Forschungszentrum Karlsruhe
in der Helmholtz-Gemeinschaft

Wissenschaftliche Berichte

FZKA 7452

Molecular Geochemistry in Hydrogeology: a Pathway to Reactive Transport Process Understanding in Natural Systems

T. Schäfer

Institut für Nukleare Entsorgung

März 2009

Forschungszentrum Karlsruhe
in der Helmholtz-Gemeinschaft

Wissenschaftliche Berichte
FZKA 7452

Molecular Geochemistry in Hydrogeology: A pathway to reactive transport process understanding in natural systems

Thorsten Schäfer
Institut für Nukleare Entsorgung

Von der Freien Universität Berlin (Germany),
Department of Earth Sciences,
genehmigte Habilitation

Forschungszentrum Karlsruhe GmbH, Karlsruhe
2009

Forschungszentrum Karlsruhe GmbH
Postfach 3640, 76021 Karlsruhe

Mitglied der Hermann von Helmholtz-Gemeinschaft
Deutscher Forschungszentren (HGF)

ISSN 0947-8620

urn:nbn:de:0005-074522

Molecular Geochemistry in Hydrogeology: A pathway to reactive transport process understanding in natural systems

Habilitation

submitted by

Thorsten Schäfer

2007

Department of Earth Sciences

Freie Universität Berlin (Germany)

Dedicated with deep love to my wife Nicole,
my little boys Finn Thorben & Peer Niklas
and daddy's little princess Jonna Marie

Phantasie ist wichtiger als Wissen, denn Wissen ist begrenzt.

(Albert Einstein)

Voraussagen sind sehr schwierig, speziell über die Zukunft.

(Nils Bohr)

Acknowledgement

I am deeply indebted to Prof. Asaf Pekdeger for giving me the opportunity to teach frequently and write together this habilitation at the Freie Universität Berlin and for supporting me all these years. I am grateful for the freedom that Prof. Jae Il Kim and Prof. Thomas Fanghänel allowed me in exploring the vast research resources available at the Institute for Nuclear Waste Disposal (INE), Forschungszentrum Karlsruhe and giving me the chance to take time for my private scientific interests. Dr. Horst Geckeis has been a source of enthusiasm and support for my research, and his untiring push and criticism were determining factors in shaping this work “Thanks Horst for all the discussion that I really enjoy!” An encompassing thank you to all colleagues & friends who have contributed in making the Institute for Nuclear Waste Disposal (INE) such an enjoyable and productive environment to work in, especially Robert Artinger, Andreas Bauer, Gunnar Buckau, Kathy Dardenne, Markus Fuss, Thomas Rabung, Wolfram Schüssler & Clemens Walther and all the members of the “8:30h coffee round”.

I feel extremely privileged that I had the opportunity to join the research group of Prof. Chris Jacobsen and Prof. Janos Kirz at Stony Brook/Brookhaven National Laboratory as well as being involved in such an exciting –*state of the art*- research method. I am deeply indebted to Sue Wirick, Michael Feser, Tobias Beetz and Mirna Lerotic for all of their guidance and scientific and political discussions at the NSLS. The stay on Long Island as a Postdoctoral Research Fellow has been wonderful. The “Schäfers” owe this to many people (especially to Meghan, Juana, the Wiricks family, the Jacobsen family, the Kirz family) who, in their own way, have helped me to work successfully and have made this stay rewarding and unforgettable for us. Sue, I hope the driveway is free for our next RV visit ☺.

Although quiet far away, the loving support of my parents in law Usch & Peter and my grandparents, Hilde, Gerda and Erich, could not have been felt closer.

I would like to thank my friends, my family, Minni, Udo, Marcel, Andreas, Rainer, Stefan & Uwe for all their friendship and encouragement.

Finally, I thank my wife Nicole, my two little boys Finn Thorben and Peer Niklas and our little princess Jonna Marie for riding with me on the inevitable rollercoaster of euphoria and depression that is inherent in writing any kind of manuscript.

Zusammenfassung

Molekulare Geochemie in der Hydrogeologie: Ein Weg zum Prozessverständnis des reaktiven Transports in natürlichen Systemen

Die sichere Prognose des Ausbreitungspfads von Radionukliden über historische (100 - 1000a) bis zu geologischen Zeiträumen (100.000a bis 1Ma) aus einem zu planenden geologischen Tiefenlager auf Basis des Multi-Barrierenkonzepts bedarf eines hohen Prozessverständnisses über den Ablauf möglichen Reaktionen und deren Auswirkungen auf die Rückhaltekapazität der Barrieren. Zum Verständnis makroskopische Beobachtungen aus Batch-, Säulen- und Feldversuchen und deren Übertragbarkeit müssen die Reaktionsprozesse auf molekularer Ebene verstanden werden. Die vorliegende Arbeit zeigt in einer Reihe von Manuskripten einen multidisziplinären Ansatz unter Kombination von nanoskopischen Methoden der Spektroskopie und der Mikroskopie in Kombination mit makroskopischen Methoden Wege auf, die zu einem besseren Prozessverständnis führen. Im Detail werden drei Schwerpunktthemen behandelt:

- Die Problematik des Kolloid-assoziierten Transports von Radionukliden wird in Säulen- und Feldversuchen unter besonderer Berücksichtigung der Reaktionskinetiken behandelt. Dabei zeigt sich in im Bereich des Huminstoff-getragenen Radionuklid- (RN) Transports, dass der überwiegende Anteil der RN reversible gebunden ist, jedoch die Dissoziationsraten einer kleinen Sub-Fraktion sehr niedrig sein können (< $10^{-8}s^{-1}$). Bei Tonmineral-Kolloiden konnte kein Einbau von RN in die Kristallstruktur und eine Bindung über „inner-sphere“ Komplexe unter Verlust von Teilen der RN-Hydrathülle festgestellt werden.

- Bei der Bildung von Sekundärphasen als Folge der Behälter-Korrosion und speziell der Transformation Ferrihydrit - Hämatit konnte ein RN- Einbau in eine deformierte Hämatit- Gitterstruktur spektroskopisch festgestellt werden, welche die beobachteten hohen Wiedererhalte in Migrationsversuchen erklärt. Die mittels Weichröntgenmikroskopie beobachtete Zonierung dieser Mischkristallphasen mit weiterer Temperierung weißt jedoch auf eine thermodynamische Instabilität hin.

- Natürlich vorhandene Ton/Organik- Assoziation in den potentiellen Wirtsgesteins-Formationen Opalinuston des Jura (Schweiz) und Callovo-Oxfordian Argillite (Frankreich) passiviert die reaktiven Oberflächen der Tonminerale und führt zu einer Stabilisierung unter hoch-alkalinen Bedingungen (pH >12) typisch für die initiale Zementkorrosion. Unter diesen alkalinen Bedingungen mobilisierte humin- und fulvinsäureartige Moleküle/Kolloide zeigen typische dreiwertige Actiniden (Cm^{3+})- Komplexierungskonstanten und können bei Mobilität ein RN- Transportpfad darstellen.

Abstract

The reliable long-term prediction over historical (100-1000a) up to geological time scales (100,000a to 1Ma) of radionuclide migration pathways out of a potential deep geological repository based on the multi-barrier concept relies on a detailed process understanding of possible reactions and their effects on the retention capacity of the several barriers. In order to transfer macroscopic observations from batch-, column- and field- studies in time and space the reaction processes on a molecular level must be understood. The manuscript at hand shows in a couple of studies a multidisciplinary pathway under combination of nano-scale spectro-microscopic techniques and macroscopic methods to elucidate reaction processes. The main emphasis of this manuscript is on three topics discussed in detail:

- The problem of colloid-borne radionuclide (RN) migration is tackled in column- and field migration studies taking especially into account RN sorption/desorption kinetics. Humic colloid associated RN transport studies revealed a predominant reversible RN bonding. However, the dissociation rates of a small sub fraction can be very small (< $10^{-8}s^{-1}$) and might be linked to structural heterogeneities observed with synchrotron-based spectro-microscopic techniques (STXM). RN sorption on clay mineral colloids is observed via inner-sphere complexation under the partly loss of the RN hydration sphere and no incorporation in the crystal lattice could be detected.
- Steel canister corrosion induces the formation of a series of ferric and ferrous iron secondary phases. Detailed spectroscopic studies on the ferrihydrite to hematite transformation showed the trivalent RN incorporation in a deformed hematite lattice. This RN binding environment changes can explain the observed high recoveries of hematite colloid associated trivalent RN's in column migration studies. Soft X-Ray microscopy studies on continuous tempered samples revealed a zoning of this solid solution system indicating a thermodynamic instability.
- Natural organics associated with clay minerals in geological formations under discussion as potential nuclear waste repository host rocks (Opalinus Clay, Switzerland; Callovo-Oxfordian Argillite, France) passivate the clay reactive surface sites and stabilize these minerals in hyper-alkaline solutions (pH >12) typical for the initial cement corrosion. Under these hyper-alkaline conditions mobilized humic- and fulvic acid like organic colloids show typical trivalent RN (Cm^{3+}) complexation constants and could, if mobile in the formation, be a potential RN transport pathway.

Content

1. Introduction

1.1 Multi-barrier concept of Nuclear Waste Storage

The long timescales over which waste from nuclear power plants remains radioactive (some hundred thousand years, see Fig. 1 & 2) led to the conception of deep geological disposal in underground repositories in stable geological formations. The principle is based on the concept that deep rock environments are largely unaffected by environmental changes for very long (geological) time periods –up to millions of years- times that span historical timescales; e.g. are longer than those since the appearance of modern humans in Africa.
Over the first 1,000 years after emplacement the fission products dominate the radio-toxicity, followed by the Americium and thereafter the major contributors to the waste radio-toxicity are the actinides ^{239}Pu, ^{240}Pu, ^{237}Np, ^{243}Am and the fission product ^{99}Tc (Toulhoat, 2002).

$$^{245}Cm \xrightarrow{8.5\cdot10^{3}a} {}^{241}Pu \xrightarrow{14.35a} {}^{241}Am \xrightarrow{4.322\cdot10^{2}a} {}^{237}Np \xrightarrow{2.14\cdot10^{6}a} {}^{233}Pa$$

$$^{241}Pu \xrightarrow{14.35a} {}^{237}U \xrightarrow{6.75d}$$

$$^{243}Am \xrightarrow{7365a} {}^{239}Np \xrightarrow{2.35d} {}^{239}Pu \xrightarrow{2.411\cdot10^{4}a} {}^{235}U \xrightarrow{7.037\cdot10^{8}a} {}^{231}Th$$

$$^{240}Pu \xrightarrow{6563a} {}^{236}U \xrightarrow{2.342\cdot10^{7}a} {}^{232}Th$$

$$^{234}U \xrightarrow{2.14\cdot10^{5}a} {}^{230}Th \xrightarrow{7.538\cdot10^{4}a} {}^{226}Ra$$

Figure 1: *Decay chains of important radionuclides remaining in a significant level of activity in spent fuel after 10,000 years*

Beside this deep geological disposal another strategy called *"partitioning and transmutation"* (P & T) focus on the reduction of waste volumes, radio-toxicity and to shorten the very long times for which the waste must be stored safely (Magill et al., 2003). The basically idea behind the *"partitioning"* step is to separate long-lived radioisotopes, namely plutonium and the so-called minor actinides (LLMA) neptunium, americium and curium from the spent nuclear fuel (Geist et al., 2002; Weigl et al., 2003). In the second *"transmutation"* step the concept foresees to transmute LLMA and plutonium via neutron capture and neutron induced nuclear fission to short-lived and eventually stable nuclides (Ahn et al., 2002). As shown in the decay chains of Fig.1 especially ^{237}Np, but also ^{241}Am and ^{241}Pu must be fissioned effectively by a transmuter to reduce significantly the radioactive mass. Assuming a P & T efficiency of

99.9% the remaining waste would reach the radio-toxicity level of natural uranium within the relatively short period of approx. 800 years (NEA, 1999) or approx. 330 years (Geist et al., 2004) compared to > 10^6 a in the direct spent fuel storage scenario (Fig. 2). The P & T step would therefore shorten the time span of secure isolation of radioactive waste from a geological timescale to a historical timescale.

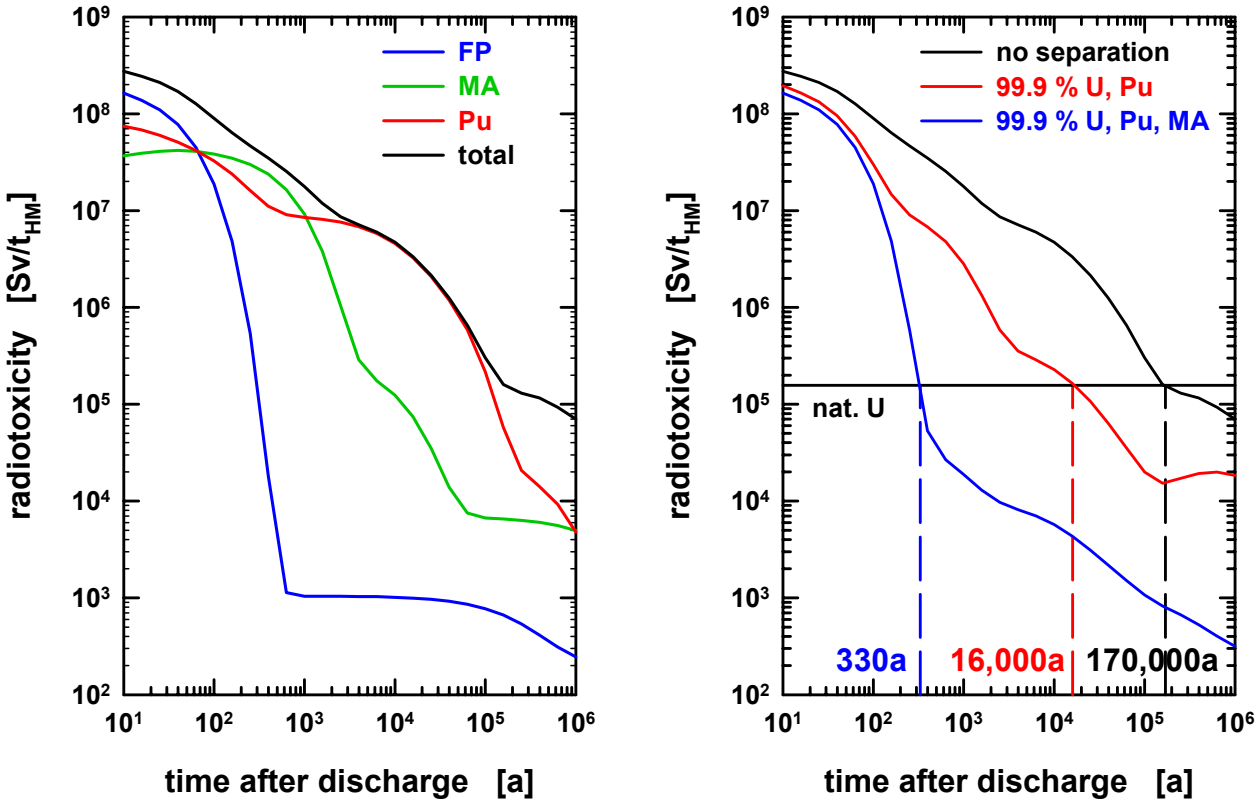

Figure 2: *(left) Time dependent radio-toxicity evolution of one ton spent fuel after 40GWd burn-up in a light water reactor, starting after one year decay time. (right) Time dependent Radio-toxicity change without separation, 99.9% Uranium and Plutonium separation or 99.9% U, Pu, and minor actinides (MA) separation. The intersection points with the horizontal line mark the time when the radio-toxicity of one ton natural uranium is reached (image modified after (Geist et al., 2004)*

The cardinal requirements of a geological disposal, as stated by the Nuclear Energy Agency (NEA) Radioactive Waste Management Committee in 1995 (NEA, 2003a) is that this deep geological formation provides a system to:

- *"isolate the wastes from the biosphere for extremely long periods of time"*
- *"ensure that residual radioactive substances reaching the biosphere will be at concentrations that are insignificant compared, for example, with the natural background levels of radioactivity"* and
- *"provide reasonable assurance that any risk from inadvertent human intrusion would be very small"*.

The International Atomic Energy Agency (IAEA) defines the term disposal as*: "The emplacement of waste in an approved, specified facility (e.g. near surface or geological repository) without the intention of retrieval."* The primary distinction between "disposal" and "storage" is the phrase *"without the intention of retrieval"*. If waste retrieval is intended, then the term "long-term storage", or even "permanent storage" is used.

Deep underground conditions in general favor the immobilization of most radionuclides by sorption due to high distribution coefficients (K_D-concept), precipitation or very low solubility. What does *"deep"* in this context mean? Based on the standard mining or civil engineering technology excavation of a deep underground repository is limited to (a) accessible locations (e.g. under land or nearshore), (b) to rock units that are reasonably stable and without major groundwater flow, and (c) to depths of between 250m and 1000m. At a depth greater than ~1000m, excavations become increasingly technically difficult and correspondingly expensive.

Waste isolation is provided by a combination of engineered and natural barriers (rock, salt, clay). This is often termed multi-barrier concept with the waste packaging, the engineered repository and the geology all providing barriers to prevent the radionuclides from reaching humans and the environment. In general, most geological disposal concepts are composed of the waste matrix, the container or the overpack, the buffer/backfill, some country dependent additions and the natural geological barrier of the host rock. The so called *"engineered barrier system"* (EBS) represents thereby the man-made, engineered materials including the waste form, waste canisters, buffer materials, backfill and seals. By definition the "near-field" consists of the EBS and those parts of the host rock, that are affected by the presence of the repository, whereas the "far-field" represents the geo- or biosphere of the undisturbed host rock. In the following the different components of the multi-barrier system are discussed in detail and the disposal programs of selected countries are compared based on the information given in (Karlsruhe, 2001; NEA, 2003a; SKB, 1996; Toulhoat, 2002). It should be mentioned here, that in the German Morsleben program and in the US/WIPP[1] program the waste matrix and the container/overpack are not considered as part of the EBS. Furthermore, there is generally a quite good consistency in EBS designs for high-level waste (HLW) and spent fuel (SF), but less for intermediate-level waste (ILW). The greater variation in the ILW disposal systems reflects the greater number of ILW waste streams and the wide range of disposal sites and host rocks considered.

Based on the in most countries favored multi-barrier concept, explained in detail in the following, degraded evolution scenarios such as oxygen intrusion, faults, colloid transport etc. must be taken into account (Toulhoat, 2002). These degraded evolution scenarios are a major concern in long-term repository retention capacity estimations and therefore the main focus

[1] United States Waste Isolation Pilot Plant (WIPP) for the disposal of transuranic waste (TRU) in salt host rock

of the papers presented in this work deal with certain aspects of barrier stability and possible radionuclide migration pathways.

1.1.1 Waste Matrix and container/overpack

The waste matrix depends greatly on the waste type, namely spent fuel (SF[2]), high level waste (HLW[3]), intermediate level waste (ILW[4]), transuranic waste (TRU) and low level waste (LLW). For HLW in several countries (Belgium, Czech Republic, France, Japan, Switzerland[5], and the US/YMP[6]) borosilicate glass or glass is planned. For spent fuel the waste matrix will be in most cases UO_2 or mixed oxides (MOX) except the US/YMP commercial and defense SF, which consists of 250 types including fuel rods, Zircalloy or stainless steel cladding, ceramic-plutonium and Pu/U alloy. ILW will have a wide variety of waste matrixes including concrete, cement or polymer grout (NEA, 2003a).

Concerning the container material one can generally distinguish between two concepts, the so called “corrosion allowance” and the “corrosion resistance” concept. In the “corrosion allowance” concept little weight is placed on the container as a barrier and relatively short-lived metals as iron and steel are used, whereas in the “corrosion resistance” concept very resistant metals such as copper and titanium are utilized. The container or overpack material will be mainly of carbon steel (Korea, Japan, Spain), modified stainless steel, e.g. with steel overpack for HLW or metal inserts for SF in the French concept or noble metal covered stainless steel (Ni-based alloy outer container in the US/YMP commercial SF concept). Deviating from that is the Swedish KBS-3 program, which foresees the use of 5 cm thick corrosion resistant copper canisters with a cast iron insert giving mechanical strength (SKB, 1996) and the French ILW program which considers also concrete containers.

The function of this waste matrix, when considered as part of the EBS, is to ensure a low release rate of radionuclides for 150,000 years[7] (Switzerland) or 100,000 years in all scenarios (France). The time span of expected radionuclide isolation by the container/overpack if considered as part of the EBS varies widely from ~1,000 years (Czech Republic, Japan, Korea, Spain, Switzerland) to >10,000 years in undisturbed scenarios of the US/YMP program to ~1,000,000 years in all scenarios of the Swedish KBS-3 program. The shown differences in the waste matrix and container/overpack functions demonstrate the different EBS designs reflecting in a way the favored host rock formations with for example a dominant role of the long-lived waste containers in isolating the waste in the Swedish KBS-3 concept.

[2] The United States differentiate between commercial spent fuel and defense spent fuel
[3] named Type C waste in France
[4] named Type B waste in France
[5] Kristallin-I concept for the disposal of HLW in crystalline host rock will be discussed within this comparison
[6] United States Yucca Mountain Program
[7] except the direct human intrusion scenario

1.1.2 Buffer/Backfill

The geo-engineered barrier is mainly designed to long-term protect (up to ~1,000,000 years in the Swedish KBS-3 concept) the waste packages from water intrusion (e.g. minimize overpack corrosion), to stabilize geo-mechanically the environment of the waste packages, to efficiently transfer the heat away from the waste, and to retard sorbing radionuclides, filter colloids or at least to assure a diffusion dominated reactive transport in the near-field. The Finish concept furthermore differentiated between the buffer function, which should decouple the canister from the flow and transport system of the surrounding rock and the backfill, which should mechanically stabilize the tunnel system and seal the disposal tunnels and access routes to prevent that this man-made constructions become major groundwater and transport pathways. The US/YMP program does not include a buffer/backfill and in the US/WIPP program the MgO buffer/backfill is expected to remove furthermore carbon dioxide. The majority of countries will use a bentonite (Sweden, Switzerland) or bentonite-sand mixture (Korea, Japan) as buffer/backfill except Germany/Morsleben (salt concrete) and United Kingdom/Nirex (cement-based vault backfill). In clay host rocks (Belgium, Netherlands, France, Switzerland/Opalinus) the waste could also be backfilled with excavated clay.
The main functions of EBS components can be summarized as follows (NEA, 2003a):

- The waste matrix is designed to provide a stable waste form that is resistant to leaching and gives slow rates of radionuclide release for the long term.
- The container/overpack is designed to facilitate waste handling, emplacement and retrievability, and to provide containment for up to 1 000 years or longer depending on the waste type.
- The buffer/backfill is designed to stabilize the repository excavations and the thermo-hydro-mechanical-chemical conditions, and to provide low permeability's and/or diffusivities, and/or long-term retardation.

1.1.3 Geological host rock formation

The presentation of favored geological host rock formation for the nuclear waste disposal will be based on the current disposal program status of the different European countries and combined in groups based on the favorite formation, namely clay, granite, salt. Volcanic tuff (i..e. Yucca Mountain) will be excluded from the discussion, as suitable tuff formations are not available throughout Europe.

Clay:

The countries i.a. Belgium, France, Netherlands and Switzerland favor currently the disposal of SF and vitrified HLW in clay. The Belgian disposal concept proposes that spent fuel and

HLW containers will be emplaced in excavated tunnels within the ductile, low permeable (average ~ 10^{-12} $m \cdot s^{-1}$) Boom clay (Cenozoic multi-layered system of the Campine Basin). Similar systems have been proposed in the Netherlands and, using less plastic clays (claystones), in France and Switzerland (details below).

The Belgium research and development (R&D) program has completed the second phase (NEA, 2003c) and after a third phase planned from 2010-2015 and a five year transition period this could lead to a project beginning around the year 2017 for the selection of a disposal site (NEA, 2003a). In France, ANDRA (Agence national pour la gestion des déchets radioactifs), in the framework of the mission entrusted by the Law of 30 December 1991, issued in 2001 the "Dossier Argile" (Andra, 2001) , which summarizes the current research status on deep geological reversible disposal of long-lived ILW and HLW in clay formations (NEA, 2003b). This report concludes that disposal of radioactive waste in clay layers, studied at the underground research laboratory in Bure (Meuse/Haute-Marne site) appears to be technically feasible and served as a test for the methology used in preparing the 2005 feasibility and complete safety assessment report. On the 30th of June 2005 Andra presented the report "Dossier Argile 2005" on the feasibility of a repository for high-level and long-lived radioactive waste in a deep geological formation (Andra, 2005). The report, representing the sum of the last 15 years of investigations, includes two parts:

- An feasibility-assessment report on clay formations, based notably on the work conducted on the site of the Meuse/Haute-Marne Underground Laboratory and in foreign laboratories;
- A report concerning the advantages of granite rocks based on the available bibliography on French granites and on the investigations carried out by Andra under research partnerships with foreign laboratories

The specific clay site (Callovo-Oxfordian argillite) in the Meuse-Haute/Marne region had been chosen in 1998, and access shaft construction for the underground laboratory (URL) began in 2000. The French R&D work in granite is currently not focused on specific host rock formations due to the ultimate rejection of preliminary site choices (NEA, 2003a). ISRN (Institut de Radioprotection et de sûreté Nucléaire) has evaluated the "Dossier Argile 2005" and states clearly, that if a fundamental decision has to be taken by the parliament in 2006, ISRN would have no obstacles against the geological formation chosen by Andra (ISRN, 2006). However, numerous points will have to be studied in greater depth in order to draw up a future safety dossier with a view to setting up a disposal facility. For example, the design of the disposal installations will have to be validated so as to show that the measures taken to confine the radioactive waste are efficient.

The Swiss HLW and SF program currently focus on the disposal in Jurassic Shale (Opalinus clay) of the Zürcher Weinland in northern Switzerland and a series of detailed reports on the

Opalinus clay option have recently been published (Berner, 2003; Nagra, 2002a; Nagra, 2002b; Nagra, 2003a; Nagra, 2003b). The comprehensive description of the post-clossure radiological safety assessment presented in these reports is part of the technical basis for the "demonstration of disposal feasibility" ("*Entsorgungsnachweis*"). One of the main objectives of this *Entsorgungsnachweis* is to demonstrate that the Opalinus Clay of the Zürcher Weinland is (a) a suitable geological environment for the repository (siting feasibility), (b) the construction and operation of a repository is practicable in such an environment (engineering feasibility) and (c) the long-term safety from the hazards presented by the wastes is assured for such a repository (safety feasibility) (Nagra, 2003a). A NEA organized international peer review by an international review team (IRT) has been carried out of a post-closure radiological safety assessment prepared by Nagra for geological disposal of SF, HLW and ILW within the Opalinus Clay of the Zürcher Weinland in northern Switzerland (NEA, 2004). The IRT concludes that, for the purposes of the current assessment the safety functions of the different barriers in the multi-barrier system have been clearly described and analyzed and given its properties, the Opalinus Clay of the Zürcher Weinland assumes a major role in contributing to safety, but other components of the multi-barrier system also contribute to, and support, the overall safety case.

However, the Swiss disposal program considers deep geological disposal in both crystalline (Kristallin-I project) (Nagra, 1994a; Nagra, 1994b; Neall et al., 1994; Smith and Curti, 1995) and clay host rocks with similar EBS designs. URL's have been developed in crystalline granite host rock at Grimsel (Smith et al., 2001) and in compacted clays at Mont Terri (Thury and Bossart, 1999). The possibilities for the disposal of SF, HLW and ILW in Switzerland are summarized together with the current state of general academic and applied geoscientific research as well as the project specific knowledge base in (Nagra, 2005). These assessments of (Nagra, 2005) lead to the results, that the required long-term stability and the relative simplicity of structure can be found in the geologic-tectonic region of the Molasse Basin and the north-eastern Tabular Jura with different host rocks and areas in this region in principle suitable to ensure the safety of a deep geological repository for SF/HLW/ILW, if the engineered barriers are adapted to the geological conditions. Between these potential host rocks the Opalinus Clay has advantages from the geological point of view over other host rocks (crystalline basement, claystones of the Lower Freshwater Molasse) and the Opalinus Clay can be found in other areas besides the Zürcher Weinland which might, in principle, be appropriate for siting a SF/HLW/ILW repository (Nördlich Lägeren, Bözberg and Jurasüdfuss*)*.

Granite

The term "crystalline host rock formation" is used for a wide variety of rocks mainly consisting of the mineral phases feldspar, quartz and silicates (mica, amphiboles and pyroxens) being

saturated and sparsely fractured. This category includes plutonic granite, basement with sedimentary cover and shield rocks (e.g. Fennoscandinavian). In the countries Finland, Sweden and Switzerland siting for a suitable geological repository environment (siting feasibility) for the three above-mentioned formations were performed and safety cases carried out (BfS, 2002). The crystalline rock formations are characterized by the following functions (SKB, 2005):

- Mechanically stable environment for constructing and operating the facility safely in depths of 500m and below.
- Potentially long and slow groundwater return pathways from the facility to the biosphere along which retention, dilution and dispersion processes operate to reduce radionuclide concentration in the groundwater.
- Long-term physical protection to the Engineered Barrier System (EBS) against the effects of surface dominated events including natural disruptive processes such as deep weathering, glaciation, river and marine erosion or flooding, asteroid or comet impact, earthquake shaking etc, and human activities such as terrorism and war,
- A geochemically stable, and benign environment to maximize the longevity of the engineered barriers such as containers, buffer and backfill in the facility,
- A natural radiation shield around the wastes, and
- A reduced likelihood of human intrusion deep into the repository, due to vandalism, excavation, drilling, quarrying and mining.

The safety concepts „Kristallin“ for the disposal or storage of SF and HLW in crystalline or fractured sedimentary rocks relies on the technical barriers and to a lesser extend on the geological barrier. The technical barriers consisting of well-defined materials with predictable RN retention capacity have the main safety function and it is expected that most RN are decayed within these technical barriers to uncritical concentrations. For example, the Swedish SR 97 assessment, conducted as a basis for the start of site investigations in Sweden in 2002 is based on data from three real sites, but it is emphasized that these are selected just to exemplify conditions in various places in Sweden. The canisters are expected to retain their containment function throughout the whole assessment period of 1 million years. Containment is therefore the main safety function with other functions having a complementary role for a small number of canisters that may be initially defective. The role of the host rock (geosphere) was nevertheless proven to be important, since the consequences of the few defective canisters vary significantly among the different sites. A sensitivity analysis shows that the “transport resistance” of the geosphere migration paths has a large impact on calculated dose (or risk) for the site with the poorest geosphere performance. The

lated dose (or risk) for the site with the poorest geosphere performance. The diffusivity of the rock matrix is somewhat sensitive, while the K_D values in the rock matrix are in general of limited sensitivity. The sensitivity of these geosphere parameters is less important for the two sites with medium and good geosphere barrier performance (i.e. sites with high transport resistance of the migration paths) (EC, 2005).

In the Finnish TILA-99 assessment carried out for four investigation sites (Hästholmen, Kivetty, Olkiluoto and Romuvaara) considered as potential alternatives for the location of a spent fuel repository (Vieno and Nordman, 1999), similar to the SR 97 safety concept, an estimated duration of the complete containment by the copper-iron canisters exceeds 100 000 years. In the geosphere-transport analyses of radionuclides, matrix diffusion was the only phenomenon assumed to cause retention and dispersion. According to the results, geosphere is an efficient barrier for the strongly and moderately sorbing nuclides ($K_D \geq 0.1$ m^3/kg), while it appears to be ineffective for weakly or non-sorbing nuclides (^{129}I, ^{36}Cl, ^{14}C, ^{135}Cs). It was concluded that from the point of view of post closure safety (safety assessment and release and transport analyses of radionuclides) all four candidate sites are suitable to host a repository for spent fuel. Olkiluoto was proposed as the location of the repository, approved by the Government in December 2000 and confirmed by the Parliament in May 2001.

Rock salt

Rock salt formation safety concepts rely in the undisturbed evolution scenario, assuming sufficient formation thickness, on the complete isolation of the emplaced waste in the host rock formation. The fundamental properties of rock salts making it most suitable as host rock formation are the impermeability and the plasticity. The open cavities between barriers will be rapidly sealed after waste emplacement by rock salt creeping and the phenomena of barrier by-pass will only temporarily be relevant. For a beneficial rock salt creeping behavior the composition, their rock salt homogeneity and a sufficient depth is important to assure a rock load and temperature driven high creeping velocity. The missing permeability of the compacted rock salt and the absence of water conducting features will give basically no possibility of RN release (Kim and Grambow, 1999). The undisturbed evolution scenario can be achieved with a high probability through the repository design and the excavation techniques used. For the disturbed scenario in a rock salt nuclear waste repository, meaning the release of RN, it has to be assumed that the safety barrier rock salt has failed. Additionally, the overlaying geological units are taken into account to be geological barriers. In the case of the Gorleben salt dome large parts are covered by cap rock except the deep erosion of the fluvio-glacial channel, the Gorleben channel, where in some locations the channel is in direct contact with the salt dome.

In the United States defense derived transuranic waste (similar to long-lived ILW) is disposed in layered salt strata, namely the Waste Isolation Pilot Plant (WIPP) operational since 1999. For this repository natural rock salt is excavated from a several metres thick layer, sandwiched between other types of rock, 650 metres below ground level. The wastes placed in these excavations contain large volumes of long-lived ILW, usually in steel containers. The steel containers are then placed in concrete overpacks. Containment of the radionuclides in the waste form mostly relies on the almost complete absence of water flow in the salt.

1.2 Why nanoscience in hydrogeology?

Nanoscience spans the size range from clusters of atoms in solution at the small end to colloidal particles at the large end and in natural environments these nano-sized solids are generally heavily hydrated. The key questions that one has to ask in the field of geochemistry and hydrogeology is:

"How can the research field really benefit from results obtained under nano-scale (1-100nm) resolution?"

Looking back in history the surprising properties of materials as e.g. antiferromagnetic coupled (AFC) media or high density xerogel-based sensors are dependent upon their physical dimension of at least on phase (Hochella, 2002a; Hochella, 2003). This dimensional limitation (typically ~1nm) causes properties that we are not familiar with in the macro-scale or in a thermodynamic perspective; a material becomes "nano" when the thermodynamic parameters differ significantly from those of the bulk. The exact size at which this happens depends both on the system and the property being considered. Nanomaterials are thermodynamically metastable with respect to bulk macrocrystalline materials, but due to slow kinetics of grain coarsening and the influence of biological processes in low-temperature earth environments (e.g. weathering and surface and groundwater systems) nano-sized materials seems to be ubiquitous (Hochella, 2002b).

Two early examples dealing with nanoscale processes, although the terminology nanoscience was not invented and vogue during that time, should be mentioned which are discussed in detail in (Banfield and Navrotsky, 2001; Hochella, 2002b). (Stöber and Arnold, 1961) could show an exponential dependency of quartz solubility with decreasing quartz mineral dimension compared to measured solubility of very large quartz grains, which could be described in a modified form of the Kelvin equation. The same phenomenon is responsible for the increased solubility of sharp features on mineral surfaces.

Typical surface energies (enthalpies) are in the order of 0.1 to 3 J/m^2 and an important point in this context is, that the enthalpy (ΔH) and free energy (ΔG) terms are small enough that the order of thermodynamic stability can be inverted by a number of factors (see Fig. 3). For nanoparticles with surface areas exceeding 100 m^2/g, the enthalpy would be raised by 2 to 60 kJ/mol affecting significantly the thermodynamic properties and resulting in a crossover in energetic stability of polymorphs, as demonstrated for alumina, titania, and zirconia (McHale et al., 1997; Navrotsky, 2004; Ranade et al., 2002). The slope of the relation between enthalpy and surface area (Fig. 2) gives the surface enthalpy and a steeper line implies a higher surface enthalpy. The observed correlation between increasing meta-stability and decreasing surface energy may represent a rather general behavior. The crossover of stability

of different polymorphs has important impacts on solubility-limiting solids in aqueous solution, i.e., on equilibrium constants for hazardous metals in aquatic environments and is very important for the long-term mobility prediction of contaminants (Fanghanel and Neck, 2002; Neck et al., 2003; Neck et al., 2002).

One way to benefit from nanotechnology is to design semiconductor nanoparticles as catalysts and/or sensing systems and optimize waste water/air treatment systems or tune environmental remediation strategies by controlling the size of the initial crystal and precipitate the desired polymorph (Kamat and Meisel, 2003). The most important benefit environmental science and especially hydrogeology can gain from the vast improvements found in synchrotron or laser based spectromicroscopic methods is to understand in detail the reaction mechanisms and -kinetics of metal/contaminant uptake and therefore reliable predict migration behavior of contaminants (SLAC, 2004). Here, the definition of nanoscience is not necessarily the change of properties going down in dimension; it is the fundamental understanding of macro-scale observations by elucidating the nanoscale mineral/water interface processes.

A classical example is the discussion about bio-availability and speciation of heavy metals using sequential extraction schemes (Heron et al., 1994; Tessier et al., 1979; Trolard et al., 1995). The disadvantage of these extraction procedures for heterogeneous mineral systems as soils and sediments is, that each extraction step is far from mineral selective and extracting agent as e.g. Na-dithionite/bicarbonate dissolves beside iron oxides also other mineral phases, i.e. clays (Haese et al., 1997). The combination of µ-focused synchrotron based techniques as X-ray fluorescence, absorption, and diffraction have given new insides in binding environments and metal oxidation states (Catalano and Brown, 2005; Manceau et al., 2005), which can lead to an optimization of remediation strategies or an assessment of the prospects of remediation success (Catalano et al., 2004; Howe et al., 2003; Scheckel and Ryan, 2004). An example of the practical use of such a multi-method approach is the uranium soil contamination of the United States Department of Energy's (DOE) former processing facility (Fernald, Ohio), where by a combination of X-Ray absorption, optical luminescence and vibrational spectroscopy the uranium oxidation state and the primary uranium host phases (hydroxides and phosphates) were identified and lead to an “intelligent” remediation strategy (Morris et al., 1996).

Although the three aspects discussed within this work cannot be separated strictly, for the convenience of the reader a splitting in three chapters, namely the

(a) Colloid transport in the far-field of potential nuclear waste repository geological formations,

(b) Influence of ferric iron phases as scavenger of radionuclides and

(c) The influence of natural organic matter on mineral dissolution reactivity is performed.

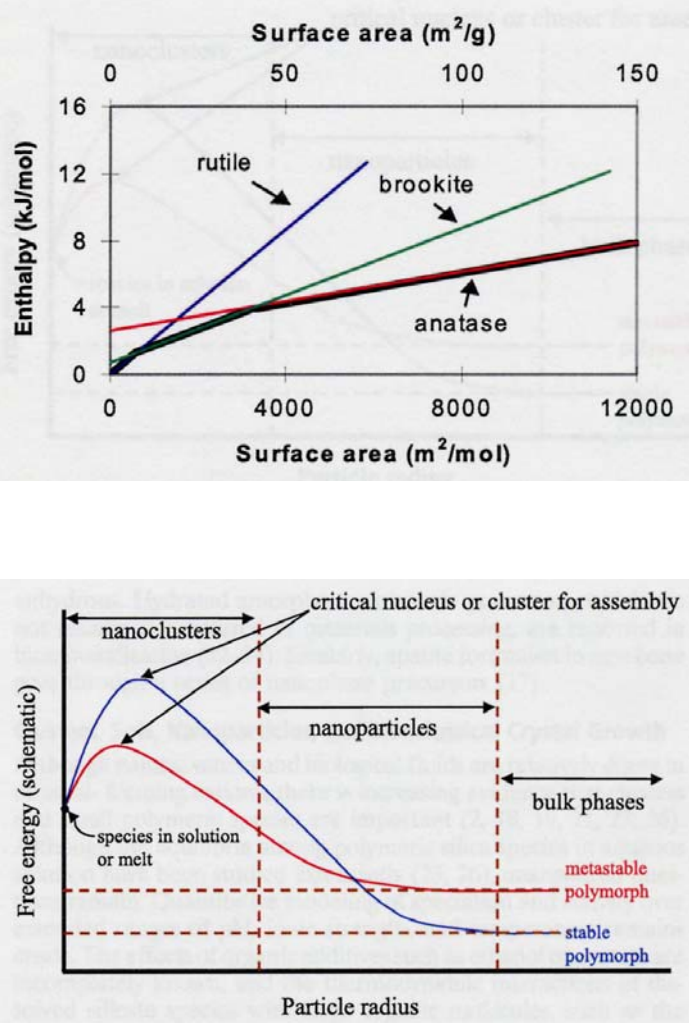

Figure 3: *(top) Enthalpy of titania polymorphs as a function of surface area. (bottom) Schematic representation of energetics of two different polymorphs as a function of particle radius. Differences in critical nucleus size and activation energy and crossover in phase stability of nanoparticles are shown. (Navrotsky, 2004)*

2.0 Colloid transport in the far-field of potential nuclear waste repository sites

Colloids (nowadays often called “nanoparticles”) can be defined as nanoscopic solids of organic or inorganic nature in the size range from ~1 nm to ~1 µm (upper size limit depending on their density) that remain suspended in water. Larger solids are usually classified as particles. Inorganic colloids are formed by alteration or physical erosion of minerals, or by direct precipitation from groundwater, and typically comprise of silica, clay minerals, calcite or Fe-oxyhydroxides. Two types of inorganic colloids are usually distinguished. The so-called intrinsic- or eigen-colloids consist essentially of polymerized complexes of a particular element (e.g. Pu(IV)-polymer, formed by condensation of hydrolysed actinide ions and consisting of actinide cations linked by anions). The carrier- or pseudo- colloids consist of mineral fragments of crystalline or amorphous solids to which a particular element/radionuclide may be attached. Organic colloids may comprise of fragments of degrading organic material, or they may be organic macromolecules (i.e. humic or fulvic acids) or microbes that are stabilized by hydrophilic coatings on their surfaces. Organic materials, especially humic and fulvic acids may form coatings on inorganic colloids, increasing their electrostatic stability.

In general, the importance of colloidal phases or nanoparticles on transport processes depends on (a) the presence of colloids, (b) the mobility and stability of these colloids and (c) the slow reversibility or “irreversibility” of metal/radionuclide interaction with these colloids (Kretzschmar and Schäfer, 2005; McCarthy and McKay, 2004; McCarthy and Zachara, 1989). Numerous publications have demonstrated, that the classical two phase flow concept of transport (stationary phase: sediment; mobile phase: ground water) has to be expanded by a third phase, namely the colloids, which are ubiquitous in aquifer systems (see (Buffle and van Leeuwen, 1993) and references therein). Neglecting the colloidal phase in groundwater systems can drastically underestimate the mobility of strong sorbing contaminants (e.g. Plutonium) (Kim, 1994). On of the most cited articles in this regard is the work of Kersting and coworkers (Kersting et al., 1999), who clearly demonstrated the mobility of Plutonium in colloidal form over 1.3 km in a 30-year period at the Nevada Test Site (NTS). Especially geochemically or hydraulically disturbed systems might generate a high concentration of colloidal phases and therefore can enhance the mobility of strong sorbing contaminants (McCarthy and Shevenell, 1998; Ryan and Gschwend, 1990; Ryan and Gschwend, 1994; Seaman et al., 1995; Swartz and Gschwend, 1998). However, colloid destabilization via aggregation can also lead to an additional retention mechanism for strong sorbing contaminants.

A recent review by (Wickham et al., 2000) considering twelve performance assessment (PA) programs for deep geological storage of high-level nuclear waste in nine countries (Belgium,

Canada, Finland, Japan, Netherlands, Sweden, Switzerland, UK, USA) showed that all programs include colloid formation in their features, events and processes (FEP) list and discuss colloids in performance assessment (PA), but not commonly model colloids in PA (SKB, 2005). PA's of repositories for SF and HLW that contain a bentonite buffer in the multi-barrier concept do not consider colloids in the source term, as they assume that colloids are filtered by the bentonite buffer (e.g. Swedish SKB's SR-95 and SR-97, Nagra's Kristallin-I). A failure of the bentonite buffer to filter colloids is not considered as an alternative scenario. PA's of waste repositories without bentonite buffer (e.g. US DOE's WIPP and Yucca Mountain) have to account for radionuclide mobilization by colloids and here the concentration of colloids formed in the repository is one of the key uncertainties.

Taking into account the multi-barrier concept (chapter 1.1) of a ILW or HLW storage site, the interface of the different barriers have to be considered as highly geochemically disturbed zones. Therefore, presence of a repository is likely to increase the concentration and range of colloids present in groundwater. This is due to the excavation carried out during repository construction, post-closure degradation of the waste form and engineered barrier system materials. Colloids formed in the near-field could be transported to the far-field by advective flow in crystalline formations, where they would add to the natural groundwater colloid population. Colloids may also be transported, albeit slowly, by diffusion.

A number of recent publications address the problem of colloid generation in different barrier compartments. This includes work on vitrified waste corrosion (Feng et al., 1994; Pirlet, 2001), steel canister corrosion (Geckeis et al., 1998; Vilks et al., 1998), cement corrosion (Fujita et al., 2003; Wieland et al., 2004), mobilization of colloids from the geo-engineered bentonite barrier (Missana et al., 2003) and site specific host rock studies (Kim et al., 1984; Kim et al., 1992). In the latter a differentiation between saturated and unsaturated flow regimes (Robinson et al., 2003) have to be taken into account. Colloid mobilization and transport in the unsaturated host rocks and from soils to the groundwater table (vadose zone) is an important research topic, which changes colloid migration mechanism (DeNovio et al., 2004; Kretzschmar and Schäfer, 2005) and has to be considered in the far-field system of the U.S. Department of Energy (DOE) Yucca Mountain (Nevada) site and the underground waste tank leakages at the Hanford Reservation (Washington State) (Chen and Flury, 2005; Chen et al., 2005; Gamerdinger and Kaplan, 2001b; Moridis et al., 2003). Understanding colloid transport in unsaturated media is complicated by the presence of dynamic air–water interfaces and the increasing discontinuity of water-filled pores with decreasing water content. Additional mechanisms of colloid retention have been suggested, such as film-straining and deposition of colloidal particles on the air–water interface (see Fig. 4). The colloids are trapped in a thin stationary film of water between the air–water interface and the water–solid interface (Wan and Tokunaga, 1997; Wan and Wilson, 1994). However, these colloidal parti-

cles may be remobilized when the water content increases and the air–water interfaces disappear due to increasing pore space saturation. In this work transport phenomena in the unsaturated zone are not discussed in detail. In general, one can state that up to now colloidal transport is not fully understood from both the experimental and modeling point of view.

Part of the problem characterizing colloidal phases is the ongoing development of high-resolution analytical methods suitable to give reliable information in the nanoscopic range.

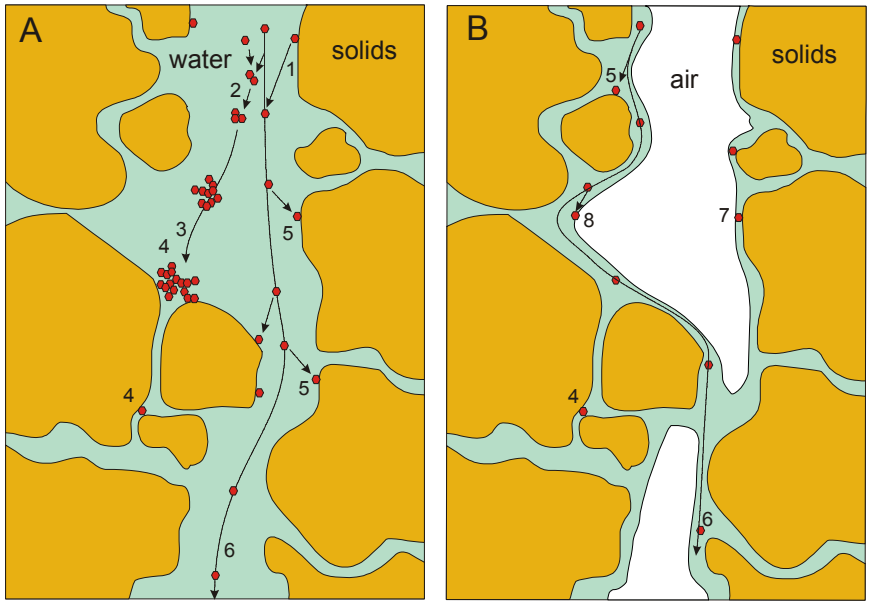

Figure 4: *(A) Processes controlling the mobility of colloidal particles in water-saturated porous media: (1) release of colloids, (2) aggregation of colloids, (3) immobilization by gravitational settling of flocks, (4) immobilization by straining of flocks or single particles, (5) immobilization by colloid deposition on solid–water interfaces, (6) transport of dispersed colloidal particles over long distances by flowing water. (B) In unsaturated porous media, additional mechanisms of colloid retardation may occur: (7) immobilization by film straining and (8) immobilization by deposition on air–water interfaces (figure taken from (Kretzschmar and Schäfer, 2005).*

Important basic information needed prior to any modeling step includes the size and/or size distribution, concentration, shape, surface charge and the chemical composition of these colloids. No analytical tool currently commercially available or under development will give all information needed for a comprehensive treatment of colloid transport using mechanistical modeling.

Colloid sizing methods include static light scattering (e.g. single particle counter; SPC (Degueldre et al., 1996)) and the frequently applied dynamic light scattering, i.e. Photon correlation spectroscopy; PCS (Duker and Ledin, 1998; Filella et al., 1997; Ledin et al., 1993; Ledin et al., 1994; Zänker et al., 2002). Light scattering methods face the disadvantage that the scattering intensity is dependent on the six power of the colloid radius (Rayleigh criteria), which make this method rather insensitive to colloids < 100nm typically predominantly found

in natural groundwater systems (Walther, 2003). Recently, a very sensitive detection method was developed, namely Laser Induced Breakdown Detection (LIBD), which is based on the formation of plasma due to a dielectrical breakdown of a colloid in a focused pulsed laser beam (Bundschuh et al., 2001; Scherbaum et al., 1996). The generated plasma is observed either by its light emission or by detection of the acoustic shock wave generated by its rapid expansion. Because each plasma event corresponds to a single colloid, the relative number of events per number of laser shots, also called breakdown probability, provides a direct measure of the colloid number concentration. This method is especially suitable to detect colloids in low concentrations (ppb range) found in natural groundwater systems and has been applied in colloid migration experiments at the Grimsel Test Site (GTS) in Switzerland (Hauser et al., 2002; Möri et al., 2003). The photon flux required for breakdown decreases with increasing colloid size. Using this dependence, even the colloid size distribution can be ascertained by varying the laser pulse energy (Walther et al. 2004). Especially the combination of this highly-sensitive sizing method with other techniques has been proven to be very efficient in characterizing natural colloids. Recent developments include the LIBD coupling with size fractionation techniques (e.g. asymmetrical flow field flow fractionation, AsymFFFF), ICP–MS to determine the size-dependent colloid composition and trace metal–colloid association and microscopically techniques as atomic force microscopy (AFM) to deduce colloid shape information (Bouby et al., 2004; Bouby et al., 2002; Geckeis et al., 2003; Plaschke et al., 2001).

Another problem is the up-scaling of colloid migration studies from small scale laboratory column experiments to the field scale important for migration phenomena in the host rock formation. Laboratory migration studies have shown that organic and inorganic colloids can be mobile under certain hydraulic and hydrochemical parameters (e.g. (Gamerdinger and Kaplan, 2001a; Grolimund et al., 1998; Kretzschmar et al., 1999; Kretzschmar and Sticher, 1997) and some studies have shown that data can be directly transferred (Higgo et al., 1993). However, field experiments are mainly performed under gradients and flow rates orders of magnitude above the natural flow conditions (Geckeis et al., 2004; Möri et al., 2003; Vilks and Bachinski, 1996; Vilks et al., 1997). Organic colloid transport under natural hydraulic conditions over large (km) distances has been detected by stable isotope composition of fulvic acids (Buckau et al., 2000a; Buckau et al., 2000b; Buckau et al., 2000c) and in combination with information derived from NMR and carbon K-edge spectromicroscopy (Scanning Transmission X-Ray Microscopy; STXM) (Schäfer et al., 2005a).

The transferability of lab-scale experiments on colloid-mediated contaminant transport to near-natural conditions is often difficult as sorption/desorption kinetics might dominate the system. Detailed lab studies under variation of the colloid-metal contact time and the column residence time of spiked groundwater have demonstrated that a small fraction of humic col-

loid associated actinides show very slow dissociation rates $<10^{-8}$ s^{-1} (Artinger et al., 2003; Artinger et al., 2002b; Schuessler et al., 2000). Kinetic controlled transport was also found for inorganic colloid (bentonite) associated actinide/lanthanide transport (Geckeis et al., 2004; Schäfer et al., 2004). Accordingly, for a reliable prediction of the long-term colloid-borne actinide migration research must focus on the mechanism of the metal colloid binding leading to an overall chemical reaction scheme for the actinide colloid interactions. Spectroscopic approaches using e.g. Time-Resolved Laser Fluorescence Spectroscopy (TRLFS) gives insights in the sorption mechanism by determining the hydration sphere of trivalent actinides. For clay minerals (kaolinite and smectite) at pH $\geq$ 5 the formation of a species equivalent to Al-O-Cm^{2+}- $(H_2O)_5$ surface complex was observed, which is replaced at higher pH by a second species either monodentate equivalent to Al-O-$Cm^{+}(OH)(H_2O)_4$ or bidentate equivalent to $(Al\text{-}O)_2\text{-}Cm^{+}(H_2O)_5$ (Bradbury and Baeyens, 2005; Geckeis et al., 2004; Stumpf et al., 2002; Stumpf et al., 2001; Stumpf and Fanghanel, 2002). No incorporation of Cm(III) into the bulk clay structure indicating an irreversibility of sorption was observed.

The given peer- reviewed publications in this chapter can be subdivided in the following topics already mentioned above:

- Colloid characterization by method coupling: (Plaschke et al., 2001)
- Laboratory studies on metal-colloid sorption kinetics (Artinger et al., 2002a; Geckeis et al., 2004; Schäfer et al., 2004)
- Field experiments on colloid-mediated radionuclide transport (Geckeis et al., 2004; Möri et al., 2003)
- Colloid transport under natural hydro-geological conditions (Schäfer et al., 2005a)

Size characterization of bentonite colloids by different methods.

Anal. Chem. (2001) **73**(17), 4338.

Plaschke M., Schäfer T., Bundschuh T., Manh T. N., Knopp R., Geckeis H., and Kim J. I.

Anal. Chem. **2001,** *73,* 4338−4347

Size Characterization of Bentonite Colloids by Different Methods

M. Plaschke,* T. Schäfer, T. Bundschuh, T. Ngo Manh, R. Knopp, H. Geckeis, and J. I. Kim

Institut für Nukleare Entsorgung, Forschungszentrum Karlsruhe GmbH, P.O. Box 3640, D-76021 Karlsruhe, Germany

The size and shape of colloids released from a natural bentonite into a low-mineralized groundwater are investigated using various colloid characterization methods. For the applied methods such as atomic force microscopy (AFM), laser-induced breakdown detection (LIBD), photon correlation spectroscopy (PCS), and flow field-flow fractionation coupled to ICP-mass spectrometric detection (FFFF-ICPMS), the respective raw size data have to be corrected in order to consider chemical composition and shape of the colloids as well as instrumental artifacts. Noncontact mode AFM of the bentonite colloids shows disklike shapes of stacked smectite platelets with a mean height-to-diameter proportion (aspect ratio) of ∼1/10. A broad particle number size distribution is determined by image processing with a mean particle diameter of 73 nm. In agreement with AFM, a broad size distribution is also found by PCS and FFFF-ICPMS. Likewise, mean particle sizes found by LIBD (67 ± 13 nm) and FFFF-ICPMS (maximum in the number size distribution, ∼70 nm) are in fair agreement with the AFM data. Somewhat higher values are obtained by PCS, where mean particle diameters of the intensity-weighted size distributions of larger than 200 nm are found (depending on the algorithm used for data processing). The influence of the disklike particle shape on the results of the individual methods is discussed. As a conclusion, the application of different colloid characterization methods is a prerequisite to get complementary information about colloid size and shape, which is essential for the understanding of natural colloidal systems.

Inorganic colloids, e.g., silicates or clay minerals, are ubiquitous in natural aquatic systems and therefore can play a distinct role in the aquatic chemistry and for the migration of groundwater trace components.[1−3] The relevance of these colloids promoting the transport of hazardous substances, i.e., long-lived radionuclides, from a waste disposal site has to be assessed by taking into account the hydrogeochemical situation, the properties of the colloidal species, and the interaction of the contaminant with these colloids. Actinide transport investigations in laboratory column[4] or block experiments as well as field-scale migration studies[5] have shown that colloid transport can enhance the actinide migration and has to be considered in the long-term safety assessment of a nuclear repository.

One of the present concepts for high-level radioactive waste disposal is to encapsulate the iron or copper canisters containing the nuclear waste into an engineered clay barrier system (EBS). Various smectitic clays are in discussion as backfill materials of such an EBS system due to their swelling properties preventing water access to the waste and their strong sorption properties toward dissolved radionuclide species. A potential scenario in this repository setup is the mobilization of colloids at the EBS/groundwater interface, possibly promoting the transport of actinides by colloid migration. Especially under the low ionic strength conditions typical for granitic groundwater systems, colloids can be stabilized by their surface charge.[2] To assess their migration properties and their potential role as radionuclide carriers, it is necessary to characterize the morphology and size distribution of such colloids.

In an earlier work, natural colloids were characterized in groundwater samples from the planned low- and intermediate-level nuclear waste repository site at the Wellenberg in Switzerland by using laser-induced breakdown detection (LIBD)[6] and other methods. The colloids found in this groundwater mainly consisted of clay particles as determined by X-ray diffraction (XRD).[7] The atomic force micrograph reveals the cylindrical shape of the colloids[7] with a major part of particles showing diameters in the range of 30−100 nm and heights of 5−15 nm. The mean particle diameter of ∼70 nm determined by LIBD[6] corresponds to an average size, which is in agreement with the size range found by atomic force microscopy (AFM) for the cylindrical colloids.

In this study, FEBEX (*f*ull-scale *e*ngineered *b*arriers *ex*periment[8]) bentonite, which is discussed as an appropriate backfill material, is placed in contact with a low ionic strength groundwater sampled from the Grimsel underground laboratory (Grimsel Test Site, GTS, Switzerland). The colloidal fraction of this material is

* Corresponding author: (phone) +49/7247/82 4747; (fax) +49/7247/82 3927; (e-mail) plaschke@ine.fzk.de.

(1) Degueldre, C.; Pfeiffer, H. R.; Alexander, W.; Wernli, B.; Bruetsch, R. *Appl. Geochem*. **1996**, *11*, 677−695.
(2) Degueldre, C.; Grauer, R.; Laube, A.; Oess, A.; Silby, H. *Appl. Geochem*. **1996**, *11*, 710.
(3) Kim, J. I. *MRS Bull.* **1994**, *19* (12), 47−52.
(4) Artinger, R.; Kienzler, B.; Schüssler, W.; Kim, J. I. *J. Contam. Hydrol.* **1998**, *35*, 261.
(5) Kersting, A. B.; Efurd, D. W.; Finnegan, D. L.; Rokop, D. J.; Smith, D. K.; Thompson, J. L. *Nature* **1999**, *397* (6714), 56−59.
(6) Bundschuh, T.; Kim, J. I. Entwicklung und Anwendung der LIBD zur Quantifizierung aquatischer Kolloide und Actinidenkolloide, *FZKA Rep.* **1999**, *6273*.
(7) Degueldre, C. *Mater. Res. Soc. Symp. Proc* **1997**, *465*, 835−846.
(8) *FEBEX, Bentonite: Origin, Properties, and Fabrication of Blocks*; Publ. Tech. 05/98; ENRESA: Madrid, Spain, 1998.

10.1021/ac010116t CCC: $20.00
Published on Web 08/02/2001

characterized by various analytical methods in order to determine size distribution and morphology.

Description of the Applied Methods. One of the most commonly applied nondestructive colloid sizing methods is photon correlation spectroscopy (PCS). PCS application to the characterization of natural aquatic colloids was reviewed and assessed by Fillela et al.[9] PCS is based on the analysis of the temporal fluctuation of the scattered laser light intensity originating from the Brownian movement of dispersed particles. By computer-assisted evaluation of the intensity autocorrelation function (ACF) $C(Q,\tau)$, a hydrodynamic diameter d_h of ideal spherical colloids using the "generalized Stokes−Einstein relation" can be calculated.[9,10]

Cumulant Method. From a simple moments expansion of $C(Q,\tau)$ by performing a polynomial fit of $\ln[C(Q,\tau) - B]^{1/2}$, known as the cumulant analysis, it is possible to get information of the *z*-average diffusion coefficient and the polydispersivity index σ. At large delay times τ, noise can produce values of $C(Q,\tau)$ that are less than the baseline constant B, creating negative numbers under the square root. The Brookhaven software[11] approach of a weighted quadratic cumulant analysis (QC) overcomes this problem by simply truncating all ACF data of larger delay time τ than the first negative data point. Commonly σ is used in the range of 0.03−0.4[12] to quantitatively describe the width of the particle size distribution. For detailed discussion on the problems of the accurately determination of higher order cumulants, see ref 13.

Multimodal Size Distribution (MSD) Analysis. Several theoretical approaches exist to estimate a full intensity distribution $G(\Gamma)$ from the ACF by the mathematically ill-conditioned inversion of the ACF. Especially the noise in the scattered intensity signal, the limited accessibility of the τ-range and the dependency of the scattered intensity on the square of the particle volume may distort broad or multimodal size distributions greatly. The effect of noise is reduced in the nonnegatively constrained least-squares algorithm (NNLS) by permitting only positive amplitudes, which passes the NNLS algorithm to calculate the MSD. Provencher[14] implemented in his widely used Laplace inversion program CONTIN a smoothing procedure to restrict the curvature in $G(\Gamma)$. The third applied method, the exponential sampling algorithm,[15] is based on the expansion of $G(\Gamma)$ by the eigenfunctions and eigenvalues of the Laplace transformation. In general, all three algorithms applied in this paper cannot resolve peaks that are separated by less than a factor of 2 for the ratio of two mean particle sizes.[16] The determined hydrodynamic diameter d_h strongly depends on the volume and the shape of the particles. Therefore, analytical expressions have been developed to consider ellipsoidal, cylindrical, or wormlike geometrical shapes.[16,17]

Finally, this intensity distribution $G(\Gamma)$ can be used to estimate the number-weighted distribution $N(r)$ for homogeneous spherical particles by weighting $N(r)$ by the sixth power of the radius.

Laser-induced breakdown detection is a very sensitive method for the direct detection of colloids at the lowest concentration level. Similar to photon correlation spectroscopy (PCS) LIBD belongs to the nondestructive colloid detection methods. LIBD is based on the plasma generation on single particles by a focused, pulsed laser beam and the detection of produced shock waves or plasma light emissions. The laser-induced breakdown effect and the principles of LIBD are described in detail in the literature.[18−22] The power density required to induce the breakdown of a dielectric medium resulting in plasma formation is significantly lower for solid matter than for liquids. Unless the laser pulse power density exceeds the breakdown threshold ($P_{A,crit}$) of the solvent in a colloidal dispersion, the plasma is generated almost exclusively on colloids. The evaluation of the number of breakdown events per number of laser shots results in a breakdown probability, which is dependent on both particle concentration and size.[19] Furthermore, the probability of a breakdown initiation on an individual particle depends on the laser power density affecting the number of particle-borne electrons.[19] The number of so-called initial electrons produced by multiphoton absorption increases with increasing particle size. These initial electrons are accelerated in the electromagnetic field of the laser beam and cause an electron avalanche by additional ionization. Therefore, the breakdown probability at a given laser power density is proportional to particle size. With increasing particle size, lower laser power density is needed to induce a dielectric breakdown on a particle.

The spatial distribution of the individual breakdown events within the focal area of the laser beam is found to be dependent on the particle diameter and independent of the particle concentration.[23] The width of the breakdown volume along the laser beam axis (effective focal length, $L_z(P)$), therefore, can be taken as a measure for the mean colloid size. $L_z(P)$ is defined as the length in which 99.7% of the plasma events are found. To determine $L_z(P)$, the light emission of single plasmas is detected by a microscope charge-coupled device (CCD) camera system. The system is calibrated by analyzing polystyrene reference particles of well-known mean particle diameters. A mean particle diameter of sample colloids is obtained by comparison the $L_z(P)$ of the sample colloids with that of the polystyrene reference particles.[23] With the known mean particle diameter of the sample colloids, the particle concentration can be calculated from the breakdown probability.[6,22] More details on the theory of LIBD and particle size evaluation can be found in ref 23.

Atomic force microscopy is a relatively new imaging technique for studying the morphology of environmental particles such as humic colloids[24] or clay particles.[7,25,26]

(9) Fillela, M.; Zhang, J.; Newman, M. E.; Buffle, J. *Colloids Surf., A* **1997**, *120*, 27−46.
(10) Berne, B. J.; Pecora, R. *Dynamic Light Scattering*; J. Wiley & Sons: New York, 1976.
(11) Brookhaven Instruments Corp. Data Analysis Software (BI-ISDA), version 8.0; Brookhaven Instruments Corp. (www.bic.com), Holtsville, NY, 1990.
(12) Burchard, W. *Adv. Polym. Sci.* **1983**, *48*, 1−124.
(13) Hanus, L. H.; Ploehn, H. J. *Langmuir* **1999**, *15*, 3091−3100.
(14) Provencher, S. W. *Comput. Phys. Commun.* **1982**, *27*, 213−227.
(15) Ostrowsky, N.; Sornette, D.; Parker, P.; Pike, R. *Opt. Acta* **1981**, *28*, 1059−1071.
(16) Yamakawa, H.; Fujii, M. *Macromolecules* **1974**, *7*, 649−654.
(17) Schurtenberger, P.; Newman, M. E. In *Environmental Particles*; Buffle, J., van Leeuven, H. P., Eds.; Lewis Publishers: Boca Raton, FL, 1992; Vol. 2, p 38−105.
(18) Bundschuh, T.; Knopp, R.; Kim, J. I. *Colloids Surf., A* **2001**, *177*, 47−55.
(19) Scherbaum, F. J.; Knopp, R.; Kim, J. I. *Appl. Phys. B* **1996**, *63*, 299−306.
(20) Fujimori, H.; Matsui, T.; Ajiro, T.; Yokose, K.; Hsueh, Y.; Izumi S. *Jpn. J. Appl. Phys.* **1992**, *31*, 1514−1518.
(21) Bettis, J. R. *Appl. Opt.* **1992**, *31*, 1382.
(22) Hauser, W.; Bundschuh, T.; Verfahren zur Bestimmung der Grösse von Partikeln in einer Lösung. Patentschrift DE 198 33 339 C1, 2000.
(23) Bundschuh, T.; Hauser, W.; Kim, J. I.; Knopp, R.; Scherbaum, F. J. *Colloids Surf., A* **2001**, *180*, 285.
(24) Plaschke, M.; Römer, J.; Klenze, R.; Kim, J. I. *Colloids Surf., A* **1999**, *160*, 269.

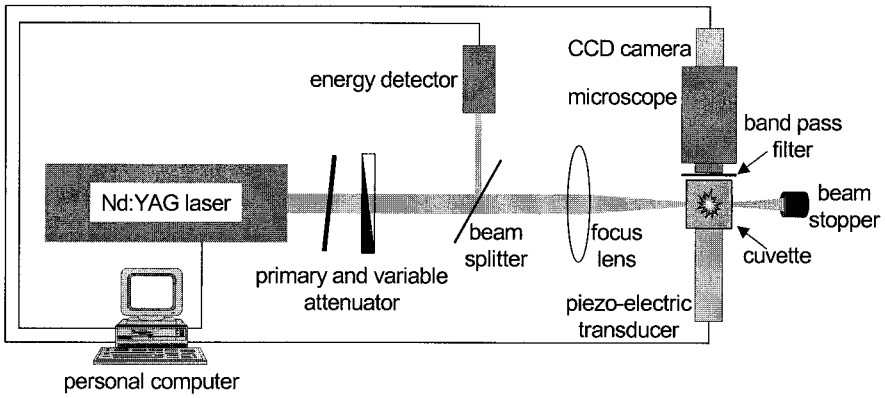

Figure 1. Experimental setup of LIBD.

Tapping mode AFM (or noncontact mode AFM) is a technique that uses oscillating cantilevers to maintain a constant distance between tip and sample.[27] Compared to electron microscopy, AFM offers more flexibility in sample preparation, three-dimensional images, and in some cases better image resolution. In the present paper, noncontact mode AFM is applied to investigate FEBEX bentonite particles on the mineral surface of cleaved mica. Different from PCS or LIBD, the AFM requires the prior deposition of colloids onto a plane surface.

Flow field-flow fractionation (FFFF) represents a colloid separation technique with no stationary phase required as, for example, in size exclusion chromatography. Thus, a less extent of interaction effects of sample components with equipment surfaces is expected. The separation of analytes by FFFF is achieved in a laminar carrier flow under the action of a flow field, which is perpendicular to the carrier flow.[28,29] The movement of colloidal species in the laminar carrier flow is determined by their diffusion coefficient and, thus, their size. Depending on the particle properties and concentration, different detectors have been applied to record the particle size distribution, e.g., UV/visible absorption,[30] laser light scattering (LLS), and LIBD.[31] In the present study, the ICPMS is used as a mass-sensitive detector.

The main focus of this study is to evaluate the results obtained by the more advanced sizing methods LIBD and AFM by comparing them with the more commonly used PCS, SEM, and FFFF.

EXPERIMENTAL SECTION

Preparation of Bentonite Samples. FEBEX bentonite is mainly composed of smectite (>90 wt %) with accessory minerals quartz, cristobalite, feldspar, and calcite.[8] The groundwater taken from the GTS is of NaCl type with a low ionic strength of 2.2×10^{-3} M and a pH value of 9.5. Stable colloid suspensions of FEBEX bentonite particles were obtained by washing 10−15 times 100 mg of bentonite with 50 mL of GTS water and centrifuging the suspension for 2 min at 15.000 rpm. The final colloid stock solution has a pH of 7.1 and a gravimetrically determined concentration of 175 mg/L. The ζ potential of the particles (ZetaPlus, PALS system; Brookhaven Inc.) is found to be -40 ± 2 mV calculated by using the Debye−Hückel potential model.[32] The colloid suspension is diluted to 17.5 mg/L for PCS, to 50 mg/L for FFFF and AFM, and to 17.5 μg/L for LIBD measurements.

Noninvasive Particle Sizing Techniques (LIBD and PCS). The experimental setup of LIBD is schematically shown in Figure 1. For plasma generation on colloids, a pulsed Nd:YAG laser (Continuum Surelite I, $\lambda_{em} = 532$ nm; repetition rate, 20 Hz; beam diameter, 4.7 mm) is used. The laser pulse energy (160 mJ) is reduced and adjusted to a value of 0.46 ± 0.03 mJ by a fixed and variable attenuator. The laser beam is focused by a plano convex lens (focal length, 40 mm) into the colloidal dispersion that is placed in a rectangular silica sample cell. To monitor the energy of the laser pulse, a part of the laser pulse is reflected onto a calibrated pyroelectric detector by a beam splitter. A monochrome full picture CCD video camera (782 × 582 pixels; JAI) with a variable macromicroscope (Leica) is arranged perpendicular to the laser beam axis in the front of one sample cell window. The microscope is used to gain an optically expanded image of the focal range that is recorded by the CCD camera. Additionally, a piezoelectric transducer (PZT)[33] is mounted to the window of the sample cell in order to monitor the amplitude of the intensive acoustic wave induced by plasma generation. Laser pulse energy, piezoelectric signal, and intensity of light emission of each plasma event are digitized and processed by a PC. Data from the CCD camera are acquired and processed via a frame grabber card by special software.

The calibration of LIBD follows a two step procedure:[6,19,34]

(1) The breakdown probability is measured in dependence on the colloid concentration from a few nanograms per liter up to some milligrams per liter for polystyrene reference colloids.[18] Commercial polystyrene reference particle dispersions (Polymer Standard Service GmbH, Mainz, Germany and Polysciences Inc.,

(25) Bickmore, B. R.; Hochella, M. F., Jr.; Bosbach, D.; Charlet, L. *Clays Clay Miner.* **1999**, *47* (5), 573−581.
(26) Lindgreen, H.; Garnaes, J.; Hansen, P. L.; Besenbacher, F.; Laegsgaard, E.; Stensgaard, I.; Gould, S. A. C.; Hansma, P. K. *Am. Mineral.* **1991**, *76*, 1218−1222.
(27) Hansma, P. K.; Cleveland, J. P.; Radmacher, M.; Walters, D. A.; Hillner, P. E.; Bezanilla, M.; Fritz, M.; Vie, D.; Hansma, H. G.; Prater, C. B.; Massie, J.; Fukunaga, L.; Gurley, J.; Elings, V. *Appl. Phys. Lett.* **1994**, *64* (13), 1738.
(28) Giddings, J. C.; Yang, F. J.; Myers, M. N. *Anal. Chem.* **1976**, *48*, 1126−1132.
(29) Giddings, J. C. *Science* **1993**, *260*, 1456−1465.
(30) Ngo Manh, T.; Geckeis, H.; Kim, J. I.; Beck, H. P. *Colloids Surf., A* **2001**, *181*, 289−301.
(31) Ngo Manh, T.; Knopp, R.; Geckeis, H.; Kim, J. I.; Beck, H. P. *Anal. Chem.* **2000**, *72*, 1−5.
(32) Debye, P.; Hückel, E. *Phys. Z.* **1923**, *24*, 185.
(33) Hauser, W.; Götz, R. Druckwellensensor. Patentschrift DE 196 02048 C2, 1999.
(34) Knopp, R.; Scherbaum, F. J.; Kim, J. I. *RCM Rep.* **1996**, *00696*.

Eppelheim, Germany) with different particle diameters (0.019, 0.032, 0.041, 0.050, 0.073, 0.155, 0.320, 0.698, 1.072 μm) are diluted with ultrapure water to the required colloid concentration and prepared in a sample cell.[18] An influence of the relatively low ionic strength of the groundwater on the LIBD signal is not expected. The effect of ionic strength up to a concentration of 1.1 mol/L NaCl was studied in an earlier work,[6] and up to this concentration only a small increase of the breakdown probability has been observed.

(2) The effective focal length ($L_z(P)$) is determined by analyzing the position of 8000 single plasma events in the laser beam axis using a microscope CCD camera. A linear relationship between $L_z(P)$ and the logarithm of the mean spherical particle diameter d_s is found:

$$\log (L_z(P)) = a + b \log (d_s) \quad (1)$$

For the given polystyrene reference particles, the empirical parameters a and b are determined to be $a = 3.248 \pm 0.009$ and $b = 0.240 \pm 0.008$ (regression coefficient $R = 0.996$).

Applying this calibration procedure, we are able to evaluate a mean particle diameter, d_s, for a given sample. From d_s and the measured breakdown probability, the particle concentration can be calculated from the calibration curves obtained in the first step of the calibration procedure. A more detailed description of the calibration procedure can be taken from.[23] It is well known that the critical laser power density required to induce a breakdown is dependent on the colloid material.[18,19] The relative critical laser power densities or so-called breakdown thresholds $P_{A,crit}$ for polystyrene latices, thoriasol, alumina, and silica are reported to be 1:1.1:1.7:1.8, respectively. Values for $P_{A,crit}$ of bentonite particles (smectite) have not yet been determined due to the nonavailability of monodisperse smectite particles. In the present work, it is assumed that $P_{A,crit}$ for smectite is similar to that of alumina and silica.

Consequently, the diameter for the polystyrene colloids has to be corrected for the actual colloid material considering eq 2 (see ref 19):

$$P_{A,\,crit} A_T = \text{const} \quad (2)$$

where A_T corresponds to the maximum particle cross section. Following this assumption, the corrected cross section for the bentonite colloids can be approximated to $A_{T(smectite)} = 1.8A_{T(polystyrene)}$. As $A_T = \pi r^2$, the corrected diameter for the bentonite colloids (d_p) is approximated by $d_p \approx 1.8^{1/2} d_s \approx 1.34 d_s$, where d_s is the corresponding diameter related to the polystyrene reference colloids.

In all experiments, ~8000 breakdown events are collected for the analysis of a sample, resulting in a measurement time of ~10 min. The samples are measured in a quartz cell with 10-mm length and 10-mm width at room temperature (24 ± 2 °C) under normal atmospheric pressure conditions.

Colloid size determination by PCS is conducted using a homodyne (single-beam) ZetaPlus system (Brookhaven Inc.) equipped with a 100-mW solid-state laser ($\lambda_{em} = 635$ nm). All measurements were performed in disposable cuvettes, and the scatter light is analyzed at a constant angle perpendicular to the incident laser beam. Ten ACF of 60-s data collection time per scan were analyzed individually and averaged to a mean intensity distribution $G(\Gamma)$. Furthermore the 10 ACFs were combined to 1 mean ACF, giving a combined intensity distribution $G(\Gamma)$. The performed analysis procedure[17] was chosen to evaluate critically the tendency of the MSD software to produce spurious peaks or multiple peaks instead of a broad unimodal distribution. The ACFs were evaluated by applying the Zetasizer III software,[11] including a linear to quartic weighted cumulant analysis and a series of MSD algorithms (NNLS,[35] CONTIN,[14] exponential sampling).

Microscopic Techniques (AFM and SEM). Muscovite mica provides a flat, atomically smooth surface with a negative charge at intermediate pH. A piece of natural muscovite (Plano, Wetzlar, Germany) with a dimension of about 1 by 2 cm is freshly cleaved and positioned vertically in a polypropylene sample beaker containing the bentonite suspension in order to avoid deposition of aggregates by sedimentation. Colloids are allowed to adsorb from the bentonite suspension with a colloid concentration of 50 mg/L to the mica surface for 24 h ($T = 22$ °C, pH 7.3). The mica sheets are then withrawn from the solution and thoroughly rinsed with deionized water in order to remove any nonadsorbed bentonite or residues from salt crystals. The mica samples are then dried in an oven at 40 °C for at least 5 h.

Noncontact mode AFM imaging is performed using a Topometrix TMX 2000 Explorer which is equipped with cantilever oscillating hardware with possible oscillation frequencies ranging from 0 to 600 kHz. Probes with silicon tips (nominal radius of curvature, <10 nm; nominal spring constant, 48 N/m; nominal resonance frequency, 190 kHz) are mounted on a scanner with a maximum range of 2.2 μm in the $x-y$ direction and 900 nm in the z direction. Imaging is performed on dried samples.

The Topometrix AFM software is applied for image processing for leveling images in a horizontal plane. A Topometrix grain analysis program that is part of the commercial image processing software is used to identify and quantify particles adsorbed on the flat surface as described in the literature.[24] The image is divided by an imaginary horizontal plane and all data points over this plane are defined as particle. Data of particle size (area, volume, average height) are exported and processed for calculation of particle size distribution. Particle diameters are calculated from the particle areas by assuming disklike particles. Since the lateral resolution of AFM is limited by the size of the AFM tip, these diameters are corrected by a geometrically estimated tip artifact which is described in the literature[36] (see Results). A particle size distribution is obtained by examination of 12 AFM images which are taken from 12 different sample sites, where ~200 particles are found.

A scanning electron microscope (CamScan, type C44 FE) equipped with a warm field emission cathode is used for characterization of bentonite particles. The sample was coated by Cr prior to the analysis.

Size Fractionation by FFFF. The fractionator used is a model F-1000 from FFFractionation, Inc. (Salt Lake City, UT). The lower frit of the channel (27.4-cm "effective" length, 2.0-cm width) is

(35) Morrison, I. D.; Grabowski, E. F.; Herb, C. A. *Langmuir* **1985**, *1*, 496–501.
(36) Eggleston, C. M. In *Scanning Probe Microscopy of Clay Minerals*; Nagy, K. L., Blum, A. E., Eds.; CMS Workshop Lectures, Vol. 7; The Clay Mineral Society: Boulder, CO, 1994; p 42.

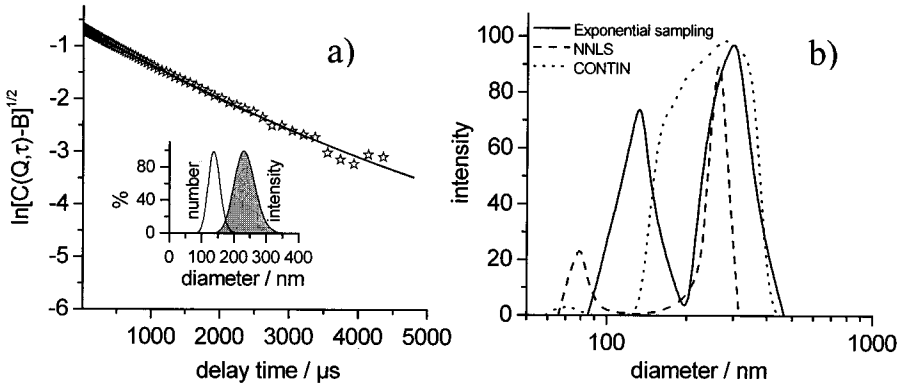

Figure 2. PCS size distribution analysis of FEBEX bentonite colloids: (a) weighted QC of the autocorrelation function $C(Q,\tau)$. Inset is the calculated intensity-weighted and number-weighted monodisperse distribution determined by QC. (b) Size distribution analysis by the ill-conditioned inverse Laplace transformation methods exponential sampling, NNLS, and CONTIN (not shape-corrected; see text).

covered with a membrane consisting of regenerated cellulose with a cutoff of 5 kDa from Schleicher & Schuell (Dassel, Germany). The carrier is degassed by a 1100 series vacuum degasser model G 1322A and delivered at constant rates to the fractionator by a 1100 HPLC Iso, pump model G 1310A from Hewlett-Packard (Waldbronn, Germany). The cross-flow is provided by a double-piston precision pump P-500 from Pharmacia Biotech AB (Sweden) in a recirculating cross-flow loop. From the channel, the effluent is directed through a DAWN-DSP-F light scattering photometer from Wyatt Technology Corp. (Santa Barbara, CA).

For detection of laser light scattering, a 5-mW HeNe laser with incident light beam $\lambda_{em} = 632$ nm is directed through the detector cell of 100-μL volume. Scattered light is detected by an array of 15 photodiodes arranged at different angles relative to the incoming laser beam. Only the signal detected by the 90° detector is taken for the present study. After LLS detection, a 5% ultrapure HNO_3 solution is mixed to the effluent at a flow rate of 0.5 mL/min by using a t-piece and led to the cross-flow nebulizer of the ICP-mass spectrometer (Elan 6000, Perkin-Elmer, Germany). More details of this experimental setup are described in the literature.[37]

A solution of 0.01% Tween 20 (polyethoxysorbitan laurate, Merck, Darmstadt, Germany), at an ionic strength of 10^{-4} mol/L ($NaClO_4$) buffered to pH ~9 using a 5×10^{-3} mol/L Tris buffer solution, is applied as a carrier. Channel flow is kept at 2 mL/min and cross-flow at 0.5 mL/min. The system is calibrated using polystyrene colloid standards (diameter: 32, 50, 102, 155, 204, 304 nm. Polysciences, Eppelheim, Germany) in ultrapure water, which are first shaken in an ultrasonic bath for ~10 min and filtered through a 450-nm syringe filter before injecting. The sample is injected (injected volume 20 μL) into the top of the FFFF channel and only the cross-flow with no channel flow is applied to the sample for 2 min. Following this step, the channel flow is started and the fractionation begins. The calibration line follows the equation, $d_s = 6.9V_r$, where d_s is the spherical particle diameter related to polystyrene reference colloids and V_r the retention volume at peak maximum.

RESULTS

Laser-Induced Breakdown Detection. First, the natural colloid background concentration of the Grimsel groundwater is determined. Only the LIBD is sensitive enough to provide reliable results on colloid concentration and size at the low background concentration. The breakdown probability varies between 0.04 and 0.09, and the mean colloid diameter is ~50 nm in all measured samples. Taking into account an average colloid density of 2.6 g/cm^3 and assuming spherical geometry, this corresponds to a colloid concentration of approximately 0.5−1.2 μg/L ((2.9−6.7) $\times 10^9$ colloid/L) colloidal material.

Due to the high sensitivity of the LIBD, the FEBEX bentonite solution has to be diluted with Grimsel groundwater to a concentration of 17.5 μg/L. Even at this low concentration, the breakdown probability lies close to the saturation of the method at 0.89; i.e., 89% of the incident laser pulses leads to a colloid breakdown. The mean colloid size of the bentonite particles in the Grimsel water is determined by evaluating the spatial distribution of breakdown events (effective focal length ($L_z(P)$) relative to the calibration with polystyrene reference particles to values of 50 ± 10 nm (error is determined by measuring the samples several times and calculating the standard deviation). After correction for the different composition of polystyrene and smectites (see Experimental Section), this corresponds to a diameter of 67 ± 13 nm. A number concentration of 3.5×10^{11} colloid/L can be calculated. Taking into account the average density of 2.6 g/cm^3 for the clay particles and a disklike shape with 1/10 height-to-diameter proportion (aspect ratio), a mass concentration in a range of 7 μg/L can be calculated. This is only ~40% of the given concentration (see Discussion).

Photon Correlation Spectroscopy. The light scatter intensity for the measured . suspension lies at ~50 000 counts. In Figure 2a, the performed weighted QC of the combined ACF for the bentonite colloid suspension can be seen truncated as described in the introduction. The intensity-weighted average hydrodynamic diameter d_h and the polydispersivity σ are 235 nm and 0.137 (fwhm 85 nm), respectively (Figure 2a inset). The averaged QC analysis results of the 10 independent data sets produced comparable results with a d_h of 234 nm and a σ of 0.141. Additionally, in Figure 2a, a number size distribution $N(r)$ is inset which was calculated using a Schultz distribution. From the maximum in the distribution curve, a mean diameter of 138 nm is determined. The QC

(37) Ngo Manh, T. Charakterisierung aquatischer Kolloide mittels Grössenausschluss-chluss-chromatografie (GPC) und der Fluss-Feldflussfraktionierung (FFFF). Ph.D. Thesis, Universität des Saarlandes, Saarbrücken, Germany, 2000.

expression provides a high goodness of fit and higher order cumulants (cubic, quartic) are small, indicating little kurtosis.

Applying the MSD algorithm NNLS, CONTIN, and exponential sampling to the measured ACF revealed in all three methods a bimodal intensity-weighted size distribution (Figure 2b) independent of the data generation (average of single ACFs or combination to one ACF). The two peaks in the bimodal size distribution obtained by all three algorithms are sufficiently separated (see introduction). Only the combined MSD analysis is shown in Figure 2b. The NNLS analysis revealed two peaks at d_h of 80 (7% intensity, 96% number) and 263 nm (93% intensity, 4% number), CONTIN peaks at d_h of 75 (3% intensity, 100% number) and 279 nm (97% intensity, 0% number), and the exponential sampling algorithm peaks at d_h of 133 (24% intensity, 89% number) and 306 nm (76% intensity, 11% number). The transformation of the intensity-weighted distribution $G(\Gamma)$ to the number-weighted distribution $N(r)$ significantly shifts the weighting of the peaks to the smaller diameter.

Atomic Force Microscopy. For the determination of particle dimensions and number by image processing, it is necessary that single bentonite particles can be distinguished on a sufficiently smooth surface. Therefore, colloidal particles are allowed to adsorb from the solution onto mica. In the case of applying an aliquot of the dispersion onto a mica surface and subsequently evaporating the solvent, the formation of aggregates during drying is likely to occur. In Figure 3a, single particles are seen on the flat mica surface. Particle diameters range from about 50 to 300 nm and their heights range from 2 to 100 nm. Most of the particles have blocky shapes typical for their monoclinic crystal symmetry. A line profile over three particles (one larger and two smaller ones) is shown in Figure 4 (indicated as broken line in Figure 3a). The smaller particles have a rather flat structure with heights in the range of 4−7 nm and with diameters in the range of 60−70 nm (aspect ratio, ∼1/10). The larger particle in contrast shows an aspect ratio in the range of 1/2 (height 100 nm; diameter 180 nm) and might correspond to stacks of smectite platelets. More particles are seen in Figure 3b where a droplet of colloid suspension has been dried. As in Figure 3a, many smaller particles with diameters in the range of 60−70 nm and some larger particles (>100 nm) can be identified.

The roughness of the mica blank substrates was found to be lower than 0.1 nm root-mean-square (RMS) value, which is sufficiently low for a precise particle analysis. Particle diameters are calculated from the determined particle areas on the assuption that particles are disklike. The lateral resolution of AFM is limited by the size and shape of the tip. For nanometric spherical particles (e.g., polystyrene nanospheres), lateral artifacts of more than 100% are found in the literature, whereas particle height is reproduced very exactly by AFM.[38] However, the lateral tip artifact markedly depends on particle height, which has to be taken into account for the flat bentonite particles (Figure 5). A tip artifact (A) can be estimated by a simple geometrical approach, according to[36]

$$A = 2S = 2\sqrt{2R_t h_p - h_p^2} \qquad (3)$$

where h_p is the particle height, R_t the radius of curvature of the AFM tip, and S the tip artifact on one side of the particle (Figure 5). The lateral tip artifact (A) is calculated individually for each particle where the height data (h_p) are determined by the grain analysis software. A radius of curvature R_t of 10 nm is assumed

(38) Ramirez-Aguilar, K. A.; Rowlen, K. L. *Langmuir* **1998**, *14*, 2562.

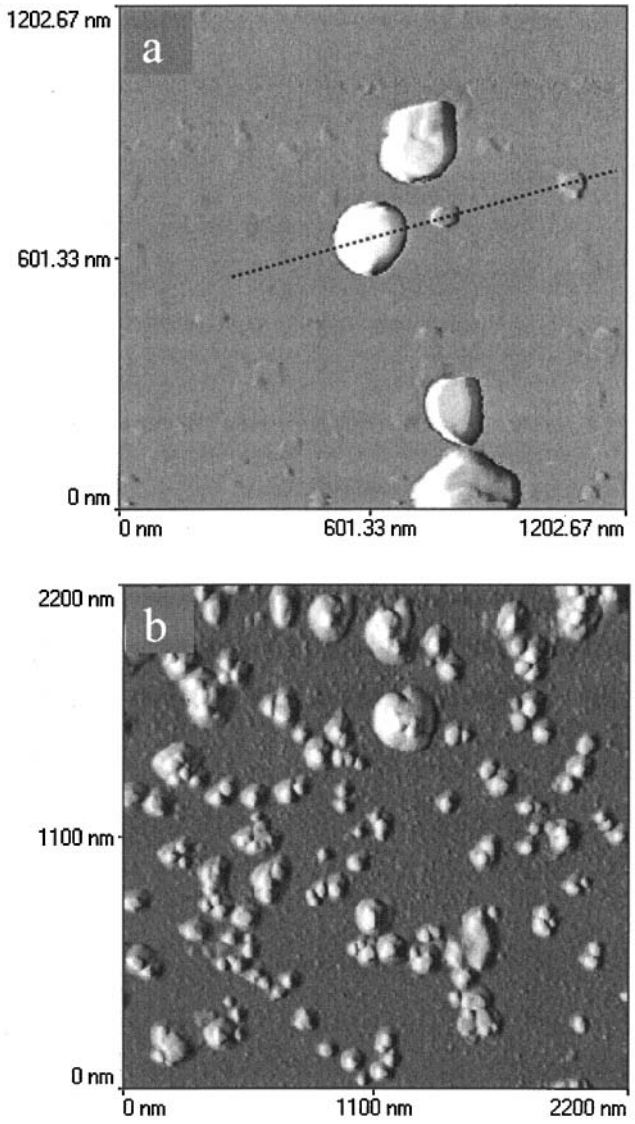

Figure 3. AFM images of FEBEX bentonite colloids adsorbed onto mica. (a) Single particles with different sizes and (b) aggregates of colloids are seen (broken line in (a) indicates the line profile of Figure 4).

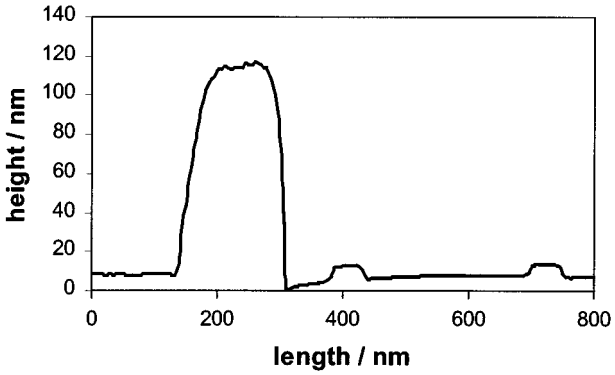

Figure 4. Line profile over three FEBEX bentonite colloids with different aspect ratios (see text).

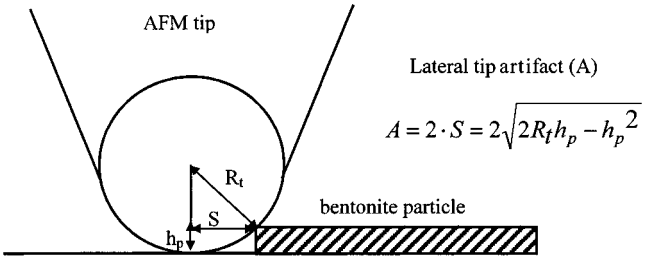

Figure 5. Geometrical estimation of the lateral AFM tip artifact (see text).

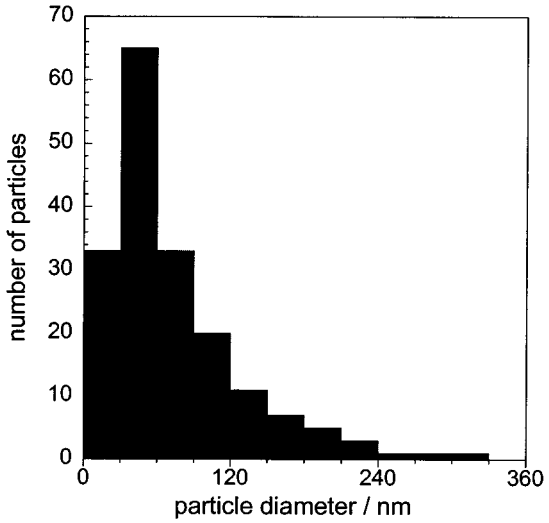

Figure 6. Particle size distribution from AFM image analysis. Particle diameters are corrected by a lateral tip artifact (see text; width of one bar, 30 nm).

according to the manufacturers specification. The particular lateral tip artifacts depending on particle heights range from 9 to 30 nm with a mean value for all particles of ~15 nm. For the few particles higher than the tip radius (R_t), a tip artifact between 20 and 30 nm is assumed depending on particle height. Particle diameters are corrected by these values of A. From the corrected particle diameters (d_p) and the average heights (h_p), a mean aspect ratio (h_p/d_p) of 0.08 is determined. This value is in fair agreement with an assumed aspect ratio of 1/10 for bentonite particles.

The number-related particle size distribution from AFM image analysis is shown in Figure 6. A relatively broad distribution with a maximum at ~45 nm and a mean particle diameter of 73 nm is found.

In addition, a mass-related size distribution is calculated from the AFM data. Particle masses are calculated for each particle under the assumption that particles have disklike shapes according to

$$m_p = (d_p/2)^2 \pi h_p \rho \qquad (4)$$

where m_p is the particle mass, d_p the tip-corrected particle diameter, h_p the particle height given by the grain analysis results, and ρ the average particle density taken as 2.6 g/cm^3. A rather broad mass-related AFM size distribution ranging from 0 to over 300 nm with a maximum at around 180 nm is seen in Figure 7. As expected, the large amount of smaller particles seen in the number-related AFM size distribution (Figure 6) play a minor role in the mass-related size distribution due to the small particle volume. In Figure 7, the mass-related AFM size distribution with a maximum at 180 nm is compared with the FFFF-ICPMS and PCS size distributions (see Discussion).

Scanning Electron Microscopy. The same samples used for AFM image analysis are covered with a Cr layer for the investigation by scanning electron microscopy (SEM). The image resolution and contrast were to low to see the smaller particles, and therefore, a particle size distribution could not be obtained. In Figure 8, a SEM image of some larger bentonite particles is shown, which have—like the larger particles found by AFM—diameters in the range of 100−150 nm.

Flow Field-Flow Fractionation. The obtained fractograms recorded by the LLS detection and ICPMS show a relatively broad size distribution for the sample colloids. Due to the high dilution of the sample during fractionation, only Mg can be detected by ICPMS as a main component of the bentonite particles. Al and Si background concentrations in the carrier solution are found to be very high, due to slight corrosion and dissolution of the ceramic frit overlying the fractionation channel at the high pH.

Note that the following values for particle diameters obtained by FFFF are related to the spherical reference colloids used for calibration and are not yet corrected for particle shapes (see next paragraph). The size distribution detected by LLS at an angle of 90° is different from that found for the ICPMS signal (not shown). Peak maximum for the fractogram detected by LLS lies at 200 nm and for the ICPMS Mg signal at ~125 nm. Dead volumes for the tubings connecting LLS and ICPMS detector are taken into consideration. The difference in the peak maximums can be explained by the strong dependency of the light scatter intensity on the particle diameter, thus overestimating the larger sized particles. As expected, the average particle size determined by fractionation and LLS detection agrees with the intensity-weighted PCS size of ~235 nm derived by QC analysis. In contrast, the ICPMS detector delivers a signal exclusively related to the analyte mass concentration. The respective fractogram, therefore, can be taken as the mass-weighted size distribution of the colloids, which ranges from ~30 to ~350 nm for the spherical equivalent diameters d_s. The shape-corrected FFFF size distribution is shown in Figure 7 and discussed in the next paragraph.

DISCUSSION

Particle Sizes and Shapes. A comparison of the size information requires the prior definition of the diameter types that are obtained by the individual methods. Only the AFM and SEM are imaging methods and provide within the inherent instrumental uncertainties the direct shape and geometric dimensions of the colloids. In the case of LIBD and FFFF, a size calibration has been made and the measured sizes are related to that of spherical polystyrene particles. Hydrodynamic diameters d_h are provided by the PCS measurement, which are derived from the particle diffusion coefficient by applying Stoke's law.

To compare the different investigation methods, it has to be understood that the colloid size obtained by AFM and LIBD gives direct information about the number-weighted mean particle diameters, whereas FFFF-LLS and PCS acquire direct information on the intensity-weighted particle diameters. Furthermore, FFFF-ICPMS includes direct mass-weighted information.

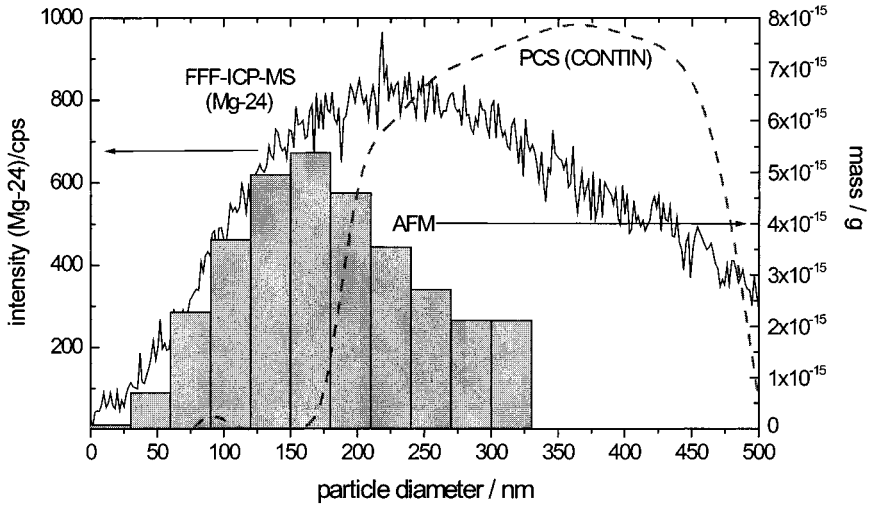

Figure 7. Shape-corrected particle size distribution determined by FFFF using the mass signal of Mg-24 and ICPMS as a detector. For comparison a mass-related size distribution calculated from AFM data and the intensity-weighted size distribution of the PCS (CONTIN, shape-corrected) analysis (dashed line) are included.

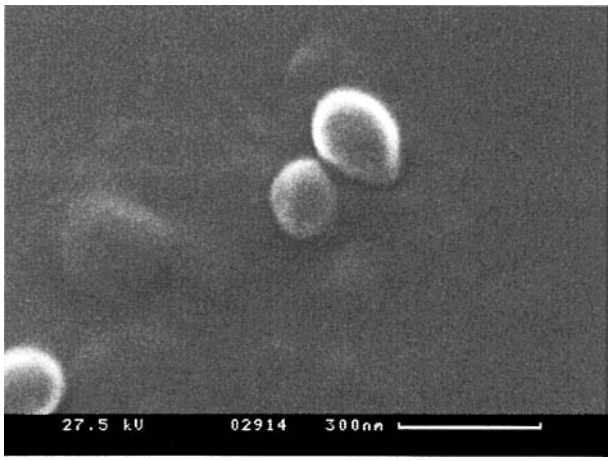

Figure 8. Shapes of FEBEX bentonite colloids imaged by SEM (see text).

For a comparison of these differently weighted particle diameters, the shape of the particles has to be considered in an appropriate way as discussed in the following paragraph. The FEBEX bentonite colloids are regarded in a geometrical shape correction as disks with a 1/10 height-to-diameter proportion (aspect ratio), which is in fair agreement with the AFM results (see Results).

The diameter obtained by LIBD for disklike-shaped particles by the above-described two-dimensional evaluation of the breakdown events in the laser focus depends on the maximum cross section of the particle A_T (see eq 2). Therefore, the diameter given by the LIBD corresponds to the diameter of the disk d_p and a shape correction is not required.

For the conversion of the hydrodynamic diameter d_h obtained by PCS to the shape-corrected d_p the following equation was applied:[16]

$$d_h = 1.5d_p\left(\left[1+\left(\frac{L}{d_p}\right)^2\right]^{1/2} + \frac{d_p}{L}\ln\left(\frac{L}{d_p}+\left[1+\left(\frac{L}{d_p}\right)^2\right]^{1/2}\right) - \left(\frac{L}{d_p}\right)\right)^{-1} \quad (5)$$

After this equation, all d_h obtained by PCS have to be multiplied by a factor of 1.30 to account for the disklike shape of the bentonite colloids. For the QC analysis, a mean intensity-weighted diameter d_p of 345 nm and a number-weighted d_p of 179 nm is calculated. As an example, the shape-corrected intensity size distribution after CONTIN analysis is shown in Figure 7. Two peaks are seen, one minor in the size range of ~90 nm and a major peak with a maximum at ~370 nm. The intensity-weighted PCS results (CONTIN) clearly demonstrate the sensitivity of this method especially for the colloid fraction of >200 nm.

To compare the mass-weighted FFFF-ICPMS size distribution with that calculated from the AFM results, it is necessary to convert the FFFF size information related to spherical reference colloids to that of disklike particles. Assuming constant volume of the particles, the diameter d_p can be derived from the spherical particle diameter d_s by using eq 6:[39,40]

$$\sqrt[3]{10\frac{2}{3}} = \frac{d_p}{d_s} \quad (6)$$

The results shown in Figure 7 are the shape-corrected mass-related size distributions obtained by AFM and FFFF. The fractogram detected by ICPMS indicates a size distribution ranging from 50 to 650 nm with a maximum at ~235 nm. The maximum of the mass-related AFM size distribution is in the range of 180 nm, which is in the same order as the FFFF result. The distribution patterns of AFM and FFFF are fairly consistent, taking into account the very different method principles. Slight differences in the distribution maximums and tailing can be attributed to (1) a limited resolution of FFFF and interactions of colloids with channel surfaces and (2) the relatively small number of particles analyzed for the AFM size distribution.

A number-weighted FFFF size distribution can be calculated by converting the mass concentration given by the ICPMS

(39) Papst, W.; Kunes, K.; Havrda, J.; Gregorová, E. *J. Eur. Ceram. Soc.* **2000**, *20*, 1429.
(40) Beckett, R.; Murphy, D.; Tadjiki, S.; Chittleborough, D. J.; Giddings, J. C.; *Colloids Surf., A* **1997**, *120*, 17.

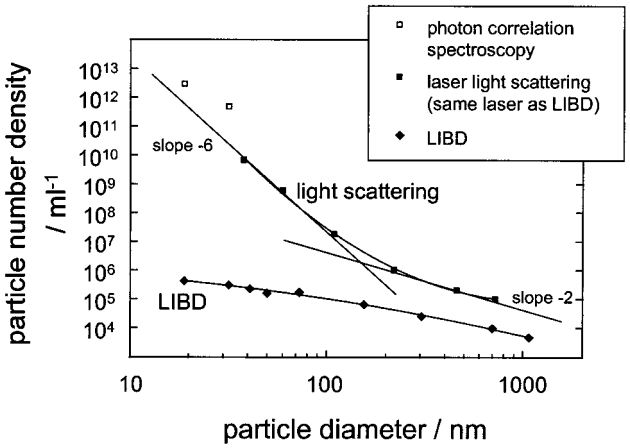

Figure 9. Detection limits of the LIBD in comparison to laser light scattering.

detector into particle numbers by using the equation

$$n = M/(V_p\rho) \tag{7}$$

where n corresponds to the particle number, M corresponds to the measured particle mass given by the ICPMS signal for Mg, V_p is the particle volume assuming again a disklike shape of platelets, and ρ is the average particle density taken as 2.6 g/cm^3. The thus calculated number-weighted size distribution shows a maximum in the range 70 nm. This value is afflicted with distinct uncertainties due to the calculation of particle numbers in a range where the particle masses are low and the detector signals are noisy.

In summary, the shape-corrected mean particle diameters found by AFM (73 nm), LIBD (67 ± 13 nm) and FFFF (~70 nm) are very consistent whereas PCS delivers distinct larger values (>200 nm). The reasons for this observation arise from the different analyzing principles.

The Methods Used. Light scattering methods such as PCS belong to the standard methods for the determination of colloid size distributions. The intensity of the scattered light strongly depends on the hydrodynamic particle diameter (d_h). In the range of Rayleigh scattering ($d_h \leq \lambda/10$), the intensity of scattered light is proportional to d_h^6, whereas for particle diameters larger than about $\lambda/6$ the intensity is proportional to d_h^2 (see slopes in Figure 9).[41] Therefore, the PCS becomes, by theory, very insensitive for small particles in the presence of larger sized particles, which produce the major part of the scattering light intensity. Thus, evaluation of the ACF for natural samples with complex composition and wide size distribution range becomes very difficult. The size distribution given in Figures 2 and 7, therefore, has to be considered under these premises. However, even the application of MSD algorithms (e.g., CONTIN) programmed to minimize curvature shows in the intensity-weighted MSD approach a detectable portion of clay colloids in the size range ~90 nm, which might dominate a number size distribution. But it has to be understood that single-angle MSD analysis could possibly generate bi- or multimodal size distributions for a broad unimodal size distribution due to the oscillations in the intensity-weighted average form factor. Therefore, recalculations of number size distributions from intensity size distributions may introduce significant error.

LIBD is a relatively new analytical technique for colloid characterization. Compared to PCS it provides a much higher sensitivity with respect to particle number densities, particle concentration, and particle dimensions. Therefore, LIBD facilitates the detection of colloids smaller than 50 nm down to the nanogram per liter range. In Figure 9, the detection limits of the LIBD are compared with conventional light scattering and PCS. It is evident that the smaller dependency of the LIBD signal on the particle size causes a much higher sensitivity of the LIBD for small colloids compared with PCS. Even though LIBD provides an averaged number-weighted particle size, a particle size distribution is not yet available.

Microscopic techniques have the advantage that both sizes and shapes of particles become visible in the images. Although SEM is a well-established method, it is not very appropriate for the investigation of flat structures with low contrast in atomic number (Figure 8). Furthermore, the colloidal system may be distinctly disturbed by sample preparation steps like drying, evaporation, or coating the sample specimen with a conductive metal layer. The AFM overcomes some of these limitations because nonconducting materials can be directly investigated in air or even in liquids. Particle sizes and shapes can be determined simultaneously from the nanometer to micrometer range. A number-weighted particle size distribution can be calculated from a number of images (Figure 6). Nevertheless, a size distribution obtained in this way is a quite time-consuming procedure and implies relatively poor statistics due to the small number of analyzed particles. Furthermore, distinct artifacts coming from size and shapes of AFM tips have to be taken into consideration. In this study, lateral particle dimensions are corrected according to a simple geometrical approach (Figure 5). After this assumption, the measured particle diameters are overestimated by an average value of 20%. The discussion of tip artifacts will become even more complex if not only sizes and shapes of particles and tips have to be considered but also the fact that the morphology of the tip may change during the measurements. Nevertheless, particle diameters obtained from the AFM number-weighted and mass-weighted particle size distributions (Figures 6 and 7) are in agreement with the corresponding LIBD and FFFF results. However, the major strength of AFM is to visualize morphologies of the nanometer-sized particles. Therefore, necessary information about particle shapes needed by the other methods for an appropriate shape correction is provided.

In contrast to the other methods applied in this study, FFFF is based on a physical fractionation of particles according to their size resulting in a complete size distribution of the bulk of particles in the sample. Combined with ICPMS, the method allows a mass-sensitive particle analysis over a widly linear measuring range that is not provided by light scattering detectors. The relative mass-weighted size distribution obtained from FFFF-ICPMS is in fair agreement with the mass-weighted distribution calculated from AFM particle dimensions (Figure 7). Unfortunately, the symmetric FFFF arrangement used in the present work revealed some drawbacks concerning the high dilution of the sample during fractionation and the presence of contamination sources inside

(41) Müller, R. H.; Schuhmann, R.; Teilchengrössenmessung in der Laborpraxis; Wissenschaftl. Verlagsgesellschaft mbH, Stuttgart, Band 38, 1996.

the channel, both reducing the sensitivity of the method. The contamination source is identified as ceramic frits being corroded, especially in high-pH carrier solutions.[31] This might be improved by modifying the channel components and performing preconcentration steps as is possible with asymmetric FFFF. Therefore, the FFFF-ICPMS combination will determine the element composition of the colloidal species as a function of their size, delivering insight into the chemical properties of the colloidal species.

SUMMARY AND CONCLUSION

In the present paper, sizes of bentonite colloids released into a low ionic strength groundwater are characterized by five different methods, namely, PCS, LIBD, AFM, SEM, and FFFF. It is pointed out that the size information given by the different colloid characterization methods strongly depends on the shape of particles. Therefore, procedures for the consideration of particle shapes are introduced and discussed. Only the shape-corrected size values can be compared in a reasonable way.

As expected for a natural colloid suspension, the FEBEX bentonite sample seems to have a rather broad number size distribution of disklike-shaped particles in the range of 10 to >300 nm. For these size ranges, the analyzing techniques used show different sensitivities and weightings. In the present broad size distribution, PCS typically overestimates the larger sized particles (maximum in the intensity size distributions: >200 nm, depending on the used algorithm). In contrast, AFM and LIBD are focused on the large number of small-sized colloids (mean particle diameters: 73 (AFM) and 67 ± 13 nm (LIBD)). As a matter of principle, these small-sized colloids play a minor role in the mass-weighted intensity distributions (maximum in the distribution curves: 235 (FFFF-ICPMS) and 180 nm (AFM)). Therefore, results obtained by the different analyzing principles are valuable and fairly consistent including more detailed information about the colloidal sample.

The present study emphasizes that complementary results of different analytical methods are required for a reasonable interpretation of more complex colloidal size distributions as typically found in natural aquatic systems.

GLOSSARY

a,b	emperical parameters
A	AFM tip artifact
A_T	maximum particle cross section
ACF	autocorrelation function (PCS)
AFM	atomic force microscopy
B	baseline constant (PCS)
$C(Q,\tau)$	experimental measured autocorrelation function (ACF)
d_h	hydrodynamic diameter (PCS)
d_p	tip or shape-corrected particle diameter (all methods)
d_s	spherical particle diameter related to polystyrene reference particles (LIBD, FFFF)
FFFF	flow field-flow fractionation
$G(\Gamma)$	weight function that gives the relative scattering contribution of the component with decay rate Γ (PCS)
GTS	Grimsel test side
h_p	average particle height (AFM)
$L_z(P)$	effective focal length (LIBD)
LIBD	laser-induced breakdown detection
M	particle mass (ICPMS)
m_p	particle mass of a single particle
n	particle number
$P_{A,crit}$	breakdown threshold (LIBD)
PCS	photon correlation spectroscopy
QC	quadratic cumulant analysis (PCS)
R_t	radius of curvature of an AFM tip
S	AFM tip artifact on one side of a particle
V_p	particle volume
V_r	retention volume (FFFF)
Γ	decay rate of the autocorrelation function
ρ	average particle density
σ	polydispersivity
τ	delay time

Received for review January 24, 2001. Accepted June 7, 2001.

AC010116T

A kinetic study of Am(III)/humic colloid interactions

Environ. Sci. Technol. (2002) **36**(20), 4358.

Artinger R., Schuessler W., Schäfer T., and Kim J. I.

Environ. Sci. Technol. **2002**, *36,* 4358−4363

A Kinetic Study of Am(III)/Humic Colloid Interactions

ROBERT ARTINGER,*
WOLFRAM SCHUESSLER,
THORSTEN SCHAEFER, AND JAE-IL KIM
Forschungszentrum Karlsruhe, Institut für Nukleare Entsorgung, P.O. Box 3640, 76021 Karlsruhe, Germany

The interaction kinetics of the Am(III) ion with aquatic humic colloids is investigated under near-natural conditions by column experiments with a sandy aquifer sample rich in humic substances for the appraisal of the migration behavior of Am. The association and dissociation kinetics of the Am ion onto and from humic colloids control the migration of colloid-borne Am. As the contact time between Am and humic colloids prior to introduction into a column is increased, the mobility of colloid-borne Am is enhanced and hence the recovery of Am in the effluent increases. On the other hand, an increase of the migration time and residence time in column, respectively, reduces the Am recovery. Considering these experimental results a refined version of the kinetic model KICAM (Kinetically Controlled Availability Model), which suggests different Am binding modes with humic colloids, was developed. Applying KICAM it is possible to predict static and dynamic experiments affected by the kinetically controlled Am/humic colloid interactions over the range of 1 h up to several months. However, to apply these experimental results to long-term conditions, the Am binding scheme as proposed in KICAM needs to be verified. This paper provides, therefore, a basis for a better understanding of the colloid-borne Am migration in porous aquifer systems.

Introduction

The behavior of radionuclides in the subsurface aquatic environment is important in the risk assessment of radioactive contaminated sites and in the long-term safety assessment of a deep geological nuclear waste disposal. Field studies in natural aquifers (*1*−*5*) and laboratory experiments (*6*−*10*) have proven that aquatic colloids enhance the mobility of actinides and lanthanides. An essential parameter controlling the colloid-borne migration of radionuclides (or other metal ions in general) is the stability of aquatic radionuclide/colloid complexes. Dissociation of radionuclides from colloids results in radionuclide retardation in aquifers compared to the migration of colloid-bound species. Therefore, knowledge of the kinetic stability of radionuclide colloid complexes in aquatic systems is an important aspect for the predictive description of the radionuclide mobility in subsurface geological media.

Humic substances are major components of aquatic organic colloids and ubiquitous in groundwater. In aquifer systems with lignite deposits, like the Gorleben site (Lower Saxony, Germany), the humic substance concentration in groundwater increases up to 300 mg dm^{-3} (*11*). Multivalent actinide ions are known to form strong complexes with humic substances (e.g. refs *12*−*17*). Whereas the kinetic interaction of divalent cations with humic substances is widely established (e.g. refs *18*−*23*), only a few publications deal with the kinetic stability of multivalent actinide complexes. Cacheris and Choppin (*24*) and Clark (*25*) investigated for Th(IV) and U(VI), respectively, the dissociation kinetics from humic colloids. The experimental data are interpreted by several first-order reactions. Furthermore, an increase in the contact time of the metal ion with humic colloids is found to enhance the kinetic stability of the metal/humic colloid complex. Here, the term contact time comprehends the reaction time between added actinide ion and the groundwater and humic substances, respectively, before the spiked groundwater is introduced into a column. This is shown for Th(IV) (*24*, *26*−*28*), Eu(III) (*29*, *30*), U(VI) (*26*, *30*), and Am(III) (*10*). Therefore, kinetically controlled metal ion/humic colloid interactions have to be considered for the appraisal of the radionuclide migration in aquifers rich in humic colloids (*31*). Column experiments (*10*) have confirmed the significance of kinetic effects for the humic colloid-borne Am migration. The fraction of mobile humic colloid-borne Am is not only controlled by the contact time of Am with humic colloids prior to the introduction into a column but also influenced by the migration time, namely the residence time in the column.

In the following, a kinetic study of Am(III) complexation with humic colloids by column experiments is presented under near natural conditions. The column experiments are designed to investigate the Am/humic colloid association kinetics as well as the dissociation kinetics. The consequences of the kinetically controlled Am/humic colloid interaction for the colloid mediated mobilization of Am(III) are discussed and compared to other studies. A refined chemical reaction scheme based on the Kinetically Controlled Availability Model (KICAM) (*32*) is proposed to describe the experimental results.

Experimental Section

Procedures and Materials. Flow-through column experiments were performed at 22 ± 2 °C under a gas atmosphere of Ar and 1% CO_2 in a glovebox using a column of 250 mm length and 50 mm inner diameter. The column was tightly packed with pleistocene quartz sand obtained from the Gorleben site. The effective pore volume of the column was 167 cm^3 which corresponds to an effective porosity of 33 ± 1%. A detailed characterization of the sand can be found elsewhere (*10*). The column was equilibrated with the Gorleben groundwater GoHy-532 over a period of 3 months. The basic physical parameters and major components of the original and equilibrated groundwater are shown in Table 1. The dissolved organic carbon (DOC) concentration of 29.9 mg dm^{-3} in the original groundwater resulted from reworked Miocene brown-coal deposits and consists of about 90% humic and fulvic acids and 10% hydrophilic compounds according to the isolation procedure with XAD-8 resin (*33*).

Aliquots of an acidic ^{241}Am(III) stock solution of about 10^{-4} mol dm^{-3} were allowed to equilibrate with the groundwater GoHy-532 at neutral pH conditions for a time period from 1 h up to 3.5 a prior to introduction into column. The resulting Am concentration was 5−30 nmol dm^{-3}. Taking into account a proton exchange capacity of 5.4 ± 0.2 (humic acid) and 5.7 ± 0.1 mequiv g^{-1} (fulvic acid), respectively, for the humic substances (*34*), the Am loading on humic colloids was found to be less than 0.1% of the total loading capacity.

* Corresponding author phone: +49-7247-6023; fax: +49-7247-3927; e-mail: artinger@ine.fzk.de.

10.1021/es025594f CCC: $22.00
Published on Web 09/18/2002

TABLE 1. Physical Parameters, Major Ions, and DOC Concentrations of the Original and Equilibrated Groundwater GoHy-532[a]

	GoHy-532 (original)	GoHy-532 (equilibrated)	GoHy-2227 (equilibrated)
pH	8.9	7.5	7.5
Eh [mV]	−160	−50	−250
Na [mmol dm^{-3}]	9.26	9.80	42.8
K [μmol dm^{-3}]	25.3	<10	166
Mg [μmol dm^{-3}]	<10	<10	122
Ca [μmol dm^{-3}]	93.3	12.5	227
Fe [μmol dm^{-3}]	15.6	14.7	41
Cl [mmol dm^{-3}]	3.71	3.78	36.1
HCO_3 [mmol dm^{-3}]	5.48	5.38	7.85
DOC [mg dm^{-3}]	29.9	32.7	102.7

[a] For the purpose of comparison (see text) the composition of equilibrated groundwater GoHy-2227 used in the previous experiments (*10*) is also shown.

TABLE 2. Basic Parameters for the Column Experiments[a]

expt no.	introduced vol [cm^{-3}]	Am concn [mol dm^{-3}]	Darcy velocity v_D [m a^{-1}]	contact time $t_{contact}$ [h]	migration time $t_{migration}$ [h]
1	157	$2.7\cdot10^{-8}$	142	1.9−4.4	5.7
2	307	$3.0\cdot10^{-8}$	60.2	3.7−21.0	12.5
3	343	$2.4\cdot10^{-8}$	21.7	0.7−65.3	34.5
4	1531	$8.5\cdot10^{-9}$	41.2	35−184	18.1
5	262	$2.3\cdot10^{-8}$	142/21.5	1.5−7.6	5.3−36.3
6	340	$5.0\cdot10^{-9}$	632/7.3	31100	1.2−104

[a] The contact time between Am and groundwater is given for the range of the Am breakthrough used for evaluation.

The Am binding onto humic colloids was confirmed by ultrafiltration experiments passing the Am spiked groundwater through polyethersulfone membranes of nominal molecular weight cutoff ranging from 10^3 to 10^6 Dalton (Filtron Co., Microsep Microconcentrators, U.S.A.). As shown in previous work (*10*), the Am species calculation for groundwater GoHy-532 resulted in almost quantitative binding onto humic colloids as Am(HA), Am(OH)HA, and $Am(CO_3)HA$.

The contact time of Am with groundwater was not varied only between different experiments but also in single experiments introducing continuously Am spiked groundwater into a column at a defined flow rate. Accordingly, the Am spiked groundwater introduced last in the column had a longer contact time with Am than at the beginning. To vary the migration time of the colloid-borne Am, the flow rate was abruptly changed during the experiment (exp. nos. 5 and 6). Tritiated water (HTO) was used as a nonsorbing tracer to determine the hydraulic properties of the column. The breakthrough of Am and HTO was measured by single fraction analysis using liquid scintillation counting. In the case of quantitative HTO elution, dispersion effects in the column could be neglected and the Am recovery was directly detectable from the breakthrough curve.

Results

Six column experiments were performed to study the mobility of Am in the presence of aquatic humic colloids. Detailed parameters for all experiments are given in Table 2. In Figure 1 the effect of contact time of Am with groundwater on the Am mobility is shown for the column experiment no. 3. The contact time is varied from 0.7 to 65 h by a slow introduction of the Am spiked groundwater. Whereas the HTO breakthrough is quantitative and remains at a constant value, the elution of humic colloid-borne Am increases with increasing

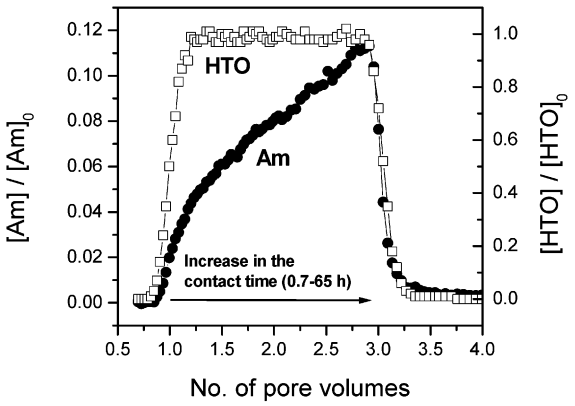

FIGURE 1. Breakthrough curves for ^{241}Am and tritiated water (HTO) in the system GoHy-532/Gorleben sand (experiment no. 3 in Table 2). The breakthrough is shown as ratio of the outlet to the inlet concentrations $[Am]_0$ and $[HTO]_0$, respectively, as a function of the eluted pore volume. For $[HTO]/[HTO]_0 \sim 1$ dispersion effects are negligible and thus the Am recovery can be directly derived from the concentration ratio $[Am]/[Am]_0$. The contact time of ^{241}Am with groundwater prior to column introduction increases during the experiment from 0.7 to 65 h.

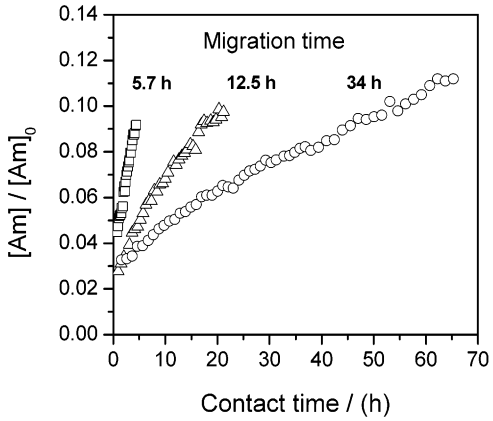

FIGURE 2. Humic colloid-borne ^{241}Am migration in the system GoHy-532/Gorleben sand as a function of the contact time between Am and the groundwater and the migration time (experiments no. 1−3 in Table 2).

the contact time. The humic colloid-borne Am fraction passes the column without retardation about 4 ± 1% ahead of the HTO flow due to the size exclusion effect (*10*). In the range of the $[HTO]/[HTO]_0$ ratio of 1.0 dispersion effects by the water flow are negligible. Accordingly, in this range the $[Am]/[Am]_0$ ratio corresponds directly to the Am recovery, e.g. a $[Am]/[Am]_0$ ratio of 0.3 corresponds a recovery of unretarded humic colloid-borne Am in the effluent of 30% based on the total Am concentration introduced into the column. To determine the Am recovery with increasing breakthrough up to 1.2 pore volume, the dispersion effect (as derived from the HTO signal) had to be taken into account.

Figure 2 summarizes the evaluated data from the column experiments no. 1−3, in which the Am elution, measured as a function of the groundwater volume passed through, is converted into the contact time between Am and groundwater. The influence of the contact time on the Am mobility is examined for three different migration times, 5.7, 12.5, and 34.5 h. In each experiment the mobility of humic colloid-borne Am increases with increasing contact time between Am and humic colloids. On the other hand, an increase of the migration time results in a decrease of mobile Am. When Am is put in contact for 20 h in the GoHy-532 groundwater, the recovery of humic colloid-borne Am

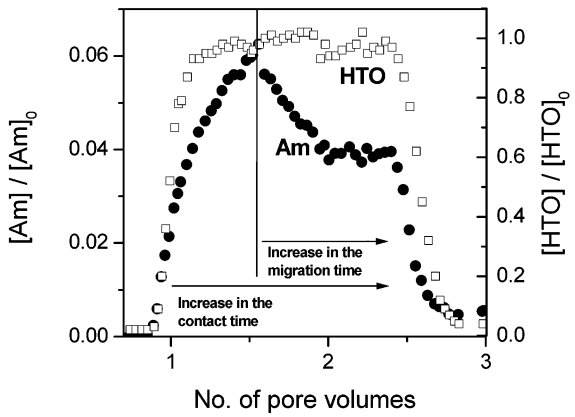

FIGURE 3. ^{241}Am and HTO breakthrough curves in the system GoHy-532/Gorleben sand (experiment no. 5 in Table 2) as a function of the Am/groundwater contact and migration time.

decreases from about 10% at 12.5 h migration to 6% at 34 h migration time. This may be ascribed to a continuous dissociation of Am from humic colloids and subsequent sorption onto the sand surface. A sorption of humic colloids onto the sand surface is unlikely as derived from previous experiments (*35*).

To study the association and dissociation kinetics of the Am/humic colloid complex in a single column experiment (experiment no. 5), both the contact and migration time were varied. The breakthrough behavior of Am and HTO is shown in Figure 3. The dependency on the migration time was obtained by an abrupt reduction of the flow rate (indicated by the vertical line in Figure 3). The Am breakthrough is characterized by two sections: (i) an increase of the eluted Am concentration up to 1.6 pore volumes due to increasing the contact time between Am and humic colloids and (ii) a subsequent decrease of the Am concentration beyond 1.6 pore volumes, which is driven by an increase of the migration time.

Modeling. The column experiments demonstrate primarily the kinetic effects on the Am migration. Therefore, a mechanistic model approach is desirable, taking into account the observed kinetic effects of the Am humic colloid interactions. For this purpose, the Kinetically Controlled Availability Model (KICAM, Figure 4 top) was developed (*32*), which is based on a reaction scheme of dissolved inorganic Am (Am^{inorg}) with two binding modes of humic colloid-bound Am, namely Am(HA^{fast}) and Am(HA^{slow}), suggesting different association and dissociation rates between Am and humic colloids. The rate constants were determined from batch and column experiments using another groundwater GoHy-2227.

Applying the KICAM model to the experimental as presented in Figure 2, a discrepancy was found between the theoretical and experimental results (Figure 5 left). The inset diagram in the left figure emphasizes that the development of the initial KICAM based mainly on data with Am humic colloid contact times longer than 100 h. That accounts for the inadequate description of the experimental data with shorter contact times. To describe the experiment an additional third Am binding mode onto humic colloids, Am($HA^{initial}$), has to be introduced to KICAM (Figure 4 bottom). This is in agreement with the proposed three first-order reactions of the Eu(III) humic colloid dissociation (*29*) and the numerous first-order components of the Th(IV) humic colloid dissociation (*24*). Furthermore, a constant positive 3% offset of the Am recovery was found for short contact times, i.e., 3% of the introduced Am migrates as colloid-borne species without any retardation through the column showing neither a significant association nor a dissociation kinetics with the colloid. From the initial KICAM such an offset is expected, but for a migration time longer than 10 h this offset is only about 1%. Consequently, another colloid-bound Am fraction, Am($Colloid^{stable}$), is introduced in KICAM (Figure 4 bottom). This mobile Am species is considered to be stable bound onto colloids in the time period of the experiment and accounts for the additional offset of 2%. Whether this stable colloid bound Am is also an integral part of the humic colloids or may be attributed to discrete colloidal inorganic entities is unknown. The extended parameter set of the refined KICAM is evaluated from the present experiments no. 1−3 (Figure 5 right) as well as the former Am batch and column experiments (*32*) using the groundwater GoHy-532 and GoHy-2227. The corresponding parameter set is given in Table 3.

The refined KICAM and the determined parameter set are used to calculate experiment no. 5. Each data point in this experiment beyond $V_p = 1.6$ corresponds to different Am/humic colloid contact and migration times. Therefore, the applicability of the refined model can be tested over a defined range of experimental conditions. Both the experimental data and model results are shown in Figure 6. The refined KICAM, which is still based on a chemical reaction scheme proposing different Am binding modes, is able to

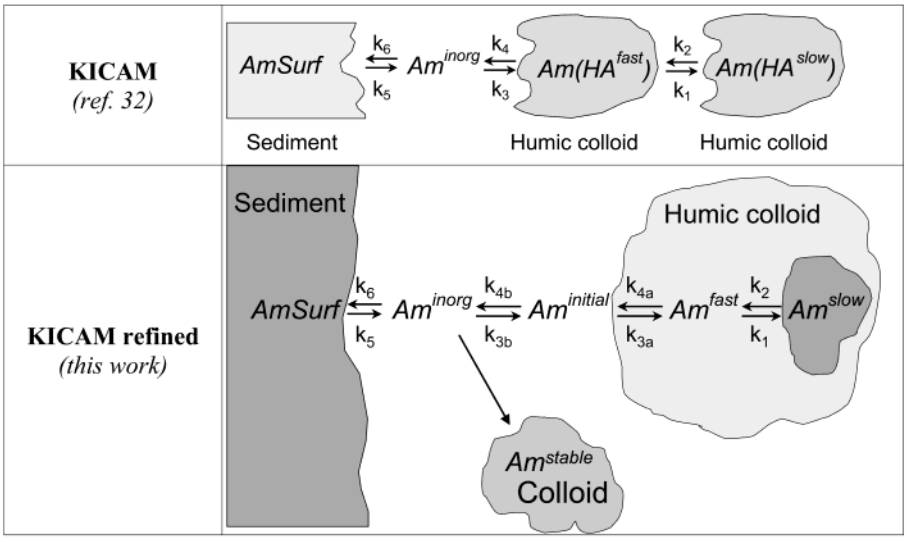

FIGURE 4. Concept of the Kinetically Controlled Availability Model (KICAM). For more details see text and ref *32*.

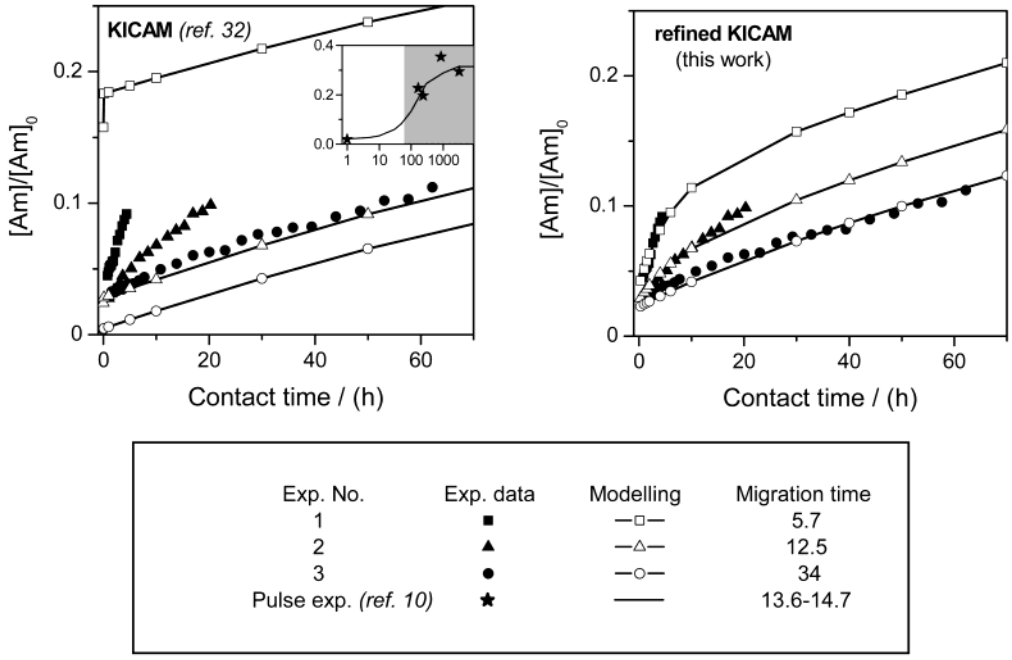

FIGURE 5. Modeling results of experiments no. 1−3 (Figure 2) using initial KICAM (left figure) and the refined version (right figure). The inset diagram in the left figure shows the calibration of KICAM based mainly on data with Am humic colloid contact times longer than 100 h.

TABLE 3. Chemical Reactions and Corresponding Rate Constants Considered in the Refined KICAM (see Figure 4)[a]

$Am(HA^{fast}) \underset{k_2}{\overset{k_1}{\rightleftarrows}} Am(HA^{slow})$	$k_1 = (3.6\cdot10^{-6} \pm 1.3\cdot10^{-6})\ s^{-1}$ $k_2 = (1.5\cdot10^{-6} \pm 0.8\cdot10^{-6})\ s^{-1}$	**(1)**
$Am(HA^{initial}) \underset{k_{4a}}{\overset{k_{3a}}{\rightleftarrows}} Am(HA^{fast})$	$k_{3a} = (8\cdot10^{-6} \pm 4\cdot10^{-6})\ s^{-1}$ $k_{4a} = (4\cdot10^{-5} \pm 2\cdot10^{-5})\ s^{-1}$	**(2)**
$Am^{inorg} + HA \underset{k_{4b}}{\overset{k_{3b}}{\rightleftarrows}} Am(HA^{initial})$	$k_{3b} = (2.5\cdot10^{2} \pm 0.6\cdot10^{2})\ mol^{-1}\ dm^3\ s^{-1}$ $k_{4b} = (3.0\cdot10^{-4} \pm 1.5\cdot10^{-4})\ s^{-1}$	**(3)**
$Am^{inorg} + Colloid \longrightarrow Am(Colloid^{stable})$	$Am(Colloid^{stable}) / Am^{tot} = 0.02 \pm 0.01$	**(4)**
$AmSurf \underset{k_6}{\overset{k_5}{\rightleftarrows}} Am^{inorg} + Surf$	$k_5 = (2\cdot10^{-5} \pm 1\cdot10^{-5})\ s^{-1}$ $k_6 = (3.0\cdot10^{1} \pm 1.5\cdot10^{1})\ mol^{-1}\ dm^3\ s^{-1}$	**(5)**

[a] Near natural column migration experiments are performed to study the colloid facilitated Am(III) transport in a porous aquifer rich in humic substances.

describe satisfactorily the experimental data. This result demonstrates the reproducibility of the kinetic effects of the Am/humic colloid binding in the aquifer system under investigation. Due to the migration velocities used in the experiment a correlation of migration and contact time is defined (Figure 6 top). The application of KICAM using this correlation allows the prediction of the breakthrough curve for an extended experiment (Figure 6 bottom, dotted line). A remarkable observation is the transitional increase of the Am mobility. Although the Am dissociation increases with increasing migration time, the build-up of stable Am humic colloid complexes (increase in contact time) acts as a counterbalance for this time period. However, in the long run the Am dissociation from the humic colloids dominates the build-up of stable Am humic colloid complexes. Therefore, the prediction clearly demonstrates that due to the complex reaction scheme only modeling enables to estimate the breakthrough in such an experiment.

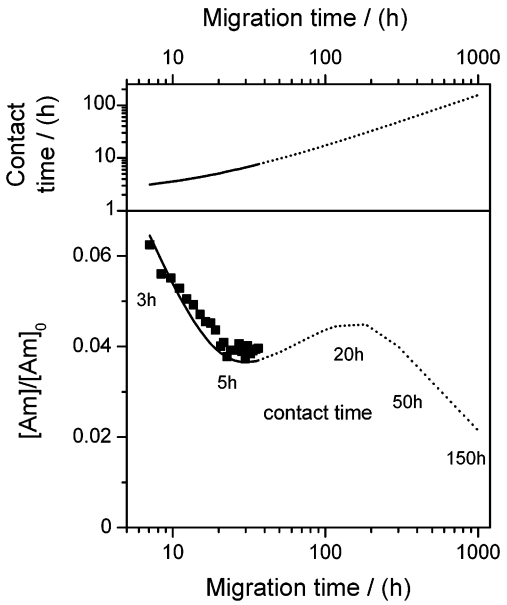

FIGURE 6. Experimental data of the experiment no. 5 (Figure 3) and calculated values of the humic colloid-borne Am migration using the refined KICAM. Each data point corresponds to different Am/humic colloid contact and migration times as pointed out in the attached diagram at the top. This correlation is defined by the different migration times used in the experiment.

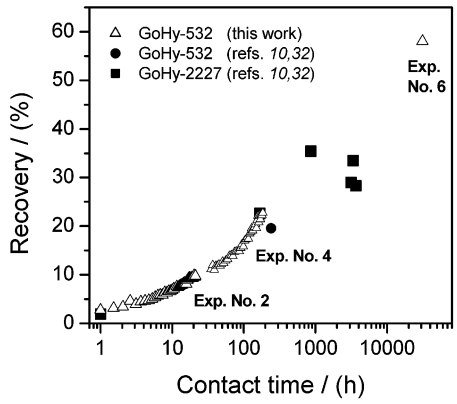

FIGURE 7. Overview of column experiments for the humic colloid-borne ^{241}Am migration as a function of the contact time of ^{241}Am with groundwater GoHy-532 and -2227 (DOC: 100 mg dm^{-3}). Common features of the experiments are as follows: same experimental setup, same Gorleben sand, column length 25−75 cm, pH 7.3−7.6, Darcy velocity 40−100 m a^{-1}, and a migration time between 12.5 and 23 h. GoHy-532 and -2227 data are also taken from refs *10* and *32*.

Discussion

The results of the present experiment show a strong influence of the association and dissociation kinetics of the Am/humic colloid complex on the Am migration in a sandy aquifer. This work corroborate other studies (*36*−*38*), suggesting that humic colloid-borne migration of multivalent metal ions depends for a given contact time exclusively on the migration time. A comparison of this work with former studies (*10*, *32*) made with groundwater GoHy-2227 (Figure 7) points out the reproducibility of the humic colloid-borne Am migration as a function of the Am/humic colloid contact time. Since the previous column experiments were made by pulse injection of 1 cm^3 Am spiked groundwater, the data are depicted on the basis of the integral Am recovery. The mobilization of Am as humic colloid-borne species increases continuously with increasing the contact time from 1 h to more than 3 years (Am recovery rises from about 3 to 58%) for both Gorleben groundwater GoHy-532 and -2227.

The influence of the contact time between Am and humic colloids is essential for the mechanistic understanding of the humic colloid-mediated Am migration. According to KICAM, the initial association rate constant k_{3b} between the added Am^{inorg} and the aquatic humic colloids is fast reflecting the observed instantaneous Am humic colloid complexation ($Am^{initial}$). Since $Am^{initial}$ shows a distinct disintegration as well, it has not to be considered for the long-term contact effect in the migration experiments with time periods from hours to years. Contrary to k_{3b}, the rate constants k_{3a} and k_1 result in the more kinetic stable binding modes Am^{fast} and Am^{slow}. They are significantly lower, compared to k_{3b}, and thus have to be considered for the contact effect. However, the process accounting for this contact effect is not clear. The following processes and their implementation in KICAM could explain the kinetics involved in the observed Am/humic colloid interaction:

(i) Structural rearrangements of humic molecules result in an Am binding in the interior of humic molecules. This kinetically controlled process may cause an enhanced steric shielding of Am versus the solution and sand surface, respectively, and thus decrease the rate constant of the Am dissociation with the increase in contact time. In consequence of that, in KICAM the binding modes Am^{fast} and Am^{slow} would be concerned. As reason for such a rearrangement Engebretson and von Wandruszka proposed the cation-enhanced formation of hydrophobic domains in humic colloids (*18*, *39*).

(ii) The metal ion charge neutralization process induces the agglomeration of several humic molecules (*40*) and surround the Am within the humic aggregate. Consequently, the Am humic colloid interaction is superposed by the kinetics of the agglomeration and separation of the humic molecules (intermolecular process). In KICAM the rate constant k_{3b} would reflect the fast primary charge neutralization and complexation process, respectively, and k_{3a} and k_1 the subsequent much slower agglomeration kinetics. Such a serial reaction pathway is also proposed by Quigley at al. (*28*) for the Th sorption onto marine colloidal organic matter. The corresponding rate constants for the disintegration of the Am humic agglomerates in KICAM are k_2 and k_{4a}. The image with metal ions as an integral part of an humic agglomerate was recently published by Simpson et al. (*41*). Simpson et al. showed that humic substances are an agglomerate of relatively low molecular weight molecules, instigated most likely by complexation with metal cations.

(iii) Due to the heterogeneous nature of humic substances Am may be bound to different binding sites with different interaction kinetics. This is exemplary proposed for the binding of UO_2^{2+} onto humic substances (*42*, *43*). However, the image of different binding sites with different interaction kinetics is not considered in KICAM showing an interdependence of these sites.

(iv) Am is not only bound to proton exchanging organic ligands within the humic molecule but also sorbed onto nanoscopic inorganic mineral phases stabilized by the humic colloids. These inorganic mineral phases may interact with Am with a kinetics that differs from that of the organic ligands. Such a colloid bound fraction is implemented in KICAM with Am^{stable} as stable colloid bound Am within the time period of the experiment. Humic colloid stabilized inorganic minerals may also account for the different dissociation rates found for added and naturally bound actinides and homologues (*44*). It is assumed that the slower desorption rates of naturally bound metal ions (e.g. Eu(III), Th(IV), U(VI)) are attributed to binding and inclusion in nanoscopic mineral phases.

Applying KICAM the experimental data in the given Gorleben groundwater sand system can be described satisfactorily for any combination of different Am humic colloid contact and migration times within a period from hours up to some months. The slowest Am dissociation rate is in the range of weeks, which is also reported for Eu(III) (*29*, *37*), Th(IV) (*26*, *28*), and U(VI) (*26*). This indicates that the multivalent actinide humic colloid interactions is possibly dominated by structural arrangements of the humic colloids (induced by charge neutralization) and not by the rapid reversible binding to functional groups. Thus, the specific properties of humic colloids and agglomerates, respectively, possibly influences the actinide dissociation in the kinetically hindered binding mode more than the overall thermodynamical stability. However, the knowledge on the processes accounting for the Am/humic colloid interaction kinetics is still insufficient, and a varying fraction of multivalent cations remains in humic colloids even after weeks to months (*26*, *29*).

In laboratory investigations the existence of very slow dissociation rates $<10^{-8}$ s^{-1} for actinides is hard to verify, and in case of batch experiments (with simultaneous association and dissociation) it is also difficult to distinguish between slow kinetics and equilibrium. Accordingly, a prediction of the humic colloid-borne Am migration for longer time periods as investigated in the laboratory is not possible so far. Therefore, future studies should focus on the mechanism of the metal humic colloid binding. The slow dissociation for actinides is of special interest, as the more stable actinide humic colloid complexes are expected to be more mobile in an aquifer. However, an overall chemical reaction scheme for the actinide humic colloid interactions must be the long-term objective, as it is the precondition for the concluding assessment of the colloid facilitated radionuclide subsurface migration.

Acknowledgments

The authors gratefully acknowledge Mr. Klotz at GSF-National Research Center for Environment and Health for his help in designing the column experiments and Mrs. Schlieker for her assistance in performing the experiments. The authors would like to thank Mr. Buckau for all his countless valuable discussions.

Literature Cited

(1) Buddemeier, R. W.; Hunt, J. R. *Appl. Geochem.* **1988**, *3*, 535−548.
(2) Marley, N. A.; Gaffney, J. S.; Orlandini, K. A.; Cunningham, M. M. *Environ. Sci. Technol.* **1993**, *27*, 2456−2461.
(3) McCarthy, J. F.; Czerwinski, K. R.; Sanford, W. E.; Jardine, P. M.; Marsh, J. D. *J. Contam. Hydrol.* **1998**, *30*, 49−77.
(4) Kaplan, D. I.; Bertsch, P. M.; Adriano, D. C.; Orlandini, K. A. *Radiochim. Acta* **1994**, *66/67*, 181−187.
(5) Kersting, A. B.; Efurd, D. W.; Finnegan, D. L.; Rokop, D. J.; Smith, D. K.; Thompson, J. L. *Nature* **1999**, *397*, 56−59.
(6) Saltelli, A.; Avogadro, A.; Bidoglio, G. *Nucl. Technol.* **1984**, *67*, 245−254.
(7) Kim, J. I.; Delakowitz, B.; Zeh, P.; Klotz, D.; Lazik, D. *Radiochim. Acta* **1994**, *66/67*, 165−171.
(8) Randall, A.; Warwick, P.; Lassen, P.; Carlsen, L.; Grindrod, P. *Radiochim. Acta* **1994**, *66/67*, 363−368.
(9) Nagasaki, S.; Tanaka, S.; Suzuki, A. *J. Nucl. Mater.* **1997**, *248*, 323−327.
(10) Artinger, R.; Kienzler, B.; Schuessler, W.; Kim, J. I. *J. Contam. Hydrol.* **1998**, *35*, 261−275.
(11) Artinger, R.; Buckau, G.; Geyer, S.; Wolf, M.; Fritz, P.; Kim, J. I. *Appl. Geochem.* **2000**, *15*, 97−116.
(12) Kribeck, B.; Podlaha, J. *Organ. Geochem.* **1980**, *2*, 93.
(13) Czerwinski, K. R.; Buckau, G.; Scherbaum, F.; Kim, J. I. *Radiochim. Acta* **1994**, *65*, 111−119.
(14) Torres, R.; Choppin, G. R. *Radiochim. Acta* **1984**, *35*, 143.
(15) Kim, J. I.; Buckau, G.; Bryant, E.; Klenze, R. *Radiochim. Acta* **1989**, *48*, 135−143.
(16) Maes, A.; De Brabandre, J.; Cremers, A. *Radiochim. Acta* **1991**, *52/53*, 41−47.
(17) Nash, K. L.; Choppin, G. R. *J. Inorg. Nucl. Chem.* **1980**, *42*, 1045−1050.
(18) Engebretson, R. R.; Von Wandruszka, R. *Environ. Sci. Technol.* **1998**, *32*, 488−493.
(19) Bonifazi, M.; Pant, B. C.; Langford, C. H. *Environ. Technol.* **1996**, *17*, 885−890.
(20) Burba, P.; Rocha, J.; Klockow, D. *Fresenius J. Anal. Chem.* **1994**, *349*, 800−807.
(21) Langford, C. H.; Cook, R. L. *Analyst* **1995**, *120*, 591−596.
(22) Sekaly, A. L. R.; Chakrabarti, C. L.; Grégoire, D. C. In *Proceedings of EnviroAnalysis, Biennial International Conference on Chemical Measurement and Monitoring of the Environment*; Carleton University: 1998; pp 611−618.
(23) Chakrabarti, C. L.; Lu, Y.; Grégoire, D. C.; Back, M. H.; Schroeder, W. H. *Environ. Sci. Technol.* **1994**, *28*, 1957−1967.
(24) Cacheris, W. P.; Choppin, G. R. *Radiochim. Acta* **1987**, *42*, 185−190.
(25) Clark, S. B. *The kinetics of uranyl-humic acid dissociation*; M.S. Thesis, Florida State University, 1987.
(26) Davis, J.; Higgo, J.; Moore, Y.; Milne, C. In *Effects of humic substances on the migration of radionuclides: complexation and transport of actinides. Second technical progress report*; Report FZKA 6324; Buckau, G., Ed.; Research Center Karlsruhe: Karlsruhe, 1999.
(27) von Wandruszka, R.; Ragle, C.; Engebretson, R. R. *Talanta* **1997**, *44*, 805−809.
(28) Quigley, M. S.; Santschi, P. H.; Guo, L.; Honeyman, B. D. *Mar. Chem.* **2001**, *76*, 27−45.
(29) King, S. J.; Warwick, P.; Hall, A.; Bryan, N. D. *Phys. Chem. Chem. Phys.* **2001**, *3*, 2080−2085.
(30) Rao, L.; Choppin, G. R.; Clark, S. B. *Radiochim. Acta* **1994**, *66/67*, 141−147.
(31) van de Weerd, H.; Leijnse, A. *J. Contam. Hydrol.* **1997**, *26*, 245−256.
(32) Schuessler, W.; Artinger, R.; Kienzler, B.; Kim, J. I. *Environ. Sci. Technol.* **2000**, *34*, 2608−2611.
(33) Thurman, E. M. In *Humic substances in soil, sediment, and water*; Aiken, G. R., MacCarthy, P., Eds.; Wiley: 1985; pp 87−103.
(34) Kim, J. I.; Buckau, G.; Li, G. H.; Duschner, H.; Psarros, N. *Fresenius, J. Anal. Chem.* **1990**, *338*, 245−252.
(35) Artinger, R.; Seibert, A.; Marquardt, C. M.; Trautmann, N.; Kratz, J. V.; Kim, J. I. *Radiochim. Acta* **2000**, *88*, 609−612.
(36) Klotz, D.; Lazik, D. *Isotopes Environ. Health Stud.* **1995**, *31*, 61−75.
(37) Klotz, D.; Wolf, M. In *Effects of humic substances on the migration of radionuclides: complexation and transport of actinides. First technical progress report*; FZKA 6124; Buckau, G., Ed.; Karlsruhe, 1998.
(38) Artinger, R.; Rabung, T.; Kim, J. I.; Sachs, S.; Schmeide, K.; Heise, K. H.; Bernhard, G.; Nitsche, H. *J. Contam. Hydrol.* **2002**, *58*, 1−12.
(39) Engebretson, R. R.; Von Wandruszka, R. *Environ. Sci. Technol.* **1994**, *28*, 1934−1941.
(40) Plaschke, M.; Römer, J.; Klenze, R.; Kim, J. I. *Surf. Interface Anal.* **2000**, *30*, 297−300.
(41) Simpson, A. J.; Kingery, W. L.; Hayes, M. H. B.; Spraul, M.; Humpfer, E.; Dvortsak, P.; Kerssebaum, R.; Godejohann, M.; Hofmann, M. *Naturwissenschaften* **2002**, *89*, 84−88.
(42) Munier-Lamy, C.; Adrian, P.; Berthelin, J.; Rouiller, J. *Org. Geochem.* **1986**, *9*, 285−292.
(43) Giesy, J. P.; Geiger, R. A.; Kevern, N. R.; Alberts, J. J. *J. Environ. Radioactivity* **1986**, *4*, 39−64.
(44) Geckeis, H.; Rabung, T.; Ngo Manh, T.; Kim, J. I.; Beck, H. P. *Environ. Sci. Technol.* **2002**, *36*, 2946−2952.

Received for review February 20, 2002. Revised manuscript received July 16, 2002. Accepted August 5, 2002.

ES025594F

U, Th, Eu and colloid mobility in a granite fracture under near-natural flow conditions.

Radiochim. Acta. (2004) **92**, 731.

Schäfer T., Geckeis H., Bouby M., and Fanghänel T.

Radiochim. Acta **92**, 731–737 (2004)

U, Th, Eu and colloid mobility in a granite fracture under near-natural flow conditions

By Thorsten Schäfer*, Horst Geckeis, Muriel Bouby and Thomas Fanghänel

Forschungszentrum Karlsruhe, Institut für Nukleare Entsorgung (INE), P.O. Box 3640, D-76021 Karlsruhe, Germany

(Received October 20, 2003; accepted March 8, 2004)

Radionuclide / Colloid / Bentonite / Carboxylated microspheres / Granite fracture / Migration experiments

Summary. Laboratory core migration experiments were performed in a granite fracture from the Grimsel Test Site (GTS, central Swiss Alps). The flow velocity was varied (46 m yr^{-1}, 94 m yr^{-1}, 187 m yr^{-1}) and solutions with 10^{-6} mol L^{-1} U(VI), 10^{-8} mol L^{-1} Th(IV) and 10^{-8} mol L^{-1} Eu(III) without (cocktail I) and with addition of 2 mgL^{-1} bentonite colloids (cocktail II) have been injected. Results are compared with those obtained in a field study at the GTS. Flow field-flow fractionation and ultrafiltration measurements show that U(VI) is not colloid borne, different from Th(IV) and Eu(III) which are associated with colloids in both spiked natural groundwaters with and without bentonite colloid addition. The partly unretarded U(VI) migration observed at short contact times (1–2 h) diminished under near-natural groundwater velocities ($\sim$ 46 m yr^{-1}) and only a weak retardation ($R_f = 19.5$) could be observed. Furthermore, the U(VI) mass recovery decreased with increasing contact time and was as expected unaffected by bentonite colloid addition. A groundwater colloid mediated Th(IV)/Eu(III) migration without bentonite colloid addition could be confirmed in the core experiments but only at fast groundwater flow rates. Experiments at a water flow rate of 94 m yr^{-1} with cocktail II demonstrated a partially bentonite colloid facilitated transport of Th(IV) and Eu(III) with 27% and 37% mass recovery, respectively. At long tracer residence times in the flow field, no breakthrough of colloidal Th(IV)/Eu(III) could be observed in both runs, indicating the strong dependence of reaction kinetics on their mobility. Reference colloid experiments using fluorescence dye labeled carboxylated polystyrene microspheres (25 nm, 50 nm and 100 nm) revealed in general a higher recovery of smaller colloid size classes increasing with groundwater velocity. Additionally, an earlier peak arrival time of colloids and colloid-associated Th(IV) and Eu(III) was observed with respect to the conservative tracer ^{3}H in all experiments due to pore-size or charge exclusion effects. In general, the colloid recoveries found in the laboratory core experiments are lower than those obtained in the field studies. The decrease of colloid mobility with increasing residence time suggests the occurrence of colloid attachment to the rock surfaces even under the colloid stabilizing groundwater conditions.

*Author for correspondence
(E-mail: thorsten.schaefer@ine.fzk.de).

1. Introduction

Transport of colloidal and dissolved species in saturated porous media or fractured rock has been a field of research during the last decade from both the experimental and the modeling viewpoint [1–5]. Large granite block scale experiments [6] as well as field migration studies [7, 8] have demonstrated the mobility of inorganic colloids. However, the sensitivity of colloidal transport on average flow velocity, colloid size [6] and colloid concentration [9] point out the general problem of field-scale experiments designed with groundwater flow velocities or colloid concentrations often orders of magnitude higher than found under natural hydraulic conditions (*e.g.* < 2 m yr^{-1} in Whiteshell research area [9]).

The *in situ* colloid migration experiments performed at the Grimsel Test site (GTS, central Swiss Alps) within the CRR (Colloid Radionuclide Retention) international joint project have demonstrated the mobility of injected Febex (full-scale engineered barrier experiment) [10] bentonite colloids in a 2.23 m length test shear zone under the given hydrodynamic conditions (injection borehole BOCR 99.002 10 mL min^{-1}; extraction borehole BOMI 87.010 150 mL min^{-1}; linear groundwater velocity $\sim$ 39 m d^{-1}) [7]. Furthermore these detailed investigations showed that even without the addition of bentonite colloids the transport of tri- and tetravalent radionuclides occurred with groundwater colloids found in the Grimsel groundwater [7]. This finding is in line with the pronounced stability of the colloids in the low ionic strength ($I = 10^{-3}$ mol/L) and high pH ($\sim$ 9.6) Grimsel groundwater. Dissolved Np(V) and U(VI) revealed a partly unretarded transport under the given experimental conditions. There are some indications that these findings may be influenced by the fast flow-field conditions. Field investigations to elucidate the effect of sorption kinetics under variation of flow velocity are however difficult to interpret due to possible changes in the 3D flow path geometry.

The aim of the ongoing laboratory studies presented in this paper is, therefore, to elucidate the effect of groundwater velocity or tracer residence time in the flow-field on the mobility of dissolved species, colloids and colloid associated lanthanides/radionuclides. The results are compared with the results of the *in situ* study performed under comparably high groundwater velocities. Experiments with carboxylated

colloids of different size were carried out to evaluate the size impact on colloid migration.

2. Materials and methods

2.1 Laboratory core experimental set-up

Laboratory migration studies are performed under argon inert gas atmosphere in a glove box (Fig. 1). The core used for the laboratory migration studies was provided by the Nationale Genossenschaft für die Lagerung radioaktiver Abfälle (NAGRA) (core CRR-FZK-2) extracted from the extension of the CRR neighborhood shear zone AU 126 from the VE gallery, tunnel meter L 463. The host rock of the shear zone is the medium to coarse grained Grimsel granodiorite, overprinted by ductile structures (mylonite) and brittle deformation. The brittle deformation caused a destruction of the mylonitic fabric, formation of fault gauge and the generation of preferential flow paths [11]. The over-cored fracture zone is approximately 2 cm thick and filled with natural infill minerals. The average mineralogical composition of this fault gauge material shows an increase in biotite content (41 vol. %), albite content (28 vol. %) and detectable amounts of clay minerals (0–1 vol. %) compared to the granodiorite host rock [11]. The core was drilled with a special 11 cm ring and 3 cm over-coring and resin polymerization technique, which however cannot completely prevent expansion of the over-cored natural fracture due to host rock pressure release [12]. The uneven core edges resulting from tearing out the core were sawed and flattened. Finally the core was cut into a section of 0.315 m length and a slab of 0.02 m length, later referred to as core #2 and core #3. All tubing and injection devices used for the migration studies are of PEEK (polyether etherketone) type. Metal ion sorption to tubing walls was found negligible under given conditions [13].

The groundwater used throughout the experiments was sampled under inert gas conditions in 50 L Teflon coated stainless steel barrels from the borehole (BOMI 87.010) in the Grimsel underground laboratory and transferred directly to the laboratory. The chemical composition of the sampled groundwater is listed in Table 1. *In situ* colloid analysis at the GTS and characterization of the sampled groundwater in the laboratory by laser induced breakdown detection (LIBD) revealed number weighted average diameters of 91 nm and 112 nm, respectively. Colloid concentrations were at 3.2 $\mu g\,L^{-1}$ (*in-situ*) and at 6.8 $\mu g\,L^{-1}$ (barreled water). Both results point to the negligible influence of the sampling procedure and storage on the groundwater colloid concentration.

Injection was performed by 100 µL Dirac-type pulses or permanent injection, as indicated for each experiment in Table 2. Tritiated water (^3H) is taken as a non sorbing tracer throughout this study. In the field migration studies iodide ($^{131}I^-$) or uranine was used [7].

Table 1. Composition of the Grimsel groundwater (borehole BOMI 87.010).

Element	concentration (µmol/L)
Na^+	530
K^+	4.1
Li^+	11.3
Ca^{2+}	203
Mg^{2+}	0.32
Sr^{2+}	2.25
Al^{3+}	0.42
Cl^-	173
SO_4^{2-}	50.8
NO_3^-	2.1
PO_4^{3-}	n.d.
F^-	339
Fe_{TOT}	n.d.
Mn^{2+}	29.0
DOC	$1.2 \pm 0.2\,mg\,L^{-1}$
DIC	$3.4\,mg\,L^{-1}$
pH	9.6

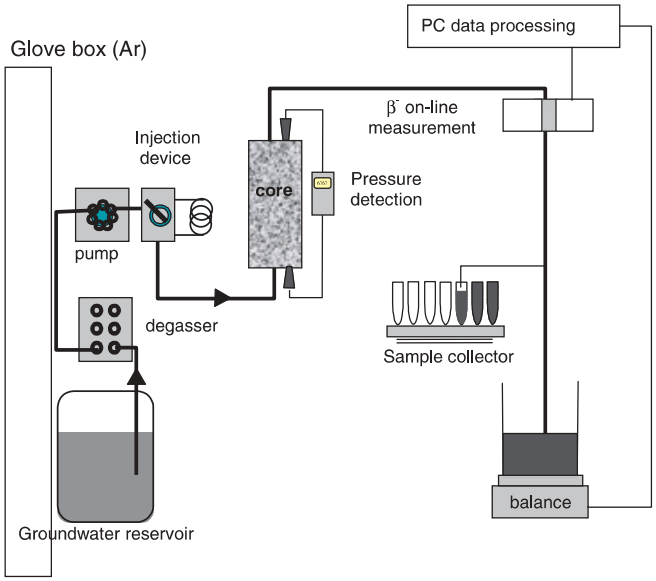

Fig. 1. Setup of core migration experiments under argon inert gas conditions in a glove box.

2.2 Colloid types and preparation

Febex bentonite colloid suspension was prepared by repeating five times cycles of suspending, centrifuging, decanting the supernantant and re-suspending the settled solid with an ultrasonic-tip [11] in Grimsel groundwater. The final suspension had a pH value of 9.2, a specific conductivity of 117 $\mu S\,cm^{-1}$ and a gravimetrically determined concentration of $540 \pm 57\,mg\,L^{-1}$. Dissolved organic carbon (DOC) measurements revealed a bentonite colloid associated organic matter content of 0.56 wt. % carbon [14]. For the colloid migration experiments the bentonite concentration was adjusted to $2\,mg\,L^{-1}$. The average number weighted size of bentonite colloids determined by LIBD is 105 nm and the intensity weighted average hydrodynamic diameter d_H measured by photon correlation spectroscopy (PCS) is 202 ± 43 nm. The size difference obtained by both methods is due to extensive dependency of scatter light intensity on the colloid size, different to the LIBD signal. The intensity weighted size obtained by PCS, therefore, tends to overemphasize the larger particles in the dispersion (see detailed

Table 2. Results of the migration experiments; ($v_{a,dom}$ represents the dominant linear groundwater velocity determined from the maximum of the ^{3}H-breakthrough curve).

Experiment number	Core number	Core length	Injected elements/colloids	Injected volume	Flow velocity $v_{a,dom}$	Recovery
C2-I	2	31.5 cm	^{3}H	72.2 mL	0.128 m d^{-1}	> 99%
C2-II	2	31.5 cm	U	144.0 mL	0.128 m d^{-1}	7% after 80 d
			Th			n.d.
			Eu			n.d.
C3-III	3	2 cm	U	48.5 mL	0.52 m d^{-1}	85% after 24 d
			Th			28% after 24 d
			Eu			24% after 24 d
C3-IV	3	2 cm	^{3}H	0.100 mL	0.52 m d^{-1}	> 99%
C3-V	3	2 cm	U	0.100 mL	0.52 m d^{-1}	> 90% after 5 d
			Th			n.d.
			Eu			n.d.
C3-VII	3	2 cm	U	0.100 mL	0.26 m d^{-1}	14% after 5 d
			Th			n.d.
			Eu			n.d.
C3-VIII	3	2 cm	U	0.100 mL	0.26 m d^{-1}	11% after 5 d
			Th			27% after 5 d
			Eu			37% after 5 d
			2 mg L^{-1} bentonite colloids			not possible
C3-IX	3	2 cm	Polystyrene coll.	0.100 mL	0.26 m d^{-1}	
			50 nm			n.d.
			25 nm			10% after 1 d
			100 nm			34% after 1 d
C3-X	3	2 cm	Polystyrene coll.			
			25 nm	0.100 mL	0.52 m d^{-1}	48% after 1 d

discussion in [15]). The result also indicates the presence of a rather broad bentonite colloid size distribution.

In addition, to investigate the effect of polydispersivity on colloid transport and mobility, migration experiments with mixtures of well defined spherical carboxylated fluorescence polystyrene colloids (25 nm, 50 nm and 100 nm; Postnova analytics) were performed. For these migration experiments, separate solutions with the individiual colloid types were prepared with concentrations adjusted to 10 mg L^{-1} for each size class. Different colloid size classes of the polystyrene colloid mixtures were detected with a SLM-Aminco Bowman Series 2 luminescence spectrometer using the excitation and emission wavelengths of the fluorescence dye given by the manufacturer.

2.3 Colloid and radionuclide/lanthanide cocktail preparation and characterization

Prior to column injection, the lanthanide cocktails were prepared by adding aliquots of U, Th and Eu standard solutions (1000 μg/ml) to Grimsel groundwater and readjusting the pH with NaOH to pH 9.6. Two injection cocktails were prepared by this way:

Cocktail I:

1×10^{-6} mol/L U; 1×10^{-8} mol/L Th;

1×10^{-8} mol/L Eu.

Cocktail II:

1×10^{-6} mol/L U; 1×10^{-8} mol/L Th;

1×10^{-8} mol/L Eu + 2 mg L^{-1} bentonite colloids.

Cocktail characterization included ultrafiltration using polyethersulfone membranes of a nominal molecular weight cut-off ranging from 10^3 to 10^6 Dalton (Filtron Co., Microsep Microconcentrators). In parallel, aliquots of the cocktail II are characterized by the asymmetric flow-field flow fractionation (AsymFFFF, Postnova Analytics, HRFFF 10.000 AF4) coupled with ICP-MS (Perkin Elmer, ELAN 6000) [16, 17]. Column outlet fractions of the migration experiments as well as ultrafiltration aliquots were analysed by ICP-MS (Perkin Elmer ELAN 6100).

3. Results and discussion

3.1 Injection cocktail characterization

The ultrafiltration of the injection cocktails with and without bentonite colloid addition (Fig. 2) shows clearly that U(VI) can be found in both cocktails as dissolved species with > 70% of the concentration passing the 1 kDa filter. In the case of the injection solution without bentonite addition (cocktail I) only 50% and 30% of Th and Eu, respectively, pass the 1000 kDa filter indicating that a major fraction of these elements is associated to > 1000 kDa colloidal phases in the groundwater or is sorbed to the filter membrane. The results are consistent with ultra-centrifugation studies on similar solutions containing Pu(IV)/Th(IV) and Am(III) at comparable concentrations [7]. Th and Eu concentrations are close to the solubility limits as has been calculated for Th and Am in the Grimsel groundwater (10^{-8} mol/L Th(IV) and 10^{-7} mol/L Am(III)) [18]. The Eu(III) solubility is assumed to be comparable to that of Am(III). The formation of Th/Eu hydroxide colloids cannot be excluded a priori either by exceeding solubility limits or by local over-saturation during the spiking procedure. Time-resolved laser fluorescence spectroscopy studies [14] point to the formation of trivalent actinide-colloid surface complexes.

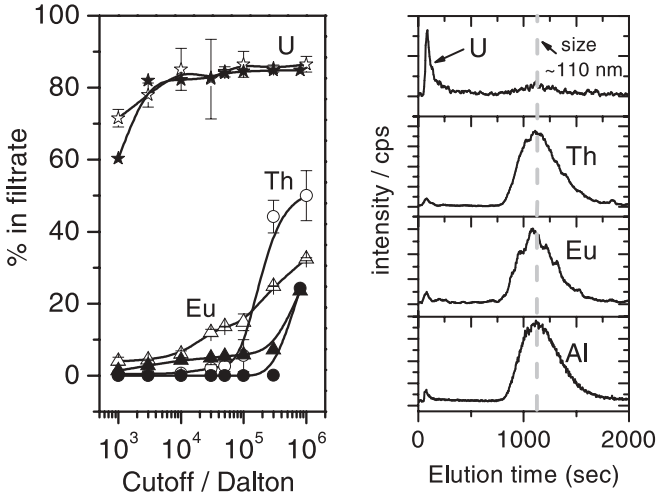

Fig. 2. Left: Ultrafiltration of cocktail I (U open stars, Th open circles and Eu open triangles) without Febex bentonite colloids and of cocktail II after 2 mg L^{-1} Febex bentonite colloid addition (filled symbols). Right: Results of the AsymFFFF analysis of cocktail II showing a clear association of Eu and Th with bentonite colloids (Al signal) and no association of U eluting in the void peak as dissolved species.

However, the groundwater colloid concentration determined by LIBD ($\sim 7\,\mu g\,L^{-1}$) is considered too low to account for adsorbing all Th(IV) and Eu(III). Under the assumption of spherical colloid shape, a distribution coefficient K_d of 2×10^6 ml/g (Am(III) K_d value to bentonite colloids; see [13]) and the above mentioned groundwater colloid concentration the calculated natural groundwater colloid bound Th and Eu fraction should be below 5%. However, we usually observe an increase of the colloid and Al concentration, taken as an indicator element for the presence of aquatic colloids, during handling of solution in glove boxes and after metal ion spiking to the groundwater. Therefore, we presently cannot exclude that the colloids bearing Th(IV) and Eu(III) may also be partly generated by contamination. Ultrafiltration results of cocktail II with 2 mg L^{-1} added Febex bentonite colloids (Fig. 2, filled symbols) revealed a clear shift to larger colloid sizes with only $\sim 20\%$ of Th and Eu passing the 1000 kDa filter. Additional experiments performed with AsymFFFF coupled to ICP-MS analysis corroborate the ultrafiltration results (Fig. 2, right). Eu(III) and Th(IV) elute together with Al representing the bentonite colloids of 110 nm mean colloid size. In the case of U(VI) only a minor fraction elutes in the region of the bentonite colloids showing a negligible association with them. The major part elutes in the void peak as dissolved species.

3.2 Breakthrough behavior of U(VI), Th(IV) and Eu(III) (cocktail I)

In the pulse injection experiments of cocktail I under variation of the flow velocity only a breakthrough of U(VI) could be detected (Fig. 3). No breakthrough was observed for Th(IV) and Eu(III) in four days. At a tracer residence time of ~ 1 h U(VI) recoveries of $> 90\%$ were obtained in the core experiments (C3-V, Table 2) (Fig. 3a) and in the field [11, 14]. Almost unretarded migration was observed in both experiments. The pronounced tailing of the U(VI) breakthrough curve in the present experiment as compared to that of the conservative tracer (Fig. 3a) and the additional hump indicate a retarded fraction with a R_f of approx. 14.6. Changing the flow velocity and therefore the tracer residence time to 5 h (C3-VII, Table 2) decreased the unretarded U(VI) fraction to 14% recovery (Fig. 3b). A retarded fraction could not be resolved from the background signal in this experiment. To study the U(VI) breakthrough behavior under near-natural flow conditions (56 h contact time or flow velocity ~ 46 m yr^{-1}), a continuous pulse injection experiment in core #2 was performed (C2-II; Table 2). No unretarded fraction could be observed (Fig. 3c). U(VI) was eluted with a retarded fraction of $R_f = 20$. The peak maximum of the U(VI) breakthrough can be observed after 42 days and the U(VI) recovery after 80 d could be quantified to be above 7%. The calculated distribution coefficient K_d based on the experimental determined retardation factor R_f with the following formula:

$$R_f = 1 + \frac{\rho_b K_d}{\Theta}\,, \tag{1}$$

where ρ_b is the bulk density (2.6 g cm^{-3}) and Θ the matrix porosity (0.2; increased matrix porosity acc. to [19]) revealed K_d values of 0.7 to 1.1 ml g^{-1} for the retarded U(VI) fraction in all experiments. Such findings are consistent with K_d values of 0.5 ml g^{-1} obtained by [20] for ^{233}U migration studies on crushed fault gauge material and are in fair agreement with K_d values around 5 ml g^{-1} obtained in batch

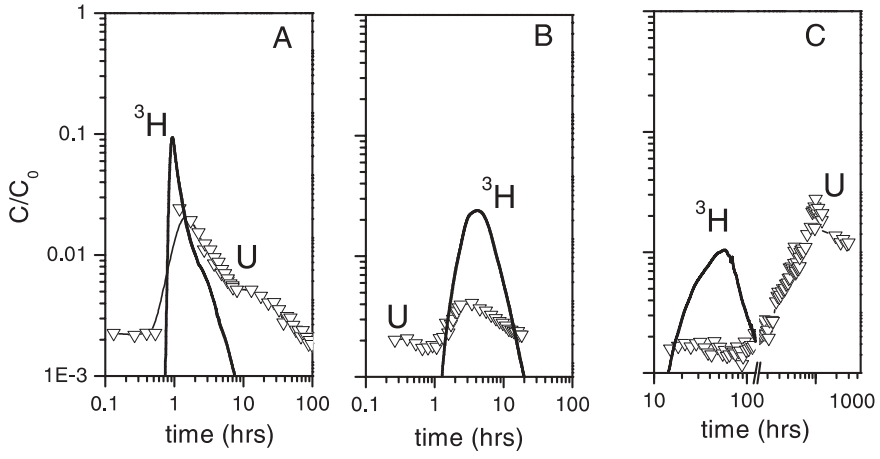

Fig. 3. Pulse and permanent injection breakthrough curves of tritiated water (solid line) and U (open triangles). (**a**) 100 µL pulse injection into the 2 cm long fracture (core #3) $v_a = 0.52$ m d^{-1}, (**b**) 100 µL pulse injection into the 2 cm long fracture (core #3) $v_a = 0.26$ m d^{-1}, (**c**) 144 mL permanent injection into the 31.5 cm long fracture (core #2) $v_a = 0.128$ m d^{-1}. For details see Table 2.

experiments with fracture infill material [14]. The only weak U(VI) sorption to surfaces can be explained by the presence of anionic carbonato complexes [18]. The existence of an unretarded U(VI) fraction at increased groundwater flow is thus due to the low collision probability of dissolved species with the fracture surfaces. Similar behavior could be observed *i.e.* for Cs^+ and Sr^{2+} in the Migration Experiment at the GTS [21]. The leading edge of the breakthrough curves in these experiments indicated a rapid advective-dispersive flow through highly transmissive zones. However, in longer flow field experiments (4.9 m) with decreased linear flow velocity ($1\,m\,h^{-1}$) a significant peak retardation and peak height reduction for the reactive radionuclides could be observed, which [21] interpreted by a sorption and matrix diffusion dominated transport process with less relevant transport through highly transmissive zones. Stochastic analysis could show that the expected peak arrival time strongly depends on the bulk retention parameter η_B [22]. This dimensionless parameter η_B is thereby defined as:

$$\eta_B = \frac{\theta^2 D^2 n\langle l_1\rangle w_0}{Q\langle \overline{b}_1\rangle R_M} \qquad (2)$$

under the consideration that the multiple-fracture pathway can be described by a single fracture with pathway length $n\langle l_1\rangle$ and aperture $\overline{b}_1$. Here, θ is the matrix porosity, D the diffusion coefficient for the solutes in the host rock, w_0 is the stream tube width at the initial release point, Q the volumetric flow rate and R_M the host rock retardation coefficient.

Values for $\eta_B > 1$ indicate the dominance of mass exchange processes (matrix diffusion, establishment of sorption equilibria) relative to advection in a segmented fracture pathway. The proportionality of this parameter η_B to the total flow path length and the inverse proportionality to the flow rate agree with the interpretation of [21] and can explain entirely the U(VI) breakthrough observed in this study.

Th(IV) and Eu(III) breakthrough could not be found at all in the pulse injection experiments. These findings are different from the field study [7], where $\sim$ 21%–34% of Pu(IV) and Am(III) showed a colloid-mediated transport, which was explained by the delayed dissociation rate of Am(III)/Pu(IV) from the aquatic colloids. It is argued that the unexpected result of the laboratory pulse injection experiments is due to limitations given by the dispersion derived dilution and the analytical detection limits. Furthermore the comparison of Th/Eu column inlet and outlet concentrations measurements prior to the start of the core migration studies showed a higher column outlet Th/Eu background concentration possibly due to the washout of fracture infill particles. Therefore, a permanent injection experiment (C3-III, Table 2) was performed. Eu(III) and Th(IV) breakthrough showed insignificant differences in the leading edge of the breakthrough curve compared to that of the conservative tracer (Fig. 4), but exhibits a steeper concentration decline after the switch back to unspiked Grimsel groundwater. This may point to the limited access of these colloidal phases to matrix pores [1]. The breakthrough of Eu and Th exhibited a plateau of C/C_0 values in the range of 0.35 to 0.39 (Fig. 4). This indicates the establishment of a steady-state condition, either due to the kinetically controlled dissociation from colloids or the time dependent attachment of colloids to the fault gauge material. The over-all recovered unretarded fraction of Eu(III) and Th(IV) transport is 24% and 28%, respectively. These values are in quite good agreement with recoveries for Am (III) and Pu(IV) in the field experiment at comparable tracer residence times. Such a colloid-borne Th(IV)/Eu(III) migration could not be observed in the experiment with the longer core (core #2, Table 2, exp.: C2-II) and a smaller groundwater velocity. We take this as a further support for the assumption that either the colloidal species or the metal ions dissociating from the colloids are retained at rock surfaces at increased contact times.

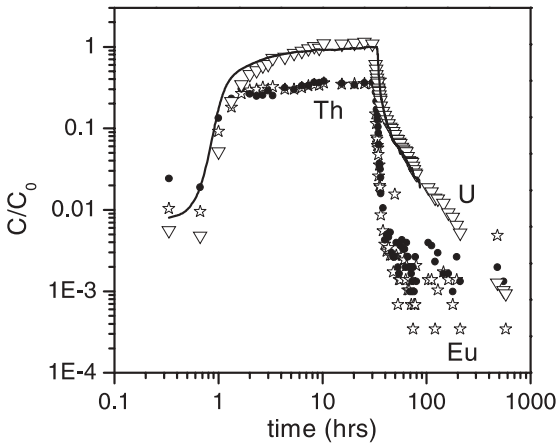

Fig. 4. Permanent injection (C3-III, see Table 2) breakthrough curves of the conservative tracer tritium (solid line) and elements U (open triangles), Th (filled circles) and Eu (open stars).

The breakthrough behavior of U(VI) in this permanent injection experiment under similar hydrodynamic conditions to the CRR field experiments (C3-III, Table 2, Fig. 4) matches with the conservative tracer in the leading edge as well as in the pronounced tailing and shows a recovery of 85% after 24 days migration time. The short residence time used in experiment C3-III, which is similar to that of the field study [14] is responsible for the mostly unretarded U(VI) migration.

3.3 Colloid breakthrough behavior (cocktail II and polystyrene microspheres)

The CRR field experiments [7, 14] have demonstrated that the presence of $20\,mg\,L^{-1}$ bentonite colloids significantly increased the mobility of tri- and tetravalent radionuclides under the given hydrodynamic conditions in a 2.23 m long fracture. In the laboratory experiments (C3-VIII, Table 2) we decreased the flow velocity to approx. $95\,m\,yr^{-1}$ (Fig. 5a). The results of these column experiment show that the U(VI) breakthrough was unaffected by the addition of $2\,mg\,L^{-1}$ bentonite colloids, as expected, and the recovery of 11% unretarded species was comparable to the previous experiment (14% recovery) under the same hydraulic conditions without bentonite (C3-VII; Table 2). The major difference in this experiment was the detection of an unretarded Th(IV) and Eu(III) breakthrough with the peak maximum slightly ahead of the conservative tracer. The recovery could be determined to be 27% (Th(IV)) and 37% (Eu(III)). This is slightly higher than the recovery of these elements under

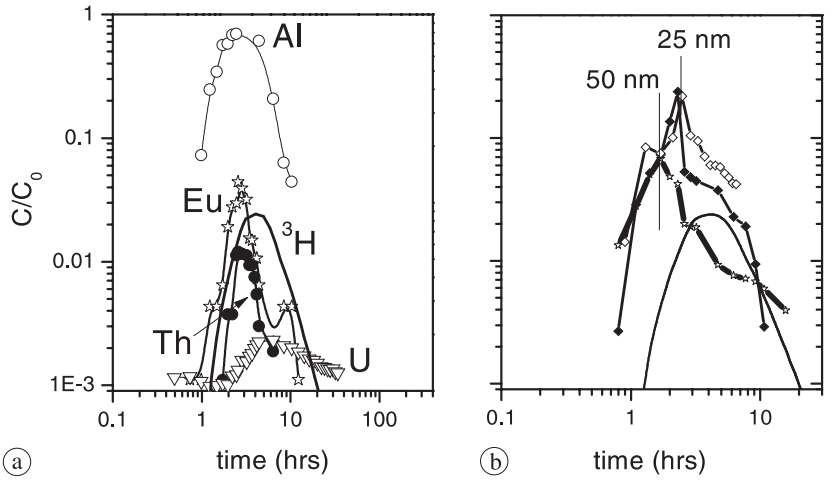

Fig. 5. (**a**) Breakthrough curves after 100 μL pulse injection of cocktail II (C3-VIII, Table 2). Tritiated water is indicated by a solid line, U as open triangles, Eu as open stars, Th as filled circles and Al as open circles. (2 cm long fracture (core #3) $v_a = 0.26\,\mathrm{m\,d^{-1}}$). (**b**) 100 μL pulse injection (C3-IX, Table 2) of carboxylated fluorescent polystyrene colloids (2 cm long fracture; core #3). Breakthrough of tritiated water is indicated by a solid line, 50 nm microsphere breakthrough as open stars, 25 nm microsphere breakthrough as filled diamonds ($v_a = 0.26\,\mathrm{m\,d^{-1}}$); Open diamonds indicate the behavior of 25 nm microspheres under a higher flow velocity of $0.52\,\mathrm{m\,d^{-1}}$ (C3-X, Table 2).

a higher flow velocity in the permanent injection experiment in absence of bentonite colloids (Fig. 4), but significantly lower than the recoveries of $70 \pm 15\%$ (Am III) and $86 \pm 9\%$ (Pu IV) observed in the CRR experiment with $20\,\mathrm{mg\,L^{-1}}$ bentonite colloids [7]. An additionally performed experiment with a flow velocity of $46\,\mathrm{m\,yr^{-1}}$ in core #2, comparable to the experiment C2-II (Table 2), except for injecting cocktail II showed no detectable Th(IV) and Eu(III) breakthrough. A quantification of the mobile bentonite colloid fraction was in both experiments not possible due to a significant mobilization of fracture derived natural colloids increasing the Al concentration background scatter to approximately 100 ppb in the column outlet before the experimental start compared to ∼11 ppb found in the natural Grimsel groundwater.

To overcome the difficulties of background differentiation and to estimate the colloid mobility of different size fractions under the given experimental conditions additional experiments with mixtures of monodisperse carboxylated fluorescent polystyrene colloids (25 nm, 50 nm and 100 nm) were performed. Under hydrodynamic conditions identical to the above mentioned bentonite colloid migration experiment (linear flow velocity of $0.26\,\mathrm{m\,d^{-1}}$) the smaller colloids were recovered to a greater extent than the larger microspheres (C3-IX, Table 2). A breakthrough of the 100 nm size class could not be detected due to detection limit constraints (d.l. ∼5 ppb), 50 nm diameter colloids showed a 10% mass recovery, whereas the 25 nm diameter colloids revealed a 34% recovery. In all cases, the mean transport velocity of the colloids was greater than the conservative tracer and the peak maximum of the larger 50 nm diameter colloids was detected ahead of the 25 nm colloid peak maximum (Fig. 5b). Similar results, but for larger carboxylated microspheres of 190 nm and 980 nm were found by [23] in both large block scale natural fractured granite as well as in fractured granite field site studies. Increasing the flow velocity to tracer residence times comparable to the CRR experiment ($0.52\,\mathrm{m\,d^{-1}}$) revealed an increased recovery (48%) of the 25 nm colloids. But surprisingly the colloid peak was not shifted significantly to lower migration times. This can partly be explained with the limited analytical resolution in this experiments due to sample volume constraints. Significant changes in the trailing edge of the colloid breakthrough curve for different size classes under investigation could not be observed indicating that size exclusion effects play a minor role. Due to the scatter of measured data and detection limit restrictions, these data have to be considered as somewhat preliminary. They nevertheless show a clear dependency of the colloid recovery on the groundwater flow rate and indicate the higher mobility of smaller colloids.

4. Conclusions

In this paper, laboratory core migration experiments under variation of linear flow velocity and therefore fracture surface contact time are presented to reveal kinetic aspects in both dissolved and colloid-associated radionuclide/lanthanide as well as colloid transport. Compared to the CRR (Colloid Radionuclide Retention) field migration studies [7] the linear flow velocity could be reduced to near-natural values as low as $46\,\mathrm{m\,yr^{-1}}$. The following conclusions can be drawn:

- The partly unretarded breakthrough of U(VI) observed under fast flow regimes ($187\,\mathrm{m\,yr^{-1}}$) diminishes with increasing tracer residence time and thus is a clear consequence of sorption kinetics.
- Th(IV) and Eu(III) serving as homologues for Pu(IV) and Am(III), respectively, revealed a partly unretarded bentonite colloid associated transport at a linear flow velocity of $\sim 94\,\mathrm{m\,yr^{-1}}$. This unretarded bentonite colloid associated Th(IV) and Eu(III) transport could not be detected under near natural groundwater velocities of $46\,\mathrm{m\,yr^{-1}}$ indicating either the dissociation of metal ions from colloids or colloid retention in the fracture.
- Th(IV) and Eu(III) transport mediated by groundwater colloids or colloids generated during sample handling in the laboratory is only found at short tracer residence times. For low groundwater velocities and long contact times with fracture infill minerals, the naturally occurring groundwater colloids should have a minor impact on actinide migration in the Grimsel granodiorite.
- Colloid migration experiments using mixtures of monodisperse fluorescent carboxylated microspheres (25 nm, 50 nm, 100 nm) revealed a decrease in mass recovery with increasing colloid size and at lowering the flow velocity. We take this as a first indication that colloid attachment to rock surfaces has to be considered even

for colloids highly stabilized by a favorable groundwater geochemistry.

In general, the kinetics of interaction with fracture surfaces play a fundamental role and control the mobility of dissolved metal species (U(VI)), colloid-associated species (Th(IV), Eu(III)) and inorganic colloids. However, to apply these experimental results to long-term repository conditions in the future, detailed studies on the mechanism of (a) colloid transport/retention in an undisturbed granite fracture and (b) the kinetics of colloid-radionuclide sorption/desorption are necessary.

Acknowledgment. The authors are indebted to A. Kersting and an anonymous reviewer for their helpful comments. This work greatly benefited from general discussions on clay mineralogy and colloid transport with A. Bauer, W. Hauser and C. Walther. We gratefully acknowledge F. Geyer, R. Götz, C. Walschburger, M. Fuss and T. Kisely for their significant analytical contribution to the work described in this paper. Finally, we thank A. Möri from the Geotechnical Institute Bern and NAGRA for providing us the bore cores and the groundwater within the CRR-project.

References

1. Oswald, J. G., Ibaraki, M.: Migration of colloids in discretely fractured porous media: effect of colloidal matrix diffusion. J. Contam. Hydrol. **52**, 213 (2001).
2. Grolimund, D., Elimelech, M., Borkovec, M., Barmettler, K., Kretzschmar, R., Sticher, H.: Transport of *in situ* mobilized colloidal particles in packed soil columns. Environ. Sci. Technol. **32**, 3562 (1998).
3. James, S. C., Chrysikopoulos, C. V.: Effective velocity and effective dispersion coefficient for finite-sized particles flowing in a uniform fracture. J. Colloid Interface Sci. **263**, 288 (2003).
4. Schäfer, T., Artinger, R., Dardenne, K., Bauer, A., Schuessler, W., Kim, J. I.: Colloid-borne Americium migration in Gorleben groundwater: Significance of iron secondary phase transformation. Environ. Sci. Technol. **37**, 1528 (2003).
5. Artinger, R., Schuessler, W., Schäfer, T., Kim, J. I.: A kinetic study of Am(III)/humic colloid interactions. Environ. Sci. Technol. **36**, 4358 (2002).
6. Vilks, P., Bachinski, D. B.: Colloid and suspended particle migration experiments in a granite fracture. J. Contam. Hydrol. **21**, 269 (1996).
7. Möri, A., Alexander, W. R., Geckeis, H., Hauser, W., Schäfer, T., Eikenberg, J., Fierz, T., De-gueldre, C., Missana, T.: The colloid and radionuclide retardation experiment at the Grimsel Test Site: influence of bentonite colloids on radionuclide migration in a fractured rock. Colloid Surf. A **217**, 33 (2003).
8. Hauser, W., Geckeis, H., Kim, J. I., Fierz, T.: A mobile laser-induced breakdown detection system and its application for the *in situ*-monitoring of colloid migration. Colloid Surf. A **203**, 37 (2002).
9. Vilks, P., Baik, M. H.: Laboratory migration experiments with radionuclides and natural colloids in a granite fracture. J. Contam. Hydrol. **47**, 197 (2001).
10. Villar, M. V., Martin, P. L., Pelayo, M., Ruiz, B., Rivas, P., Alonso, E., Lloret, A., Pintado, X., Gens, A., Linares, J., Huertas, F., Caballero, E., Jimenz de Cisneros, C., Obis, J., Perez, A., Velasco, J.: FEBEX bentonite: origin, properties and fabrication of blocks (full-scale engineered barriers experiment in crystalline host rock). Technical report 05/98, Enresa (empresa nacional de residuos radiactivos, s.a.), Madrid, Spain (1998).
11. Möri, A., Geckeis, H., Fierz, T., Eikenberg, J., Degueldre, C., Hauser, W., Geyer, F. W., Schäfer, T.: The CRR final project report series: 1. Description of the Field Phase – Methologies and Raw Data. Nagra Technical Report 03-01, Nagra, Wettingen, Switzerland (in press).
12. Ota, K., Möri, A., Alexander, W. R., Frieg, B., Schild, M.: Influence of the mode of matrix po-rosity determination on matrix diffusion calculations. J. Contam. Hydrol. **61**, 131 (2003).
13. Missana, T., Mingarro, M., Gutierrez, M. G., Alonso, U., Geckeis, H., Schäfer, T., Rabung, Th., Vejmelka, P., Marquardt, C.: GTS Phase V (CRR Experiment): Supporting laboratory experiments with radionuclides and bentonite colloids. Nagra Technical Report 03-02, Nagra, Wettingen, Switzerland (in press).
14. Geckeis, H., Schäfer, T., Hauser, W., Rabung, Th., Missana, T., Degueldre, C., Möri, A., Eikenberg, J., Fierz, Th., Alexander, W. R.: Results of the Colloid and Radionuclide Retention experiment (CRR) at the Grimsel Test Site (GTS), Switzerland. Impact of reaction kinetics and speciation on radionuclide migration. Radiochim. Acta **92**, 765 (2004).
15. Plaschke, M., Schäfer, T., Bundschuh, T., Manh, T. N., Knopp, R., Geckeis, H., Kim, J. I.: Size characterization of bentonite colloids by different methods. Anal. Chem. **73**, 4338 (2001).
16. Bouby, M., Geckeis, H., Ngo Manh, T., Yun, J. I., Dardenne, K., Schäfer, T., Walther, C., Kim, J. I.: Laser-induced breakdown detection combined with asymmetrical flow field-flow fractionation: application to iron oxy/hydroxide, J. Chrom. A **1040**, 97 (2004).
17. Schimpf, E., Caldwell, K., Giddings, J. C.: *Field-flow fractionation Handbook*. Wiley-Interscience, John Wiley & Sons, Inc., New York (2000).
18. Duro, L.: Prediction of the solubility and speciation of radionuclides in Febex and Grimsel waters. Nagra Aktennotiz 99-218, Nagra, Wettingen, Switzerland (1999).
19. Möri, A., Mazurek, M., Adler, M., Schild, M., Siegesmund, S., Vollbrecht, A., Ota, K., Ando, T., Alexander, W. R., Smith, P. A., Haag, P., Bühler, C.: Grimsel Test Site Investigation Phase IV (1994–1996). The Nagra-JNC *in situ* study of safety relevant radionuclide retardation in frac-tured crystalline rock IV: The *in situ* study of matrix porosity in the vicinity of a water conducting fracture. Nagra Technical Report 00-08, Nagra, Wettingen, Switzerland (2003).
20. Missana, T., Garcia-Gutierrez, M., Turrero, M. J., Alonso, U., Mingarro, M.: The role of colloids in the radionuclide transport in a deep geological repository. Technical Report 05/2003, Enresa (empresa nacional de residuos radiactivoa, s.a.), Madrid, Spain (2003).
21. Hoehn, E., Eikenberg, J., Fierz, T., Drost, W., Reichlmayr, E.: The Grimsel Migration Experiment: field injection-withdrawal experiments in fractured rock with sorbing tracers. J. Contam. Hydrol. **34**, 85 (1998).
22. Painter, S., Cvetkovic, V.: Stochastic analysis of early tracer arrival in a segmented fracture pathway. Water Resour. Res. **37**, 1669 (2001).
23. Becker, M. W., Reimus, P. W., Vilks, P.: Transport and attenuation of carboxylate-modified latex microspheres in fractured rock laboratory and field tracer tests. Ground Water **37**, 387 (1999).

The colloid and radionuclide retardation experiment at the Grimsel Test Site: influence of bentonite colloids on radionuclide migration in a fractured rock.

Colloids Surf. A (2003) **217**(1-3), 33.

Möri A., Alexander W. R., Geckeis H., Hauser W.,
Schäfer T., Eikenberg J., Fierz T., Degueldre C.,
and Missana T.

ELSEVIER

Colloids and Surfaces A: Physicochem. Eng. Aspects 217 (2003) 33–47

COLLOIDS AND SURFACES A

www.elsevier.com/locate/colsurfa

The colloid and radionuclide retardation experiment at the Grimsel Test Site: influence of bentonite colloids on radionuclide migration in a fractured rock

A. Möri [a,*], W.R. Alexander [b], H. Geckeis [c], W. Hauser [c], T. Schäfer [c], J. Eikenberg [d], Th. Fierz [e], C. Degueldre [d], T. Missana [f]

[a] *Geotechnical Institute Ltd., Bern, Switzerland*
[b] *National Co-operative for the Disposal of Radioactive Waste (NAGRA), Wettingen, Switzerland*
[c] *Forschungszentrum Karlsruhe, Institut für Nukleare Entsorgung (FZK-INE), Karlsruhe, Germany*
[d] *Paul Scherrer Institute (PSI), Villigen, Switzerland*
[e] *Solexperts AG, Schwerzenbach, Switzerland*
[f] *CIEMAT, Madrid, Spain*

Abstract

The colloid and radionuclide retardation (CRR) experiment is dedicated to the study of the in situ migration behaviour of selected actinides and fission products in the absence and presence of bentonite colloids in a water-conducting feature (shear zone) in the Grimsel Test Site (GTS). The technical scenario considers the bentonite backfill/host rock interface as a potential source for colloids. The experiment investigates the migration behaviour of U, Th, Pu, Am, Np, Sr, Cs, I and Tc and the influence of smectitic bentonite colloids by two in situ tracer injections in a well-characterised dipole. The field experiments are supported by an extended laboratory and modelling programme. Colloid breakthrough is determined on-line by a mobile, laser-induced breakdown detection apparatus (LIBD), a mobile photon correlation spectrometer (PCS) and, afterwards in the laboratory, by a single particle counting method (SPC) using a laser light scattering technique. Bentonite colloids generated from bentonite backfill material were found to be stable in the experimental groundwater and the influence of pH and salinity on colloid stability was investigated. The in situ monitored breakthrough of the tri- and tetravalent actinides Am and Pu and of Cs followed the colloid breakthrough indicating some degree of colloid-mediated migration of these radionuclides in the experimental shear zone. But even when no colloids had been added to the tracer cocktail, part of Am(III) and Pu(IV) appears to migrate as colloids. The different colloid detection techniques revealed a colloid recovery between 80 and 90% of the injected bentonite colloids. The CRR experimental results are considered from the perspective of understanding the likely long-term behaviour of a deep geological repository for radioactive waste and as an indicator of the way forward to the next generation of in situ experiments.

Keywords: Colloid and radionuclide retardation experiment; Bentonite colloids; Radionuclides; Grimsel Test Site; In situ tracer injection

* Corresponding author. Tel.: +41-31-389-3431.
E-mail address: andreas.moeri@geo-online.com (A. Möri).

0927-7757/03/$ - see front matter
doi:10.1016/S0927-7757(02)00556-3

1. Introduction

In most high-level radioactive waste repository designs, the waste is packed in massive metal canisters which are surrounded by a large volume of bentonite clay, all of which constitute the engineered barrier system (EBS). The canisters will slowly degrade and eventually fail, releasing some radionuclides, most of which are expected to be retained and to decay within the bentonite. However, it is conceivable that, for example, gas production may induce potential flow paths in the bentonite allowing a limited amount of radionuclides to escape the EBS. Erosion of the bentonite at the EBS/host rock interface is expected to produce bentonite colloids (see Fig. 1) and any radionuclides released from the EBS may become associated with these colloids and migrate through water conducting features (e.g. shear zones) towards the biosphere.

Much information now exists on the behaviour of natural and artificial colloids in deep and shallow groundwaters but, despite this, it has not yet been possible to completely define the likely impact of colloid-facilitated transport of radionuclides released from a repository. This is partly because the potential role of colloids in radionuclide transport is quite complicated. As noted in Ref. [1], five requirements must be fulfilled (the so-called colloid ladder, see Fig. 2) to prove that colloid-facilitated transport of radionuclides in a potential repository host rock may be of significance to the long-term performance of a waste repository: colloids must be present, mobile and stable under the given groundwater conditions (geochemical and hydrogeological environment), radionuclide association with the colloids must take place and the association must be irreversible.

The colloid and radionuclide retardation (CRR) experiment is dedicated to study the in situ migration behaviour of selected actinides and fission products in the absence and presence of bentonite colloids in fractured rock at Nagra's Grimsel Test Site (GTS) in the central Swiss Alps. In addition to the programme of in situ experiments, the project partners, namely ANDRA (F), ENRESA (E), FZK-INE (D), JNC (J), USDoE/Sandia (USA) and Nagra (CH), funded an extensive programme of laboratory and modelling work. The modelling programme was focussed on calculations of radionuclide solubility in both the test site groundwater and bentonite porewater in addition to flow field modelling (geostatistical, inverse modelling of crosshole pumping tests) and reactive transport modelling (evaluation of preparatory tracer tests and predictive transport

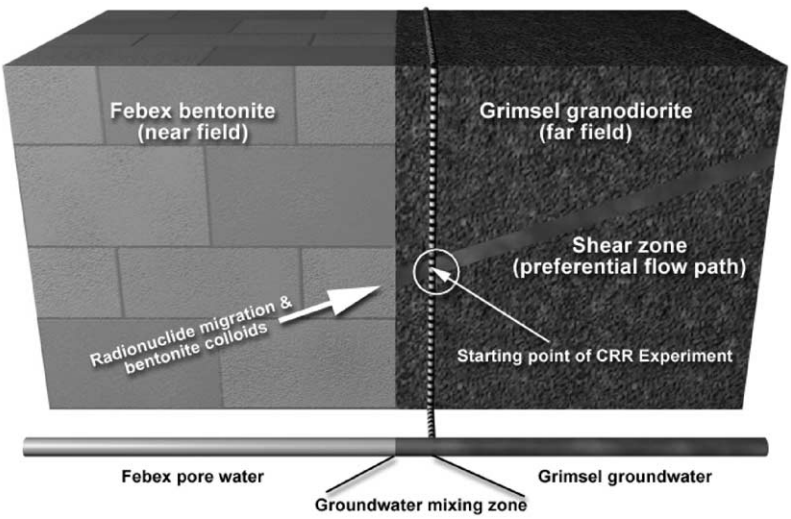

Fig. 1. Conceptual model of the CRR experiment.

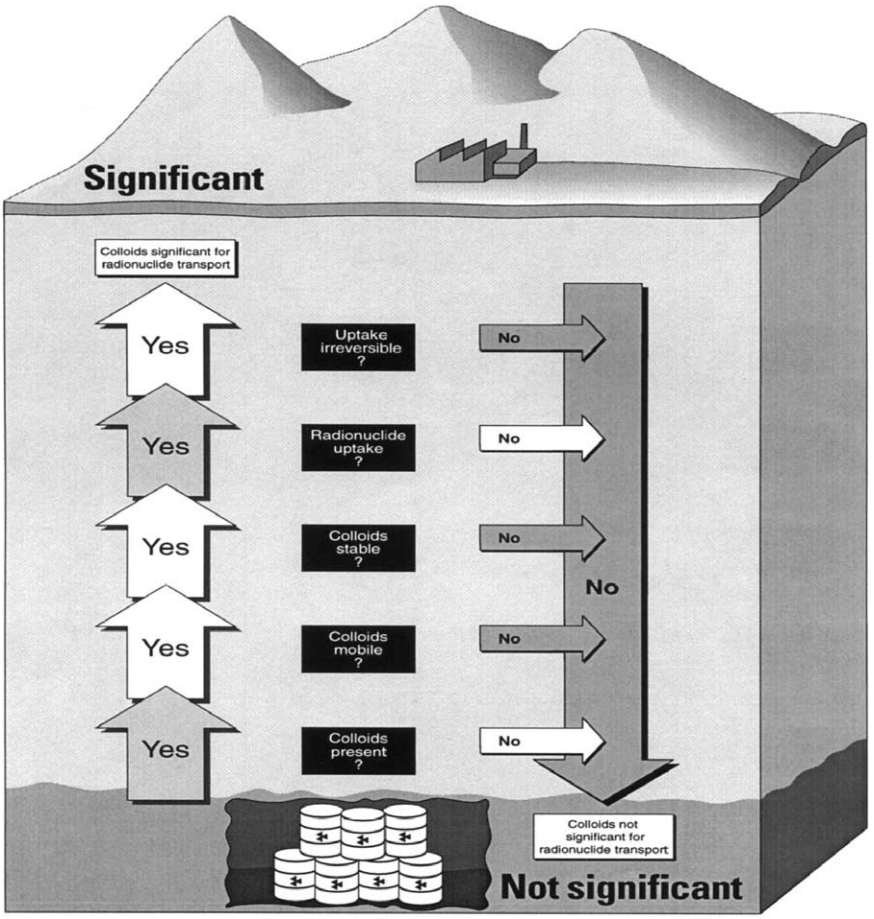

Fig. 2. The 'colloid ladder' indicates when colloid-facilitated radionuclide transport in the host rock may become significant to the long-term performance of deep geological waste repositories (from Re. [1]).

modelling). The laboratory programme concentrated on batch experiments with different solids (Grimsel granodiorite, fault infill material, bentonite, etc.) in the absence and presence of bentonite colloids. The results of the laboratory programme and predictive modelling of the in situ behaviour of the radionuclides will be compared with the in situ data on radionuclide and colloid behaviour.

Between January and March 2002, the final tracer injection campaign was carried out in a test shear zone (a complex, multi-fracture zone with fault infilling material; see Refs. [2,3] for details) at the GTS. Six tracer injections were performed with the fluorescent dye uranine in combination with the conservative radiotracer ^{131}I (the latter was intended to be used as conservative tracer, measured online, during the main injections) to compare the behaviour of both tracers and to confirm the reproducibility of the injection functions. The two main tracer injections were performed with

- $^{243}Am(III)$, $^{237}Np(V)$, $^{242}Pu(IV)$, $^{238}Pu(IV)$, $^{238}U(VI)$, $^{85}Sr(II)$, $^{131}I(I)$ and $^{232}Th(IV)$ in the absence of bentonite colloids and
- $^{241}Am(III)$, $^{237}Np(V)$, $^{244}Pu(IV)$, $^{238}Pu(IV)$, $^{233}U(VI)$, $^{99}Tc(IV)$, $^{137}Cs(I)$, $^{85}Sr(II)$, $^{131}I(I)$ and $^{232}Th(IV)$ in the presence of 20 mg l^{-1} of bentonite colloids.

Whenever possible, it was decided to use different radioisotopes of the injected elements in order to distinguish the measured element concentrations from the two runs in the outlet solutions.

The work presented here was produced by a large team of co-workers (who are identified in the acknowledgements below). The aim of this paper is to give an insight into the presently performed work related to colloid-mediated radionuclide migration studies at the GTS. Some selected experimental results of laboratory studies and in situ migration experiments are presented and discussed below in order to demonstrate the colloid relevance to the migration of some radionuclides in a given granitic environment. However, further evaluation of the data obtained in laboratory and field experiments is currently underway and several publications will follow this overview paper, describing in more detail the methodologies, results and final conclusions of the project (see Refs. [4–7]).

2. Grimsel Test Site (GTS)

2.1. Site description

The CRR in-situ experiments were carried out at Nagra's GTS which is located at about 1730 m above sea level under a ~450 m overburden of crystalline rock. The test shear zone which was selected for the CRR experiment is located at the former migration (MI) site which has the advantage of being a well characterised site due to previous work carried out there in two projects over the previous 15 years (see Refs. [8–11] for details). Fig. 3 shows the test site with the AU gallery, the boreholes and the four CRR dipoles. The preparatory tracer tests were performed in each of the four dipole flow field configurations under varying flow conditions. The dipoles consist of existing boreholes from the former Migration Experiment (MI boreholes; see Refs. [8,9] for details) and of new CRR boreholes which all have been instrumented with triple packer systems. The final tracer injections were performed in dipole 1 (see D-1 in Fig. 3) which has a straight-line length of 2.23 m.

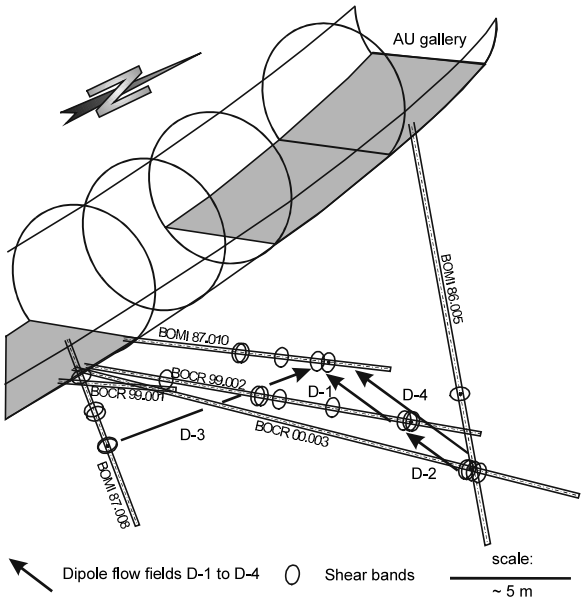

Fig. 3. 3D view of the CRR test site (viewed from the south) showing the more important boreholes used in the experiment. The plane of the page represents the idealised plane of the shear zone (the grey section in the gallery indicates the concrete floor which is missing in the area where the shear zone intersects the gallery)

2.2. Hydrogeochemical overview

The host rock of the test shear zone is the Grimsel granodiorite, which was affected by greenschist metamorphism and deformation about 25 Ma BP where the original plutonic rocks were partially metamorphosed to gneisses. The Grimsel granodiorite is medium to coarse grained and is transected by a series of shear zones and scattered lamprophyre and aplite dykes. The granodiorite consists mainly of 23 vol% quartz, 23 vol% plagioclase, 20 vol% potassium feldspar and 25 vol% sheet silicates (biotite, muscovite and chlorite). The ductile deformation, which formed extended shear zones (mylonites) was followed by brittle deformation, which can be attributed to the post metamorphic regional uplift. The CRR test shear zone is characterised as a WSW-ENE striking, steeply dipping (to the SSE) cleavage parallel shear plane. The original shear direction was sub-vertical, parallel to the mineral stretching lineation with a minimum value for shear displace-

ment of 3 m. The thickness of the shear zone varies between 0.15 and 0.90 m. Brittle reactivation of the shear zone resulted in a reduction in the internal cohesion of the shear zone and in the formation of fault infill between the sheared planes which has an increased sheet silicate content compared to the matrix and to the mylonites (about 45 vol%, for details see Ref. [2]). This increase in sheet silicates (along with the presence of secondary clay minerals produced by the greenschist facies overprint) in the fault infill and a relatively large porosity of 30–40%, are responsible for the observed (see Fig. 4 for details) preferential retardation of radionuclides in this material as seen also in the EP experiment (for details see Ref. [3]).

The evaluation of the borehole outflow tests in the MI and CRR boreholes crosscutting the test shear zone at the east side of the gallery indicated transmissivities around 10^{-6} m^2 s^{-1}. The test site groundwater is a Na^+/Ca^{2+}–HCO_3^-–SO_4^{2-} groundwater type with a pH of 9.6 and an E_h below −300 mV. The electrical conductivity is 103 μS cm^{-1} and the ionic strength 0.0012 M. The natural colloid background of the test site groundwater was found to be about 10^{10} colloids l^{-1} between 40 and 1000 nm (for details see Ref. [12]) and additional studies of the natural background are currently ongoing.

2.3. Experimental set-up

The flow field was established between the injection borehole BOCR 99.002 (10 ml min^{-1}) and the extraction borehole BOMI 87.010 (150 ml min^{-1}) and has a straight-line length of 2.23 m (see Fig. 3). The hydraulic flow along the dipole points to the gallery, thus following the natural groundwater flow towards the galleries. The packed off interval in BOCR 99.002 is 40 cm (115 ml) and in BOMI 87.010 is 31 cm (83 ml). The new CRR boreholes were arranged in a way which enables shear zone parallel overcoring of the resulting dipole flow fields from the gallery if significant amounts of tracer and/or colloids were retarded within the shear zone (cf. [3,13]).

Specially designed triple packer systems were installed in the two boreholes in such a way that the shear zone interval of the borehole was tightly sealed. The test intervals were equipped with a pressure measurement line, a flow line and a quartz fibre pair for downhole detection of the fluorescent uranine dye. In addition, all parts

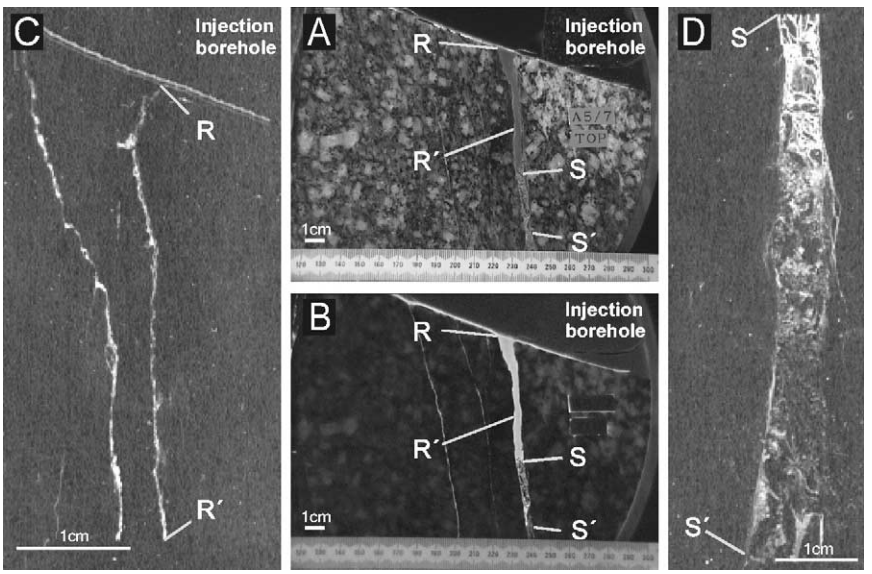

Fig. 4. (A,B) Slab photographs under normal and UV light; (C,D) α-autoradiograph images from the channel type structure. The major flow paths within the shear zone are located in the fault infill as flow channels. Note that the injected α-emitting radionuclides were preferentially retarded at the flow channel surface and within the fault infill; details in Ref. [3].

within the interval exposed to groundwater were PEEK (polyether etherketone) coated in order to minimise tracer sorption on the test equipment while using radionuclide tracers.

The injected water was in situ groundwater and was pumped with a HPLC pump through pH and E_h flow-through cells and then passed a flow meter-all instruments were directly linked to the data acquisition system. The radionuclide cocktails were injected with a newly developed tracer dosage system (see Ref. [4] for details) into the PEEK tubing of the injection line by applying a N_2 overpressure to the vial containing the cocktail. This procedure allowed avoiding the contact of the solution with the aerobic atmosphere. The actual injection flow rate (10 ml min^{-1}) was monitored by measuring the mass loss from the cocktail container.

The extraction side was also equipped with an HPLC pump, pH, O_2 and E_h flow-through cells and a flow meter (see Fig. 5). The bentonite colloids at the borehole outflow were detected on-site and on-line using a laser induced breakdown detector (LIBD) [14] and by photon correlation spectroscopy (PCS) [15]. The particle size distribution of the effluent colloids was determined off-site by using a single particle counter (SPC). On-site, real-time analysis of the ^{131}I and ^{85}Sr activity was performed by γ-spectrometry with a HPGe detector. During the two main tracer injections, about 600 samples were collected from the outflow solution for further element analysis by ICP-MS (determination of radionuclides in the extraction solution and determination of Al content as an indicator for the presence of bentonite colloids) and additional γ- and α-measurements were performed in the laboratory.

3. Preparatory laboratory testing

Different types of colloids have been considered to be relevant for the scenario defining the framework of the CRR experiment. Colloidal species can be generated in the EBS of a repository due to a variety of processes:

- corrosion of the waste container could produce metaloxide/hydroxide colloids,
- corrosion of the waste form itself might generate colloidal silica, and/or clay (from vitrified waste) or uranium or other actinide phases (from spent Pu/U or mixed fuel, MOX),
- colloidal species may be derived from the bentonite (smectite, etc.) and
- natural colloids can be present in the ambient groundwater.

Radionuclides can either attach to such colloidal species by sorption or association (heterogeneous radiocolloids) or may even be the main component of such colloids, e.g. due to polymerisation of

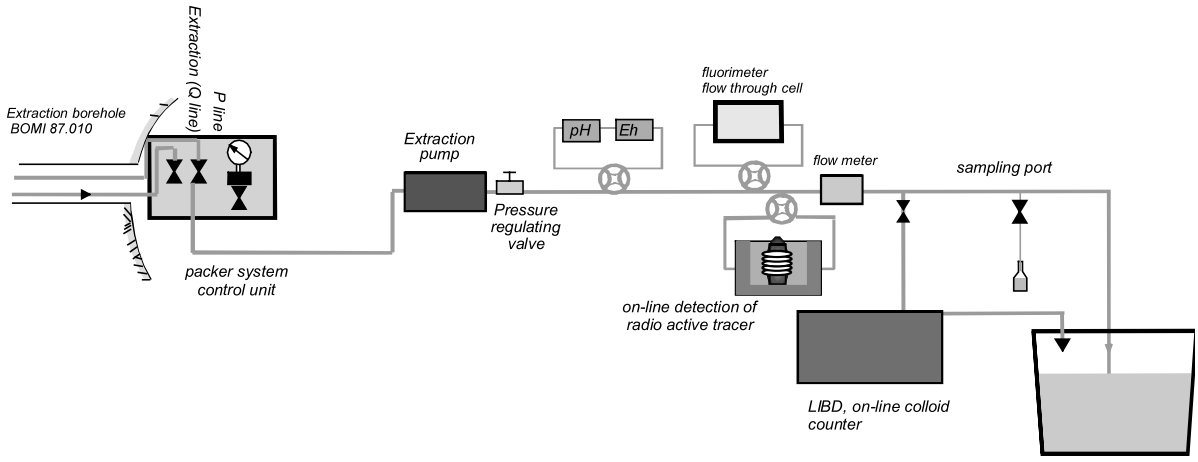

Fig. 5. Extraction borehole sampling and monitoring equipment.

hydrolysed actinide species (homogeneous radiocolloids). Laboratory studies were therefore performed with different types of colloids in test site groundwater and in the porewater of the bentonite. The experimental bentonite consists mainly of smectite (93±2%) with quartz (2±1%), plagioclase (3±1%), cristobalite (2±1%), potassic feldspar, calcite and trydimite as accessory minerals and is already in use at the GTS for the full-scale high level waste engineered barriers experiment (FEBEX, for details see Ref. [16]).

The first studies within the CRR project concentrated on the investigation of the formation of bentonite colloids at the bentonite/host rock interface, on the stability of different types of colloids and on the radionuclide uptake of the bentonite colloids.

3.1. Bentonite colloids

Bentonite colloids were obtained from crushed bentonite blocks. The material was sieved (size fraction <64 μm) and washed with Milli-Q deionised water and finally equilibrated with test site groundwater. The colloidal fraction was obtained by centrifugation. The structure of these colloids was investigated by scanning electron microscopy (SEM) techniques. SEM samples were obtained by filtering the suspension through an Amicon XM 50 membrane (pore size 3 nm), drying and subsequent covering by an Au film. The SEM image of these bentonite colloids shows that the largest number of these colloids is around 200 nm (Fig. 6, left image).

The exchange properties of bentonite colloids in the test site groundwater have been determined and the main exchangeable cations were found to be: Mg^{2+} ($\sim$31%), Ca^{2+} ($\sim$29%), Na^{+} ($\sim$29%) and K^{+} ($\sim$3%).

Two experimental set-ups have been designed in order to simulate the in situ conditions for colloid generation at the bentonite/host rock interface in the laboratory [17]: a first scenario where advection dominates colloid mobilisation (dynamic experiment) and a second where diffusion is predominant (quasi-static experiment). However, since very low flow conditions are expected to exist around the EBS in a repository, the water flow rates in the dynamic experiments were also very low (from 0.17 to 0.48 ml day^{-1}). Despite this, bentonite colloids were generated at the bentonite surface and mobilised at the bentonite/hostrock interface (for more details see Refs. [5,17]) which is in agreement also with earlier work (see, for example Ref. [18]).

The water flow at the simulated host rock/bentonite interface produced erosion on the exposed bentonite surface and solid material was found in the eluted water. The fact that the water flow actually ran at the interface, and not within the bentonite or along the external walls of the column, was confirmed by adding the fluorescent dye, uranine, to the injected water and then visually examining the sample.

The particulate matter generated at the interface contained large fragments (up to 3 μm) and smaller particles that could be clearly observed upon filtering the eluted water with a 0.45 μm pore size filter membrane. The total solid fraction was fairly polydispersed and the colloidal fraction had a mean hydrodynamic diameter, determined by PCS, ranging from 200 to 300 nm in size. Fig. 6

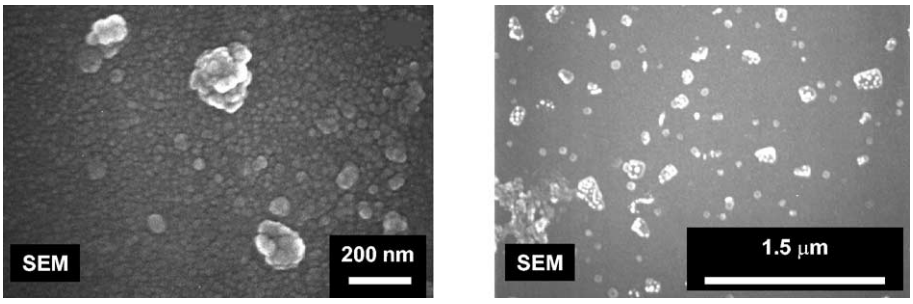

Fig. 6. Scanning electron microscope images of bentonite colloids.

(right image) shows a SEM image of a sample of the colloidal material observed in the eluted water. The 200–300 nm sized colloids (aggregates) were actually formed by smaller spherical particles. Chemical analysis, performed with EDX, identified Si, Al, Mg, Ca and Fe (probably clay minerals and metal oxides) as the main components of the colloidal material generated at the interface. The ζ potential of the colloidal material found in the eluate was always negative, and the final value lay in the expected range for smectite clay colloids of -20 and -30 mV, respectively. The concentration of both colloidal and total solid fraction generated at the interface was observed to increase with increasing water flow. It is worth mentioning that colloids were also observed in the experiments performed under quasi-static conditions which implies that colloids may be produced even in the absence of mechanical forces driving the erosion processes.

3.2. Stability of bentonite colloids

To investigate the influence of ionic strength on the stability of the Febex bentonite colloids, gradual concentration changes from 0.001 M (comparable to the ionic strength of the test site groundwater) to 0.22 M using NaCl, $NaClO_4$ or $CaCl_2$ solution were accomplished. The pH was controlled by adding NaOH or 0.1 M HCl. Fig. 7 (left image) shows the evolution of the hydrodynamic mean diameter obtained by dynamic light scattering of colloids obtained from bentonite as a function of the ionic strength of the water. An increase in the mean size clearly indicates that coagulation is occurring (in agreement with the observations in the colloid erosion experiment). The pH of the suspensions varied slightly with the addition of the electrolyte but the final values were in the range of pH 8.7 ± 0.5.

Another set of experiments was performed to study the effect of the pH and the hydrodynamic mean diameter of bentonite colloids (see Fig. 7 right image). At fixed ionic strength, the stability of the colloids strongly depends on the pH of the suspensions. The curves obtained for pH > 6 (pH 8 and 11) are flat and no substantial change in the mean size was observed during the experiment. The curve at pH 6 shows an increase of approximately 100 nm in the mean hydrodynamic diameter after 45 min whereas, at pH 5, the coagulation of colloids is practically immediate. The curve at pH 2 is very similar to the curve obtained for the fast coagulation regime at pH 5.

The pH-dependent stability behaviour of smectitic colloids depends, in fact, on the small pH-dependent charge of the amphoteric aluminol groups at the edge sites. Edge to face coagulation processes may occur at pH < 6.5 as the charge emerging at the edges is positive whereas the layer

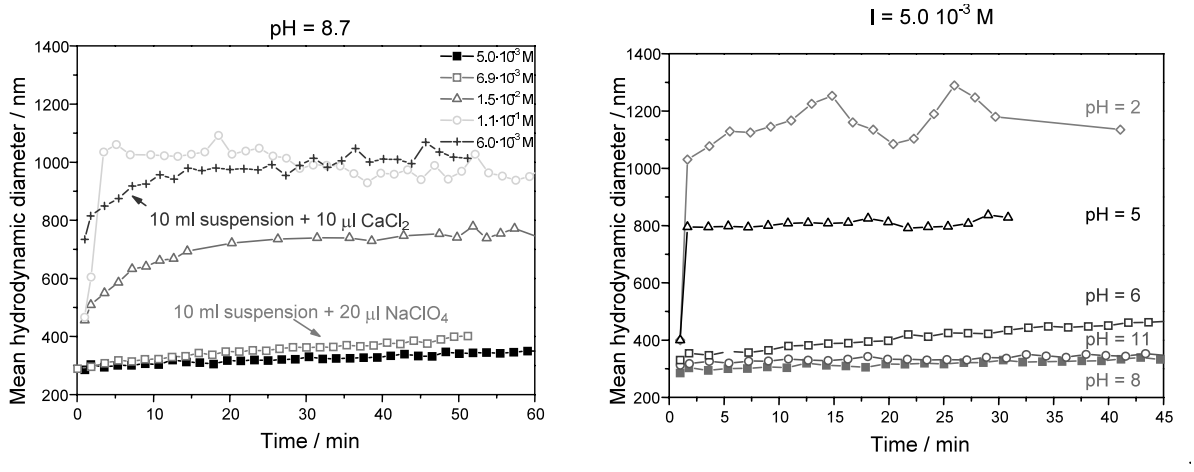

Fig. 7. Evolution of the hydrodynamic mean diameter of bentonite colloids (1.3 ± 0.3 g l^{-1}) at different ionic strengths (left) and at different pH (right).

charge at the planar face of the smectitic platelets is always negative widely independent of pH. As a consequence, bentonite colloids are expected to show high stability under the experimental groundwater conditions ($I = 10^{-3}$ M and pH 9.5) [19]. In order to verify this issue, the colloid size distribution was investigated also for longer time periods. Colloids obtained from previously washed bentonite and conditioned in the test site groundwater were prepared. The concentration of the suspension was approximately 2000 mg l^{-1}. The colloid size distribution was found to be rather invariant over a period of approximately 5 months.

3.3. Batch experiments with radionuclides and bentonite colloids

The sorption of the actinides and the fission products onto different solids, namely Grimsel granodiorite, fracture infill material and Febex bentonite colloids, was experimentally investigated in the laboratory for a number of radioelements relevant to long term safety of a repository: Cs(I), U(VI), Se(IV) and Tc(VII and IV), Am(III), Np(V) and Pu(IV and VI) (details in Ref. [5]). Not all of them were finally studied in the in situ experiment. The following main findings resulted from these studies:

- Pu, Am, U and Cs sorption on bentonite colloids is in general stronger than that found for the bulk bentonite, possibly due to the large surface area of the colloids. For the other radionuclides, sorption on the colloids appears to be much less significant. K_d-values in the range of 10^6 ml g^{-1} for Am are almost constant after short contact times similar to those for Cs ($\sim 7 \times 10^3$ ml g^{-1}), the values for Pu increase from initially 10^5 to 10^6 ml g^{-1} after 3 weeks. A similar trend is found for U where the K_d values increased from 8×10^2 to 1.5×10^3 ml g^{-1} within 12 weeks.
- Sorption of Am, Pu, Se and U on fracture infill and granodiorite displays a strong kinetic control. Even after experimental periods of 12 weeks, equilibria are not yet attained. It is not yet clear which is the dominant underlying process (redox and/or mineralisation reactions). In general, Am sorption is stronger than that of Pu and almost no sorption takes place for Np. U is much more strongly sorbed on the granodiorite than on the fracture infill. For Cs the opposite is true.
- Despite the low redox potential of the test site groundwater in the batch experiments, Np remains in oxidation state V. At least in the case of U and Se, slow reduction to oxidation state IV might contribute to the slow sorption kinetics. For Tc, a clear increase of sorption with time is found under anaerobic conditions, probably indicating that reduction to Tc(IV) occurs in the system.
- Strong sorption of Am and Pu on bentonite colloids was observed. K_d-values in the range of 10^6 ml g^{-1} for Am are almost constant after short contact times, whereas the values for Pu increase from initially 10^5 to 10^6 ml g^{-1} after 3 weeks.
- Sorption of Pu and Am onto Grimsel granodiorite or on the fault infill is decreased by more than one order of magnitude in the presence of 20 mg l^{-1} bentonite colloids. No sorption of bentonite colloids can be detected on either solid. There is some indication that actinide sorption on the bentonite colloids may be reversible, as sorption on granodiorite and fracture infill increases slightly over a time period of 1 week even in presence of the bentonite colloids.

4. In situ experiments

Eight tracer tests were performed between January and March 2002 in the test dipole. The entire test programme was performed within a very tight time plan and laboratory analyses of the field samples began immediately after in situ injections were completed.

On-site radiation protection measures were already applied during the preliminary tracer testing and were intensified during the injection of the actinides. The on-site surveillance concentrated on personal dosimetry and monitoring of potential contamination and external dose rates (note that

Table 1
Radioisotope activity, mass concentration, assumed oxidation state and colloidal fraction as determined by ultracentrifugation in radionuclide cocktails 1 and 2

	Injected activity Bq for 100 ml	Concentration (M)	Assumed oxidation state	Colloidal fraction (%)	Analytical method
Run #1 (without bentonite colloids)					
^{131}I	$7.46 \times 10^{+4}$	1.24×10^{-12}	−I	0	γ-spec.
^{85}Sr	$9.52 \times 10^{+4}$	1.28×10^{-11}	II	~0	γ-spec.
^{232}Th	1.06×10^{-3}	1.12×10^{-8}	IV	20-30	ICP-MS
^{238}U	2.82×10^{-1}	9.50×10^{-7}	VI	0–12	ICP-MS
^{237}Np	$5.82 \times 10^{+2}$	9.44×10^{-7}	V	0–10	ICP-MS/α-spec.
^{238}Pu	$6.70 \times 10^{+2}$	4.44×10^{-11}	IV	5–58	α-spec.
^{242}Pu	$3.50 \times 10^{+1}$	9.94×10^{-9}	IV	5–58	ICP-MS
^{243}Am	$1.06 \times 10^{+3}$	5.93×10^{-9}	III	6–58	ICP-MS/α-spec.
Run #2 (incl. 20 mg l^{-1} bentonite colloids)					
^{131}I	$5.56 \times 10^{+4}$	9.23×10^{-13}	−I	0	γ-spec.
^{85}Sr	$8.24 \times 10^{+4}$	1.11×10^{-11}	II	~0	γ-spec.
^{137}Cs	$6.07 \times 10^{+5}$	1.38×10^{-8}	I	8	γ-spec.
^{99}Tc	$6.55 \times 10^{+1}$	1.04×10^{-8}	IV	12	ICP-MS
^{232}Th	1.03×10^{-3}	1.10×10^{-8}	IV	94	ICP-MS
^{233}U	$7.22 \times 10^{+3}$	8.69×10^{-7}	VI	6	ICP-MS
^{237}Np	$6.72 \times 10^{+2}$	1.09×10^{-6}	V	0–1	ICP-MS
^{238}Pu	$7.20 \times 10^{+2}$	4.77×10^{-11}	IV	84	α-/γ-spec.
^{244}Pu	1.11×10^{-1}	6.70×10^{-9}	IV	84	ICP-MS
^{241}Am	$2.04 \times 10^{+3}$	1.15×10^{-8}	III	99	α-spec.

no contamination occurred and no doses above those expected from the natural background radiation were measured). The breakthrough solution, if not sampled, was collected within six 2000 l PVC tanks. Solid radioactive wastes were collected and transported elsewhere for handling and disposal.

4.1. Preparation of the injection cocktail

The final two radionuclide cocktails were prepared by adding the radionuclides and colloids to previously collected test site groundwater under anoxic conditions (in argon gloveboxes with <1 ppm oxygen). 125 ml of the solution were prepared and 100 ml were injected (the remaining 25 ml were used for laboratory analysis). Table 1 shows the radioisotopes used with their assumed[1] oxidation state, the injected activity and mass concentration and the colloidal fraction for each element in the injection solutions for both runs. In the injection cocktail for run 1, where no bentonite colloids had been added, colloid-bound tri- and tetravalent actinides were identified. Ultracentrifugation for 1 h at 90 000 rpm, however, yielded a considerable scatter for the colloidal radionuclide fraction, which may be due to the presence of very small colloids that cannot be sedimented under the given conditions or due to the existence of colloids of a very low density close to that of water, e.g. gel-like aggregates with a high water content. The fact that, in at least some of the ultracentrifugation experiments, colloids are detected for Pu, Th and Am indicates the relevance of colloids under these conditions.

For the second in situ experiment a 10 g l^{-1} bentonite colloid suspension was prepared by repeated suspending, centrifuging, decanting the supernatant and re-suspending the suspension in Grimsel groundwater with an ultrasound tip. The final suspension had a pH of 9.21, a specific conductivity of 117 μS cm^{-1} and a gravimetrical

[1] The oxidation states noted in Table 1 are based on thermodynamic databses and expert knowledge. In a number of cases, these were confirmed by solution speciation measurements (see Ref. [4] for details).

determined concentration of 540 ± 57 mg l^{-1}. For the injection cocktail the bentonite colloid concentration was adjusted to 20 mg l^{-1}.

The average size of bentonite colloids in the cocktail for run 2 (concentration: 20 mg l^{-1}) was 109 ± 10 nm, determined by LIBD. This time, ultracentrifugation shows clearly and reproducibly the presence of tri- and tetravalent actinides in the colloidal state, i.e. adsorbed on bentonite colloids. A small fraction of Cs also appears to be sorbed on colloids.

4.2. Breakthrough curves of the radionuclides

The determination of radionuclide concentrations in the individual samples was done by ICP-mass spectrometry (ICP-MS) and by α- and γ-spectrometry. As indicated before, only the behaviour of some of the injected radionuclides will be discussed here (for details see Refs. [4–7]).

Two main groups of breakthrough curves could be distinguished in run 1 where no bentonite colloids were added (Fig. 8): the peak maxima for tri- and tetravalent Am and Pu respectively appear about 10 min earlier than those found for the conservative non sorbing tracer ^{131}I. Twenty to thirty percent of the injected Am and Pu were recovered, which is clearly less than found for ^{131}I ($> 90\%$). It was already observed in preparatory in situ tracer tests that, in the test shear zone, colloids migrated slightly faster than the conservative tracers [14]. Therefore, it could be concluded that a certain fraction of the reduced actinides might form homogeneous or heterogeneous radiocolloids, even in the absence of added bentonite colloids and it is reasonable to speculate that the recovered Am and Pu simply represents the colloidal fraction of the injection cocktail.

Fig. 9 shows resulting breakthrough curves obtained by the measurements performed after run 2.

Again, there is a significant difference between the peak times of the tri- and tetravalent elements and the conservative tracer ^{131}I. The peak time of the more rapidly eluted radionuclides coincides with the peak time of the bentonite colloids, detected by LIBD, PCS and SPC (see below) and are not very different from those in run 1. This confirms the run 1 interpretation that a considerable fraction of the tri- and tetravalent elements was transported in a colloidal state. The main difference in the findings obtained from run 2 as

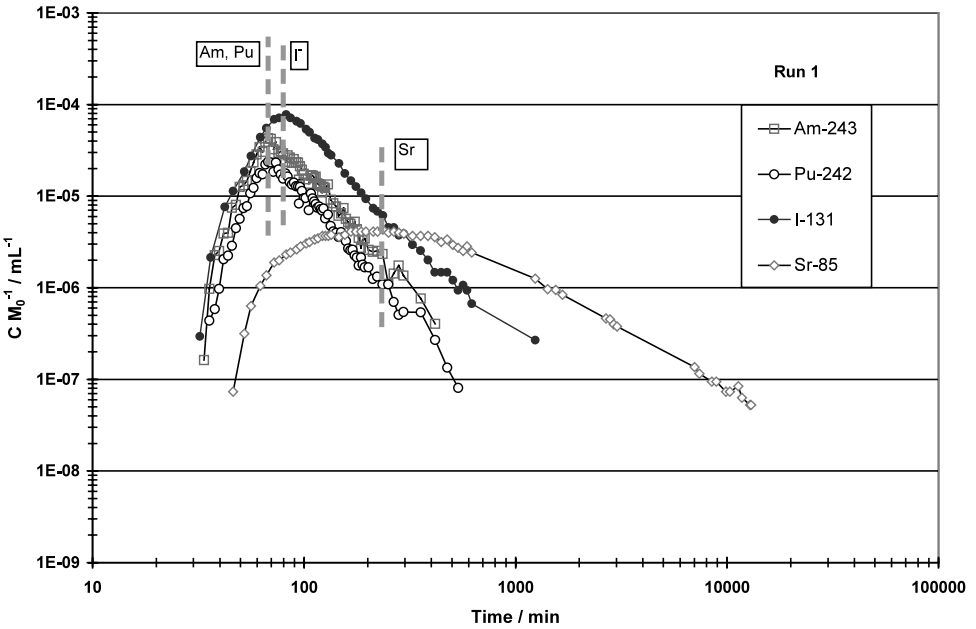

Fig. 8. Breakthrough curves of ^{243}Am, ^{242}Pu, ^{131}I and ^{85}Sr (run 1) without bentonite colloids.

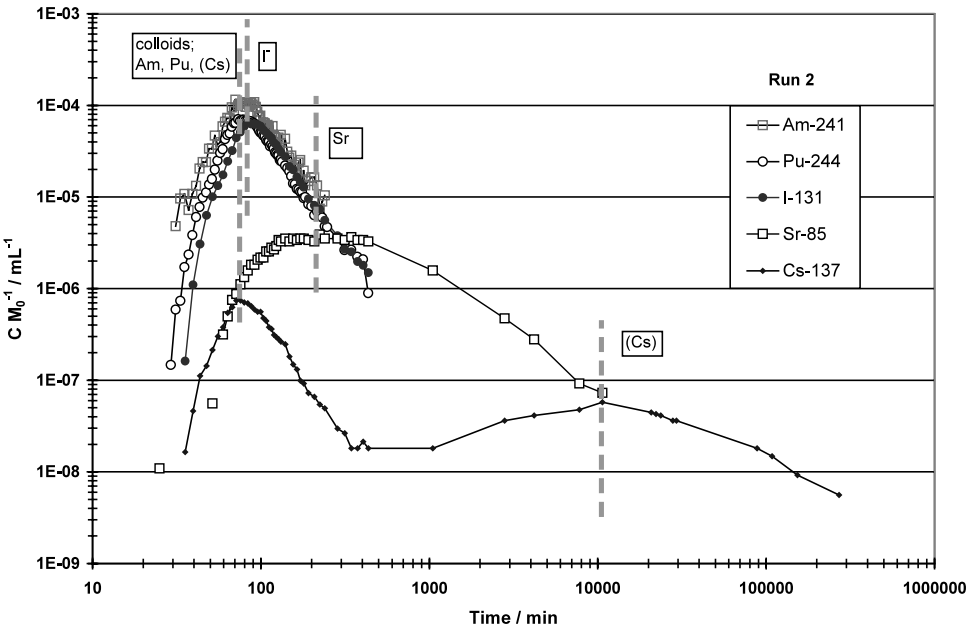

Fig. 9. Breakthrough curves of ^{241}Am, ^{244}Pu ^{131}I, ^{85}Sr and ^{137}Cs (run 2) with bentonite colloids.

compared to run 1 is the increased recovery of the tri- and tetravalent actinides (see Table 2). This is easily explained by the predominantly colloidal state of these metal ions as revealed by the ultracentrifugation experiment. This explanation is supported by the almost identical breakthrough curves obtained for ^{244}Pu and the colloids shown in Fig. 10. Cs clearly shows two different peaks (see Fig. 9) indicating that a certain fraction of this element was probably transported in a colloid state (first peak) while a second fraction appeared retarded. This interpretation is supported by laboratory ultracentrifugation tests (see Ref. [5] for details). Sr experiences a retardation during migration through the fracture due to sorption to fracture surfaces as already observed in earlier migration experiments (e.g. [8]).

4.3. Colloid analysis in breakthrough solutions

Breakthrough curves for the bentonite colloids and the curve for ^{244}Pu fit quite well and the peak maximum is slightly shifted to earlier elution times compared to the peak of the conservative tracer ^{131}I (Fig. 10), as expected from analogy to earlier colloid in situ experiments [14]. Slightly different colloid recoveries obtained by the different methods are partly due to the analytical uncertainties of the methods (notably, the PCS measurements are close to the detection limit of the method) and partly due to uncertainties given by the difficulty of precisely defining the colloid background baseline. However, consideration of the SPC, PCS, ICP-MS and LIBD data suggests that 80–90% of the colloids are passing through the test shear zone with little significant retardation. The precise mechanisms involved are currently unclear and are being further investigated in the laboratory (results will be reported in Ref. [6]).

Single particle counting revealed that the natural colloid background in the Grimsel migration groundwater was 2.1×10^5 ml^{-1} for sizes of 50–100 nm and 6.25×10^6 ml^{-1} for the same size range during the breakthrough of the bentonite colloids. The recovery of the smallest measured colloids by this technique revealed a nearly complete recovery for this size class of between 90 and 100%.

Table 2
Calculated recoveries of Am, Pu, Sr and I in run 1 and 2

Element	Run 1 (without bentonite colloids) Element recovery (%)	Run 2 (with bentonite colloids) Element recovery (%)
Am(III)	34±4	70±15
Pu(IV)	21±3	86±9
Sr(II)	87	90
I(I)	100	92

Under the experimental conditions employed here, there is short-term retardation of certain tracers within the experimental shear zone. Calculations (see Ref. [4]) show that the retarded portion of the tracers are slowly eluted over a period of several weeks at very low concentrations (several orders of magnitude below the detection limits of the analytical techniques).

5. Summary and conclusions

The presented experimental findings show that, under the given conditions in the test shear zone, bentonite colloids influence the in situ retardation behaviour of tri- and tetravalent actinides in a significant way. In the laboratory, it was confirmed that, depending on the advective flow rate of the host rock groundwater, bentonite colloid formation at the bentonite/host rock interface can occur and, thus, substantiate the colloidal scenario taken as a basis of the experimental layout. Once such colloids are produced, their stability, which is strongly dependent on the pH and salinity of the groundwater, is very high in the test site groundwater. The in situ experiment confirmed the laboratory results and the injected bentonite colloids showed a recovery of 80–90% after passing through the 2.23 m long dipole flow field. Colloid facilitated transport was shown to be faster than the transport of dissolved species. The migration behaviour of the tri- and tetravalent actinides Am and Pu was strongly mediated by the bentonite colloids and recovery increased from 20 to 30% in the absence of bentonite colloids, to about 60–80% in the presence of bentonite colloids. A part of Cs follows that behaviour while the Sr breakthrough can be explained by reversible sorption to fracture surfaces without significant interaction with colloids. Data for the migration of Np(V) and U(VI) are currently evaluated and

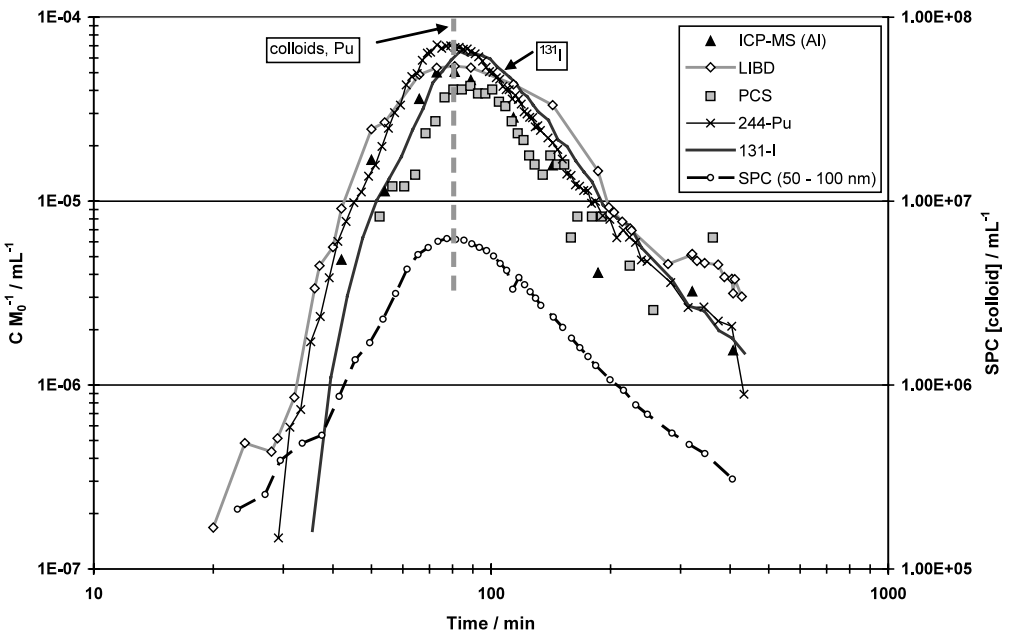

Fig. 10. Colloid breakthrough curves detected by LIBD, PCS, SPC and ICP-MS compared with the breakthrough of ^{131}I and ^{244}Pu (SPC data in colloids ml^{-1}); in case of ICP-MS detection, Al is measured as representing the bentonite colloids.

require some more interpretation. These results will be reported in a forthcoming paper.

As noted above (see Fig. 2), five requirements must be fulfilled to prove that colloid-facilitated transport of radionuclides in a potential repository host rock may be of significance to the long-term performance of a waste repository. The results presented here for the CRR test shear zone conditions indicate that the answer to the first four questions above is probably affirmative. However, before any conclusive statements can be made about the likelihood of significant colloid-facilitated radionuclide transport in the vicinity of a deep geological waste repository, two further points must be addressed:

- first, the last question about reversibility or irreversibility of radionuclide-colloid association must be investigated further in a simple system such as the CRR test shear zone and
- second, this, and the other processes examined here in CRR, must be investigated in repository-relevant systems.

Although the in situ work carried out to date has been on a longer temporal and spatial scale than laboratory experiments, the flow system transmissivities tested in URLs are usually much higher than would be expected in a suitable repository host rock (e.g. in the CRR test shear zone, the transmissivity is around 10^6 times greater). This is common with in situ work carried out and ongoing around the world today and is simply a question of practicalities (i.e. conducting in situ experiments within reasonable time scales and budgets; see examples of this in Ref. [11]). Nevertheless, even if process and mechanism understanding for colloid migration and colloid facilitated radionuclide transport has now increased (through complex experiments such as CRR), future work must consider significantly longer time scales than has been the case so far and focus on, for example, semi-stagnant groundwater systems, to try to better match the conditions in and around a waste repository. Although at an early stage, proposals are currently under consideration for the next period of work at the GTS (phase VI) for experimental durations of up to several decades — or several orders of magnitude longer than has been the case in any rock laboratory anywhere in the world to date. Further information and regular updates will be available on www.grimsel.com.

Acknowledgements

The authors would like to thank the following people for their significant contribution to the work described in this paper F. Geyer, R. Goetz, Th. Rabung and Ch. Marquardt (FZK); M. Rüthi, G. Kosakowski and A. Laube (PSI); V. Fernández, M.G. Gutiérrez, U. Alonso and M. Mingarro (CIEMAT) and F. van Dorp (NAGRA). Special thanks go also to the funding organisations, namely Nagra (CH), ANDRA (F), ENRESA (E), BMWi/FZK-INE (D), JNC (J) and USDoE/SANDIA (USA).

References

[1] W.M. Miller, W.R. Alexander, N.A. Chapman, I.G. McKinley, J.A.T. Smellie, Geological Disposal of Radioactive Wastes and Natural Analogues. Waste Management Series, vol. 2, Pergamon, Amsterdam, 2000.
[2] P. Bossart, M. Mazurek, Grimsel Test Site: Structural Geology and Water Flow-Paths in the Migration Shear Zone. Nagra Technical Report 91-12, Nagra, Wettingen, Switzerland, 1991.
[3] A. Möri, B. Frieg, K. Ota, W.R. Alexander (Eds.), The Nagra-JNC In Situ Study of Safety Relevant Radionuclide Retardation in Fractured Crystalline Rock III: the RRP Project Final Report, Nagra Technical Report NTB 00-07, Nagra, Wettingen, Switzerland, 2002, in preparation.
[4] A. Möri (Ed.), The CRR Final Project Report Series: 1—Description of the Field Phase-Methodologies and Raw Data Nagra Technical Report NTB 03-01, Nagra, Wettingen, Switzerland, 2003, in preparation.
[5] H. Geckeis, T. Missana (Eds.), The CRR Final Project Report Series: 2—Results of the Supporting Laboratory Programme Nagra Technical Report NTB 03-02, Nagra, Wettingen, Switzerland, 2003, in preparation.
[6] J. Guimerà, G. Kosakowski (Eds.), The CRR Final Project Report Series: 3—Results of the Supporting Modelling Programme Nagra Technical Report NTB 03-03, Nagra, Wettingen, Switzerland, 2003, in preparation.
[7] W.R. Alexander, A. Möri (Eds.), The CRR Final Project Report Series: 4—Project Overview and Synthesis of

Results Nagra Technical Report NTB 03-04, Nagra, Wettingen, Switzerland, 2003, in preparation.

[8] U. Frick, W.R. Alexander, B. Baeyens, P. Bossart, M.H. Bradbury, CH. Bühler, J. Eikenberg, Th. Fierz, W. Heer, E. Hoehn, I.G. McKinley, P.A. Smith, The Radionuclide Migration Experiment—Overview of Investigations 1985–1990, Nagra Technical Report NTB 91-04, Nagra, Wettingen, Switzerland, 1992.

[9] P.A. Smith, W.R. Alexander, W. Heer, P.M. Meier, B. Baeyens, M.H. Bradbury, M. Mazurek, I.G. McKinley, The Nagra-JNC In Situ Study of Safety Relevant Radionuclide Retardation in Fractured Crystalline Rock I: The Radionuclide Migration Experiment—Overview of Investigations 1990–1996, Nagra Technical Report NTB 00-09, Nagra, Wettingen, Switzerland, 2001.

[10] P.A. Smith, W.R. Alexander, W. Kickmaier, K. Ota, B. Frieg, I.G. McKinley, Development and Testing of Radionuclide Transport Models for Fractured Rock: Examples from the Nagra/JNC Radionuclide Migration Programme in the Grimsel Test Site, Switzerland, J. Contam. Hydrol. 47 (2001) 335–348. Also published in Japanese in JNC Technical Review 11, JNC TN1340 2001-006, JNC, Tokai, Japan.

[11] W.R. Alexander, P.A. Smith, I.G. McKinley, Modelling radionuclide transport in the geological environment: a case study from the field of radioactive waste disposal, in: E.M. Scott (Ed.), Modelling Radioactivity in the Environment, Ch. 5, Elsevier, Amsterdam, 2002, in press.

[12] C. Degueldre, B. Baeyens, W. Goerlich, J. Riga, J. Verbist, P. Stadelmann, Colloids in water from a subsurface in granitic rock, Grimsel Test Site, Switzerland Geochim. Cosmochim. Acta 53 (1989) 603–610.

[13] W.R. Alexander, B. Frieg, K. Ota, P. Bossart, The RRP project: investigating radionuclide retardation in the host rock, Nagra Bull. 27 (1996) 43–55.

[14] W. Hauser, H. Geckeis, J.I. Kim, Th. Fierz, A mobile laser-induced breakdown detection system and its application for the in situ-monitoring of colloid migration, Colloids Surf. A: Physicochem. Eng. Aspects 203 (2002) 37–45.

[15] M. Plaschke, T. Schäfer, T. Bundschuh, T. Ngo Manh, R. Knopp, H. Geckeis, J.I. Kim, Size characterization of bentonite colloids by different methods, Anal. Chem. 73 (2001) 4338–4347.

[16] F. Huertas, J.L. Fuentes-Cantillana, F. Jullien, P. Rivas, J. Linares, P. Fariña, M. Ghoreychi, N. Jockwer, W. Kickmaier, M.A. Martinez, J. Sampe, E. Alonso, F.J. Elorza, Full Scale Engineered Barriers Experiment for a Deep Geological Repository for High-Level Radioactive Waste in Crystalline Host Rock, EC Final report EUR 19147, EC, Luxembourg, 2000.

[17] T. Missana, U. Alonso, M.J. Turrero, Generation and stability of bentonite colloids at the bentonite/granite interface of a deep geological radioactive waste repository, J. Contam. Hydrol. (2002) in press.

[18] Japan Nuclear Cycle Development Institute, Properties of the buffer, in: H12: Project to Establish the Scientific and Technical Basis for HLW Disposal in Japan, Supporting Report 2: Repository Design and Engineering Technology, Appendix B, JNC Technical Report, JNC TN1410 2000-003, JNC, Tokai, Japan, 2000.

[19] T. Missana, A. Adell, On the applicability of DLVO theory to the prediction of clay colloids stability, J. Colloid Interface Sci. 230 (2000) 150–156.

Results of the Colloid and Radionuclide Retention experiment (CRR) at the Grimsel Test Site (GTS), Switzerland - Impact of Reaction Kinetics and Speciation on Radionuclide Migration -.

Radiochim. Acta (2004) **92**, 765.

Geckeis H., Schäfer T., Hauser W., Rabung T., Missana T.,
Degueldre C., Möri A., Eikenberg J., Fierz T.,
and Alexander W. R.

Radiochim. Acta **92**, 765–774 (2004)

Results of the colloid and radionuclide retention experiment (CRR) at the Grimsel Test Site (GTS), Switzerland – impact of reaction kinetics and speciation on radionuclide migration

By H. Geckeis[1,*], T. Schäfer[1], W. Hauser[1], Th. Rabung[1], T. Missana[2], C. Degueldre[3], A. Möri[4], J. Eikenberg[5], Th. Fierz[6] and W. R. Alexander[7]

[1] Forschungszentrum Karlsruhe, Institut für Nukleare Entsorgung (INE), Postfach 3640, D-76021 Karlsruhe, Germany
[2] Ciemat, Avenida Complutense, 22, E-28040 Madrid, Spain
[3] Paul-Scherrer Institut, Villigen, Switzerland
[4] Geotechnisches Institut, Gartenstrasse 13, CH-3001 Bern, Switzerland
[5] PSI, Würenlingen and Villigen, CH-5232 Villigen PSI, Switzerland
[6] Solexperts, CH-8603 Schwerzenbach, Switzerland
[7] Nagra, CH-5430 Wettingen, Switzerland

(Received September 26, 2003; accepted March 5, 2004)

Actinides / Fission products / Aquatic colloids / Migration / TRLFS / STXM / SPC / LIBD

Summary. The influence of smectite colloids on the migration behaviour of U(VI), Th(IV), Pu(IV), Am(III), Np(V), Sr(II) and Cs(I) is investigated within the Colloid and Radionuclide Retardation experiment (CRR). Two *in situ* experiments in a well-characterized granitic fracture zone are carried out in presence and absence of bentonite colloids. Radionuclide retardation observed in the field studies increases in the sequence Np(V) ~ U(VI) < Sr(II) < Cs(I), where a small fraction of colloid borne breakthrough is only stated for Cs(I) in presence of bentonite colloids. Am(III) and Th/Pu(IV) mainly migrate as colloids without retardation in the presence and absence of smectitic colloids. The radionuclide migration behaviour is discussed on the basis of results obtained in laboratory batch sorption experiments and spectroscopic studies. Consistent with the field observation, laboratory derived K_d values increase in the order Np(V) ~ U(VI) < Sr(II) < Cs(I). Significant kinetic hindrance for the sorption to fault gauge minerals is observed for Sr(II) and Cs(I), but notably for Am(III) and Pu(IV). The slow sorption reaction of tri- and tetravalent actinide ions is explained by their kinetically hindered dissociation from colloidal species. In order to explain the colloidal behaviour of tri- and tetravalent actinides even in absence of bentonite colloids, ultracentrifugation and spectroscopic experiments are performed. It is found that up to 60% of Pu(IV) and Am(III) species can be centrifuged off. Adding Cm(III) (5×10^{-8} mol L^{-1}) into both injection solutions instead of Am(III) allows for a spectroscopic study by using the time resolved laser fluorescence spectroscopy (TRLFS). Peak position and fluorescence lifetimes ($\lambda = 604$ nm, $\tau = 110$–114 μs) together with the fact that Cm(III) can be widely separated by ultracentrifugation, suggest the existence of inner-sphere surface complexes on groundwater and bentonite colloids. Carbon *K*-edge XANES analysis of the bentonite colloids reveal the presence of natural organic constituents. They are mainly of aliphatic nature containing high fractions of carboxylate groups. A contribution of these organic species towards the bentonite colloid stability and sorption of actinides is assumed to be likely.

Introduction

A number of recent studies carried out in the laboratory or *in situ* demonstrated the relevance of aquatic colloids as potential carriers for the radionuclides under natural groundwater conditions [1–3]. Organic humic/fulvic acids [1, 3], inorganic clay, silica or iron oxide/hydroxide nanoparticles [2, 4] have been identified as relevant colloidal species. It is now well established that under certain geochemical conditions especially the tri- and tetravalent actinides are prone to colloid formation and to colloid borne migration [2, 5]. The generation of colloidal species conflicts with the generally assumed low mobility and low solubility of these elements and, therefore, belong to the key uncertainties of nuclear waste disposal performance assessment considerations.

The aim of the Colloid and Radionuclide Migration experiment (CRR) at the Grimsel Test Site, Switzerland, is to investigate the bentonite colloid influence on the radionuclide migration at the near field/far field interface of a high level nuclear waste repository in crystalline rock. The CRR experiment is carried out in the frame of an international project conducted by ANDRA (F), ENRESA (E), JNC (J), USDOE/Sandia (USA), FZK-INE (D) and NAGRA (CH). The smectite clay colloids investigated in this study originate from a natural bentonite (FEBEX, Spain [6]) that is considered as an appropriate backfill and barrier material in a nuclear waste repository in fractured hostrock. They exhibited a considerable stability under the given groundwater conditions of the site [7–9, 17]. The geochemical reactions of Pu, Th, Am, Np, U, Cs and Sr within the ternary system consisting of fault gouge minerals, groundwater and colloids

*Author for correspondence (E-mail: geckeis@ine.fzk.de).

are investigated in laboratory batch experiments and in field studies by injecting radionuclide and colloid containing solutions into an established dipole flow field in a natural shear zone at NAGRA's Grimsel Test Site, Switzerland. Two *in situ* runs were performed, where in run 1 a groundwater solution containing the actinide ions U(VI), Np(V), Th(IV), Pu(IV), Am(III), Sr(II) and iodide as a non-sorbing tracer has been injected. The injection solution in run 2 contained additionally Cs(I) and 20 mg L^{-1} bentonite colloids. In a previous paper we reported first results of the CRR *in situ* radionuclide migration experiments [9]. It was shown that tri- and tetravalent actinide mobility is clearly enhanced in the presence of colloids.

The present paper

- completes the outcome of the field study by adding data on the migration of U(VI) and Np(V);
- attempts to explain the radionuclide elution sequence observed in the field study in a qualitative way by considering batch sorption experiments performed in the laboratory, and
- discusses the chemical nature of the actinide-colloid binding with respect to its reversibility on the basis of spectroscopic results.

Site description

The test shear zone at Nagra's Grimsel Test Site (GTS) is located at about 1730 m above sea level under a $\sim$ 450 m thick overburden of crystalline rock [9, 10]. The thickness of the shear zone varies between 0.15 and 0.90 m. The fault gouge material (mylonite/protomylonite) is mainly composed of muscovite, biotite, chlorite, epidote, K-feldspar, plagioclase and quartz. Carbonate minerals are not found [11]. Transmissivities of around 10^{-6} m^2 s^{-1} have been measured. The transmissivity gives the amount of water [m^3/s] transported in a 1 m wide aquifer under a unit hydraulic gradient. For the tracer tests reported below, a dipole of 2.23 m length was used. The relevant geometrical data of the boreholes and dipoles are summarised in Möri *et al.* [9]. The groundwater at the site is characterized by low ionic strength, low carbonate concentration and high pH [12] (Table 1).

Table 1. Chemical composition of the Grimsel groundwater [12]; the alkalinity determined by potentiometric titration in [eq L^{-1}] represents the total concentration of dissolved carbonate ([HCO_3^-] + 2[CO_3^{2-}]).

Parameter	
pH	9.6 ± 0.2
Temp. [°C]	12 ± 1
E_h [V]	≤ -0.2
	mol L^{-1}
Na^+	6.9×10^{-4}
K^+	5.0×10^{-6}
Mg^{2+}	6.2×10^{-7}
Ca^{2+}	1.4×10^{-4}
Sr^{2+}	2.0×10^{-6}
Rb^+	2.5×10^{-8}
Cs^+	5×10^{-9}
SO_4^{2-}	6.1×10^{-5}
F^-	6.1×10^{-5}
Cl^-	1.6×10^{-4}
Br^-	3.8×10^{-7}
I^-	1.0×10^{-9}
Alkalinity [eq L^{-1}]	4.5×10^{-4}

Experimental details

Experimental *in situ* parameters and instrumentation

The dipole flow field injection and withdrawal flow rates of 10 and 150 mL min^{-1}, respectively, were established by two HPLC pumps. A more detailed description of the experimental arrangement is available from Refs. [9, 13]. The tracer solutions were stored under Ar atmosphere in a 250 ml bottle made of high density polyethylene. An aliquot of 100 ml was introduced into the flow field by pressurised N_2 *via* a valve. The extraction side contained an extraction pump (HPLC), pH, O_2 and E_h flow through cells and a flow meter. Various on-line and off-line analytical methods were applied to monitor breakthrough of radionuclides and colloids.

Analysis of tracers in the dipole extraction fluid

A portable Ge-detector was used for *in situ* γ-spectrometric analysis of I-131, Sr-85 and Cs-137 in the dipole extraction fluid [9]. Selected samples were additionally analysed in the laboratory. In order to increase the detection sensitivity larger sample volumes were taken and counting times enhanced. Pu-238, Am-241, Am-243, Np-237 and U-233 concentrations were determined in sampled aliquots by α-spectrometry in the laboratory after evaporation on stainless steel plates. Due to the limited energy resolution of the method, Pu-238 and Am-241 as well as Np-237 and U-233 could not be differentiated. In samples where those nuclides coexisted (samples of run 2) only the sum activity of both nuclides could be given. Element analysis of sample aliquots collected from the dipole effluent and the injection cocktail was done with an ICP-mass spectrometer equipped with an ultrasonic nebuliser and a desolvation device. Beside the actinide isotopes, Al was measured in dipole effluent aliquots as an indicator for the presence of smectite colloids.

Colloid detection

On-line colloid analysis during the second field experiment was done by laser light scattering (photon correlation spectroscopy; PCS) and a mobile laser-induced breakdown detection (LIBD) system for the sensitive colloid analysis. In both cases, the dipole extraction fluid was led *via* a bypass to the quartz flow through cuvettes of the PCS and LIBD arrangement. During detection the bypass flow was stopped. The LIBD method and modes of calibration and data evaluation are described elsewhere [14]. Details of the on-line colloid analysis by both PCS and LIBD are available from [9, 13, 14]. Colloid analysis of selected samples in the laboratory was performed additionally by using another laser light scattering method, the Single Particle Counting (SPC) in a flow-through mode as described earlier [15]. 50 mL samples aliquots were collected at the end of the

Table 2. Composition of the injection solutions for run 1 and run 2 in Grimsel groundwater; Colloidal fractions have been determined by ultracentrifugation.

Injection solution for run 1						
	Anal. meth.	Activity conc. $Bq\,L^{-1}$	Mass conc. $g\,L^{-1}$	Mass conc. $mol\,L^{-1}$	Rel. analyt. uncertainty %	Colloidal fraction % coll
^{131}I	γ-spec.	7.46×10^{5}	1.62×10^{-10}	1.24×10^{-12}	1.1	0
^{85}Sr	γ-spec.	9.52×10^{5}	1.09×10^{-9}	1.28×10^{-11}	4.6	0
^{232}Th	ICP-MS	1.06×10^{-2}	2.60×10^{-6}	1.12×10^{-8}	10	20–30
^{238}U	ICP-MS	2.82	2.26×10^{-4}	9.50×10^{-7}	10	0–12
^{237}Np	ICP-MS/α-spec.	5.82×10^{3}	2.24×10^{-4}	9.44×10^{-7}	5	0–10
^{238}Pu	α-spec.	6.70×10^{3}	1.06×10^{-8}	4.44×10^{-11}	2	5–58
^{242}Pu	ICP-MS	3.50×10^{2}	2.40×10^{-6}	9.94×10^{-9}	8	5–58
^{243}Am	ICP-MS/α-spec.	1.06×10^{4}	1.44×10^{-6}	5.93×10^{-9}	4	6–58
Injection solution for run 2 (solution contains additionally 20 $mg\,L^{-1}$ bentonite colloids)						
	Anal. meth.	Activity conc. $Bq\,L^{-1}$	Mass conc. $g\,L^{-1}$	Mass conc. $mol\,L^{-1}$	Rel. analyt. uncertainty %	Colloidal fraction % coll
^{131}I	γ-spec.	5.56×10^{5}	1.21×10^{-10}	9.23×10^{-13}	2.9	0
^{85}Sr	γ-spec.	8.24×10^{5}	9.41×10^{-10}	1.11×10^{-11}	2.5	0
^{137}Cs	γ-spec.	6.07×10^{6}	1.90×10^{-6}	1.38×10^{-8}	2.3	8
^{232}Th	ICP-MS	1.03×10^{-2}	2.55×10^{-6}	1.10×10^{-8}	8	94
^{233}U	ICP-MS	7.22×10^{4}	2.02×10^{-4}	8.69×10^{-7}	8	6
^{237}Np	ICP-MS	6.72×10^{3}	2.58×10^{-4}	1.09×10^{-6}	8	0–1
^{238}Pu	α-/γ-spec.	7.20×10^{3}	1.14×10^{-8}	4.77×10^{-11}	10	84
^{244}Pu	ICP-MS	1.11	1.64×10^{-6}	6.70×10^{-9}	8	84
^{241}Am	γ-spec.	2.04×10^{4}	1.61×10^{-7}	6.66×10^{-10}	8	99

extraction line and analysed in the laboratory. Colloid concentrations were determined for different size classes. The method was calibrated by reference polystyrene colloids as described in [16].

Preparation of tracer solutions

Two injection solutions were prepared by spiking the radionuclides to Grimsel groundwater under Ar atmosphere. The composition of both solutions is given in Table 2. More detailed description of the tracer cocktail preparation is available from [9, 13]. The colloid stock suspension for the *in situ* migration experiment was prepared from a batch of FEBEX bentonite (grain size $< 63\,\mu m$) as described in [9, 17].

Laboratory batch sorption experiments

Batch sorption experiments were carried out under anaerobic conditions ($O_2 < 1$ ppm, Ar or N_2 atmosphere). Bentonite colloid dispersions in Grimsel groundwater were prepared as described in [9]. The fault gouge minerals were crushed and equilibrated with Grimsel groundwater. The final pH of the solution in all batch sorption studies always remained between 9.2 and 9.6. Samples were taken at variable time periods to investigate the time dependency of the sorption reaction. Experimental conditions for Cs(I) and U(VI) sorption studies were: Solid:liquid ratio for experiments with bentonite colloids was 1 : 435 and 1 : 4 for studies with crushed fault gouge minerals (grain size: $< 300\,\mu m$). 7.6×10^{-8} $mol\,L^{-1}$ Cs-137 and 6.8×10^{-7} $mol\,L^{-1}$ U-233 were spiked to the groundwater in contact with the solid in separate batch experiments. The evolution of the radionuclide concentration was followed by liquid scintillation counting (LSC) for uranium and gamma counting for Cs.

Conditions for investigations on Np(V), Pu(IV) and Am(III) sorption were: Solid : liquid ratio is 1 : 4 for experiments with fault gouge minerals. In these experiments a size fraction of 250–800 μm was chosen in order to avoid extensive colloid generation from the fine grains of the mylonite. Such colloids may interact with actinide ions and, thus, influence the sorption behaviour. Np-237 (1.1×10^{-8} $mol\,L^{-1}$), Pu-244 (7×10^{-10} $mol\,L^{-1}$), and Am-243 (1.4×10^{-9} $mol\,L^{-1}$) were spiked simultaneously to a batch experiment and concentrations were analysed in sample aliquots by ICP-MS. Np and Pu-stock solutions were checked prior to dilution and spiking to the groundwater by UV-Vis absorption and were found to consist to more than 90% of Pu(IV) and exclusively of Np(V), respectively. Sorption of Np(V) (1.4×10^{-8} $mol\,L^{-1}$), Pu(IV) (3.8×10^{-11} $mol\,L^{-1}$) and Am(III) (9×10^{-10} $mol\,L^{-1}$) onto bentonite colloids (solid:liquid ratio: 1 : 50 000) and colloid influence on the sorption to fault gouge minerals was studied by spiking 20 $mg\,L^{-1}$ bentonite colloids to the groundwater and to groundwater in contact with the fault gouge minerals, respectively. Bentonite colloid concentration was then monitored indirectly by following the Al-concentration measured by ICP-MS. Radionuclide species were determined in the supernating solution and in ultracentrifuged aliquots (90 000 rpm; *ca.* 5×10^{5} g) in order to quantify the colloidal radionuclide fraction.

Time resolved laser spectroscopy (TRLFS)

An aliquot of a Cm-248 ($t_{1/2} = 3.49 \times 10^{5}$ a; 89.9 mass. % Cm-248, 9.4 mass. % Cm-246, 0.7 mass. % Cm-244) stock solution with a concentration of 1.27×10^{-4} $mol\,L^{-1}$ stored in 0.1 $mol\,L^{-1}$ $HClO_4$ was spiked to pure Grimsel ground-

water and groundwater containing 20 mg L^{-1} bentonite colloids under inert gas atmosphere (Ar; < 1 ppm O_2). Another two samples (absence and presence of bentonite colloids) contained additionally 10^{-8} mol L^{-1} Th-232 and Pu-244, in order to simulate the injection solutions. The final Cm concentration was adjusted to 5×10^{-8} mol L^{-1}. Solution pH after spiking the metal ions to the groundwater was adjusted to 9.2 by adding dropwise NaOH solution. After 5 d storage, solution aliquots were analysed by the time-resolved laser spectroscopy (TRLFS) and Cm-248 concentrations before and after 30 min ultracentrifugation (90 000 rpm, *ca.* 5×10^5 g) were determined by liquid scintillation counting.

TRLFS measurements were performed with a pulsed Nd:YAG pumped dye laser system (Continuum, Powerlite 9030, ND 6000). The fluorescence emission was detected by an optical multichannel analyzer consisting of a polychromator (Chromex 250) with a 1200 lines/mm grating. To fade out any light scattering and background fluorescence, the emission spectra of Cm(III) were recorded 1 μs after the exciting laser pulse in the range of 580–620 nm and at a constant excitation wavelength of 396.6 nm (laser dye: Exalite 398) and in a time window of 1 ms. For lifetime measurements the time delay between the laser pulse and the camera gating was scanned with time intervals between 10 and 15 μs.

Carbon *K*-edge XANES analysis

Measurements were performed at the Scanning Transmission X-Ray Microscope (STXM), National Synchrotron Light Source (NSLS) at Brookhaven National Laboratories (BNL), undulator beamline X1A1, operated by the State University of New York at Stony Brook [18]. The principle of this method is described in detail elsewhere [18, 19]. STXM images of Febex smectite colloids were recorded in the energy range from 280 eV to 305 eV with the image stack option [20] using an undulator gap of 36.5 mm. Details on sample preparation, energy calibration and energy resolution are given in [21, 22]. Only spectra with at least 1% X-ray transmittance of the incoming flux were used to avoid spectral distortion. The baseline corrected and normalized carbon XANES spectrum was then further resolved into its individual arctangent [23, 24] and Gaussian curve components, using the nonlinear least-squares fitting routine SOLVER of Microsoft Excel. Details on the de-convolution procedure of the main $1s-\pi^*$ or Rydberg/mixed valence transitions can be found in [22].

Results and discussion

In situ migration studies

A complete summary of the outcome of the migration tests run 1 and 2 is given in Table 4, Fig. 1a,b. Radionuclide concentrations in both figures are normalized to the injected mass or activity m_0. Such normalization allows for a comparison of tracer breakthrough curves performed at variable tracer concentration ranges. The colloids in the injection solution of run 2 are found to have a size of 109 ± 10 nm as determined by LIBD. SPC finds the colloids mainly in a size range of 50–100 nm (94%). Only 4% are attributed to a size range of 100–150 nm. Results determined by both methods appear to be fairly consistent. The intensity weighed average size obtained by PCS by using the quadratic weighted cumulant analysis (QC) [25] is at 202 ± 45 nm. An overestimation of the intensity weighed size by PCS can be explained by the strong size-dependent increase of scatter light intensity. Thus, a small fraction of larger particles may easily cover a larger number of smaller ones (see *e.g.* [25]). No significant change of the colloid size distribution after passage of the fracture could be stated by LIBD. SPC detects less recovery for colloids > 100 nm. All methods including ICP-MS monitoring of the Al concentration as an indicator for the smectite colloids point to a quite high colloid recovery > 85%.

The tri- and tetravalent actinide migration is clearly dominated by colloidal species in the presence of bentonite colloids (run 2; Fig. 1b). Peak maxima of their breakthrough curves appear about ten minutes ahead of the non-sorbing tracer I^- together with the colloid breakthrough detected with the different colloid detection methods. The shift points to the existence of size or charge exclusion effects typical to colloid migration. A part of tri- and tetravalent actinide ions (20%–40%) shows as well the colloid pattern breakthrough curve even in absence of the bentonite colloids in run 1. The nature of these colloids, however, is unclear and calls for further investigations (see discussion below). Sr(II) behaves as expected and as already observed in earlier migration ex-

Table 3. Bentonite colloid bound radionuclide fractions in the injection solution of run 2 as determined experimentally by ultracentrifugation and as calculated from K_d-values.

	U(VI)	Np(V)	Pu(IV)	Am(III)	Cs(I)
K_d (ml g^{-1}) sorption to bentonite coll.	8.2×10^2	$< 5.0 \times 10^3$	1.0×10^5	2.0×10^6	8.8×10^3
Total RN conc. in cocktail (mol L^{-1})	8.7×10^{-7}	1.0×10^{-6}	6.7×10^{-9}	8.0×10^{-10}	1.6×10^{-8}
Colloid bound RN fraction (%)					
(Calculated)	2	< 9	67	98	15
(Measured by ultracentrifugation)	6	< 1	84	99	8
Colloid bound RN conc. (mol L^{-1})	1.4×10^{-8}	$< 1 \times 10^{-7}$	4.5×10^{-9}	6.5×10^{-10}	2.1×10^{-9}

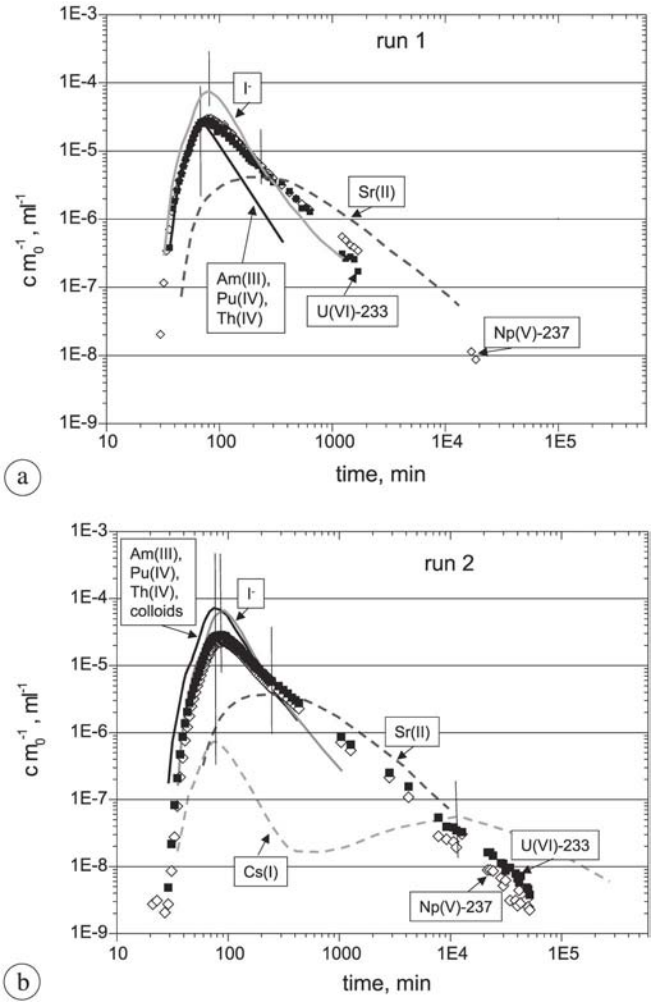

Fig. 1. (**a**) Breakthrough curves for I-131, Sr-85, Am-243, Pu-242, Np-237, U-238 in run 1 (no bentonite colloids). (**b**) Breakthrough curves for I-131, Sr-85, Cs-137, Am-241/Pu-238, Pu-244, Np-237, U-233 in run 2 (20 mg L^{-1} bentonite colloids); radionuclide concentrations are normalized to the injected mass or activity of the respective radionuclide.

periments at the GTS [26, 27] like a weakly retarded tracer and is not influenced by the presence of bentonite colloids. Less than 1% of Cs(I) migrates colloid borne in run 2 while the major part experiences strong retardation. These findings have been already discussed in our previous paper [9].

Evaluation of analytical data for Np(V) and U(VI) elution in run 1 and 2 obtained by ICP-MS and α-spectrometry is now implemented in Fig. 1a, b and Table 4. The migration of both actinide ions appears to be identical and unbiased by the presence of colloids. Both nuclides are completely eluted after 14 to 30 days. The shape of the breakthrough curves, however, suggests an ambivalent migration behaviour: A fraction of both actinide ions moves like the conservative tracer I^-. However, the Np(V), U(VI) breakthrough curves show a significantly more pronounced tailing than found for I^-. Similar breakthrough curves have been stated already at the GTS for the sorbing tracers Sr(II) and Cs(I) in *in situ* experiments at a short dipole distance (1.7 m) [28]. The observation is explained by rapid flow through open flow field channels with residence times around 1 h, giving the tracers not sufficient time to interact with the rock surface [27]. Increasing the flow field distance to 4.9 m resulted in a clear increase of the retardation factors (Sr(II): 54; Cs(I): 767 [27]). At longer residence time, the radionuclides are able to access pores and to undergo sorption reactions [26, 27]. The dipole distance and residence times in our studies lie in between those of the two previous experiments and so are the retardation ratios for Sr(II) and Cs(I). The discussion shows that tracer retardation strongly depends on residence times within the dipole flow field of the water conducting shear zone. The following section, therefore, deals with the examination of kinetics involved into the sorption reaction.

Sorption and desorption kinetics

Sorption onto bentonite colloids

Sorption to bentonite colloids for Cs(I), Np(V), U(VI), Am(III) and Pu(IV) determined in batch experiments shows slight time dependence in a period ranging from 1 h to weeks but partly obscured by the uncertainty of the ultracentrifugation separation. K_d values are highest for Am(III) (1.2×10^6–2.7×10^6 ml g^{-1}) and Pu(IV) (1.0×10^5–8.0×10^5 ml g^{-1}). Data for Am(III) lie in a range comparable to those found for the sorption of its chemical homologue Eu(III) onto Na-montmorillonite under similar conditions [29]. The larger scatter of the Pu(IV) K_d values and the fact that they are smaller than those found for Am(III) may be explained by the presence of a small fraction of Pu species with higher oxidation states ($< 10\%$) in the Pu stock solution showing weaker sorption. No interaction of Np(V) with bentonite colloids could be observed, which demonstrates that no significant reduction to the tetravalent state occurs. The upper limit for the respective K_d values ($< 5 \times 10^3$ ml g^{-1}) is, however, quite high due to the small solid:liquid ratio (1 : 50 000) used in those experiments. K_d values for Cs(I) (6.4×10^3–8.7×10^3 ml g^{-1}) are found to be somewhat higher compared to those obtained for U(VI) (0.8×10^3–2.5×10^3 ml g^{-1}). For Cs(I) and U(VI) non-linear sorption isotherms have been established [30], so that K_d values are expected to increase at lower metal ion concentrations. Despite the uncertainties adhering to these K_d-values, they are reflecting the radionuclide partitioning between colloids and dissolved species in the injection solution of run 2 fairly well (see Table 3).

Sorption to fault gouge minerals

K_d-values for Cs(I) rapidly raise to ~ 550 ml g^{-1} and then slowly increase to > 1000 ml g^{-1} within several weeks (Fig. 2). These data are compatible with those given by Aksoyoglu *et al.* [31], who found a similar time dependency for the sorption of Sr(II) onto Grimsel mylonite [31]. For the crushed solid with a grain size < 250 μm, they report K_d-values of 67–75 ml g^{-1} for Sr(II) after 30–40 days (see Fig. 2). The pattern of Cs and Sr-sorption kinetics might be explained by a two-step sorption reaction as suggested in [31–33]: A fast surface adsorption reaction (ion exchange, isotope exchange) is followed by the surface diffusion into micropores of the solid. Aquatic speciation of Cs(I) and Sr(II) ions under given conditions is dominated by the aquo cations. The prevailing existence of anionic

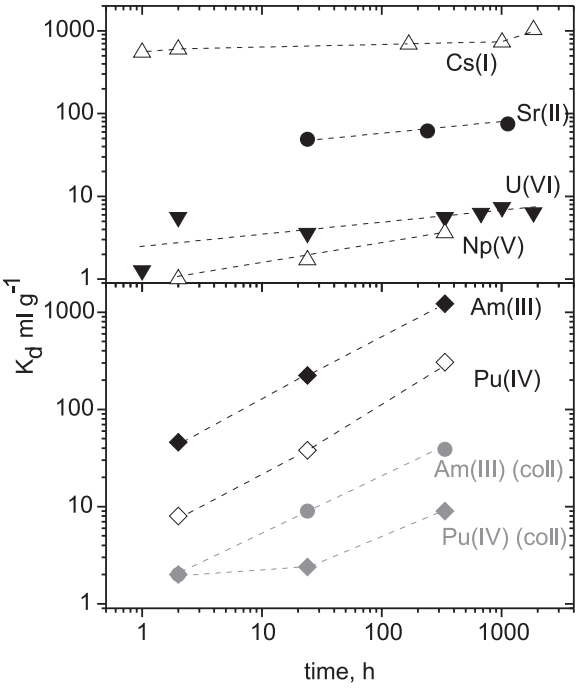

Fig. 2. Sorption coefficients (K_d; ml g^{-1}) obtained in batch experiments for Np-237, U-233, Pu-244, Am-243, Cs-137, Sr-85 in Grimsel groundwater in contact with fault gouge minerals; Solid to liquid ratio is: 1 : 4; data plotted in grey are obtained in the presence of 20 mg L^{-1} bentonite colloids; Sr-85 K_d-values are taken from [31].

carbonato complexes (see Table 4) counteracting the interaction with the rock surface may explain the comparably weak sorption of Np(V) and U(VI). For Np(V) and U(VI) only a weak time dependent increase is observed. Due to the low redox buffer capacity in the groundwater and the low content of Fe(II) in the mylonite, no reduction of the oxidized actinide species can be observed within the period of our experiments. Time dependence of the sorption reaction is significantly more pronounced for Am(III) and Pu(IV) where the K_d-values determined after ultracentrifugation increase by more than one order of magnitude within two weeks. Without centrifugation much lower K_d-values are obtained. Thermodynamic calculations [12] suggest the presence of dissolved $Pu(OH)_4$ and hydroxo- and carbonato complexes for Am(III). Pu(IV) concentrations spiked to the groundwater are exceeding calculated solubility limits (1×10^{-10}–2×10^{-9} mol L^{-1} [12]) so that precipitation of colloidal $Pu(OH)_4$ or oxihydroxide species is likely under the experimental conditions. On the other hand, the calculations indicate undersaturation of Am(III) taking into account the available solubility data for $AmOHCO_3$ and $Am(OH)_3$(am) solids ($c_{sol} \geq 1.1 \times 10^{-7}$ mol L^{-1} [12]). Our experimental data, however, indicate both actinides being present to a considerable fraction as colloidal species in batch experiments and in the injection solution of run 1. The colloidal fractions (see Table 2) determined by ultracentrifugation experiments reveal a considerable scatter. This fact suggests that colloids are of low density and/or small size and, thus, are not completely separated by ultracentrifugation. Slow desorption of the actinide ions from such colloids or sorption of the actinide bearing colloids to the rock surface could explain the observed sorption kinetics which is obviously not completed after weeks. The instability of those colloidal actinide species with time is also demonstrated by the analysis of the injection solution after 19 months. ∼ 90% of Am(III) and Pu(IV) disappeared from solution due to sorption to container walls.

Influence of bentonite colloids on sorption to fault gouge material

The influence of 20 mg L^{-1} bentonite colloids on the sorption to fault gouge material is studied for Am(III) and Pu(IV). Frequent ICP-MS analysis of the supernatant in those batch experiments shows Al concentrations remaining constant with time and corresponding to the nominal Al content of the 20 mg L^{-1} colloid solution. The constant Al concentration demonstrates that within the observation time period, bentonite colloids do not sorb onto the fault gouge material. Ultracentrifugation of the solution yields Al-concentrations close to the natural content of the groundwater (∼ 50 µg L^{-1}). Am(III) and Pu(IV) K_d-values decrease by about one order of magnitude in presence of the colloids proving their strong influence on these actinide ions (Fig. 2). It is, however, interesting to note that the K_d values in presence of colloids show a time dependence similar to that obtained in absence of bentonite colloids. The similar time dependence in both experimental series supports the hypothesis that the kinetics of actinide ion desorption from colloids is primarily responsible for the pronounced increase of K_d values with time in both solutions. The results, moreover, indicate the reversibility of the actinide-colloid binding within a time period of days and weeks.

The sorption coefficients (K_d-values) determined in the present study are not appropriate to gain quantitative insight into sorption reactions and the underlying mechanisms. Crushed fault gouge material had to be used in the present experiments. Hence, the K_d-values will be influenced by the generation of fresh surfaces. In order to apply such K_d-values to describe the migration experiments, they have to be scaled to the available surface sorption sites within the flow field (see [34]). Sorption reactions are moreover influenced by the heterogeneity of the given natural system. Sorption data obtained in the laboratory using a small aliquot of natural minerals may not adequately describe sorption phenomena in an *in situ* experiment of larger spatial scale. The data presented here, therefore, should primarily be considered as an information on the time dependent sorption behaviour of the individual radionuclides and represent an estimate on the order of magnitude of radionuclide sorption. Sorption data are not directly comparable as they are partly obtained with mylonitic fault gouge material of different grain size. A comparison of K_d-values for Sr(II), Cs(I) and U(VI) obtained by varying the mylonite grain size shows maximum variations by a factor of 4 [13, 31]. Despite the experimental uncertainties, the sequence of radionuclide retardation in run 1 and 2 following the order U(VI) ∼ Np(V) < Sr(II) < Cs(I) is in accordance with the K_d-values. The partly unretarded U(VI) and Np(V) migration results from the quite weak sorption behaviour in combination with short residence times in the fracture.

Pu(IV) and Am(III) migration can only be explained by the presence of colloidal species and their kinetically inhibited desorption from colloids. Breakthrough of those frac-

Table 4. Results of the *in situ* migration experiments; R_p: Peak elution time; R_f: Retardation factor ($R_f = R_{p\,(radionuclide)}/R_{p\,(I\text{-}131)}$); Predominant chemical species are included in the table for the individial radionuclides as calculated in [12]; Recoveries are given as determined by the different analytical methods after certain times.

Run 1					
Tracer	Calculated chemical speciation [9]	R_p [min]	R_f	Recovery [%]	Recoveries after certain times determined by the different analytical methods
I-131	I^-	76–82 (79)	1	100	after 1.1×10^3 min; γ-spec
Sr-85	Sr^{2+}	236	3	87	after 1.3×10^4 min; γ-spec
Np-237	$NpO_2CO_3^-$ NpO_2^+	81	1	110 ± 13 70 ± 8 67	after 2×10^4 min; ICP-MS after 1.7×10^3 min; ICP-MS after 590 min; α-spec
U-238	$UO_2(CO_3)_3^{4-}$ $UO_2(CO_3)_2^{2-}$ $UO_2(OH)_3^-$	78–82	1	62 ± 9	after 1.7×10^3 min, ICP-MS
Am-243	$AmOHCO_3$ $Am(CO_3)_2^-$ $Am(OH)_2^+$	68–72	0.88	34 ± 4 43	after 416 min; ICP-MS after 588 min; α–spec
Pu-238/242	$Pu(OH)_4$	68–70	0.87	21 ± 3 29	after 536 min; ICP-MS after 236 min; γ-spec
Th-232	$Th(OH)_4$	68	0.86	–	
		Run 2			
Tracer		R_p [min]	R_f	Recovery [%]	Recoveries after certain times
I-131		84–90 (88)	1	92	after 1.1×10^3 min; γ-spec
Sr-85		178–284 (223)	2.5	88	after 1.1×10^4 min; γ-spec
Cs-137		1) 71 2) 10 663	0.81 121	70	after 2.7×10^5 min; γ-spec
Np-237		89–93	1	82 ± 4 83 ± 12 81 (U+Np)[a]	after 5.1×10^4 min; ICP-MS after 1.7×10^3 min; ICP-MS after 4.2×10^3 min, γ-spec
U-233		78–82	1	103 ± 5 81 (U+Np)[a]	after 5.1×10^4 min; ICP-MS after 4.2×10^3 min; γ-spec
Am-241		75–81	0.9	70 (Am+Pu)[a]	after 4.2×10^3 min; γ-spec
Pu-238/244		75–83	0.9	86 ± 9 70 (Am+Pu)[a]	after 434 min; ICP-MS after 4200 min; γ-spec
Th-232		75–81	0.9	63 ± 8	after 171 min; ICP-MS
Bentonite Colloids		78–81	0.9	85–100	LIBD, SPC, PCS

R_p-values in brackets are taken as mean values;
a: Recovery is related to both radioelements; the nuclides could not be differentiated by α-spectrometry.

tions of Pu(IV) and Am(III) which are not eluted as colloid borne species in run 1 can not be detected due to the limited sensitivity of the analytical methods.

Spectroscopic examination of the actinide binding to colloids

The question towards the reversibility and the kinetics of actinide-colloid binding is not only important for the interpretation of the present *in situ* migration experiment. The answer to this question has considerable impact on the assessment the colloid relevance for the long term safety of a nuclear waste repository [9, 35] and calls for the closer inspection of the nature of colloid binding to actinides. Spectroscopic methods like Extended X-Ray Absorption Fine Structure (EXAFS) and the Time-resolved laser induced fluorescence spectroscopy (TRLFS) have been applied to gain information on the structure and chemical bonding of colloidal and surface sorbed actinide species on a molecular scale. TRLFS using Cm(III) as a fluorescent probe has

the striking advantage to provide spectroscopic information even at trace concentrations down to 10^{-8} mol L^{-1} [36], *i.e.* at concentrations relevant to natural groundwater systems. Cm(III) has been proven in numerous studies to exhibit an almost identical geochemical behaviour as compared to Am(III) (*e.g.* [37]). TRLFS results on Cm(III), therefore, are applied to describe the colloidal behaviour of Am(III) in Grimsel groundwater.

Fluorescence spectra of a 5×10^{-8} mol L^{-1} Cm(III) solution in Grimsel groundwater alone, in groundwater spiked with 20 mg L^{-1} bentonite colloids and as a reference, a spectrum of Cm(III) sorbed onto Ca-montmorillonite at pH = 9.2 (taken from [38]) are plotted in Fig. 3. All spectra show a peak maximum at around 603.8 nm. For all spectra fluorescence lifetimes range from 100 to 114 μs. The red shift of the Cm(III) fluorescence emission bands in the samples and the increase of the fluorescence lifetime relative to the spectrum of the free Cm(III) aquo ion (peak maximum: 593.8 nm; lifetime: 65–68 μs) indicate the formation of inner-sphere complexes. By applying the empirical correlation of Kimura [39], we can derive from the fluorescence lifetime that 4.8 to 5.6 H_2O molecules or OH^- ions exist in the inner coordination sphere of the Cm(III)

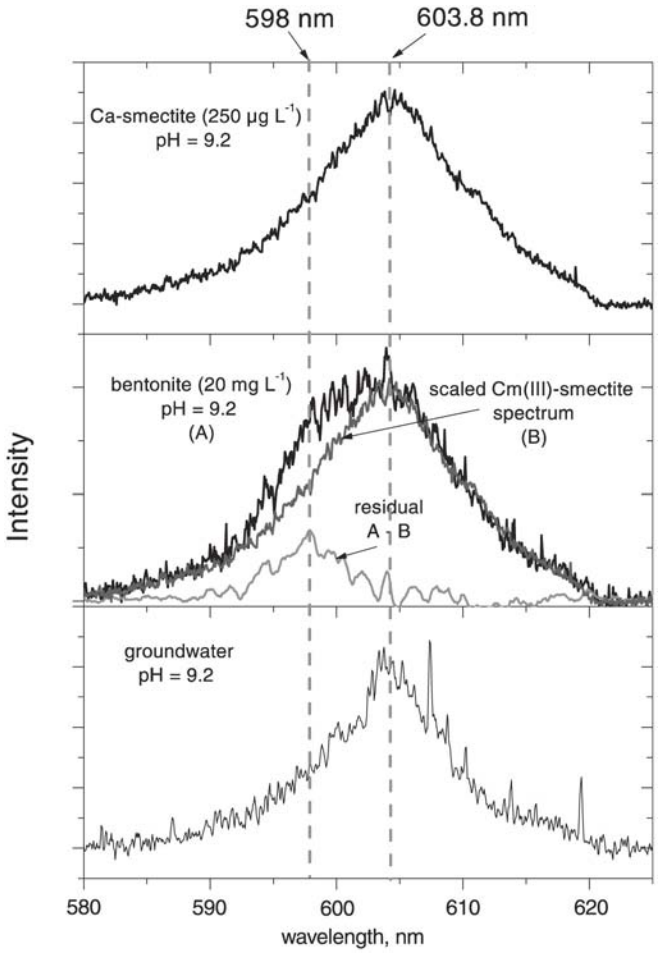

Fig. 3. TRLFS spectra for Cm-(Ca-montmorillonite) (upper spectrum) [38], Cm-bentonite colloid (middle spectrum) and Cm-groundwater colloid (lower spectrum); the spectrum in the middle (Cm-bentonite colloid) (**a**) is deconvoluted by subtraction of the scaled Cm-(Ca-montmorillonite) (**b**) spectrum. The residual spectrum is plotted in grey.

in each sample. These spectroscopic findings are in agreement with a number of TRLFS studies on Cm(III) sorption on mineral surfaces [37]. The suggestion of surface complexes like $>Al-O-Cm(H_2O)_{(5-x)}(OH)_x$ matches the spectroscopic findings [40]. Spectra are not influenced by adding 10^{-8} mol L^{-1} of both Th(IV) and Pu(IV) simultaneously with Cm(III) in order to simulate the injection solution composition of runs 1 and 2.

The TRLFS study suggests the existence of Cm(III) complexed to colloid surfaces in the groundwater even in the absence of added bentonite colloids. Ultracentrifugation proves the presence of colloidal Cm(III) species. 45%–65% of the Cm(III) can be separated from solution (consistent with Th, Pu and Am behaviour in injection solution of run 1). We cannot decide on the basis of the present experiments whether these colloids are natural groundwater colloids, which have been detected in Grimsel groundwater up to concentrations of 5 μg L^{-1} [14], or if the colloids have been introduced as contamination during preparation in the Ar-glove box. At least we can exclude the generation of colloidal hydroxides ('eigencolloids') for An(III) during the solution preparation due to local oversaturation effects or by exceeding solubility limits. In this case, Cm(III) fluorescence would be strongly quenched due to concentration quench effects and lifetimes would be clearly decreased [41]. It is furthermore noted that > 90% of the Cm(III) disappears from the solution when being left in the quartz cuvette after 3 weeks and is found sorbed to the cuvette walls.

Spectra for Cm(III) interacted with bentonite colloids indicate as well the presence of surface sorbed Cm(III) species. However, the band appears to be significantly broadened as compared with the Cm(III)-montmorillonite band obtained at the same pH. Spectral deconvolution performed by subtracting the scaled Cm-montmorillonite spectrum from the Cm(III)-bentonite spectrum yields a residual band with a peak at 598 nm (Fig. 3). A straightforward contribution of this band is presently not possible. However, we assume that natural organics associated with the natural bentonite used in this study may contribute to the Cm(III) adsorption. Carbon analysis reveals a content of 0.56 ± 0.01 mass. % organic carbon in the bentonite which is in agreement with earlier analyses [6]. In order to characterize the smectite/organic associates, carbon *K*-edge XANES (X-Ray Absorption Near Edge Spectroscopy) is performed on a bentonite sample. The average spectra of Febex bentonite colloid associated natural organic matter is given in Fig. 4 (upper part) showing the measured spectra (open circles), the fit (straight line), the Gaussian peaks used for de-convolution and the quantification of functional group distribution. Taking into account detailed XANES investigations on the carbonyl $C(1s) \rightarrow \pi^*_{C=O}$ transition [42, 43] that have shown shifts as much as 3.8 eV with aldehyde type structure $C(1s) \rightarrow \pi^*_{C=O}$ transitions around 286.3 eV [44], ketone type structures at 286.6–286.8 eV [44] and amide type structures around 288.2 eV [42], the broadened absorption of bentonite associated natural organic matter (NOM) indicate highly functionalized aliphatics. This high variety of carbonyl type groups and their π^* transition energy variation point out furthermore one of the difficulties of quantitative C(1*s*) spectral de-convolution. However, both the

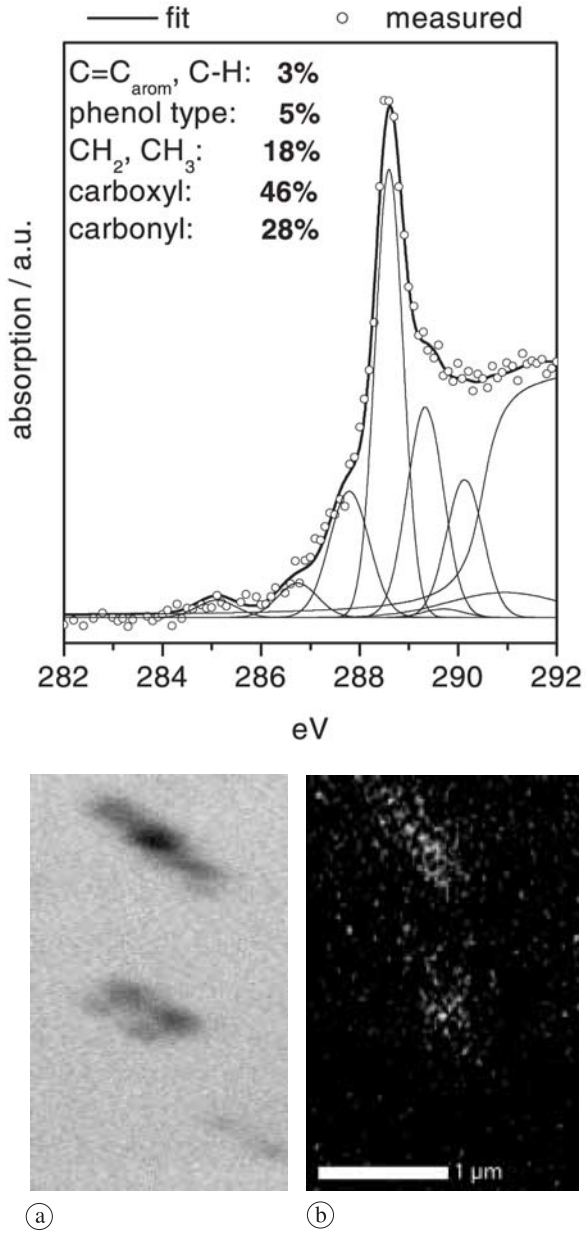

Fig. 4. Upper graph: C(1*s*) XANES spectra de-convolution and functional group quantification of Febex bentonite associated natural organic matter. Lower images: STXM spectromicroscopic images of Febex bentonite colloids. (**a**) Absorption image at 280 eV showing inorganic bentonite colloid aggregates. Dark grey values represent high X-ray absorption/colloid thickness. (**b**) Ratio image of carboxyl group (288.6 eV) distribution on natural untreated Febex bentonite. Bright grey values in the ratio image indicates high concentrations of selected carboxylate groups.

spectral deconvolution and the spectral shape show a highly functionalized natural organic matter. High resolution ratio images ($I(E) = 288.6$ eV; $I_0(E) = 280$ eV) of the carboxyl group distribution in comparison with an absorption image taken at 280 eV below the carbon edge (Fig. 4, lower part) shows a clear association of smectite with carboxyl groups. Contamination with organic material can be ruled out by analyzing blank samples.

These impurities of natural organic matter associated to bentonite can (a) contribute significantly to the overall smectite metal complexation and (b) may increase the colloid stability by changing the pH dependent smectite edge charge. The evaluation of the spectra indicates the presence of organic matter containing only minor content of aromatic constituents but rather aliphatic carboxylic acid components. Such highly functionalized organic matter is known to interact strongly with actinide ions and, thus, may easily be responsible for the additional band in the Cm(III)-bentonite TRLF-spectrum.

Conclusions

The study proved that smectite colloids eroding from bentonite can exhibit a considerable mobility in a granitic shear zone under the investigated groundwater velocities. Under given geochemical conditions, they act as carriers notably for the tri- and tetravalent actinide migration. Np(V) and U(VI) interaction with colloids is negligible. Combining the outcome of laboratory investigations with those of the field study, however, reveals the necessity of considering kinetics of the radionuclide interactions at the mineral-groundwater and the colloid-groundwater interface. Spectroscopic studies indicate actinide binding to aquatic colloids *via* inner-sphere surface complexation. The surface complexed colloid borne actinide ion still keeps a part of its hydration sphere and remains in contact with the surrounding solution. Dissociation of such complexes may be considered kinetically hindered but reversible over a time period of weeks or months [45]. Reversibility of the actinide-colloid binding is indeed observed in batch sorption studies. The origin of kinetic effects noted in batch and field experiments are of physical and/or chemical nature. While diffusion into pores is primarily assumed to cause the kinetic effects for Cs(I) and Sr(II) sorption, it is the release rate from colloids which may control retardation of tri- and tetravalent actinide ions. The quantitative assessment of radionuclide migration requires the deeper understanding of radionuclide geochemical reaction kinetics and the underlying mechanisms.

Acknowledgment. The authors would like to thank Christian Marquardt for providing Np(V) and Pu(IV) stock solutions and valuable help for oxidation state characterization. The unflagging assistence of F. W. Geyer (sampling, ICP-MS analysis), and R. Götz (LIBD measurements) is gratefully acknowledged. We are grateful for beamtime allotment by BNL/NSLS. Spectromicroscopic data were collected using the X1-A1 STXM developed by the group of Janos Kirz and Chris Jacobsen at SUNY Stony Brook, with support from the Office of Biological and Environmental Research, U.S. DoE under contract DE-FG02-89ER60858, and from the NSF under grant DBI-9605045. The zone plates were developed by Steve Spector and Chris Jacobsen of Stony Brook and Don Tennant of Lucent technologies Bell Labs with support from the NSF under grant ECS-9510499. Finally, we would like to thank all organisations contributing to the funding of the CRR programme: ANDRA (France), BmWA (Federal ministry for economy and employment, Germany), ENRESA (Spain), JNC (Japan), NAGRA (Switzerland), USDoE (USA).

References

1. Artinger, R., Kienzler, B., Schüßler, W., Kim, J. I.: J. Contam. Hydrol. **35**, 261 (1998).
2. Kersting, A. B., Efurd, D. W., Finnegan, D. L., Rokop, D. J., Smith, D. K., Thompson, J. L.: Migration of plutonium in ground water at the Nevada Test Site. Nature **397**, 56 (1999).
3. Vilks, P., Baik, M. H.: Laboratory migration experiments with radionuclides and natural colloids in a granitic fracture. J. Contam. Hydrol. **47**, 197 (2001).

4. Degueldre, C., Triay, I., Kim, J. I., Vilks, P., Laaksoharju, M., Miekeley, N.: Groundwater colloid properties: a global approach: Appl. Geochem. **15**, 1043 (2000).
5. Kim, J. I.: Actinide colloid generation in groundwater. Radiochim. Acta **52–53**, 71 (1991).
6. 'FEBEX bentonite: Origin, Properties and fabrications of blocks'. ENRESA Technical Publication 05/98, Madrid (1998).
7. Missana, T., Adell, A.: On the Applicability of DLVO theory to the prediction of clay colloids stability. J. Coll. Interface Sci. **230**, 150 (2000).
8. Missana, T., Alonso, U., Turrero, M. J.: Generation and stability of bentonite colloids at the bentonite/granite interface of a deep geological radioactive waste repository. J. Contam. Hydrol. **61**, 17 (2002).
9. Möri, A., Alexander, W. R., Geckeis, H., Hauser, W., Schäfer, Th., Eikenberg, J., Fierz, Th., Degueldre, C., Missana, T.: The colloid and radionuclide retardation experiment at the Grimsel Test Site: Influence of bentonite colloids on radionuclide migration in a fractured rock. Coll. Surf. **217**, 33 (2003).
10. Bossart, P., Mazurek, M.: Grimsel Test Site: Structural geology and water flow-paths in the migration shear zone. Nagra Technical Report 91-12. Nagra, Wettingen, Switzerland (1991).
11. Frick, U. (ed.): The Radionuclide Migration Experiment – Overview of the Investigations 1985–1990. Paul-Scherrer-Institut, PSI-Report 120 (1992).
12. Duro, L., Bruno, J., Rollin, C., Guimerà, J., Geckeis, H., Schüßler, W., Vejmelka, P., Shibata, M., Yoshida, Y., Ota, K., Yui, M.: Prediction of the solubility and speciation of RN in Febex and Grimsel waters. Colloid and Radionuclide Retardation project. Nagra Report, Nagra 99-218, Nagra, Wettingen, Switzerland (2000).
13. Möri, A. (ed.): The CRR final project report series: 1-description of the field phase – methodologies and raw data. Nagra Technical Report NTB 03-01 (in prep.). Nagra, Wettingen, Switzerland.
14. Hauser, W., Geckeis, H., Kim, J. I., Fierz, Th.: A mobile laser-induced breakdown detection system and ist application for the *in situ* monitoring of colloid migration. Coll. Surf. **203**, 37 (2002).
15. Degueldre, C., Pfeiffer, H. R., Alexander, W., Wernli, B., Bruetsch, R.: Colloid properties in granitic groundwater systems. I. Sampling and characterisation. Appl. Geochem. **11**, 677 (1996).
16. Wieland, E., Spieler, P.: Colloids in the mortar backfill of a cementitious repository for radioactive waste. Waste Management **21**, 511 (2001).
17. Schäfer, Th., Bauer, A., Bundschuh, T., Rabung, Th., Geckeis, H., Kim, J. I.: Colloidal stability of inorganic colloids in natural and synthetic groundwater. Applied Mineralogy in Research, Economy, Technology and Culture. Proc. of the 6th Internat. Congress ICAM 2000, Göttingen, July 13–21. A. A. Balkema, Rotterdam, Vol. 2 (2000) pp. 675–678.
18. Jacobsen, C., Williams, S., Anderson, E., Browne, M. T., Buckley, C. J., Kern, D., Kirz, J., Rivers, M., Zhang, X.: Diffraction-limited imaging in a scanning transmission X-ray microscope. Opt. Commun. **86**, 351 (1991).
19. Zhang, X., Ade, H., Jacobsen, C., Kirz, J., Lindaas, S., Williams, S., Wirick, S.: Micro-XANES: chemical contrast in the scanning transmission X-ray microscope. Nucle. Instrum. Methods Phys. Res. A **347**, 431 (1994).
20. Jacobsen, C. J., Zimba, C., Flynn, G., Wirick, S.: Soft X-ray microscopy from sub-100 nm regions. J. Microscopy **197**, 173 (2000).
21. Claret, F., Bauer, A., Schäfer, T., Griffault, L., Lanson, B., Experimental investigation of the interaction of clays with high-pH solutions: A case study from the Callovo–Oxfordian formation. Meuse-Haute Marne underground laboratory (France). Clays Clay Mineral **50**, 633 (2002).
22. Schäfer, T., Hertkorn, N., Artinger, R., Claret, F., Bauer, A.: Functional group analysis of natural organic colloids and clay association kinetics using C (1*s*) spectromicroscopy. J. Phys. IV **104**, 409 (2003).
23. Hitchcock, A. P., Ishii, I.: Carbon K-shell excitation spectra of linear and branched alkanes. J. Electron. Spectrosc. Relat. Phenom. **42**(1), 11 (1987).
24. Hitchcock, A. P., Urquart, S. G., Rightor, E. G.: Inner shell spectroscopy of benzaldehyde, terephthalaldehyde, ethylbenzoate, terephthaloyl chloride, and phosgene: Models for core excitation of poly (ethylene terephathalate). J. Phys. Chem. **96**, 8736 (1992).
25. Plaschke, M., Schäfer, T., Bundschuh, T., Ngo Manh, T., Knopp, R., Geckeis, H., Kim, J. I.: Size characterization of bentonite colloids by different methods. Anal. Chem. **73**, 4338 (2001).
26. Hadermann, J., Heer, W., The Grimsel (Switzerland) migration experiments: integrating field experiments, laboratory investigations and modeling, J. Contam. Hydrol. **21**, 87 (1996).
27. Hoehn, E., Eikenberg, J., Fierz, T., Drost, W., Reichlmayr, E.: The Grimsel Migration Experiment: field injection-withdrawal experiments in fractured rock with sorbing tracers. J. Contam. Hydrol. **34**, 85 (1998).
28. Heer, W., Smith, P. A., Modelling the radionuclide migration experiments at Grimsel. What have we learned? Mat. Res. Soc. Symp. Proc. **506**, 663 (1998).
29. Bradbury, M., Baeyens, B.: Sorption of Eu on Na- and Ca-montmorillonites: Experimental investigations and modelling with cation exchange and surface complexation. Geochim. Cosmochim. Acta **66**, 2325 (2002).
30. Möri, A. (ed.): GTS Phase V, CRR Experiment, Supporting laboratory experiments with radionuclides and bentonite colloids. NAGRA Technical Report, NTB 03-02 (in print), Nagra, Wettingen, Switzerland.
31. Aksoyoglu, S., Bajo, C., Mantovani, M.: Batch Sorption Experiments with Iodine, Bromine, Strontium, Sodium and Cesium on Grimsel Mylonite. PSI Report No. 83, Paul-Scherrer-Institute, Villigen, Switzerland (1990).
32. Axe, L., Trivedi, P.: Intraparticle surface diffusion of metal contaminants and their attenuation in microporous amorphous Al, Fe, and Mn oxides. J. Coll. Interface Sci. **247**, 259 (2002).
33. Strawn, D. G., Scheidegger, A. M., Sparks, D. L.: Kinetics and mechanisms of Pb(II) sorption and desorption at the aluminum oxide–water interface. Environ. Sci. Technol. **1998**, 2596 (32).
34. Bradbury, M. H. (ed.): Laboratory Investigations in Support of the Migration Experiments at the Grimsel Test Site. PSI Report No. 28, Paul-Scherrer-Institute, Villigen, Switzerland (1989).
35. Ryan, J. N., Elimelech, M.: Colloid mobilization and transport in groundwater. Coll. Surf. **107**, 1 (1996).
36. Kim, J. I., Rhee, D. S., Wimmer, H., Buckau, G., Klenze, R.: Radiochim. Acta **62**, 35 (1993).
37. Stumpf, Th., Rabung, Th., Klenze, R., Geckeis, H., Kim, J. I.: Spectroscopic study of Cm(III) sorption onto γ-alumina. Coll. J. Interface Sci. **238**, 219 (2001).
38. Pierret, M. C., Rabung, Th., Bauer, A., Geckeis, H., Klenze, R., Kim, J. I., Bradbury, M. H., Baeyens, B.: Interaction of Cm(III) and Eu(III) with Ca-montmorillonite: Surface Complexation Modelling and Spectroscopic studies (to be published).
39. Kimura, T., Choppin, G. R.: Luminescence study on determination of the hydration number of Cm(III). J. Alloys Compd. **213**/**214**, 313 (1994).
40. Geckeis, H., Rabung, Th.: Solid-water interface reactions of polyvalent metal ions at iron oxide/hydroxide surfaces. In: *Encyclopedia of Surface and Colloid Science*. (Hubbard, A., ed.) Dekker (2002).
41. Tits, J., Stumpf, Th., Rabung, Th., Wieland, E., Fanghänel, Th.: Uptake of trivalent actinides (Cm(III)) and lanthanides (Eu(III)) by calcium silicate hydrates: a wet chemistry and time-resolved laser fluorescence spectroscopy (TRLFS) study. Env. Sci. Technol. **37**, 3568 (2003).
42. Urquhart, S. G., Ade, H.: Trends in the carbonyl core (C 1*s*, O 1*s*) $\rightarrow \pi^*_{C=O}$ transition in the near-edge X-ray absorption fine structure spectra of organic molecules. J. Phys. Chem. B **106**(34), 8531 (2002).
43. Dhez, O., Ade, H., Urquhart, S. G.: Calibrated NEXAFS spectra of some common polymers. J. Electron. Spectrosc. Relat. Phenom. **128**, 85 (2003).
44. Hitchcock, A. P., Brion, C. E.: Inner-shell excitation of formaldehyde, acetaldehyde and acetone studied by electron impact. J. Electron. Spectrosc. Relat. Phenom. **19**(2), 231 (1980).
45. Rabung, T., Stumpf, T., Geckeis, H., Klenze, R., Kim, J. I.: Sorption of Am(III) and Eu(III) onto γ-alumina: experimental results and modeling. Radiochim. Acta **88**, 711 (2000).

Origin and Mobility of Fulvic Acids in the Gorleben Aquifer system: Implications from Isotopic Data and Carbon/Sulfur XANES.

Org. Geochem. (2005) **36**, 567.

Schäfer, T., Buckau, G., Artinger, R., Kim, J.I., Geyer, S., Bleam, W.F., Wirick, S., Jacobsen, C.

Available online at www.sciencedirect.com
SCIENCE DIRECT®
Organic Geochemistry 36 (2005) 567–582
Organic Geochemistry
www.elsevier.com/locate/orggeochem

Origin and mobility of fulvic acids in the Gorleben aquifer system: implications from isotopic data and carbon/sulfur XANES

T. Schäfer [a,*], G. Buckau [a], R. Artinger [a], J.I. Kim [a], S. Geyer [b], M. Wolf [c], W.F. Bleam [d], S. Wirick [e], C. Jacobsen [e]

[a] *Forschungszentrum Karlsruhe, Institut für Nukleare Entsorgung, P.O. Box 3640, 76021 Karlsruhe, Germany*
[b] *UFZ-Umweltforschungszentrum Leipzig-Halle, Sektion Hydrogeologie, Theodor Lieser Str., 06120 Halle, Germany*
[c] *GSF-National Research Center for Environment and Health, Institute of Groundwater Ecology, 85764 Neuherberg, Germany*
[d] *University of Wisconsin, Department of Soil Science, Madison, WI 53706-1299, USA*
[e] *State University of New York at Stony Brook, Department of Physics and Astronomy, Stony Brook, NY 11794, USA*

Received 8 March 2004; accepted 29 October 2004
(returned to author for revision 14 June 2004)
Available online 21 January 2005

Abstract

The Gorleben aquifer system, overlaying a Permian salt dome, has been under investigation for more than two decades for the potential to host a nuclear waste repository. Groundwater in the system shows a range of compositions, especially with respect to salt content and dissolved organic carbon (DOC) concentration. An uncertainty for safety analysis is the mobility of metal-complexing dissolved organic acids. Hence, isotopic data and carbon/sulfur K-edge X-ray absorption near edge structure (XANES) spectroscopy have been used in order to determine the mobility of fulvic acids (FAs). Isotopic data (^{13}C, ^{14}C, ^{3}H) show that FAs from the recharge zone are mobile over the entire depth, including into the salt dome influenced brines. ^{14}C and $\delta\ ^{34}S$ (up to 34‰) analysis shows furthermore that enhanced DOC (mainly humic and fulvic acids) concentrations originate from microbiologically mediated turnover of lignite intercalations in sandy Miocene sediments (''in situ generation''). XANES revealed that these in situ generated FAs have a high C_{arom}/C_{aliph} ratio (~2.8), a decreased carboxyl/carbonyl content (less hydrophilic), a red shift in the $C_{arom} = C_{arom}$ peak at 285.2eV, indicating heteroatom substitution and aromatic ring distortion, and feature a high reduced S content (~69%). Shallow recharge groundwater and deep brine derived FAs exhibit a similar C_{arom}/C_{aliph} ratio (1.1–1.4), indicating invariance in the backbone structure against higher residence times and variation in geochemical conditions. XANES data also suggest that only heteroatom-substituted, destabilized aromatic ring structures of the FAs are stable in the brines and revealed 43% reduced S in recharge FAs and high (61%) reduced S with higher sulfate content in the channel brine FAs. Sulfur redox speciation therefore reflects geochemical conditions/reactions and shows a high stability of reduced sulfur species in more aerobic channel brine environments. The application of carbon and sulfur XANES shows that key structural information can be obtained from small sample amounts. The high mobility of

* Corresponding author. Tel.: +49 7247 82 5494; fax: +49 7247 82 3927.
E-mail address: schaefer@ine.fzk.de (T. Schäfer).

0146-6380/$ - see front matter
doi:10.1016/j.orggeochem.2004.10.011

FAs over a range of groundwater conditions and residence times verifies the potential for dissolved humic substances to enhance radionuclide transport.

1. Introduction

Colloid facilitated contaminant transport is attracting growing attention with respect to the risk assessment of contaminated sites and the long term safety assessment of deep geological nuclear waste disposal (Honeyman, 1999; Kim, 1994; McCarthy and Zachara, 1989). Aquatic fulvic acids (FAs) and humic acids (HAs) are ubiquitous in aquifer systems and represent a major fraction of the dissolved organic carbon (DOC). Because humic substances interact with metal ions and non-polar organic substances, they may play a crucial role for the geochemical behaviour of non-polar organic pollutants, heavy metal ions and a variety of radionuclides, especially multivalent actinide ions (Artinger et al., 2002; Kim et al., 1989; Manahan, 1989; Schäfer et al., 2003a).

A key question for evaluating the influence of natural organic substances in performance assessment (PA) is the mobility and long term stability of humic substances (OECD-NEA, 1994). In case of a well defined sandstone aquifer, mobility over a distance of more than 20 km and long term stability of about 15,000 years were found for FAs (Buckau et al., 2000a). The origin and fate of humic substances in an aquatic environment depends on the specific properties of that aquifer system. There is no single indicator that can be used in order to obtain an unambiguous answer to the origin and fate of humic substances in groundwater. Instead, a thorough understanding of the overall hydrological and geochemical situation is required, including possible changes over the past. Such knowledge in combination with different humic substance specific indicators can provide the desired understanding.

In this work the fate of aquatic FAs in the Gorleben aquifer (Lower Saxony, Germany) is studied. The aquifer extends to 280 m below the surface and is situated in sediments covering and surrounding a Permian salt dome. The salt content varies from fresh recharge water to saturated brines close to the dome. One specific feature of this aquifer is the large variety of DOC concentrations, from <1 to >100 mgC/L. The high concentrations result from microbiological turnover of near surface peat or Miocene brown coal (sedimentary organic carbon, SOC) in deep sandy sediments. The microbiological turnover of carbon sources is driven by reduction of sulfate originating from salt dome dissolution. Several papers have dealt with the fate of aquatic humic substances in this complex aquifer system (Artinger et al., 1999, 2000; Buckau et al., 2000b,c,d). From this work it is known that in situ generation from SOC dominates the humic substance inventory in deep groundwater with high DOC concentrations ($>\approx$5 mgC/L). This applies especially to the HAs and makes identification of possible minor fractions of different origin difficult. FAs in groundwater with enhanced DOC concentrations are less dominated by the in situ origin than are HAs. Therefore, delineation of FAs with different origins is more promising. Furthermore, FAs occur in recharged groundwater and in brines in much higher concentrations than HAs, thus enabling the isolation of sufficient quantities for characterization.

Previous attempts to correlate different properties of FAs with their origin did not lead to firm conclusions (Artinger et al., 2000). The two main problems are that some characteristic properties may vary depending on the physicochemical environment and that an unambiguous indicator is required for determining the respective contributions from different sources/origins. Compared to previous studies, the new approach in this paper analyzes the recharge contribution via the ^{14}C content of FAs. Different characteristic properties may be invariant with respect to changes in physico-chemical conditions, while others may not. For this reason, seven FAs isolated from different parts of the Gorleben aquifer have been characterized using X-ray absorption near edge structure (XANES) spectroscopy at the Carbon and Sulfur K-edge and structural information deduced from the spectra. Variations in characteristic properties deduced from XANES are also interpreted in terms of the varying contributions from the two principal origins, namely recharge and in situ generation.

2. Materials and methods

2.1. Gorleben site hydrogeology: insights from carbon isotope geochemistry

A detailed description of the Gorleben aquifer system, sampling positions for selected groundwater and complete data sets on groundwater chemistry can be found in Artinger et al. (2000) and Buckau et al. (2000b,c). Key data for the groundwater samples relevant for this study are given in Table 1. The groundwater samples are divided into four classes, reflecting the chemical composition and differences in HA and FA concentration. The different groundwater classes have the following characteristics:

Table 1
Key data including important chemical parameters (DIC, Cl^-, SO_4^{2-}), FA concentration, ^3H, ^{14}C content and $\delta\ ^{34}S$ values. Data from Kim et al. (1995) and Artinger et al. (2000) where also additional data can be found

Water type	Sample Gohy-	Depth (m)	Tritium (TU)[a]	FA (mgC/L)	E_H (mV)	$\delta\ ^{13}$DIC (‰ V-PDB)[b]	^{14}C(FA) (pmc)[c]	^{14}C (DIC)[d] (pmc)[c]	DIC (mmol/L)	SO_4^{2-} (μmol/L)	$\delta\ ^{34}SO_4$ (‰ CDT)[e]	Cl^- (μmol/L)
Recharge												
	421	10–13	20.0	0.53	189 ± 94	−23.1	92.5	68.5	0.84	823	2.3	430
	711	6–9	29.2	0.35	398	−22.1	100.9	70.4	0.59	532	2.3	344
Transition												
	182	70–73	<0.3	0.13	−48	−13.4	46.1	27.9	1.07	35	15.1	198
Enhanced DOC												
	412	65–68	<0.2	2.6	92	−6.8	8.1	8.6	3.66	<1.0	n.d.[f]	507
	2211	83–85	0.32	22	29 ± 13	−10.0	13.4	5.2	9.52	198	n.d.[f]	37746
	2227	128–130	<0.3	5.9	−24 ± 82	−12.8	10.6	5.0	8.17	324	34	36704
Channel brine												
	653	216–219	<0.3	1.0	218 ± 126	−15.1	40.0	7.6	4.40	45993	10.7	4079000

[a] TU tritium unit (1 TU = 0.118 Bq/L).
[b] Relative to the $^{13}C/^{12}C$ ratio in Vienna-Pee Dee Belemnite (V-PDB) standard.
[c] Percent modern carbon (100 pmc = 0.23 Bq/gC).
[d] Dissolved inorganic carbon.
[e] Relative to the $^{34}S/^{32}S$ ratio in Canon Diablo Troilite (CDT) standard.
[f] Not detected.

(i) Recharge: young groundwaters at depths down to about 25 m situated in fluviatile quartz sands low in organic content, deposited during the most recent Weichsel/Visconsin ice age. These groundwaters have significant concentrations of tritium from nuclear atmospheric testing. The FA concentrations are low, with variations reflecting different land use.
(ii) Transition groundwaters: comparable to the recharge ones, but, with negligible tritium concentrations.
(iii) Enhanced DOC groundwaters: high DOC concentrations, including high FA concentrations.
(iv) Channel brines: the high salt content reflects the proximity to the salt dome. The FA concentrations in these brines are comparable to those from the recharge and transition waters.

The generation process for the FAs (and DOC) in the Gorleben aquifer system is illustrated in Fig. 1. FAs show δ ^{13}C values around $-27‰$ relative to Vienna-Pee Dee Belemnite (V-PDB; Kim et al., 1995). This shows that they originate from C_3 plant material and do not exchange significantly with dissolved inorganic carbon (DIC). The concentration of DIC of biogenic origin is calculated via the δ ^{13}C value of $-27‰$ rel. V-PDB (cf. Table 1) and $0‰$ for sedimentary carbonate dissolution. The ^{14}C concentrations of biogenic DIC and FAs correlate with each other due to their common origin (microbiological turnover of organic material of C_3 plant origin) where the absolute values reflect the ^{14}C concentrations in the different sources. Present recharge is affected by elevated ^{14}C concentrations from atmospheric nuclear testing. Recharge prior to testing has lower ^{14}C concentrations. The organic material in old sediments (for example brown coal sand) is basically ^{14}C-free. Deviations are expected where the isotopic composition of the DIC is amended via, for example carbonate precipitation and methane generation. In the former case the ^{14}C concentration of DIC is decreased. In the latter case the calculated ^{14}C concentration is too high due to an incorrect δ ^{13}C value being used in the calculation of the biogenic DIC. In addition, deviations due to dissolution of carbonate of unknown δ ^{13}C content cannot be completely excluded. Examples may be salt dome carbonate dissolution or the existence of non-marine sedimentary carbonates.

Fig. 1 confirms the common origin of biogenic DIC and FAs. A few samples with elevated values for the calculated ^{14}C concentration of biogenic DIC coincide with methane in the groundwater (cf. Buckau et al., 2000d). A few with particularly low ^{14}C concentration of biogenic DIC presumably reflect carbonate precipitation, especially in brines. The generation process is independent of the type and origin of the groundwater and source material. On average, a ^{14}C activity ratio of ~0.8 is calculated for the biogenic DIC and FAs. Molecules enriched in the lighter isotope of an element react with a lower activation energy and are therefore concentrated in the reaction products of metabolic processes.

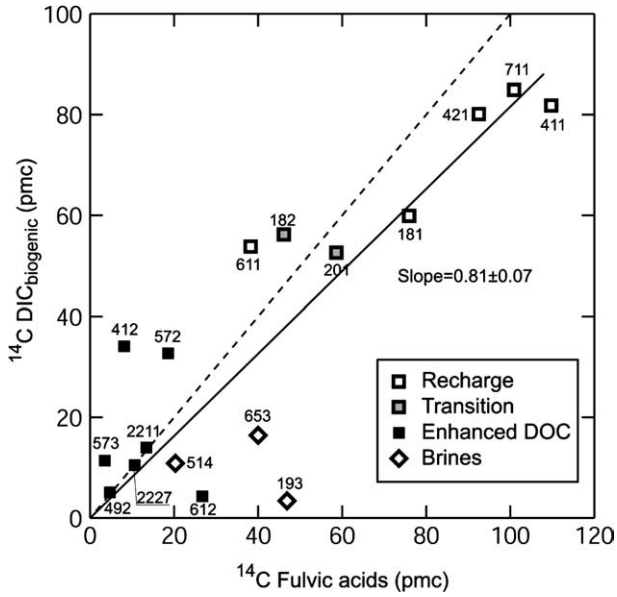

Fig. 1. ^{14}C concentration of biogenic DIC (dissolved inorganic carbon) versus the ^{14}C concentration of FAs.

2.2. Fulvic acids

The isolation of FAs from groundwaters is described in detail in Artinger et al. (2000) and consists of the following steps: enrichment, isolation, separation from HAs and purification. For groundwaters with low FA concentrations and low salinity (Gohy-182, -421 and -711), a mobile field operation system combining reverse osmosis and sorption on to XAD-8 (Rohm and Haas Co., USA) at low pH is used. This system allows the on-site processing of 5000 L of groundwater per day. Because brines (Gohy-653) do not allow reverse osmosis, up to 1 m^3 of groundwater was directly processed in the field using a XAD-8 column of 8 L volume. After enrichment/isolation of HAs and FAs, the FAs were separated from the HAs via centrifugation of HA flocculate at pH 1 (addition of HCl). Humic substances from groundwaters with high DOC concentrations (Gohy-412, -2211 and -2227) were directly isolated from groundwater samples transported to the laboratory (acidification, flocculation of HAs, sorption of FAs onto XAD-8). The isolated FAs were purified twice by sorption on XAD-8 (at pH 1) followed by alkaline elution. Before freeze drying, excess salt was removed by cation exchange of pH neutralized solution over BIO REX 70 or AG MP-50 (BIO RAD Co., Germany). The FA samples were characterized using elemental analysis, UV/VIS spectroscopy, gel permeation chromatography (GPC), fluorescence spectroscopy and ^{14}C measurements (results reported in Artinger et al., 2000).

2.3. X-ray absorption near-edge structure analysis

2.3.1. Carbon K-edge XANES

The application of carbon XANES in environmental studies includes work on coal, aquatic HAs and FAs (Cody et al., 1995, 1996; Plaschke et al., 2002; Schäfer et al., 2003c; Scheinost et al., 2002) and the reactivity of natural-organic matter (NOM) inorganic mineral associations (Claret et al., 2002; Schäfer et al., 2003b). Measurements were performed at the Scanning Transition X-ray Microscope (STXM), National Synchrotron Light Source (NSLS) at Brookhaven National Laboratories (BNL), undulator beamline X1A1, operated by the State University of New York at Stony Brook (Jacobsen et al., 1991). The principle of this method is described in detail elsewhere (Jacobsen et al., 1991; Zhang et al., 1994). STXM images of FA isolates were recorded at the carbon K-edge using an undulator gap of 36 mm. Sample preparation was performed by drying a 0.5–1 μL droplet of resuspended freeze-dried FA on a 100 nm thick Si_3N_4 window. Only spectra with at least 1% X-ray transmittance were used to avoid spectral distortion.

The Fresnel zone plate used had a diameter of 160 μm and an outermost zone width of 45 nm, giving a theoretical spatial resolution (Rayleigh criterion) of 55 nm at a focal length of 1.7 mm (Spector et al., 1997). The exit and entrance slit set-up was chosen to obtain an energy resolution Δ eV of 0.1 eV at the C K-edge (Winn et al., 1996). Energy calibration of the spherical grating monochromator was performed by using the photon energy of the CO_2 gas adsorption band at 290.74 eV (Hitchcock and Mancini, 1994; Ma et al., 1991). XANES spectra were recorded in the energy range from 280 eV to 310 eV by using the image stack option (Jacobsen et al., 2000). STXM measurements yield information on the product of sample thickness d and the mass absorption coefficient $\mu(E)$ which is related to the quotient of the incident flux on the sample $I_0(E)$ and the flux detected behind the sample $I(E)$ via $\mu(E) * d = \ln[I_0(E)/I(E)]$. Image stacks are measured as a function of photon energy and the XANES spectra can be extracted after stack alignment. Image regions free from particles or separately measured XANES spectra without samples gave the $I_0(E)$ information.

2.3.2. Sulfur K-edge XANES

All sulfur K-edge spectra were collected at the CSRF-DCM (CSRF = Canadian Synchrotron Radiation Facility, DCM = double-crystal monochrometer) beamline owned by CSRF at the SRC (Synchrotron Radiation Center) built around the electron storage ring Aladdin at the University of Wisconsin-Madison. The electron energy operation condition of the Aladdin storage ring during sample measurement was 800 MeV. The DCM beamline works in the energy range 1500–4000 eV with a beam size of 1×5 mm (horizontal × vertical) using a Quartz (1010) crystal monochromator with an energy resolution of <0.7 eV. All the energies were measured with respect to the position of the white line of the elemental sulfur K-edge (2472 eV) spectrum. Each XANES spectrum shown represents the average of three scans with a 0.45 eV step size. The FA samples were mounted on 0.5 mm thick acrylic holders with Mylar film (Chemplex Industries), pressed into a thin film with a sample press and supported with boron nitride for measurement.

2.3.3. Spectra treatment

For comparison, all XANES spectra were baseline corrected and normalized prior to peak fitting. Each normalized carbon or sulfur spectrum was then further resolved into its individual arctangent (Stöhr, 1996) and Gaussian curve components, using the nonlinear least-squares fitting routine SOLVER of Microsoft Excel. The normalization step is mandatory for determining the changes in organic material or sulfur oxidation state, respectively.

Two ionization thresholds (IPs) were set for C(1s) spectrum deconvolution (arctangent function at 290.4 eV for aromatic/aliphatic carbon (Hitchcock and Ishii,

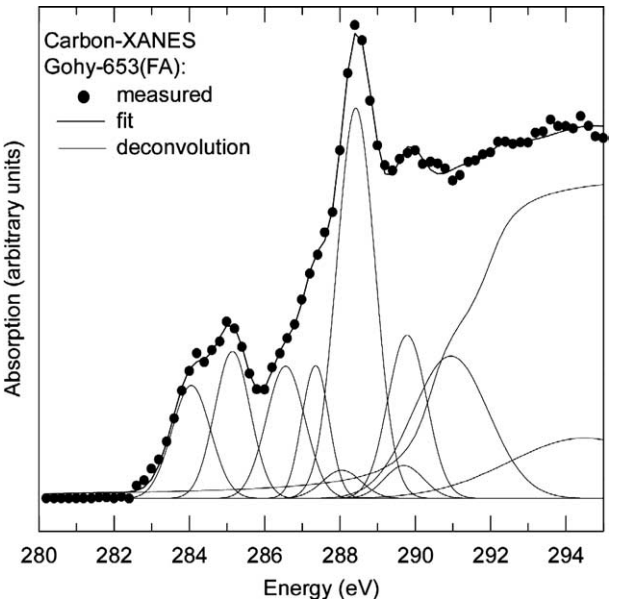

Fig. 2. Deconvolution of carbon C(1s) XANES of different functionalities shown as an example for sample Gohy-653(FA). Two ionization thresholds (IP) were simulated by arctangent functions, six Gaussian functions represent the main 1s-π* or Rydberg/mixed valence transitions (284.4, 285.2, 286.6, 287.6, 288.6 and 289.4 eV) and two higher energy (1s-2π*) transition are implemented. σ*-transitions (~293, ~294 eV) were simulated by simplified Gaussian shape function.

1987; Hitchcock et al., 1992) and at 292 eV for hydroxylated aromatic carbon) with full width at half maximum (FWHM) of 0.5 eV to generate the continuum spectrum up to 300 eV. The parameter choice over emphasizes contributions to the continuum absorption at low energies and represents a conservative choice. The IPs magnitude was assessed by the atomic ratio of carbon to oxygen tabulated in Artinger et al. (2000). FWHM of Gaussian peaks was loosely constrained between 0 and 0.5 eV, and 6 Gaussian functions representing the main 1s-π* or Rydberg/mixed valence transitions (284.4, 285.2, 286.6, 287.6, 288.6 and 289.4 eV) were used (Fig. 2). Following the work of Cody et al., 1995, 1996, this energy of inner-shell transition (1s-π*) is accompanied by a second, higher energy transition (1s-2π*) occurring approximately 4 eV above the energy of the 1s-π* transition with nearly one-quarter of its intensity. In order to achieve quantitative information on spectral deconvolution this transition was implemented; σ*-transitions (~293, ~294 eV) were simulated using a simplified Gaussian shape function with a FWHM of <1 and <2 eV.

Sulfur K-edge XANES spectra correlate with changes in the oxidation state speciation of sulfur in humic substances, i.e., HAs and FAs, but cannot identify the exact chemical form of each species (Xia et al., 1999). A number of publications have quantitatively resolved using XANES spectroscopy the major S containing functional groups into their formal oxidation states including, e.g., anaerobic marine sediments (Vairavamurthy et al., 1997), HAs and FAs (Hundal et al., 2000; Morra et al., 1997) and photooxidation of crude

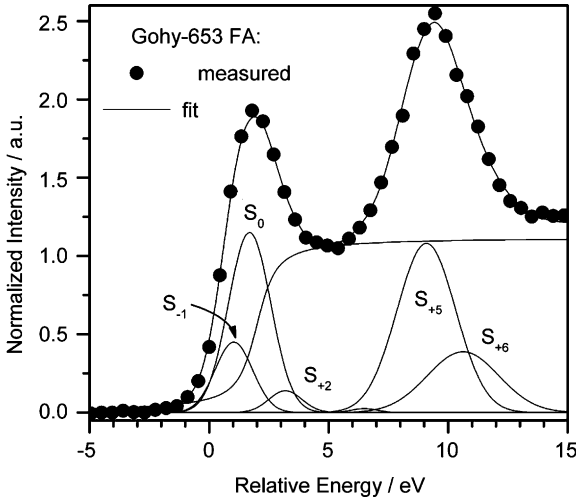

Fig. 3. Deconvolution of different oxidation states (S_{-1}/thiol, S_0/thiophene; disulfide, S_{+2}/sulfoxide, S_{+4}/sulfone, S_{+5}/sulfonate, S_{+6}/sulfate) by sulfur K-edge XANES is shown for sample Gohy-653(FAs) as an example. Experimental XANES spectra were fitted using six Gaussian peaks (1s → 3p transitions) and two arctangent step functions that represent the transition of ejected photoelectrons in the continuum.

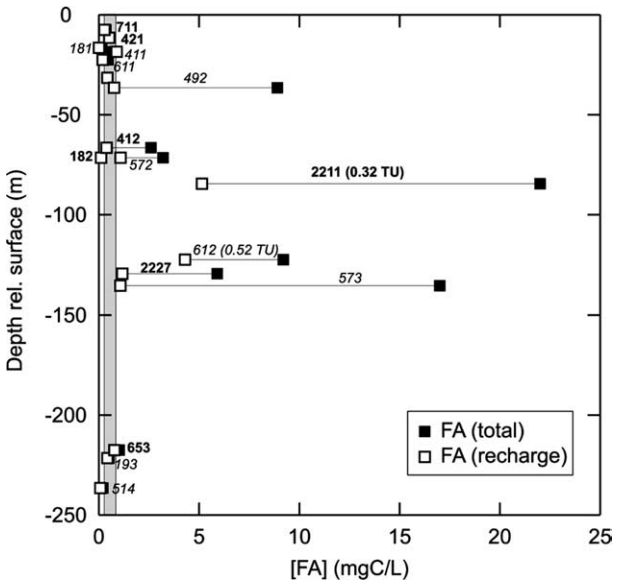

Fig. 4. Concentrations of FAs as a function of groundwater sampling depth. Total FA concentrations are shown together with those of FAs originating from recharge (via ^{14}C).

oil (Garrett et al., 1998). Sulfur XANES spectroscopy was used to determine the percentage of S in each of the following oxidation groups (oxidation state/representative organic sulfur compound): S_{-1}/thiol, S_0/thiophene;disulfide, S_{+2}/sulfoxide, S_{+4}/sulfone, S_{+5}/sulfonate, S_{+6}/sulfate. Experimental XANES spectra were fitted using six Gaussian peaks ($1s \rightarrow 3p$ transitions) and two arctangent step functions that represent the transition of ejected photoelectrons in the continuum. The areas under the particular Gaussian peaks were corrected for the change in absorption cross section with increasing oxidation state. For details on the assumptions made in the fitting procedure see Xia et al. (1999) and Hundal et al. (2000). A typical deconvolution of a sulfur XANES spectrum is shown in Fig. 3.

3. Results and discussion

3.1. Origin of FAs (isotopic data)

Evaluation of the ^{14}C concentration of biogenic DIC for the purpose of groundwater dating revealed a value of 54 ± 2 pmc (percent modern carbon, see footnote in Table 1) prior to atmospheric nuclear testing (Buckau et al., 2000c). The impact of atmospheric nuclear testing on the ^{14}C content was deduced from correlation with tritium from the same source (see Fig. 8 in Buckau et al., 2000c). Application of the same approach to the ^{14}C concentration of the corresponding FAs using the given correlation between ^{14}C $DIC_{biogenic}$ and ^{14}C FA (Fig. 1) revealed a starting value for recharge FAs prior to atmospheric nuclear testing to be 55 ± 6 pmc (cf. 54 ± 2 for $DIC_{biogenic}$). This value was used to quantify the amount of FAs in deep groundwaters originating from recharge under the conditions prior to atmospheric nuclear testing.

In Fig. 4 the concentrations of FAs in the different groundwaters are shown as a function of sampling depth. The total FA concentrations show large variations, with strongly elevated values in the depth range where in situ generation takes place via microbiologically mediated turnover of brown coal sand intercalations. The FA concentrations originating from recharge are in the same low range for most of the groundwaters. Exceptions are Gohy-612 and -2211 where tritium is also found at considerable depth. Of great interest is the fact that the FA concentrations in the brines are comparable to those in the recharge groundwaters.

Groundwaters from the enhanced DOC depth range will exchange with both recharge groundwaters and brines. In the recharge groundwaters dilution takes place by way of the relatively fast groundwater transport (recharge and discharge). This will mask the inflow of elevated FA concentrations in this region. The age of the brines is difficult to determine. The FA concentrations and their ^{14}C content indicate that the brines are young compared to the ^{14}C half-life ($T_{1/2} \approx 5730$ years). A higher age partly indicated from the ^{14}C of the DIC (Buckau et al., 2000c) is probably overestimated due to carbonate precipitation (cf. above discussion, Fig. 1). Exchange with the brines should result in inflow not only of recharge FAs but also inflow of ''old''

^{14}C-free ones from in situ generation in overlying groundwater. The latter is expected to be minor (see Fig. 4) and thus the FAs from in situ generation (from brown coal) can be expected to be less hydrophilic and to preferentially precipitate at high ionic strength. The mainly recharge-dominated origin of brine-derived FAs requires a considerable exchange of groundwater over the entire depth for timescales short compared to that of ^{14}C decay. This is also supported by the identification of tritium down to a depth of 125 m and the mainly exponential mixing of salt over the entire depth (Buckau et al., 2000b). Therefore, isotopic data evaluation suggests a transport of FAs from recharge through the various groundwaters down to the deep brines. At the intermediate depths, considerable amounts of FAs are generated from old carbon deposits. These FAs are primarily precipitated at the high ionic strength of the brines. A considerable contribution of "young" ^{14}C-containing FAs from wetland/marsh is not found in the groundwaters above and south of the salt dome.

3.2. Carbon K-edge XANES

Polarization dependency XANES or NEXAFS studies have clearly shown that the spectral features at 285.2, 286.6, 288.6 and 289.5 eV are all of π symmetry (Francis and Hitchcock, 1992). The discussion of the carbon K-edge results is based on the general characteristic ordered from the lowest to the highest antibonding π* transition energy. The averaged spectrum of each sample is given in Fig. 5 and the deconvolution results are shown in Table 2. The energy region above the ionization potential typical for σ*-resonances did not show significant features for the FAs and is therefore not discussed in the context of this paper.

XANES spectra of the channel brine (Gohy-653) and enhanced DOC (Gohy-2227) FAs are considerably different from all the others. There is a significant 1.2 eV red shift in the lowest π* resonance (285.2 eV), attributed to the C 1s (C–H) 1 π* transition. The red shift must be associated with a lower π^*_{LUMO} (lowest unoccupied molecular orbital) energy that can be interpreted as a loss of aromatic stabilization as found in studies of *p*-benzoquinone (shift to 284 eV) due to quinoid distortion (Francis and Hitchcock, 1992). EHMO (Extended Hückel Molecular Orbital) calculations by Francis and Hitchcock (1992) on the isolated C=C moiety spectrum evolution of *p*-benzoquinone distortion show comparable features to the Gohy-653 FAs if the C_2H_2 units are pulled away approximately 0.5 Å from the axis of the carbonyl groups. Similar effects in the low energy feature ($1\pi^*_{C=C}$ at 284.4 eV) can occur by extensive conjugation, and hence delocalization of orbitals, resulting in an energy splitting as observed in poly(ethylene naphthalate) (Dhez et al., 2003). Heteroatom substitution can also shift the transition of the carbon atoms in the conjugated side chain ring ($1\pi^*_{C=C}$ at 284.8 eV), as demonstrated on poly(2-vinyl pyridine), due to the presence of nitrogen (Dhez et al., 2003). The red shift observed in

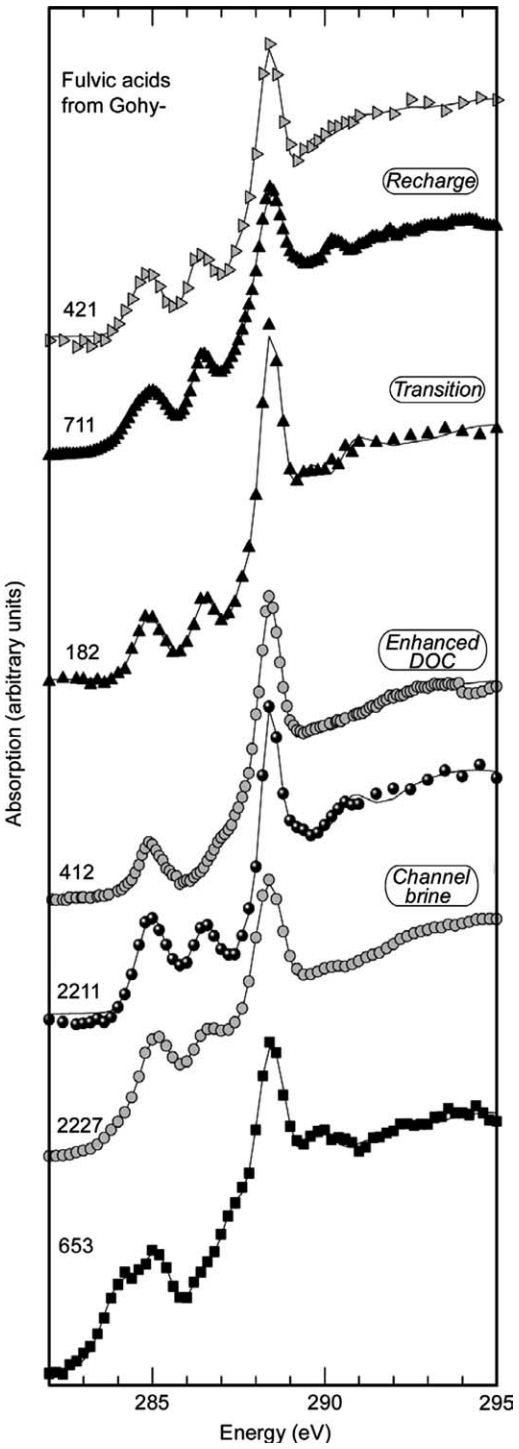

Fig. 5. Average carbon K-edge XANES spectra of the different isolated FAs.

Table 2
Distribution of carbon functionality of FA samples from carbon K-edge XANES, given as relative peak area. More detailed information on allocation of functionalities to different absorption energies is given in the text

Carbon functionality:	Red shift area[a]	C_{arom}=C_{arom} C_{arom}–H	Phenol	CH_2, CH_3	Carboxyl	Carbonyl	∑(Carboxyl + Carbonyl)	C_{arom}/C_{aliph}
Energy (eV):	284.2	285.2	286.6	287.4	288.6	289.5		
Sample								
Relative peak area								
Recharge								
-421	–	12	12	10	41	25	66	1.2
-711	–	13	9	12	43	23	66	1.1
Transition								
-182	–	10	14	8	43	25	67	1.3
Enhanced DOC								
-412	–	10	4	13	49	24	73	0.8
-2211	–	17	16	6	37	24	61	2.8
-2227	4	18	19	7	40	12	52	2.7
Channel brine								
-653	11	13	13	9	38	16	54	1.4

[a] Red shift due to heteroatom substitution/aromatic ring destabilization or benzoquinone type functional groups.

the FAs of Gohy-653 and Gohy-2227 therefore strongly indicates a higher heteroatom substitution/aromatic destabilization in the saline and enhanced DOC FAs compared to recharge dominated ones. However, it is also consistent with the presence of catechol-like rings typical of chemical structures in lignitic wood and huminite (Hatcher and Clifford, 1997).

The next lower transition at 285.2 eV is typical for aromatic carbon bonded either to carbon or a proton (Cody et al., 1995; Stöhr et al., 2001). The intensity of this transition depends on the amount of associated hydroxyl groups and it can be found to be 20% less intense in phenol compared to benzene (Francis and Hitchcock, 1992), and is even weaker in hydroquinone. The aromatic carbon absorption intensity is approximately twice as high in the enhanced DOC FAs Gohy-2227 and -2211 than in the recharge dominated and transition ones. The brine FAs of Gohy-653 and the recharge FAs are comparable in their contribution of aromatic carbon.

Recent detailed NEXAFS investigations on the carbonyl C(1s) → $\pi^*_{C=O}$ transition by Dhez et al. (2003) and Urquhart and Ade (2002) have shown that this transition can shift as much as 3.8 eV, which points out the difficulties in quantitative spectral deconvolution without detailed knowledge of the chemical components and suitable structural models. In particular, the spectral features of FAs Gohy-711 and Gohy-653 are remarkably different. The Gohy-711(FAs) spectrum shows good resolved sharp peaks in the 286–288 eV region, whereas the saline Gohy-653(FAs) one is almost featureless in this region. Taking into account that the aldehyde type structure C(1s) → $\pi^*_{C=O}$ transition lies around 286.3 eV (Hitchcock and Brion, 1980), the carbon 1s excitation of ketone type structures would be expected at 286.6–286.8 eV (Hitchcock and Brion, 1980) and that of amide type structures around 288.2 eV (Urquhart and Ade, 2002), then the flattened, broadened absorption of Gohy-653(FAs) can be interpreted as an indication of highly functionalized aliphatic carbon and heteroatom substitution in the FAs of brine and enhanced DOC origin. These signatures are typical of huminite (brown coal) from lignin-derived material (Hatcher and Clifford, 1997; Stankiewicz et al., 1996).

The ketone type excitation around 286.6 eV is superimposed on a prominent absorption that can be assigned to aromatic carbon bonded to oxygen [C(1s) → π^*_{C-OH}] as found in phenol or halogenated aromatics (Cody et al., 1995). The splitting is due to symmetry reduction and/or chemical shifts (higher electron affinity) associated with the ligand group (Stöhr, 1996). The band intensity (peak height) ratios of the C(1s) → π^*_{C-OH} to C(1s) → $\pi^*_{C=C,\ C-H}$ transition is slightly higher in the recharge FAs with ~1.3 compared to values of ~0.5–1.0 in the enhanced DOC FAs. However, in the peak deconvolution of the spectra both intensities are comparable, except for Gohy-412(FAs). The observed ratio of the above mentioned π* intensities in comparison with data for *p*-benzoquinone and hydroquinone (Francis and Hitchcock, 1992) indicates an average hydroxylation of two hydroxyl groups per aromatic ring and potentially higher hydroxylation in the recharge FAs. The aromatic carbon-associated hydroxylation found in the enhanced DOC FAs is not uncommon and can also be found in huminite (Argonne Premium Coal Sample Bank No. 2) spectra, a maceral group of brown coals also termed sub-bituminous B rank coal (Cody et al., 1995).

The next higher excitation around 287.6 eV is not a π* state but a low-lying 1s carbon transition to a mixture of 3p Rydberg orbital with a symmetrical antibonding C–H* orbital (Ade et al., 1992; Stöhr, 1996), resulting in a relatively intense absorption band. Detailed studies on various polymers have shown that this transition is located around 287.1–287.9 eV, but it can present a second transition at energies around 288.0–288.6 eV in unsaturated polymers with carbon–carbon double bonds in the main chain (Dhez et al., 2003). Studies by Cody et al. (1995, 1996) have demonstrated that this transition correlates with the concentration of aliphatic methyl and methylene groups in huminite, the main component of Tertiary coal. However, linear correlation studies on C(1s) XANES – ^{13}C NMR signal comparison (Schäfer et al., 2003c) revealed a rather weak, mixed Rydberg/valence (C–H*) transition intensity compared to the C(1s) π*-transitions and, therefore, a lower carbon XANES sensitivity to aliphatics. A detailed study of the intensity ratio (Table 2) between the aromatic carbon transition ($1\pi^*_{C=C;\ C-H}$ at 285.2 eV) and the mixed Rydberg/valence (C–H*) transition at 287.6 eV reveals uniform values (1.1–1.3) for the recharge and transition FAs and a slightly elevated ratio of 1.4 for the channel brine, whereas the enhanced DOC samples show a strong increase in aromatics and reduction in aliphatics, respectively (2.7–2.8). Taking into account the functional group sensitivity differences in C(1s) XANES – ^{13}C NMR linear regression comparison (Schäfer et al., 2003c), with a slope of 0.27 ± 0.03 for aliphatics and a slope of 0.70 ± 0.10 for aromatics, the aliphaticity in recharge dominated FAs is even more pronounced.

The most intense band in all the FAs spectra is centered around 288.6 eV and can be assigned to the large oscillation strength of the $1\pi^*_{C=O}$ of aromatic and aliphatic associated carboxylic groups. Elaborate polymer studies have demonstrated a variation in band energy between 288.2 and 288.8 eV (Dhez et al., 2003). Studies on amino acids and peptides (Boese et al., 1997; Carravetta et al., 1998) have shown a very small effect of peptide bond shift (0.3 eV) in the corresponding $1\pi^*_{C=O}$ resonance towards lower energy on the XANES spectra. This implies that carbon K-edge XANES spectroscopy is rather insensitive for distinguishing between carboxylic acid derivatives and peptides in complex systems and so chemical information must rely on other analytical methods. Taking again the C(1s) XANES – ^{13}C NMR linear regression analysis of Schäfer et al.

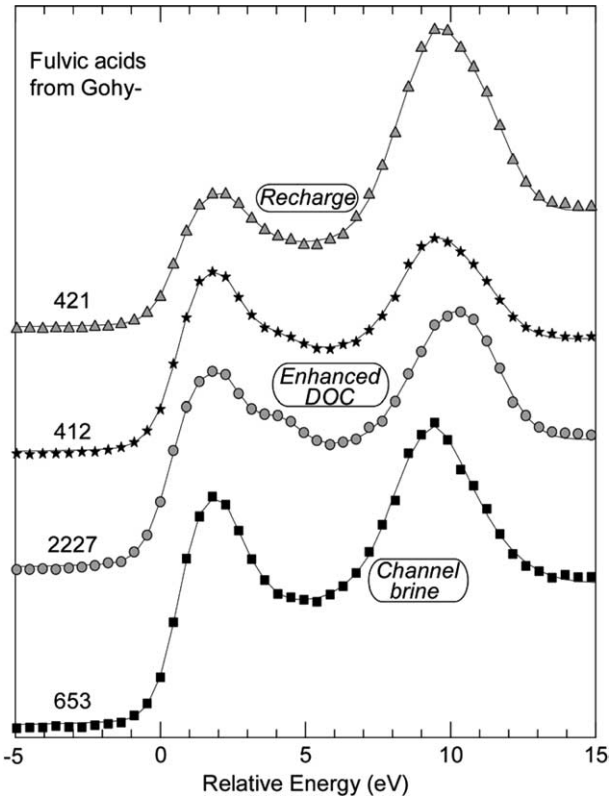

Fig. 6. Average sulfur K-edge XANES spectra of the different isolated FAs.

(2003c) for C=O groups (slope 2.40 ± 0.1) a quantitative carboxyl type group content of 15–20% for all the FAs could be estimated.

The transition at 289.5 eV is typically assigned to the O-alkyl group of alcohols and carbohydrates (Hitchcock and Mancini, 1994), but the C(1s) $\pi^*_{C=O}$ transition of carbonyl groups in urea and diphenyl urea (Urquhart and Ade, 2002) is shifted due to inductive effects of the neighbouring nitrogen atom in the same binding energy region (289.5–289.9 eV). A linear correlation of the ^{13}C NMR chemical shifts assigned to carbonyl groups (185–220 ppm) with the C(1s) resonance at 289.5 eV shows a correlation coefficient r^2 0.953 (Schäfer et al., 2003c). We therefore assigned this C(1s) transition to carbonyl groups. However, the deconvolution of this transition should not be over interpreted due to the overlap with the arctangent function of the ionization potential and the overlapping σ*-transition. The results from carboxyl and carbonyl functional group quantification show the highest content in the recharge and transition FAs and a significant decrease in the enhanced DOC (exception Gohy-412) and channel brine derived FAs (Table 2).

3.3. Sulfur K-edge XANES

The deconvolution of the average Gorleben FA sulfur XANES spectra (Fig. 6, Table 3) reveals an increase in reduced S (electronic oxidation state ⩽2) from 43% to 69% with the transition from shallow recharge dominated groundwater FAs (Gohy-421) to enhanced DOC groundwater FAs (Gohy-412 and -2227). Thiols (S_{-1}) follow this trend with an increase from 4% to 31 %. The remarkable difference in the reduced sulfur species between the two enhanced DOC groundwater FAs Gohy-2211 and Gohy-2227 might reflect the lower redox potential in the latter groundwater (Fig. 7). The measured isotope fractionation in Gohy-2227 is 31.7‰ or 23.3‰, respectively, taking either the atmospheric fallout sulfate δ ^{34}S value of 2.3‰ or the channel brine δ ^{34}S value of 10.7 as source (Fig. 8, Table 1). These isotope fractionation values lie within/above the sulfate reduction to sulfite (SO_3^{2-}) of 22–24‰ and below the highest fractionation of 45–50‰ obtained by summing up all sulfate to sulfide fractionation steps measured in closed laboratory systems (Canfield, 2001). However, the results are in good agreement with data on the extent of fractionation during sulfate reduction in natural systems (Habicht et al., 1998). The sulfur K-edge XANES show contributions of oxidized sulfur ($S_{+5/+6}$) of approximately 30% in the enhance DOC FA samples. Compared to literature values found for leonardite-derived HA and lignites (coals and oil shales; Olivella et al., 2002a,b) with an average oxidized sulfur content of 50 ± 15% (n = 9), the enhanced DOC FAs show a lower amount of oxidized sulfur. This may reflect both the remobilization of hydrophobic compounds via partial oxidation of Miocene brown coal sand, comparable to observations made by Hundal et al. (2000), or be the result of incorporation of reduced sulfur during microbiological sulfur reduction associated with the in situ generation process. The findings suggest that S is predominantly in the "reduced" form (electronic oxidation state ⩽2), likely composed of sulfides, thiols, thiophenes and sulfoxides in enhanced DOC and channel

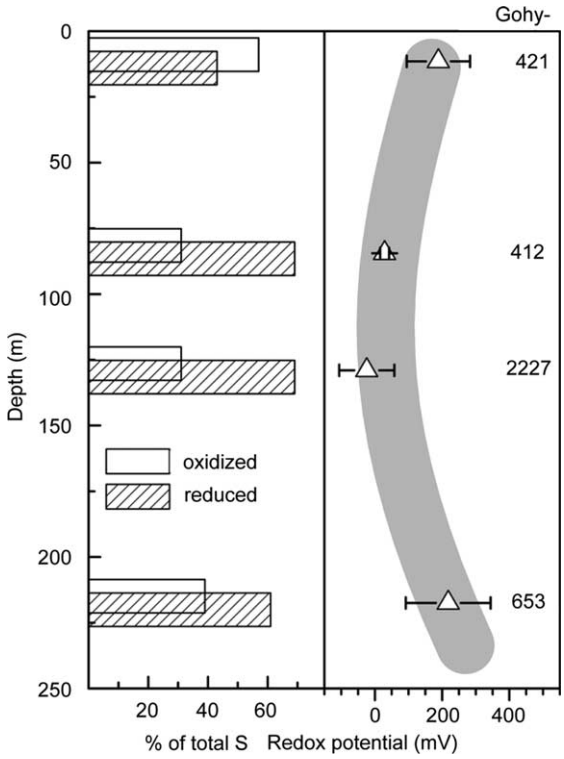

Fig. 7. Left: Block chart of oxidized and reduced sulfur determined by sulfur K-edge XANES as a function of groundwater depth. Right: Average groundwater redox potential for the respective groundwater with variation detected for various sampling campaigns.

Table 3
Distribution of sulfur oxidation states in FA samples from sulfur K-edge XANES, given as relative amount of total S

	Reduced S			Oxidized S		
Formal oxidation state:	−1	0	+2	+4	+5	+6
Sample						
Recharge						
-421	4	36	3	–	44	13
Enhanced DOC						
-412	12	53	4	–	27	4
-2227	31	31	7	–	30	1
Channel brine						
-653	16	42	3	(0.3)	28	11

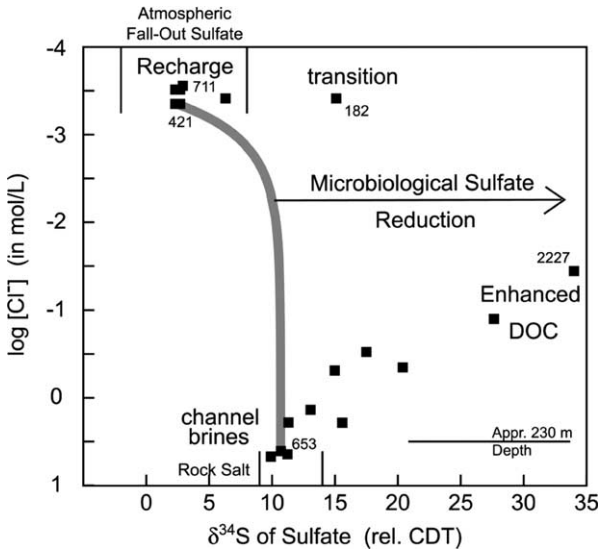

Fig. 8. δ ^{34}S sulfate values plotted as a function of chloride concentration used as conservative tracer for influence of brines. Discrimination of recharge dominated areas influenced by atmospheric fallout sulfate and channel brines showing Zechstein evaporite δ ^{34}S signatures is given. Grey line represents pure mixing path. Enhanced DOC groundwater shows microbial sulfate reduction and brine influence; transition groundwater Gohy-182 shows no brine influence.

brine-derived FAs. In combination with the ^{34}S isotopic fractionation data (Fig. 8) showing a preferential turnover of $^{32}SO_4^{2-}$ and enrichment in ^{34}S in the remaining sulfate of the enhanced DOC groundwaters, a bacterially mediated FAs generation via SO_4^{2-} reduction in the vicinity of a SO_4^{2-} supply can be identified as a predominant process.

The saline groundwater FAs sample Gohy-653 shows a somewhat lower reduced S content (61%), with thiols (S_{-1}) and sulfides/disulfides (S_0) percentages closer to values found for Gohy-2227(FAs) than for -412(FAs). The reduced S groups of Gohy-653(FA) are not significantly influenced by the redox environment of the channel brine (E_H 218 ± 126 mV, Table 1, Fig. 7), indicating a high stability of the reduced organic S. Similar results were found for HA samples under variation in aeration and pH by Hutchison et al. (2001). Within the oxidized S groups in Gohy-653(FAs) the percentage of ester bound sulfates (S_{+6}) is increased to values in the range of the recharge dominated Gohy-421(FAs). It has been shown by Lou and Warman (1994) that labile ester sulfate can accumulate in organic matter with an increase of inorganic sulfate input. Therefore, in the channel brine groundwater Gohy-653 the high inorganic SO_4^{-2} concentration of 46 mmol/L may be responsible for the increase in ester sulfate in the isolated FAs. The δ ^{34}S signature of the channel brine groundwater Gohy-653 shows a value of 10.7‰ which is comparable to Permian Zechstein evaporite values of 9.6–11.9‰ (Berner et al., 2002) and clearly indicates dissolved gypsum/anhydrite from the salt dome cap rock as SO_4^{2-} source.

Overall, the high valent S measured for the FAs here is dominated by sulfonic acids with an oxidation state of +5, whereupon the recharge dominated FAs from Gohy-421 show the maximum percentage. High sulfonic acid content in the total S pool is typical of FAs as pointed out by Morra et al. (1997) and represents a major form of forest soil organic sulfur (Autry and Fitzgerald, 1990), which can be enhanced due to agricultural activities (van Loon et al., 1993). The high sulfonic acid content found in Gohy-421(FAs) together with the high ^{14}C inventory (Buckau et al., 2003) clearly indicates a soil perturbed by agricultural activity as the FAs source.

3.4. XANES and isotopic data correlation

Finally, the general properties of the FAs deduced from carbon and sulfur XANES are correlated with the fraction of FAs originating from recharge as determined by isotopic data analysis (Figs. 1 and 4). Thereby, the respective contribution is set to 100% in recharge groundwaters and calculated from the measured ^{14}C FA concentration relative to the value of 56 pmc for recharge conditions prior to atmospheric nuclear testing. The results are shown in Fig. 9. Data for carbonyl groups are excluded because of the above mentioned uncertainty in carbon XANES spectral deconvolution. Data for the enhanced DOC Gohy-412 FAs are also excluded because of strongly deviating results, possibly due to inorganic contamination. The carbon content is significantly lower than in the other samples. Furthermore, the sample showed considerable contribution of

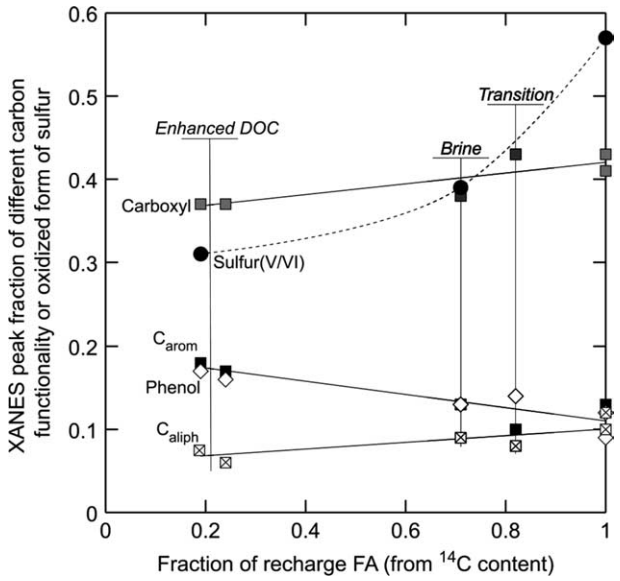

Fig. 9. Peak fractions of different carbon functionality determined from carbon K-edge XANES and oxidized form of sulfur from sulfur K-edge XANES against fraction of recharge FAs within the total FA derived from ^{14}C content back calculation (see text).

inorganic substances, indicating that purification was not very successful (Kim et al., 1995).

As a general trend, the carboxyl group content increases with the fraction of recharge FAs. A corresponding decrease is seen in the C=C/aromatic content and in the content of phenolic groups. The aliphatic group content does increase slightly with the fraction of recharge FAs. Despite the uncertainty in the data and the correlations shown in Fig. 9, the composition of in situ generated FAs can be estimated. Extrapolation to zero contribution of recharge FAs leads to relative peak areas for different carbon entities/functionalities as follows: carboxylic groups 0.35 ± 0.02, C=C/aromatic groups 0.19 ± 0.02, phenolic groups 0.18 ± 0.01 and aliphatic groups 0.08 ± 0.02. This would lead to a residue of about 0.2 consisting of carbonyl groups, which is difficult to quantify. Sulfur functional groups in the oxidized form (S_{+5}/S_{+6}) show almost the doubled peak area for recharge FAs compared to in situ generated FAs. The brine FAs have a value in between, tending more towards the in situ generated FAs which cannot be explained by simple mixing. The relative peak areas of oxidized/reduced forms of sulfur in the channel brine-derived FAs does not correlate with the groundwater redox potential (Fig. 7). The sulfur inventory may reflect both the inherent form of sulfur in Miocene brown coal material and also geochemical (microbial) reactions, including the in situ generation process.

Attempts to correlate the relative peak areas for different carbon functionalities with physicochemical conditions were not successful. Therefore, the overall result is that the content of these carbon functionalities appears to reflect the respective contribution of recharge and enhanced DOC FAs. The successful correlation between functionalities and the mixing between recharge and in situ generation also verifies the high mobility of FAs following relatively rapid groundwater exchange over the entire depth of the aquifer system, with strong local variation. This is seen directly for the high contribution of recharge FAs in the groundwater Gohy-2211 sample at 83–85 m depth, verified both by the ^{14}C content and the carbon functionality distribution from carbon XANES. Not only is fallout tritium found in this groundwater, but it also contains a surprisingly high content of recharge FAs.

The red shift area (heteroatom substitution, aromatic distortion, benzoquinone type groups) might be one possible exception from the general conclusion that the carbon functional group content reflects mainly mixing of two sources. This content is relatively high in the brine sample Gohy-653(FAs) but is not identified in the recharge and transition FAs. A small but significant amount is also found in Gohy-2227 FAs. Two different processes could result in the observed red shift: (a) Heteroatom-substituted portions of FAs generated in the enhanced DOC groundwaters (i.e., Gohy-2227) are preferentially stable under channel brine conditions and coagulate to a lower extent. (b) Inflow takes place from the neighbouring Gorleben channel with net flow of groundwater from depth towards the surface (Artinger et al., 2000). Consequently, the carbon functionality responsible for the red shift may be generated under brine conditions and found in Gohy-2227 as a result of upward FAs movement.

4. Conclusions

Through a combination of isotopic and spectroscopic (XANES) observations it is possible to identify the origin and mobility of FAs in the Gorleben aquifer system:

(i) Isotopic data analysis of FAs revealed a common origin (microbiological turnover of organic material of C_3 plant origin) as the generation process irrespective of the source documented by the absolute ^{14}C values.
(ii) Back calculation of the recharge-derived FA fraction, taking a ^{14}C value of 55 ± 6 pmc prior to atmospheric nuclear testing, showed a rapid vertical groundwater exchange and an unhindered transport of recharge FAs to deep channel brine groundwaters.
(iii) Carbon K-edge XANES revealed for recharge and brine derived FAs a very similar C_{arom}/C_{aliph} ratio (1.1–1.4), indicating the invariance in the FA backbone structure against high residence time and variation in geochemical conditions. In situ generated FAs have a high C_{arom}/C_{aliph} ratio (~2.8), a decreased carboxyl/carbonyl functional group content (less hydrophilic) and a red shift of the $C_{arom} = C_{arom}$ peak, indicating heteroatom substitution and/or aromatic ring distortion. Furthermore, the C(1s) XANES data suggest that only heteroatom substituted, destabilized aromatic ring structures of the enhanced DOC FAs are stable in the brines and do not flocculate at the high ionic strength.
(iv) Sulfur XANES revealed only 43% reduced S in recharge FAs and the highest reduced S content (~69%) in in situ generated enhanced DOC FAs. A slightly lower value (61%) of reduced S, with an increase in labile bond ester sulfate content due to the presence of inorganic sulfate, can be found in the channel brine FAs. Sulfur oxidation state analysis reflects primarily geochemical conditions/reactions and shows a high stability of reduced sulfur species in FAs in higher redox potential (channel brine) aquatic environments.
(v) Carbon and sulfur XANES provide a broad spectrum of structural information. This information is comparable to that obtained by for example ^{13}C NMR; however, in contrast to ^{13}C NMR only very small samples are required.

Acknowledgements

We thank Dr. Claude Largeau and an anonymous reviewer for their helpful suggestions. Furthermore, we are grateful for beamtime allotment by BNL/NSLS. Spectromicroscopic data were collected using the X1-A1 STXM developed by the group of Janos Kirz and Chris Jacobsen at SUNY Stony Brook, with support from the Office of Biological and Environmental Research, U.S. DoE under contract DE-FG02-89ER60858, and from the NSF under grant DBI-9605045. The zone plates were developed by Steve Spector and Chris Jacobsen of Stony Brook and Don Tennant of Lucent Technologies Bell Labs, with support from the NSF under Grant ECS-9510499.

Associate Editor—**Lorenz Schwark**

References

Ade, H., Zhang, X., Cameron, S., Costello, C., Kirz, J., Williams, S., 1992. Chemical contrast in X-ray microscopy and spatially resolved XANES spectroscopy of organic specimens. Science 258, 972–975.

Artinger, R., Buckau, G., Geyer, S., Fritz, P., Wolf, M., Kim, J.I., 2000. Characterization of groundwater humic substances: influence of sedimentary organic carbon. Applied Geochemistry 15, 97–116.

Artinger, R., Buckau, G., Kim, J.I., Geyer, S., 1999. Characterization of groundwater humic and fulvic acids of different origin by GPC with UV/Vis and fluorescence detection. Fresenius Journal of Analytical Chemistry 364, 737–745.

Artinger, R., Schuessler, W., Schäfer, T., Kim, J.I., 2002. A kinetic study of Am(III)/humic colloid interactions. Environmental Science & Technology 36, 4358–4363.

Autry, A.R., Fitzgerald, J.W., 1990. Sulfonate sulfur: a major form of forest soil organic sulfur. Biology and Fertility of Soils 10, 50–56.

Berner, Z.A., Stuben, D., Leosson, M.A., Klinge, H., 2002. S- and O-isotopic character of dissolved sulphate in the cover rock aquifers of a Zechstein salt dome. Applied Geochemistry 17, 1515–1528.

Boese, J., Osanna, A., Jacobsen, C., Kirz, J., 1997. Carbon edge XANES spectroscopy of amino acids and peptides. Journal of Electron Spectroscopy and Related Phenomena 85, 9–15.

Buckau, G., Artinger, R., Kim, J.I., Geyer, S., Fritz, P., Wolf, B., Frenzel, B., 2000a. Development of climatic and vegetation conditions and the geochemical and isotopic composition in the Franconian Albvorland aquifer system. Applied Geochemistry 15, 1191–1201.

Buckau, G., Artinger, R., Fritz, P., Geyer, S., Kim, J.I., Wolf, M., 2000b. Origin and mobility of humic colloids in the Gorleben aquifer system. Applied Geochemistry 15, 171–179.

Buckau, G., Artinger, R., Geyer, S., Wolf, M., Fritz, P., Kim, J.I., 2000c. ^{14}C dating of Gorleben groundwater. Applied Geochemistry 15, 583–597.

Buckau, G., Artinger, R., Geyer, S., Wolf, M., Fritz, P., Kim, J.I., 2000d. Groundwater in situ generation of aquatic humic and fulvic acids and the mineralization of sedimentary organic carbon. Applied Geochemistry 15, 819–832.

Buckau, G., Wolf, M., Geyer, S., Artinger, R., Kim, J.I., 2003. Origin and mobility of aquatic humic substances from wetland recharge in the Gorleben aquifer system. In: Buckau, G. (Ed.), Humic Substances in Performance Assessment of Nuclear Waste Disposal: Actinide and Iodine Migration in the Far-Field (First Technical Progress Report), Research Center Karlsruhe Report FZKA 6800, Karlsruhe, Germany, pp. 39–51.

Canfield, D.E., 2001. Biogeochemistry of sulfur isotopes, Stable Isotope Geochemistry. Reviews in Mineralogy and Geochemistry 43, 607–636.

Carravetta, V., Plashkevych, O., Agren, H., 1998. A theoretical study of the near-edge X-ray absorption spectra of some larger amino acids. Journal of Chemical Physics 109, 1456–1464.

Claret, F., Bauer, A., Schäfer, T., Griffault, L., Lanson, B., 2002. Experimental investigation of the interaction of clays with high-pH solutions: a case study from the Callovo-Oxfordian formation, Meuse-Haute Marne underground laboratory (France). Clays and Clay Minerals 50, 633–646.

Cody, G.D., Botto, R.E., Ade, H., Behal, S., Disko, M., Wirick, S., 1995. Inner-Shell Spectroscopy and imaging of a subbituminous coal: in situ analysis of organic and inorganic microstructure using C(1s)-, Ca(2p)-, and Cl(2s)-NEXAFS. Energy and Fuels 9, 525–533.

Cody, G.D., Botto, R.E., Ade, H., Wirick, S., 1996. The application of soft X-ray microscopy to the in situ analysis of sporinite coal. International Journal of Coal Geology 32, 69–86.

Dhez, O., Ade, H., Urquhart, S.G., 2003. Calibrated NEXAFS spectra of some common polymers. Journal of Electron Spectroscopy and Related Phenomena 128, 85–96.

Francis, J.T., Hitchcock, A.P., 1992. Inner-shell spectroscopy of *p*-benzoquinone, hydroquinone, and phenol: distiguishing quinoid and benzenoid structures. The Journal of Physical Chemistry 96, 6598–6610.

Garrett, R.M., Pickering, I.J., Haith, C.E., Prince, R.C., 1998. Photooxidation of crude oils. Environmental Science and Technology 32, 3719–3723.

Habicht, K.S., Canfield, D.E., Rethmeier, J., 1998. Sulfur isotope fractionation during bacterial reduction and disproportionation of thiosulfate and sulfite. Geochimica et Cosmochimica Acta 62, 2585–2595.

Hatcher, P.G., Clifford, D.J., 1997. The organic geochemistry of coal: from plant materials to coal. Organic Geochemistry 27, 251–262.

Hitchcock, A.P., Brion, C.E., 1980. Inner-shell excitation of formaldehyde, acetaldehyde and acetone studied by electron impact. Journal of Electron Spectroscopy and Related Phenomena 19, 231–250.

Hitchcock, A.P., Ishii, I., 1987. Carbon K-shell excitation spectra of linear and branched alkanes. Journal of Electron Spectroscopy and Related Phenomena 42, 11–26.

Hitchcock, A.P., Mancini, D.C., 1994. Bibliography of atomic and molecular inner-shell excitation studies. Journal of Electron Spectroscopy and Related Phenomena 67, 1–132.

Hitchcock, A.P., Urquhart, S.G., Rightor, E.G., 1992. Inner shell spectroscopy of benzaldehyde, terephthalaldehyde, ethyl benzoate, terephthaloyl chloride, and phosgene: models for core excitation of poly (ethylene terephathalate). The Journal of Physical Chemistry 96, 8736–8750.

Honeyman, B.D., 1999. Colloidal culprits in contamination. Nature 397, 23–24.

Hundal, L.S., Carmo, A.M., Bleam, W.L., Thompson, M.L., 2000. Sulfur in biosolids-derived fulvic acid: characterization by XANES spectroscopy and selective dissolution approaches. Environmental Science and Technology 34, 5184–5188.

Hutchison, K.J., Hesterberg, D., Chou, J.W., 2001. Stability of reduced organic sulfur in humic acid as affected by aeration and pH. Soil Science Society of America Journal 65, 704–709.

Jacobsen, C., Williams, S., Anderson, E., Browne, M.T., Buckley, C.J., Kern, D., Kirz, J., Rivers, M., Zhang, X., 1991. Diffraction-limited imaging in a scanning transmission X-ray microscope. Optics Communications 86, 351–364.

Jacobsen, C.J., Zimba, C., Flynn, G., Wirick, S., 2000. Soft X-ray microscopy from sub-100nm regions. Journal of Microscopy 197, 173–184.

Kim, J.I., 1994. Actinide colloids in natural aquifer systems. Material Research Society Bulletin 19, 47–53.

Kim, J.I., Artinger, R., Buckau, G., Kardinal, C., Geyer, S., Wolf, M., Halder, H., Fritz, P., 1995. Grundwasserdatierung mittels ^{14}C-Bestimmungen an gelösten Humin- und Fulvinsäuren (Abschlußbericht), RCM report 00895, Institute of Radiochemistry, Technical University Munich, Munich, Germany, pp. 221.

Kim, J.I., Buckau, G., Rommel, H., Sohnius, B., 1989. The migration behaviour of transuranium elements in Gorleben aquifer systems: colloid generation and retention process. Material Research Society Symposium Proceedings 127, 849–854.

Lou, G.Q.J., Warman, P.R., 1994. Characterization of Ester Sulfate in a Gypsum-Amended Podzol Using an Immobilized Sulfatase Reactor. Biology and Fertility of Soils 17, 276–280.

Ma, Y., Chen, C.T., Meigs, G., Randall, K., Sette, F., 1991. High-resolution-shell photoabsorption measurements of simple molecules. Physical Review A 44, 1848–1858.

Manahan, S.E., 1989. Interactions of hazardous-waste chemicals with humic substances. Advances in Chemistry Series 219, 81–92.

McCarthy, J.F., Zachara, J.M., 1989. Subsurface transport of contaminants: mobile colloids in the subsurface environment may alter the transport of contaminants. Environmental Science and Technology 23, 497–502.

Morra, M.J., Fendorf, S.E., Brown, P.D., 1997. Speciation of sulfur in humic and fulvic acids using X-ray absorption near-edge structure (XANES) spectroscopy. Geochimica et Cosmochimica Acta 61, 683–688.

OECD-NEA, 1994. Binding models concerning natural organic substances in performance assessment. In: Proceedings of the NEA workshop organized in co-operation with the Paul Scherrer Institut (PSI), Bad Zurzach (Switzerland).

Olivella, M.A., del Rio, J.C., Palacios, J., Vairavamurthy, F.X.C., de las Heras, F.X.C., 2002a. Characterization of humic acid from leonardite coal: an integrated study of PY-GC-MS, XPS and XANES techniques. Journal of Analytical and Applied Pyrolysis 63, 59–68.

Olivella, M.A., Palacios, J.M., Vairavamurthy, A., del Rio, F.X.C., de las Heras, F.X.C., 2002b. A study of sulfur functionalities in fossil fuels using destructive- (ASTM and

Py-GC-MS) and non-destructive- (SEM-EDX, XANES and XPS) techniques. Fuel 81, 405–411.

Plaschke, M., Rothe, J., Schäfer, T., Denecke, M.A., Dardenne, S., Pompe, S., Heise, K.H., 2002. Combined AFM and STXM in situ study of the influence of Eu(III) on the agglomeration of humic acid. Colloids and Surfaces A: Physicochemical and Engineering Aspects 197, 245–256.

Schäfer, T., Artinger, R., Dardenne, K., Bauer, A., Schuessler, J.I., Kim, J.I., 2003a. Colloid-borne Americium migration in Gorleben groundwater: significance of iron secondary phase transformation. Environmental Science and Technology 37, 1528–1534.

Schäfer, T., Claret, F., Bauer, A., Griffault, L., Ferrage, E., Lanson, B., 2003b. Natural organic matter (NOM)-clay association and impact on Callovo-Oxfordian clay stability in high alkaline solution: spectromicroscopic evidence. Journal de Physique IV 104, 413–416.

Schäfer, T., Hertkorn, N., Artinger, R., Claret, F., Bauer, A., 2003c. Functional group analysis of natural organic colloids and clay association kinetics using C(1s) spectromicroscopy. Journal de Physique IV 104, 409–412.

Scheinost, A.C., Kretzschmar, R., Christl, I., Jacobsen, C., 2002. Carbon group chemistry of humic and fulvic acid: a comparison of C-1s NEXAFS and ^{13}C NMR spectroscopies. Special Publications – Royal Society of Chemistry 273, pp. 39–47.

Spector, S., Jacobsen, C., Tennant, D., 1997. Process optimization for production of sub-20 nm soft X-ray zone plates. Journal of Vacuum Science and Technology B 15, 2872–2876.

Stankiewicz, B.A., Kruge, M.A., Mastalerz, M., 1996. A geochemical study of macerals from a Miocene lignite and a Eocene bituminous coal, Indonesia. Organic Geochemistry 24, 531–545.

Stöhr, J., 1996. NEXAFS Spectroscopy. Springer, Berlin.

Stöhr, J., Samant, M.G., Lüning, J., Callegari, A.C., Chaudhari, P., Doyle, J.P., Lacey, J.A., Lien, S.A., Purushothaman, S., Speidell, J.L., 2001. Liquid crystal alignment on carbonaceous surfaces with orientational order. Science 292, 2299–2302.

Urquhart, S.G., Ade, H., 2002. Trends in the carbonyl core (C 1s, O 1s) $\rightarrow \pi^*$ C═O transition in the near-edge X-ray absorption fine structure spectra of organic molecules. Journal of Physical Chemistry B 106, 577–585.

Vairavamurthy, M.A., Manowitz, B., Maletic, D., Wolfe, H., 1997. Interactions of thiols with sedimentary particulate phase: studies of 3-mercaptopropionate in salt marsh sediments from Shelter Island, New York. Organic Geochemistry 26, 577–585.

van Loon, W.M.G.M., Boon, J.J., Groot, B., 1993. Quantitative analysis of sulfonic acid groups in macromolecular lignosulfonic acids and aquatic humic substances by temperature-resolved pyrolysis-mass spectroscopy. Environmental Science and Technology 27, 2387–2396.

Winn, B., Ade, H., Buckley, C., Howells, M., Hulbert, S., Jacobsen, C., Kirz, J., McNulty, I., Miao, J., Oversluizen, I., Pogorelsky, I., Wirick, S., 1996. X1A: second generation undulator beamlines serving soft X-ray spectromicroscopy experiments at the NSLS. Reviews of Scientific Instruments 67, 1–4.

Xia, K., Skyllberg, U.L., Bleam, W.F., Bloom, P.R., Nater, P.A., Helmke, P.A., 1999. X-ray absorption spectroscopic evidence for the complexation of Hg(II) by reduced sulfur in soil humic substances. Environmental Science and Technology 33, 257–261.

Zhang, X., Ade, H., Jacobsen, C., Kirz, J., Lindaas, S., Williams, S., Wirick, S., 1994. Micro-XANES: chemical contrast in the scanning transmission X-ray microscope. Nuclear Instruments and Methods in Physics Research A 347, 431–435.

3.0 Radionuclide scavenging by ferric iron phases

Iron oxides and hydroxides are widespread in environmental systems and have been identified in the atmosphere, hydrosphere, lithosphere, pedosphere and biosphere (Cornell and Schwertmann, 1996). Recent global ocean circulation and carbon cycle models include seawater iron geochemistry and tuned to match the observed ocean Fe distribution (Archer and Johnson, 2000). An interesting point in this perspective is the work of (Wu et al., 2001) who demonstrated, that a substantial portion of the previously presumed “dissolved” iron is present in the colloidal size range. The formation of secondary phases including the predominant ferric iron phases is of major importance for the fate of both organic and inorganic substances/contaminant in natural systems. Work in the past decades has been focused on the characterization of low crystalline hydrous ferric oxides (HFO), or more crystallographic precisely 2-line and 6-line ferrihydrite (Drits et al., 1993; Jambor and Dutrizac, 1998; Manceau and Drits, 1993; Manceau and Gates, 1997), the metal surface complexation/precipitation in the binary system metal - ferrihydrite (Bruno et al., 1995; Charlet and Manceau, 1992; Dardenne et al., 2001; Dardenne et al., 2002; Dzombak and Morel, 1990; Zänker et al., 2003), the ternary system metal – ferrihydrite – organics (Payne et al., 1996; Schäfer et al., 2003a) and especially the fate of metals during the transformation of meta-stable ferrihydrite to stable end members as goethite and hematite (Dardenne et al., 2002; Lerotic et al., 2004; Lichtner and Waber, 1992; Nagano et al., 1999; Sakamoto et al., 1994; Sun et al., 1996).

Various technical applications use or have to deal with iron oxide/hydroxide phases in form of colloids or as scaling. The oil industry has performed a lot of research over at least the last three decades especially in the area of formation damage studies in oil reservoir rocks, where iron colloids are beside clays the major concern changing dramatically the productivity of reservoirs via permeability reduction (Pittman and King, 1986; Potter and Dibble Jr., 1985). Ferric iron encrustations are also a common problem that seriously affects the performance of drinking water wells and drains (Houben, 2004). Their formation is induced by the mixing of reduced ground water containing ferrous iron with oxic shallow ground water and exposure to air. In Finland for example treatment plants of anoxic groundwater have been simply based on atmospheric oxidation and co-precipitation of heavy metals with iron and manganese oxides (Carlson and Schwertmann, 1987). A ferric chloride flocculation step is routinely used in wastewater treatment plants and effectively removes heavy metals, but difficulties with organic contaminant such as pharmaceuticals were observed (Ternes et al., 2002).

Furthermore, remediation strategies, as permeable reactive barrier (PRB) systems (Blowes et al., 2000; Naftz et al., 2002) using e.g. zero-valent iron (ZVI) are based i.e. on the formation of ferrous and ferric iron phases by corrosion of steel or Fe(0) nanoparticles (Cantrell and Kaplan, 1997a; Cantrell and Kaplan, 1997b; Kaplan et al., 1996). The concept of a PRB

is relatively simple. Reactive material is placed in the subsurface where a plume of contaminated ground water must move through it as it flows, typically under its natural gradient creating a passive treatment system (see Figure 5). The PRB is not a barrier to the water, but it is a barrier to the contaminant. Due to the passive nature of PRBs and the potential of PRBs to mitigate the spread of contaminants that have proven difficult and expensive to manage with other cleanup methods (e.g. pump-and-treat) they offer good cost/benefit ratios. The majority of installed PRBs use ZVI with more than 80 full-scale ZVI-based PRBs installed worldwide (ITRC, 2005).

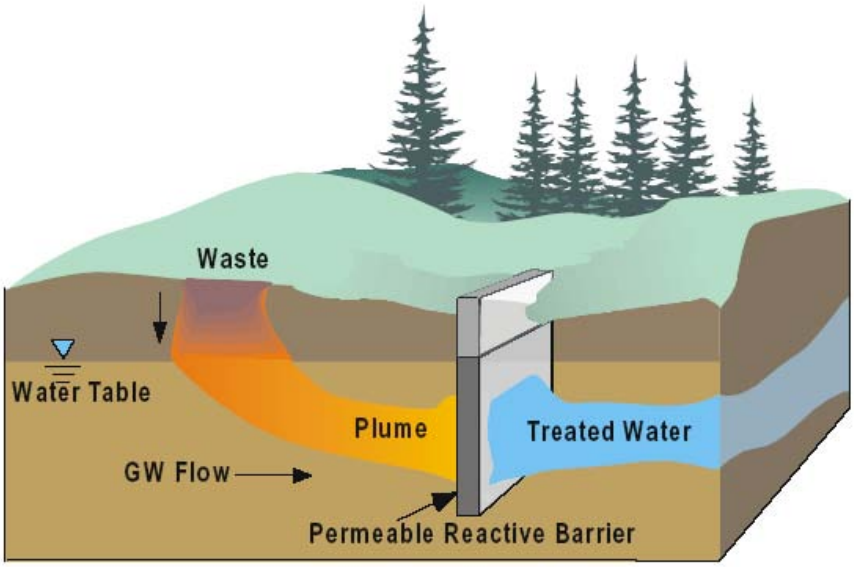

Figure 5: *Example of a waste plume being treated by a permeable reactive barrier wall. (Figure taken from (EPA, 1998).*

Commercial PRBs are currently built in two basic configurations, namely the funnel-and-gate and the continuous PRB. Both have required some degree of excavation and been limited to fairly shallow depths (16m to ~22.5m). Newer techniques for emplacing reactive media, such as the injection of slurries/colloid suspensions, hydrofracturing, driving mandrels, etc., may serve to overcome some of these emplacement limitations. The funnel-and-gate design PRB uses impermeable walls (sheet pilings, slurry walls, etc.) as a “funnel” to direct the contaminant plume to a “gate(s)” containing the reactive media (i.e. ZVI), whereas the continuous PRB completely transects the plume flow path with reactive media. In both designs it is necessary to keep the reactive zone permeability equal to or greater than the permeability of the aquifer to avoid diversion of the flowing waters around the reactive zone. ZVI based PRB’s have been successfully used in tests to treat groundwater contaminated by chromium (Powell and Puls, 1997; Pratt et al., 1997; Puls et al., 1999), organic solvents (O’Hannesin and Gillham, 1998), uranium (Morrison et al., 2001) and anion forming elements such as Tc(VII) (Blowes et al., 2000; Cantrell et al., 1995). For the later, treatment was evaluated in large-scale experiments at the US Department of Energy, Oak Ridge National Laboratory Y-

12 site and preliminary results indicate the re-movement of Tc(VII) and U(VI) by ZVI and the importance of reaction kinetics (Liang et al., 2005).

Regarding the multi-barrier system of a SF and HLW nuclear-waste repository site, in the "corrosion allowance concept" stainless steel canister corrosion will form a sequence of secondary iron phases quite comparable to the ZVI corrosion products with green rust, magnetite, hematite and oxy-hydroxides like ferrihydrite as precursor phases. The formation of ferrous or ferric iron phases depends on the scenario. The possibility that the copper/iron canister breaches earlier as expected cannot be entirely ruled out, as material and/or manufacturing defects can arise in the canister fabricating procedures (e.g. unsuccessful electron beam weld) (Bowyer, 1999). As a result, a defective canister might be penetrated by groundwater at ~1000 years after disposal (Bond et al., 1997) and redox conditions near the fuel pellets may well be modified as a result of the radiolysis of groundwater (Werme et al., 1990). Groundwater radiolysis produces equivalent quantities of oxidizing (mainly H_2O_2 and O_2) and reducing (mostly H_2) species (Werme et al., 1990). The strong γ- and β- fields associated with the fuel will decrease by a factor of $>10^3$ in the first few hundred years after disposal (Sunder and Shoesmith, 1991) and groundwater will thus be subject mainly to α- radiolysis. Approximately ~99 % of the oxidants originally generated will back react with the simultaneously generated reducing species, and only ca. 1 % are available to oxidize the fuel matrix (Liu and Neretnieks, 1996), which is however sufficient to increase the redox potential near the fuel pellets. The release of the major fraction of the nuclide inventory will be controlled primarily by the dissolution of the fuel matrix. In particular, they will be subject to a variety of redox reactions within the canister, as shown schematically in Fig. 6, due mainly to the anoxic corrosion of the cast iron insert that continuously provides ferrous iron to the intervening solution. The system as shown in Fig. 6 can be divided into three regions, in which the dominant reactions are quite different.

1. In the first region (fuel rod), the oxidative dissolution of the fuel matrix plays the most important role in determining the chemistry near the fuel pellets. It acts, in essence, as the only source releasing hexavalent uranium (UO_2^{2+}) and other RN's into solution. H_2 generated both by the radiolysis of groundwater and by the anoxic corrosion of the cast iron insert will rapidly build-up and the expected high H_2 partial pressures are seen to suppress fuel oxidation very effectively in the presence of radiation (King et al., 1999; Spahiu et al., 2000). Therefore, the largest amount of dissolved hexavalent uranium will be reduced by dissolved H_2, using UO_2 (s) on the fuel pellets as a catalyst (Liu, 2001).
2. In the second region, i.e. the intervening solution between the fuel rod and the corrosion film of the cast iron insert, the only redox reaction is the oxidation of ferrous iron by radiolytic oxidants. The reduction of dissolved hexavalent uranium by dissolved

ferrous iron is thermodynamically possible, but it was not found to take place in recent studies (Liger et al., 1999).

3. In the third region, an iron corrosion film grows very slowly as the cast iron insert is oxidized and partly dissolves. A porous hydroxide or oxide thin layer film would then gradually build up on top of the inner iron surface providing a great transport resistance and a large number of sorption sites for the outgoing radiolysis-produced oxidants and the dissolved nuclides. The oxidation of ferrous iron by O_2 or radiolysis-produced oxidants is favored thermodynamically and kinetically not only by hydrolysis but also by specific adsorption to iron-corrosion products (Tamura et al., 1976). As a result, a Fe^{3+}/Fe^{2+} redox front will form within the corrosion film (Fig. 6) to the left of which only Fe^{3+}(s) exists and to the right of which Fe^{2+}(s) co-exists with Fe^{3+}(s). Given that the redox reactions are fast in comparison with the mass transport, the oxidants would be depleted near the Fe^{2+}/Fe^{3+} (s) front. The composition of the corrosion film that consists of Fe^{2+}(s), Fe^{3+}(s) and perhaps UO_2 (s) will dynamically change from the outer layer to the cast iron surface.

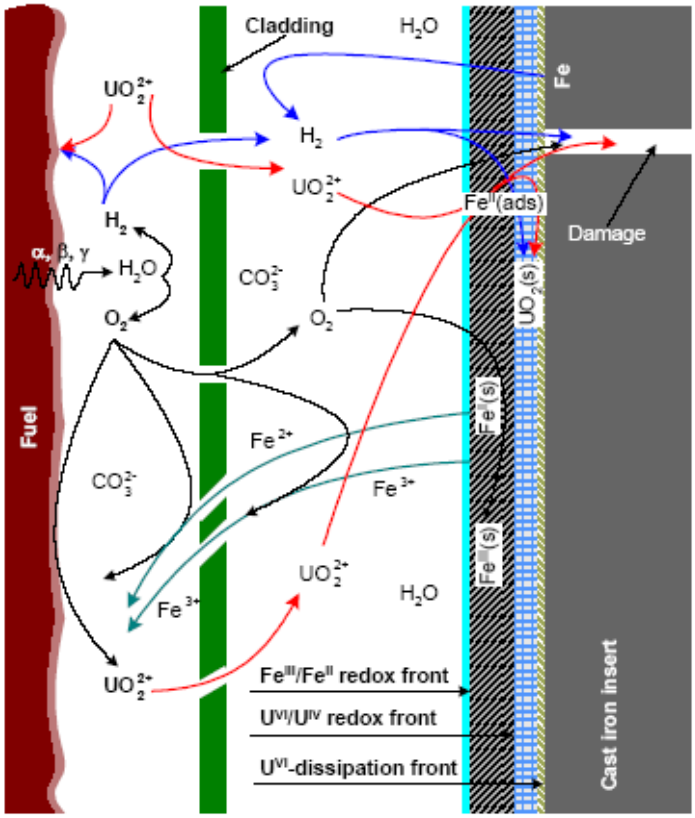

Figure 6: *Schematic view of the main processes occurring within the canister with a small damage through its iron insert, which conceptually denotes all the cracks/defects that exist. (Figure taken from (Liu, 2001).*

Overall, the anoxic corrosion of the cast iron insert plays a very important role in determining the redox chemistry within the canister, and in retarding the transport of dissolved nuclides

out of the canister. The possibility that oxidising species produced by radiolysis diffuse out of the canister and into the surrounding bentonite cannot be completely excluded, although this could only occur in the case of passivation of magnetite (Johnson and Smith, 2000).

Redox conditions in the near field outside the canister will be initially oxidizing, as a result of the presence of air trapped in pores of the backfill bentonite and the oxidation of the host rock due to shaft and tunnel excavation/ventilation. The low moisture content and slow saturation of the backfill bentonite will initially hinder consumption of O_2 by the steel canister and this situation may last for a considerable time. In the expected case of slow water inflow rates, the relatively high reactivity of pyrite towards O_2, the high moisture content of the host rock compared to the backfill bentonite, and the high rate of O_2 diffusion in unsaturated bentonite will favor consumption of O_2 by pyrite present in the excavation disturbed zone (EDZ) and steel in the emplacement tunnels (rails, mesh). Depending on the rate of saturation of the bentonite, the consumption of O_2 may take a few years (if bentonite saturation is rapid) to a few decades (for a longer unsaturated period). Beside the consumption of oxygen through small amounts of pyrite and siderite present in the backfill material or in the host rock (Clay formations) possible microbial activity can be considered. In crystalline rock detailed investigations suggest that microbiology-mediated reducing conditions will occur less than one year after repository closure (Pedersen, 2002).

All this examples mentioned above show that ferric and ferrous iron secondary phases will occur in various redox-fronts in the multi-barrier system of a SF and HLW nuclear-waste repository site and a thorough evaluation of the radionuclide retention on these phases is important in order to give precise information on the radionuclide source term. The peer- reviewed publications given in this chapter can be subdivided in the following topics:

- Surface complexation and sorption species identification of trivalent lanthanides (trivalent actinide homologues) on 2-line ferrihydrite by spectroscopic methods (Dardenne et al., 2001)
- Structural incorporation of sorbed actinides/lanthanides during ferrihydrite to hematite/goethite transformation (Dardenne et al., 2002; Lerotic et al., 2004; Schäfer et al., 2003a)
- Mobility of ferric iron colloidal phases in DOC rich ground water (Schäfer et al., 2003a)

As a connection to the following chapter and giving a brief idea about the close relationship of element cycles in natural systems the hot topic of CO_2 sequestration should be mentioned at this point. Recent scientific challenges include the technical feasibility of “greenhouse gas” CO_2 sequestration by enhancing i.e. the natural “sinks” or processes to remove CO_2 from the

atmosphere. One of the various controversial discussed ideas is to add naturally limited nutrients to surface ocean waters in order to manipulate the marine biological cycle and therewith stimulating the biologically (phytoplankton) mediated uptake of atmospheric CO_2 (Buesseler and Boyd, 2003). In general, marine chemists distinguish between “macro-nutrients” as nitrogen, phosphorus and silicon and “micro-nutrients” such as iron, which are pumped up from the deep ocean by physical perturbation. The very interesting point about using iron as a catalyst is the average nutrient uptake of phytoplankton, which is in the following ratio (Adhiya and Chisholm, 2001): *106 C : 16 N : 1 P : 0.005 Fe*.

In other words, adding one iron atom can cause by theory the biological uptake of over 100.000 atoms of carbon. Three ocean regions have been identified as high dissolved nutrient, low photosynthetic biomass or “high-nutrient-low-chlorophyll” (HNLC) zones, namely the Eastern Equitorial Pacific, the NE Subarctic Pacific and the Southern Ocean (Adhiya and Chisholm, 2001). In the Southern ocean iron-enrichment experiments it has already been demonstrated that iron fertilization induces a notable increase in biomass and associated decrease in dissolved inorganic carbon and macro-nutrients (Buesseler et al., 2004; Buesseler and Boyd, 2003; Coale et al., 2004). However, the sinking of particulate organic carbon (POC) was very limited. New seawater models incorporated into a global ocean circulation the iron geochemistry and tuned to match the observed ocean Fe distribution. The model is based on the idea that the concentrations of organic iron-binding ligands in seawater control the subsurface Fe concentration and predicts that a majority (70-80%) of the global carbon export production can be sustained by upwelling of dissolved iron in seawater rather than by atmospheric deposition. Ocean recycling of Fe appears to play a major role in determining the strength of the biological pump in the ocean and the $pCO_{(2)}$ of the atmosphere.

Identification and characterization of sorbed lutetium species on 2-line ferrihydrite by sorption data modeling, TRLFS and EXAFS.

Radiochim. Acta (2001) **89**(7), 469.

Dardenne K., Schäfer T., Denecke M. A., Rothe J., and Kim J. I.

Radiochim. Acta **89**, 469–479 (2001)

Identification and characterization of sorbed lutetium species on 2-line ferrihydrite by sorption data modeling, TRLFS and EXAFS

By K. Dardenne*, T. Schäfer, M. A. Denecke, J. Rothe and J. I. Kim

Forschungszentrum Karlsruhe, INE, P.O. Box 3640, D-76 021 Karlsruhe, Germany

(Received January 9, 2001; accepted January 11, 2001)

Lutetium / Sorption / EXAFS / Hydrous ferric oxide / Ferrihydrite / Sorption modeling

Summary. The Lu(III) sorbed species onto synthetic hydrous ferric oxide (HFO), commonly called ferrihydrite, has been identified. Characterization of the synthetic 2-line HFO shows that its synthesis is reproducible. Potentiometric titration of freshly synthesized HFO, modeled using the constant capacity model ($\kappa_1 = 0.5\ \mathrm{F/m^2}$) in the FITEQL code, yields a specific surface area S_a of $360 \pm 35\ \mathrm{m^2/g}$ (N_2-BET), a site density N_d of 2.86 sites/nm^2 (concentration of hydroxyl groups, $N_s = 1.71 \times 10^{-3}$ mol sites/g HFO), and acidity constants $pK_{a1}^{int} = 6.37$ and $pK_{a2}^{int} = 9.25$.

Evaluation of chemical sorption data reveals the presence of two different Lu surface sorbed species, dependent on pH; a monodendate species forms at low pH and a polydentate species at pH > 5. Satisfactory fits to the sorption data are obtained using a combination of monodentate and bidentate surface species. The combination of species is chosen, based on extended X-ray absorption fine structure (EXAFS) results. The sorption constants obtained from these fits are $pK_s = -1.89(\pm 0.1)$ and $pK_s = -1.69(\pm 0.1)$ for the monodentate species $\equiv \mathrm{FeOLu(H_2O)_5}^{2+}$ for fits to the pH edge and to the isotherm at pH 5.9, respectively. A value of $pK_s = 3.69(\pm 0.01)$ is found for the bidentate species $\equiv \mathrm{Fe(O)_2Lu(H_2O)_5}^{+}$ for both fits. EXAFS analysis of sorption samples prepared at $4.5 <$ pH < 8 shows that Lu is surrounded by a single first shell of 7 ± 1 oxygen atoms, at a distance of (2.30 ± 0.01) Å in all samples. A second coordination shell of Fe neighboring atoms at a distance of (3.38 ± 0.01) Å is observed for sorption samples pH ≥ 5.5. This distance is associated with the formation of a bidendate complex with bonding via edge sharing to iron octahedra. The samples prepared at pH < 5.1 show no Fe shell, as expected for monodentate coordination. No evidence for surface precipitation and no noticeable difference between wet paste and dried powder samples is found.

1. Introduction

Knowledge of the interaction of actinide cations with mineral surfaces is prerequisite to long-term performance assessment of nuclear repositories. Sorption models and corresponding equilibrium constants describing the actinide-mineral interaction are obtained from modeling of sorption data, i.e., the measured amount of actinide cations sorbed onto a mineral surface as a function of pH, ionic strength, and actinide concentration. These models and the determined constants describing determinant aqueous/mineral-interface processes and mechanisms are used in predictive transport models for the long-term behavior of radionuclides. A mechanistic understanding of the processes involved, e.g., identification of the actinide species formed on the mineral surface, is important in modeling sorption data because the numerical equilibrium constant values extracted from the data are dependent upon the surface complexation reactions postulated. The reactants and reaction products assumed to participate in the sorption processes, i.e., the mineral sorption sites, actinide cation speciation, the sorbed surface species and their stoichiometries, influence the overall constants obtained in the modeling.

We have studied the surface sorption reaction of Lu(III) with low crystalline, metastabile 2-line ferrihydrite, synonymously described in the literature [1] as hydrous ferric oxide (HFO). Lu is chosen as a homologue for the trivalent actinides. The equilibrium constants for the surface complexation reaction obtained from modeling sorption data are based on spectroscopic identification of the Lu sorbed species formed on the surface and experimental characterization of the HFO sorbent. Time resolved laser fluorescence spectroscopy (TRLFS) is not applicable for Lu(III) due to its full $4f$ shell. Therefore a TRLFS study is done using Eu and comparative studies of Eu and Lu sorption (pH edge and isotherms) are performed in parallel. Both lanthanides exhibit a similar HFO sorption behavior allowing transfer of Eu results to Lu. Lu is used for EXAFS studies instead of Eu because of the spectral interference of Eu L edges with the Fe K edge.

2. Materials and methods

2.1 2-line ferrihydrite (2*L*-HFO)

2.1.1 Preparation

Dispersion of HFO was freshly prepared according to Schwertmann and Cornell [2]. All chemicals were of analytical grade. The product was washed five times with Milli-Q water and separated after each washing by centrifugation. The concentrated suspension was dialyzed by a 3.0–3.5 nm dialysis membrane in a Milli-Q water bath for three days in

*Author for correspondence (E-mail: dardenne@ine.fzk.de).

the dark. The bath water was periodically changed. The resulting HFO stock solution had an electrical conductivity not greater than ten-times that of Milli-Q water and a concentration of approximately 14 g/mol. As HFO is a metastable phase, experiments were performed within three weeks to avoid the presence of HFO transformation products (hematite, goethite). Reproducibility of 15 separate syntheses was established by comparing physicochemical characterization of a freeze-dried aliquot from each charge.

2.1.2 Characterization

The synthetic HFO products were characterized by powder X-ray diffraction (XRD), Fourier transform infrared spectroscopy (FTIR), and surface area determination. The XRD patterns of powder samples were recorded using a Seifert 3000TT diffractometer with Cu K_α radiation. The patterns of all 15 charges were comparable, showing only two broad diffraction peaks at d spacings of 0.26 nm (110) and 0.15 nm (300), as expected for 2-line HFO [3]. No traces of 6-line HFO, transformation products (hematite or goethite), or impurities were detected.

FTIR analysis on KBr pellets (1.5 wt. % HFO) using a Bruker IFS55 spectrometer confirmed the purity of the synthetic 2-line HFO. Only characteristic hydroxyl bands at 450 and 650 cm^{-1} (bulk OH deformations), $\sim$ 3440 cm^{-1} (bulk OH stretch), and an adsorption band at 1620 cm^{-1} (molecular water) were observed.

Specific surface area, S_A, measurements were performed by the BET [4] method using N_2 adsorption (Quantachrome, Autosorb1) and the modified ethylene-glycol-monoethyl-ether (EGME) method of Carter *et al*. [5]. The latter method is a widely accepted procedure [6] to measure the total (external and internal) surface area, where the molecular area occupied by an EGME molecule is defined as 0.52 nm^2. Pre-treatment of BET samples included a drying and gas removal procedure at 105 °C. The S_A determined by EGME adsorption was 675 ± 56 m^2g^{-1} (number of determinations, $N = 31$) and from BET N_2-adsorption, 360 ± 35 m^2g^{-1} ($N = 7$). These results are comparable to published values: 590 m^2/g by EGME adsorption [7] and BET-N_2(g) values of 340 m^2/g [8] and 313 m^2/g [9]. The S_A values from both methods are smaller than the theoretically calculated value of 840 m^2/g [10], assuming 2 nm diameter ferrihydrite spheres with a 3.57 g/cm^3 density.

2.2 Potentiometric and sorption experiments

2.2.1 Experimental procedure

Potentiometric titration experiments were performed to determine acidity constants and total concentration of the surface hydroxyl groups. An aqueous suspension of 1 g/L 2-line HFO was titrated with CO_2-free $HClO_4$ or NaOH, over a pH range 4–10, at three different ionic strengths (0.1, 0.01, 0.001 mol/L $NaClO_4$), under inert gas atmosphere (Ar). The pH was measured using a Ross type standard combination electrode. During each titration, a maximum of ten to fifteen minutes between each incremental addition of base or acid were allowed for pH to equilibrate. This was to ensure that only ionization of surface hydroxyl groups contributed to the determination of the surface acidity constants [11].

Lu(III) sorption batch experiments were performed on a 4.8 g/L aqueous suspension of HFO in 20 mL total volume, containing 10^{-3} mol/L Lu(III), at constant ionic strength (0.1 mol/L $NaClO_4$), and under inert gas atmosphere. Polypropylene or polyethylene vessels and storage containers were used for all sorption experiments. Lutetium was added from an acidic stock solution and 0.1 mol/L NaOH or $HClO_4$ used for pH adjustment. The pH was held constant at the desired value using a 10^{-3} mol/L 2-(N-morpholino)ethanesulfonic acid (MES) buffer in the pH range 5–6 and β-(4-pyridil)ethanesulfonic acid (PES) near pH 4. A maximum surface coverage of 12% to 24% was expected under these experimental conditions (2.1×10^{-4} mol Lu per g HFO), assuming a mono- or bidentate complexation. The samples were agitated regularly over three days. Lu and Fe concentrations of the supernatant solution following 35 min ultra-centrifugation at 450 000 g (XL90 Ultracentrifuge, Beckman) were determined by ICP-AES and ICP-MS (Perkin-Elmer PLASMA 400 & ELAN 6000). Fe concentrations were determined to avoid erroneously high Lu supernatant concentrations due to an possibly presence of HFO colloids. An portion of the separated solid phase, rinsed with Milli-Q water, was freeze-dried or dried 12 hours at 45 °C under aerobic conditions for spectroscopic investigations.

2.2.2 Fitting procedure

Surface acidity constants and Lu complexation constants were obtained by fitting the experimental pH titration and sorption data to surface complexation models (SCM) using the FITEQL 3.2 code [12]. The constant capacitance model (CCM) and diffuse double layer model (DDLM) were used for the titration data. The main indicator of the goodness of fit is the overall variance, V_y, which is the weighted sum of squares of residuals divided by the degree of freedom (SOS/DF). The weighting factor is the experimental error estimate calculated from the given experimental error so that the numerical value of V_y depends on experimental error estimates. A reasonably good fit is generally indicated by V_y values between 0.1 and 20 [12].

The error estimates used to fit the titration data are 7% for the relative error for pH, corresponding to an absolute error of 0.03 pH unit, and a relative error of 1% for the total proton concentration, corresponding to an absolute error of 10^{-6} mol/L. Fits to the pH-edge sorption data were performed using 4.6% (0.02 pH unit) as a relative error for pH and 10^{-5} mol/L as the absolute error for the sorbed species concentration. The isotherm sorption data was fitted using 9.2% (0.04 pH unit) as a relative error for pH. Relative errors of 1.5% and 3% were used for the total Lu concentration and the concentration of Lu remaining in solution.

2.3 Spectroscopic investigations

Time-resolved laser fluorescence spectroscopic (TRLFS) lifetime measurement of Eu(III) ($^5D_0 \rightarrow {}^7F_x$) was used to determine the number of water molecules coordinated to Eu sorbed onto HFO. Eu was used as Lu does not fluoresce.

A dye laser (Exalite 398), pumped by a pulsed Nd:YAG laser (Continuum, Powerlite 9030, ND 6000) with a pulse energy of 3 mJ, was used. TRLFS study was performed on KBr pellets containing Eu(III) sorbed onto HFO at pH 5.7 (1.1 wt. % HFO, 4.9×10^{-4} mol Eu/g HFO, maximal surface site coverage 28%). The Eu sorption onto HFO was achieved by the same procedure as described for Lu above. An excitation wavelength of 396.5 nm was used to promote the Eu^{3+} ions from the ground state ^7F_x into the $^5L_7$ state, which decayed to the emitting $^5D_0$ level through non-radiative relaxation. Fluorescence emitted in the 540 nm to 740 nm range from the $^5D_0 \rightarrow {}^7F_x$ transition was detected by an optical multi-channel analyzer (polychromator Chromex 250) with a 300 lines/mm grating. The WINSPEC data acquisition software was used to register spectra. The time dependent emission was scanned by recording 51 spectra with increasing the delay time between laser pulse and camera gating from 1 μs to 1.5 ms by 30 μs interval.

EXAFS spectra were measured at the Hamburger Synchrotronstrahlungslabor (HASYLAB) positron storage ring DORIS, operating at 4.44 GeV with a maximal current of 150 mA, at beamline A1, as well as at the European Synchrotron Radiation Facility (ESRF), operating at 6 GeV with a maximal current of 200 mA, at the ROBL beamline. At HASYLAB, a double-bounce monochromator with a Si(111) channel-cut crystal was used. The monochromator was equipped with a piezo-driven feedback to stabilize the intensity of the incident X-ray beam [13]. The crystals were detuned to 50% of the incident intensity in order to obviate higher harmonic contamination of the beam. At the ROBL station, Si(111) crystals were used for the double-crystal monochromator, which was also stabilized with a feedback system. Higher harmonics were rejected by two Pt coated mirrors. All data were collected at ambient temperature in transmission mode, using ionization chambers filled with nitrogen gas.

A list of the samples investigated, their Lu loadings, experimentally measured Lu L_3 edge jumps, and the facility where their spectra were recorded are given in Table 1. EXAFS spectra were recorded at the Lu L_3 edge (9244 eV) for five Lu(III):HFO sorption samples prepared at varying pH and two reference samples, a 0.02 M aqueous Lu(III) solution and Lu_2O_3. Powdered samples were measured dispersed in polyethylene (PE) powder and pressed into 13 mm ∅ pellets. The wet paste sample was measured loaded into a stoppered PE tube of 400 μL volume and a diameter of 5 mm. No drying occurred during data collection.

Sample spectra were energy calibrated using the first inflexion point in the K-edge spectrum of a zinc metal foil, defined as 9659 eV [14], which was recorded simultaneously. The EXAFS was extracted from the absorption spectrum by fitting μ_0 with a cubic spline function. The autobak program was also used to extract $\chi(k)$ from the absorption spectrum for comparison [15]. Data analysis was performed based on conventional methods [16] using the WinXAS97 software [17]. Theoretical backscattering amplitude and phase functions for fitting the experimental data were calculated with the multiple scattering code FEFF8 [18] either using single scattering Lu−O atom pairs or a 6 atom cluster with atomic positions calculated from the structural data reported for Lu_2O_3 [19].

3. Results and discussion

3.1 Titration modeling

The pH titration curves for three different ionic strengths are shown in Fig. 1. The curves are shifted along the ordinate to align the "pristine" point of zero charge at zero addition of base and acid [20]. The crossing point of these curves, called PZSE (point of zero salt effect), is found at a pH value of 7.8 and taken as the point of zero net proton charge, PZNPC. This value is comparable to 7.8–7.9 found by Charlet and Manceau [21] and Davies and Leckie [11] and to 7.9 to 8.2, with an average of 8.0, reported by Dzombak and Morel [1] using different methods including acid/base-titration, electrophoresis, and salt titration. This PZNPC is on the lower end of the range of published values. However, it cannot be interpreted as transformation of 2-line HFO to goethite, because such a conversion was not confirmed by IR spectroscopic and powder XRD results.

The point of zero net proton charge, PZNPC, is related to the intrinsic acidity constants, K_a^{int}, by the following expression:

$$\mathrm{PZNPC} = 0.5\left(\mathrm{p}K_{a1}^{int} + \mathrm{p}K_{a2}^{int}\right) .$$

The apparent acidity constant, K_a^{app}, can be calculated from K_a^{int} via the expression:

$$\mathrm{p}K_a^{app} = K_a^{int} \exp(-\Delta Z F \Psi / \mathrm{RT}) ,$$

Table 1. EXAFS samples, Lu(III) loadings, Lu L_3 edge jumps, and the facility where they were measured.

Samples	pH	Loading (mg Lu/g)	Lu in pellet (mg)	Measured edge jump	Facility
Lu(III):HFO	7.7	51	2.5 ± 0.1	0.11	HASYLAB
	6.1	93	[a]	0.094	ESRF
	6.1	93	5.20 ± 0.01	0.43	ESRF
	5.5	61.4–64.5	3.3 ± 0.1	0.28	ESRF
	5.1	22–29	1.4 ± 0.2	0.092	HASYLAB
	4.6	0.1–9	0.3 ± 0.3	0.054	ESRF
Lu_2O_3	–	879	9.0	0.84	HASYLAB
Lu aquo species in 0.5 M $HClO_4$	–	–	–	0.22	HASYLAB

a: wet paste sample.

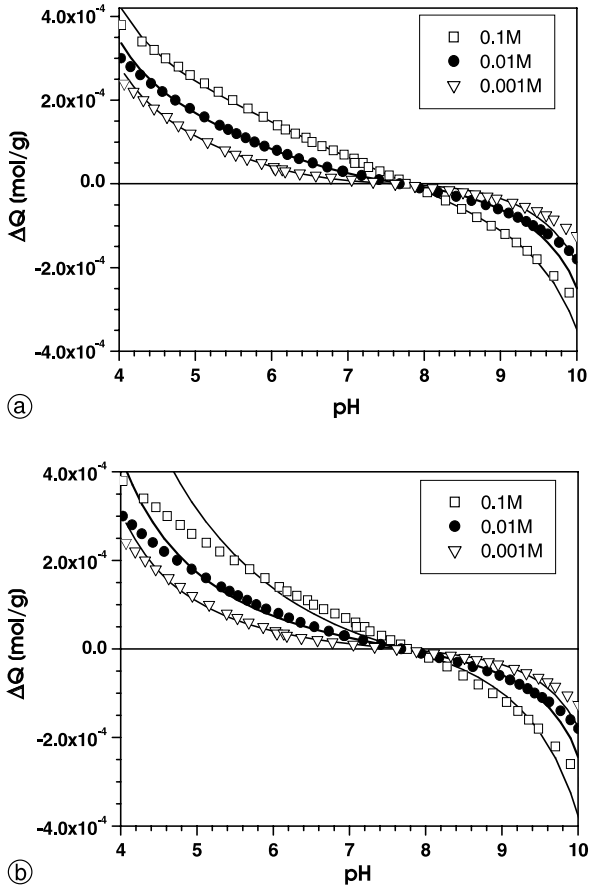

Fig. 1. Titration data (symbols) and resulting curves from FITEQL modeling (solid lines) using CCM top (**a**) and DDLM bottom (**b**).

where ΔZ corresponds to the net charge change of the surface species and Ψ is the HFO surface potential in volt.

The isoelectrical point (IEP) was determined from electrophoretic mobility measurements for two ionic strengths 0.1 mol/L and 0.001 mol/L $NaClO_4$ and was found at a pH value of 8.7. This is in good agreement with the 8.5–8.8 values reported by Parks [22].

Surface acidity constants to describe the amphoteric character of the HFO surface hydroxyl groups

$$\equiv FeOH_2^+ \Leftrightarrow \equiv FeOH + H^+ \quad K_{a1}{}^{app}$$
$$\equiv FeOH \Leftrightarrow \equiv FeO^- + H^+ \quad K_{a2}{}^{app}$$

are calculated from the titration data using FITEQL 3.2. The constant capacitance, κ_1, $K_{a1}{}^{int}$, $K_{a2}{}^{int}$, and the total concentration of surface hydroxyl groups, N_s, are the variable parameters for the three different ionic strengths investigated. Titration data was fitted in the manner described by Hayes *et al.* [23]), in which κ_1 and N_d (site density in sites/nm^2) are held constant, while the values for $K_{a1}{}^{int}$ and $K_{a2}{}^{int}$ are varied, and the fit is repeated for various incremental values of κ_1 and N_d. The value for N_d is varied between 1 and 100 sites/nm^2 using literature values and κ_1 is varied between 0.2 and 1.2 F/m^2 in 0.1 increments. Due to the large difference in S_A determined by different methods, fits are performed for three S_A values: the BET-N_2 adsorption result (360 m^2/g), the EGME adsorption result (675 m^2/g), and the value recommended by Davis (600 m^{2}g^{-1}) [1, 10, 11].

The best fit for all three ionic strengths is obtained using the CCM (see Fig. 1a, Table 2). With the DDLM (Fig. 1b,

Table 2. Results of fits to the titration data using CCM. DDLM results for a selected density of site (1.71×10^{-3} mol/g) are given for comparison.

I [mol/L]	pK_{a1}	pK_{a2}	PZC	WSOS/ DF	κ_1 [F/m^2]	N_d [sites/nm^2]	N_S [mol/g]	S_A [m^2/g]
0.1	6.56	9.06	7.81	2.10				
0.01	5.63	9.92	7.78	4.59	0.5	1.97[c]	1.178×10^{-3}[c]	360
0.001	4.92	10.46	7.69	6.83				
0.1	6.37	9.25	7.81	2.08				
0.01	5.46	10.09	7.77	4.76	0.5	2.86	1.710×10^{-3}*	360
0.001	4.75	10.62	7.69	6.94				
0.1	6.30	9.32	7.81	2.08				
0.01	5.39	10.15	7.77	4.82	0.5	3.28[c]	1.960×10^{-3}	360
0.001	4.69	10.69	7.69	6.98				
0.1	6.56	9.06	7.81	2.10				
0.01	5.63	9.92	7.78	4.59	0.3	1.18[d]	1.178×10^{-3}	600
0.001	4.92	10.46	7.69	6.83				
0.1	6.37	9.25	7.81	2.08				
0.01	5.46	10.09	7.77	4.76	0.3	1.72	1.710×10^{-3}*	600
0.001	4.75	10.62	7.69	6.94				
0.1	6.30	9.32	7.81	2.08				
0.01	5.39	10.15	7.77	4.82	0.3	1.97[a]	1.960×10^{-3}	600
0.001	4.69	10.69	7.69	6.97				
DDLM								
0.1	5.69	−9.79	7.742	53.88				
0.01	5.79	−9.71	7.751	12.36	–	2.86[e]	1.710×10^{-3}[e]	360
0.001	6.14	−9.32	7.730	5.26				

a: values determined by Charlet & Manceau [21];
b: calculated from N_d and S_A and held constant during the fit procedure, excluding the two values marked*;
c: held constant during the fit and used to compared to the $S_A = 600$ m^2/g results;
d: held constant during the fit and used to compared to the $S_A = 360$ m^2/g results;
e: held constant during the fit and used to compared to the CCM results.

Table 3. Experimentally determined PNZPC for hydrous ferric oxides(*) and low crystalline 2-line HFO and acidity constants at a ionic strength 0.1 M.

PZNPC	pK_{a1}	pK_{a2}	N_s (10^{-3} mol sites/g HFO)	Reference
7.85*	6.6	9.1	1.12	Farley *et al.* (1985) [28]
8.00	7.18	8.82	2.04	Dzombak & Morel (1990) [1]
7.83	6.93	8.72	2.04	Hansen *et al.* (1994) [20]
7.9*	5.1	10.7	9.86	Davis & Leckie (1978) [11]
7.8	6.37	9.25	1.71	This work

Table 2), only the lowest ionic strength in the pH-range 4.8 to 9.4 can be satisfactorily modeled. This fit, however, is not significantly better than that obtained using the CCM approach. The value used for κ_1 is found to be the most critical parameter. Best κ_1 values are 0.5 F/m^2 for $S_A = 360$ m^2/g, 0.3 F/m^2 for $S_A = 600$ m^2/g, and 0.25 F/m^2 for $S_A = 675$ m^2/g. Using these values, fits of the titration data yield identical acidity constants for a given N_s, with comparable SOS/DF values for each S_A. We retain the surface area obtained by BET because it does not include micro pores, which might not be available for "fast" sorption processes. It is evident from the results in Table 2 that it is impossible to select the "true" acidity constants based on the SOS/DF variation obtained for the three best fits. Therefore the set of values obtained by optimizing N_s is selected. The following acidity constants are found: $pK_{a1}^{int} = 6.37$ and $pK_{a2}^{int} = 9.25$, $N_s = 1.71 \times 10^{-3}$ mol/g with $N_d = 2.86$ sites/nm^2 for $S_A = 360$ m^2/g in 0.1 mol/L $NaClO_4$. These values are used for modeling the Lu sorption described below.

A range of acidity constants, derived from experimental data for HFO, has been reported in the literature and is given Table 3. In the present investigation, the reproducibility of each solution of 2-line HFO is painstakingly validated. Only freshly precipitated products are used for potentiometric and Lu sorption investigations.

Surface speciation calculated with these constants shows that more than 80% of the proton exchangeable groups are in the form ≡ FeOH; the relative ≡ FeOH concentration variation is less than 6% in the pH range 4–10.

3.2 pH-edge and isotherm sorption modeling

The Lu pH-edge sorption curve is shown in Fig. 2. The sorption edge is graphically found to be at pH = 5.2. The maximal sorption is attained at pH 6 under the conditions investigated. The sorption equilibrium reaction can be written as follows:

$$\mathrm{Lu(H_2O)_{8-9}}^{3+} + n{\equiv}\,\mathrm{FeOH} \Leftrightarrow {\equiv}\,\mathrm{Fe(O)}_n\mathrm{Lu(OH)}_p\mathrm{(H_2O)_{(5\ or\ 6-p)}}^{(3-n-p)+} + (n+p)\mathrm{H}^+ , \quad (1)$$

where ≡ FeOH describes one surface HFO hydroxyl group and ≡ $Fe(O)_n$ defines the number of hydroxyl groups reacting with a Lu^{3+} cation. Lutetium bound to hydroxyl groups connected to the same iron atom on the HFO surface (edge sharing polyhedron) or to hydroxyl groups connected to different, adjacent iron atoms (corner sharing iron polyhedron) are not distinguished in this description.

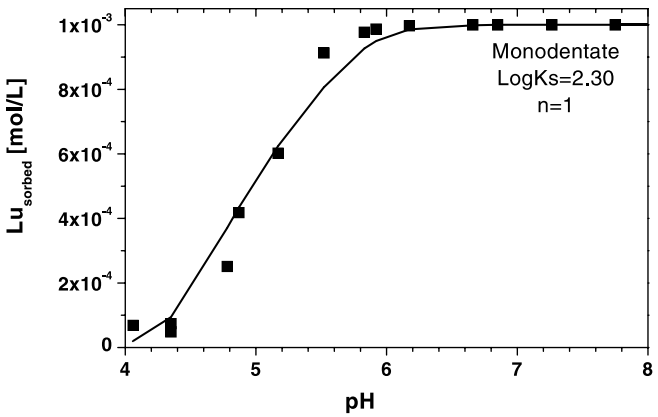

Fig. 2. Experimental pH edge (symbols) and theoretical fit using a monodendate species (WSOS/DF: 11.9) and CCM.

The rearrangement of the expression for the sorption constant, K_s, defined by Eq. (1) yields:

$$\log \frac{[\mathrm{Lu_{sorbed}}]}{[\mathrm{Lu^{3+}}]_{aq}} = (n+p)\mathrm{pH} + \log K_s + n \log [{\equiv}\,\mathrm{FeOH}]_{free} ,$$

where $[Lu_{sorbed}]$ represents the concentration of surface sorbed species, $Fe(O)_nLu(OH)_p(H_2O)_{(5-p)}^{(3-n-p)+}$, and $[Lu^{3+}]_{aq}$ the concentration of aquo species in solution, $Lu(H_2O)_8^{3+}$. The relative concentration variation of free surface hydroxyl groups is near 2, 5, and 10%, for a monodentate (**M**; $n = 1$), bidentate (**B**; $n = 2$), or tridentate (**T**; $n = 3$) sorbed species, respectively. As a first approximation, this concentration variation is small and can be neglected. Then a linear relationship exists between pH and

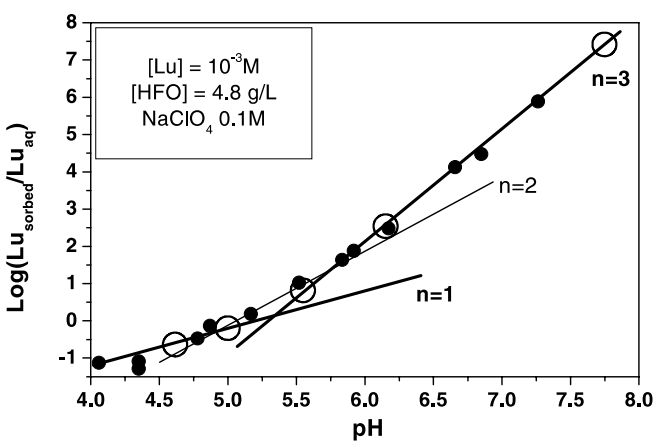

Fig. 3. Log–log plot of the pH edge. Experimental points are small filled circles; EXAFS samples are indicated as large open circles. Differentiation into three regions of different slopes is based on CCM modeling and results from EXAFS experiment described in Sect. 3.4.

$\log \frac{[Lu_{sorbed}]}{[Lu^{3+}]_{aq}}$. The corresponding so-called "log-log" plot is shown in Fig. 3. Each slope gives the total number of protons exchanged in the sorption process, $(n+p)$. At least two different regions can be distinguished in Fig. 3: one region at pH < 5.3 with a slope 1 and one at pH > 5.3 with a slope in the range 2.65–2.75, or near 3. The graphical approximation indicates that at least two types of sorbed surface species are formed. The sorbed species at pH < 5.3 should satisfy the relation $(n+p)=1$ and at pH > 5.3$(n+p) \sim 3$. The value of n gives the dentate character of the sorbed species and can vary from 1 to 3. The value p defines the degree of hydrolysis and varies from 0 to 2. Refinement to the graphical approach by including the variation of the surface hydroxyl group concentration does not noticeably change the slope of the "corrected" log–log plot. Differentiation of the log–log plot into three regions of slopes 1, 2, and 3 indicated in Fig. 3 is based on subsequent modeling and the results from EXAFS experiment described in Sect. 3.4. If the slope in the log-log plot is determined within the pH range limited to 4.7–6.2, i.e., above the pH where a single monodentate species forms and below the pH where hydrolysis occurs, then a value of about 2 is obtained, the value expected for the formation of a bidendate species without hydrolysis.

The Lu(III):HFO sorption data are also modeled using the FITEQL 3.2 code and various $Fe(O)_n Lu(OH)_p \cdot (H_2O)_{(5-p)}{}^{(3-n-p)+}$ surface species. The quality of the fit obtained using a single sorbed species is poor. An example for a single, monodentate surface species is shown in Fig. 2. The best fit results are achieved when including two species in the model, one with $(n+p)=1$ and the other with $(n+p)=3$. The combination $(n+p)=1$ and $(n+p)=2$ species also leads to good quality fit results. Depending on which combination is used, monodentate $(n+p)=1$ and a $(n+p)=2$ species or monodentate $(n+p)=1$ and a $(n+p)=3$ species, two general speciation curves are obtained as shown in Fig. 4. The pK_s values obtained for the combined species fits are listed in Table 4.

Fig. 5 compares the best fit results for a single species fit with that obtained using a fit model of a combination of species. Modeling the isotherm sorption measured at pH 5.9 yields the same results for pK_s (Table 5) as found for modeling the pH edge. Similar to the pH-edge results, a satisfactory fit is only possible for a combination of two surface species. The relative concentrations of the two Lu sorbed species found for the isotherm at pH 5.9 are in good agree-

Table 4. Sorption constants (pK_s) obtained with CCM modeling of Lu(III):HFO pH edge data for the surface species $Fe(O)_n Lu(OH)_p (H_2O)_{(5-p)}{}^{(3-n-p)+}$ using $S_A = 360\,m^2/g$, $N_d = 2.86$. 1:2 indicates using a model of combined monodentate (**M**; $n=1$) and bidentate (**B**; $n=2$) species; 1:3 a combination of **M** and tridendate (**T**; $n=3$).

$n+p$	M	MOH	$M(OH)_2$	B	BOH	T	WSOS/DF
1	−2.30						11.9
2		5.52					7.8
				3.31			7.1
			12.80				12.9
3					10.55		11.1
						8.23	8.2
1:2	−1.89			3.69			4.3
	−1.91	5.91					4.1
	−2.03		13.95				3.7
1:3	−2.03				11.75		3.7
	−2.02					9.52	3.8

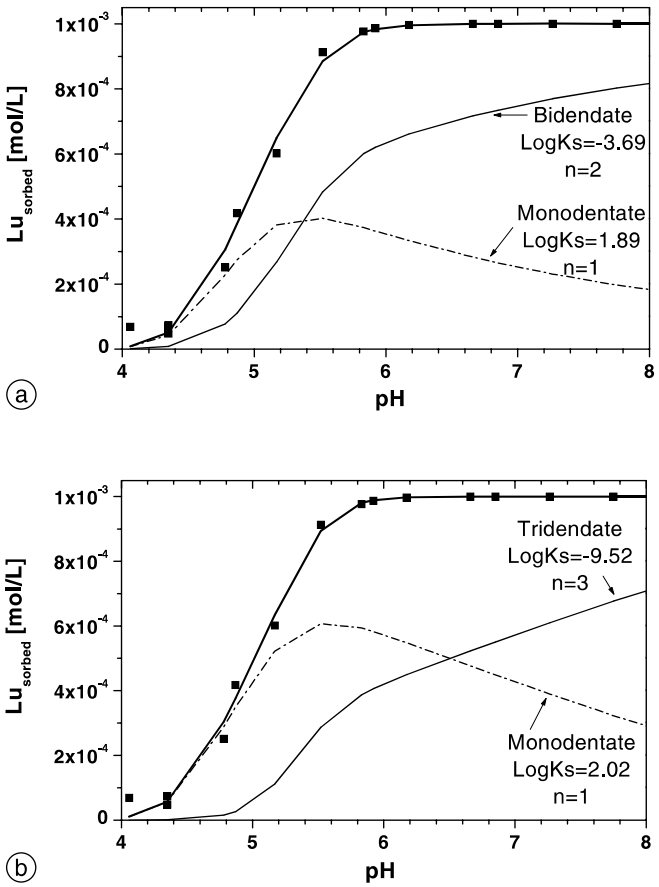

Fig. 4. (**a**): Speciation curves calculated from modeling results (WSOS/DF = 4.1–4.3) for combination of monodentate $n=1$ and $n=2$ species. (**b**): corresponding curves from modeling results (WSOS/DF = 3.7–3.8) obtained for a combination of monodentate $n=1$ and $n=3$ species.

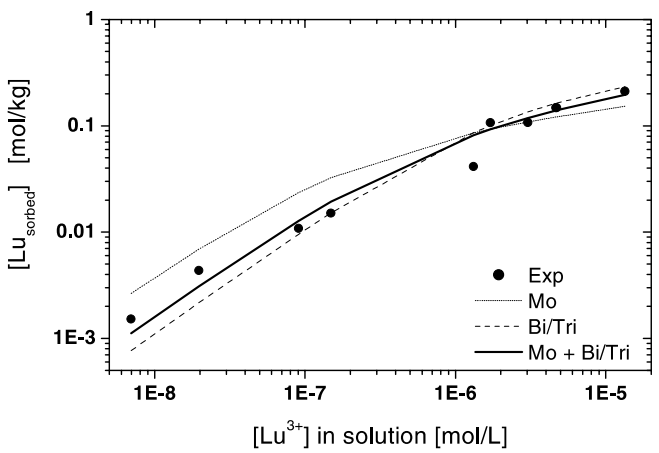

Fig. 5. CCM fits to the sorption isotherm at pH 5.9 from results listed in Table 5. Mo is using $(n+p)=1$ species. Bi/Tri are actually two results for $n=2$ and another for $n=3$.Mo+Bi/Tri is also two results for 1:2 and 1:3 species combination in Table 5. In both cases, the two results yield curves which are identical to within the line width shown.

Table 5. Sorption constants (pK_s) obtained with CCM modeling of the Lu(III):HFO pH isotherm at pH 5.9 for the surface species $Fe(O)_n Lu(OH)_p(H_2O)_{(5-p)}^{(3-n-p)+}$ using $S_a = 360\,m^2/g$, $N_d = 2.86$. 1:2 indicates using a model of combined monodentate (**M**; $n = 1$) and bidentate (**B**; $n = 2$) species; 1:3 a combination of **M** and tridendate (**T**; $n = 3$).

$n+p$	M	B	BOH	T	WSOS/DF
1	−2.30				19.3
2		3.44			4.98
3			10.86		9.52
				8.63	4.34
1:2	−1.69	3.69			3.1
1:3	−1.90		11.8		2.7
	−1.89			9.57	2.7

ment to those obtained from analysis of the pH-edge. The relative concentrations calculated are either ∼ 33% **M** and 64% **B** or ∼ 57% **M** and 42% **T**, depending on the polydentate species which is assumed.

No final conclusion can be drawn concerning the nature of the sorbed species based only on modeling of the sorption data. One may conclude that two different Lu sorbed species appear to form on the HFO surface in the pH and concentration range studied. One of these species is a monodentate species; further information is needed in order to identify the second, polydentate species.

3.3 TRLFS results

The variation of the lifetime with the number of coordinated water molecules is explained by the de-excitation through vibronic coupling process. In the case of lanthanides, it has been shown that the rate of deexcitation via a vibronic coupling between OH oscillators and Ln(III) ions can be assumed to be "directly proportional to the number of OH oscillators in the first coordination sphere" [24].

As mentioned in Sect. 1, laser fluorescence measurements can not be performed on Lu due to its $4f$ full shell. Therefore, Eu, which shows a similar sorption behavior is chosen for TRLFS experiments. The Eu sorption sample is obtained by the same experimental procedure used for Lu. The TRLFS studies are performed on KBr pellets containing Eu(III) sorbed onto HFO at pH 5.7 (1.1 wt. % HFO, 4.9×10^{-4} mol Eu/g HFO, maximal surface site coverage of 28%). The Eu sorption species is characterized by a lifetime of 205 µs. An increase of the lifetime over the lifetime of the aquo species (110 µs) indicates that the number of water molecules in the first Eu(III) coordination sphere is reduced from nine (or ten) in the aquo species [24] to five water molecules (including OH) in this sorption sample.

3.4 EXAFS results

In order to identify the two Lu surface sorbed species, EXAFS experiments are performed on Lu(III):HFO sorption samples. Samples are specifically selected distributed across regions in the log-log representation of the pH edge (Fig. 3): pH 4.6, 5.1, 5.5, 6.1, and 7.7. Lutetium L_3 edge

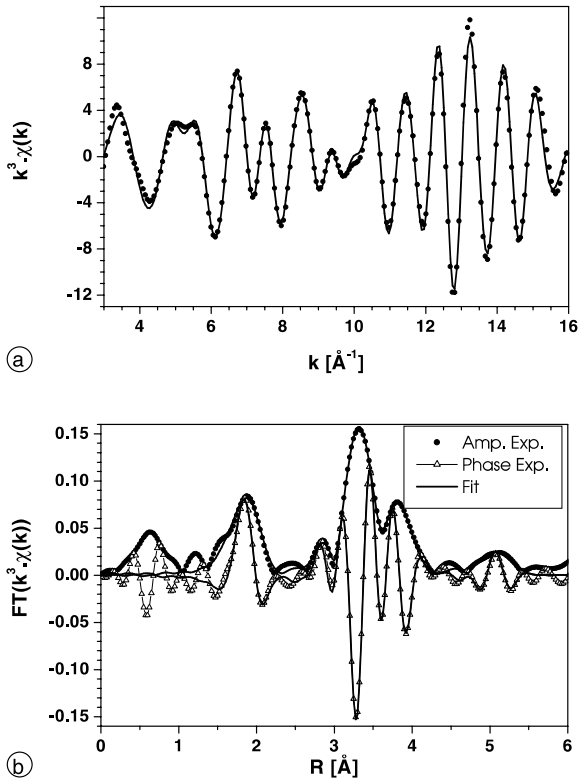

Fig. 6. (**a**) k^3-weigthed Lu L_3 edge EXAFS for Lu_2O_3 (line) and best fit results (dots) using phase and backscattering functions obtained from single scattering phase and amplitude functions. (**b**) Corresponding Fourier transform (Bessel window, k range = 3.0–16.0 Å^{-1}). The fit in this curve is depicted as a line.

EXAFS spectra of the reference samples are analyzed in order to test the theoretical backscattering amplitude and phase functions used in the data analysis. Fig. 6 shows the k^3-weighted EXAFS spectrum for Lu_2O_3, its corresponding Fourier transform (FT) and the theoretical functions obtained from fits of the experimental data to the EXAFS equation using the functions obtained from the atom cluster FEFF8 calculation. Fits are performed to both

Table 6. Structural parameters obtained from fits to Lu_2O_3 EXAFS in both R-space and k-space (*italics*) and shown in Fig. 5. The amplitude reduction factor, S_o^2, was held constant at 1. The shift in ionization energy, ΔE_o, was held constant at 7.46 eV for fits in R-space and at 7.50 eV for those in k-space. Average bond lengths and coordination numbers calculated from XRD structure determination (JCPDS-ICDD 43-1021, Saiki, 1985) are given in parentheses.

Bond	R [Å]	N	σ_2 10^{-3} [Å^2]
Lu–O	2.22	6.5	6.8
	2.22	*6.0*	*6.0*
	(2.246)	(6)	
Lu–Lu	3.45	7.1	4.9
	3.45	*6.4*	*4.5*
	(3.453)	(6)	
Lu–Lu	3.93	5.1	4.6
	3.93	*5.2*	*4.8*
	(3.933)	(6)	
Lu–Lu	5.19	8.1	8.2
	5.19	*7.9*	*8.3*
	(5.223)	(6)	

the EXAFS oscillations and to the FT spectra (i.e., fits in *k*-space and *R*-space). The coordination number, *N*, interatomic distance, *R*, and EXAFS Debye–Waller factor, σ^2, obtained from the fits are listed in Table 6. The results are in good agreement with the XRD structure determination [19, JCPDS-ICDD 43-1021].

The fit to the Lu(III) aquo species spectrum, used as a reference sample, using FEFF8 scattering functions from the cluster calculation gives 8 oxygen neighbors at a distance of 2.31 Å with $\sigma^2 = 0.0058$ Å^2. The smaller σ^2 value for the Lu−O sphere in the aquo species compared to Lu_2O_3 reflects the smaller distribution of bond lengths in the solution species. In the Lu_2O_3 structure, there are two crystallographic Lu sites with a distribution of bond lengths from 2.18 to 2.28 Å. This leads to a larger σ^2 value of 0.0068 Å^2 for the Lu−O shell. Fits to the aquo species EXAFS using single scattering FEFF8 files give 9 oxygen neighbors at a 2.31 Å distance with $\sigma^2 = 0.0078$ Å^2. The fits using FEFF8 functions obtained from single scattering and cluster calculations yield the same results to within the range of error generally associated with an EXAFS analysis, i.e. ±10% for the coordination number and ±0.02 Å for the interatomic distance. Thus the backscattering amplitudes and phase functions obtained from the single scattering calculations are used to analyze the Lu−O shell in the sorption sample spectra. Single scattering amplitude and phase functions for the Lu−Fe scattering pair are also used in fits to those sorption samples exhibiting a further distant Fe coordination shell.

The k^3-weighted Lu L_3 edge EXAFS spectra for air-dried Lu(III): HFO sorption samples and their corresponding FT's are shown Fig. 7. From visual comparison of the spectra, it is evident that the sample prepared at pH 4.6 shows a larger oscillatory amplitude than the other samples. Furthermore, this sample shows no evidence for further distant coordination shells, whereas the other four samples all exhibit a FT peak at ∼ 3.1 Å. Although the intensity of this peak is small, its presence corresponds to the perturbation of the main oscillation frequency in the EXAFS spectra at around 7 Å^{-1}.

The EXAFS equation is fit to the spectra in both *R*- and *k*-space. Fits are repeated after applying different EXAFS extraction procedures. Fits of the FT data for a single Lu−O shell are initially performed within a 1.35–2.50 Å *R*-space window. Results for the Lu−O shell are introduced as starting parameters for fits in the 1.35–3.60 Å range using two

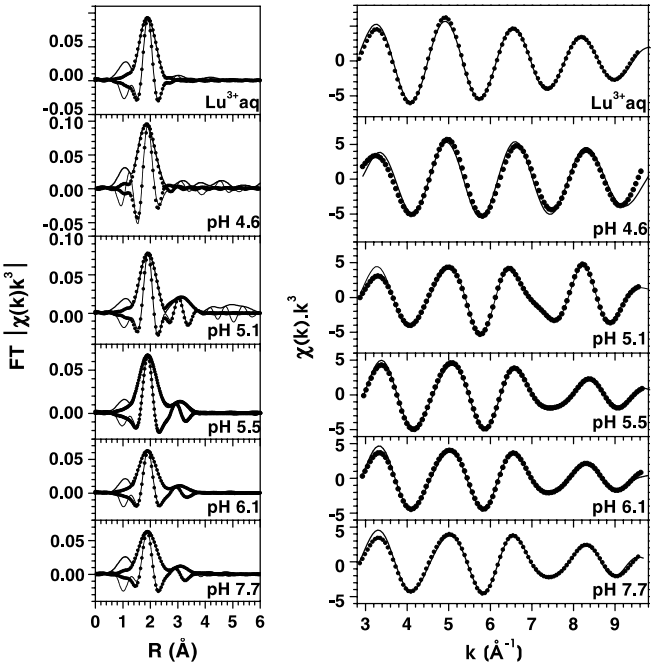

Fig. 7. Right: k^3-weighted Lu L_3 edge filtered EXAFS (two first shells) and best fit results. Left: Fourier transform of the experimental EXAFS (Bessel window, *k* range = 2.6–9.9 Å^{-1}). Theoretical curves are depicted as dots and experimental as continuous lines.

shells, both Lu−O and Lu−Fe shells. Fits in *k*-space are done on Fourier filtered FT spectra using a single oxygen coordination shell for the pH 4.6 sample and a model of one Lu−O and one Lu−Fe coordination shell for the other sorption sample spectra. These fits result in slightly greater σ^2 values and ∼ 0.5 larger *N* than the fits in *R*-space. ΔE_o is allowed to vary in the fits because not all spectra are recorded during the same experimental run or at the same facility. Setting $\Delta E_o = 6.5$ eV constant for the three samples measured at ROBL during the same run yields the same results within the experimental error range.

Average values of all results obtained from fits in *R*- and *k*-space and for different EXAFS extraction procedures are summarized in Table 7. The standard deviations given in Table 7 are the statistic standard deviations of the numerous fit results. A comparison of structural parameters for the sorption samples reveals that the Lu−O distance is 2.30 Å for all samples; no splitting of the Lu−O coordination sphere upon binding to the HFO surface is observed. Within the experimental error, *N* is invariant for all

Table 7. Average structural parameters *N*,*R* and their statistical error obtained from fits described in the text. S_o^2 was held constant at 1.

Sample	pH	Lu–O				Lu–Fe			
		N	*R* [Å]	σ^2 10^{-3} [Å^2]	ΔE_o [eV]	*N*	*R* [Å]	σ^2 10^{-3} [Å^2]	ΔE_o [eV]
Lu(III):HFO	4.6	6.2±0.8	2.28	2.5±0.5	3.9		–		
Lu(III):HFO	5.1	6.5±0.5	2.31	6.1±0.5	5.6	1.7±0.3	3.48	6.3±1.7	4.6
Lu(III):HFO	5.5	7.7±1.0	2.30	10.3±1.3	7.0	2.7±0.8	3.38	15±3	3.9
Lu(III):HFO	6.1	7.6±0.6	2.30	10.5±1.0	6.5	3.2±0.8	3.38	21.5±3	3.4
Lu(III):HFO[a]	6.1	7.3±0.4	2.30	7.7±0.6	6.5[b]	2.7±0.4	3.38	17±2	3.4[b]
Lu(III):HFO	7.7	7.0±0.5	2.30	9.2±0.7	6.1	3.3±0.3	3.38	20.5±0.4	3.2
Lu(III) aquo		9.1±0.3	2.31	7.8±0.5	4.9				

a: wet paste sample;
b: held constant at the value obtained for the dried sample, pH 6.1.

Lu(III):HFO sorption, 6–8. The only change in the metrical parameters as a function of sample preparation pH is in σ^2. The larger Lu−O EXAFS intensity observed for the sample prepared at pH 4.6 is due to a smaller σ^2 (0.0025 Å^2), which is even smaller than that observed for the Lu aquo species (0.0078 Å^2), and not a larger N. The proximity of the HFO surface has an effect of lowering the mean square displacement of oxygen atoms coordinated to Lu(III). The oxygen atoms coordinating Lu belong mostly to water molecules. This means that the proximity of the HFO surface lends rigidity and/or increased order to the coordinating aquo sphere.

As expected from the TRLFS results, N is reduced by two to three for the sorption samples as compared to the aquo species. From TRLFS it is known that, following the sorption process at pH 5.7, five water molecules remain coordinated to the metal cation. Combining this information with the EXAFS results ($N \sim 7$), indicates that two next neighbor oxygen atoms belong to the HFO surface, i.e., a bidendate surface complex is apparently formed.

In order to interpret the results for the Lu−Fe parameters listed in Table 7, a discussion of the possible Lu−Fe interactions is required. Possible binding sites for Lu(III) onto a FeO_6-octahedron located on the HFO surface are depicted in Fig. 8: a monodentate species (**M**), two possible bidendate species (bidentate edge-sharing **B1** and bidentate geminal corner-sharing **B2**), and a tridentate species (**T**). A double-edge sharing tridentate species is not included in these considerations because it is considered not to be energetically favorable [25]. The expected Lu−Fe distances for the different binding modes are also indicated in Fig. 8. Relatively long distances in the 3.7–4.4 Å range, depending on binding angle (∠ Fe−O−Lu), are expected for **M**. Species **B2** is expected to have Lu−Fe distances near 4.1 Å; **T** near 3.2 Å. **T** is bound to a FeO_6-octahedron face and expected to have a shorter Lu−Fe distance, ∼ 2.9 Å. These Lu−Fe distances are based on the proposed structure for HFO basic tetrameric unit composed of four planar $Fe(O, OH)_6$ octahedra [3], the d spacings from the HFO XRD pattern, and the Lu−O bond length from our EXAFS analysis.

Returning to the interpretation of Lu(III):HFO EXAFS fit results, no Lu−Fe interaction is observed for the pH 4.6 sample. This corroborates sorption results, which indicate the formation of **M** species at this pH. Due to both the long length expected for this interaction and the dynamic atomic displacements possible for **M** binding, a Lu−Fe interaction is not expected in the EXAFS. The appearance of a second peak at ∼ 3.1 Å (uncorrected for phase shift) for pH 5.1 and above results from scattering on a heavy atom and is attributed to a Lu−Fe interaction. No reliable fit of the data using Lu−Lu phase and amplitude scattering function is possible. The lack of a Lu−Lu interaction excludes the presence of sorbed polynuclear surface species or significant surface precipitation. A minor fraction of poorly ordered Lu-precipitate might not be detected. The ∼ 3.1 Å peak indicates the formation of a species different from species **M**, present at pH 4.6. The species **B1**, **B2**, and **T** have shorter Lu−Fe distances than species **M**, as well as a more rigid structure so that a Lu−Fe interaction should be observed in the EXAFS. The mean Lu−Fe distance found in the fits, 3.38 Å, is the same for all sorption samples above pH 5.1, i.e. in the region where the slope in the log–log plot is around 3. This 3.38 Å distance is too short for a **M** or **B2** species and too long to be associated with a tridentate species **T**. This distance better matches that expected for **B1**. These iron oxide polyhedron edge sites are high affinity bonding sites in HFO [25, 26]. A value of one for N (Lu−Fe) is expected for species **B1** but values ranging

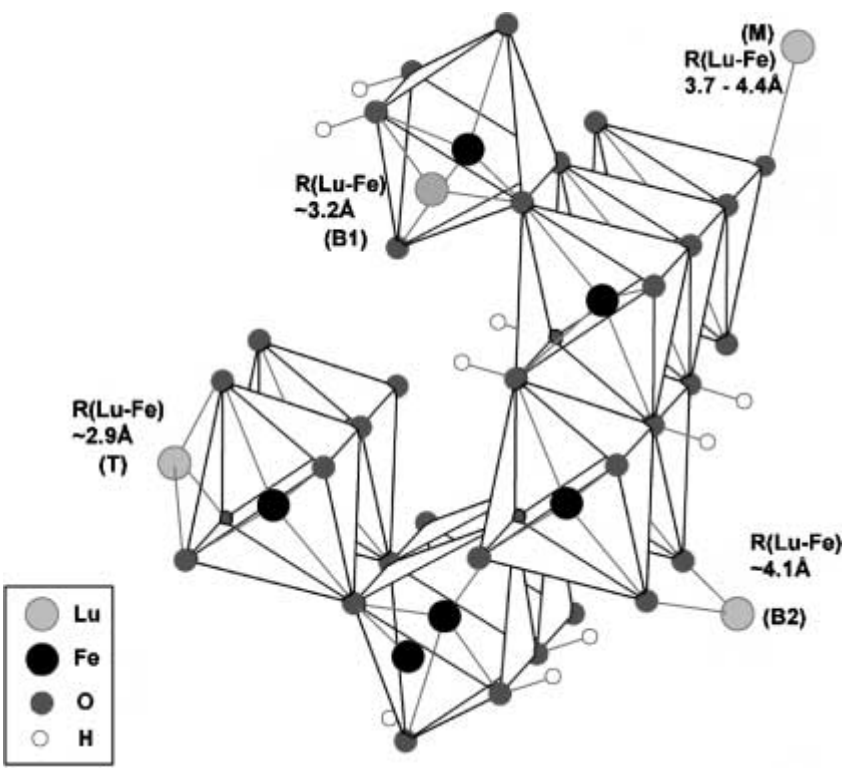

Fig. 8. Schematic, arbitrary structural representation of HFO surface sites available for Lu sorption and their calculated expected bond lengths (see text).

from 1.7 to 3.3 are obtained in the EXAFS analysis. This discrepancy may be do to the strong correlation between fit parameters N and σ^2 or to the Fe backscattering amplitude function used in the fit. We had no reference compound to test the amplitude function.

The σ^2 factor for the Lu−O shell increases with increasing pH. In addition, Lu−Fe shell exhibits a relatively large σ^2 factor. The Lu−O distance for a Lu−OH interaction should be different than the remaining Lu−O distances in the surface complex. Therefore, the introduction of an OH ligand into the Lu coordination sphere upon hydrolysis is expected to lead to an increase in the σ^2 factor of the Lu−O shell. The large Lu−Fe σ^2 values may indicate the presence of a distribution of Lu−Fe bond lengths. This might be expected for low crystalline HFO as sorbent, especially when hydrolysis occurs.

The pH 6.1 sorption sample is investigated both as a wet paste and a dried powder. However, no significant difference in their EXAFS spectra is observed. Fit results of the paste sample yield the same distances and comparable results for N, but a slightly smaller σ^2 value for both Lu−O and Lu−Fe coordination shells. Obviously, drying the sorption sample does not greatly alter the primary interaction of Lu(III) with the HFO surface. This is important to establish the relevance of the TRLFS hydration number, obtained for a dried sample.

4. Conclusions

Potentiometric titration of freshly synthesized HFO, modeled using the constant capacity model ($\kappa_1 = 0.5\ \mathrm{F/m^2}$) with the FITEQL code, yields the following characteristics: a specific surface area of $360 \pm 35\ \mathrm{m^2/g}$ (N_2-BET), a site density N_d of $2.86\ \mathrm{sites/nm^2}$ ($N_\mathrm{s} = 1.71 \times 10^{-3}\ \mathrm{mol\ sites/g}$ HFO), and acidity constants $\mathrm{p}K_{\mathrm{a}1} = 6.37$ and $\mathrm{p}K_{\mathrm{a}2} = 9.25$. Chemical sorption studies shows that two different Lu species are sorbed onto HFO as a function of pH: a monodendate species forms at pH values < 5.1 and a polydentate species dominates at $\mathrm{pH} > 5.1$.

The combination of modeling chemical sorption data and spectroscopic investigations, which probe the local structure of sorbed species, allows identification of the sorbed species. EXAFS results for Lu(III):HFO sorption samples prepared in the pH range 4.6 to 7.7 show that their EXAFS spectra exhibit a single first shell of 7 ± 1 oxygen atoms around Lu atoms at a distance of (2.30 ± 0.01) Å. The coordination number of Lu sorbed onto HFO is lower than that of the aquo species (9 ± 1), but the Lu−O bond lengths are comparable, without evidence of any splitting of the first coordination shell into more than one distance. No evidence of surface precipitation is found. No noticeable difference is discernable between wet paste and dried powder samples.

At pH values below 5.1 the formation of the Lu sorption species takes place according the reaction $\equiv \mathrm{Fe{-}OH} + \mathrm{Lu^{3+}(H_2O)_{8-9}} \rightarrow \equiv \mathrm{Fe{-}O{-}Ln(H_2O)_5^{2+}} + \mathrm{H^+} + 3\text{–}4\mathrm{H_2O}$. A second shell of neighboring Fe atoms at a distance near 3.4 Å is found for the sorption samples prepared at pH values 5.1 and above. This Lu−Fe distance indicates that Lu forms a bidendate complex, with bonding via edge sharing with FeO_6-octahedra on the HFO surface.

The sorption data are well fit using a combination of monodentate and bidentate species. The sorption constants of $\mathrm{p}K_\mathrm{s} = -1.89(\pm 0.1)$ and $\mathrm{p}K_\mathrm{s} = -1.69(\pm 0.1)$ for the monodentate species are found for fits to the pH edge and to the isotherm at pH 5.9, respectively. A value of $\mathrm{p}K_\mathrm{s} = 3.69(\pm 0.01)$ is obtained for the bidentate species $\equiv \mathrm{Fe(O)_2Lu(H_2O)_5^{+}}$. The fact that the slope of the pH edge log–log plot is apparently greater than two, the value expected for the formation of the bidentate species, is interpreted as resulting from the hydrolyzed form of the bidentate complex. Above pH 6.5 the first hydrolysis $\mathrm{Lu(OH)^{2+}}$ species forms [27]. The EXAFS Debye-Waller factor for the sorption samples is observed to increase slightly with increasing pH. This is likely due to an increase in distribution of bond lengths in the Lu coordination sphere upon increasing the amount of hydrolyzed complexes.

Acknowledgment. We acknowledge the European Synchrotron Radiation Facility and the Hamburger Synchrotronstrahlungslabor (HASYLAB) for beamtime allotment and C. Hennig and T. Reich (ROBL„ ESRF) and K. Attenkofer and E. Welter for their assistance.

References

1. Dzombak, D. A., Morel, F. M. M.: *Surface complexation modeling – hydrous ferric oxide*. John Wiley & Sons, New York (1990).
2. Schwertmann, U., Cornell, R. M.: *Iron Oxides in the Laboratory (Preparation and Characterization)*. VCH-Verlag, Weinheim (1991).
3. Cornell, R. M., Schwertmann, U.: *The Iron Oxides – structure, properties, reactions, occurrence and uses*. VCH-Verlag, Weinheim (1996).
4. Brunauer, S., Emmett, P. H., Teller, F.: Adsorption of gases in multimolecular layers. J. Am. Chem. Soc. **60**, 309 (1938).
5. Carter, D. L., Heilman, M. D., Gonzales, C. L.: Ethyleneglycol monoethyl ether for determining surface area of silicate minerals. Soil Sci. **100**, 356 (1965).
6. USDA.: Procedures for collecting soil samples and methods analysis for soil survey. U.S. Gov. Print. Office, Washington DC (1982).
7. Pyman, M. A. F., Posner, A. M.: The surface areas of amorphous mixed oxides and their relation to potentiometric titration. J. Colloid Interface Sci. **66**, 85 (1978).
8. Eggleton, R. A., Fitzpatrick, R.: New data and a revised structural model for ferrihydrite. Clays Clay Min. **36**, 111 (1988).
9. Weidler, P. G.: Oberflächen synthetischer Eisenoxide. Dissertation, Techn. Universität München (1995).
10. Davis, J. A.: Adsorption of trace metals and complexing ligands at the oxide/water interface. PhD, Stanford University, California (1977).
11. Davis, J. A., Leckie, J. O.: Surface ionization and complexation at the oxide/water interface. II. Surface properties of Amorphous Iron Oxyhydroxide and Adsorption of Metal Ions. J. Colloid Interface Sci. **67**, 90 (1978).
12. Herbelin, A., Westall, J.: FITEQL, A computer program for determination of chemical equilibrium constants from experimental data, Version 3.2. Oregon State University (1996).
13. Krolzig, A., Materlik, G., Swars, M., Zegenhagen, J.: A feedback control system for synchrotron radiation double crystal instruments. Nucl. Instr. Methods **219**, 430 (1984).
14. McMaster, W. H., Kerr Del Grande, N., Mallett, J. H., Hubbell, J. H.: Compilation of X-ray cross sections. Lawrence Livermore National Laboratory (1969).
15. Newville, M., Livins, P., Yacoby, Y., Rehr, J. J., Stern, E. A.: Phys. Rev. B **47**, 14 126 (1993).
16. Koningsberger, D. E., Prins, R.: *X-ray Absorption: Principles, Applications, Techniques for EXAFS, SEXAFS and XANES*. Wiley Interscience, New York (1988).

17. Ressler, T.: WinXAS: A New Software Package not only for the Analysis of Energy-Dispersive XAS Data. J. Physique IV **7**, 269 (1997).
18. Ankudinov, L. A., Ravel, B., Rehr, J. J., Conradson, S. D.: Real-space multiple scattering calculation and interpretation of X-ray-absorption near-edge structure. Phys. Rev. B **58**, 7565 (1998).
19. Saiki, A., *et al.*: J. Ceram. Assoc. Jpn. **93**, 649 (1985).
20. Hansen, H. C. B., Wetche, T. P., Raulung-Rasmussen, K., Borggaard, O. K.: Stability constants for silicate adsorbed to ferrihydrite. Clay Minerals **29**, 341 (1994).
21. Charlet, L., Manceau, A. A.: X-ray absorption spectroscopic study of the sorption of Cr(III) at the oxide/water interface. II. Adsorption, coprecipitation, and surface precipitation on hydrous ferric oxide. J. Colloid Interface Sci. **148**, 443 (1992).
22. Parks, G. A.: The isoelectric points of solid oxides, solid hydroxides, and aqueous hydroxo complex systems. Chem. Rev. **65**, 177 (1965).
23. Hayes, K. F., Redden, G., Wendell, E., Leckie, J. O.: Surface complexation models: an evaluation of model parameters estimation using FITEQL and oxide mineral titration data. J. Colloid Interface Sci. **142**, 448 (1991).
24. Horrocks, W. D. J., Sudnick, D. R.: Lanthanide Ion Probes of structure in biology. Laser-Induced Luminescence decay constants provide a direct measure of the number of metal coordinated water molecules. J. Am. Chem. Soc. **101**, 334 (1979).
25. Randall, S. R., Sherman, D. M., Ragnarsdottir, K. V., Collins, C. R.: The mechanism of cadmium surface complexation on iron oxyhydroxide minerals. Geochim. Cosmochim. Acta **63**, 2971 (1999).
26. Spadini, L., Manceau, A., Schindler, P. W., Charlet, L.: Structure and stability of Cd^{2+} surface complexes on ferric oxides. 1. Results from EXAFS spectroscopy, J. Colloid Interface Sci. **168**, 73 (1994).
27. Rizkala, E. N., Choppin, G. R.: *Handbook on the physics and chemistry of Rare Earths*. (Gschneidner, K. A. J., Eyring, L., Eds.), Elsevier Science, Amsterdam, North-Holland (1991), p. 393.
28. Farley, K. J., Dzombak, D. M., Morell, F. M. M.: A surface precipitation model for the sorption of cations on metal oxides. J. Colloid Interface Sci. **106**, 226 (1985).

Low temperature XAFS investigation on the lutetium binding changes during the 2-line ferrihydrite alteration process.

Environ. Sci. Technol. (2002) **36**(23), 5092.

Dardenne K., Schäfer T., Lindqvist-Reis P., Denecke M. A., Plaschke M., Rothe J., and Kim J. I.

Environ. Sci. Technol. **2002**, *36,* 5092−5099

Low Temperature XAFS Investigation on the Lutetium Binding Changes during the 2-Line Ferrihydrite Alteration Process

K. DARDENNE,* T. SCHÄFER, P. LINDQVIST-REIS, M. A. DENECKE, M. PLASCHKE, J. ROTHE, AND J. I. KIM

Forschungszentrum Karlsruhe, INE, P.O. Box 3640, 76021 Karlsruhe, Germany

The time dependent changes of Lu speciation (used as Am(III) homologue), initially sorbed onto 2-line ferrihydrite at pH 5.9, during tempering (70 °C) to stable crystalline transformation products, goethite and hematite, is studied. Microscopies (AFM, SEM), XRD and FTIR spectroscopy confirm transformation to both goethite and hematite, with a predominance of hematite. XRD investigation of another transformation series at pH 8.0 (75 °C, $[Lu(III)_{initial}]$ 7 times higher) shows that the cell volume of hematite increases, suggesting the incorporation of Lu in the crystal structure. Extended X-ray absorption fine structure (EXAFS) (pH 5.9 series, 70 °C) reveals a shortening of the Lu−O bond distance and an increase in asymmetry of the first shell with increasing tempering time in the intermediate temper time samples. The intensity of the second peak in the Fourier transform (FT) of the EXAFS increases and splits into two components. The EXAFS data of the end product can be modeled well using a hematite-like cluster, with an isotropic expansion of distances to account for incorporation of Lu into the hematite structure. These results demonstrate that the Lu is incorporated in the crystal lattice of the transformation product, as opposed to being occluded or remaining a sorbed species on the surface.

Introduction

Iron oxides and hydroxides are one of the predominant secondary phases in the weathering of igneous and sedimentary rocks (*1*) and also occur as precipitates from Fe-bearing waters (*2*). Commonly found secondary iron phases are 2-line ferrihydrite (2LFh) and its transformation products, goethite and hematite. Drum steel corrosion in the near field of a nuclear repository site can produce iron oxides/hydroxides as products. Such corrosion products may serve as a sink for radionuclides through their entrapment into the transformation products, thereby immobilizing them.

Iron oxides/-hydroxide phases play a crucial role in the bioavailability and migration behavior of heavy metal cations (*3,4*) and radionuclides (*5*−*9*) in natural systems. Due to the 2LFh metastability, knowledge of changes in sorption properties (e.g., reversibility) during the dissolution/recrystallization process and the possible entrapment of metal cations into transformation products are essential for predictive migration modeling.

* Corresponding author phone: +49 7247 82 6669; fax: +49 7247 82 3927; e-mail: dardenne@ine.fzk.de.

A number of publications on the 2LFh transformation in the presence of metal cations exists. Ferrihydrite aging studies reported in refs *10* and *11* point out that sorption increases and reversibility decreases for Cu, Mn, and Ni, whereas Pb and Cd show the opposite behavior. The concentration of background electrolyte (*12*), as well as metal concentration (*13, 14*), can reduce the rate of transformation or promote the formation of, e.g., hematite at the expense of goethite.

Systematic radionuclide sorption studies onto ferrihydrite include U (*15*−*17*), Np (*18*−*20*), Sr (*21*) and the Am(III) homologues Eu and Lu (*22*−*24*). However, only a limited number of investigations on lanthanide/actinide entrapment into crystalline 2LFh transformation products have been carried out (*25*−*27*).

A previous room temperature (RT) extended X-ray absorption fine structure (EXAFS) study on a pH 8.0 transformation series combined with selective extraction revealed that Lu is likely incorporated in the crystalline phase structure of the hematite transformation product (*28*). Lu was chosen for the EXAFS study to avoid the Fe interference occurring for Eu due to the proximity of the Fe K edge to the Eu L2, L3 edges. The Lu L3 edge EXAFS of the Lu containing transformation products differed from that of Lu sorbed onto either 2LFh or hematite at the same pH value 7.85. The EXAFS spectra varied with the temper time. The first peak in the Fourier transform (FT), corresponding to the Lu−O coordination shell, shifted toward shorter distances and its intensity and symmetry decreased. In addition, the second coordination shell, corresponding to a Lu−Fe interaction in the Lu:2LFh sorbed species, increased in intensity and progressively split into two components with increasing temper time (from 0 to 212 h at 75 °C). However, fits to this shell were inconclusive due to the thermal dampening of the EXAFS oscillations at room temperature, which is stronger for the more distant atoms, i.e., the Fe atoms in our study. To better determine the Lu environment in the crystalline transformation phases, EXAFS measurements of a new sample series tempered at 70 °C for varied times (0 h, 84 h, 155 h and 238 h) were performed at 16 K. In addition to this low-temperature EXAFS investigation, changes in the Lu structural environment during the 2LFh transformation are studied using Fourier transform infrared spectroscopy (FTIR), atomic force microscopy (AFM) and scanning electron microscopy (SEM) on the whole sample series (0 h, 39 h, 84 h, 155 h, 238 h and 5 months). The FTIR results are compared to those obtained for Eu(III), where the sorption samples were prepared at pH 5.9 with a similar Ln(III) initial concentration and tempered at 45 °C. The powder X-ray diffraction (XRD) pattern of the 238 h tempered sample and of the pH 8.0 transformation sample series are discussed.

Experimental Section

2-Line Ferrihydrite (2LFh). An aqueous suspension of 2LFh was freshly prepared according to ref *29*. The synthetic 2LFh product was characterized by XRD, FTIR, and surface area determinations (*24*). The powder XRD pattern recorded using a Seifert 3000TT diffractometer with Cu Kα radiation shows only two broad diffraction peaks at *d* spacings of 0.26 nm (110) and 0.15 nm (300), as expected for 2LFh (*30*). No diffraction peaks from 6-line ferrihydrite, transformation products (hematite or goethite) or impurities were detected.

10.1021/es025513f CCC: $22.00

Published on Web 10/23/2002

Sorption and Tempering Experiments. The Lu(III) sorption experiments were performed in a 2.7 g/dm^3 aqueous suspension of 2LFh, 40 cm^3 total volume, containing 157 μmol/dm^3 Lu(III). Polyethylene (PE) vessels were used for all transformation experiments. Lutetium was added from an acidic stock solution and 1 mol/dm^3 NaOH used for pH adjustment to pH 6.0. The ionic strength achieved was 0.004 mol/dm^3 $NaClO_4$. A maximum surface coverage of ~7% was expected under these experimental conditions (5.8×10^{-5} mol Lu/g 2LFh), assuming a bidentate complexation (*24*). The solution was then distributed into 20 vessels and kept for 24 h at RT before being tempered for different times (0 h−5 months) at 70 °C.

For the pH 8.0 transformation sample series tempered at 75 °C $[Lu]_{initial}$ was 3.95×10^{-4} mol/g 2LFh. The pH after sorption at RT was 7.85. The pH was readjusted to 8.0 ± 0.3 after each sampling for the first week and freely evolved afterward.

Sample Characterization. Following filtration through a 0.2 μm syringe filter, the Lu and Fe concentration of the supernatant solution was determined using ICP-AES and ICP-MS (Perkin-Elmer PLASMA 400 & ELAN 6000). Fe concentration was also determined to avoid erroneously high Lu supernatant concentration due to possible presence of 2LFh colloids. The solid phase from the tempering experiments was separated by filtration through a 0.1 μm membrane filter, rinsed with Milli-Q water (except for the 238 h sample) and dried at RT under atmospheric conditions.

Microscopic Techniques (AFM and SEM). Noncontact mode AFM imaging was performed in water using a Topometrix TMX 2000 Explorer, equipped with a cantilever oscillating hardware. Triangular probes with silicon nitride tips (nominal radius <50 nm; nominal resonance frequency 17 kHz) were mounted on a liquid scanner with a maximum range of 2.2 μm in the $x-y$ direction and 900 nm in the z direction.

A piece of natural muscovite (Plano, Wetzlar, Germany), with ~1 × 2 cm^2 dimensions was freshly cleaved and positioned vertically in a polypropylene sample beaker containing the particle suspension. Particles were allowed to adsorb from the fluid onto the mica surface for 24 h (T = 22 °C). The mica sheets were then withdrawn from the solution and thoroughly rinsed with deionized water in order to remove any nonadsorbed particles. AFM measurements were performed in Milli-Q water.

A SEM (CamScan, type C44 FE) equipped with a warm field emission cathode was used for characterization of iron oxide particles coated with Cr.

Spectroscopic Investigations. FTIR spectra on KBr pellets (1.2 wt % 2LFh) were measured using a Bruker IFS55 spectrometer.

Lutetium L3 edge EXAFS spectra were recorded at the European Synchrotron Radiation Facility (ESRF), operating at 6 GeV with a maximal current of 200 mA, at the ROBL beamline. Si(111) crystals were used in the double-crystal monochromator. Higher harmonic rejection was done with two Pt coated mirrors. All data were collected at 16K in transmission mode, using ionization chambers filled with nitrogen gas.

Sample spectra were energy calibrated using the first inflection point in the K-edge spectrum of a zinc metal foil (9659 eV) (*31*). Data analysis was performed based on conventional methods (*32*); the AUTOBK program for extracting χ(k) from the absorption spectrum and the FEFFIT software for modeling data from the UWXAFS package (*33*) were used.

Four Lu:2LFh samples tempered for various times (see open circles in Figure 1) were investigated. Samples were measured dispersed in boron nitride (BN) powder and pressed into 13 mm diameter pellets.

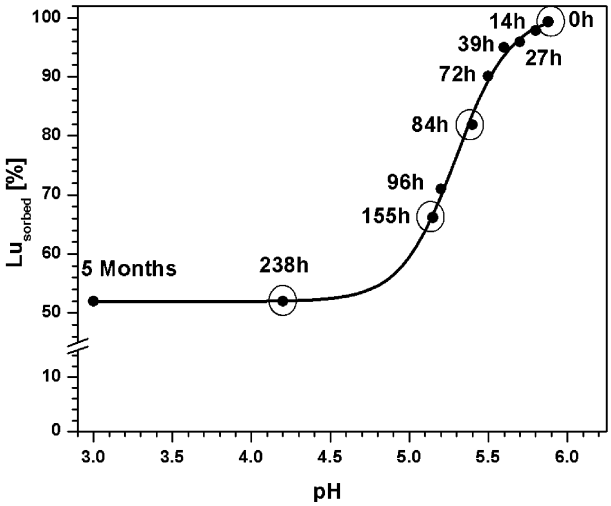

FIGURE 1. Percent Lu associated with iron oxide/hydroxide transformation product as a function of pH change with temper time (filled circles). Open circles indicate EXAFS samples.

Theoretical backscattering amplitude and phase functions for fitting the experimental data from the transformation samples were calculated with the multiple scattering code FEFF8 (*34*) using an 59 atom cluster with atomic positions calculated from structural data reported for hematite (*35*). Fits were carried out in R-space between 1.4 and 4.0 Å (k range of 2.75−10.6 Å^{-1})

Results and Discussion

Overall Sample Characteristics. The color of the transformation products changed from dark red-brown for the 2LFh to a light red for the 238 h and the 5 months tempered samples. This suggests that hematite was formed.

Figure 1 depicts the pH evolution and amount of Lu associated with the solid phase during the total alteration time of 5 months. The pH of the solution decreased from 5.9 (value after sorption) to 3.0. The amount of Lu associated with the iron oxide/hydroxide phase was observed to decrease with decreasing pH. At pH values below ~5, the amount of Lu released varied slowly and attained a constant value of 52% Lu in the solid phase from pH 4.2 (238 h sample) to 3.0 (5 months sample). This indicates that Lu, initially reversibly bound to the iron phase, becomes more strongly bound with time, e.g., through incorporation into the solid phase. The more strongly bound Lu(III) species cannot be re-mobilized into solution upon a pH decrease. This is in agreement with our previous results showing that the amount of Lu extracted with crystalline Fe-phases increases with temper time for Lu sorbed onto 2LFh at pH 7.85 (*28*).

Microscopy Results (AFM, SEM). The variation of the morphology and size of 2LFh and its transformation products was investigated by noncontact mode AFM. Particles were studied in their hydrated state so that morphologies were not disturbed by possible drying artifacts (*36*, *37*). Figure 2a shows an AFM image of 2LFh particles in water. These exhibit a broad distribution of lateral and vertical dimensions in the range of 25−200 nm and 2−34 nm, respectively. In addition, ~100 nm long needles with ~15 nm height and diameter were observed. An image of the 2LFh samples sorbed with Lu at pH 5.9 before tempering is depicted in Figure 2b. Large aggregates of 2LFh particles with diameters in the range of 80−200 nm were formed. In the 238 h tempered sample (Figure 2c), goethite needles with length, diameter and height of about 250, 40 and 10 nm, respectively, and small 40−60 nm particles (probably hematite) were found. Upon temper-

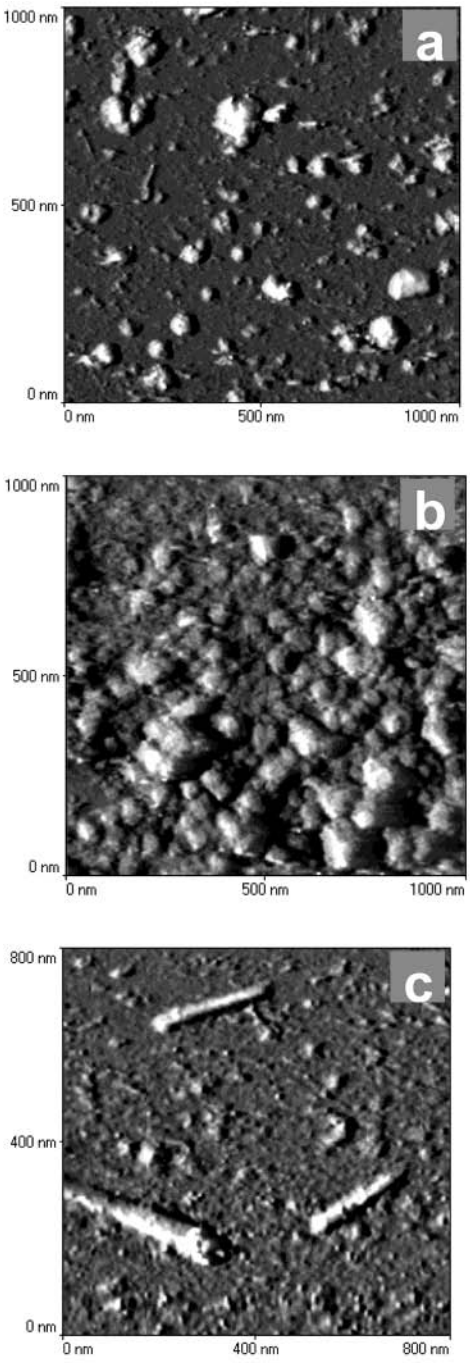

FIGURE 2. AFM images of (a) 2LFh particles, (b) 2LFh particles sorbed with Lu at pH 5.9, I = 0.004 M, and (c) transformation products of particles shown in (b) following tempering for 238 h at 70 °C. All measurements in water: total image heights: (a) 38 nm; (b) 43 nm; and (c) 22 nm.

ing the Lu:2LFh aggregate size decreased and formation of goethite needles is observed. Note that all lateral dimensions may be overestimated due to a tip artifact typical for AFM (*38*).

Figure 3 compares SEM images of the transformation samples (Figure 3c−f) with those of synthetic 2LFh (Figure 3g), low crystalline goethite (Figure 3a) and hematite (Figure 3b). The sample aged 84 h (Figure 3e) was very similar to 2LFh itself. The major transformation product morphologies were <100 nm rounded hexagonal and/or cubic shaped hematite particles (Figure 3c,d). Some goethite needles were observed as in the AFM study.

Energy dispersive analysis of X-ray (EDAX) from different zones of all the samples did not reveal any Lu enriched regions.

XRD Results. The powder diffraction pattern of the 238 h tempered sample from the pH 5.9 series (Figure 4) showed the presence of goethite and hematite. Rietveld refinement using the FullProf software (*39*, *40*) was used to determine crystal lattice parameters of the hematite and goethite phases and to estimate the composition of this sample (hematite ~62 wt %, goethite ~38 wt %). Four reflexes were observed, neither belonging to goethite, nor to hematite. They were located at *d* spacing values 4.67 Å, 3.11 Å, 2.82 Å and 1.87 Å with 9%, 35%, 4% and 3% peak intensities relative to the 2.698 Å hematite peak. The lattice parameters obtained were $a = 0.50355(5)$ nm, $c = 1.3752(2)$ nm, $V = 301.98(7)$ Å^3 for hematite and $a = 0.9966(2)$ nm, $b = 0.30244(8)$ nm, $c = 0.4604(1)$ nm, $V = 138.76(5)$ Å^3 for goethite. Similar values were listed in the JCPDS-International center for diffraction database for the pure synthetic compounds (reference 86-0550 for hematite and 81-0464 for goethite).

Powder X-ray diffractograms of the pH 8.0 transformation samples (75 °C, [Lu(III)$_{initial}$] 7 times higher than for the "pH5.9" series) were recorded using a Bruker diffractometer, model D8, $\lambda_{Co} = 1.78901$ Å ($K_{\alpha 1}$), step time 5 s, step size 0.02°. They showed reflexes for hematite and additional lines belonging to the sodium perchlorate monohydrate salt (Figure 5). With increasing tempering time, the reflexes characteristic for hematite appeared in the diffraction pattern (see Figure 5, 2LFh:Lu sorption, 212 h and 2.5 months). Cell parameter refinement for the hematite formed by transformation of 2LFh in the presence of Lu yielded a larger unit cell ($a = 0.5047(4)$ nm, $c = 1.3801(5)$ nm, $V = 304.4(6)$ Å^3 for the 2LFh:Lu 212 h, $a = 0.5043(3)$ nm, $c = 1.3796(5)$ nm, $V = 303.8(4)$ Å^3 for the 2LFh:Lu 2.5 months) than for the 238 h tempered sample of the previous series ($V = 301.98(7)$ Å^3). A comparable variation of cell parameters was found for Nd incorporation into hematite (*25*). The hematite synthesized from iron nitrate salt according to ref *29* showed smaller lattice parameters ($a = 0.5022(3)$ nm, $c = 1.3728(6)$ nm, $V = 299.7(5)$ Å^3) than in the database. The synthetic hematite samples showed no noticeable change in cell parameters following Lu sorption. The full width half-maximum (fwhm) values (2θ degrees) determined using a pseudovoigt function are much larger for the pure hematite (104: 0.630, 110: 0.469, 116: 0.619) than for the 2.5 months hematite transformation product of 2LFh (104: 0.312, 110: 0.315, 116: 0.328). The fwhm was similar for the pH 8 series 212 h and 2.5 months tempered samples.

FTIR Spectroscopy Results. Figure 6 compares FTIR spectra of the transformation samples with those from the initial sorption sample (Figure 6f), goethite (Figure 6g) and hematite (Figure 6a). In the spectrum of the Lu:2LFh sorption sample characteristic hydroxyl bands at 450 and 650 cm^{-1} (bulk OH deformations), ~3380 cm^{-1} (bulk OH stretch), and an adsorption band at 1620 cm^{-1} (molecular water) were observed. The small, sharp band at 1384 cm^{-1} is due to nitrate still present in the 2LFh. In the transformation product spectra the bands characteristic for goethite and hematite increased in intensity while the 2LFh bands decreased and disappeared. This proved the coexistence of the three phases during the transformation. The two sharp bands characteristic of goethite (*30*) at 895 (δ_{OH}) and 803 cm^{-1} (γ_{OH}) appeared and their intensity increased with increasing temper time.

The γ_{OH} out of plane bending band at 803 cm^{-1} shifted toward higher wavenumbers compared to that observed for pure synthetic goethite (795 cm^{-1}). This shift can be due to incorporation of lutetium into the goethite crystal structure and/or to a change in crystallinity. The simultaneous decrease in difference between the wavenumber for the observed δ_{OH}

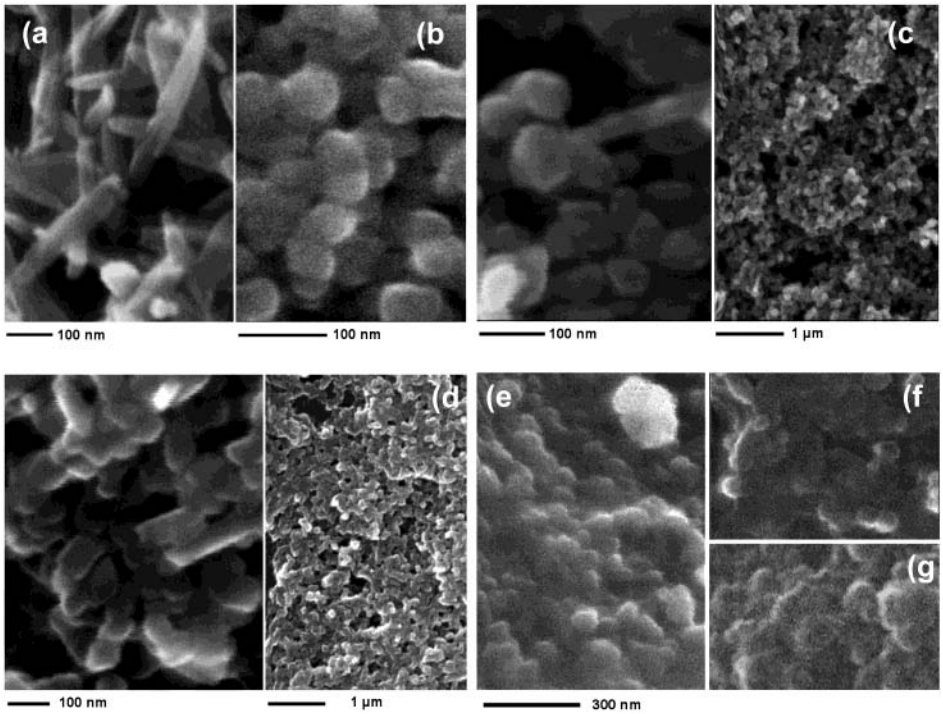

FIGURE 3. SEM images of the transformation samples (a) low-crystalline synthetic goethite, (b) synthetic hematite, (c) 2LFh:Lu, 238h at 70 °C at two different magnifications, (d) 2LFh:Lu, 5 months at 70 °C at two different magnifications, (e) 2LFh:Lu, 84 h at 70 °C, (f) 2LFh:Lu sorption, 1 week at 20 °C, and (g) pure synthetic 2LFh.

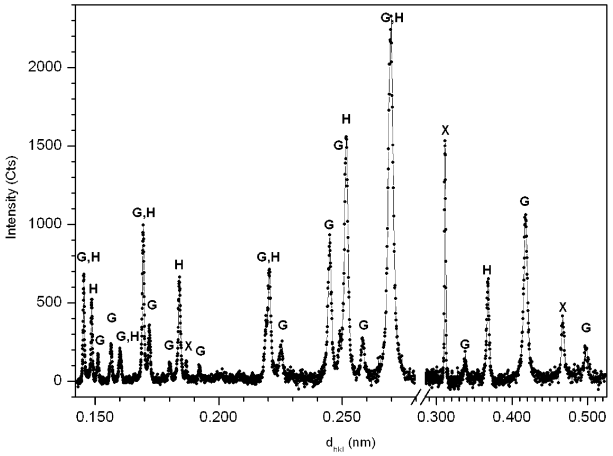

FIGURE 4. XRD pattern of the 238 h tempered sample measured at the synchrotron radiation source ANKA, Germany (accumulation of 10 scans: $\lambda = 1.818$ Å, step time 1s, step size 0.02°). Background (broad band 2.4−3.7 Å, ∼180 counts) due to the sample holder (adhesive tape) was removed; data was not smoothed. Most of the goethite (G) and hematite (H) lines are marked. (X) corresponds to the nonidentified phase.

and γ_{OH} bands (from 103 cm^{-1} in goethite to 92 cm^{-1} in the transformation product) suggests a lower crystallinity in the transformation product. We observed a similar frequency shift of the goethite γ_{OH} characteristic band for tempered Eu(III):2LFh sorption samples (pH 5.9; 45 °C) (spectrum not shown). In this investigation, Eu and 2LFh concentrations were similar to the Lu and 2LFh concentrations reported here. However, goethite, and not hematite, was the main transformation product formed.

The large band at 3410 cm^{-1} in the hematite spectrum corresponds to surface hydroxyl stretch vibrations. The intensity of this band decreased when the sample was stored a few days at 40 °C (spectrum not shown), which is in agreement with results described in ref *30*. Intense characteristic bands at 630 cm^{-1} (A_{2u} mode), 597 and 537 cm^{-1} (E_u mode) and 455 cm^{-1} (E_u mode) are also observed.

EXAFS Results. Figure 7 shows the k^2-weighted Lu L_3 edge experimental EXAFS and the R-space fit results of the Lu:2LFh transformation samples studied. Visual comparison of these spectra and their FT suggests that the Lu environment changes with increasing tempered time, i.e., with increasing transformation. The intensity and symmetry of the first shell FT peak decreased and its maximum shifted toward shorter distances as a function of the temper time while the transformation progressed, similar to previous results of a Lu:2LFh series, pH 8.0 (*28*). Symmetry and intensity increases again for the 238 h tempered sample where the transformation is completed.

The intensity of the second shell FT peak increased and the peak split into two discernible components. In addition, the white line intensity in the absorption spectra decreased with increasing the temper time, suggesting that Lu is incorporated in a condensed bulk phase (*41*).

The initial sorption sample (temper time 0 h) EXAFS was fit using two coordination shells, an oxygen (O′) and an iron shell. This fit yielded seven oxygen atoms at a mean bond distance of 2.30 Å and a Lu−Fe distance of 3.39 Å. This is in good agreement with previous results (*24*).

The tempered samples were fit using structural models of the two transformation end products (goethite and hematite). The models taken into account were ∼59 atom clusters having hematite-like (Figure 8) and goethite-like structures, with an isotropic expansion of 4% to account for Lu incorporation into the crystal. The average bond lengths and coordination numbers calculated for these samples are listed in Table 1.

Because XRD and SEM results indicated hematite to be the main transformation product, the hematite-like model was first used to fit the EXAFS data for the 238 h tempered sample. The coordination numbers were held constant during the fit. Results of these fits are given in Table 2 and shown in Figure 7. The experimental EXAFS was fit well using the hematite-like model. To obtain good results, the inclusion

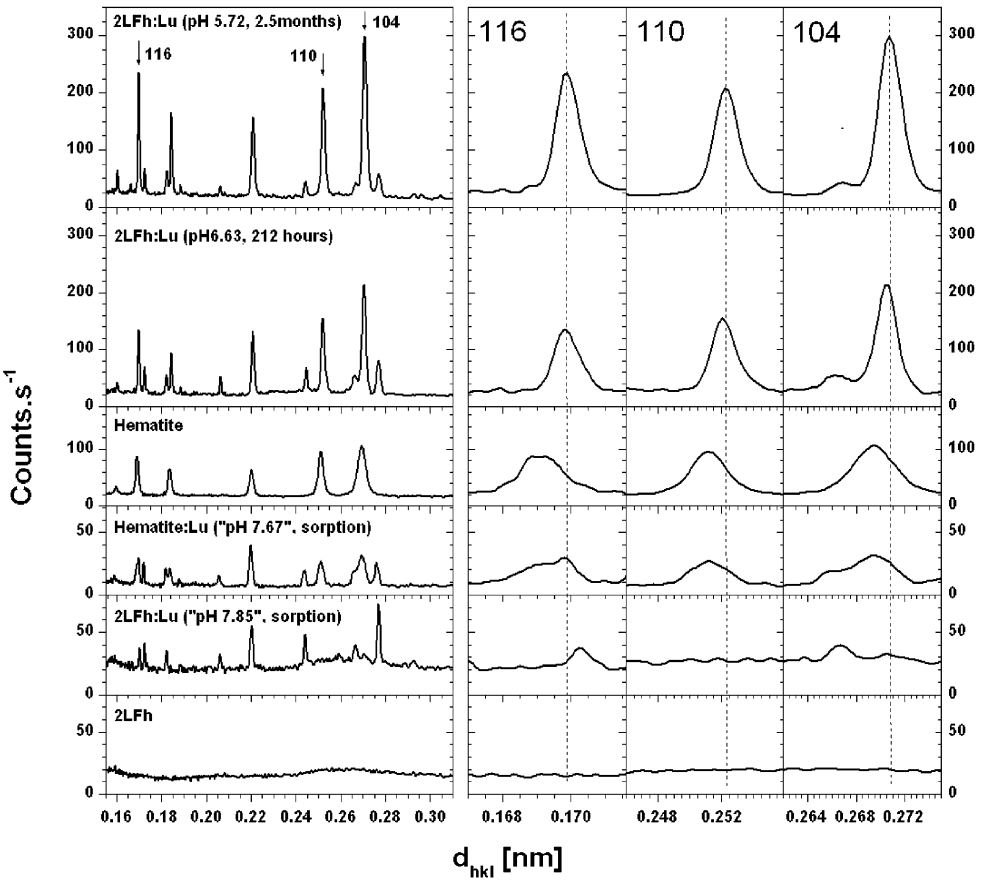

FIGURE 5. XRD pattern (background not removed) of synthetic 2-line ferrihydrite and hematite, pure and after Lu sorption (bottom) compared with XRD pattern of transformation samples at 75 °C (sorption at pH 7.95) (top).

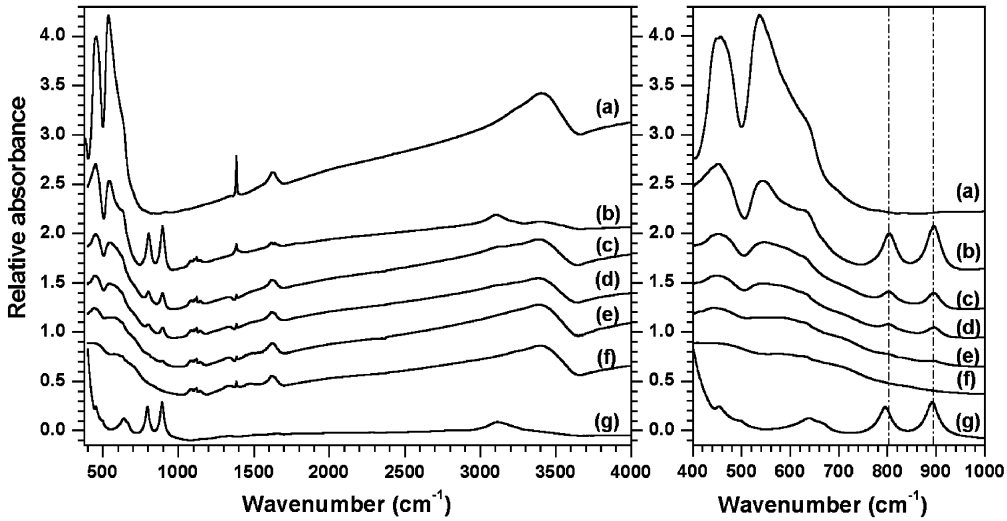

FIGURE 6. FTIR spectra at left and an enlargement of the 400−1000 cm^{-1} range at right: (a) synthetic hematite, (b) 2LFh:Lu, tempered 238 h at 70 °C, (c) 2LFh:Lu, tempered 155 h at 70 °C, (d) 2LFh:Lu, tempered 84 h at 70 °C, (e) 2LFh:Lu, tempered 39 h at 70 °C, (f) 2LFh:Lu sorption, aged 1 week at 20 °C, and (g) synthetic goethite.

of a Lu−Fe distance near 3.9 Å was required. This distance is absent in the goethite-like cluster. No good fit was possible using solely the goethite-like model. If Lu is incorporated into goethite, its EXAFS contribution is completely masked by Lu in hematite. The fit to the data was initially performed on the shorter k range in order to lower the influence of eventual multiple scattering (MS) contributions. The fit to the data over the range 1.7−10.7 $Å^{-1}$ required including the 4-legged ($Lu_c \rightarrow O_1 \rightarrow Lu_c \rightarrow O_2 \rightarrow Lu_c$, $\angle O_1,Lu_c,O_2 = 180°$) MS contribution. This suggests that the environment of Lu incorporated into the hematite structure has a high symmetry. Otherwise, one would not expect to observe this 4-legged MS path.

Principal component analysis (*42*) of the four EXAFS spectra (nonweighted (0Wt) and k^2-weighted (2Wt)) yielded 2 principal components with eigenvalues representing 85.9% of the signal (56.8% and 29.1%). The two last components (7.3% and 6.8%) contained only noise. The uniqueness test

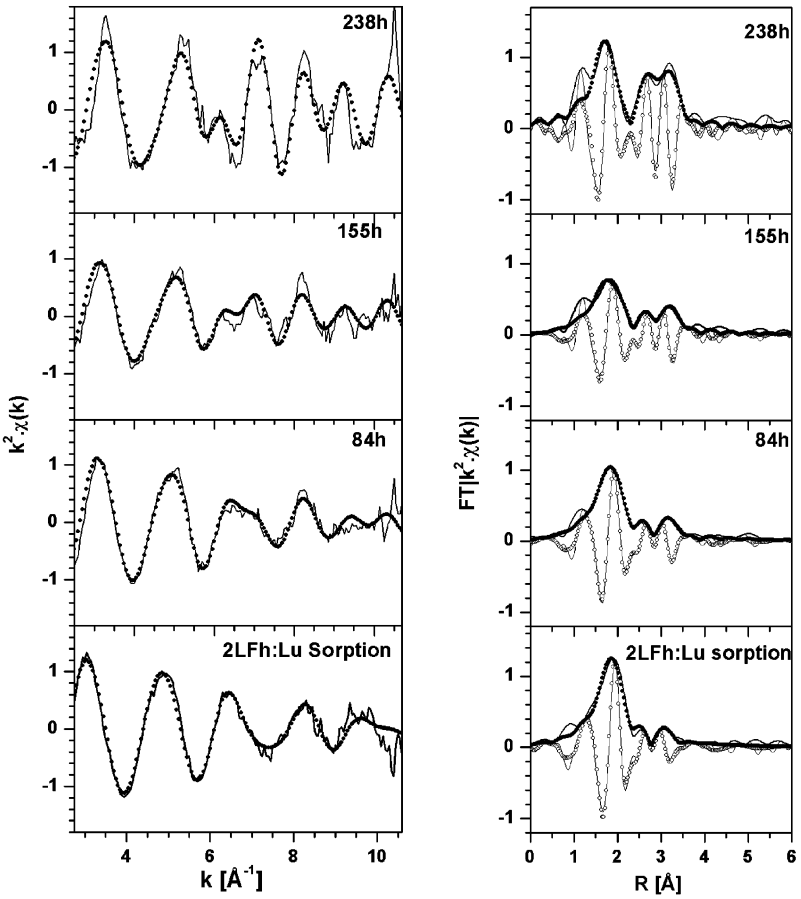

FIGURE 7. Left: k^2-weighted Lu L_3 edge experimental EXAFS and back transformed R-space fit results (1.4 to 4.0 Å); right: corresponding Fourier transforms (Hanning windows, k range = 2.75−10.6 Å. Theoretical curves are depicted as dots and experimental ones as continuous lines.

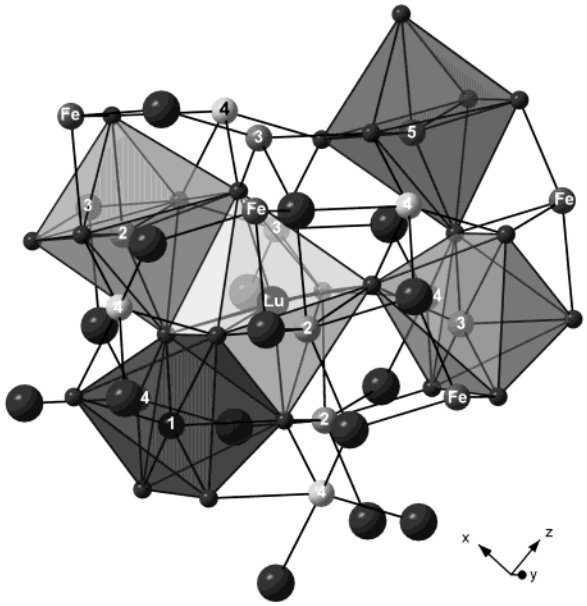

FIGURE 8. 59 atom cluster with hematite-like structure. Numbers correspond to Fe atoms in Table 1 (e.g. 1 is Fe1).

showed that the 0 h and 238 h species had nothing in common. These samples were therefore used as "standards" to perform the rotation of the matrix and reproduce the intermediate temper time samples in terms of a combination of 0 h and 238 h tempered samples. The rotation of the PCA matrix over the standard base yielded ~23% (i.e., 0Wt: 22.1%/2Wt: 24.3%) of the 238 h species in the 84 h tempered sample and ~45.7% (0Wt 45.6%/2Wt 45.8%) of the 238 h species in the 155 h tempered sample.

TABLE 1. Average Bond Lengths and Coordination Numbers Calculated for the Hematite-like and Goethite-like Model Clusters from XRD Structure (*29, 35*)

	hematite		goethite		2LFh	
backscattering atom	distance (Å)	N	distance (Å)	N	distance (Å)	N
O	2.02	3	2.03	2+1	1.75	1
O	2.20	3	2.20	2+1	2.16	1+1
O					2.40	1+1
O					2.69	1
Fe1	3.02	1	3.14	2	3.11	1
O			3.34	1		
Fe2	3.09	3	3.44	2	3.19	2
Fe3	3.50	3	3.58	4	3.49	2
O	3.53	3	3.73	2	3.66	1+1
O	3.74	3	3.83	2	3.74	1+1
O			3.90−4.78	10	3.81	1
Fe4	3.85	6			3.90	2

Simultaneous fits to the data of the 84 h and 155 h tempered samples were done using a combination of results for the temper times 0 h and 238 h species. We introduced a ratio factor (rf) as a measure of transformation progress into these fits. The value of rf gives the proportion of Lu incorporated into hematite and was varied during the fit procedure. The value 1-rf is the proportion of initial Lu:2LFh remaining in the sample. The first coordination shell bond lengths were held constant at 2.19 Å and 2.30 Å, i.e., the

TABLE 2. Structural Parameters Obtained from Fits in R-Space to Transformation Sample EXAFS Shown in Figure 7[a]

sample temp time (h)	neighbor	N[d]	R [Å]	ΔE0 [eV]	σ^2 [10^{-3} Å^2]	% final product[e]
0	O′	7.2	2.30	7.4	7.42	0
	Fe′	1[b]	3.39	2.2	3.86	
84 h[c]	O		2.19[b]		7.66	24
	O′		2.30[b]		7.66	
	Fe1 + Fe2		3.15		9.87	
	Fe4		3.93		10.66	
155 h[c]	O		2.19[b]		8.77	44
	O′		2.30[b]		8.77	
	Fe1 + Fe2		3.15		8.64	
	Fe4		3.93		10.67	
238 h	O	6[b]	2.19	7.0	7.30	100
	Fe1 + Fe2	4[b]	3.09	1.1	10.5	
	Fe3	3[b]	3.42	1.1	1.87	
	Fe4	6[b]	3.89	1.1	12.7	

[a] For the 84 h and 155 h tempered samples, the coordination numbers and ΔE0 were held constant at the values for the 0 h and 238 h tempered samples. The ratio factor (rf), a measure of the transformation progress, is fit. [b] Held constant at this value. [c] Fe3 and Fe′ parameters are fixed at the values from 0 h and 238 h, N is varied. [d] N(O′)=(1-rf)*7.2, N(O)=rf*6 and N(Fe′)=(1-rf)*1, N(Fe3)= rf*3, N(Fe1+Fe2)=rf*4, N(Fe4)=rf*6. [e] %final product = 100*rf.

values obtained from fits to the 0 h and 238 h tempered sample data. The Debye−Waller factors for both O shells were constrained to the same value in the fit as they were similar for the 0 h and the 238 h samples. The Lu−Fe3 and Lu−Fe′ were too close to be fit separately and were fixed to values obtained from 0 h and 238 h (fit with a unique distance yielded 3.42 Å). The other Lu−Fe distances were varied but constrained to evolve identically for both samples.

Both 84 h and 155 h tempered sample EXAFS spectra were fit well with this model. A trend in the progress of the transformation is seen in the rf values obtained in the fits: 24% hematite-like product at a temper time of 84 h and 44% at 155 h. These results indicate that both species, Lu sorbed onto 2LFh and Lu incorporated into the hematite crystal structure, coexist in the intermediate temper time samples. Standard EXAFS analysis fully agrees with the PCA of the data set.

In summary, combining microscopy, diffraction and spectroscopy, we showed that the major transformation product of Lu:2LFh is hematite (XRD, AFM, SEM). The three phases 2LFh, goethite, and hematite coexist during the transformation process (FTIR), and Lu is distributed at least among 2LFh and hematite (EXAFS). We demonstrated (EXAFS, pH evolution) that the actinide trivalent homologue, Lu, is incorporated into an hematite-like structure during the alteration of the 2LFh, which is of crucial importance for the actinide mobility in the geosphere.

Acknowledgments

We acknowledge the European Synchrotron Radiation Facility (ESRF) for beamtime allotment and the ROBL staff, especially André Rossberg, for support. We also thank Steven Doyle for the XRD measurement of the 238 h tempered sample at the Angströmquelle Karlsruhe (ANKA).

Note Added after ASAP Posting

This paper was released ASAP on 10/23/2002 with a typographical error in the second line of the Abstract. The correct version was posted on 11/12/2002.

Literature Cited

(1) Jambor, J. L.; Dutrizac, J. E. *Chem. Rev.* **1998**, *98*, 2549−2585.
(2) Carlson, L.; Schwertmann, U. *Geochim. Cosmochim. Acta* **1981**, *45*, 421−429.
(3) Lion, L. W.; Altmann, R. S.; Leckie, J. O. *Environ. Sci. Technol.* **1982**, *16*, 660−666.
(4) Davies-Colley, R. J.; Nelson, P. O.; Williamson, K. J. *Environ. Sci. Technol.* **1984**, *18*, 491−499.
(5) Lu, N.; Kung, K. S.; Mason, C. F. V.; Triay, I. R.; Cotter, C. R.; Pappas, A. J.; Pappas, M. E. G. *Environ. Sci. Technol.* **1998**, *32*, 370−374.
(6) Payne, T. E.; Davis, J. A.; Waite, T. D. *Radiochim. Acta* **1994**, *66/67*, 297−303.
(7) Barnes, C. E.; Cochran, J. K. *Geochim. Cosmochim. Acta* **1993**, *57*, 555−569.
(8) Sato, T.; Murakami, T.; Yanase, N.; Isobe, H.; Payne, T. E.; Airey, P. L. *Environ. Sci. Technol.* **1997**, *31*, 2854−2858.
(9) Murakami, T.; Ohnuki, T.; Isobe, H.; Sato, T. *Am. Mineral.* **1997**, *82*, 888−899.
(10) Ford, R. G.; Bertsch, P. M.; Farley, K. J. *Environ. Sci. Technol.* **1997**, *31*, 2028−2033.
(11) Karthikeyan, K. G.; Elliott, H. A.; Cannon, F. S. *Environ. Sci. Technol.* **1997**, *31*, 2721−2725.
(12) Baltpurvins, K. A.; Burns, R. C.; Lawrance, G. A.; Stuart, A. D. *Environ. Sci. Technol.* **1997**, *31*, 1024−1032.
(13) Sun, T.; Paige, C. R.; Snodgrass, W. J. *Water, Air, Soil Pollut.* **1996**, *91*, 307−325.
(14) Cornell, R. M.; Giovanoli, R.; Schneider, W. *J. Chem. Technol. Biotechnol.* **1992**, *53*, 73−79.
(15) Waite, T. D.; Davis, J. A.; Payne, T. E.; Waychunas, G. A.; Xu, N. *Geochim. Cosmochim. Acta* **1994**, *58*, 5465−5478.
(16) Reich, T.; Moll, H.; Arnold, T.; Denecke, M. A.; Hennig, C.; Geipel, G.; Bernhard, G.; Nitsche, H.; Allen, P.; Bucher, J.; Edelstein, N.; Shuh, D. *J. Spectrosc. Relat. Phenom.* **1998**, *96*, 237−248.
(17) Payne, T. E.; Davis, J. A.; Waite, T. D. *Radiochim. Acta* **1996**, *74*, 239−243.
(18) Nagasaki, S.; Tanaka, S.; Suzuki, A. *Nucl. Sci. Technol.* **1994**, *31*, 143−150.
(19) Tochiyama, O.; Endo, S.; Inoue, Y. *Radiochim. Acta* **1995**, *68*, 105−111.
(20) Combes, J. M.; Chrisholm-Brause, C. J.; Brown, G. E., Jr.; Parks, G. A.; Conradson, S. D.; Eller, P. G.; Triay, I. R.; Hobart, D. E.; Meijer, A. *Environ. Sci. Technol.* **1992**, *26*, 376−382.
(21) Collins, C. R.; Sherman, D. M.; Ragnarsdottir, K. V. *Radiochim. Acta* **1998**, *81*, 201−206.
(22) Music, S.; Ristic, M. *J. Radioanal. Nucl. Chem.* **1988**, *120*, 289−304.
(23) Music, S.; Gessner, M.; Wolf, R. H. H. *J. Radioanal. Chem.* **1979**, *50*, 91−100.
(24) Dardenne, K.; Schäfer, T.; Denecke, M. A.; Rothe, J.; Kim, J. I. *Radiochim. Acta* **2001**, *89*, 469−479.
(25) Nagano, T.; Mitamura, H.; Nakayama, S.; Nakashima, S. *Clays Clay Min.* **1999**, *47*, 748−754.
(26) Sorensen, M. A.; Stackpoole, M. M.; Frenkel, A. I.; Bordia, R. K.; Korshin, G. V.; Christensen, T. H. *Environ. Sci. Technol.* **2000**, *34*, 3991−4000.
(27) Martinez, C. E.; Sauvé, S.; Jacobson, A.; McBride, M. B. *Environ. Sci. Technol.* **1999**, *33*, 2016−2020.
(28) Dardenne, K.; Schäfer, T.; Denecke, M. A.; Rothe, J. *XAFS investigation of lanthanides(III) sorption onto ferrihydrite with aging*; Proceedings of 2nd OECD-NEA Workshop on Speciation, Techniques and Facilities for Radioactive Materials at Synchrotron Light Sources, 10−12 Sept. 2000 Grenoble, France, 222−228.
(29) Schwertmann, U.; Cornell, R. M. *Iron Oxides in the Laboratory* (*Preparation and Characterization*); Dyllick-Brenzinger, Chr. Ed.; VCH Verlagsgesellschaft mbH: Weinheim, 1991.
(30) Cornell, R. M.; Schwertmann, U. *The Iron Oxides: Structure, Properties, Reactions, Occurrence and Uses*; VCH−Verlag: Weinheim, 1996.
(31) McMaster, W. H.; Kerr Del Grande, N.; Mallett, J. H.; Hubbell, J. H. *Compilation of X-Ray Cross Sections*; Lawrence Livermore National Laboratory: 1969.
(32) Koningsberger, D. E.; Prins, R. *X-ray Absorption: Principles, Applications, Techniques for EXAFS, SEXAFS and XANES*; Wiley-Interscience: New York, 1988.
(33) Newville, M.; Livins, P.; Yacoby, Y.; Rehr, J. J.; Stern, E. A. *Phys. Rev. B* **1993**, *47*, 14126−14131.
(34) Ankudinov, L. A.; Ravel, B.; Rehr, J. J.; Conradson, S. D. *Phys. Rev. B* **1998**, *58*, 7565−7576.
(35) Blake, R. L.; Hessevick, R. E.; Zoltai, T.; Finger, L. W. *Am. Mineral.* **1966**, *51*, 123−129.
(36) Maurice, P. A.; Leeb, Y.-J.; Hersmanc, L. E. *Geochim. Cosmochim. Acta* **2000**, *64*, 1363−1374.

(37) Nagtegaala, M.; Stroeveb, P.; Tremela, W. *Thin Solid Films* **1998**, *327*−*329*, 571−575.
(38) Plaschke, M.; Schäfer, T.; Bundschuh, T.; Ngo Manh, T.; Knopp, R.; Geckeis, H.; Kim, J. I. *Anal. Chem*. **2001**, *73*, 4338−4347.
(39) Rodrigez-Carvajal, J. *FULLPROF: A program for Rietveld refinement and pattern matching analysis;* Proceedings of Powder diffraction, Abstracts of the satellite Meeting of the XVth Congress of the IUCr, 1990 Toulouse, France.
(40) Rodrigez-Carvajal, J. *FULLPROF.2k version 1.9c*; Laboratoire Léon Brillouin (CEA-CNRS): Saclay, 2001.
(41) Rothe, J.; Denecke, M. A.; Neck, V.; Mueller, R.; Kim, J. I. *Inorg. Chem*. **2002**, *41*, 249−258.
(42) Wassermann, S. R.; Allen, P. G.; Shuh, D. K.; Bucher, J. J.; Edelstein, N. M. *J. Synchrotron Rad*. **1999**, *6*, 284−286.

Received for review January 8, 2002. Revised manuscript received August 29, 2002. Accepted September 5, 2002.

ES025513F

Cluster analysis of soft x-ray spectromicroscopic data.

Ultramicroscopy (2004) **100**, 35.

Lerotic M., Jacobsen C., Schäfer T., and Vogt S.

Available online at www.sciencedirect.com
SCIENCE DIRECT®
Ultramicroscopy 100 (2004) 35–57
ultramicroscopy
www.elsevier.com/locate/ultramic

Cluster analysis of soft X-ray spectromicroscopy data

M. Lerotic[a,*], C. Jacobsen[a], T. Schäfer[b], S. Vogt[c]

[a] *Department of Physics and Astronomy, State University of New York at Stony Brook, Stony Brook, NY 11794-3800, USA*
[b] *Forschungszentrum Karlsruhe, INE, P.O. Box 3640, 76021 Karlsruhe, Germany*
[c] *Argonne National Laboratory, Argonne, IL 60439-4856, USA*

Received 13 August 2003; received in revised form 6 January 2004; accepted 26 January 2004

Abstract

Soft X-ray spectromicroscopy provides spectral data on the chemical speciation of light elements at sub-100 nm spatial resolution. When all chemical species in a specimen are known and separately characterized, existing approaches can be used to measure the concentration of each component at each pixel. In other cases (such as often occur in biology or environmental science), some spectral signatures may not be known in advance so other approaches must be used. We describe here an approach that uses principal component analysis to orthogonalize and noise-filter spectromicroscopy data. We then use cluster analysis (a form of unsupervised pattern matching) to classify pixels according to spectral similarity, to extract representative, cluster-averaged spectra with good signal-to-noise ratio, and to obtain gradations of concentration of these representative spectra at each pixel. The method is illustrated with a simulated data set of organic compounds, and a mixture of lutetium in hematite used to understand colloidal transport properties of radionuclides.

PACS: 07.05.Kf; 07.85.Tt; 61.10.Ht; 78.70.Dm

Keywords: X-ray microscopy; X-ray spectromicroscopy; Principal component analysis; Cluster analysis

1. Introduction

Spectromicroscopy is a powerful tool which provides a way to see chemical speciation with the spatial resolution of a microscope. It can be carried out using photon absorption (from X rays to the infrared), X-ray fluorescence excitation, or electron energy loss, especially when plural inelastic scattering can be ignored. In studies of specimens where only a few chemical species are present (such as polymer blends), the data can be interpreted straightforwardly using reference spectra of pure components. In other situations such as in biology or environmental science, this approach may not be possible due to compositional complexity.

We describe here a method to find natural groupings of data without prior knowledge of the spectra of all components [1]. Drawing upon prior discussions of multivariate statistical analyses of energy loss electron microscopy data [2,3], we

*Corresponding author. Tel.: +1-631-632-8093; fax: +1-631-632-8101.
E-mail address: lerotic@xray1.physics.sunysb.edu (M. Lerotic).

0304-3991/$ - see front matter © 2004 Elsevier B.V. All rights reserved.
doi:10.1016/j.ultramic.2004.01.008

describe a particular approach that provides experimentally useful information for X-ray spectromicroscopy. We use principal component analysis [4] to orthogonalize spectromicroscopy data, and discard much of the noise present in the data. We then use cluster analysis or unsupervised pattern matching [5] to classify pixels according to the similarity of their spectra, and then recover gradations of thicknesses of representative materials using these observable spectra. This approach can nicely visualize nanoscale speciation in complex specimens.

1.1. Data sets

In order to illustrate clustering methods, we will make use of two soft X-ray spectromicroscopy data sets. One is an experimental data set acquired at the oxygen K absorption edge using the Stony Brook STXM IV microscope [6,7] at the beamline X1A2 at the National Synchrotron Light Source. The other is a simulated data set, using experimentally determined carbon K edge spectra of several amino acids [8]. The experimental data are acquired as a series of transmission images in (x, y) at nearby photon energies E [9], which provides the same (x, y, E) data as would be obtained by acquiring a series of spectra at adjacent pixels.

The experimental data come from the application of soft X-ray spectromicroscopy to studies in environmental science. It is drawn from a study of lutetium structural incorporation in hematite, which has already been intensively characterized including Lu L-edge EXAFS and colloid migration studies [10–12]. Lutetium is commonly used as lanthanide homologue for the trivalent actinide americium. The understanding of Am(III) crystal structure entrapment and the maximum incorporation capacity in either stationary (e.g., canister corrosion) or mobile (e.g., colloidal transport at large distances to the "far field") iron phases is of paramount importance to the reliable prediction of radionuclide mobility in deep geological nuclear waste repositories. Studies on the oxygen K-edge pre-peak intensity, attributed to the unoccupied bands of primary O(2p)–Fe(3d) character, have shown that this pre-peak can be directly correlated with the proportion of Fe–O–Fe bonds or Fe substitution present in the mineral structure [13]. This pre-peak feature shows in addition a splitting (with absorption peaks at 530.0 and 531.7 eV) due to a crystal-field-induced difference between the energy levels of the t_{2g} and e_g orbitals. To investigate the maximum trivalent lanthanide/actinide entrapment capacity and possible recrystallization kinetics which would remove structurally incorporated Lu out of the hematite lattice, samples were prepared by crystallizing various mixtures (0–100 mol% Lu per mol Fe) precipitates of ferrihydrite according to the hematite synthesis conditions described by Schwertmann et al. [14]. Only the data of 5 mol% Lu per mol Fe substituted hematite will be discussed within this paper. The washed and freeze dried sample was re-suspended in purified, deionized water and directly dried on a Si_3N_4 window for measurement. This preparation procedure produced a sample with variations in both thickness and composition.

In order to explore the characteristics of the method in an example where the specimen composition and component spectra are known in advance, we will also use a simulated data set. This was formed by using experimentally-measured absorption spectra of pure thin films of collagen and the amino acids leucine and tyrosine ([8]; see Fig. 1). With the exception of a 10×10 pixel hole at the lower left corner, the specimen (in a 128×128 pixel array, giving $P = 16,384$ pixels) was assumed to have a uniform thickness of 200 nm. Most of the specimen was assumed to be 100% collagen; however, specific regions (in the shape of letters) were assumed to have different compositions. The letters A, B, and C were given a composition of 90%, 50%, and 10% leucine, respectively, and the letters D, E, and F were given a composition of 90%, 50%, and 10% tyrosine, respectively, with collagen making up the rest of the composition in each case. This artificial specimen was then "illuminated" with 1000 photons per pixel at each of 133 photon energies evenly spaced between 282 and 302 eV, corresponding to the near-edge absorption region of carbon. At each pixel and energy, the square root of the "transmitted" photons was multiplied by a normally distributed random number (Gaussian

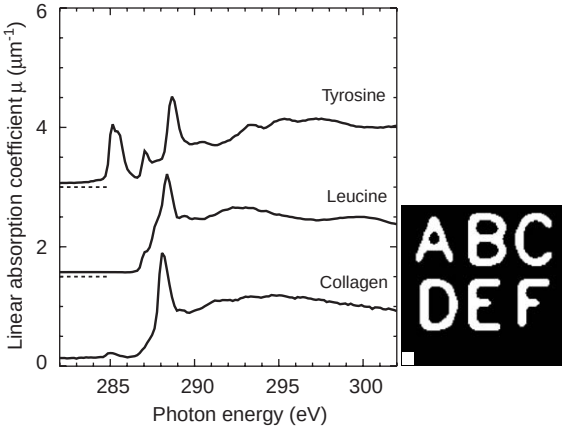

Fig. 1. Simulated soft X-ray spectromicroscopy data (left) used for constructing a simulated specimen. The spectra of the amino acids tyrosine and leucine were measured by Kaznacheyev et al. [8], and the collagen spectrum was measured by A. Osanna (unpublished). The black area in the specimen (right) was assigned the transmission spectrum of 200 nm of collagen. Letters A, B, and C were assigned the transmission spectra of 90%, 50%, and 10% leucine, respectively, with collagen to make a total thickness of 200 nm. Letters D, E, and F were assigned the transmission spectra of 90%, 50%, and 10% tyrosine, respectively, with collagen to make a total thickness of 200 nm. The square at lower left was assigned to be nonabsorbing so as to provide an I_0 flux normalization region.

distribution with a mean of zero and a standard deviation of one) and added to the transmitted photons (with the result constrained to be $\geqslant 0$) to approximate the Poisson statistics of photon counting.

2. Analysis of X-ray spectromicroscopy data

When an X-ray flux $I_0(E)$ is incident on a thin film with thickness t, the transmitted flux $I(E)$ is given by the Lambert–Beer law as

$$I(E) = I_0(E)\exp[-\mu(E)t]. \tag{1}$$

The linear absorption coefficient $\mu(E)$ can be written as

$$\mu(E) = 2r_e\frac{hc}{E}n_a f_2(E), \tag{2}$$

where f_2 represents the complex number of effective electrons per atom $[f_1(E) + if_2(E)]$ [15]. In this expression, $r_e = 2.818 \times 10^{-15}$ m is the classical radius of the electron, and $hc = 1239.852$ eV nm. The number density of atoms $n_a = (\rho N_A)/M$ is found from the mass density ρ, Avogadro's number N_A, and molar mass M; compound mixtures can be represented by calculating an element-weighted average of the product $\bar{n}_a\bar{f}_2(E)$. We define optical density $D(E)$ of the film to be

$$D(E) = -\ln\left(\frac{I(E)}{I_0(E)}\right) = \mu(E)t \tag{3}$$

so that we can obtain the thickness from $t = D(E)/\mu(E)$ if $\mu(E)$ is known.

2.1. Matrix treatment of spectromicroscopy

Spectromicroscopy data consist of a series of energy spectra at adjacent positions forming an image [16], or a "stack" of images [9,17] over a series of spectroscopically interesting energies. From these data indexed at $n = 1, \ldots, N$ energies, we form a data matrix $D_{N\times P}$ with columns indexed by $p = 1, \ldots, P$ for pixels, which in our case correspond to image positions as $p = i_{col} + (i_{row} - 1)n_{rows}$ where i_{col} and i_{rows} are both indexed from a starting value of 1. If we have $s = 1\ldots, S$ spectroscopically distinct components in the specimen, we can express the optical density at particular energy n and pixel p summed over all components as the sum of the thicknesses t_{sp} of all components s at the pixels p, and the spectra μ_{ns} of all components s at the energies n, as

$$D_{np} = \mu_{n1}t_{1p} + \mu_{n2}t_{2p} + \cdots + \mu_{nS}t_{Sp} = \sum_{s=1}^{S}\mu_{ns}t_{sp} \tag{4}$$

or, for all N energies indexing rows and P pixels indexing columns in matrix notation,

$$D_{N\times P} = \mu_{N\times S}\cdot t_{S\times P}. \tag{5}$$

If we know the set of exact absorption spectra $\mu_{N\times S}$ for all of the $s = 1\ldots S$ known components, we can calculate spatially-resolved thickness maps $t_{S\times P}$ of the components by matrix inversion of Eq. (5) as

$$t_{S\times P} = (\mu_{N\times S})^{-1}\cdot D_{N\times P}. \tag{6}$$

The inversion of the matrix $\mu_{N\times S}$ can be accomplished using singular value decomposition (see Appendix A), leading to quantitative maps of specimen composition [18,19]. Equivalent results have also been obtained using curve-fitting methods to obtain thickness maps based on known spectra (A. Hitchcock, personal communication).

2.2. Principal component analysis

In many cases, particularly in biology or environmental science, the specimen cannot be assumed to be made up of a simple combination of a limited number of components for which reference spectra are known a priori. One approach to handle these cases involves the use of principal component analysis (PCA) to characterize the data set in terms of its most significant variations without prior knowledge of their characteristics. From its origin in the social sciences, it has been used extensively in chemistry [4] and, more recently, in X-ray absorption spectroscopy [20], electron energy-loss spectrum imaging [3], and X-ray spectromicroscopy [21,22].

The goal in PCA is to describe the specimen by a set of $s = 1 \ldots S_{\text{abstract}}$ abstract components (where $S_{\text{abstract}} \leqslant N$) [4]. These abstract components describe the main spectroscopic signatures in the data; each signature may in fact arise from a linear combination of several different chemical species, so that there is not a simple, direct relationship between one particular abstract component and one particular chemical component of the specimen. As a result, in PCA we seek to characterize the specimen not in terms of known spectra $\mu_{N\times S_{\text{physical}}}$ and thicknesses $t_{S\times P}$, but in terms of column and row matrices

$$D_{N\times P} = C_{N\times S_{\text{abstract}}} \cdot R_{S_{\text{abstract}}\times P}, \tag{7}$$

where the column matrix $C_{N\times S_{\text{abstract}}}$ contains in each column a spectrum (with N points) of one of the S_{abstract} components, while the row matrix $R_{S_{\text{abstract}}\times P}$ contains in each row an image (with P pixels) of one of the S_{abstract} components.

One method for calculating the column matrix $C_{N\times S_{\text{abstract}}}$ is to use the covariance of the data (singular value decomposition can also be used, as described in Appendix B, but at a much greater cost in terms of computer storage and calculation time). One can calculate either a spectral covariance $Z_{N\times N}$ or a spatial covariance $Z_{P\times P}$ (see Appendix C); we describe here the calculation based on spectral covariance $Z_{N\times N}$ which is preferred when $N < P$. The spectral covariance matrix is formed from the data matrix as

$$Z_{N\times N} = D_{N\times P} \cdot D^{\mathrm{T}}_{P\times N}, \tag{8}$$

so that it measures the correlation between images at various energies. Because the correlation of the image at energy n_1 with the image at energy n_2 is the same as the correlation of n_2 with n_1, the covariance matrix $Z_{N\times N}$ is symmetric. We then wish to find the eigenvectors (which we will henceforth call eigenspectra) and eigenvalues $\lambda(s)$ that fully span the covariance matrix:

$$Z_{N\times N} \cdot C_{N\times S_{\text{abstract}}} = C_{N\times S_{\text{abstract}}} \cdot \Lambda_{N\times N}, \tag{9}$$

where $S_{\text{abstract}} = N$, and $\Lambda_{N\times N}$ is a diagonal matrix whose diagonal elements are given by the eigenvalues $\lambda(s)$ for $s = 1 \ldots N$. Columns of the eigenspectra matrix $C_{N\times S_{\text{abstract}}}$ consist of the N eigenspectra sorted in the order of decreasing magnitude of corresponding eigenvalues $\lambda(s)$, as anticipated by Eq. (7), with $S_{\text{abstract}} = N$. We can also find a corresponding eigenimage matrix $R_{S_{\text{abstract}}\times P}$ from

$$R_{S_{\text{abstract}}\times P} = C^{\mathrm{T}}_{S_{\text{abstract}}\times N} \cdot D_{N\times P}, \tag{10}$$

where we have used the fact that C is orthogonal (being composed of eigenvectors) so that its inverse is its transpose, $C^{-1} = C^{\mathrm{T}}$. It should be emphasized that the eigenspectra $C_{N\times S_{\text{abstract}}}$ and eigenimages $R_{S_{\text{abstract}}\times P}$ are calculated directly from the data with no prior assumptions.

Examination of the eigenspectra and eigenimages by themselves can provide considerable insight into the data [21,22]. As an example, the first few eigenspectra of the lutetium/hematite data are shown in Fig. 2. The first eigenspectrum is essentially an average of the spectra at all P pixels, so it looks like a recognizable X-ray absorption spectrum, and the first eigenimage shows an average of all N images corresponding roughly to a thickness map of the specimen. The second eigenspectrum gives the first correction to that average, and the third eigenspectrum gives the next

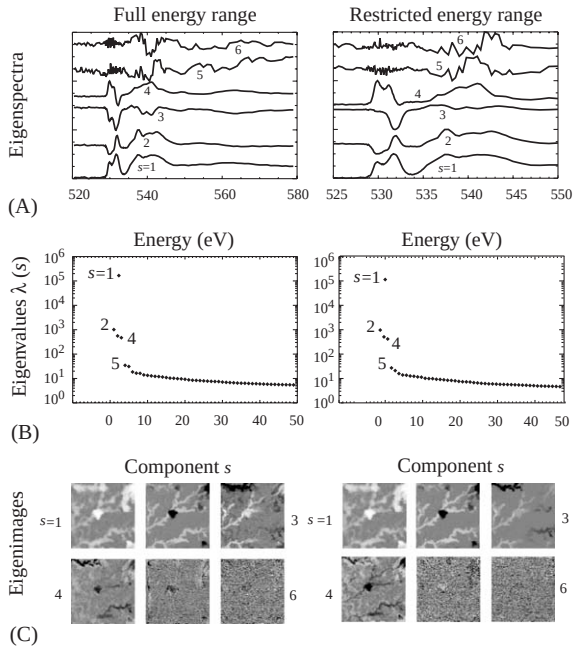

Fig. 2. Illustration of eigenspectra (A), eigenvalues (B), and eigenimages (C) for the lutetium/hematite data. Results for both the full 520–580 eV energy range with $\bar{S}_{\text{abstract}} = 5$, and also for a restricted 525–550 eV energy range with $\bar{S}_{\text{abstract}} = 4$, are shown. Of the eigenspectra $C_{N\times s}$ (from Eq. (9)) shown in (A), the first represents an average absorption spectrum, while subsequent eigenspectra represent successive corrections to this average that are required to represent the spectra present in the pixels of the data until eigenspectra 5 and 6 begin to represent mostly variations in noise from pixel to pixel. The eigenvalues $\lambda(s)$ of Eq. (9) shown in (B), which multiply the eigenspectra when reproducing the covariance matrix $Z_{N\times N}$, also indicate the decreasing significance of successive components. The eigenimages $R_{s\times P}$ (from Eq. (10)) shown in (C) go from showing something that is close to total thickness at $s = 1$ to only noise at $s = 6$ (full energy range) or $s = 5$ (restricted energy range). It should be noted that the eigenimages can have positive and negative values; they are shown here on a grey scale where white corresponds to maximum positive values, black corresponds to maximum negative values, and zero is the shade of grey exactly halfway between black and white.

correction to the first two, and so on, so that eigenspectra beyond the first do not look like recognizable X-ray absorption spectra. This emphasizes the point that the components we have found are *abstract* rather than physical. As the eigenspectrum index s is increased, we reach a point where the eigenspectra show increasingly random fluctuations from one energy n to another, and the eigenimages have the "salt and pepper" appearance of noise images. At this point, the variations being represented are no longer those of significant spectral variations in the data, but simply represent random variations due to noise. We therefore conclude that there is a subset of *significant* components $\bar{S}_{\text{abstract}}$ that fully represent the meaningful variations in the data. There may in fact still be imbedded errors due to experimental errors (such as detector nonlinearities) that are mixed in with the $\bar{S}_{\text{abstract}}$ correct factors, but the significant components $\bar{S}_{\text{abstract}}$ exclude the extracted error [23,4, Chapter 4].

It is of course desirable to find a measure of $\bar{S}_{\text{abstract}}$, and one such measure that is said to be particularly robust is the factor indicator function IND(s) [4, Eq. (4.63)] which reaches a minimum when $s = \bar{S}_{\text{abstract}}$. However, in our experience the factor indicator function is not a good predictor of $\bar{S}_{\text{abstract}}$ for X-ray spectromicroscopy data sets, and one must instead determine an appropriate value of $\bar{S}_{\text{abstract}}$ by examining several factors:

(1) Examination of the eigenvalues $\lambda(s)$. The first few eigenvalues decrease rapidly as they measure increasingly subtle variations in spectral signature. One then enters a regime where there is a slow decrease in the eigenvalues associated with successive components of noise. The correct number of reduced components $\bar{S}_{\text{abstract}}$ is approximately at the "knee" of the eigenvalue plot.
(2) Examination of the quality of the reproduction of an experimental spectrum using only $\bar{S}_{\text{abstract}}$ eigenspectra, as will be discussed below (see Figs. 3 and 14).
(3) Examination of the eigenimages to see if there appears to be significant structure present, or if only random pixel-to-pixel variations ("salt and pepper" noise) appear.

In the lutetium/hematite data set of Fig. 2, examination of the data over the entire energy range of 520–580 eV suggests a value of $\bar{S}_{\text{abstract}} = 5$ so as to fully represent all nonnoise variations of the data. However, the small amount of structure shown in the $s = 5$ eigenimage seems to be primarily due to slight differences in absorption in the spectroscopically uninteresting range of

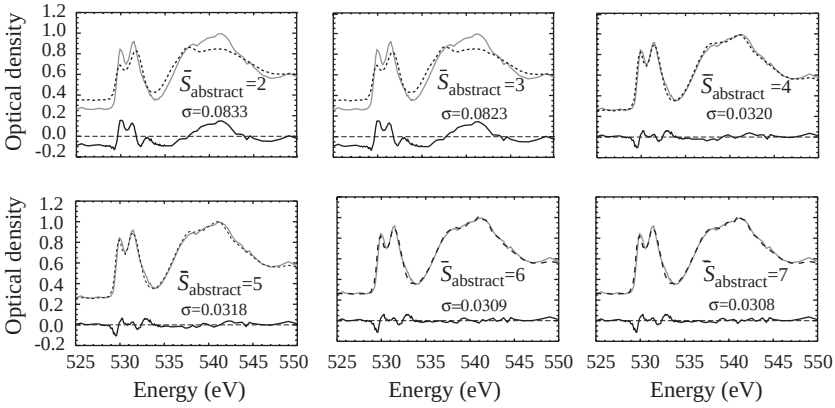

Fig. 3. Example of the fitting of a single physical spectrum according to Eq. (13) with several choices of $\bar{S}_{abstract}$. The physical spectrum (solid line) in this case was obtained in a separate measurement of a pure hematite specimen; we show here the results of fitting this spectrum using increasing number of eigenspectra from the reduced energy range lutetium/hematite components of Fig. 2. The fitted spectra are shown as dashed lines, and the residual errors of the fit are shown below along with their root variance σ. A significant decrease in the root variance σ results when the $s = 4$ eigenspectrum is added to the fit, in agreement with the observation in Fig. 2 that $\bar{S}_{abstract} = 4$ is appropriate for the lutetium/hematite data. Little further improvement in the fit is obtained by including subsequent eigenspectra. Some slight systematic error between the pure hematite spectrum and the lutetium/hematite data remains even as the number of eigenspectra are increased; this was possibly caused by slightly different specimen thicknesses and background signals leading to subtle changes in peak shapes between the two measurements.

550–580 eV, as illustrated by the $s = 5$ eigenspectrum for the full energy range data. We have therefore re-calculated the components using only the data in the energy range 525–550 eV, where most of the oxygen near-edge structure is contained. The resulting components, also shown in Fig. 2, indicate that the important near-edge variations in the data are adequately represented by $\bar{S}_{abstract} = 4$. It is our experience that restricting the energy range of the data in this manner is usually desirable. We will use this restricted energy range with $\bar{S}_{abstract} = 4$ in subsequent analysis of the lutetium/hematite data.

We can now determine a reduced version of our data which we define by

$$D'_{N\times P} = C_{N\times \bar{S}_{abstract}} \cdot R_{\bar{S}_{abstract}\times P}, \tag{11}$$

which of course differs from Eq. (7) only by the restriction of using only $\bar{S}_{abstract}$ significant components rather than the full set of $S_{abstract} = N$ components. If we have been careful in our choice of $\bar{S}_{abstract}$, this reduced data matrix should represent all the meaningful information of our original data, with the extracted error [23,4, Chapter 4] removed. This reduced data matrix has an additional important feature that will be exploited in cluster analysis: it is formed out of orthogonal eigenspectra ordered in degree of their significance (as determined by their eigenvalues $\lambda(s)$ in Eq. (9)), separating successively important variations in the data into successive indices s of $\bar{S}_{abstract}$. This orthogonalized, noise-filtered representation of the data is a good "space" to search for patterns in the data.

2.3. Fitting physical spectra using principal components

Having found a reduced set of eigenspectra and eigenimages that describes the data, we assume that there must exist a transformation matrix T that allows one to re-create actual spectra $\mu_{N\times S_{physical}}$ and thickness images $t_{S_{physical}\times P}$ from the $\bar{S}_{abstract}$ number of principal components. This transformation must satisfy

$$D'_{N\times P} = (C_{N\times \bar{S}_{abstract}} \cdot T_{\bar{S}_{abstract}\times S_{physical}}) \cdot (T^{-1}_{S_{physical}\times \bar{S}_{abstract}} \cdot R_{\bar{S}_{abstract}\times P}), \tag{12}$$

whereas the reduced data matrix of Eq. (11) is assumed to be formed from $D'_{N\times P} = C_{N\times \bar{S}_{abstract}} \cdot R_{\bar{S}_{abstract}\times P}$. Comparing Eq. (12) with Eq. (5), it can

be seen that physical spectra can be associated with eigenspectra by

$$\mu_{N\times S_{\text{physical}}} = C_{N\times \bar{S}_{\text{abstract}}} \cdot T_{\bar{S}_{\text{abstract}}\times S_{\text{physical}}}. \quad (13)$$

The transformation matrix T can therefore be determined from the eigenspectra and physical spectra to be

$$T_{\bar{S}_{\text{abstract}}\times S_{\text{physical}}} = C^{\text{T}}_{\bar{S}_{\text{abstract}}\times N} \cdot \mu_{N\times S_{\text{physical}}}, \quad (14)$$

where we have again used the fact that C is orthogonal so $C^{-1} = C^{\text{T}}$. With T thus determined, we can also represent the thickness maps $t_{S_{\text{physical}}\times P}$ from the eigenimages by

$$t_{S_{\text{physical}}\times P} = T^{-1}_{S_{\text{physical}}\times \bar{S}_{\text{abstract}}} \cdot R_{\bar{S}_{\text{abstract}}\times P}. \quad (15)$$

While the transformation matrix $T_{\bar{S}_{\text{abstract}}\times S_{\text{physical}}}$ involves the matrix of orthogonal eigenspectra $C^{\text{T}}_{\bar{S}_{\text{abstract}}\times N}$, it also involves the matrix of target spectra $\mu_{N\times S_{\text{physical}}}$ which has no guarantee of being orthogonal. We therefore must invert the transformation matrix without assuming orthogonality; this can be accomplished using singular value decomposition as described in Appendix A.

Evaluating the quality of the reproduction of an experimental spectrum $\mu_{N\times s_{\text{physical}}}$ from $\bar{S}_{\text{abstract}}$ eigenspectra according to Eq. (13) provides a very good means of judging the proper choice of $\bar{S}_{\text{abstract}}$ in X-ray spectromicroscopy. As Fig. 3 shows, selection of a reasonable value of $\bar{S}_{\text{abstract}}$ allows one to obtain a fitted spectrum that recreates the physically significant elements of the experimental spectrum while rejecting noise. Of course, if the physical spectrum is not well represented by either the full $S_{\text{abstract}} = N$ or restricted $\bar{S}_{\text{abstract}}$ set of eigenspectra (meaning the eigenspectra do not fully span the spectral set in which the physical spectrum lies), it will be impossible to fully recreate its spectral signature. This can happen if the physical spectrum is acquired in a separate measurement where different systematic errors apply. This effect can be seen in the residual to the physical spectrum fit in Fig. 3, but it is absent when reconstructing cluster spectra as will be shown in Fig. 14.

2.4. Comments on data preprocessing

It is not uncommon for researchers in spectromicroscopy or spectrum imaging analysis to carry out a number of preprocessing operations on their data. We therefore comment on them from a point of view of applying them to X-ray spectromicroscopy data, and illustrate results using some of these approaches in Fig. 4:

- In infrared spectroscopy, it is common to take the second derivative of spectra prior to classifying them [24] to increase their visual distinguishability. This is a less desirable step in X-ray and electron approaches because radiation damage considerations lead the experimentalist to acquire quantum-noise-limited spectra which result in very noisy derivatives. In addition, it is reasonable to expect that a covariance test of spectral difference might work just as well on raw data as well as on second-derivative data, since the same energy-to-energy difference information is contained in both representations.
- It is tempting to consider applying some sort of spectral smoothing to the data prior to principal component analysis. We have succumbed to this temptation in explorations of different approaches, but we have subsequently rejected it. Spectral filtering slightly alters the shape of the eigenvalue versus component curves such as are shown in Fig. 2B, but the "knee" in these curves still exists and the characteristics of the eigenspectra at the transition from $\bar{S}_{\text{abstract}}$ significant to $S > \bar{S}_{\text{abstract}}$ insignificant components are much the same. Indeed, the goal of working with a reduced data representation based on $\bar{S}_{\text{abstract}}$ components is to remove those components with poor correlation, which naturally include quantum noise, and pre-smoothing of the data may be counterproductive by removing some of the noise that would otherwise be removed as extracted error [23,4, Chapter 4].
- Many researchers use covariance about the mean or mean centering. This involves subtracting the average spectrum from the spectrum of each

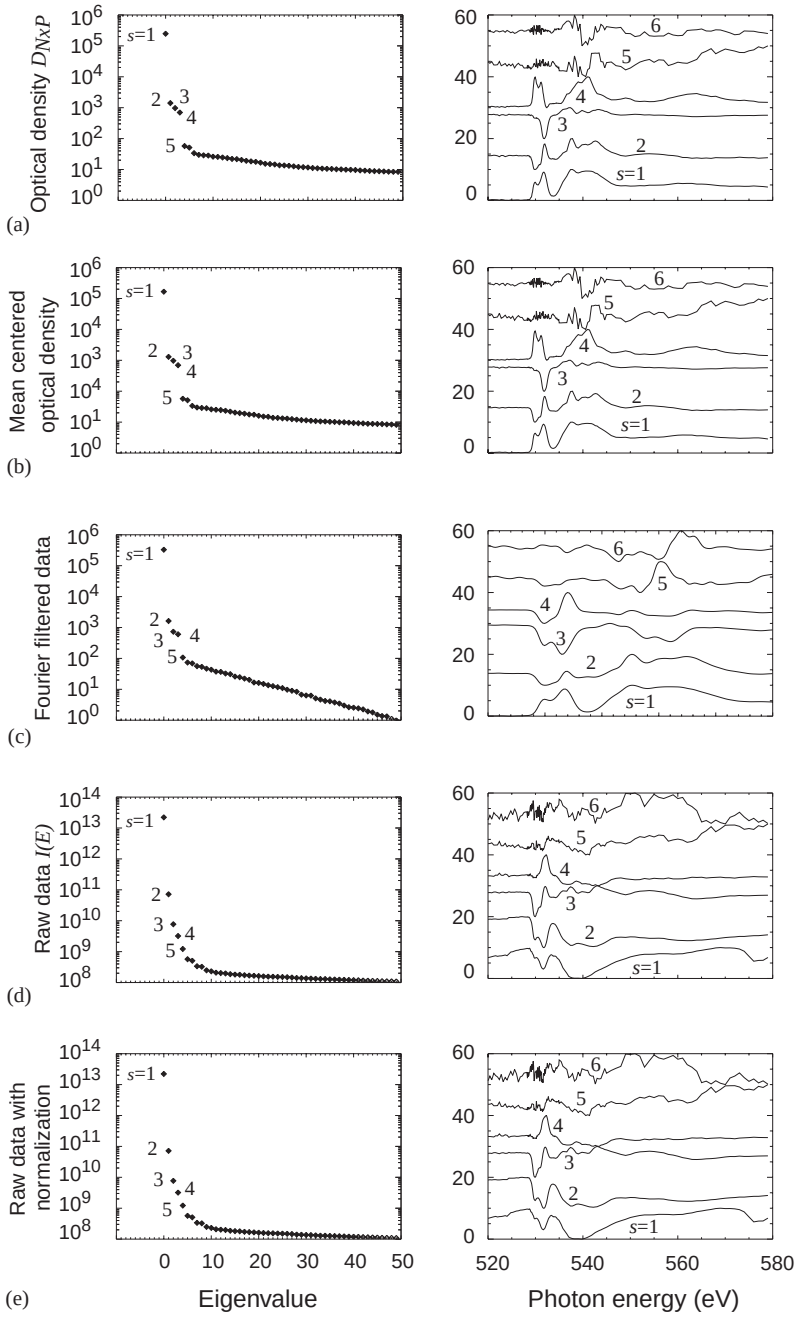

Fig. 4. Comparison of eigenvalues and eigenspectra obtained by PCA after various preprocessing operations have been applied to the data (see Section 2.4). We have chosen to work with the optical density $D_{N\times P}$.

pixel according to

$$D^{\#}_{N\times P} = D_{N\times P} - B_{N\times P}, \tag{16}$$

where $B_{N\times P}$ is a matrix where each row n consists of repeats of the value

$$b_n = \frac{1}{P}\sum_{p=1}^{P} D_{np}. \tag{17}$$

If mean centering is applied, information about the zero point of the experimental scale is lost [4] which is useful information in X-ray spectromicroscopy where one wants to distinguish absorbing from nonabsorbing regions. Indeed, the shapes of the eigenspectra obtained with and without mean centering are identical (Fig. 4), with differences only in pixel weights for the first eigenspectrum (which in the mean centered case have partly negative values, caused by centering the origin of the eigenspace at the average of the data points). As a result, we do not use mean centering in our analysis.

- In electron energy loss spectroscopy, plural inelastic scattering effects mean that one cannot do a simple normalization of the data to obtain a linear optical density $D(E) = -\ln[I(E)/I_0(E)]$. As a result, several authors renormalize the raw data $I(E)$ according to the square root of row or column averages as required for factorial analysis of correspondence [25] rather than covariance analysis. This weights individual pieces of data according to their statistical significance. We have not chosen to apply this approach because of our desire to preserve a data matrix $D_{N\times P}$ or reduced, noise-filtered data matrix $D'_{N\times P}$ which can be used in proportional equations (Eqs. (6) and (15)) to obtain thickness maps. Different adjustments applied to each energy n or pixel p would violate that simple proportionality. In particular, by using the reduced data matrix $D'_{N\times P}$ in principal component analysis, we have removed the spectral components with poor covariance (such as uncorrelated quantum statistical noise) as extracted error, which may provide much of the same effect of emphasizing data with good statistics.

For these reasons we have chosen to adopt the "first analyze, then process" philosophy advocated by Trebbia and Bonnet [25].

3. Cluster analysis

Application of principal component analysis to spectromicroscopy data has given us a very useful intermediate result: we can now gain insight into our data matrix $D_{N\times P}$ in terms of a reduced set of principal eigenspectra $C_{N\times \bar{S}_{\text{abstract}}}$ and eigenimages $R_{\bar{S}_{\text{abstract}}\times P}$. These eigenspectra and eigenimages are noise-filtered and orthogonalized into components sorted by their degree of covariance, and thus significance. However, it is only in the case where we know of the spectra of all physical components of the specimen, and thus the full matrix $\mu_{N\times S_{\text{physical}}}$, that we are able to calculate the transformation matrix $T_{\bar{S}_{\text{abstract}}\times S_{\text{physical}}}$ of Eq. (14) to allow us to interpret our eigenspectra as real spectra, and our eigenimages as real images. In other words, we have to know the answer in order to interpret the answer, which of course is unsatisfying if one has an unknown specimen. Other strategies exist; for example, one can use oblique analysis [26] to seek a transformation matrix T from the $\bar{S}_{\text{abstract}}$ orthogonal coordinates provided by principal component analysis to a set of S coordinates that have the properties of being pure positive and lying near groupings of data.

We adopt here an alternative strategy: we seek a method of grouping pixels with similar experimentally-determined spectra together, and then analyze the entire data according to these major spectral themes found in the data. We implement this theme-with-variations approach using cluster analysis or unsupervised pattern matching algorithms [5].

Cluster analysis typically involves evaluation of groupings of data points in some data representation, followed by classification or assignment of subsets of data to specific clusters. What data representation might be best for seeking clusters? Let us compare our set of principal eigenimages $R_{\bar{S}_{\text{abstract}}\times P}$ of Eq. (10) with the original data matrix $D_{N\times P}$ of Eq. (5) or even its reduced version $D'_{N\times P}$ of Eq. (11). The data matrix expresses the signal at

each pixel p in terms of its spectral response over N energies, whereas the eigenimage matrix expresses the signal in terms of its degree of incorporation of each of $\bar{S}_{\text{abstract}}$ orthogonal components; of course, $\bar{S}_{\text{abstract}} < N$. It is natural therefore that we look for clustering of the data in the eigenimage matrix $R_{\bar{S}_{\text{abstract}} \times P}$ over the set of dimensions $\bar{S}_{\text{abstract}}$, so that we can take advantage of the eigenimage matrix properties of orthogonality and reduced dimensionality. Each pixel p is then represented by a weighting $R_{s,p}$ in each of the $s = 1 \ldots \bar{S}_{\text{abstract}}$ components. We can then attempt to locate cluster centers in this $\bar{S}_{\text{abstract}}$-dimensional space, and classify pixels according to their distances from these cluster centers. While a great many distance metrics are available [5], we will use here a simple Euclidian distance measure (that is, $\sqrt{x^2 + y^2 + z^2}$ if we have three data dimensions x, y, and z). However, we will make further modifications to the data before searching for clusters:

(1) As can be seen from Fig. 2, some eigenimages (in particular, the first eigenimage where $s = 1$) can have positive values for nearly all pixel weightings $R_{s,p}$. However, the clustering algorithm described below starts with initial guesses for cluster centers that are uniformly distributed about the origin. We therefore calculate the average value of each eigenimage

$$\langle R_s \rangle = \sum_{p=1}^{P} R_{s,p} \tag{18}$$

and subtract it from the eigenimage. This will shift the weighting coefficients of all P pixels for the sth component to be centered about the origin in that dimension, removing any offset bias in finding cluster centers on one side of the origin versus the other side. This modification will be used only for clustering of the data; the unmodified eigenimage matrix $R_{\bar{S}_{\text{abstract}} \times P}$ will be used in subsequent calculations.

(2) We noted above that the first component ($s = 1$) had an eigenspectrum that was representative of the average absorption spectrum. This first component will therefore in some sense measure only the thickness of the sample. Chemical variations are represented primarily in subsequent components $s = 2 \ldots \bar{S}_{\text{abstract}}$. We therefore allow the option of searching for clusters only over the dimensions $s = 2 \ldots \bar{S}_{\text{abstract}}$, rather than over all dimensions $s = 1 \ldots \bar{S}_{\text{abstract}}$.

(3) When orthonormalized eigenspectra are determined from the covariance of the data (Eq. (9)), the amplitudes for all eigenspectra are similar to each other even when weak variations of the data (and increasing imbedded error) are represented by increasing component indices s. Since the eigenimages $R_{S_{\text{abstract}} \times P}$ are calculated from the eigenspectra $C_{N \times S_{\text{abstract}}}$ according to Eq. (10), pixels will have similar amplitudes for weighting coefficients $R_{s,p}$ for all component indices. This may be undesirable, since we may want to give greater or lesser weighting to the components with increasing index s that describe increasingly subtle variations in the spectral signatures of the data, or ever decreasing contribution of a spectral component that is present in few pixels.

We therefore introduce a power-law scaling parameter γ that will multiply the origin-centered eigenimage weightings $R_{s \times P}$ for the P pixels at each component $s = 1 \ldots \bar{S}_{\text{abstract}}$ according to

$$R^{\text{scaled}}_{s \times P} = (R_{s \times P} - \langle R_s \rangle) \left(\frac{\lambda(1)}{\lambda(s)} \right)^{\gamma}. \tag{19}$$

Setting $\gamma = 0$ will eliminate any rescaling of eigenimage weightings $R_{s \times P}$. The sensitivity to higher component indices will be increased with $\gamma > 0$, and decreased with $\gamma < 0$. Setting γ to too large a value opens one to the risk of clustering pixels according to variations in their imbedded error [23,4, Chapter 4] which becomes more significant in higher index component indices s; in practice, we find that values of $\gamma \lesssim 0.5$ work well.

The combined result of these two adjustments gives us a scaled set of eigenimages $R^{\text{scaled}}_{\bar{S}_{\text{abstract}} \times P}$ where the $s = 1$ component can optionally be removed from consideration in classifying the data.

3.1. Cluster analysis algorithm: learning vector quantization

In the ideal situation, data points are arranged in a few tightly packed, well separated groups. The goal of the clustering algorithm is to find a partitioning that minimizes distances within the groups and maximizes distances between them. While a great number of clustering algorithms exist, we use here a learning vector quantization (LVQ) algorithm [27,28] (closely related to self-organizing map algorithms) over K iterations as illustrated on Fig. 5:

(1) We begin by assigning random positions to each of G cluster centers. The number of cluster centers G will usually be larger than the number of significant components $\bar{S}_{\text{abstract}}$; determination of the number of clusters G will be discussed later. The starting position or component "weight"

$$W_{\bar{S}_{\text{abstract}},g} = [w_{1,g}, \ldots, w_{S_{\text{abstract}},g}] \tag{20}$$

of the gth cluster center is randomly assigned on a uniform distribution over the range -1 to $+1$ in each dimension s.

(2) We now choose one pixel p^* at random and calculate the distance from that pixel to each of the G cluster centers. The "winning" cluster center g^* which is closest to the pixel in question is then moved toward the pixel by adjusting its weights according to

$$w'_{s,g^*} = w_{s,g^*} + \alpha_k[R^{\text{scaled}}_{s,p^*} - w_{s,g^*}] \times \text{for } s = 1 \ldots \bar{S}_{\text{abstract}}, \tag{21}$$

where $[R^{\text{scaled}}_{s,p^*} - w_{s,g}]$ is a component of the Euclidian vector distance from the old cluster center position $W_{\bar{S}_{\text{abstract}}}$ to the pixel position $R^{\text{scaled}}_{\bar{S}_{\text{abstract}} \times p^*}$. The coefficient α_k is a learning rate, which we adjust linearly from 0.3 to 0.1 over $K = 20$ iterations in the present work. Cluster centers other than the "winning" cluster g^* are not adjusted.

(3) We now repeat step 2 for all remaining pixels P, and then for all iterations K as the outer index of a nested loop with the learning rate α_k adjusted as noted above. We have found it important to iterate over a randomized ordering of pixels P; otherwise, cluster centers will acquire a bias towards the pixels at the lower left corner of the image (in our case, the starting pixel locations) if these pixels are used in succession at the start of the algorithm.

(4) After K iterations have been completed, we now assign each pixel p to be a member of the cluster g which the pixel is closest to the center of.

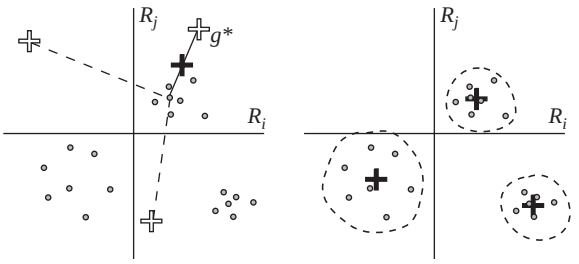

Fig. 5. Illustration of the learning vector quantization cluster algorithm used in this work (drawn from example IDL code by Habbersett [31]). Shown here are data points (pixels p) plotted based on their weights $R_{i,p}$ and $R_{j,p}$ in two eigenimages i and j. Left: a specified number of cluster centers G are originally located at random positions (open crosses). For each pixel p, the distance to all cluster centers is calculated, the "winning" cluster center g^* closest to the pixel is determined, and this cluster center is then moved towards the pixel (filled cross) according to the learning rate α_k. Right: at the conclusion of K iterations of this process through all pixels P, cluster centers are located in the midst of groups of pixels, and pixels are assigned to their "winning" cluster g^*.

We note that it is possible that some cluster centers g might be distant from all pixels p and thus never be chosen as the "winning" cluster g^* to be moved closer to a pixel. At the end of the algorithm, these cluster centers have no members, and they are removed from the list of clusters and the number of clusters G is adjusted accordingly. That is, bad initial guesses of cluster center positions will be abandoned rather than bias the clustering. We note that while in principle one can get different clustering results each time the algorithm is run due to different random choices of initial cluster positions, in practice we find good consistency between different runs of the algorithm on the same data. Finally, we have also implemented a K-means algorithm for locating cluster centers [5]. The results we have obtained

using K-means are quite similar to those obtained using the learning vector quantization method, except that we find that the boundaries of cluster regions in images are slightly smoother when using the learning vector quantization algorithm. As noted before, both algorithms use a measure of the distance from cluster centers, so in both cases the data are implicitly assumed to be clustered in hyperspheres.

Having assigned a cluster index g to all pixels P, we can visualize our result in several standard ways. A pseudo-color image of the specimen can be generated where each cluster index g is assigned a different color (see e.g., Fig. 6), and we can also display the number of pixels assigned to each cluster center. Histograms of distances of pixels from their respective cluster centers can be generated. These distances can also be shown for each pixel in a greyscale image where bright regions are those which are poorly classified by the number of cluster centers G chosen (see Fig. 7). Scatterplots provide another means to view the result of cluster analysis. For any pair of significant components i and j, one can plot the position of each pixel p based on its eigenimage weightings $R_{i,p}^{\text{scaled}}$ and $R_{j,p}^{\text{scaled}}$. The pixels can be color-coded based on their assigned cluster index g, and a number for the cluster index can be plotted based on its coordinates $(w_{i,g}, w_{j,g})$ in these two components. An example of such a scatterplot is shown in Fig. 8, which demonstrates that it is not always possible to recognize cluster center positions based on only two components. Fortunately, the clustering algorithm is able to "see" the data in all $\bar{S}_{\text{abstract}}$ components, and cluster the data accordingly.

3.2. Dendrograms and the number of clusters G

We now wish to determine the number of clusters G that should be chosen for classifying the data. A commonly used method for aiding this choice is to examine hierarchical trees or dendrograms of the clustered data [5,29]. These hierarchical

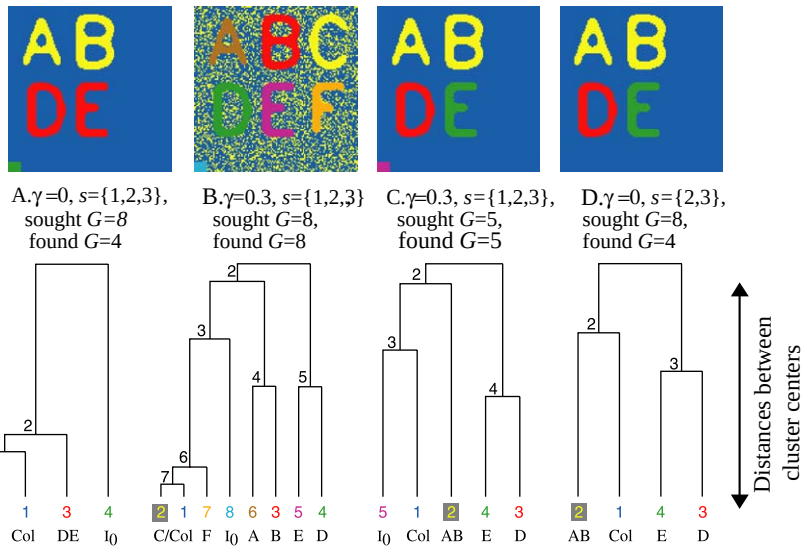

Fig. 6. Cluster analyses examples for the simulated data of Fig. 1. Cluster analysis was carried out where the number of clusters sought G and the eigenvalue power-law scaling term γ of Eq. (19) was adjusted as shown for each figure. In the rightmost figure, clustering was carried out based only on components $s = 2, 3$ rather than on the full set $s = 1, 2, 3$. The clustering results shown are representative rather than identically reproducible when seeking many clusters from different random starting cluster center locations. Note that if one were to merge clusters to a total number $G = 4$, the letters "A" and "B" (which are both made of different mixtures of leucine and collagen) would be clustered together, and letters "D" and "E" (which are both made of different mixtures of tyrosine and collagen) would clustered together in all cases. The letters "C" and "F" of only 10% leucine and tyrosine, respectively, are not often found by cluster analysis, though they show up in the cluster-spectrum-based thickness maps of Fig. 9.

Fig. 7. Error maps from cluster analysis. These images show the distance from a particular pixel to its cluster center. All displayed images are shown on the same scale, with the largest distance error shown as pure white. Regions which are not well described by a given number of clusters stand out clearly as being far from any cluster center.

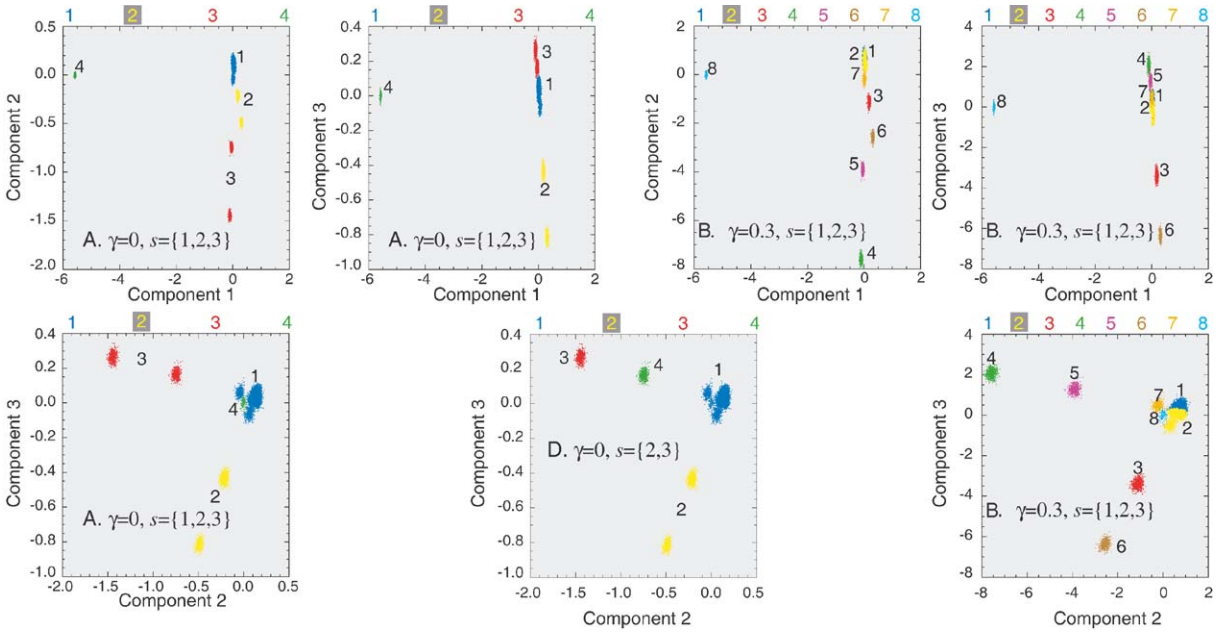

Fig. 8. Scatterplots of the simulated test data. Each pixel p has a weighting $R_{s,p}^{\text{scaled}}$ (Eq. (19)) in each of the $\tilde{S}_{\text{abstract}}$ components. These scatterplots show the position of all pixels (colored according to their assigned cluster in online version only) in any two of these components or dimensions, and the locations of the respective cluster centers (numbers offset slightly from their true locations for clarity) in these same dimensions. Clustering results A, B, and D from Fig. 6 are shown.

methods can be used as clustering algorithms in their own right, as well. Divisive hierarchical methods start with one cluster which contains all pixels P, and successively splits the pixels into increasing numbers of clusters based on distances from current cluster centers. Agglomerative hierarchical methods start out with each pixel in its own cluster; the two closest pixels are merged into a new common cluster, and this process is continued until all pixels are merged into one cluster. In our case, we will use hierarchical agglomeration not at the starting point of individual clusters for each pixel, but at a starting point of having already classified the data into G clusters. In other words, we use hierarchical agglomeration not to cluster individual pixels (which would be very time consuming); instead, we use hierarchical agglomeration on cluster

centers that have already been obtained using the LVQ or K-means algorithm.

For agglomerating clusters, distances between clusters can be determined by methods including measuring the distance between cluster centers (the centroid linkage), or determining the average of distances between all pairings of pixels from the two clusters (the average linkage). Having measured the distance between all clusters, one then merges the two clusters that are closest to each other into one new cluster with a position that is then set by using a distance matrix updated using the average linkage version of a recurrence formula [5, Eq. (4.2)]. Distances between clusters are then re-measured, and the process is repeated until there is only one cluster left. When using centroid linkage to calculate dendrograms, inversions or reversals can occur (see e.g., Fig. 4.8 of Everitt et al. [5]) which make interpretation more difficult. Such inversions do not occur when the average linkage is used, so this is the measure we have used for calculating the dendrograms shown here.

Agglomerative clustering is commonly visualized using a dendrogram (see e.g., Fig. 6), which illustrates the merger made at each step of the analysis. At the bottom are shown all G clusters provided by the initial cluster analysis; these are called the terminal nodes because they represent where division of the dendrogram ends. As two clusters are merged together into one, the distance between them serves as the branch distance along the vertical. In the final step, there is only one cluster left, which is called the root of the dendrogram.

This dendrogram can often be used to gain insight into a better choice of the number of clusters G. When many clusters are merged over a short distance along the dendrogram the distances between them are not very large so their characteristics are fairly similar. However, when the distance along the abscissa is large before two clusters are merged, then their characteristics are rather different. As a result, if one has a dendrogram which resembles several "arms" reaching down which eventually branch out into many "fingers" and "thumbs," a good estimate of the number of clusters is the number of "wrists" present in the dendrogram. This measure can be used along with other information the user has about the specimen.

3.3. Cluster spectra and thickness maps

Cluster analysis has provided us with a means to classify our data based on similarities between spectra. However, a disadvantage of the approach is that it provides an either/or answer: a pixel is determined to be a member of either one cluster or another. (We note that fuzzy clustering methods, where pixels are assigned a weight for membership in more than one cluster, also exist.) This is often helpful for understanding X-ray spectromicroscopy data, but of course a real specimen may well have gradations of composition which gradually change from one position to another. These gradations in composition will be masked by nonfuzzy cluster analysis, unless one uses a very large number G of clusters in which case the simplification one originally sought through cluster analysis is lost!

In order to reach our final goal of characterizing a sample based on continuous thicknesses of representative spectral signatures, we first obtain these signatures by calculating the average spectrum $\bar{D}_{N\times g}$ of all pixels within a cluster as

$$\bar{D}_{N\times g} = \sum_{j=1}^{P_g} D_{N\times j}/P_g, \tag{22}$$

where j indexes the P_g pixels p that are members of cluster g, and N is the array of photon energies. Because each cluster's spectrum $\bar{D}_{N\times g}$ will represent an average of all pixels with nearly identical spectra, it will have a signal-to-noise ratio that is greatly improved relative to individual pixel spectra. Now that we have this set of physical spectra that are present within the specimen, we can define a transformation matrix where the "signature" spectra matrix $\bar{D}_{N\times G}$ stands in for the measured physical spectra matrix $\mu_{N\times S_{\text{physical}}}$ to allow us to define a transformation matrix analogous to Eq. (14) of

$$T_{\bar{S}_{\text{abstract}}\times G} = C^{\mathrm{T}}_{\bar{S}_{\text{abstract}}\times N}\cdot \bar{D}_{N\times G}, \tag{23}$$

which in turn allows us to follow Eq. (15) to obtain pseudo-thickness maps $t_{G\times P}$ for the set of G "signature" spectra as

$$t_{G\times P} = T^{-1}_{G\times \bar{S}_{\text{abstract}}} \cdot R_{\bar{S}_{\text{abstract}}\times P} = T^{-1}_{G\times \bar{S}_{\text{abstract}}} \cdot C^{\mathrm{T}}_{\bar{S}_{\text{abstract}}\times N} \cdot D'_{N\times P}, \quad (24)$$

where we will use singular value decomposition to invert the matrix $T_{\bar{S}_{\text{abstract}}\times G}$. We note that $\mu_{N\times S_{\text{physical}}}$ could be assumed to contain spectra expressed as linear absorption coefficients in a reciprocal physical length, allowing $t_{S_{\text{physical}}\times P}$ to be interpreted as thicknesses in physical units. Because the cluster "signature" spectra $\bar{D}_{N\times G}$ are due to unknown thicknesses of unknown compounds, we cannot directly interpret the pseudo-thickness maps $t_{G\times P}$ in terms of physical thicknesses. (The same can be said of oblique analysis, where one determines a set of oblique spectra to be mapped [26].) Even so, the pseudo-thickness maps $t_{G\times P}$ and cluster spectra $\bar{D}_{N\times G}$ are immensely useful in allowing us to view continuous transitions from one "signature" spectrum to another at cluster boundaries.

4. Cluster analysis of simulated data

In order to illustrate the performance of the analysis methods described above, we first consider the case of the simulated specimen of Fig. 1. In Fig. 2 we saw that it is better to carry out PCA and subsequent cluster analysis only over a narrow, near-edge energy range. Examination of the spectra in Fig. 1 would suggest that for the test data a restricted energy range of 284–292 eV would be appropriate for examination; however, as a more demanding test we used the full energy range of 282–302 eV for the analyses shown here. Principal component analysis gave $\bar{S}_{\text{abstract}} = 3$ components, as one would expect for this simulated specimen composed of collagen, leucine, and tyrosine. We then carried out cluster analysis using the variations discussed in Section 3: we chose the eigenvalue power law scaling term γ of Eq. (19) to be either 0 or 0.3, we changed the number of clusters G sought, and we chose in one case to seek clusters only among components $s = 2, 3$ rather than the full set $s = 1, 2, 3$. As Fig. 6 shows, one can get slightly different clustering results with each choice of parameters, and indeed even with repeated clusterings with the same choice of parameters due to the fact that random cluster center positions are used as the starting point for each calculation. This would seem to indicate a lack of robustness in clustering, but examination of the dendrograms of Fig. 6 shows that in fact all clustering examples give the same classification of the essentials of the data: letters A and B are either grouped together or closely spaced on the same dendrogram branch, and the same applies to letters D and E. That is, the algorithm finds regions based on the similarity of their spectroscopic components, and also to a lesser extent based on their fractional thickness. In the case where overly aggressive clustering led to "salt and pepper" noise in the collagen background region, the erroneous result is readily recognizable, and the "salt and pepper" regions represent the last branch on the dendrogram which would be merged in the first step of agglomeration.

In addition to the dendrograms, it is helpful to look at the cluster distance error maps of Fig. 7. These figures show on a greyscale image the distance from each pixel to its "winning" cluster center g^*, and also several metrics of cluster distances: the maximum, the root mean squared, and the distance within which 95% of all pixels are located to their respective cluster centers. In a clustering run where the lowest-concentration letters C and F were not found, the distance error map very clearly shows that there are regions which were not properly clustered. It is also useful to consider the scatterplots of Fig. 8 of clustering runs A ($\gamma = 0$, components $s = 1, 2, 3$, sought $G = 8$, found $G = 4$ clusters), B ($\gamma = 0.3$, components $s = 1, 2, 3$, sought $G = 8$, found $G = 8$ clusters), and D ($\gamma = 0$, components $s = 2, 3$, sought $G = 8$, found $G = 4$ clusters) along with their respective cluster maps of Fig. 6. The scatterplot for clustering run B shows most clearly how each letter of the test data can be separated in principal component space, and also how clusters 1 and 2 are strongly overlapping and thus are the first to merge in the dendrogram of Fig. 6.

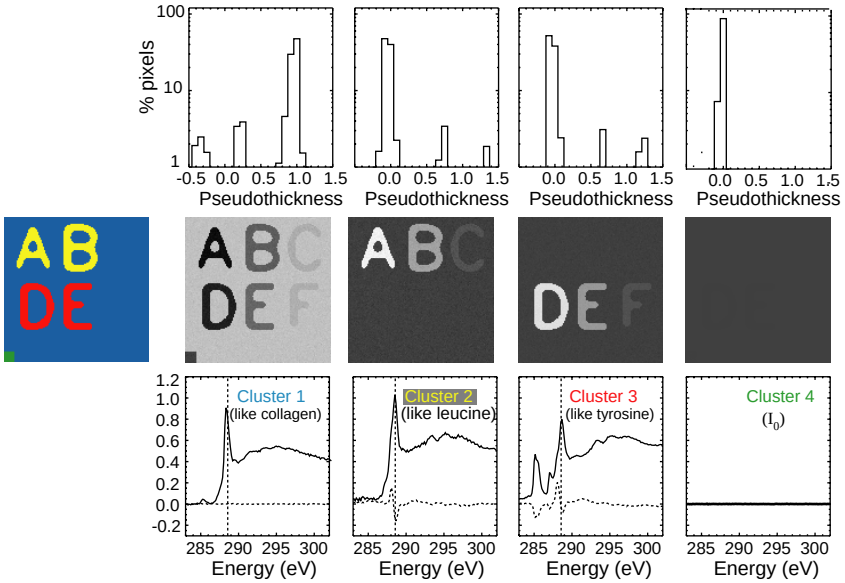

Fig. 9. Pseudo-thickness maps calculated using Eq. (24) for the spectra obtained from clustering run A ($\gamma = 0$, $s = 1, 2, 3$, sought $G = 8$ clusters) of Fig. 6. The thickness maps are shown in the middle image; the thicknesses for cluster 4 are all zero so the darker regions in the cluster 1 pseudo-thickness map are negative values as indicated by the histograms above each map. Plots of the cluster spectra are shown below, along with deviations from the spectra of the materials used to "build" the simulated data: collagen (with an absorption peak at 288.08 eV) associated with cluster 1, leucine (with a peak at 288.57 eV) associated with cluster 2, tyrosine associated with cluster 3, and the empty I_0 region of the specimen.

Our ultimate goal is to be able to come up with representative spectra for an unknown data set, and map thicknesses corresponding to these spectra. For our simulated data, we will use the results of clustering run A of Fig. 6. With these clusters, we show in Fig. 9 the cluster spectra $\bar{D}_{N\times g}$ calculated according to Eq. (22), and pseudo-thickness maps $t_{G\times P}$ calculated according to Eq. (24). As can be seen, the cluster spectra are very close to the collagen, leucine, and tyrosine spectra used to build the simulated data, with slight differences due to the fact that the pixels that were clustered together involved mixtures of leucine and collagen, or tyrosine and collagen, rather than the respective pure substances. Because the collagen spectrum is mixed into the spectra of clusters 2 and 3, the cluster 1 pseudo-thickness map shows some negative values. However, we also note that the low-concentration letters C and F do indeed show up in the pseudo-thickness maps even though they were not found by the clustering algorithm. This figure indicates how cluster analysis can be used to recover representative spectra from the data, and pseudo-thicknesses corresponding to these representative spectra.

5. Cluster analysis of lutetium/hematite data

We have carried out the analysis methods described above on the lutetium/hematite data described in Section 1.1. As shown in Fig. 2, $\bar{S}_{\text{abstract}} = 4$ principal components were used to describe the data in the energy range 525–550 eV. Examination of clustering results and dendrograms analogous to those shown in Fig. 6 showed that $G = 5$ clusters calculated using $\gamma = 0$ provided a reasonable segmentation of the data, as shown in Fig. 10. Cluster 1 is a mostly open region with very little optical density, while the spectrum of cluster 5 is similar to the pure hematite spectrum shown in Fig. 3 with nearly equal optical density at 530.0 and 531.7 eV. We can gain further insight into the

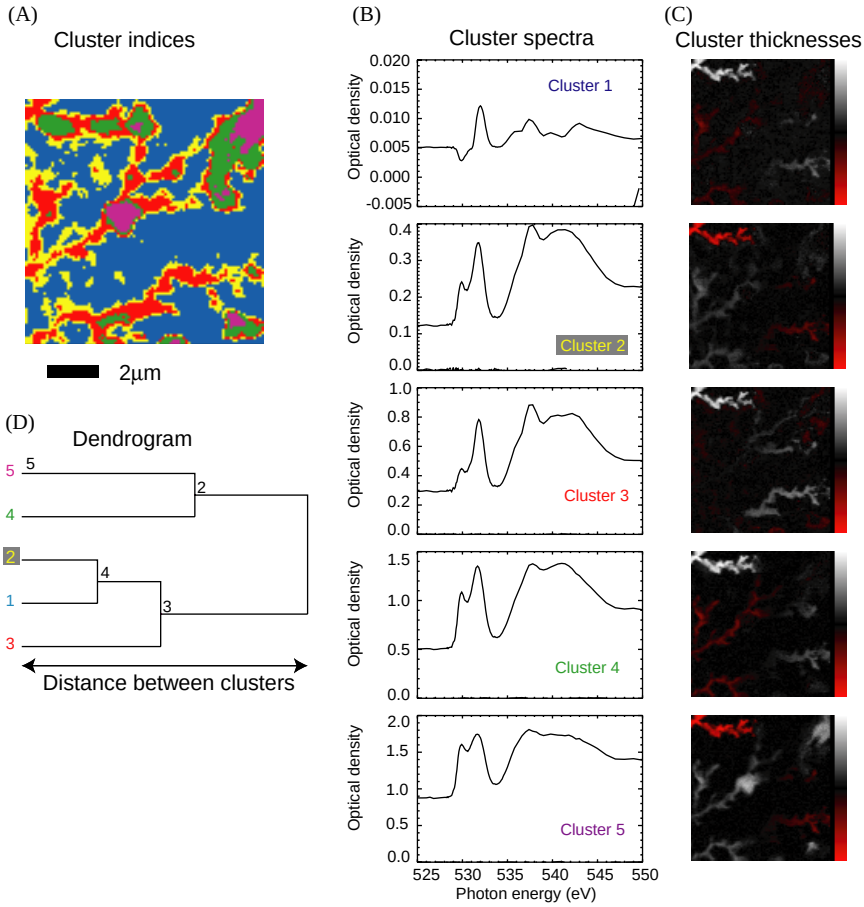

Fig. 10. Results of cluster analysis of the lutetium/hematite data, showing the cluster index image (A), cluster spectra $\bar{D}_{N\times G}$ (B), cluster pseudo-thickness maps $t_{G\times P}$ (C), and dendrogram (D). These results were obtained with the $s = 1$ component included in the cluster analysis, which was carried out with $\gamma = 0$. Cluster 1 shows very little absorption, cluster 5 is reminiscent of the pure hematite spectrum shown in Fig. 3, and clusters 2–4 show various degrees of incorporation of lutetium.

data by consideration of the dendrogram in Fig. 10. This shows that clusters 1 and 2 are most similar to each other in terms of weak absorption, even though their spectral signatures are rather different. Cluster 3 is then merged with these first two clusters, and its spectrum appears to be quite similar to that of cluster 2. Since clusters 2 and 3 both have decreased absorption at 530.0 eV relative to 531.7 eV, they can be interpreted as representing an increasing degree of substitution of Lu^{3+} for Fe^{3+} in the hematite matrix. Cluster 4 is merged with cluster 5; since its spectral shape is more similar to cluster 2 than cluster 5, cluster 4 can also be assumed to have a lesser but nonnegligible degree of lutetium incorporation into the hematite matrix. Its similarity to the nearly-pure-hematite of cluster 5 therefore must be based primarily on its greater optical density rather than on its chemical characteristics.

One problem in the clustering results of Fig. 10 is that the structure in the upper left appears not in one but in several pseudo-thickness maps, either as a positive pseudo-thickness (clusters 1, 3, and 4; grey regions) or as a negative one (clusters 2 and 5; red regions; color scale in online version only). Spectroscopically, clusters 2, 3 and 4 are fairly similar to each other, except in their overall scale of optical density, as noted above. These effects

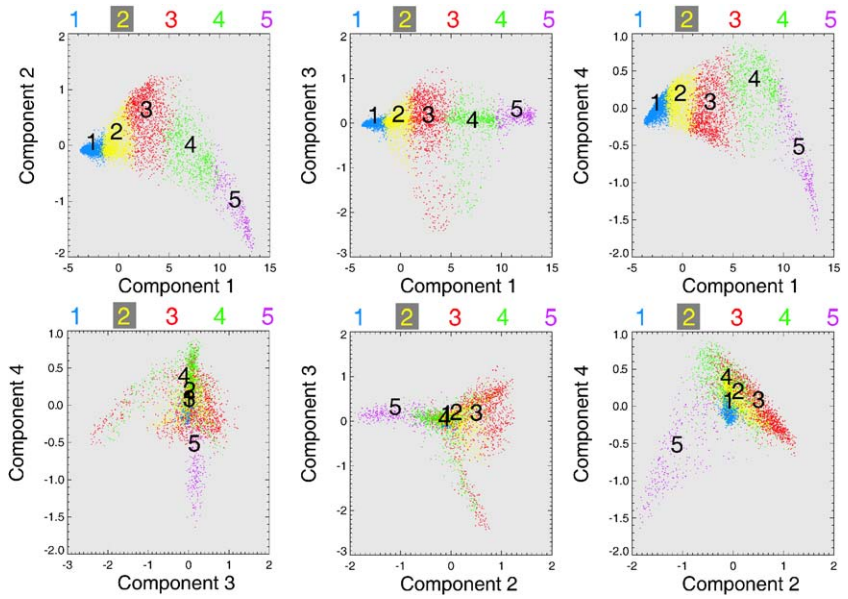

Fig. 11. Scatterplots of the pixel weightings $R^{\text{scaled}}_{s,p}$ of Eq. (19) for the lutetium/hematite data with the $s = 1$ component included in the analysis. The data are separated most distinctly by variations in component $s = 1$, which means that specimen thickness was responsible for most of the classification.

signal that the clustering algorithm classified pixels in part due to similarities in thickness, as can be confirmed by examination of the scatterplots involving component 1 in Fig. 11. A more desirable outcome might be to instead classify the data according to similarities in spectroscopic signature with thickness effects disregarded. As was noted in Section 2.2, the first or $s = 1$ component of principal component analysis is dominated by the average absorption spectrum of the entire specimen, and the $s = 1$ eigenimage is in some sense a map of thickness in the specimen without regard for composition.

We have therefore recalculated the clustering of the lutetium/hematite data with the first $s = 1$ eigenimage excluded, as described in Section 3. We again sought $G = 5$ clusters with an eigenvalue scaling factor of $\gamma = 0$. The results are shown in Figs. 12 and 13. The scatterplots of Fig. 13 now do not show the data separated based on one and only one component. The cluster spectra $\bar{D}_{N\times g}$ of Fig. 12 now show differences that are more pronounced in spectral signature than in overall optical density. (One can also carry out a cross-check of the correct number of abstract components $\bar{S}_{\text{abstract}}$ by examining the target spectrum fits of Eq. (13) for the real, physical spectra of selected clusters, as shown in Fig. 14.) It is perhaps even more informative to note that Fig. 12 now shows few red (online only), negative pseudo-thickness regions $t_{G\times P}$. As before, cluster 1 shows mostly residual weak absorption throughout the specimen. Cluster 2 has a spectrum very similar to that of the pure hematite spectrum shown in Fig. 3; cluster 5 has a spectrum which is quite similar but may show the onset of the well-known "thickness effect" in absorption spectroscopy where spectral shapes can become distorted due to less-strongly-absorbed, higher diffraction orders from the X-ray monochromator. What is particularly interesting is that clusters 3 and 4 show differing intensities of the 530 eV absorption peak indicating a changing degree of lutetium incorporation into the hematite matrix.

The cluster analysis of the lutetium/hematite oxygen K-edge spectromicroscopic data demonstrates that lutetium (5 mol% per mol Fe) is initially structurally incorporated in the hematite

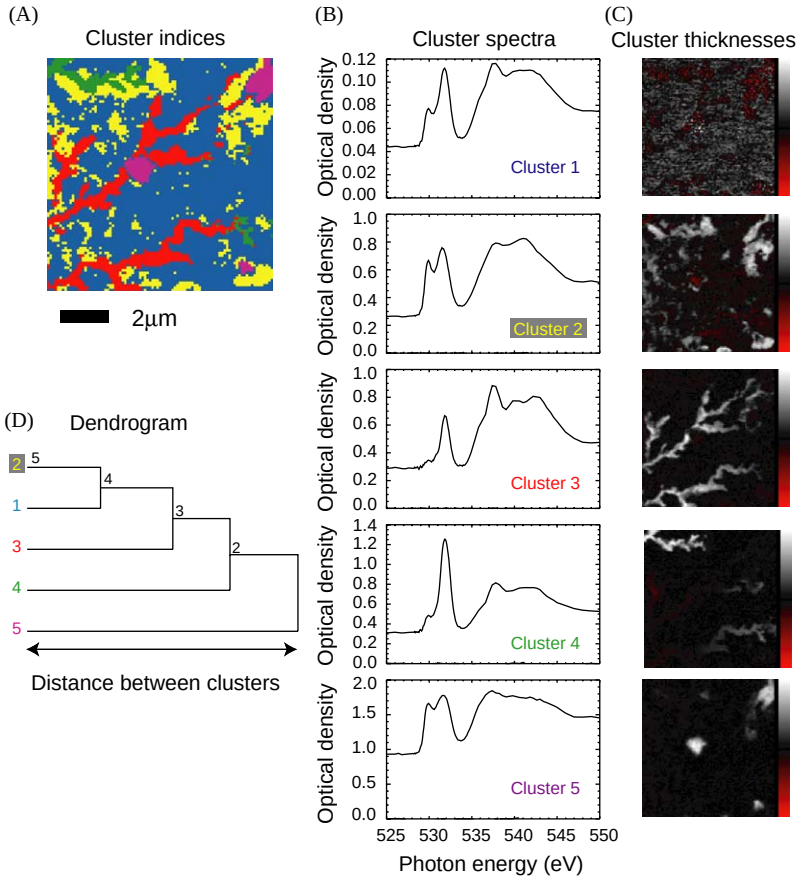

Fig. 12. Cluster analysis of the lutetium/hematite data with the first component excluded, showing the cluster index image (A), cluster spectra $\bar{D}_{N\times g}$ (B), cluster pseudo-thickness maps $t_{G\times P}$ (C), and dendrogram (D). These results were obtained with $\gamma = 0$. Compared to the $s = 1$–4 cluster results of Fig. 10, these $s = 2$–4 clustering results show few regions of negative pseudo-thickness $t_{G\times P}$ and clearer classification of the data based on chemical speciation as opposed to thickness.

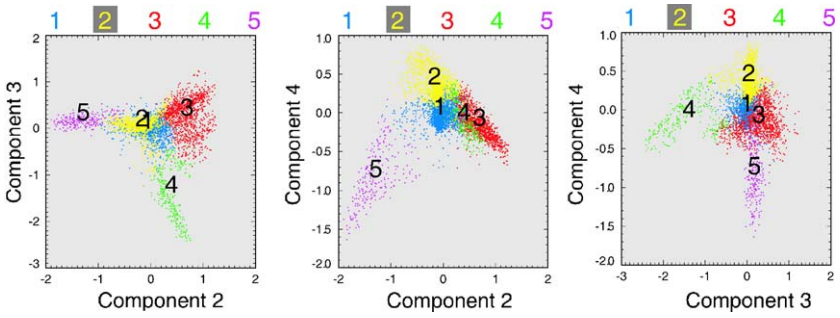

Fig. 13. Scatterplots of pixel weightings $R_{s,p}^{\text{scaled}}$ for the lutetium/hematite data clustered with the first component excluded. Compared to the $s = 1$–4 cluster results of Fig. 11, the data are now clustered by a combination of components, rather than based on one component only. This approach classifies the data more on its spectroscopic variations and less on its thickness.

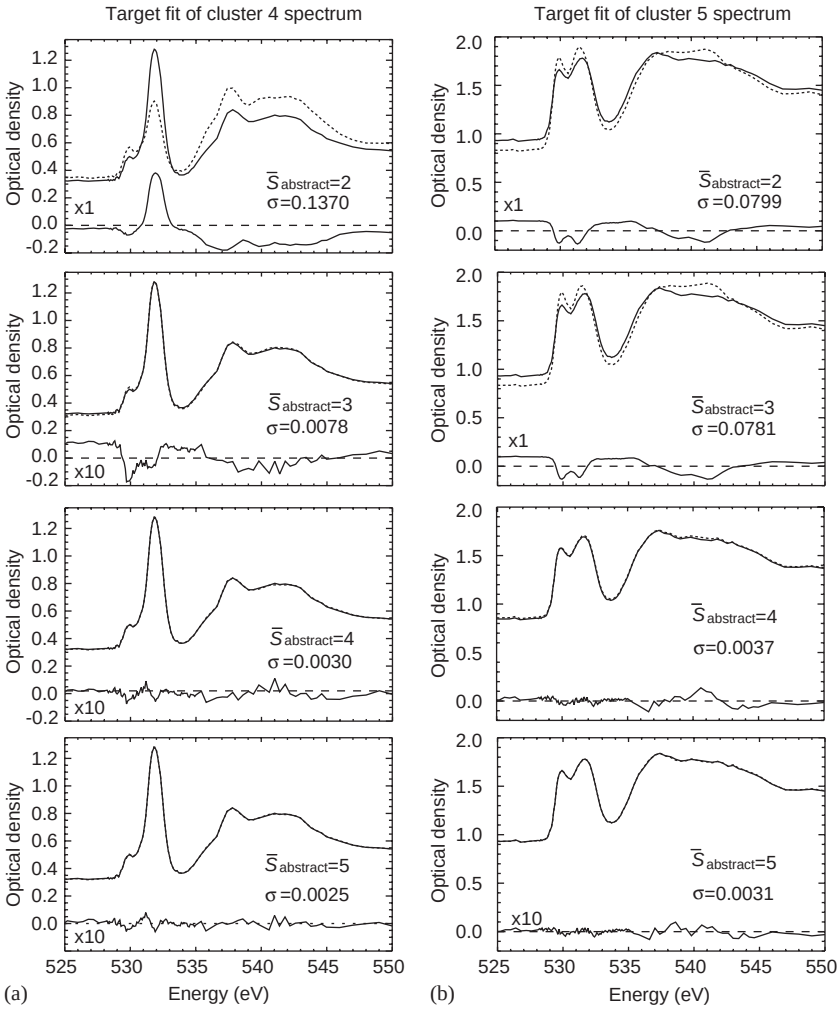

Fig. 14. Fits of the spectra of clusters 4 and 5 of Fig. 12 according to Eq. (13) for various values of $\bar{S}_{abstract}$, shown as dashed line. Actual cluster spectra are shown as solid lines, and the residual errors of the fit are shown below together with their root variance σ. As expected, $\bar{S}_{abstract} = 4$ works well in describing all the significant variations in the data. Calculations like this can serve as a cross-check to see that the correct value of $\bar{S}_{abstract}$ was chosen prior to carrying out cluster analysis.

crystal structure, as indicated by significant pre-edge changes in clusters 3 and 4 of Fig. 12. It also shows a nanoscale separation into regions compatible with pure hematite (clusters 2 and 5) and mixed Fe/Lu hematite crystals with distinct Lu concentrations (clusters 3 and 4). These results suggest that lutetium-substituted hematite might not be the thermodynamic stable phase, and that re-crystallization processes structurally exclude lutetium. Such kinetic information is of paramount importance to identify the essential mineral phases determining long-term radionuclide mobility, and further investigations of these phenomena are presently underway.

6. Conclusion

We have described the use of principal component analysis to orthogonalize and noise-filter spectromicroscopy data, and cluster analysis to classify the data into regions with similar spectra.

This allows one to obtain characteristic, physically-meaningful spectra, and pseudo-thicknesses associated with these spectra, from specimens with no prior information on composition. One can "tune" the degree to which chemical variations are weighted relative to thickness variations by excluding the first component from consideration by the clustering algorithm, by using a eigenvalue scaling parameter γ to increase the sensitivity to higher components, or both. Ongoing investigations concern the use of distance metrics other than Euclidian, and the combination of clustering with oblique analysis.

This approach has been examined using simulated data where the known composition was recovered, and data obtained as part of a study of the incorporation of lutetium (a lanthanide homologue for the trivalent actinide americium) in hematite with implications for groundwater colloidal transport of radionuclides.

Acknowledgements

We wish to thank Michael Feser, Jörg Maser, Sue Wirick, and Kathy Dardenne for many helpful discussions, and Angelika Osanna for her role in bringing multivariate statistical analysis methods to our research. We gratefully acknowledge funding from the National Institutes for Health under Contract R01 EB00479-01A1, and from the National Science Foundation under Contracts OCE-0221029 and CHE-0221934. Data were acquired using the Stony Brook scanning transmission X-ray microscopes which operate at the National Synchrotron Light Source (NSLS) at Brookhaven National Laboratory, which is supported by the U.S. Department of Energy, Division of Materials Sciences and Division of Chemical Sciences, under Contract No. DE-AC02-98CH10886.

Appendix A. Matrix inversion using singular value decomposition (SVD)

Singular value decomposition is based on the Eckart–Young theorem of linear algebra, which states that an array A with $N \geqslant S$ can be decomposed as

$$A_{N\times S} = U_{N\times S} \cdot W_{S\times S} \cdot V^{\mathrm{T}}_{S\times S}, \tag{A.1}$$

where the matrix $U_{N\times S}$ has orthogonal columns, the matrix $W_{S\times S}$ is zero everywhere except for its diagonal elements which are all zero or positive (these diagonal elements are called the *singular values*), and the matrix $V_{S\times S}$ has orthonormal rows. That is, these matrices have the properties that $U^{\mathrm{T}}_{S\times N} \cdot U_{N\times S} = 1_{S\times S}$, and $V^{\mathrm{T}}_{S\times S} \cdot V_{S\times S} = 1_{S\times S}$. The singular value decomposition algorithm [30, Section 2.6] can be used to numerically construct these arrays. With them, one can find the inverse of $A_{N\times S}$ as

$$A^{-1}_{S\times N} = V_{S\times S} \cdot W^{-1}_{S\times S} \cdot U^{\mathrm{T}}_{S\times N}, \tag{A.2}$$

where the inverted matrix $W^{-1}_{S\times S}$ is again a diagonal matrix with elements $W^{-1}_{i,i}$ that are the inverse of the singular values $W_{i,i}$, or zero when $W_{i,i} = 0$.

Appendix B. Calculation of eigenspectra using singular value decomposition

Besides using covariance, the eigenspectrum matrix can also be determined from the singular values of the data matrix. Following [4, Eq. (3.81)] and realizing that we have defined the data matrix as (see Eq. (5))

$$D_{N\times P} = C_{N\times S_{\mathrm{abstract}}} \cdot R_{S_{\mathrm{abstract}}\times P}$$

rather than $D_{P\times N}$, we can express the data matrix using singular value decomposition (SVD) as

$$D^{\mathrm{T}}_{P\times N} = U_{P\times S_{\mathrm{abstract}}} \times W_{S_{\mathrm{abstract}}\times S_{\mathrm{abstract}}} \times V^{\mathrm{T}}_{S_{\mathrm{abstract}}\times N}. \tag{B.1}$$

The eigenvalues of the data matrix are then given by [4, Eq. (3.84)]

$$\lambda(s) = W^2_{S_{\mathrm{abstract}}} \tag{B.2}$$

from diagonal matrix $W_{S_{\mathrm{abstract}}\times S_{\mathrm{abstract}}}$, the eigenspectra are given by [4, Eq. (3.83)]

$$C_{N\times S_{\mathrm{abstract}}} = V_{N\times S_{\mathrm{abstract}}} \tag{B.3}$$

and the eigenimages are given by [4, Eq. (3.82)]

$$R_{S_{\mathrm{abstract}}\times P} = U^{\mathrm{T}}_{S_{\mathrm{abstract}}\times P} \times W_{S_{\mathrm{abstract}}\times S_{\mathrm{abstract}}}. \tag{B.4}$$

In case like ours, where we have very large number of pixels P and small number of energies N, calculating eigenspectra and eigenimages using SVD takes significantly longer and uses much more data storage than calculating it by using the covariance matrix $Z_{N\times N}$. SVD generates square matrices with the larger dimension of N or P, while $Z_{N\times N}$ or $Z_{P\times P}$ can be formed based on the lesser of N or P.

Appendix C. Eigenspectra and eigenimages from spatial covariance

In soft X-ray spectromicroscopy, the intrinsic width of near-absorption-edge resonances is about 0.06-0.2 eV, while the energy range over which they lie is typically 20–30 eV. Data sets with $N = 100$–500 photon energies are thus typical, while the number of pixels may be $P = 100 \times 100 = 10^4$ or more, so that $N \ll P$. It is for this reason that we have here used the spectral covariance $Z_{N\times N}$ as defined by Eq. (8). If, on the other hand, one has $P < N$ (such as in infrared microspectroscopy), the spatial covariance $Z_{P\times P}$ of the data can be obtained from

$$Z_{P\times P} = D_{P\times N} \cdot D^{\mathrm{T}}_{N\times P}, \tag{C.1}$$

where data matrix $D_{P\times N}$ is given by

$$D_{P\times N} = C_{P\times S_{\mathrm{abstract}}} \cdot R_{S_{\mathrm{abstract}}\times N}. \tag{C.2}$$

Eigenimage matrix $C_{P\times S_{\mathrm{abstract}}}$ is obtained from the spatial covariance as

$$Z_{P\times P} \cdot C_{P\times S_{\mathrm{abstract}}} = C_{P\times S_{\mathrm{abstract}}} \cdot \Lambda_{P\times P}. \tag{C.3}$$

Columns of the eigenimage matrix $C_{P\times S_{\mathrm{abstract}}}$ now consist of the P eigenimages. The row matrix $R_{S_{\mathrm{abstract}}\times N}$ is now an eigenspectra matrix, and it can be obtained from

$$R_{\bar{S}_{\mathrm{abstract}}\times N} = C^{\mathrm{T}}_{\bar{S}_{\mathrm{abstract}}\times P} \cdot D^{\mathrm{T}}_{P\times N}. \tag{C.4}$$

The spatial and spectral covariances will yield the same conclusions about the number of principal components [4], target spectrum fitting, and so on, so it is sensible to choose whichever one gives the smaller and faster computation.

References

[1] C. Jacobsen, M. Feser, M. Lerotic, S. Vogt, J. Maser, T. Schäfer, J. Phys. IV 104 (2003) 623.
[2] N. Bonnet, J. Microsc. 190 (1/2) (1998) 2.
[3] N. Bonnet, N. Brun, C. Colliex, Ultramicroscopy 77 (1999) 97.
[4] E. Malinowski, Factor Analysis in Chemistry, 2nd Edition, Wiley, New York, 1991.
[5] B. Everitt, S. Landau, M. Leese, Cluster Analysis, 4th Edition, Arnold Publishers, London, 2001.
[6] M. Feser, M. Carlucci-Dayton, C.J. Jacobsen, J. Kirz, U. Neuhäusler, G. Smith, B. Yu, Applications and instrumentation advances with the Stony Brook scanning transmission X-ray microscope, in: I. McNulty (Ed.), X-ray Microfocusing: Applications and Techniques, Vol. 3449, Society of Photo-Optical Instrumentation Engineers (SPIE), Bellingham, Washington, 1998, pp. 19–29.
[7] M. Feser, T. Beetz, C. Jacobsen, J. Kirz, S. Wirick, A. Stein, T. Schäfer, Scanning transmission soft X-ray microscopy at beamline X-1A at the NSLS–advances in instrumentation and selected applications, in: D.A. Tichenor, J.A. Folta (Eds.), Soft X-ray and EUV Imaging Systems II, Vol. 4506, Society of Photo-Optical Instrumentation Engineers (SPIE), Bellingham, Washington, 2001, pp. 146–153.
[8] K. Kaznacheyev, A. Osanna, C. Jacobsen, O. Plashkevych, O. Vahtras, H. Ågren, V. Carravetta, A. Hitchcock, J. Phys. Chem. A 106 (13) (2002) 3153.
[9] C. Jacobsen, G. Flynn, S. Wirick, C. Zimba, J. Microsc. 197 (2) (2000) 173.
[10] K. Dardenne, T. Schäfer, M. Denecke, J. Rothe, XAFS investigation of lanthanide sorption onto ferrihydrite and transformation products by tempering at 75°C, in: Speciation, Techniques and Facilities for Radioactive Materials at Synchrotron Light Sources, Nuclear Energy Agency, Organisation for Economic Co-operation and Development, Grenoble, France, 2000, pp. 222–228, http://www.nea.fr/html/science/docs/pubs/nea3054/nea3054-speciation.pdf.
[11] K. Dardenne, T. Schäfer, P. Lindqvist-Reis, M. Denecke, M. Plaschke, J. Rothe, J. Kim, Environ. Sci. Technol. 36 (23) (2002) 5092.
[12] T. Schäfer, R. Artinger, K. Dardenne, A. Bauer, W. Schuessler, J.I. Kim, Environ. Sci. Technol. 37 (2003) 1528.
[13] A. Gloter, J. Ingrin, D. Bouchet, C. Colliex, Phys. Rev. B 61 (2000) 2587.
[14] U. Schwertmann, R. Cornell, Iron Oxides in the Laboratory (Preparation and Characterization), VCH Verlagsgesellschaft mbH, Weinheim, 1991.
[15] B.L. Henke, Low energy X-ray interactions: photoionization, scattering, specular and Bragg reflection, in: D.T. Attwood, B.L. Henke (Eds.), Low Energy X-ray Diagnostics, Vol. 75, American Institute of Physics, New York, 1981, pp. 146–155 (Monterey, 1981).
[16] S. Pennycook, L. Boatner, Nature 336 (1988) 565.

[17] H. Ade, X. Zhang, S. Cameron, C. Costello, J. Kirz, S. Williams, Science 258 (1992) 972.
[18] X. Zhang, R. Balhorn, J. Mazrimas, J. Kirz, J. Struct. Biol. 116 (1996) 335.
[19] I.N. Koprinarov, A.P. Hitchcock, C.T. McCrory, R.F. Childs, J. Phys. Chem. B 106 (2002) 5358.
[20] S.R. Wasserman, J. Phys. IV 7 (C2) (1997) 203.
[21] P.L. King, R. Browning, P. Pianetta, I. Lindau, M. Keenlyside, G. Knapp, J. Vac. Sci. Technol. A 7 (6) (1989) 3301.
[22] A. Osanna, C. Jacobsen, Principle component analysis for soft X-ray spectromicroscopy, in: W. Meyer-Ilse, T. Warwick, D. Attwood (Eds.), X-ray Microscopy: Proceedings of the Sixth International Conference, American Institute of Physics, Melville, New York, 2000, pp. 350–357.
[23] E. Malinowski, Anal. Chem. 49 (4) (1977) 606.
[24] J. Kneipp, M. Beekes, P. Lasch, D. Naumann, J. Neurosci. 22 (8) (2002) 2989.
[25] P. Trebbia, N. Bonnet, Ultramicroscopy 34 (1990) 165.
[26] H. Harman, Modern Factor Analysis, 3rd Revised Edition, The University of Chicago Press, Chicago, 1976.
[27] T. Kohonen, Self-Organization and Associative Memory, 3rd Edition, Springer, Berlin, 1989.
[28] T. Kohonen, Proc. IEEE 78 (9) (1990) 1464.
[29] J. Hartigan, Clustering Algorithms, Wiley, New York, 1975.
[30] W.H. Press, B.P. Flannery, S.A. Teukolsky, W.T. Vetterling, Numerical Recipes in Fortran 77: The Art of Scientific Computing, Cambridge University Press, Cambridge, UK, 1986.
[31] J. Steinkamp, R. Habbersett, R. Hiebert, Rev. Sci. Instrum. 62 (11) (1991) 2751.

Colloid-borne Americium migration in Gorleben groundwater: Significance of iron secondary phase transformation.

Environ. Sci. Technol. (2003) **37**(8), 1528.

Schäfer T., Artinger R., Dardenne K., Bauer A.,
Schuessler W., and Kim J. I.

Environ. Sci. Technol. **2003**, *37,* 1528−1534

Colloid-Borne Americium Migration in Gorleben Groundwater: Significance of Iron Secondary Phase Transformation

THORSTEN SCHÄFER,*
ROBERT ARTINGER, KATHY DARDENNE,
ANDREAS BAUER,
WOLFRAM SCHUESSLER, AND JAE IL KIM
Institut für Nukleare Entsorgung (INE), Forschungszentrum Karlsruhe, P.O. Box 3640, D-76021 Karlsruhe, Germany

The mobility of actinides in natural water may be enhanced by colloid-mediated transport. In this context the reversibility of actinide colloid interaction is a key factor. Iron is an element that can generate colloids under conditions found in natural waters. In this paper, the impact of hematite and the low-crystalline precursor 2-line ferrihydrite on colloid-mediated transport of americium(III) is investigated. Am(III)-containing iron colloids are generated from two different approaches, namely contact between the two in aqueous solution or coprecipitation of Am(III) during iron colloid generation. Dissolved organic carbon (DOC), especially humic substances, has a strong influence on the stability of inorganic colloids. In addition, humic substances interfere in the distribution and kinetics of exchange between groundwater and sediments. Four groundwaters from the Gorleben aquifer system are used with DOC concentrations varying between 0.9 and 81.6 mgC/L together with Pleistocene Aeolian quartz sand from this site. Batch and column experiments are conducted under near-natural conditions (Ar + 1% CO_2). To study the influence of kinetics, contact times up to one month are studied. The dynamic light-scattering investigations show that the colloidal stability of the 2-line ferrihydrite increases with increasing DOC concentration. The low-crystalline iron colloids have a marginal influence on the Am(III) transport due to reversibility of americium sorption. Contrary to this, the crystalline hematite generated from coprecipitation of Am(III) leads to an increase of unretarded colloid-mediated Am(III) transport up to a factor of almost five. Chemical characterization of these hematite colloids shows that Am(III) is structurally entrapped in the hematite. The distribution of Am(III) and 2-line ferrihydrite between groundwater and sand sediment remained in disequilibrium even after one month. This shows that the kinetics of Am(III) distribution between the different phases (bulk solution/colloidal form/sediment) is a key issue.

Introduction

In natural aquifers, aquatic colloids are ubiquitous and take part in geochemical solid−water interface reactions (*1*, *2*). Because of their strong interaction with multivalent actinide ions (*3*, *4*), humic colloids, as well as inorganic colloids, exert a crucial influence on the mobility of actinides in natural (*5*, *6*) and anthropogenically influenced aquifer systems (*7*, *8*). Groundwater and quaternary sand used in this study originate from the Gorleben aquifer system (Lower Saxony, Germany). The strata covering a Permian salt dome consists of sandy sediments and represents a complex system of confined and unconfined groundwater horizons (*9*). This aquifer system has been intensively studied in a large number of programs over more than twenty years for the purpose of determining the safety of nuclear waste disposal in the underlying salt dome. Dissolved organic carbon (DOC) concentrations in groundwater vary from around 0.1 to 200 mgC/L (*10*). The humic and fulvic acid content varies between around 50% in low-DOC waters up to around 80% at high DOC concentrations. Detailed information on the isolated fulvic and humic acids is presented elsewhere (*11*, *12*).

Numerous column experiments show that humic colloids in natural sandy sediments are transported about 5% faster than the conservative tritium tracer (*13*, *14*). The amount of actinides transported unretarded with these colloids depends on the actinide humic colloid desorption kinetics (*13*, *14*). Consequently, kinetics is a key issue in actinide transport predictions (*15*).

Inorganic colloids are stabilized by charge reversal through sorption of humic substances (*16*, *17*). Similarly, sediment grain dissolution and mobilization of clay colloids by sorption of humic substances is observed (*18*). The metastable, low-crystallinity iron oxyhydroxide 2-line ferrihydrite ("2LFh") is frequently found as the dominant inorganic Fe-colloid species in aquatic systems. The 2LFh is also frequently found in natural grain surface coatings where it determines sediment sorption properties. Np(V) is found to be reversibly bound to 2LFh (*19*), whereas Pu(V/VI) exhibits a very slow desorption rate from iron oxide surfaces (*20*). Coprecipitation of Pu(IV) and Np(IV) generates mixed hydroxides with Fe(III) (*21*). The 2LFh is metastable with respect to goethite/hematite as stable end products. With this transition, Np(V) binding is shown by Sakamoto et al. (*22*) to change from a reversible form (1 M $MgCl_2$ extractable) into stable incorporation (6 M HCl extractable). Similarly, alteration of 2LFh is shown to generate structural replacement of Nd(III) in hematite as documented by a Rietveld refinement analysis (*23*).

The aim of this study is to investigate the influence of metastable 2-line ferrihydrite (2LFh) and its thermal transformation product (i.e., hematite) on the mobility of Am(III) in natural groundwater, including the role of humic substances. Time-resolved laser light scattering is used to study the stability of 2LFh colloids, especially the influence of groundwater with different DOC concentrations. The mobility of iron oxide/hydroxide colloids and the influence on Am(III) transport is studied by batch and column experiments using radioactively labeled iron colloids (^{59}Fe).

Experimental Section

2-Line Ferrihydrite (2LFh) Colloid Preparation and Characterization. For the preparation of ^{59}Fe-spiked iron colloids, 260.6 mg of an irradiated 99.99+ % pure iron foil (GoodFellow, Germany) was dissolved in 5 M HNO_3. The final stock solution had an Fe concentration of 0.21 mol/L.

(*i*) 2LFh was formed by leaving the solution for 2 h at 25 °C after neutralization (pH 7−8) by rapid addition of 5 M KOH (*24*). Reproducibility of the pure 2LFh synthesis by various characterization methods is described elsewhere (*25*).

* Corresponding author phone: ++49 (7247) 82 5494; fax: ++49 (7247) 82 3927; e-mail: schaefer@ine.fzk.de.

10.1021/es015832r CCC: $25.00
Published on Web 03/07/2003

TABLE 1. Physicochemical and Chemical Data for Gorleben Groundwater Sampled and Handled under Near-Natural Conditions (Ar + 1% CO_2), Including GoHy-182 and -532 after Conditioning with Sediment for Three Months

groundwater	GoHy-182	GoHy-412	GoHy-532	GoHy-2227	equilibrated GoHy-182	equilibrated GoHy-532
pH	8.1	7.7	8.9	7.7	6.6	7.5
E_h [mV]	−90	−70	−160	−120	−260	−140
Na [μmol/L]	171.7	2545	9257	40530	178.3	9800
K [μmol/L]	n.d.[a]	15.9	25.3	179.8	5.1	16.6
Mg [μmol/L]	41.6	n.d.	n.d.	193.4	51	1.2
Ca [μmol/L]	646.9	557.1	46.6	668.1	326.2	12.5
Si [μmol/L]	16.0	26.7	13.2	22.1	171.5	156.2
Fe [μmol/L]	2.2	2.7	5.2	5.9	59.5	14.7
Cl^- [μmol/L]	263.5	509.9	3710	33673	222.3	3783
HCO_3^- [μmol/L]	1051	3287	5477	8003	442.6	5270
SO_4^{2-} [μmol/L]	28.1	1.0	5.2	282	0.8	6.5
ionic strength I [mol/L]	2.2×10^{-3}	4.4×10^{-3}	9.6×10^{-3}	44×10^{-3}	1.5×10^{-3}	9.8×10^{-3}
DOC [mgC/L]	0.9 ± 0.1	5.0 ± 0.3	22.6 ± 0.3	81.6 ± 0.8	7.1 ± 0.1	32.7 ± 0.4
saturation index (SI)						
ferrihydrite	−0.98	−1.82	−0.02	−2.58	−6.82	−2.94
hematite	11.84	10.15	13.76	8.64	0.17	5.90

[a]n.d. not detected.

(*ii*) 2LFh/Am coprecipitates (hereinafter referred to as 2LFh/Am) were synthesized by adding 2 mL of the ^{59}Fe stock solution (pH < 1) to a 3 mL aliquot of the $^{241}Am(III)$ stock solution ($\sim 10^{-4}$ mol/L in 0.1 M perchloric acid) and adjusting the suspension to pH 6 with 1 M KOH.

(*iii*) Tempering 2LFh/Am over a period of 7 d at 70 °C in an oven generated the transformation product hematite (hereinafter referred to as Hae/Am). The pH value was set to 6 and adjusted once a day. According to X-ray diffraction analysis of the transformation products, hematite was the major mineral component.

Washing with Milli-Q water (centrifugation, decantation, and re-dispersion) was performed up to five times to purify the synthesized iron colloids. The final stock solutions had an electrical conductivity comparable to that of the Milli-Q water, and the colloids remained stable. Photon correlation spectroscopy (PCS) analysis using a Brookhaven ZetaPlus system (Brookhaven Inc.) equipped with a solid-state laser ($\lambda_{em.} = 532$ nm) yielded an intensity-weighted mean colloid size of 259 ± 127 nm and 186 ± 113 nm for the 2LFh and the 2LFh/Am samples, respectively. PCS analysis of Hae/Am colloids showed a slightly lower mean colloid size of 180 ± 80 nm. All chemicals used in this study were of analytical grade or better.

Am Exchange Stability. The Am exchangeability in 2LFh precursor and the colloidal transformation products was determined by a three-step extraction scheme. The method is specific for iron oxides (*26*). The total metal content ($Fe_{[T]}$, $Am_{[T]}$) was determined using a citrate−dithionite−bicarbonate extraction procedure (*27*). The poorly crystalline or "active" metal content ($Fe_{[O]}$, $Am_{[O]}$) was extracted by a NH_4−oxalate−oxalic acid for 2 h in the dark at pH 3 (*28*). For the exchangeable, salt-extractable metal content ($Fe_{[E]}$, $Am_{[E]}$), a 1 M $MgCl_2$ procedure was applied (*26*).

Colloid Stability Analysis. The influence of humic substance concentration on the colloid stability of 2LFh was investigated in Gorleben groundwater with DOC concentrations ranging from 0.9 to 81.6 mgC/L (GoHy-182, -412, -532, -2227 (cf. Table 1)). 2LFh colloid concentrations of 1.8 mg/L or 5.6 mg/L were used based on 89 g 2LFh/mol Fe for the stoichiometry $Fe_2O_3 \cdot xH_2O$ (*29*). The selected colloid concentration range simulates the uppermost colloid concentration (1−60 mg/L) expected in highly chemically disturbed groundwater systems (*30*). Coagulation kinetics were monitored by PCS over a period of 14 days. Assuming a spherical colloid geometry, the hydrodynamic diameter d_H was evaluated by means of the quadratically weighted cumulant analysis (QC) implemented in the Brookhaven software package (*31*). A further discussion of the critical evaluation of the errors associated with the PCS technique compared to that of other colloid detection systems is provided by Plaschke et al. (*32*).

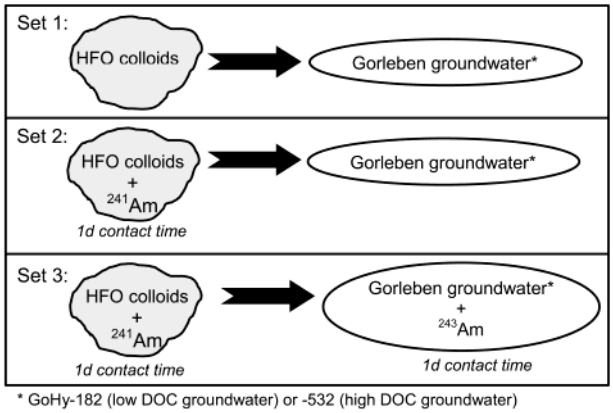

FIGURE 1. Schematic illustration of the three sets used for batch experiments.

Chemical stability analysis of the ferric iron colloids was performed by calculating the saturation indices (SI) of the original and column-equilibrated groundwater (Table 1) using PHREEQC (*33*). Dissolved ferric iron concentrations are below analytical detection limits for all samples. On the basis of the total Fe concentration and the measured E_h, the saturation indices for ferrihydrite and hematite were calculated (Table 1). Furthermore, possible dissolution of ferrihydrite colloids was monitored in the batch experiments by an ICP-MS analysis of dissolved iron, operationally defined as the fraction <1 kDa. A kinetically enhanced dissolution of iron colloids in column experiments, which had been observed by Roden and Urrutia (*34*) in flow-through experiments, was minimized by a three months' preequilibration of the groundwater (see below).

Batch Experiments. Batch and column experiments were performed under inert gas atmosphere (Ar + 1% CO_2) in a glovebox. Three sets of sorption kinetics experiments were conducted over a period of 21 days using a three months' equilibrated Gorleben groundwater (GoHy-182 and GoHy-532) sediment system (Figure 1). Pleistocene Aeolian quartz sand was used as sediment (*13*) and batches were performed at a liquid-to-solid ratio of L/S = 4.27 mL/g. All experiments were conducted in triplicate. The distribution coefficient K_d

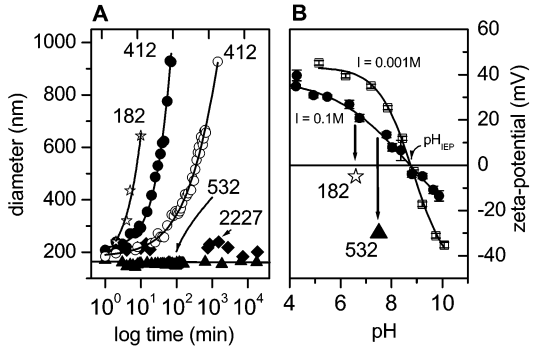

FIGURE 2. (A) Hydrodynamic diameter (d_H) of 2LFh colloids in Gorleben groundwater determined by photon correlation spectroscopy (PCS) as a function of time. Samples vary by DOC concentrations (☆ GoHy-182, 0.9 mg/L DOC; ●,○ GoHy-412, 5.0 mg/L DOC; ▲ GoHy-532, 22.6 mg/L DOC; ◆ GoHy-2227, 81.6 mg/L); and 2LFh colloid concentration (filled symbols, 5.6 mg/L; and open symbols, 1.85 mg/L). (B) 2LFh zeta potential as a function of pH in 0.001 M and 0.1 M NaCl and in the Gorleben groundwaters GoHy-182 and -532. Increasing DOC content results in increasing stabilization of 2LFh colloids through sorption of humic substances resulting and charge reversal.

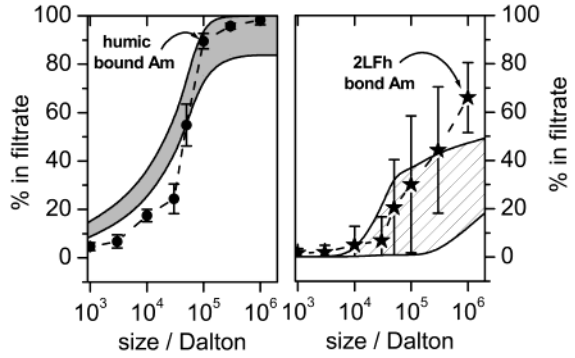

FIGURE 3. Ultrafiltration results of GoHy-532 groundwater prior to injection. Left graph: DOC size distribution without 2LFh addition is given as gray-shaded area and the humic-bound Am is shown as filled circles. Right graph: 2LFh colloid size distribution is indicated as striped pattern and the 2LFh-associated Am is shown as filled stars.

(colloids are treated as belonging to the solution) or colloid distribution coefficient $K_{d,C}$ is defined as

$$K_{d,C} \text{ or } K_d = \frac{C_S}{C_W}\frac{V}{m} \quad (1)$$

where C_s is the sediment-sorbed metal/colloid concentration (mol/L), C_w is the metal/colloid concentration in the solution (mol/L), V (mL) is the groundwater volume, and m (g) is the sediment mass. The averaged distribution coefficients K_d or $K_{d,C}$ (mL/g) and the standard deviation detected are shown in Figure 4. Three different sets were used for adding ^{59}Fe-spiked 2LFh and Am(III) to the groundwater/sediment system. Thereby, two different Am(III) isotopes are used (^{241}Am and ^{243}Am) for determination of isotope exchange kinetics. The sets prepared for these experiments were the following.

Set 1. Addition of ^{59}Fe-spiked-2LFh to the Gorleben groundwater/sediment system, resulting in an iron concentration of 5.0×10^{-6} mol/L and a 2LFh concentration of 0.44 mg/L, assuming 89 g 2LFh/mol Fe (*29*).

Set 2. Addition of ^{59}Fe-spiked-2LFh as described in set 1, previously contacted with ^{241}Am for 1 d to obtain a final Am concentration of 3.2×10^{-8} mol/L.

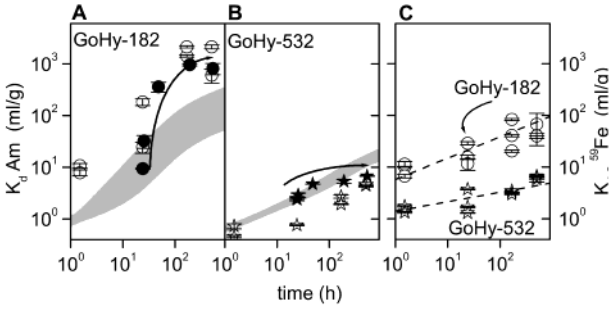

FIGURE 4. Americium sorption by Pleistocene quartz sand with the Gorleben groundwaters GoHy-182 and GoHy-532 (A, B) and 2LFh colloids (Fe_T 5 μM) (C) as a function of time. The shaded area shows the results of Artinger et al. (*13*) for the case where 2LFh colloids are absent. ^{241}Am sorption coefficients are represented by open symbols (set 2), and ^{243}Am (set 3) are shown as filled symbols (A, B). 2LFh colloid/sediment distribution coefficients $K_{d,C}$ are determined by ^{59}Fe measurements (C).

TABLE 2. Hydraulic Parameters of Column Experiments

parameter	
column length/diameter [m]	0.25/0.05
effective porosity ϵ_{eff} [%]	33 ± 1
Darcy velocity v_D [m·s^{-1}]	$4.3 \times 10^{-6} \pm 1 \cdot 10^{-7}$

Set 3. Groundwater preequilibration with 4.7×10^{-7} mol/L ^{243}Am (1 d) before the addition of the 2LFh-^{241}Am mixture as described in set 2.

Column Experiments. For the column experiments, conditioned groundwater (GoHy-182 and -532)/ Pleistocene quartz sand (*13*) systems were used. The basic physical parameters and the major chemical compositions and DOC concentrations of the original and the equilibrated groundwater are shown in Tables 1 and 2.

Conditioning of groundwater with sediment under Ar + 1% CO_2 atmosphere results in lowering of pH and redox potential with simultaneous increase in DOC and Fe concentration. The size distribution of humic colloids remains unchanged, as was determined by ultrafiltration (*13*). The dissolved Am or Am associated with iron colloids was brought into contact with the Gorleben groundwater reservoir for 1 h. A size distribution analysis of humic colloids or Am associated with 2LFh colloids was performed prior to sample injection and of groundwater leaving the column outlet. This was done by ultrafiltration using polyethersulfone membranes with a nominal molecular weight cutoff ranging from 10^3 to 10^6 Dalton (Filtron Co., Microsep Microconcentrators). Continuous injection of approximately one pore volume of Am or Am/iron-colloid-spiked groundwater was applied. The Fe concentration varied between 8.5 and 22 μmol/L depending on the colloid type used. This resulted in a 2LFh colloid concentration of 0.8 to 1.9 mg/L. The initial ^{241}Am concentration injected varied from 4×10^{-10} to 3×10^{-8} mol/L (Table 3) between the runs.

Taking into account that the column has a total of 6×10^{-2} mol/L surface sorption sites (*35*), the Fe concentration injected into the column (4.7×10^{-6} mol) or ferrihydrite concentration calculated (2.9×10^{-6} mol) over all experiments amounts to 0.3−0.5‰ of the total sorption sites. For Am, the equivalent number is ~0.001‰. Therefore, no significant reduction in sediment sorption capacity occurs in these experiments. Flow velocity of the colloid-bound Am was held constant at a Darcy velocity of 4.3×10^{-6} m·s^{-1} in all experiments. Tritiated water (HTO) was used as a conservative tracer to determine the hydraulic properties of the columns.

TABLE 3. Results from Americium Migration Experiments with Gorleben Groundwater

groundwater	iron colloid type:	colloid-induced iron concn. mol/dm^{-3}	^{241}Am concn. in injected solution mol/dm^{-3}	recovery R (^{241}Am) %	retardation factor R_f (^{241}Am)	recovery R (^{59}Fe) %	retardation factor R_f (^{59}Fe)	$R(^{241}Am)/R(^{59}Fe)$ ratio
GoHy-182	2LFh/Am	1.4×10^{-5}	4.5×10^{-10}	0.5	n.d.[a]	n. d.	n.d.	-
GoHy-532	no	-	2.9×10^{-8}	7.9	0.97 ± 0.01	-	-	-
GoHy-532	2LFh	8.5×10^{-6}	3.1×10^{-8}	10.2	0.85 ± 0.04	31.3	0.85	0.33
GoHy-532	2LFh/Am	1.6×10^{-5}	3.8×10^{-10}	17.9	0.89 ± 0.02	43.6	0.93	0.41
GoHy-532	Hae/Am	2.2×10^{-5}	7.6×10^{-10}	39.0	0.89 ± 0.02	46.0	0.92	0.85

[a]n.d. Not detected.

Several parameters were determined from these experiments. The chemical retardation, R_f, is defined as

$$R_f = \frac{v_p}{v_c} \tag{2}$$

where v_p is the velocity of the ideal tracer (HTO) through the column and v_c denotes the velocity of the colloid/metal through the column. Chemical retardation is larger than 1 when the solute interacts with the sediment and less than 1 when pore size exclusion effects (colloidal transport) or anion exclusion occur. The recovery R (%) is defined as

$$R = \left[\int_{t_0}^{t_f} \frac{C(t)}{C_0} \mathrm{d}t\right] \times 100 \tag{3}$$

where C_0 is the concentration in the substance injected (mol/L), $C(t)$ is the concentration (mol/L) at time t, and t_0 and t_f are the times elapsed from injection to the beginning and the end of the breakthrough, respectively.

In a single-column experiment, the contact time of Am with humic colloids or the contact time of iron colloids with humic groundwater is varied by continuous injection of approximately one pore volume of Am-spiked groundwater into the column. Accordingly, the 2LFh/humics last introduced into the column have a longer contact time than those injected at the beginning. In the case of quantitative HTO elution, dispersion effects in the column could be neglected and Am recovery was detected directly from the breakthrough curve. The isotopes to be investigated (^{241}Am, ^{243}Am, ^{59}Fe, and HTO) in the batch and column experiments (single fraction) were detected by γ-spectrometry and/or liquid scintillation counting.

Results and Discussion

Colloid Stability Analysis and Am Association. The PCS measurements regarding the colloidal stability of 2LFh yielded a concentration of 1.85 mg/L or 5.6 mg/L in the different Gorleben groundwaters and revealed a strong dependence of aggregation on the DOC concentration (Figure 2A). Fast coagulation of 2LFh colloids could be observed for the groundwater GoHy-182 and -412, whereas the colloids were stabilized in the groundwater having a higher DOC content. Although a fast aggregation/colloid diameter increase was detected within the first 10 minutes in GoHy-182 groundwater (Figure 2A), the laser light scattering (LLS) intensity started to decrease not before a reaction time of 3 h (data not shown separately). This indicates the delayed onset of the sedimentation processes. Additional tests performed at different 2LFh concentrations in the groundwater (GoHy-412) showed aggregation kinetics increasing with a rising 2LFh colloid concentration.

Zeta potential (ζ) measurements of the purified 2-line ferrihydrite colloids at variable ionic strengths (I) revealed an isoelectrical point at pH_{IEP} 8.7 (Figure 2B). Measurements at ionic strengths of 0.001 M and 0.1 M (10 times higher than the maximum ionic strength of the groundwater under investigation) showed a positive ζ-potential of +40 mV and +22 mV at pH 6.5 (GoHy-182) and +32 mV and +16 mV at pH 7.5 (GoHy-532), respectively. In the Gorleben groundwater, the positively charged 2LFh colloid surface decreased from −5 mV in GoHy-182 to −30 mV in GoHy-532 (Figure 2B), concurrent with an increase in the DOC content. Similar results were obtained from fatty acid and Suwannee humic/fulvic acid sorption experiments on hematite colloids (*36*) and for natural organic matter sorption on goethite (*37*). An increase in the organic acid concentration causes a destabilization of hematite colloids which reach a minimum stability ratio, whereas the stability ratio increases sharply with a further increase in the polyelectrolyte concentration (*36*). The results presented here demonstrate that neither pH changes nor ionic strength variations in the different groundwaters can explain the observed change in the zeta potential. It may therefore be concluded that negatively charged humics sorb onto the 2LFh surface and, via charge neutralization, lead to a 2LFh colloid destabilization in Gorleben groundwater of low (0.9−5.0 mgC/L) DOC concentration (GoHy-182, -412). High DOC concentrations of 22.6−81.6 mgC/L in GoHy-532 and -2227 were sufficient to exceed the domain of nearly uncharged colloids and stabilize negatively charged 2LFh/humic colloid associates in the mg/L range. Consequently, the colloid stability results demonstrate the importance of humic substances as stabilizing agents for an inorganic colloid-mediated mobilization.

Even under the reducing groundwater conditions (Table 2), the chemical stability of ferrihydrite monitored during the batch experiments showed a 3.5% and 2.3% ferrihydrite dissolution in GoHy-182 and GoHy-532 within 30 d, respectively. According to (*34*), the stability of Fe(III) iron phases in the reducing groundwater can be explained by an initial Fe(II) solid-phase sorption resulting in a blockage of reduction-sensitive surface sites. The experimental setup used for the batch and column experiments in this study and the groundwater preequilibration time of three months were to limit the ferrihydrite colloid dissolution rate measured.

The saturation indices calculated for all groundwaters (Table 2), however, indicate an undersaturation (SI < 0) regarding ferrihydrite [$Fe(OH)_3(nH_2O)$] and a supersaturation (SI > 0) with respect to the hematite ferric iron mineral phase (Fe_2O_3). Nevertheless, the mineral saturation data imply an uncertainty as far as the Fe(III) activity assumption made is concerned.

For GoHy-532 without the addition of 2LFh, ultrafiltration results revealed only 10−15% of the Am activity in the operationally defined soluble fraction <1 kDa, which suggested that 85−90% of the Am was bound onto humic colloids (Figure 3). This result is in agreement with speciation calculations and the DOC size analysis performed by Artinger et al. (*13*), indicating the predominant existence of ternary $Am(CO_3)HA(I)$ with minor fractions of Am(OH)HA(II) and AmHA(III). Size distribution analysis of Am sorbed quantitatively onto 2LFh that had been in contact with GoHy-532 groundwater for 1 h exhibited a significant shift of Am to larger colloid size fractions, which is in good agreement with

^{59}Fe ultrafiltration results for 2LFh colloids (Figure 3). The ultrafiltration results illustrate that Am is associated with 2LFh in the injection fluid and column outlet fractions (not shown separately). The size distribution variations of 2LFh colloids can be attributed partly to pore-plugging effects of the polyethersulfone membranes. As a result, filter cutoff and reproducibility of the filtration are changed drastically. A comparable variability of iron colloidal fractions retained by individual filters of the same manufacturer was found in the cross-flow ultrafiltration intercomparison studies performed by Reitmeyer et al. (*38*). Here, the inconsistency and lacking correlation between the artifacts, filter types, and manufacturers were attributed to differences in system composition and system cleanup.

Batch Experiments. The time-dependent sorption behavior of ^{59}Fe-spiked 2LFh colloids and Am(III) in batch experiments is shown in Figure 4. The results can be summarized as follows.

Set 1. The experimental results show that the 2LFh colloid distribution coefficient ($K_{d,C}$) for the GoHy-182 system exceeds that of the GoHy-532 system by an order of magnitude (Figure 4C). In the batch experiments at low DOC concentrations (GoHy-182), ~ 90% ($K_{d,C} \sim 10$) of the iron colloids as well as of ^{241}Am (Figure 4A) were found to be sediment sorbed after a reaction time of 1 h. In comparison, colloid stability measurements (Figure 2A) show a fast aggregation of iron colloids, although the colloid sedimentation indicated by the LLS intensity decrease cannot be detected in this time range. Therefore, the fast association kinetics of iron colloids with the sediment are responsible for the higher ^{241}Am K_d values (Figure 4A, open circles) compared to the absence of 2LFh (Figure 4A, gray-shaded area).

The results demonstrate the crucial importance of humic colloids to the stabilization of colloidal metal oxides on one hand and to counter-balancing charge heterogeneities on the other hand. The sediment charge heterogeneities lead to high colloid attachment. In addition, the batch experiments show that the equilibrium state for 2LFh colloid attachment/sorption ($K_{d,C}$) onto the Gorleben sand is not reached after the period of 30 days in either of the groundwater systems. Consequently, kinetic aspects have to be taken into account in colloid-sediment association and colloid/radionuclide migration studies.

Set 2. Comparison of the 2LFh/Am sorption experiments in the presence of inorganic 2LFh colloids presented here with the Am sorption experiments without the addition of inorganic colloids (initial Am concentration 5×10^{-8} mol/L) performed by Artinger et al. (*13*) (Figure 4, gray-shaded areas) shows a significant change of Am sorption for both groundwaters (Figure 4, open symbols). The addition of 2LFh colloids to GoHy-182 groundwater results in higher Am sorption due to fast 2LFh colloid-sediment association kinetics (Figure 4C) observed within the first hour and colloid aggregation (Figure 2A).

However, comparison of the $K_{d,C}$ values of the iron colloids with the higher K_d values of the Am sorption additionally suggests a fast Am/iron colloid dissociation in the sediment. On the other hand, 2LFh addition to GoHy-532 groundwater results in a stabilization of the colloid-bound Am in the solution (Figure 4B, open stars). This is reflected by the K_d values after an equilibrium time of 30 days being almost an order of magnitude smaller than those of the system without 2LFh colloid addition (gray-shaded area). Furthermore, the equilibrium state for ^{241}Am sorption onto the Gorleben sand is not reached after the period of 30 days in either of the groundwater systems.

Set 3. Preequilibration of the groundwater humic colloids with ^{243}Am (4.7×10^{-7} mol/L) did not have any significant effect on the ^{241}Am and 2LFh sorption trends, as indicated by the variation of the data points in Figure 4 (open symbols).

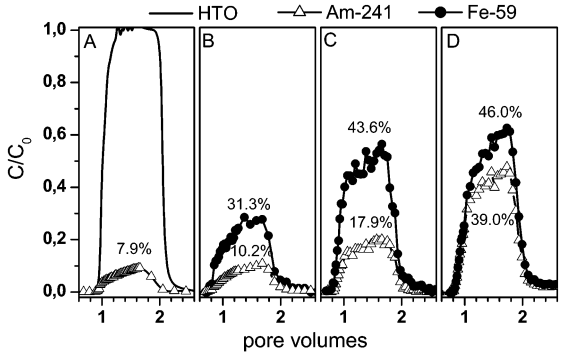

FIGURE 5. Column breakthrough curves of ^{241}Am (ρ), ^{59}Fe (★), HTO (solid line), and recoveries R (%) as a function of the colloid type (A, humic colloid-bound Am; B, 2LFh colloid-sorbed Am; C, 2LFh/Am coprecipitate colloids; D, hematite colloid-bound Am) in GoHy-532 groundwater. Here, C/C_0 is the ratio of the outlet to inlet concentration of ^{241}Am, ^{59}Fe colloids, and HTO.

^{243}Am sorption changes in GoHy-182 (Figure 4A, filled symbols) after the addition of 2LFh colloids followed the ^{241}Am K_d trend, which suggested a humic colloid sorption on 2LFh colloids and their fast attachment onto the sediment. The assumption of the combination of humic colloid 2LFh association and 2LFh colloid attachment being the rate-limiting step in GoHy-182 may explain this change of Am sorption. The K_d changes of initial 1 d GoHy-532 humic colloid-equilibrated ^{243}Am (Figure 4B, filled symbols) showed that the ^{243}Am data followed roughly the data of (*13*), which had been obtained without 2LFh colloid addition over a period of 7 d. After 21 d, the K_d values dropped to the 2LFh-associated ^{241}Am values. Here, it is obvious from the ^{243}Am K_d values derived from the gray-shaded area (pure humic system) as a function of time that ^{243}Am dissociates from humics and associates with colloidally stable iron colloids. The retarded behavior of ^{243}Am compared to the ^{241}Am trend in GoHy-532 might be explained by a more kinetically stable Am/humic substance complex which is observed by Artinger et al. (*13*) with increasing contact time.

Column Experiments. The results of the migration experiments, including Am and 2LFh recoveries R and retardation factors R_f, are listed in Table 3. The R values are inserted in Figure 5 in percent.

One pore volume of spiked groundwater was injected followed by conditioned groundwater. ^{59}Fe is used for quantification of iron colloids. HTO breakthrough is quantitative ($[HTO]/[HTO]_0 = 1.0$) except for at the beginning and the end of breakthrough (Figure 5A). This shows that dispersion is limited. Consequently, in the region where ($[HTO]/[HTO]_0 = 1.0$, $[Am]/[Am]_0$ corresponds directly to the recovery of Am by unhindered transport.

Because of the low recovery of Am and ^{59}Fe, results from experiments with GoHy-182 could not be quantified easily. No significant Am transport enhancement could be observed through addition of 2LFh colloids ($R = 0.5\%$). Contrary to this, Am and ^{59}Fe transport was sufficient for quantitative evaluation with the GoHy-532 groundwater system.

The transport velocity of humic-colloid-borne Am is about 3% faster (retardation factor $R_f = 0.97$) than that of HTO (Table 3). These results are comparable to findings from pulse injection experiments (*13*). The transport velocity of iron colloids is found to be about 15% faster than that of HTO (Table 3). This indicates a higher degree of size exclusion, and thus larger size of these colloids. Recovery of iron colloids was found to be 31.3, 43.6,% and 46%, for 2LFh colloids, 2LFh colloids from the experiment with Am co-generation (2LFh/Am), and hematite colloids (Hae/Am), respectively (Figure 5). This increase in recovery correlates with a decrease

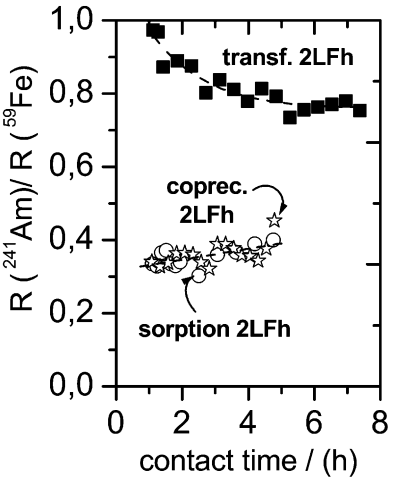

FIGURE 6. Variation of the recovery ratio of ^{241}Am/^{59}Fe as a function of contact time, as derived by the column experiment. The contact time is the time prior to the injection of the spiked groundwater into the column.

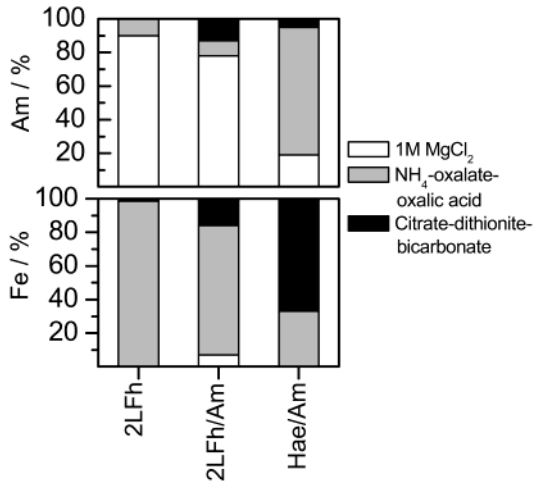

FIGURE 7. Sequential extraction of 2LFh, 2LFh/Am, and Hae/Am. The extracted percentage of iron is plotted at the bottom and ^{241}Am is plotted at the top.

in colloid size as found by PCS and variation in R_f values (Table 3). This demonstrates that initially positively charged 2LFh colloids are partly mobile in near-neutral pH Gorleben groundwater rich in humic substances. The recovery of iron colloids increases with contact time (Figure 5). This can be interpreted by means of sorption of different dissolved organic carbon (DOC) compounds with a varying ability to stabilize the colloids (*39*). In the beginning, both weakly and strongly binding (stabilizing) groundwater DOC components adsorb onto free available sorption sites of the iron colloids. With increasing contact time, strongly binding stabilizing DOC components competitively displace the weakly binding components (*40*).

For 2LFh recoveries in column experiments neglecting the filter efficiency of the sediment and using the $K_{d,C}$ values of the batch experiments with a comparable contact time, values of >90% sorption in GoHy-182 and ~60% sorption in GoHy-532 were estimated. These values are in good agreement with the observed recoveries.

Upon addition of 2LFh colloids, the Am recovery increased from 7.9 to 10.2% (Figure 5B). A further increase in Am recovery is found for co-generation with 2LFh (17.9%) and hematite (39.0%). In this sequence, the ratios of Am eluted with the iron colloids (recoveries of Am to ^{59}Fe) are increasing (0.33, 0.41, and 0.85 for Am contact with 2LFh colloids, Am co-generation with 2LFh colloids, and Am inclusion in hematite colloids, respectively). This shows the increasing stabilization of Am with iron colloid and decreasing Am reversibility in this sequence.

The ratio ^{241}Am to ^{59}Fe remains relatively unaffected by the contact time prior to injection in column experiments for co-generation and contact with 2LFh colloids (Figure 6). The slight ratio increase with contact time observed in these experiments can be attributed to the Am−HS association/dissociation kinetics (*15*, *38*) of the reversible iron colloid bond Am fraction. Therefore, this is an Am-humic interaction phenomenon rather than a strengthening of Am-2LFh binding.

In contrast to the unaltered 2LFh experiments, the Am/Fe ratio for hematite colloids in the column outlet fractions decreases from almost 1 to stabilize around a value of about 0.8. This can be attributed to a kinetically controlled desorption of the reversibly bound Am fraction from hematite during the initial stage of the experiments (Figure 6).

The iron phases and the impact on the Am interaction was studied by selective iron extraction (Figure 7). The fraction of $Fe_{(O)}$ (iron extractable by ammonium−oxalate−oxalic acid) decreases from 99% to 77% and 33%, in the sequence 2LFh with Am sorbed, 2LFh with co-generated Am (2LFh/Am), and hematite/Am (Hae/Am), respectively. This shows the changes in iron mineralogy between these samples.

The higher stability of the Am co-generated 2LFh colloids is also verified by size distribution (cf. above). The fraction of Am that can be exchanged by competition with salt (1 M $MgCl_2$) decreases from 90% to 78% and 19%, respectively, in the same sequence. This shows that the Am interaction with iron colloids is strongly dependent on the iron phase mineralogy with 2LFh recrystallization and secondary mineral formation (i.e., hematite) drastically changing the Am/mineral interaction kinetics. The Am binding to hematite, however, is also influenced by heterogeneity of the iron colloids. Although only 33% of iron is extracted by the $Fe_{(O)}$ procedure, 76% of Am is released. This shows that Am is preferentially sorbed onto a fraction of iron in hematite, which is less crystalline or of small crystal size.

To resolve the underlying recrystallization reactions on an atomic scale, metrical parameters describing the Lu coordination were derived from the extended Lu L_3 edge X-ray absorption fine structure (EXAFS) spectra (*41*, *42*). Lu is used as a lanthanide homologue for the trivalent actinide Am. Lu_2O_3, Lu sorbed onto goethite and hematite are investigated as references. The Lu first oxygen coordination shell in the transformation product differs from that in the sorbed species and varies with the tempering duration at 70 °C. The intensity and symmetry of this first shell's Fourier transformation (FT) peak decreases and shifts toward shorter distances as a function of ferrihydrite aging. Similar to Lu sorbed onto ferrihydrite, the aged products exhibit an FT peak at ~3.0 Å which is not present in the Lu sorbed onto goethite or hematite. This peak is attributed to a second coordination shell of Fe atoms (FT peak at 3.0−3.05 Å) and shows a higher peak intensity with peak splitting with increasing tempering time. From this we conclude that the Lu coordination differs from that of a Lu species sorbed onto ferrihydrite, goethite, or hematite, and that the Lu coordination changes significantly during the transformation process. Consequently, these results document Lu incorporation into hematite during aging of 2LFh, thus corroborating the interpretation of the extraction results.

The overall conclusion of the results is that the mobility of trivalent actinide ions by both entrapment in stationary phases (sediment) or in mobile mineral phases (colloids), as shown in this work, is a direct function of the iron phase mineralogy and their formation and stabilization pathway.

Acknowledgments

We gratefully acknowledge the assistance of Ms. Schlieker in performing the experiments. Furthermore, we thank the staff of the Hahn-Meitner Institute (Berlin) and the Technical University of Munich for performing neutron activation at BER II (Berlin) and FRM (Munich), respectively. We are indebted to three anonymous reviewers for their valuable constructive suggestions.

Literature Cited

(1) McCarthy, J. F.; Zachara, J. M. *Environ. Sci. Technol.* **1989**, *23*, 497−502.
(2) Honeyman, B. D. *Nature* **1999**, *397*, 23−24.
(3) Kim, J. I. In *Handbook on the Physics and Chemistry of the Actinides*; Freeman, A. J., Keller, C., Eds.; Elsevier Science: Amsterdam, The Netherlands, 1986; Chapter 8.
(4) Kim, J. I.; Czerwinski, K. R. *Radiochim. Acta* **1996**, *73*, 5−10.
(5) Kim, J. I.; Buckau, G.; Rommel, H.; Sohnius, B. *Mater. Res. Soc. Symp. Proc.* **1989**, *127*, 849−854.
(6) Vilks, P.; Miller, H. G.; Doern, D. C. *Appl. Geochem.* **1991**, *6*, 565−574.
(7) Buddemeier, R. W.; Hunt, J. R. *Appl. Geochem.* **1988**, *3*, 535−548.
(8) McCarthy, J. F.; Czerwinski, K. R.; Sanford, W. E.; Jardine, P. M.; Marsh, J. D. *J. Contam. Hydrol.* **1998**, *30*, 49−77.
(9) BGR. *Übertägige geowissenschaftliche Erkundung des Standortes Gorleben*. Report 108880, Bundesanstalt für Geowissenschaften und Rohstoffe, 1991.
(10) Buckau, G. Komplexierung von Americium (III) mit Huminstoffen in natürlichen Grundwässern. Ph.D. Thesis, Technical University Munich, Munich, 1991.
(11) Buckau, G.; Artinger, R.; Fritz, P.; Geyer, S.; Kim, J. I.; Wolf, M. *Appl. Geochem.* **2000**, *15*, 171−179.
(12) Artinger, R.; Buckau, G.; Geyer, S.; Wolf, M.; Fritz, P.; Kim, J. I. *Appl. Geochem.* **2000**, *15*, 97−116.
(13) Artinger, R.; Kienzler, B.; Schuessler, W.; Kim, J. I. *J. Contam. Hydrol.* **1998**, *35*, 261−275.
(14) Artinger, R.; Seibert, A.; Marquardt, C. M.; Trautmann, N.; Kratz, J. V.; Kim, J. I. *Radiochim. Acta* **2000**, *88*, 609−612.
(15) Schuessler, W.; Artinger, R.; Kienzler, B.; Kim, J. I. *Environ. Sci. Technol.* **2000**, *34*, 2608−2611.
(16) Kretzschmar, R.; Sticher, H. *Environ. Sci. Technol.* **1997**, *31*, 3497−3504.
(17) Puls, R. W.; Paul, C. J.; Clark, D. A. *Colloids Surf. A* **1993**, *73*, 287−300.
(18) Swartz, C. H.; Gschwend, P. M. *Environ. Sci. Technol.* **1998**, *32*, 1779−1785.
(19) Girvin, D. C.; Ames, L. L.; Schwab, A. P.; McGarrah, J. E. *J. Colloid Interface Sci.* **1991**, *141*, 67−78.
(20) Lu, N.; Triay, I. R.; Cotter, C. R.; Kitten, H. D.; Bentley, J. *Reversibility of sorption of Plutonium-239 onto colloids of hematite, goethite, smectite, and silica*. Report LA-UR-98-3057, Los Alamos National Laboratory: Los Alamos, NM, 1998.
(21) Grigoriev, M. S.; Fedoseev, A. M.; Gelis, A. V.; Budantseva, N. A.; Shilov, V. P.; Perminov, V. P.; Nikonov, M. V.; Krot, N. N. *Radiochim. Acta* **2001**, *89*, 95−100.
(22) Sakamoto, Y.; Ohnuki, T.; Senoo, M. *Radiochim. Acta* **1994**, *66/67*, 285−289.
(23) Nagano, T.; Mitamura, H.; Nakayama, S.; Nakashima, S. *Clays Clay Miner.* **1999**, *47*, 748−754.
(24) Schwertmann, U.; Cornell, R. M. *Iron Oxides in the Laboratory (Preparation and Characterization)*; VCH Verlagsgesellschaft mbH: Weinheim, 1991.
(25) Dardenne, K.; Schäfer, T.; Denecke, M. A.; Rothe, J.; Kim, J. I. *Radiochim. Acta* **2001**, *89*, 469−479.
(26) Loeppert, R. H.; Inskeep, W. P. In *Methods in Soil Analysis. Part 3. Chemical Methods*; Bartels, J. M., Ed.; SSAS & ASA, Inc.: Madison, WI, 1996; Vol. 5, pp 639−664.
(27) Mehra, O. P.; Jackson, M. L. *Clays Clay Miner.* **1960**, *7*, 317−327.
(28) Schwertmann, U. *Z. Pflanzenernaehr. Düng. Bodenkund.* **1964**, *105*, 194−202.
(29) Dzombak, D. A.; Morel, F. M. M. *Surface Complexation Modeling - Hydrous Ferric Oxide*; Wiley & Sons: New York, 1990.
(30) Kaplan, D.; Bertsch, P.; Adriano, D.; Miller, W. P. *Environ. Sci. Technol.* **1993**, *27*, 1193−1200.
(31) Brookhaven Instruments Corporation's Data Analysis Software (BI-ISDA); Version 8.0 ed.; Brookhaven Instruments Corporation (www.bic.com): Holtsville, NY, 1990.
(32) Plaschke, M.; Schäfer, T.; Bundschuh, T.; Ngo Manh, T.; Knopp, R.; Geckeis, H.; Kim, J. I. *Anal. Chem.* **2001**, *73*, 4338−4347.
(33) Parkhurst, D. L.; Appelo, C. A. J. *User's Guide to PHREEQC (Version 2)- A computer program for speciation, batch-reaction, one-dimensional transport, and inverse geochemical calcultions*. Water Resources Investigations Report 99-4259, U.S. Department of the Interior: Washington, DC, 1999.
(34) Roden, E. E.; Urrutia, M. M. *Environ. Sci. Technol.* **1999**, *33*, 1847−1853.
(35) Schuessler, W.; Artinger, R.; Kim, J. I.; Bryan, N. D.; Griffin, D. *J. Contam. Hydrol.* **2001**, *47*, 311−322.
(36) Liang, L.; Morgan, G. G. *Aquat. Sci.* **1990**, *52*, 32−55.
(37) Day, G. M.; Hart, B. T.; McKelvie, I. D.; Beckett, R. *Colloids Surf. A* **1994**, *89*, 1−13.
(38) Reitmeyer, R.; Powell, R. T.; Landing, W. M.; Measures, C. I. *Mar. Chem.* **1996**, *55*, 75−91.
(39) Amirbahman, A.; Olson, T. M. *Environ. Sci. Technol.* **1993**, *27*, 2807−2815.
(40) Gu, B.; Mehlhorn, T. L.; Liang, L.; McCarthy, J. F. *Geochim. Cosmochim. Acta* **1996**, *60*, 1943−1950.
(41) Dardenne, K.; Schäfer, T.; Lindquist-Reis, P.; Denecke, M. A.; Plaschke, M.; Rothe, J.; Kim, J. I. *Environ. Sci. Technol.* **2002**, *36*, 5092−5099.
(42) Dardenne, K.; Schäfer, T.; Denecke, M. A.; Rothe, J. In *2nd Euroconference and NEA Workshop on Speciation, Techniques, and Facilities for Radioactive Materials at Synchrotron Light Sources*, September 10−12: Grenoble, France, 2000; pp 223−228.

Received for review December 7, 2001. Revised manuscript received January 13, 2003. Accepted January 29, 2003.

ES015832R

4.0 Influence of natural organic matter (NOM) on reaction processes

The sorption of organic materials can alter the physicochemical properties of mineral surfaces in many ways, i.e. rate and extent of dissolution, the sorption capacity for other solution species including contaminants, and the physical stability of colloids suspended in solution. Understanding the inorganic mineral sorption mechanism of NOM is of fundamental interest in order to understand on one hand the global carbon cycle and the anthropogenic influences on the CO_2 sequestration and on the other hand to identify major carbon preservation processes, e.g. leading to oil and gas reservoirs.

Minerals in natural systems are often associated with organics (e.g. in soils) as a result of pedogenic processes and anthropogenic impacts. Several aspects of organic-mineral particles, such as the type of layer silicates, intercalation of organic matter, and contents/types of metal oxides, are decisive for organic-mineral bonds. Literature data evaluation by comparing different sheet silicates revealed, that fractions rich in kaolinite often have small C_{org} contents, smectite-rich fractions contain C_{org} within a wide range, and fractions dominated by allophane have the largest C_{org} contents due to the small particle sizes and the large specific surface areas ($\leq 478\ m^2\ g^{-1}$) (Schulten and Leinweber, 2000). Comparatively large C_{org} contents appear to be characteristic for chlorite-rich fractions < 2µm, possibly due to low pH, which favors the simultaneous formation of secondary chlorites and poorly crystalline pedogenic oxides, both with large surface area, and inhibiting the decomposition of organic matter. Intercalation of organic matter in clay minerals has only seldom been found under natural conditions (Kennedy et al., 2002). One reason is that macromolecules such as humic acids (HAs) are larger than the interlayer spaces of up to 1.8 nm (smectite), which can be shown unequivocally by molecular modeling (Schulten and Leinweber, 2000). Hence, the properties of external surfaces are much more important for the binding of organic matter than the inner-particle crystal structure of clay minerals.

The adsorption of organic molecules on mineral surfaces can proceed through simple electrostatic and hydrogen bond interactions with surface hydroxyl groups (*outer-sphere complexation*) and/or through ligand exchange reactions to form direct bonds between the organic ligands and surface cations (*inner-sphere surface complexation*). Inner sphere complexation is widely considered to be important in mineral dissolution processes. Basic geochemical books (e.g. (Stumm and Morgan, 1996) show that organic ligands (e.g oxalate, citrate, salicylate, catechol and phthalate) promote dissolution rate of silicates and oxides under acidic conditions far from equilibrium compared to single inorganic acids at the same pH (Fig. 7). The ligand-promoted dissolution R_L is dependent on the surface ligand concentration $\{\equiv MeL\}$ (Eq. 1) and the type of ligand that forms inner-sphere complexes. The mineral dis-

solution reaction rate far from equilibrium is generally described by at least three mechanisms, (a) through decreasing solution pH or forming complexes with cations at the mineral surface, (b) by changing the saturation state of the solution with respect to the mineral phase and (c) by affecting the speciation in solution of ions such as Al^{3+} that themselves influence mineral dissolution rate (Drever, 1994; Drever and Stillings, 1997). The enhanced rate of e.g. kaolinite dissolution is usually interpreted in terms of the concentration of an Al-centered organic surface complex. On the basis of this hypothesis, the enhanced rate of kaolinite dissolution is related to the complexing ability of the anions of the organic acid chosen, especially with Al^{3+}. The larger the complexing constant of the organic acid, the higher the concentration of Al-centered organic surface complex and the higher the rate of kaolinite dissolution. Citrate, oxalate, and malate anions have higher complexing constants with Al than acetate anion and the rates of kaolinite dissolution in citric, oxalic, and malic acids are consequently higher than that in acetic acid (Wang et al., 2005).

$$R_L = \frac{d\{Me_{aq}\}}{dt} = k_L \{\equiv MeL\} \quad (1)$$

(Furrer and Stumm, 1986; Zinder et al., 1986) have proposed that organic ligand anions chelating surface metal cations as a bidentate mononuclear inner-sphere complex enhance dissolution kinetics. The reason is a considerable electron density transfer into the coordination sphere of the surface metal cation polarizing and weakening the mineral metal-oxygen bonds and therefore leaving the complexed metal cations more susceptible to be released from the surface. Spectroscopic studies focusing on the downscaling to nanoscopic resolution in order to understand macroscopic determined dissolution rates have demonstrated that organics as oxalate and malonate are indeed capable to form inner-sphere complexes (Duckworth and Martin, 2001; Duckworth and Martin, 2003).

Furthermore, it has been demonstrated that bidentate, binuclear, inner-sphere organic ligand complexes on mineral surfaces inhibit mineral dissolution (Biber et al., 1994). The stabilizing effect against dissolution by such binuclear complexes can be mainly attributed to the low probability, or in other words, the high activation energy associated with the simultaneous detachment of two metal cations from the mineral surface. Monodentate ligands (benzoate ion), though readily adsorbed, do not enhance dissolution rates (Furrer and Stumm, 1986; Zinder et al., 1986). The above mentioned subject of inner-sphere low molecular weight (LMW) organic acids sorption on mineral stability (weathering) has received considerable attention in the scientific community and a couple of reviews have been published over the years (i.e. (Drever and Stillings, 1997; Stumm, 1993)).

Therefore, in complex (natural) systems consisting of multiple LMW anionic species, the overall dissolution behavior is given by the balance of dissolution-enhancing and dissolution-inhibiting properties of organic ligands adsorbed in different modes. The adsorption modes

are themselves a function of the individual, relative, and overall concentration of these multiple LMW anionic species and the solution pH.

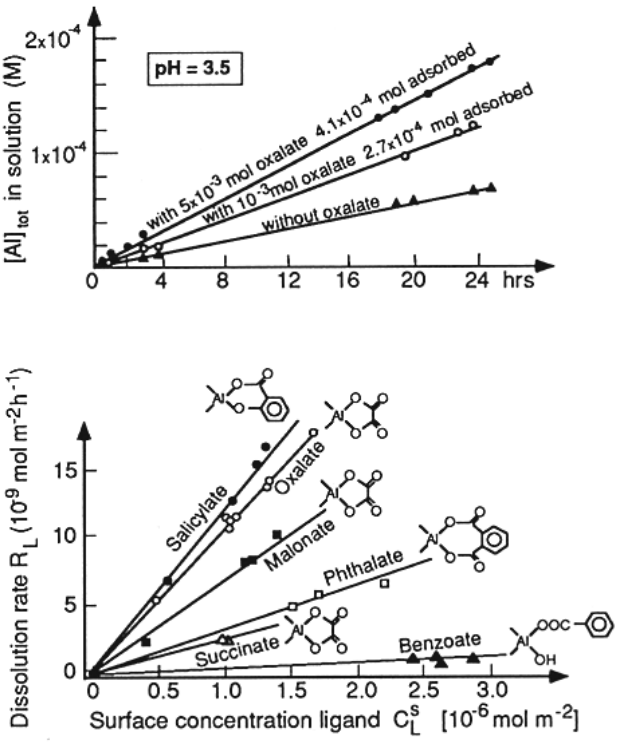

Figure 7: *Organic ligand promoted dissolution of alumina-oxide as a function of organic ligand surface coverage (upper graph) and type of organic ligand (lower graph) (images taken from (Stumm and Morgan, 1996)*

The role of outer-sphere LMW organic anions in mineral dissolution processes has been addressed a fewer attention in the literature and basically three potential outcomes can be found:

(a) The organic anions adsorbed, as outer sphere complexes, do not transfer significant electron density into the coordination sphere of the surface cations and therefore have little direct effect on dissolution kinetics. This hypothesis is supported by the correlation of aqueous metal complex reactivities with ligand-induced mineral dissolution rates, which shows that outer-sphere bound ligands have little impact on the kinetics of water exchange around solution based cations (Ludwig et al., 1995).

(b) The adsorption of an anionic ligand to the surface as an outer-sphere complex effectively decreases the surface charge, which in turn increases the surface protonation at a given pH. Thus, part of the ligand promotion effect might actually be a proton-promoted dissolution. Consequently, the effect of outer-sphere complexes on dissolution rates should primarily be due to a lowering of surface charge, and therefore indirectly a proton promoted dissolution rate increase (Persson et al., 1998).

(c) LMW multivalent organic anions, although adsorbed in an outer-sphere mode, bind tightly to the mineral surface via electrostatic and/or hydrogen bonding and therewith effectively hinder or block the attack of dissolution-promoting species such as protons. An overall reduction in the dissolution rate is the result. Studies by (Johnson et al., 2004) on maleate[8] induced corundum dissolution have demonstrated that such steric protection mechanisms indeed are observable.

Concerning the adsorption of natural organic matter fractions (fulvic acids) on metal oxyhydroxide surfaces (e.g. goethite) (Filius et al., 2003) have presented a detailed model of the macroscopic FA adsorption as a function of pH and ionic strength. This work suggests that FA inner-sphere surface complexation is of greatest importance at low pH with higher affinity of carboxyl groups to form inner-sphere complexes with decreasing pH, while outer-sphere complexes dominate at high pH. Similar results have been recently published by (Yoon et al., 2004) studying Suwannee River fulvic acid (SRFA) adsorption to aluminum (oxyhydr)-oxides, which predominantly sorbs in a outer-sphere manner forming only minor inner-sphere species under quite acidic pH conditions. Studies on the effect of natural macromolecular organic substances (NOM analogue pyromellitate and SRFA) on corundum dissolution at pH 3 showed an inhibition via sterically protection of dissolution-active surface sites against protolytic attack (Johnson et al., 2005). Furthermore, the dissolution-inhibiting effect of SRFA was substantially greater than that observed for pyromellitate, indicating that (1) SRFA is more strongly outer spherically bound to specific dissolution-active surface sites, (2) free (uncomplexed) SRFA charge groups are binding to (and therefore effectively trapping) Al^{3+} cations as they are released from the corundum surface, and/or (3) each SRFA anion is interacting with multiple dissolution-active surface sites on the corundum surface. The latter is understandable given the substantially larger predicted sizes of SRFA molecules compared to pyromellitate anions.

The simple organic molecules mentioned above represent building blocks of humic substances that are transformed from plant residues by microorganism (generation of amino compounds). Possible pathways include (a) the sugar – amino compound polymerization (i.e. Maillard reaction), (b) the poly-phenol theory via quinone – amino compound polymerization and (c) the classical theory of modified lignin – amino compound polymerization (Stevenson, 1982). A rather new aspect of organic matter mineral interaction has to be investigated in the light of considerations to use deep geological formations or geo-engineered materials for the final storage of high nuclear waste (HLW). This includes:

[8] Maleate is a simple dicarboxylate LMW anion, that has unfavorable monodentate or bidentate inner-sphere binding due to the formation of energetically unfavorable seven- or eight- membered chelate rings)

- Clay-rich low carbon formations as potential host rocks for HLNW[9] (e.g. Callovo-Oxfordian argillite, Opalinus clay or Boom Clay).
- Bentonite buffer/backfill will be used as one compartment of the engineered barrier system (EBS) in the multi barrier concept of HLNW storage (Arcos et al., 2003).
- The far-field aquifer system of salt formations considered as host rocks for HLNW (e.g. Gorleben) may contain high dissolved carbon concentrations (DOC) or chemically disturbed systems (hyperalkaline plume) can release organic compounds. These organic compounds can have a considerable metal complexation capability and additionally stabilize inorganic colloids and therefore might enhance the mobility of radionuclides.

Going to the first bullet, one concept of LLW[10] and ILW[11] waste storage (e.g. France) foresees the use of cement as waste confining container material. Initial cement corrosion will lead to hyper- alkaline conditions (Atkinson, 1985) and batch type studies have already demonstrated the dissolution of purified clay minerals in KOH solutions (Bauer and Berger, 1998). However, high alkaline treatment of the separated host rock clays (Callovo-Oxfordian argillite, France) have shown very different reaction behavior with low to undetectable dissolution of clay phases (Claret, 2001; Claret et al., 2002).

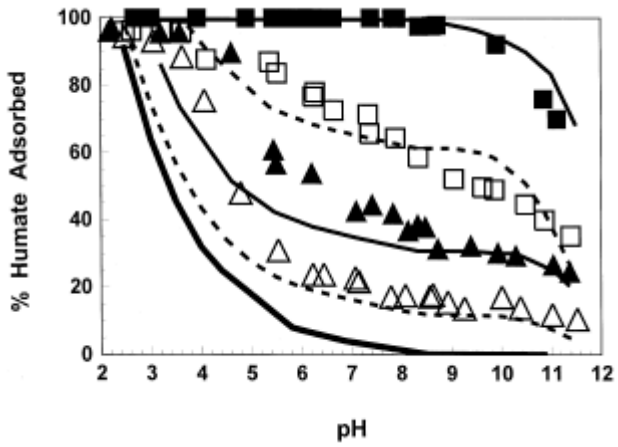

Figure 7: *Humic acid (0.1g/L) adsorption onto Al_2O_3 as a function of solution pH (0.1M NaNO3) Different symbols represent experiments with various Al_2O_3 concentrations; filled squares 20g/L, open squares 5g/L, filled triangles 2.5g/L, open triangles 1.0g/L. The thick solid line shows the percentage of total HA removed by precipitation from solution. The thin curves represents model fits using FITEQL to the data (Fein et al., 1999)*

Detailed carbon X-ray absorption near-edge structure (XANES) investigations on the separated clay phases showed organic coatings of clay edge-sites even after one-year reaction time in hyper-alkaline solution. The results are cooperated by studies on HA uptake of Al_2O_3

[9] HLNW: High Level Nuclear Waste
[10] LLW: Low Level Waste
[11] ILW: Intermediate Level Waste

under low surface loadings (Fig. 7) which also show a considerable amount of HA remaining on the mineral surface at alkaline pH (Fein et al., 1999). Additionally, organic matter polymerization processes during the diagenetic burial history contribute to the passivation of reactive clay edge sites, as shown by the low amount of oxygen-containing functional groups in the clay-associated organic matter (Claret et al., 2002; Schäfer et al., 2003b). The outcome of this work point out that study on HA/FA mineral surface sorption might be inappropriate to simulate the natural organic/mineral- association in sedimentary rocks. However, the evolution of pore/reaction water shows a release of DOC (dissolved organic carbon) and functional group changes in both the reaction water and on clay associated organics (Claret et al., 2003; Schäfer et al., 2003b) which indicates that kinetics play a dominant role and a clay dissolution after complete natural organic carbon release might start. The released organic material showed comparable Cm(III) complexation behavior to brown coal derived humic acid (Aldrich) (Claret et al., 2005).

Considering the second bullet, the process of radionuclide bentonite interaction has to be understood in detail in order to reliable predict the retention capacity of different compartments of the EBS. In real systems having complex porewater chemistries, metal complexes such as carbonates, hydroxy-carbonates and sulfates will be present. Their role needs to be elucidated and quantified. Organic ligands may be present, and could form coatings on mineral surfaces. This would imply that they, and not the component minerals, might control the uptake on immobile phases. Spectroscopic investigations on trivalent actinide (Cm^{3+}) clay (Febex bentonite; Spanish bentonite backfill material) interaction using time-resolved laser fluorescence spectroscopy (TRLFS) have demonstrated, that clay associated organics have some complexation capabilities (Geckeis et al., 2004) and fluorescence spectra are different compared to pure clay phases (Bradbury et al., 2005; Rabung et al., 2005; Stumpf et al., 2002; Stumpf et al., 2001). The combination with carbon C(1s) XANES spectromicroscopy showed furthermore the association of these highly functionalized organic ligands with bentonite minerals (Geckeis et al., 2004). The research in this field is ongoing, but it is clearly important to achieve an understanding of uptake processes, and develop mechanistic models to quantify them. The ultimate goal is that such models will be capable of predicting sorption values over the spectrum of conditions in the near- and far-fields of a radioactive waste repository.

The third bullet concerns the mobility of natural organic matter (humic and fulvic acids) in geological environments. (Artinger et al., 2000; Buckau et al., 2000a) have demonstrated by stabile isotope analysis that fulvic acids can be mobile over long distances (km) in aquifer systems. The combination of stable isotopic data (^{13}C, ^{14}C, ^{3}H) and carbon/sulfur K-edge XANES spectroscopy has been used to determine the mobility of fulvic acids (FAs) in the Gorleben aquifer system and the results indicate the invariance of the FA backbone structure

against high residence times and variation in geochemical conditions and a vertical transport from recharge dominated region to the cap rock influenced channel brines (Schäfer et al., 2005a; Schäfer et al., 2003c). The peer- reviewed publications given in this chapter can be subdivided in the following topics:

- Clay reactivity under high alkaline solution conditions typical for the initial cement corrosion (Claret et al., 2002; Taubald et al., 2000).
- Hydrophilic organic matter characterization in clay-rich host rock formations (Callovo-Oxfordian argillite and Opalinus Clay) and the in the Gorleben aquifer system, overlaying a Permian salt dome (Claret et al., 2003; Claret et al., 2005; Schäfer et al., 2005a)
- Source of organic matter and OM metal complexation behavior (Claret et al., 2005; Plaschke et al., 2002; Schäfer et al., 2005b)

Experimental investigation of the effect of high-pH solutions on the Opalinus Shale and the Hammerschmiede Smectite.

Clay Min. (2000) **35**(3), 515.

Taubald H., Bauer A., Schäfer T., Geckeis H., Satir M., and Kim J. I.

Clay Minerals (2000) **35**, 515–524

Experimental investigation of the effect of high-pH solutions on the Opalinus Shale and the Hammerschmiede Smectite

H. TAUBALD[1], A. BAUER[2,*], T. SCHÄFER[2], H. GECKEIS[2], M. SATIR[1] AND J. I. KIM[2]

[1]*Universität Tübingen, Institut für Mineralogie, Petrologie und Geochemie, Lehrstuhl fuer Geochemie, Wilhelmstr. 56, D-72074 Tübingen, and* [2]*Forschungszentum Karlsruhe, Institut für Nukleare Entsorgungstechnik, PO Box 3640, D-76021 Karlsruhe, Germany*

(*Received 20 June 1999; revised 20 September 1999*)

ABSTRACT: The alteration and transformation behaviour of the Tertiary Hammerschmiede Smectite and the Jurassic Opalinus Shale in an alkaline solution was studied in column experiments. The Hammerschmiede Smectite is proposed as potential backfill material and the Opalinus Shale as host rock for the Swiss low-level nuclear waste storage site. Over a period of 18 months, the evolution of permeability, pH and solution concentrations were measured. After the experiment, the columns were cut into pieces to study the mineralogical and the chemical evolution of the clays. X-ray diffraction (XRD) revealed no significant appearance or disappearance of diffraction peaks at the end of the experiments. The scanning electron micrographs of the clays revealed that both clays exhibited a precipitation zone, which extends from 0 to 2 cm below the infiltration surface. Both clays showed significant differences in the evolution of pH and hydraulic conductivity. The solution front crossed the Opalinus Shale column entirely after only 11 weeks and the initial values for K^+ and Na^+ were conserved in the solution. For both clays, the salt concentrations in the percolating fluids mirror the evolution of pH.

KEYWORDS: Opalinus Shale, Hammerschmiede Smectite, hydraulic conductivity.

The effect of alkaline solutions on clay minerals has been the subject of study for a number of years (Velde, 1965; Eberl & Hower, 1977; Mohnot *et al*., 1987; Carroll-Webb & Walther, 1988; Carroll & Walther, 1990; Chermark, 1992; Chermark, 1993; Eberl *et al*., 1993; Huang, 1993; Adler *et al*., 1998; Bauer *et al*., 1998; Bauer & Velde, 1999). The stability of kaolinite in aqueous solutions of varying pH has been the object of more numerous investigations (May *et al*., 1986; Carroll-Webb & Walther, 1988; Carroll & Walther, 1990; Nagy *et al*., 1991; Wieland & Stumm, 1992; Ganor *et al*., 1995; Bauer *et al*., 1998; Bauer & Berger, 1998). One objective of such studies has been to determine the ultimate stability of clays as barriers to the migration of aggressive solutions emanating from man-made repositories. These clay barriers are designed to contain nuclear waste products, as well as municipal waste concentrates. The major concern in these cases is the rate of reaction of clays. Such information is important for risk assessments or evaluations and calculations concerning the safety of repositories.

High-pH solution-mineral reactions occur in a variety of natural geological environments as well in environments modified by human activity in various engineering projects. Two common 'engineered' high-pH environments include emplaced concrete (Atkinson, 1985; Andersson *et al*., 1989; Lunden & Andersson, 1989; Savage *et al*., 1992)

* E-mail: bauer@ine.fzk.de

and alkaline flooding of sandstone reservoirs (Novosad & Novosad, 1984; Mohnot *et al*., 1987). Concrete and cement are proposed as matrix material, backfill material and as structural components of radioactive waste repositories (Bath *et al*., 1987). The amount of concrete and cement associated with these repositories, especially in low-level waste facilities, is often quite large (e.g. 8.2×10^5 m^3, Karlson *et al*., 1986). Solidification or disaggregation of concrete in natural environments will produce high-pH solutions. The initial pore fluids in hydraulic cement range in pH from 12.5 to 13.5, have high ionic strengths, and are dominated by Na and K in concentrations ranging from 300–4200 ppm and 100–7500 ppm, respectively (Andersson *et al*., 1989; Lunden & Andersson, 1989). The Ca concentrations in these pore-fluids are much lower and range from 20–130 ppm. The release of this alkaline, high-pH plume to the surrounding media has been modelled (Haworth *et al*., 1989; Reardon, 1990; Jeffries *et al*., 1988; Berner, 1990; Vieillard & Rassineux, 1992). Results show that there is an initial period of NaOH and KOH release (pH >13), followed by a solution composition controlled by portlandite $Ca(OH)_2$ and finally a solution composition controlled by calcium silicate hydrate (CSH) gels (pH to 9–10).

The present study was designed to provide a description of the reaction relations between two different clays and basic aqueous solutions typical of the initial alteration of concrete. In this study, we combined chemical and mineralogical methods to describe the possible long term behaviour of clays in a repository under alkaline conditions.

MATERIALS AND METHODS

Experimental set-up

Column experiments were performed for 18 months at room temperature. A batch of ~2 kg of Hammerschmiede Smectite (HS) and Opalinus Shale (OP) raw material were crushed carefully to obtain an homogeneous mass, and deionized (DI) water was added until a water content of 21.0% was reached to obtain a proctor density of 95% (wet side). The HS and OP were then compacted in a proctor device and cylindrical samples formed, reaching a density of 1.705 g/cm^3 for HS and 1.621 for OP (95% of 1.795 g/cm^3 and 1.706 respectively) (German TA-Abfall (1991), for details see German DIN regulation No. 18127). These samples were then inserted into the permeability cells (8 cm high and 9 cm in diameter) and saturated with DI water, reaching a constant permeability of about 3×10^{-10} m/s after four weeks (according to DIN regulation 18130). The resulting exchange of one pore volume probably caused a weak leaching which is negligible with regard to the further treatment of the sample. The high pH solution was percolating from the top to the bottom of the column. The hydraulic gradient in our experiments was achieved by compressed air. We used this experimental configuration to simulate possible influences of limited amounts of CO_2 in the pore-spaces of compacted backfill material in a nuclear waste disposal site.

The initial hydraulic gradient was $i = 20$ for both materials, where i is the ratio of the water level in cm above the column divided by the height of the column in cm. The value $i = 20$ was chosen because it represents a standard value in applied geology. After 40 weeks, the hydraulic gradient was reduced to $i = 1$ for the OP and raised to $i = 90$ for the HS. This change was necessary to prevent leakage from the OP column and to obtain enough solution for the HS column measurements. Values for the hydraulic conductivity (k) were measured at 20°C (DIN procedure 18130). After the experiments, the columns were cut into 5–6 horizontal segments to study the mineralogical and chemical evolution of the system.

Starting materials

The starting materials were the Opalinus Shale and the Hammerschmiede Smectite. The initial fluid used was designated the simple young fluid (SYF). They were characterized as follows:

Starting solution. The chemical composition of the SYF is supposed to be typical for solutions resulting from the initial stages of cement alteration (Nagra, internal report, 1995). The starting solutions were prepared from analytical reagent grade KOH, NaOH and $Ca(OH)_2$ salts. The solution composition and the initial pH are given in Table 1.

EQ 3 (Wolery, 1983) calculations, in the absence of CO_2, were performed to determine the distribution of the aqueous species in solution (Fig. 1). At the initial pH, the solution is slightly oversaturated with respect to portlandite (log Q/K = 0.407). The starting solutions were nevertheless clear and showed no precipitation with time, when not exposed to air.

TABLE 1. Solution composition of the simple young fluid (SYF) and the initial solution pH.

NaOH	2.606 g/l
KOH	9.033 g/l
$Ca(OH)_2$	0.166 g/l
pH (initial) = 13.22	

Starting clays. The OP and the HS were characterized by XRD, X-ray fluorescence (XRF), scanning electron microscopy (SEM) and gas absorption surface area analysis with N_2 (BET). The XRD determination of the amount of quartz and calcite was carried out on the bulk clays using LiF internal standard mixture (Brindley, 1980). Semi-quantitative analysis of the <4 μm fraction was determined by comparing patterns to those of standard clay mineral mixtures (Brindley, 1980). Table 2 gives the mineral and chemical composition of the starting clays as determined by XRF. The weight loss on ignition (LOI) was determined gravimetrically. The specific surface area determined by the BET (Brunauer *et al.*, 1938) method using N_2 adsorption was found to be 15 m^2/g for the OP and 41 m^2/g for the HS. The presence of S and C in the starting material was analysed using a LECO-125 C/S analyser. The total organic content (TOC) in the OP was <0.4 wt.% and 0.1 wt.% SO_2 was measured. No S or C was found in the HS.

Identification of the reacted products

XRF and ICP-MS. To follow the chemical evolution of the two clays chemical analyses of the starting and the reacted materials were carried out. Elemental analysis for major components was performed on a Siemens SRS 300 XRF spectrometer. The ICP-MS measurements were carried out on an ICP-MS Elan 6000 (Perkin-Elmer) to determine the concentration of the rare earth elements (*REE*) and other trace elements.

XRD. After the experiments, the material was homogenized and crushed gently in a mortar. The solids were then washed with 250 ml distilled/DI water. The suspensions were passed through a Millipore filter (0.1 μm) in order to concentrate the material for XRD. To follow the reaction trend of the clays, 4 g of sample material were suspended in 300 ml DI water and the pH adjusted to 4.8 with 0.01 M HCl until the pH remained constant. After stirring for 24 h in high density PE bottles, the solid was separated by centrifugation, resuspended in 100 ml DI water, filtered and washed with 50 ml 1 M $SrCl_2$ at 50°C for 24 h to obtain homoionic clays with two water-layers in the interlayer. The 0.2 μm fractions of the clays were separated by sedimentation techniques (Day, 1965). The suspensions were passed through a Millipore filter (0.1 μm) in order to concentrate the material and to orient the clay particles for XRD (Moore & Reynolds, 1997).

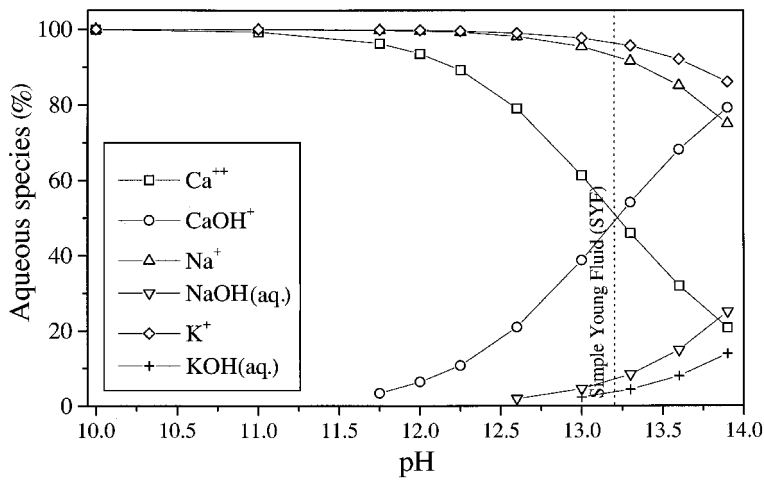

FIG. 1. EQ3 calculation of the distribution of the aqueous species (%) in a solution with the simple young fluid composition as function of pH. The dashed line indicates the initial SYF.

TABLE 2. Estimated mineral composition, the BET surfaces and the oxide composition as determined by XRF (wt.%) of the starting clays.

Mineral composition (%)	OP	HS	Oxide composition	OP	HS
smectite	–	53	SiO_2	60	48.8
illite	25	7	Al_2O_3	14.1	15.6
chlorite	5	–	CaO	6.65	9
kaolinite	20	19	Fe_2O_3	4.8	6.2
illite/smectite	8	–	K_2O	2.8	4.2
quartz	30	5	Na_2O	0.4	0.45
calcite	10	16	MgO	1.4	2.5
dolomite	–	–	LOI	9.23	13.7
siderite	2	–	SO_2	0.1	–
			TOC	<0.4	–
Total	100	100		99.88	100.45
BET	15 m^2/g	41 m^2/g			

The XRD patterns of the samples were recorded using a Philips PW 1050/20 diffractometer with a stepping-motor drive goniometer and Ni-filtered Cu-$K\alpha$ radiation (fine focus tube, Philips PW 2213/20). Motor displacement and intensity acquisition (Siemens proportional detector) commands were effected using a Socabim DACO system. The divergence slit, receiving slit and scatter slit were 1°, 0.1 mm and 1°, respectively. Usual step size and counting times were 0.01°2θ and 3 s, respectively.

These methods allowed precise determinations of diffraction peak characteristics such as position and width which were analysed using the deconvolution program DECOMPXR (Lanson & Velde, 1992; Lanson & Besson, 1992). A detailed description of the deconvolution procedure can be found in Lanson (1997).

The portion of expandable and non-expandable interlayers were determined using the NEWMOD program (Reynolds, 1985). Quantitative determination of mineral phases in shales is quite difficult and in this study only relative changes in mineral proportions are discussed (i.e. total disappearance of diffraction peaks and appearance of new ones).

SEM. Scanning electron micrographs of the untreated, reacted material were made in order to observe minor components not revealed by XRD and to observe the relative stability of the different reaction products. The SEM micrographs were obtained using a JEOL GSM-6100 instrument with a KEVEX energy dispersive detector, used for semi-quantitative analysis (ratio of peak heights).

Solution compositions. The cation composition of the fluids was measured using a Perkin-Elmer Analyst 300 atomic absorption spectrometer. The Ca^{2+}, Mg^{2+}, Na^{+} and K^{+} were measured with the flame technique and Si^{4+} with the graphite furnace technique on diluted solutions. The pH was measured using a WTW 537 pH meter calibrated using five standard solutions (pH 7, 9, 10, 11, 13).

EXPERIMENTAL RESULTS

Solids

After 18 months, the two columns showed (1–2 cm) a change in colour in the upper zone, due to the precipitation of a fine white veil of secondary phases. After the experiments, the columns were cut into segments and analysed to study the distribution of the elements. While cutting the columns, the growth of white secondary phases along discrete planar features of enhanced permeability such as bedding planes and micro-cracks were observed for the OP. To follow the evolution, we used the ratio concentration of the initial clays to the concentration found in the two treated samples.

Mineralogy. No significant appearance or disappearance of diffraction peaks were observed for the OP and HS column within a range of 2 to 56°2θ throughout the whole sample. Only the chlorite disappeared in the first two segments of the OP columns. The decomposition of the XRD patterns

indicated no significant changes in the diffraction domain size of kaolinite for OP.

A reduction of the coherent scattering domain size was noted for the first two segments of HS, but without illitization. The SEM revealed a precipitation zone in both clays, extending from 0 to 2 cm above the infiltration surface and made up of fibrous to honeycomb-textured CaAlSi hydroxide phases (CASH). In this zone, neoformed Ca carbonate, portlandite and brucite also occur. In all segments of HS, a small number of very fine but blocky crystallites can be found under SEM. These appear to be randomly distributed and EDAX analysis showed that they have a Ca,Mg hydroxide composition. In most of the EDAX analysis a small Sr peak was observed on the spectra.

Major elements. The CaO, K_2O and Na_2O are relatively more abundant in the top of both columns. This observation was true for the first 2 cm of the HS column (Fig. 2). For the OP, this zone of enrichment is smaller, and the 10–20 mm level even shows a small depletion in CaO, K_2O and Na_2O. There was no evolution of K_2O in lower segments. The Hammerschmiede sample exhibited a slight increase of CaO and MgO concentrations at the bottom of the column, accompanied by a depletion in Na_2O. The last two segments of the OP showed no changes.

The Fe_2O_3, MgO and Al_2O_3 are depleted in the first 20 mm of the column in both clays but showed no significant change in the lower part, except for MgO in the HS column. Both clays showed only a slight decrease in relative SiO_2 abundance at the top of the columns but no change with increasing depth.

REE and trace elements. The *REE* and trace elements Pb, Mn, Th, Cu, Li and Cs showed no significant changes and no fractionation throughout the column.

Solutions

The evolution of the salt concentrations in the percolating fluids reflect the pH evolution (see Figs. 3a, 4). The Na^+ and K^+ increase, while Ca^{2+} and Mg^{2+} decrease with increasing pH, indicating the breakthrough of the high pH plume through the column. This is especially true for the HS column, where pH and cation concentration correlate perfectly. With increasing pH, the concentration of Ca^{2+} and Mg^{2+} were below detection limits for both clays. The Fe^{3+} solution concentrations increased for the OP for 20 weeks and then decreased (Fig. 3a). It is striking that after only 11 weeks, the solution front crossed the OP column entirely and the initial solution values for K and Na were conserved (Fig. 3a).

The concentrations for Si^{4+} and Al^{3+} also correlate with the evolution of the solution pH (Fig. 3b). However, a slight increase in Si^{4+} and Al^{3+} concentrations was observed for HS before the breakthrough of high pH in the fluid correlating with a slight pH increase.

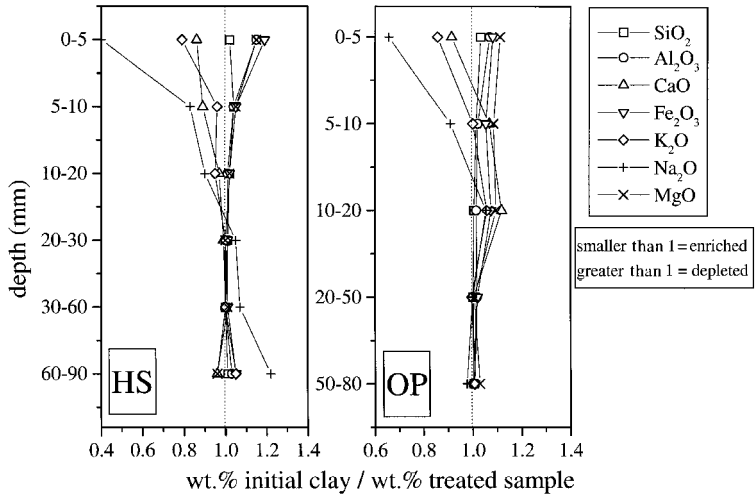

FIG. 2. Evolution of the major elements, plotted as $conc._{(initial\ clay)}/conc._{(altered\ clay)}$, as a function of column depth after the experiments.

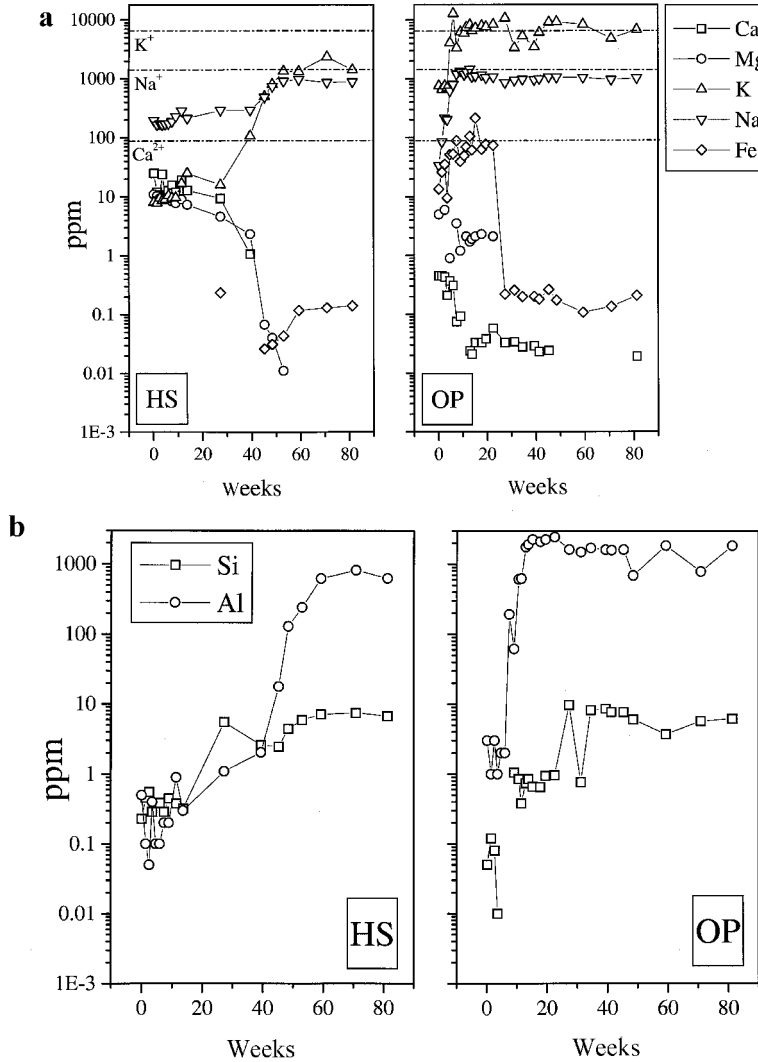

FIG. 3. Evolution of the percolate solution concentrations as a function of time. (a) Ca, Mg, K, Na and Fe solution concentrations as a function of time. (b) Si and Al solution concentrations as a function of time.

Evolution of the pH. The two different clays exhibit different changes in pH with time (Fig. 4). In the first 40 weeks, the pH showed only a slight increase for the HS (8.5 to 9.2). After this period, the pH increased continuously to 12.42 at 59 weeks, after which it remained constant until the end of the experiments (Fig. 4). The OP showed no pH change for the first 6 weeks. This period was followed by an increase of the pH from 7.31 to 12.74 within 5 weeks. After this the pH showed only a slight increase, reaching a maximum after 45 weeks (13.21) to come down again to a value of 12.72 at the end of the experiment.

Evolution of the hydraulic conductivity. At the beginning of the experiment, both materials showed the same hydraulic conductivity of 3×10^{-10} m/s for pore-water (Fig. 4). The hydraulic conductivity of OP stayed more or less constant for 40 weeks. After 40 weeks, the hydraulic conductivity exhibited a significant increase (Fig. 4). It was necessary to reduce the hydraulic gradient to $i = 1$ to prevent the total failure of the OP column. The permeability

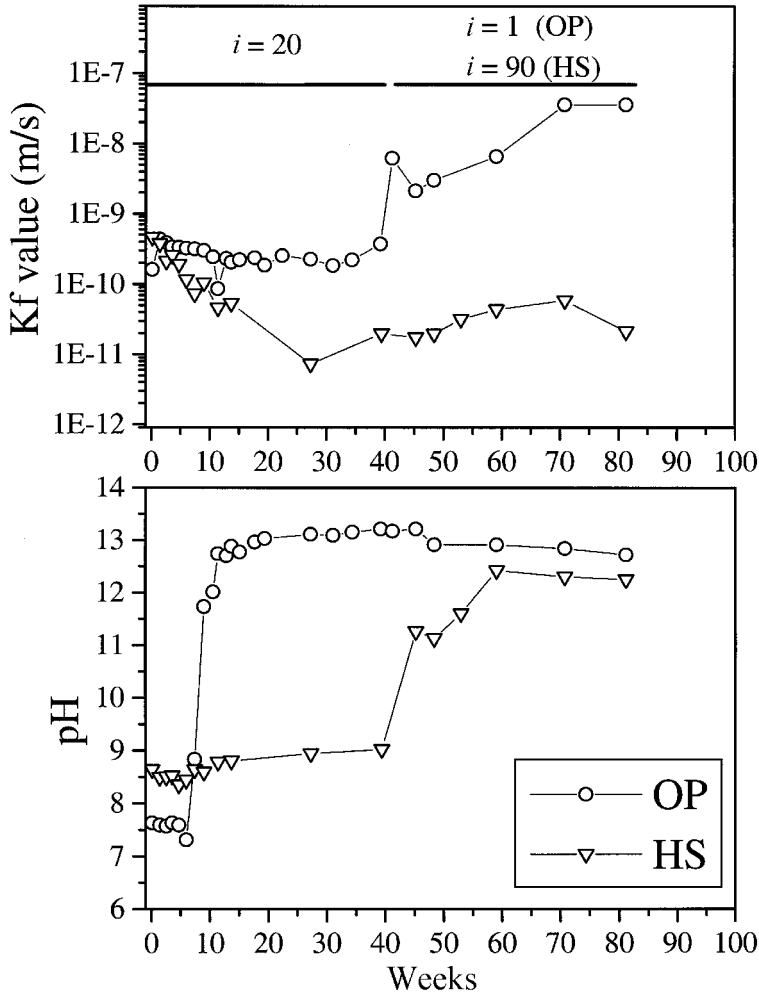

FIG. 4. Evolution of the percolate pH and the hydraulic gradient of the columns as a function of time.

increase continued up to a value more than two orders of magnitude (3.51×10^{-8} m/s) greater, until the end of the experiment.

The hydraulic conductivity of HS decreased by two orders of magnitude to a value of 7.27×10^{-12} m/s after 27 weeks. After 40 weeks, the hydraulic gradient was increased to $i = 90$, to assure enough percolating fluid for sampling. Then the hydraulic conductivity increased slowly again until the end of the experiment, to a value of 2.1×10^{-11} m/s. The total amount of percolating fluid was ~900 ml for HS and ~2400 ml for OP (see Fig. 5).

DISCUSSION

The main purpose of this experimental investigation was to determine the effect of basic solutions on the mineralogy and chemistry of clays under conditions which might be expected in a low-level nuclear waste disposal. All standards for the preparation of clay liners proposed by the German law have been respected (German TA-Abfall, 1991; German DIN regulation No. 18127; DIN regulation 18130). Although both clays started with the same hydraulic conductivity for pure water, the alkaline solution front crossed the OP column after only 11 weeks,

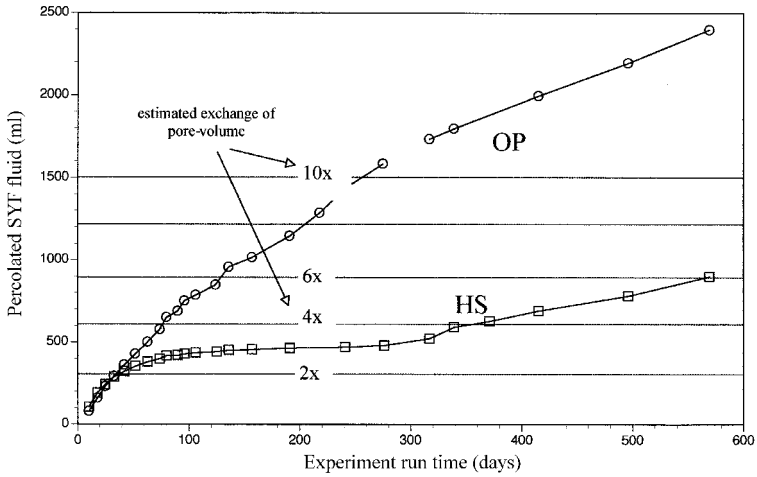

FIG. 5. Total amount of percolated fluid for HS and for OP.

when pore-volume was exchanged four times. The initial concentrations for K^+ and Na^+ were found after percolation. Breakthrough of the high-pH plume occurs after 40 weeks for the HS, which correlates approximately to a four-fold pore-volume exchange (see Fig. 5).

A significant increase in hydraulic conductivity from 4×10^{-10} (39 weeks) to 6.2×10^{-9} was observed for the OP after 40 weeks. It was necessary to reduce the hydraulic gradient to $i = 1$ to prevent the leakage of the OP column. The evolution of hydraulic conductivity was different for the HS: it decreased to a value of 7.3×10^{-12} m/s after 27 weeks. After 40 weeks, the hydraulic gradient was changed to $i = 90$ but remained below the starting value (3×10^{-10} m/s) even after the breakthrough of the high pH solution. The Na^+ concentrations in percolated solutions for HS showed the starting value of Na^+ after 53 weeks. The K^+ concentration increased with time but remained one order of magnitude below the initial value at the end of the experiment.

The hydraulic gradient was provided in our experiments by compressed air. A regular control of the pH of the percolated fluid showed no significant decrease of the pH due to carbonatization of the solutions. It is important to note that the solution pH did not change significantly while the solutions passed through the columns. This observation is important because it indicates that there is no significant reaction between the fluid and the clay. If a reaction had occurred, a drop in pH due to the speciation of Al^{3+} and Si^{4+} would have been observed. Chermark (1992) measured a drop in the quenched pH from 12.91 down to 6.68 after 35 days at 200°C in his batch experiments with fine-grained Opalinus Shale. Bauer (1997) observed the same evolution of solution pH in his batch experiments at 35°C and 80°C for kaolinite and smectite for initial KOH concentrations below 0.1 M KOH. In the case of the HS, mass balance calculations showed that the difference between the initial pH (13.2) and final pH (12.4) is consistent with the decrease in K^+ concentration, so that the mass balance is conserved. The initial interlayer cations, Ca^{2+} and Mg^{2+}, were obviously exchanged for K. The liberated cations precipitated to form Ca,Mg hydroxide, which was observed using SEM.

The evolution of the major and trace elements showed no such significant differences along the profile of the column that might explain the observed differences in the evolution of the hydraulic conductivity. Both clays showed a leached layer enriched in CaO, K_2O and Na_2O. The same association of new phases in the upper part of the column was observed for both clays. The *REE* concentrations for both clays showed no evolution and there is no correlation between the formation of secondary phases and *REE* in either case.

The XRD revealed that only chlorite, which is highly unstable under oxidizing conditions, was eliminated in the upper segments of the OP column. The dissolution of the chlorites may also be

responsible for the evolution of the Fe^{3+} concentration in the percolating solutions of the OP. In the lower segments chlorite was not dissolved; this may indicate that the permeability increased significantly after 40 weeks and the SYF fluid passed through the sample along preferential pathways. The alteration of clays under high-pH conditions was described by Eberl *et al*. (1993), Bauer *et al*. (1998) and Bauer & Velde (1999). Bauer & Velde (1999) observed in their smectite experiments an initial decrease in the coherent diffracting domain size of the smectites followed by a decrease of the expandability of the clays. In kaolinite experiments, Bauer *et al*. (1998) described the transformation of kaolinite to K-feldspar in high molar KOH conditions at low temperatures. The decomposition of XRD patterns in our experiments indicated no significant changes in the diffraction domain size of kaolinite for the OP and a reduction of the coherent scattering domain size of smectites only in the first two segments, but without illitization. According to Bauer *et al*. (1998) and Bauer & Velde (1999), this observation indicates that the experiments are in the dissolution phase of the reactions between clay mineral and solution.

Due to the observed chemical reactions, including precipitation of secondary phases, advective transport in the columns was reduced. This decrease in permeability indicates that diffusion controlled transport processes must gain importance with increasing run time in the case of the HS. As mentioned above, pore-volume normalized breakthrough curves indicate no significant difference between the OP and the HS. The hydraulic conductivity for the HS decreased from the initial value for pore-water to that for SYF (Fig. 4). The phenomena can probably be explained by Ca,Mg hydroxide precipitation reducing the effective pore-space in the HS. This, however, can not explain the enhanced hydraulic conductivity for the OP. Continuation of the dissolution reactions for the kaolinite-rich OP might force development of preferential pathways after 40 weeks. Even a reduction of the experimental adjusted gradient could not prevent a further increase in hydraulic conductivity. These results indicate a negative evolution of the hydraulic properties of the illite/kaolinite-rich OP shale, when used as an engineered barrier system in contact with an alkaline solution. Further investigations concerning the coupled chemical-hydraulic transport processes are in progress to test this hypothesis.

REFERENCES

Adler M., Mäder U. & Waber N. (1998) Experiment vs modelling: Diffusive and advective interaction of high-pH solution in argillaceous rock at 35°C. Abstracts of the Goldschmidt Conference 1998, *Mineral. Mag*. **62A**, 15–16.

Andersson K., Allard B., Bengtsson M. & Magnusson B. (1989) Chemical composition of cement pore waters. *Cement Concrete Res*. **19**, 327–332.

Atkinson, A. (1985) *The Time Dependence of the pH within a Repository for Radioactive Waste Disposal*. AERE R11 777, HMSO, London.

Bath A. H., Cristofi N., Neal C., Philp J. C., McKinley I. G. & Berner U. (1987) *Trace Element and Microbial Studies of Alkaline Groundwater in Oman, Arabian Gulf: A Natural Analogue of Cement-Pore Waters [rep.]*. Nagra NTB, 90-12, Baden, Switzerland.

Bauer A. (1997) *Etude du comportement des smectites et de la kaolinite dans des solutions potassiques (0.1–4 m)*. Thèse de 3ème cycle, Univ. Paris 6.

Bauer A. & Berger G. (1998) Kaolinite and smecite dissolution rate in high molar KOH solutions at 35 and 80°C. *Appl. Geochem*. **13**, 905–916.

Bauer A. & Velde B. (1999) Smectite transformation in KOH solutions. *Clay Miner*. **34**, 261–276.

Bauer A., Velde B. & Berger G. (1998) Kaolinite transformation in high molar KOH solutions. *Appl. Geochem.* **13**, 619–629.

Berner U. (1990) *A Thermodynamic Description of the Evolution of Porewater Chemistry and Uranium Speciation during the Degradation of Cement [rep.]*. Nagra NTB, 90-12, Baden, Switzerland.

Brindley G.W. (1980) Quantitative X-ray mineral analysis of clays. Pp. 411–438 in: *Crystal Structures of Clay Minerals and their X-ray Identification* (G.W. Brindley & G. Brown, editors). Monograph **5**, Mineralogical Society, London.

Brunauer S., Emmett, P.H. & Teller E. (1938) Adsorption of gases in multimolecular layers. *J. Am. Chem. Soc*. **60**, 309–319.

Carroll S.A. & Walther J.A. (1990) Kaolinite dissolution at 25°, 60° and 80°C. *Am. J. Sci*. **290**, 797–810.

Carroll-Webb S. & Walther J. V. (1988) A surface complex reaction model for the pH-dependence of corundum and kaolinite dissolution. *Geochim. Cosmochim. Acta*, **52**, 2609–2623.

Chermark J.A. (1992) Low temperature experimental investigation of the effect of high pH NaOH solutions on the Opalinus Shale, Switzerland. *Clays Clay Miner*. **40**, 650–658.

Chermark J.A. (1993) Low temperature investigation on the effect of high pH KOH on the Opalinius Shale Switzerland. *Clays Clay Miner*. **41**, 365–372.

Day P.R. (1965) Particle fractionation and particle size analysis. Pp. 545–567 in: *Methods of Soil Analysis* (C.A. Black, editor). American Society of

Agronomy, Inc.
DIN 18127, *Proctorversuch*, April 1976, Beuth Verlag.
DIN 18130, Teil 1: *Bestimmung des Wasserdurchlässigkeitsbeiwerts*, November 1989, Beuth Verlag.
Eberl D.D. & Hower J. (1977) The hydrothermal transformation of sodium and potassium smectite into mixed layer clays. *Clays Clay Miner.* **25**, 215–227.
Eberl D.D., Velde B. & McCormick T. (1993) Synthesis of illite-smectite from smectite at earth surface temperatures and high pH. *Clay Miner.* **28**, 49–60.
Ganor J., Mogollon J.L. & Lasaga A.C. (1995) The effect of pH on kaolinite dissolution rates and on activation energy. *Geochim. Cosmochim. Acta*, **59**, 1037–1052.
Haworth A., Sharland S.M. & Tweed C.J. (1989) Modelling of the degradation of cement in a nuclear waste repository. *Proc. Mat. Res. Soc. Symp.* **127**, 447–454.
Huang W.J. (1993) The formation of illitic clays from kaolinite in KOH solution from 225°C to 350°C. *Clays Clay Miner.* **6**, 645–654.
Jeffries N.L., Tweed C.J. & Wisbey S.J. (1988) The effects of changes in pH in a clay surrounding a cementitious repository. *Mat. Res. Soc. Symp. Proc.* **112**, 43–52.
Karlson L.G., Höglund L.O. & Pers K. (1986) *Nuclide Release from the Near-Field of a L/ILW Repository [rep.].* Narga NTB, 85-33, Baden, Switzerland.
Lanson B. (1997) Decomposition of experimental X-ray diffraction patterns (profile fitting): A convenient way to study clay minerals. *Clays Clay Miner.* **45**, 132–146.
Lanson B. & Besson G. (1992) Characterisation of the end of smectite to illite transformation: decomposition of X-ray patterns. *Clays Clay Miner.* **40**, 40–52.
Lanson B. & Velde B. (1992) Decomposition of X-ray diffraction patterns; A convenient way to describe complex diagenetic evolutions. *Clays Clay Miner.* **40**, 629–643.
Lunden I. & Andersson K. (1989) Modelling the mixing of cement pore water and groundwater using the PHREEQE code. *Mat. Res. Soc. Symp. Proc.* **127**, 949–956.
May H.M., Kinniburgh D.G., Melmke P.A. & Jackson M.L. (1986) Aqueous dissolution, solubilities and thermodynamic stabilities of common aluminosilicate clay minerals: Kaolinite and smectites. *Geochim. Cosmochim. Acta*, **50**, 1667–1677.
Mohnot S.M., Bae J.H. & Foley W.L. (1987) A study of alkali/mineral reactions. *SPE Reservoir Engineering*, **Nov. 1987**, 653–663.
Moore M.D. & Reynolds R.C., Jr. (1997) *X-ray Diffraction and the Identification and Analysis of Clay Minerals*. Oxford University Press.
Nagra Interner Bericht 95-70 (1995) *Column Experiments: Results of experiments and modelling* (unpublished report).
Nagy K.L., Blum A.E. & Lasaga A.C. (1991) Dissolution and precipitation kinetics of kaolinite at 80°C and pH 3. *Am. J. Sci.* **291**, 649–686.
Novosad Z. & Novosad J. (1984) Determination of alkalinity losses resulting from hydrogen ion exchange in alkaline flooding. *SPE of AIME*, 49–52.
Reardon E.J. (1990) An ion interaction model for the determination of chemical equilibrium in cement/water systems. *Cement Concrete Res.* **20**, 175–192.
Reynolds R.C., Jr. (1985) *NEWMOD, a computer program for the calculation of basal diffraction intensities of mixed layer clay minerals*. R.C. Reynolds, editor, 8 Brook Rd., Hanover, New Hampshire 03755, USA.
Savage D., Bateman K., Hill P., Hughes C., Milodowski A., Pearce J., Rae E. & Rochelle C. (1992) Rate and mechanism of the reaction of silicates with cement pore waters. *Appl. Clay Sci.* **7**, 33–45.
TA-Abfall (1991) *Zweite Allgemeine Verwaltungsvorschrift zum Abfallgesetz, Teil 1: Technische Anleitung zur Lagerung, chemisch/physikalischen, biologischen Behandlung, Verbrennung und Ablagerung von besonders überwachungsbedürftigen Abfällen*. GMBI, *42*, 12.
Velde B. (1965) Experimental determination of muscovite polymorph stabilities. *Am. Miner.* **50**, 436–449.
Vieillard P. & Rassineux F. (1992) Thermodynamic and geochemical modelling of the alteration of two cement matrices. *Appl. Geochem.* **1**, 125–136.
Wieland E. & Stumm W. (1992) Dissolution kinetics of kaolinite in acid aqueous solutions at 25°C. *Geochim. Cosmochim. Acta*, **56**, 3339–3355.
Wolery T.J. (1983) *EQ3NR, a computer program for geochemical aqueous speciation-solubility calculations: user's guide and documentation*. Lawrence Livermore Nat. Lab., Livermore, CA, USA, UCRL-53414-report.

Experimental investigation of the interaction of clays with high-pH solutions: A case study from the Callovo-Oxfordian formation, Meuse-Haute Marne underground laboratory (France)

Clay Clay Min. (2002) **50**(5), 633.

Claret F., Bauer A., Schäfer T., Griffault L., and Lanson B.

Clays and Clay Minerals, Vol. 50, No. 5, 633–646, 2002.

EXPERIMENTAL INVESTIGATION OF THE INTERACTION OF CLAYS WITH HIGH-pH SOLUTIONS: A CASE STUDY FROM THE CALLOVO-OXFORDIAN FORMATION, MEUSE-HAUTE MARNE UNDERGROUND LABORATORY (FRANCE)

FRANCIS CLARET[1,2], ANDREAS BAUER[3], THORSTEN SCHÄFER[3], LISE GRIFFAULT[2] AND BRUNO LANSON[1,*]

[1] Environmental Geochemistry Group, LGIT - Maison des Géosciences, University J. Fourier – CNRS, BP 53, 38041 Grenoble Cedex 9, France

[2] ANDRA, Parc de Croix Blanche, 1-7 rue Jean Monnet, 92298 Châtenay-Malabry Cedex, France

[3] Forschungszentum Karlsruhe, Institut für Nukleare Entsorgung, PO Box 3640, D-76021 Karlsruhe, Germany

Abstract—The impact of alkaline solutions (pH = 13.2) on the clay mineralogy of the Callovo-Oxfordian formation hosting the French underground laboratory for nuclear waste disposal investigation (Meuse-Haute Marne site) has been studied experimentally. Initially, each of the four samples selected as representative of the mineralogical transition in this Callovo-Oxfordian formation consists of a mixture of three main clay phases: discrete illite, discrete smectite and a randomly interstratified mixed-layered mineral (MLM) containing ~65% of non-expandable layers. Clay separates were altered in batch reactors at 60°C using high solution:solid ratios. The mineralogy of this clay fraction and solution chemistry were monitored as a function of reaction time. In addition, the interactions between organic matter and clay particles were investigated using scanning transmission X-ray microscopy (STXM).

The clay mineralogy is little affected even though the pH is still high after 1 y reaction time. The only significant mineralogical evolution is the partial dissolution of the discrete smectite component leading to the formation of a new randomly interstratified illite-expandable MLM. Additional mineralogical transformations lead, for one sample, to the dissolution of micro-crystalline quartz and, for another sample, to the crystallization of a tobermorite-like phase. The low reactivity of clay minerals may be attributed to the presence of organic matter in the samples. In their initial state, all outer surfaces of clay particles are indeed covered with organic matter. After 1 y reaction time, STXM studies showed the basal surfaces of clay particles to be devoid of organic matter, but their edges, which are the most reactive sites, were still protected.

Key Words—High pH, French Underground Laboratory, Organic Matter, STXM, XRD.

INTRODUCTION

Nuclear waste disposal in deep geological formations is currently under investigation in several countries. Based on a directive of December 31st 1991, France is conducting research in a clay-rich formation, the 'Callovo-Oxfordian argilite', in the Meuse-Haute Marne site (MHM, Eastern Paris basin). An underground laboratory will soon be operational allowing investigation of the confinement properties of this host formation. However, disposal in such deep environments demands technical solutions which ensure that waste is stored in a safe way preventing harmful effects to the population. In particular, concrete is often thought of as a civil engineering material in such deep storage facilities or as a component of the waste package, especially for intermediate-level long-lived waste (ILLW – 'B type' according to the French nuclear waste classification). However, the water-induced alteration of concrete generates alkali-rich high-pH (12.5–13.6) solutions (Anderson *et al*., 1989; Lunden and Andersson, 1989), the release of which to the surrounding media has been modeled (Jeffries *et al*., 1988; Haworth *et al*., 1989; Berner, 1990; Reardon, 1990; Vieillard and Rassineux, 1992). Such modeling shows that solution composition is first controlled by the release of NaOH and KOH leading to very high solution pH (pH >13). In a second step, the solution composition is controlled by portlandite ($Ca(OH)_2$ – pH 12), and finally by calcium-silicate-hydrate (CSH) phases (pH 9–10).

As a consequence, numerous investigations have been conducted on the stability of clays in such high pH conditions (Mohnot *et al*., 1987; Carroll-Webb and Walther, 1988; Carroll and Walther, 1990; Chermak, 1992, 1993; Eberl *et al*., 1993; Huang, 1993; Bauer and Berger, 1998; Bauer *et al*., 1998; Bauer and Velde, 1999; Cama *et al*., 2000; Taubald *et al*., 2000; Huertas *et al*., 2001). These studies consistently indicate that the clay minerals described in the Callovo-Oxfordian formation of the MHM site (smectite, illite and mixed-layer illite-smectite – Bouchet and Rassineux, 1997; Claret, 2001) would react when in contact with high-pH alkali-rich solutions. For example, recent high-pH experimental investigations on smectite-type minerals indicated a fast montmorillonite-to-beideillite transformation (Rassineux *et al*., 2001). On the other hand, the bulk mineralogy of the formation offers a good buffering capacity, especially in the presence of silicates such as quartz (~20 wt.%) and of carbonates. Similar studies on natural formations such as in the Maqarin analog site depict an

* E-mail address of corresponding author:
bruno.lanson@obs.ujf-grenoble.fr

alteration halo restricted to a few mm thick along a conducting fracture (Cassagnabere *et al*., 2001).

The main objective of this study was to investigate the specific behavior of the natural clay mineral assemblages from the Callovo-Oxfordian formation in the MHM site when in contact with Ca-Na-K-rich solutions at high pH (>13). The experimental work was conducted on <2 μm clay separates. These reactive size fractions were altered hydrothermally in closed systems for periods varying from 1 day to 1 y. Both fluids and solids were recovered and analyzed.

MATERIALS

Starting materials

The French underground laboratory will be located in Bure (eastem Paris Basin), between the Haute-Marne and Meuse departments. This laboratory will be hosted in the Callovo-Oxfordian formation the burial depth of which ranges from 422 to 552 m in the exploration drill hole EST 104. This clay formation is a hard shale containing 40–45% clay minerals, and ~50% of calcite and quartz. Bouchet and Rassineux (1997) showed that this clay formation included a mineralogical transition from smectitic 'R0' mixed-layered minerals (MLM) at the top of the formation to more illitic 'R1' MLM in its deeper section. In the sampled well, EST 104, four core samples were selected at 447, 490, 494 and 516 m below ground level as being representative of the whole mineralogical sequence covered by the clay formation. Two 'R0' samples were chosen, the first with a high smectite content (~65%) and the other one with ~50% smectite in the 'R0'. These I-S compositions were estimated from the method developed by Inoue *et al*. (1989). Another two samples were selected in the 'R1' part of the drillhole, the first one with ~60% illite, and the other with ~70% illite. These compositions were estimated from X-ray diffraction (XRD) patterns using the criteria defined by Velde *et al*. (1986). Their chemical composition was determined by Bouchet and Rassineux (1997), and additional analyses of S and C in the starting material were performed using a LECO-125 C/S analyzer. The total organic matter (TOC) and the S concentration in the initial solids are given in Table 1, the organic matter having been described exhaustively by Faure *et al*. (1999). Because organic matter is known to react with alkali solutions, particular attention was paid to this component.

Table 1. Total organic carbon (TOC) and sulfur content (wt.%) of the initial clay samples.

Sample	TOC	Sulfur
447	1.32	0.2439
490	1.31	0.2133
494	1.32	0.135
516	1.36	0.2596

Before extracting the <2 μm size-fraction by centrifugation, carbonates were removed using the acetic acid-acetate buffer method described by Moore and Reynolds (1989), but organic matter was not removed before size fractionation. Finally the clays were saturated with Ca. The mineralogy of the clay samples was investigated in detail by XRD (Claret, 2001) and scanning electron microscopy (SEM). All four clay samples consist of a mixture of three main phases: discrete illite, discrete smectite and a randomly interstratified mixed-layer mineral (MLM) containing ~65% of non expandable illite layers (Table 2; Claret, 2001). As a function of burial depth, the relative proportion of smectite decreases from 20 to 2% whereas that of discrete illite increases from 15 to 25%. The relative amount of the MLM phase (65%), as well as its composition, remains unchanged throughout the depth profile (Table 2; Claret, 2001). As a consequence, the mineralogical transition initially described, as for a diagenetic series, by a progressive illitization of I-S MLMs, corresponds to the progressive removal of discrete smectite with increasing depth together with the progressive increase of a discrete illite component.

Small amounts of kaolinite, chlorite and/or quartz may also exist in the different samples, sample 447 showing the highest concentration of quartz, which is detectable even in the $\leqslant 0.2$ μm size-fraction.

Starting solution

The simple young fluid (SYF) chemical composition is typical of solutions resulting from the initial stages of cement alteration (Nagra, 1995). The starting solutions were prepared from analytical reagent grade KOH, NaOH and $Ca(OH)_2$ salts. The solution composition and the initial pH are given in Table 3.

EQ3 (Wolery, 1983) calculations were performed to determine the distribution of aqueous species in solution in the absence of CO_2. At the initial pH, the solution is slightly oversaturated with respect to portlandite (log Q/K = 0.407). The starting solutions were nevertheless clear and showed no evidence of precipitation with time, when not exposed to air.

Table 2. Mineralogical composition of the clay (<2 μm) size-fraction of the initial clay samples as determined by Claret (2001) from experimental XRD profile fitting using the multi-specimen technique (Sakharov *et al*., 1999).

Sample	Smectite		MLM		Illite		Kaolinite	Chlorite
	%Sm	Ab.	%Sm	Ab.	%Sm	Ab.	Ab.	Ab.
447	100	20	65	65	5	15	0	0
490	100	13	65	66	5	20	0	1
494	100	2	65	74	5	19	4	1
516	100	2	65	63	5	23	9	2

The data were derived from the characterization of the Ca-saturated and EG-solvated samples. %Sm indicates the relative proportion of expandable layers in randomly interstratified mixed-layer minerals (MLM). Ab. indicates the relative proportion of the various phases in the clay fraction.

Experimental set-up and sample preparation

Clay samples weighing 0.5 g were added to 10 mL [liquid/solid ratio (L/S) = 20] and 40 mL (L/S = 80) of SYF solution. Batch experiments were performed for up to 12 months at 60°C in Savilex containers. The temperature control was precise to ±2°C and accurate to ±4°C. The bottles were shaken twice a week. The containers were removed at specific intervals, quenched in cold water (25°C), and opened. After the experiments, the reacted material and the solution were separated by centrifugation. The supernatant suspensions were filtered through a 0.45 μm filter before analysis.

The solids were then washed six times with bidistilled water (Milli-Q/18.2 MΩ cm^{-1}). After each washing step the solid was separated by centrifugation and resuspended in 50 mL Milli-Q water. In the next step the clays were re-suspended in 50 mL of 1 M $SrCl_2$ solution in order to ensure the presence of two water layers in the expandable interlayers. To promote complete cation exchange, the suspensions were stored for 4 h at 50°C. Following the cation exchange, the clays were dialyzed in tubes prepared by boiling in distilled water for one day with repeated changes of the water to remove any excess organic material.

METHODS

X-ray diffraction

Oriented slides were prepared by pipetting a slurry of the Sr-saturated samples on a glass side and drying it at 40°C for a few hours to obtain an air-dried (AD) preparation. Ethylene glycol (EG) solvation was achieved by exposing the oriented clay slides to ethylene glycol vapor at 70°C for 12 h. The XRD patterns were recorded with a Bruker D5000 diffractometer using a 0.04° step size and 6 s counting time per step. The divergence slit, two Soller slits, antiscatter slit and resolution slit were 0.5°, 2.3°, 2.3°, 0.5° and 0.06°, respectively.

To characterize the structural modification of the reacted clay samples, their structure was determined using the multi-specimen fitting procedure described by Sakharov *et al*. (1999). This method, which may be used to describe complex polyphasic clay parageneses, requires the recording of XRD patterns of each sample after different treatments (*e.g.* Sr-saturated in AD and EG solvated states). For each XRD pattern, structural parameters such as the composition of the MLM phases (proportions of the different layer types), their stacking mode (Reichweite parameter R, junction probabilities), and an estimate of their relative proportions are adjusted to fit the experimental XRD pattern (Sakharov *et al*., 1999; Claret, 2001). Because the different treatments may change the thickness and scattering power (nature, amount and position of interlayer species) of the swelling interlayers but not the distribution of the different 2:1 layer types, a consistent structural model is obtained for one sample when the structural parameters obtained from all XRD patterns of the same sample coincide.

Table 3. Composition of the Simple Young Fluid (SYF) and the initial solution pH.

NaOH	2.606 g/L
KOH	9.033 g/L
$Ca(OH)_2$	0.166 g/L
pH	13.22

To fit the experimental XRD patterns, the program of Drits and Sakharov (1976) was used over the 2–50°2θ CuKα range. Instrumental and experimental factors such as horizontal and vertical beam divergences, goniometer radius, dimensions and thickness of the samples were measured and introduced. The sigmastar value was set to 12 and the mass absorption coefficient (μ*) to 45, as recommended by Moore and Reynolds (1989). The *Z* coordinates of atoms proposed by Moore and Reynolds (1989) were used for all 2:1 layer types. The d_{001}-values used for simulations are given in Table 4. The K content in the illite interlayers was set at 0.75 atoms per $O_{10}(OH)_2$. The lognormal thickness distributions of coherent scattering domain sizes (CSDS) were characterized by the mean and maximum CSDS (Drits *et al*., 1997).

Scanning electron microscopy, scanning transition X-ray microscopy

Scanning electron microscope (SEM) images of untreated and reacted materials were recorded to identify minor components which may not be detected by XRD and to determine the relative stability of the different reaction products. These micrographs were obtained using a JEOL GSM-6100 instrument equipped with a KEVEX energy dispersive detector.

Scanning transmission X-ray microscopy (STXM) investigations were performed at beamline X1-A of the National Synchrotron Light Source (Brookhaven National Laboratory) operated by the State University of New York at Stony Brook. The principle of the method is described in detail in Jacobsen *et al*. (1991) and Zhang *et al*. (1994). Sample preparation was performed by squeezing 1 μL of aqueous colloid suspensions between Si_3N_4 windows, using a wet-cell assembly to maintain the hydration state (Neuhäusler *et*

Table 4. *d*-spacings (d_{001}) (in Å) of the different layer types used for the calculation of mixed-layer mineral XRD patterns.

	Illite	Smectite 2 layers	Smectite 1 layer
Ethylene glycol solvated	9.98	16.65–16.7	12.9–13.3
Air-dried state	9.98	14.8–15	12.5–12.8

al., 1999). Initial clay samples ($\leqslant$2 μm size-fraction) were kept in suspension in deionized water, whereas reacted samples were kept in suspension in reacted SYF.

The Fresnel zone plate used for these measurements had a diameter of 160 μm and a outermost zone width of 45 nm giving a theoretical lateral resolution of 55 nm (Rayleigh criterion), at a focal length of 1.7 mm (Spector *et al.*, 1997). The exit and entrance slit set-up was chosen to obtain an energy resolution ΔeV of 0.1 eV at the C K-edge (Winn *et al.*, 1996). Energy calibration of the spherical grating monochromator was performed by using the photon energy of the CO_2 gas adsorption band at 290.74 eV (Ma *et al.*, 1991; Hitchcock and Mancini, 1994).

The STXM images of clay suspensions were recorded at the C K-edge and K L-edge. The STXM measurements yield information on the product of sample thickness (d) and of its mass absorption coefficient $\mu(E)$ through the relation $Abs(E) = \mu(E)*d = \ln[I_0(E)/I(E)]$ in which $I_0(E)$ is the incident flux on the sample and $I(E)$ the flux measured behind the sample at the energy E. $I_0(E)$ is obtained from regions free of particles or from XANES spectra measured without sample. Low-resolution image stacks can be measured as a function of energy.

High-resolution images were collected at selected energies below and above C (E_{below} = 280 eV, E_{above} = Σ(285–290 eV)) and K (E_{below} = Σ(280–290 eV), E_{above} = 297.3 eV) edges. Ratio images were subsequently calculated giving to each pixel the corresponding $-\log(Abs_{E_{above}}/Abs_{E_{below}})$ ratio to visualize the distribution of K and C, to image the association between clay and organic matter in untreated and reacted samples (Figure 1).

In addition, X-ray absorption near-edge structure (XANES) spectra were extracted from low-resolution image stacks in the 280–310 eV range after a careful stack alignment (Jacobsen *et al.*, 2000). In the XANES spectra, clay minerals are identified using the X-ray absorption of structural interlayer K, and more precisely the absorption band double feature at 297.3 eV (L_3-edge) and 300 eV (L_2-edge). These energy values are shifted by 3 eV as compared to the values tabulated for K by Henke *et al.* (1993), because potassium is present as K^+ in these interlayers.

For XANES comparison, all spectra were corrected for the baseline and normalized to the absorption intensity of the K L_3-edge energy (297.3 eV).

Determination of solution composition

The pH was measured using an Orion 525A pH meter calibrated with five standard solutions (pH 7, 9, 10, 11, 13). Because pH measurement of high-pH solutions is always critical, each measured value was checked against a pH 13 standard. A maximum drift of ±0.1 pH unit was observed during pH measurements.

The concentrations of dissolved Si, Al, Na, K, Ca and Fe were determined for all samples on a Plasma 400

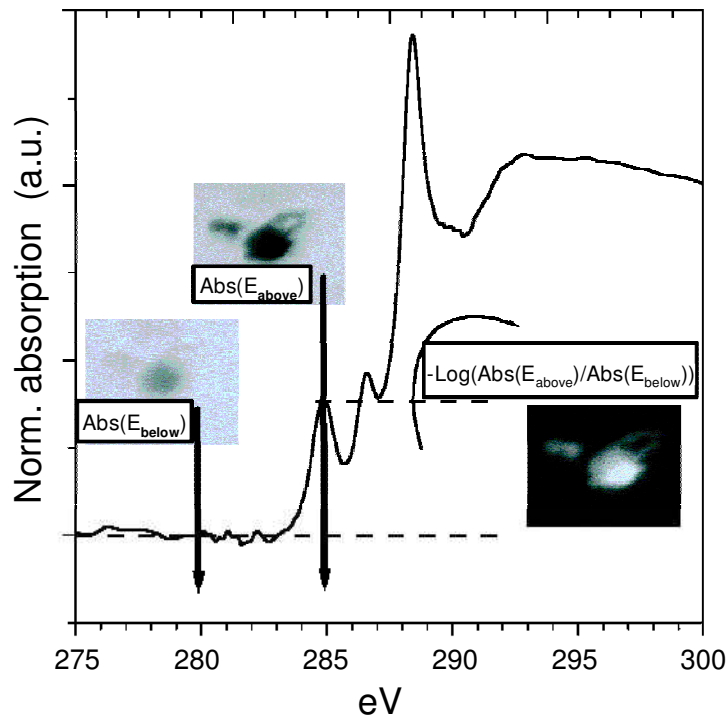

Figure 1. Absorption of a smectite suspension in organic-containing solution. The image collected at E_{below} illustrates the very limited absorption of this dilute suspension of thin smectite particles. The ratio-image $-\log(Abs_{E_{above}}/Abs_{E_{below}})$ allows us to localize specifically organic functional groups absorbing, in this case, at 285 eV.

Table 5. Concentration of the different aqueous species as a function of time.

Reaction time (days)	pH	Si (mg/L)	Al (mg/L)	Na (mg/L)	K (mg/L)	DOC (mg/L)	Sulfate (mg/L)
Sample 447 L/S 20							
1	13.17	53.7	14.4	1433.6	4632.0	30.3	29.5
3	13.15	193.6	12.5	1452.7	4416.0	46.9	52.8
6	13.21	348.5	9.4	1402.0	4113.0	67.2	79.2
9	13.16	500.0	7.6	1426.7	4186.0	80.3	92.0
16	13.13	1101.0	5.8	1411.0	4138.0	101.9	92.4
30	13.09	1512.6	5.7	1408.4	4148.0	132.8	100.3
74	12.97	2139.0	5.4	1498.0	4489.0	170.1	132.0
145	12.56	2720.8	5.3	1466.6	4645.8	229.1	145.5
350	12.25	4134.5	6.2	1472.0	4427.0	269.5	181.4
Sample 490 L/S 20							
2	13.21	53.0	14.8	1452.7	4289.0	27.3	27.3
4	13.21	79.7	24.6	1405.1	3995.0	36.6	36.8
9	13.18	99.2	32.9	1448.0	4226.0	76.8	59.4
16	13.17	139.4	41.1	1436.2	4190.0	110.5	80.4
30	13.13	158.1	46.2	1451.0	4148.0	131.8	120.4
74	13.1	215.0	54.8	1499.5	4289.0	139.6	145.0
145	13.06	334.2	48.4	1498.0	4268.4	147.8	192.0
350	13.04	269.5	49.4	1492.4	4057.6	150.9	195.1
Sample 494 L/S 20							
1	13.19	33.2	11.6	1494.5	4603.0	15.3	13.9
3	13.2	62.0	23.2	1422.3	4450.0	20.0	18.4
6	13.21	86.3	33.5	1422.0	4330.0	34.0	23.4
9	13.2	100.2	42.7	1428.8	4254.0	42.8	28.2
16	13.19	136.9	48.2	1422.6	4267.0	73.6	36.6
30	13.19	142.3	57.7	1439.6	4326.0	92.1	54.7
74	13.18	144.2	73.1	1484.1	4356.0	110.4	78.0
145	13.08	195.7	73.8	1457.6	4425.8	134.2	79.4
350	13.04	223.7	76.2	1418.0	4286.2	180.1	81.7
Sample 516 L/S 20							
1	13.22	31.2	21.0	1417.8	4913.0	21.1	22.6
3	13.19	46.6	29.6	1435.7	5156.0	23.1	41.3
6	13.22	70.4	50.2	1462.1	4157.0	60.9	68.0
9	13.25	82.2	65.7	1469.3	4378.0	48.0	99.1
16	13.22	93.4	92.5	1447.3	4404.0	76.2	118.2
30	13.22	118.6	114.1	1481.0	4480.0	99.1	149.9
74	13.2	159.4	148.8	1497.0	4789.0	101.0	201.0
150	13.09	176.9	162.0	1498.0	4662.0	113.4	219.9
350	13.05	141.4	191.8	1491.6	5083.8	119.5	239.9
Sample 447 L/S 80							
1	13.24	7.7	7.1	1507.1	5301.0	17.2	10.0
3	13.22	50.5	10.2	1482.7	5079.0	20.8	21.3
6	13.2	142.9	11.3	1504.9	5059.0	28.6	25.8
9	13.18	227.6	11.1	1492.7	4890.0	32.8	28.2
16	13.18	385.3	10.5	1504.6	4721.0	37.2	33.9
30	13.17	826.9	11.6	1509.2	4978.0	45.5	36.9
74	13.16	997.0	15.4	1467.6	4813.0	67.4	44.0
145	12.98	1225.4	7.6	1503.0	4950.6	77.9	51.6
350	12.95	1835.0	6.5	1506.4	5165.4	81.8	55.9
Sample 490 L/S 80							
1	13.21	11.4	7.3	1434.4	5243.0	10.3	7.5
3	13.21	21.0	11.4	1483.1	5048.0	10.5	11.9
6	13.18	34.4	16.3	1495.7	5496.0	10.4	13.3
9	13.21	47.4	23.7	1479.2	4861.0	12.9	18.5
16	13.19	71.9	29.0	1512.7	4766.0	26.9	21.3
30	13.17	80.9	33.7	1514.9	4849.0	34.9	24.6
74	13.16	128.3	55.2	1451.5	4859.0	47.8	34.0
145	13.17	180.4	54.1	1453.8	5342.4	57.8	44.5
350	13.14	233.1	79.2	1472.6	5058.0	66.6	47.3

Table 5. (*Contd.*)

Reaction time (days)	pH	Si (mg/L)	Al (mg/L)	Na (mg/L)	K (mg/L)	DOC (mg/L)	Sulfate (mg/L)
Sample 494 L/S 80							
1	13.23	7.2	6.3	1463.1	5000.0	6.9	3.5
3	13.21	19.1	12.5	1466.6	4945.0	7.7	5.1
6	13.23	32.0	18.3	1420.7	4978.0	11.3	8.7
9	13.22	46.1	25.1	1509.1	4918.0	14.7	11.2
16	13.21	53.8	29.0	1492.3	4771.0	20.5	13.3
30	13.23	59.7	35.2	1511.8	4906.0	24.5	14.8
74	13.24	90.8	60.9	1495.0	4886.0	28.4	18.0
145	13.16	124.0	55.8	1457.2	5042.4	37.3	17.3
350	13.15	131.4	76.4	1443.4	5424.8	48.8	20.8
Sample 516 L/S 80							
1	13.21	9.5	12.5	1482.7	5206.0	5.3	11.6
3	13.22	12.7	14.1	1468.0	5156.0	8.3	13.8
6	13.21	26.6	22.7	1444.0	5009.0	14.6	18.5
9	13.23	33.1	29.9	1519.6	5139.0	20.4	20.9
16	13.2	52.9	42.8	1506.9	4935.0	25.7	24.0
30	13.24	62.4	66.4	1514.7	4956.0	32.0	33.5
74	13.22	100.1	116.5	1411.3	4933.0	36.1	46.0
145	13.16	160.6	135.4	1461.0	5248.8	46.4	50.7
350	13.16	141.1	164.8	1477.0	5257.2	47.9	55.9

ICP-AES (Perkin Elmer) after appropriate dilution. The sulfate concentrations were determined using a DX-300 ion chromatograph. The dissolved organic carbon (DOC) was measured using a Shimadzu TOC-5000, after appropriate dilution, and pH adjustment with concentrated HCl (pH 2–3).

To determine the size distribution of released colloidal material, the reacted solutions were passed through polyethersulfone membranes of nominal molecular weight cut off ranging from 10^3 to 10^6 Dalton (Microsep™ Microconcentrators). Each filter was washed 15 times with Milli-Q water before use.

EXPERIMENTAL RESULTS

Solutions

All reacted solutions showed a change in color during the experiment. This change was not the same for the different samples, and was most intense for sample 447. For this sample, the solution was dark brownish after 74 days and opaque at the end of the experiment (L/S = 20). Filtration through a 0.45 μm filter for solution analysis purposes did not modify this strong coloration. Even after ultra-filtration through a 10^3 Dalton filter (1 nm) the solution still showed a dark brownish color, which is induced by colloidal organic material.

Dissolved organic carbon and sulfate. A similar evolution of DOC and sulfate concentrations was observed for all samples (Table 5). With increasing reaction time, the positive slope of these concentration curves decreased, maximum DOC concentration (270 mg/L) being obtained for sample 447 (L/S = 20) at the end of the experiment (350 days). The DOC was the dominant species in solution for the two L/S ratios except for sample 516 for which the solution is dominated by sulfate for the two L/S ratios. Maximum sulfate concentration (240 mg/L) was found in sample 516 (L/S 20) after 350 days (Table 5).

To determine the size distribution of this colloidal organic material as a function of reaction time, reacted solutions were filtered through polyethersulfone membranes, and DOC was measured in the filtrate and compared with the initial DOC in solution. The evolution of this size distribution as a function of time was the same for all four samples, the average size of the organic material decreasing with increasing reaction time, independently of L/S ratio (Figure 2). For example, in sample 516 (L/S = 80) ~50% and 80% of the initial DOC was present in the filtrate of a 1000 Dalton

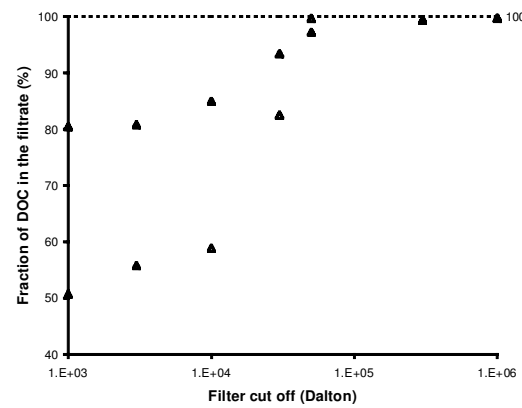

Figure 2. Evolution of the dissolved organic carbon (DOC) size distribution as a function of time for sample 516 (L/S = 80). Open and solid triangles show the DOC size-distribution after 74 days and 1 y reaction times, respectively.

Filter after 74 and 350 days reaction times, respectively (Figure 2).

Si and Al. The evolution of Si and Al concentrations with time was different for sample 447 when compared to the other three samples (Table 5). For sample 447, the initial increase of [Si] was followed by a decrease in the slope of the concentration curve for both L/S ratios. However, the slope was still positive after 1 y and no steady-state concentration was reached. For this sample, [Al] decreased after the initial increase to reach the same final [Al] for the two L/S ratios (6 mg/L). For the other three samples (490, 494 and 516), the evolution of Si and Al concentrations showed the same trend for both L/S ratios, the positive slope of the concentration curve decreasing with increasing time. Typical values were ~150–300 and 50–200 mg/L for Si and Al, respectively (Table 5). In addition, it is notable that there was a decrease of [Si] at the end of the experiment for sample 490 (L/S = 20) (Table 5).

The Al and Si concentrations in solution were not correlated with the presence of organic material as shown on Figure 3. In this figure, one may note that for sample 516 (L/S = 80, 350 days) Al and Si concentrations were constant whatever the filter cut off was. On the contrary, DOC concentration decreased with this parameter to indicate that Al and Si are present as aqueous species, rather than sorbed on organic colloids.

Na, K, Ca, Mg and Fe concentrations. After the initial fast decrease, [Na] and [K] were constant (~1400 and 5000 mg/L, respectively) throughout the experiment for the two L/S ratios (Table 5). In all experiments, the Ca, Mg and Fe concentrations were below the detection limit.

Evolution of pH. Contrasting pH evolutions as a function of time were observed for the different samples (Table 5). In samples 490, 494 and 516, the pH was constant throughout the experiment for both L/S ratios, whereas in sample 447, the pH decreased to 12.2 (L/S = 20) and to 12.9 (L/S = 80) at the end of the experiment (350 days).

Solids

SEM. The SEM analysis of sample 447 showed a strong dissolution of quartz in this initially quartz-rich sample. In all samples a small number of very fine blocky crystals can be found. These appear to be randomly distributed and to have a mixed Ca, Mg hydroxide composition. In most samples, limited precipitation of fibrous to honeycomb-textured CaAlSi-hydroxide phases (CASH) was also observed. Finally, rare occurrences of newly formed portlandite and brucite also appeared in most samples. Apart from the limited presence of these newly-formed phases, no significant textural modification was observed in the reacted clay samples.

X-ray diffraction. The XRD patterns obtained from reaction products are very similar to those of the initial raw materials, and in most cases no significant dissolution or neoformation was detected. Kaolinite and chlorite, whose proportions increase with depth in the sequence, showed no tendency to react during the experiments, whereas quartz disappeared in sample 447 for both L/S ratios. No significant modification of the clay mineralogy could be detected for samples 447 and 516 (Figure 4). On the contrary, a significant neoformation was observed for sample 494 (L/S = 20), the new phase being characterized by a rational series of basal reflections (d_{001} = 11.45 Å) which may be observed for the 74 and 350 days, reaction times experiments (L/S = 80, Figure 5). The saturation of this sample with different cations, its solvation with EG or its complete dehydration under secondary vacuum (10^{-5} Torr) did not alter its XRD pattern (Figure 6). Even though it was

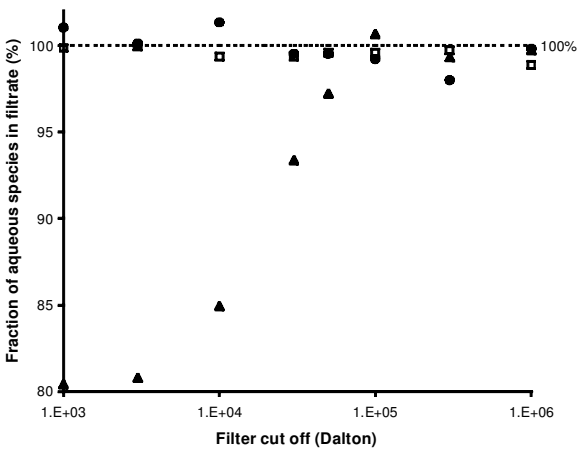

Figure 3. Distribution of aqueous species as a function of time for sample 516 after 1 y reaction time (L/S = 80). Si, Al and DOC are shown as open squares, solid circles, and solid triangles, respectively.

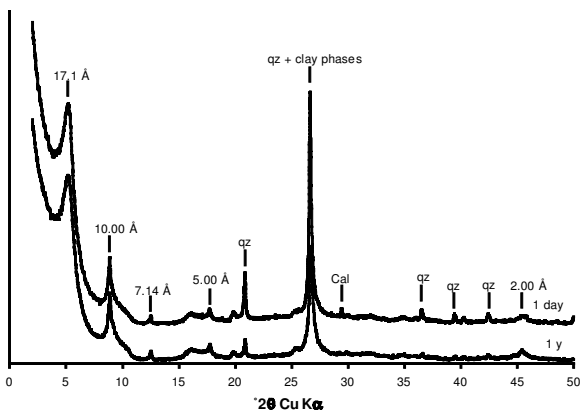

Figure 4. XRD patterns of sample 447 as a function of reaction time (L/S = 80 – Sr-saturation and EG solvation). The positions of the diffraction maxima are indexed. Quartz (qz) and calcite (Cal) impurities are labeled.

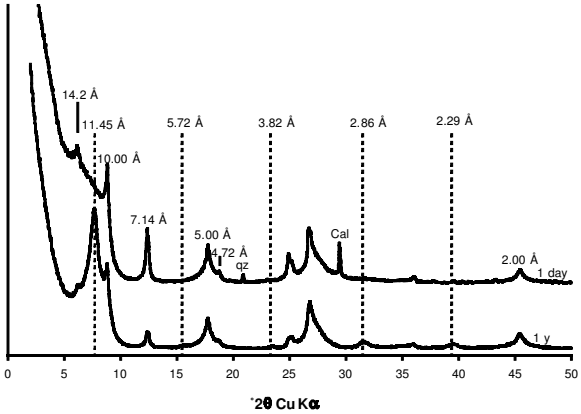

Figure 5. XRD patterns of sample 494 as a function of reaction time (L/S = 80 – Sr-saturation and ethylene glycol solvation). The positions of the diffraction maxima are indexed. Quartz (qz) and calcite (Cal) impurities are labeled. The rational series of reflections associated with the newly-formed tobermorite-like phase are shown as dashed lines.

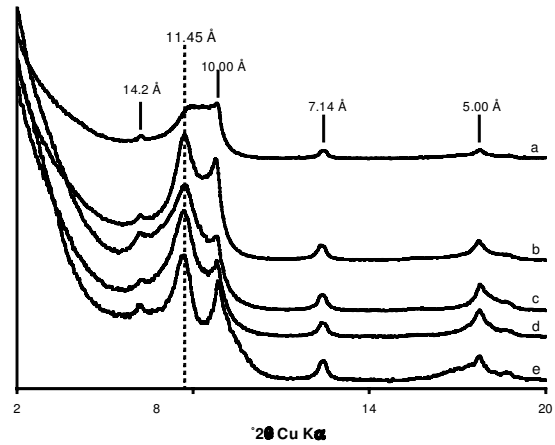

Figure 6. XRD patterns of sample 494 as a function of sample preparation (L/S = 80 – 1 y). The positions of the diffraction maxima are indexed, and the reflections attributed to the tobermorite-like phase are shown as dashed lines. (a) Na saturation and deep vacuum conditions (10^{-5} torr) during data collection, to ensure complete dehydration of expandable interlayers. (b) Na saturation and air-dried (AD) state. (c) Mg saturation and AD state. (d) Sr saturation and AD state. (e) Sr saturation and ethylene glycol solvation.

possible to reproduce the set of peak positions using a 2:1 layer with d_{001} = 11.45 Å, it was impossible to obtain a correct distribution of intensities between these reflections whatever the occupancy of the interlayer space. These reflections are more likely related to a newly-formed tobermorite-like phase (11 Å variety) which is reminiscent of the CASH phases observed using SEM.

A detailed study of XRD patterns recorded for sample 490 showed a continuous decrease of the smectite contribution at 17.3 Å with increasing reaction time, and the presence of a new peak at ~12.0 Å in the EG pattern (Figure 7). These modifications were more obvious for L/S = 80. In this case, the diffraction maximum at 12.0 Å is probably related to a phase different from that described for sample 494, because the series of reflections was not rational and because the contribution of this phase to the diffracted intensity varied as a function of sample state (cation saturation, EG solvation).

Application of the multi-specimen method indicates that after 1 y the reacted material is composed of five different phases. In addition to illite, chlorite and kaolinite which were initially present, two randomly interstratified MLM phases are also present. The first one with a 70% illite content and R = 0 ordering (random interstratification), is similar to the MLM phase present in the starting material (Claret, 2001). Fitting both AD and EG Sr-saturated patterns it was possible to estimate a 50% illite content for the other randomly interstratified MLM phase (Figure 8). In addition, the multi-specimen method confirmed the assumed disappearance of the initial smectite phase with reaction time.

Spectromicroscopic results. Spectroscopic investigation of untreated clay suspensions systematically showed the coexistence of K and C in the same area (Figure 9). To investigate these ubiquitous associations between K in clay minerals and C from organic matter, a detailed STXM study was carried out on sample 447 because the experimental alteration of this sample led to high DOC concentration in solution (Table 5). The absorption of the unaltered sample 447 was measured at the K L_3 edge (297.3 eV), above the C edge (Figure 10a). Dark gray values (regions 1–3) indicate a high combined absorption of K and C, showing large aggregates of clay-sized particles (~1 μm). The comparison of the ratio images of K (Figure 10b) and C (Figure 10c) distributions provided qualitative information on the relative contents of K and C, light gray values indicating high K or C content. The presence of high K concentrations over the

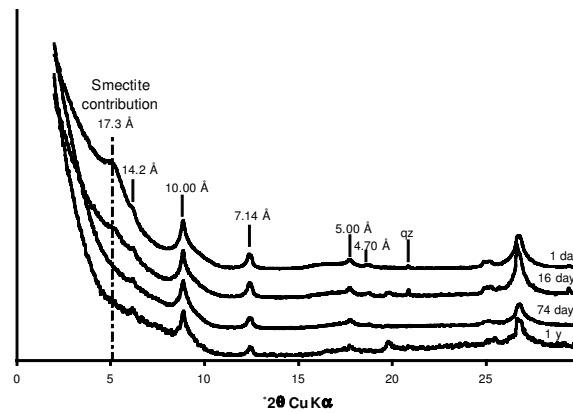

Figure 7. XRD patterns of sample 490 as a function of reaction time (L/S =80 – Sr saturation and EG solvation). The positions of the diffraction maxima are indexed, and quartz (qz) impurities are labeled. The position of the smectite contribution is shown as an irregular dashed line.

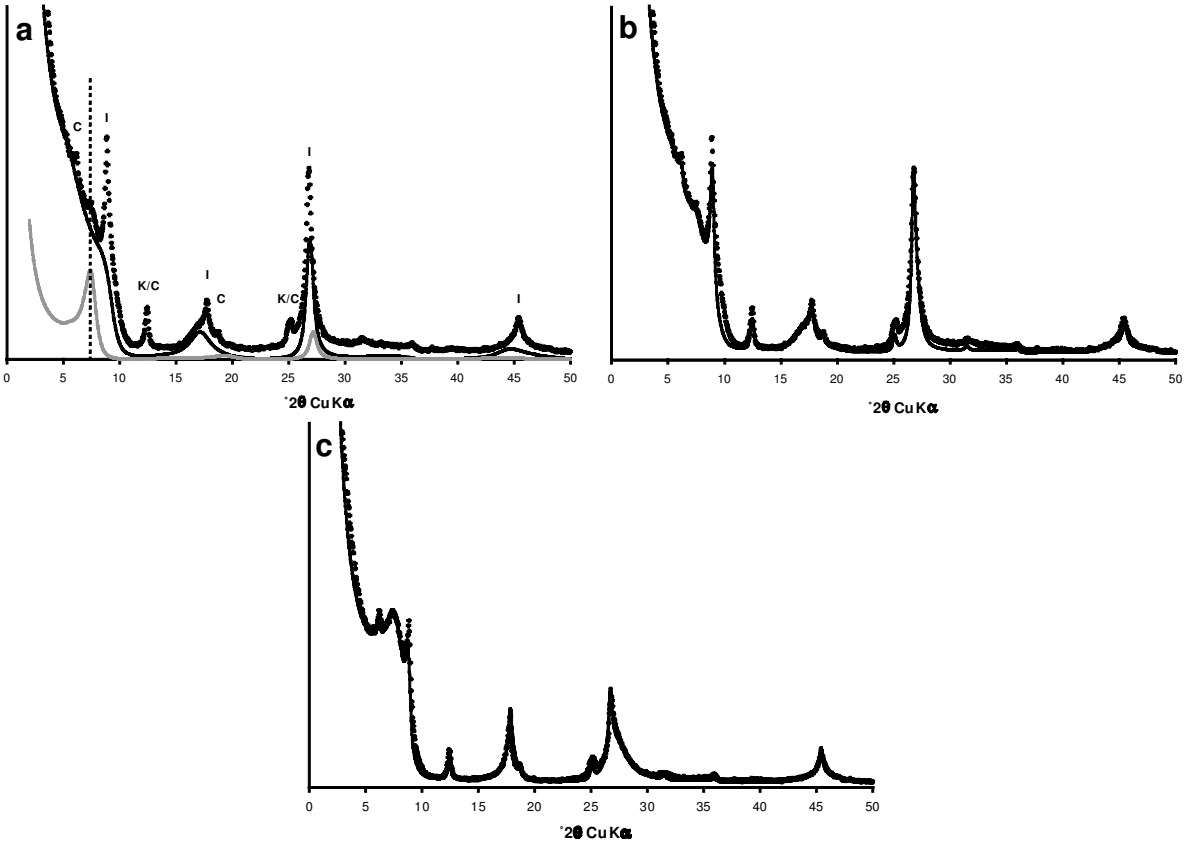

Figure 8. Mineralogical characterization of sample 490 (L/S = 80 – 1 y) using the multi-specimen method described by Sakharov *et al*. (1999). Experimental XRD patterns are shown as crosses, whereas calculated patterns are shown as solid lines. (a) Sr saturation and EG solvation. Contributions of the initial MLM phase with ~70% of illite layers and of the newly-formed MLM phase with ~50% illite layers are shown as solid and thin gray lines, respectively. The position of the latter contribution is shown as a dashed line. I, K and C labels indicate the positions of diffraction lines for illite, kaolinite, and chlorite respectively. (b) Sr saturation and EG solvation. Optimum fit to the experimental data is shown as a solid line. In addition to the two contributions from the MLM phases shown in part a, this calculated pattern includes that of discrete illite, kaolinite and chlorite. (c) Sr saturation and AD state. Optimum fit to the experimental data is shown as a solid line. The contributions to the diffracted intensity are similar to that in part b.

absorbing domains (regions 1–3) allowed their identification as K-rich phyllosilicates, such as the MLM, containing ~65% of non-expandable layers which makes up most of the clay-size fraction in all samples. Furthermore, these ratio images confirmed the association of organic material with these clays deduced from the XANES spectra (Figure 9). As shown by the similar distributions of K (Figure 10b) and C (Figure 10c), organic material covered clay plate surfaces and clay particle edges as well as inter-particle contacts for this unreacted sample. After reaction of sample 447 (350 days, L/S = 20), the contrast of the K ratio image (Figure 10e) is not as good as for the unreacted sample (Figure 10b). The concentration of this sample is very high and does not always allow a clear identification of the K contribution to the high global absorption (regions 4, 7). However, such an identification is possible in the low-absorption zones (regions 6, 8) of the reacted sample image. Furthermore, the unreacted sample was put in suspension in deionized water and, as a consequence, contained K only in the solid fraction. By contrast, both liquid and solid components of the reacted sample suspension in reacted SYF contain K, thus lowering the contrast (region 5). However, the identification of the large absorbing domains as K-rich phyllosilicates is beyond doubt.

In turn, the C ratio image of this reacted sample 447 (Figure 10f) showed a global depletion in the C content, and more especially a reduced amount of C on basal surfaces of clay particles whereas high C contents were still observed on particle edges and at inter-particle contacts (lighter gray values outlining regions 4 and 7). In particular, one may note that in the lower left corner of the reacted sample image (region 8) the K distribution is homogeneous (Figure 10e) whereas additional details (particle edges?) are visible on the C ratio image (Figure 10f).

Further investigation of the C (1s) absorption edge for untreated sample 447 showed characteristic features of aromatic carbon at 285 eV and 289 eV, carboxylic

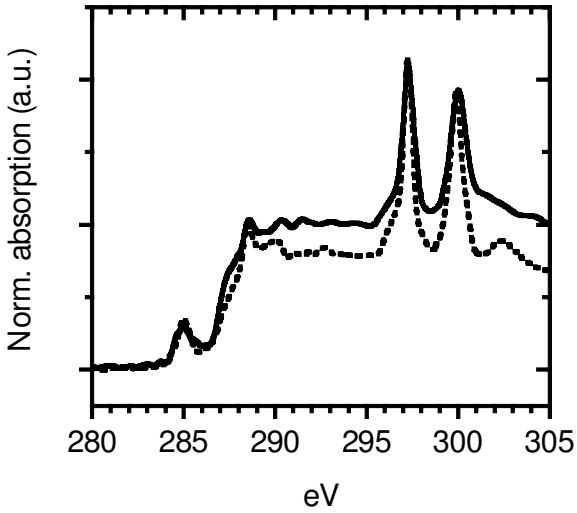

Figure 9. XANES spectra recorded at the carbon K-edge on unreacted sample 447 (solid line), and on sample 447 after 1 y reaction time (dashed line). The intensity is normalized to the L_3 absorption band of K at 297.3 eV. An additional peak at 300 eV corresponds to the L_2 absorption band of K (Henke *et al*., 1993).

groups at 289 eV and a broad shoulder at 287–288 eV (Table 6, Figure 9), which may be attributed either to a resonance of aromatic carbon bond to oxygen or to methyl and methylene groups of aliphatic carbon (Cody *et al*., 1995). The XANES spectrum (Figure 9) of reacted sample 447 (350 days in SYF; L/S 20) showed equivalent features with comparable intensities of absorption bands at 285 eV (aromatic carbon bonded to either proton or carbon) and at 289 eV (aromatic and/or aliphatic carboxylic acids).

After normalization to the K L_3-edge intensity, the continuum step of C absorption (*i.e.* the plateau after the absorption edge) decreased after 1 y reaction time to indicate that a smaller amount of organic material is associated with clay particles. However, this apparent decrease may be overestimated because of the different K concentrations in initial and reacted samples.

Table 6. Assignment of energy bands to block building groups of organic matter.

Energy (eV)	Transition (s)	Functional group
285	1s-π*	$C_{arom.}$-C, $C_{arom.}$-H[a]
287	1s-π*	$C_{arom.}$-OH[a,b]
288	1s-3p/σ_{C-H*}	CH_2, CH_3[c]
289	1s-π*	C=O, COOH, COOR[c,d,e]
	1s-2π*	$C_{arom.}$-H, $C_{arom.}$-C[b]
290	1s-4p	CH_2, CH_3[c]
291	1s-2π*	$C_{arom.}$-OH[e]
297	L_{III}	Potassium[f]
300	L_{II}	Potassium[f]

Note: [a](Hitchcock *et al*., 1992); [b](Francis and Hitchcock, 1992) [c](Hitchcock *et al*., 1986); [d](Ishii and Hitchcock, 1987); [e](Robin *et al*., 1988); [f](Henke *et al*., 1993)

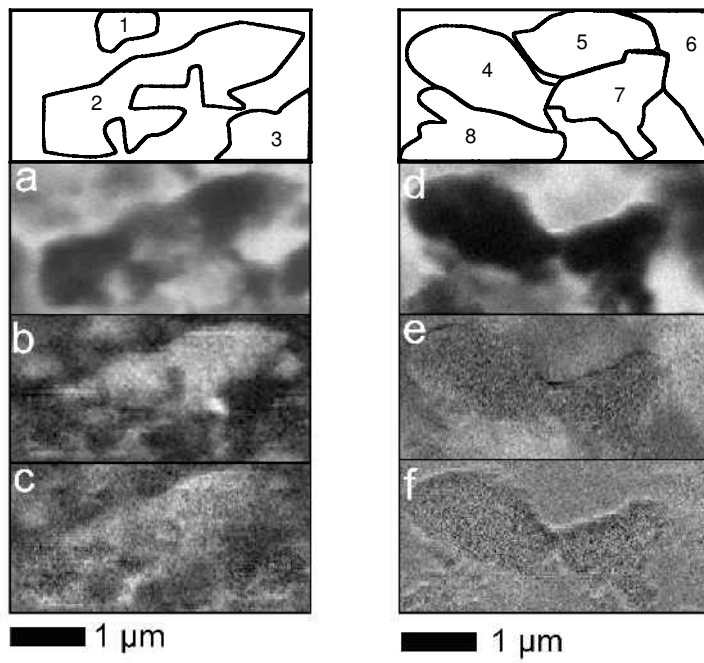

Figure 10. STXM images of unreacted sample 447 (a,b,c) and of sample 447 after 1 y reaction time with the Simple Young Fluid (L/S = 80 (d,e,f). The two sets of images are topped by a labeled sketch of the images for descriptive purposes (see text). Images 10a and 10d were taken at 297.3 eV. The dark gray values indicate a combined absorption by C and K. Images 10b and 10e are ratio images to visualize the distribution of K (E_{below} = Σ(280–290 eV), E_{above} = 297.3 eV). Images 10c and 10f are ratio images to visualize the distribution of C (E_{below} = 280 eV, E_{above} = Σ(285–290 eV)). The light gray values in ratio images indicate high K (b,e) or C (c,f) contents (see text).

DISCUSSION

Mineralogical evolution

The main goal of this experimental investigation was to determine the possible effects of basic solutions which might result from the initial alteration of concrete on the crystal chemistry of typical clays from the geological environment of the future French Meuse-Haute Marne underground laboratory. Such alteration of clays under low-to-moderate temperature and high-pH conditions was described previously by Eberl *et al*. (1993), Bauer and Berger (1998) and Bauer and Velde (1999). During their smectite alteration experiments, Bauer and Velde (1999) observed an initial decrease in the smectite CSDS followed by a decrease of the clay expandability via illite-smectite (I-S) MLM phases, *i.e.* illitization, in agreement with Eberl *et al*. (1993).

In our experiments, XRD pattern modeling indicates that a limited proportion of smectite transforms into a randomly interstratified MLM containing ~50% of illite layers after 1 y (L/S = 80). Indeed, XRD shows that in reacted sample 490, the amount of smectite, which was initially ~10% (Claret, 2001), decreases with reaction time simultaneously with the neoformation of this MLM phase (Figures 7, 8). On the other hand, no precipitation of this MLM phase or dissolution of smectite is observed in reacted samples 447 and 494 even though they initially contain discrete smectite. The contrasting scattering powers of the various phases present in the clay fraction may account for this apparent inconsistency as the presence of phases with high scattering powers in these samples could conceal the presence of a MLM phase similar to that identified in sample 490. For example, the presence of a newly-formed 11.45 Å tobermorite-like phase in sample 494 or the overwhelming intensity of smectite in sample 447 can impede the characterization of such a MLM phase. The very high scattering amplitude of the smectite phase may also conceal the possibility that it decreases with increasing reaction time if the initial discrete smectite is not strongly depleted as in sample 490.

The very high pH conditions of the experiments were found to be compatible with the neoformation of tobermorite-like phases in sample 494 (L/S = 80–74 days to 1 y terms) as these phases are usually formed under similar conditions during the binding process of Portland cements (Taylor, 1992). The SEM data indicate that this phase is present as traces in all altered samples although XRD detected its presence only in sample 494. At present there is no consistent explanation for the higher proportion of this tobermorite-like phase in altered sample 494.

In conclusion, except for the unusual precipitation of this tobermorite-like phase, the observed mineralogical evolution of clay minerals, and especially that of the discrete smectite phase, is compatible with earlier experiments (Eberl *et al*., 1993; Bauer and Velde, 1999) and leads to the formation of randomly interstratified MLM phases. However, one may note that the observed evolution is very limited and affects only the discrete smectite phase, leaving all other clay phases unaltered. In particular, the randomly interstratified MLM containing ~65% of illite layers which make up most of the clay-size fraction (Claret, 2001) and the discrete illite phase seem unaltered in all experiments. In addition, the discrete smectite phase is only partly affected, as its decreasing proportion could be observed only for sample 490 which initially contained ~10% of this phase (Table 2). This decrease was undetectable for sample 447 which initially contained ~20% of discrete smectite, probably because of the high scattering amplitude of this phase. On the contrary, the evolutions described in the literature affect all of the smectite phase (Eberl *et al*., 1993; Bauer and Velde, 1999). The origin of such a limited reactivity of clay phases when in contact with alkaline solutions will be discussed below.

Evolution of solution chemistry

Except for sample 447 for which the observed pH drop was induced by the dissolution of micro-crystalline quartz, the solution pH did not change significantly throughout the experiments. Consistent with the limited mineralogical evolution of clays, this steady pH indicates that there is no significant fluid-clay reaction as a pH drop is expected as a result of clay-fluid interaction because of the speciation of Al^{3+} and Si^{4+}. Chermak (1992) measured such a drop, from 12.91 down to 6.68, of the quenched pH in his batch experiments with fine-grained Opalinus Shale (35 days, 200°C). Decarreau (1999) also observed such a pH drop in the experiments conducted with samples from the Callovo-Oxfordian formation in alkaline solution. After one week, depending on starting solution, the pH decreased from 12.6 to 7.0 or from 13.5 to 10 as a result of the OH^- consumption. One may note that in these experiments the limited liquid:solid ratio (3:1) enhanced this pH drop. Bauer and Berger (1998) observed the same evolution of solution pH in the batch experiments at 35 and 80°C for kaolinite and smectite, respectively, for initial KOH concentrations below 0.1 M.

The limited reactivity of clays is confirmed by the rather low Si and Al concentrations measured in solution. The only high [Si] value (4134 mg/L), which was measured for sample 447, results from the dissolution of micro-crystalline quartz. All other measured values are similar, or lower, to that measured by Bauer and Berger (1998) in KOH 0.1 M solution (initial *in situ* pH 11.47 at 80°C).

The initial interlayer cation (Ca^{2+}) is likely to have been exchanged rapidly for K^+ at the beginning of the reaction as shown by the initial reduction of [K^+] in solution. Liberated Ca, as well as that introduced in the initial SYF solution, are not retrieved in solution, and probably precipitated as CASH or tobermorite-like

phases, which were observed by SEM. This hypothesis is supported by the systematic dissolution of calcite traces in reacted sample 494 in which the tobermorite-like phase was observed (not shown).

Influence of organic matter

The measured increase of DOC concentration with reaction time indicates that the organic material is much more affected than clays by alkaline solutions. This was expected as treatment with basic NaOCl solutions, for example, is recommended to remove organic material from clay samples (Moore and Reynolds, 1989). With increasing reaction time, organic matter in solution is gradually decomposed as shown by the evolution of the DOC size-distribution (Figure 2).

The STXM investigations indicate that the organic material is preferentially released from the basal surfaces of clay particles whereas the edges of these particles are still covered after one year. As will be discussed below, it is likely that this specific reactivity of the organic clay coverage is responsible for the observed limited alteration of clay minerals in the present high-pH experiments. This hypothesis is supported by the strong dissolution features observed by SEM on mineral species, *e.g.* quartz, which were not initially covered by organic material.

Because of the preferential desorption of the organic material from their basal surfaces, an important proportion of clay particle surface area is accessible to alkaline solution after several months of reaction. However, in spite of this increased direct contact surface between the clay minerals and the solution, the evolution of these minerals remains very limited. Bauer and Berger (1998) explained contrasting reactivity observed between kaolinite and smectite in high molar KOH solutions at 35 and 80°C by structural considerations and emphasized the main role of crystal edges. The essential role played by crystal edges in the alteration process of clay minerals may also account for the low alteration rate observed in our experiments, as access to these edges is blocked by organic material throughout the experiments as shown by STXM investigations.

The dominant influence of edge surface sites on the dissolution rate has also been demonstrated for biotite based on macroscopic experiments conducted at low pH (Turpault and Trotignon, 1994). Consistently, Bosbach *et al.* (2000) observed that the proton-promoted dissolution of hectorite particles takes place exclusively at the crystal edges, the basal surfaces being completely unreactive on the experiment time scale. Furthermore, crystal edges are readily blocked by the presence of organic material as demonstrated by Chin and Mills (1991). The latter authors showed clearly that the presence in solution of humic acids from soils (50 mg L^{-1}) inhibit kaolinite dissolution, and hypothesized that large humic acid molecules bind to multiple surface Al sites preventing the adsorption of both H^+ and small organic ligands. Such a passivation of the reactive clay edges by organic material coverage was demonstrated by Taubald *et al.* (2000) who showed that chlorite which is unstable under oxidizing conditions showed no tendency to react during their experiment.

CONCLUSIONS

The effect of alkaline solutions on clay mineralogy was investigated experimentally at 60°C as a function of time to mimic the effect of a pH plume resulting from the alteration of cements on the clay formation hosting the future French underground laboratory. From the three clay phases initially present, *i.e.* discrete smectite, discrete illite, and a randomly-interstratified MLM phase containing ~65% of illite layers, only the smectite was shown to transform. The evolution of discrete smectite to a randomly interstratified MLM phase containing ~50% of illite layers is consistent with earlier similar experiments (Eberl *et al.*, 1993; Bauer and Velde, 1999). The neoformation of a tobermorite-like phase was the only additional significant mineralogical evolution.

Coverage of clay mineral outer surfaces, and more especially of the crystal edges, may be responsible for the very limited character of the observed mineralogical transformation by blocking the access of the alkaline solution to these most reactive sites. After 1 y of reaction time, the bonding of organic ligands to crystal edges is still effective whereas basal surfaces appear to be free of the initial organic coverage. As a result, aqueous concentration of DOC is high but does not promote clay mineral dissolution by complexing Al or Si. The average size of this colloidal organic material tends to decrease with increasing reaction progress.

At lower pH values than those used in this study (*e.g.* 7–8) such humic material may influence the sorption of metal ions, and more especially that of actinides. Their complexation both in solution and on solid surfaces will be an essential parameter for their fate.

ACKNOWLEDGMENTS

The results presented in the present article were collected during a PhD thesis granted by Andra (French National Agency for Nuclear Waste Disposal). Andra is thanked for permission to publish this manuscript. BL and FC acknowledge financial support from Andra. Spectromicroscopic data were collected using the X-1A STXM developed by the group of Janos Kirz and Chris Jacobsen at SUNY Stony Brook, with support from the Office of Biological and Environmental Research, U.S. DoE under contract DE-FG02-89ER60858, and from the NSF under grant DBI-9605045. The zone plates were developed by Steve Spector and Chris Jacobsen of Stony Brook and Don Tennant of Lucent Technologies Bell Labs with support from the NSF, under grant ECS-9510499.

REFERENCES

Anderson, K., Allard, B., Bengtsson, M. and Magnusson, B. (1989) Chemical composition of cement pore waters. *Cement and Concrete Research*, **19**, 327–332.

Bauer, A. and Berger, G. (1998) Kaolinite and smectite dissolution rate in high molar KOH solutions at 35°C and 80°C. *Applied Geochemistry*, **13**, 905–916.

Bauer, A. and Velde, B. (1999) Smectite transformation in high molar KOH solutions. *Clay Minerals*, **34**, 259–273.

Bauer, A., Velde, B. and Berger, G. (1998) Kaolinite transformation in high molar KOH solutions. *Applied Geochemistry* , **13**, 619–629.

Berner, U. (1990) *A Thermodynamic Description of the Evolution of Porewater Chemistry and Uranium Speciation during the Degradation of Cement*. Nagra NTB, Report 90-12, Baden, Switzerland.

Bosbach, D., Charlet, L., Bickmore, B. and Hochella, M.F. (2000) The dissolution of hectorite: In-situ, real-time observations using atomic force microscopy. *American Mineralogist* , **85**, 1209–1216.

Bouchet, A. and Rassineux, F. (1997) *Echantillons d'Argiles du Forage EST 104: Etude minéralogique Approfondie*. Andra, Report DR-P-0ERM-98-007A, Chatenay-Malabry, France, 107 pp.

Cama, J., Ganor, J., Ayora, C. and Lasaga, A.C. (2000) Smectite dissolution kinetics at 80 degrees C and pH 8.8. *Geochimica et Cosmochimica Acta*, **64**, 2701–2717.

Carroll, S.A. and Walther, J.V. (1990) Kaolinite dissolution at 25°, 60° and 80°C. *American Journal of Science*, **290**, 797–810.

Carroll-Webb, S.A. and Walther, J.V. (1988) A surface complex reaction model for the pH-dependence of corundum and kaolinite dissolution. *Geochimica et Cosmochimica Acta*, **52**, 2609–2623.

Cassagnabere, A., Parneix, J.C., Sammartino, S., Griffault, L., Maeder, U. and Milodowski, T. (2001) Mineralogical evolution of bitumimous marl adjacent to an alkaline water conducting feature at the Maqarin analogue site. Pp. 367–370 in: *Water-Rock Interaction* (R. Cidu, editor). Balkema, Liss, Tokyo.

Chermak, J.A. (1992) Low temperature experimental investigation of the effect of high pH NaOH solutions on the Opalinus shale, Switzerland. *Clays and Clay Minerals*, **40**, 650–658.

Chermak, J.A. (1993) Low temperature experimental investigation of the effect of high pH KOH solutions on the Opalinus shale, Switzerland. *Clays and Clay Minerals*, **41**, 365–372.

Chin, P.F. and Mills, G.L. (1991) Kinetics and mechanisms of kaolinite dissolution: effect of organic ligands. *Chemical Geology*, **90**, 307–317.

Claret, F. (2001) Caractérisation structurale des transitions minéralogiques dans les formations argileuses: Contrôles et implications géochimiques des processus d'illitisation. Cas particulier d'une perturbation alcaline dans le Callovo-Oxfordien Laboratoire souterrain Meuse-Haute-Marne. PhD thesis, Université Joseph Fourier, Grenoble, France, 174 pp.

Cody, G.D., Botto, R.E., Ade, H., Behal, S., Disko, M. and Wirick, S. (1995) Inner-shell spectroscopy and imaging of a subbituminous coal: In-situ analysis of organic and inorganic microstructure using C(1s)-, Ca(2p)-, and Cl(2s)-NEXAFS. *Energy and Fuels*, **9**, 525–533.

Decarreau, A. (1999) *Etude Expérimentale des Réactions entre Argiles de sites de Stockage Français et Eaux Cimentaires*. Andra, Report D-RP-1UPT-99-001, Chatenay-Malabry, France, 38 pp.

Drits, V.A. and Sakharov, B.A. (1976) *X-ray Structure Analysis of Mixed-layer Minerals*. Doklady Akademii Nauk, SSSR, Moscow, 256 pp.

Drits, V.A., Środoń, J. and Eberl, D.D. (1997) XRD measurement of mean crystallite thickness of illite and illite/smectite: Reappraisal of the Kübler index and the Scherrer equation. *Clays and Clays Minerals*, **45**, 461–475.

Eberl, D.D., Velde, B. and McCormick, T. (1993) Synthesis of illite-smectite from smectite at Earth surface temperatures and high pH. *Clay Minerals*, **28**, 49–60.

Faure, P., Landais, P. and Griffault, L. (1999) Behavior of organic matter from Callovian shales during low-temperature air oxidation. *Fuel*, **78**, 1515–1525.

Francis, J.T. and Hitchcock, A.P. (1992) Inner-shell spectroscopy of p-benzoquinone, hydroquinone, and phenol: Distiguishing quinoid and benzenoid structures. *Journal of Physical Chemistry*, **96**, 6598–6610

Haworth, A., Sharland, S.M. and Tweed, C.J. (1989) Modeling of the degradation of cement in a nuclear waste repository. *Material Research Society Symposium Proceedings*, **127**, 447–454.

Henke, B.L., Gullikson, E.M. and Davis, J.C. (1993) X-ray interactions: Photoabsorption, scattering, transmission, and reflection at E=50–30000 eV, Z=1–92. *Atomic Data and Nuclear Data Tables*, **54**, 181–342.

Hitchcock, A.P. and Mancini, D.C. (1994) Bibliography and database of inner-shell excitation spectra of gas phase atoms and molecules. *Journal of Electron Spectroscopy and Related Phenomena*, **67**, 1–132.

Hitchcock, A.P., Newbury, D.C., Ishii, I., Stöhr, J., Horsley, J.A., Redwing, R.D., Johnson, A.L. and Sette, F. (1986) Carbon K-shell excitation of gaseous and condensed cyclic hydrocarbons: C_3H_6, C_4H_8, C_5H_8, C_5H_{10}, C_6H_{10}, C_6H_{12}, and C_8H_8. *Journal of Chemical Physics*, **85**, 4849–4862.

Hitchcock, A.P., Urquart, S.G. and Rightor, E.G. (1992) Inner shell spectroscopy of benzaldehyde, terephthalaldehyde, ethyl benzoate, terephthaloyl chloride, and phosgene: Models for core excitation of poly (ethylene terephathalate). *Journal of Physical Chemistry*, **96**, 8736–8750.

Huang, W.L. (1993) The formation of illitic clays from kaolinite in KOH solution from 225°C to 350°C. *Clays and Clay Minerals*, **41**, 645–654.

Huertas, F.J., Caballero, E., de Cisneros, C.J., Huertas, F. and Linares, J. (2001) Kinetics of montmorillonite dissolution in granitic solutions. *Applied Geochemistry*, **16**, 397–407.

Inoue, A., Bouchet, A., Velde, B. and Meunier, A. (1989) Convenient technique for estimating smectite layer percentage in randomly interstratified illite/smectite minerals. *Clays and Clay Minerals*, **37**, 227–234.

Ishii, I. and Hitchcock, A.P. (1987) A quantitative experimental study of the core excited electronic states of foramide, formic acid, and formyl fluoride. *Journal of Chemical Physics*, **87**, 830–839.

Jacobsen, C., Williams, S., Anderson, E., Browne, M.T., Buckley, C.J., Kern, D., Kirz, J., Rivers, M. and Zhang, X. (1991) Diffraction-limited imaging in a scanning transmission x-ray microscope. *Optics Communications*, **86**, 351–364.

Jacobsen, C., Wirick, S., Flynn, G. and Zimba, C. (2000) Soft X-ray spectroscopy with sub-100 nm spatial resolution. *Journal of Microscopy*, **197**, 173–184.

Jeffries, N.L., Tweed, C.J. and Wisbey, S.J. (1988) The effects of changes in pH in a clay surrounding a cementitious repository. *Material Research Society Symposium Proceedings* , **112**, 43–52.

Lunden, I. and Andersson, K. (1989) Modelling the mixing of cement pore water and groundwater using the PHREEQC code. *Material Research Society Symposium Proceedings*, **127**, 949–956.

Ma, Y., Chen, C.T., Meigs, G., Randall, K. and Sette, F. (1991) High-resolution K-shell photoabsorption measurements of simple molecules. *Physical Review A*, **44**, 1848–1858.

Mohnot, S.M., Bae, J.H. and Foley, W.L. (1987) A study of alkali/mineral reactions. *SPE Reservoir Engineering*, 653–663.

Moore, D.M. and Reynolds, R.C., Jr. (1989) *X-ray Diffraction*

and the Identification and Analysis of Clay Minerals. Oxford University Press, Oxford and New York, 322 pp.

Nagra (1995) *Column Experiments: Results of Experiments and Modelling*. Nagra NTB, Report 95–70, Baden, Switzerland.

Neuhäusler, U., Abend, S., Jacobsen, C. and Lagaly, G. (1999) Soft X-ray spectromicroscopy on solid-stabilized emulsions. *Colloid Polymer Science*, **277**, 719–726.

Rassineux, F., Griffault, L., Meunier, A., Berger, G., Petit, S., Viellard, P., Zellagui, R. and Munoz, M. (2001) Expandability-layer stacking relationship during experimental alteration of a Wyoming bentonite in pH 13.5 solutions at 35 and 60°C. *Clay Minerals*, **36**,197–210.

Reardon, E.J. (1990) An ion interaction model for the determination of chemical equilibrium in cement/water systems. *Cement and Concrete Research*, **20**, 175–192.

Robin, M.B., Ishii, I., McLaren, R. and Hitchcock, A.P. (1988) Fluorination effects on the inner shell spectra of unsaturated molecules. *Journal of Electron Spectroscopy and Related Phenomena*, **47**, 53–92.

Sakharov, B.A., Lindgreen, H., Salyn, A. and Drits, V.A. (1999) Determination of illite-smectite structures using multispecimen X-ray diffraction profile fitting. *Clays and Clays Minerals*, **47**, 555–566.

Spector, S., Jacobsen, C. and Tennant, D. (1997) Process optimization for production of sub-20 nm soft X-ray zone plates. *Journal of Vacuum Science and Technology B*, **15**, 2872–2876.

Taubald, H., Bauer, A., Schafer, T., Geckeis, H., Satir, M. and Kim, J.I. (2000) Experimental investigation of the effect of high-pH solutions on the Opalinus Shale and the Hammerschmiede Smectite. *Clay Minerals*, **35**, 515–524.

Taylor, H.F.W. (1992) Tobermorite, jennite, and cement gel. *Zeitschrift für Kristallographie*, **202**, 41–50.

Turpault, M.P. and Trotignon, L. (1994) The dissolution of biotite single crystals in dilute HNO_3 at 24°C: Evidence of an anisotropic corrosion process of micas in acidic solutions. *Geochimica et Cosmochimica Acta*, **58**, 2761–2775.

Velde, B., Suzuki, T. and Nicot, E. (1986) Pressure-temperature-composition of illite/smectite mixed-layer minerals: Niger delta mudstones and other examples. *Clays and Clay Minerals*, **34**, 435–441.

Viellard, P. and Rassineux, F. (1992) Thermodynamic and geochemical modelling of the alteration of two cement matrices. *Applied Geochemistry*, **1**, 125–136.

Winn, B., Ade, H., Buckley, C., Howells, M., Hulbert, S., Jacobsen, C., Kirz, J., McNulty, I., Miao, J., Oversluizen, T., Pogorelsky, I. and Wirick, S. (1996) X1A: second generation undulator beamlines serving soft x-ray spectromicroscopy experiments at the NSLS. *Reviews of Scientific Instruments* , **67**, 1–4.

Wolery, T.J. (1983) *EQ3NR a computer program for geochemical aqueous speciation-solubility calculations: User's guide and documentation*. Lawrence Livermore National Laboratory UCRL-53414, Livermore, CA, USA, 202 pp.

Zhang, X., Ade, H., Jacobsen, C., Kirz, J., Lindaas, S., Williams, S. and Wirick, S. (1994) Micro-XANES: chemical contrast in the scanning transmission x-ray microscope. *Nuclear Instruments and Methods in Physics Research A*, **347**, 431–435.

(*Received 6 December 2001; revised 29 March 2002; Ms. 612; A.E. David A. Laird*)

Natural organic matter (NOM)-clay association and impact on Callovo-Oxfordian clay stability in high alkaline Solution: Spectromicroscopic evidence.

J. Phys. IV (2003) **104**, 413.

Schäfer T., Claret F., Bauer A., Griffault L., Ferrage E., and Lanson B.

J. Phys. IV France **104** (2003)

DOI: 10.1051/jp4:20030111

Natural organic matter (NOM)-clay association and impact on Callovo-Oxfordian clay stability in high alkaline solution: Spectromicroscopic evidence

T. Schäfer[1], F. Claret[1,2], A. Bauer[1], L. Griffault[2], E. Ferrage[3] and B. Lanson[3]

[1] *Forschungszentrum Karlsruhe, Institut für Nukleare Entsorgung, INE, P.O. Box 3640, 76021 Karlsruhe, Germany*
[2] *ANDRA, Parc de Croix Blanche, 1-7 rue Jean Monnet, 92298 Châtenay-Malabry cedex, France*
[3] *Environmental Geochemistry Group, LGIT, Maison des Géosciences, Université J. Fourier, CNRS, BP. 53, 38041 Grenoble cedex 9, France*

Abstract. The understanding of chemical association between natural organic matter (NOM) and clay minerals is of paramount importance to predict the long term stability of host rock formations for deep geological nuclear waste repositories. Synchrotron-based soft X-ray spectromicroscopy demonstrates a strong association between K-rich clay phases (illite) and NOM in the Callovo-Oxfordian argillite (Meuse-Haute Marne, or MHM site, France) and a weaker association in the Opalinus clay (Benken, Switzerland). C(1s) spectra show no significant depth dependent variation in the MHM site (447-516m). Alteration experiments under oxidizing conditions and high pH of the Callovo-Oxfordian clay indicate a passivation of chemically reactive sites by NOM that is responsible for the kinetic hindered clay dissolution/transformation. These experiments lead to a significant release of humic/fulvic acid colloids in the alkaline solution with time dependent variation in size and functional group content.

1. INTRODUCTION

Host rocks considered for deep geological storage of nuclear waste include clay-rich formations as (e.g.) the Callovo-Oxfordian argillite (MHM site, France) and the Opalinus shale (Zürcher Weinland, Switzerland). However, there are concerns that the mineralogical composition of these clay formations will not be stable under alkaline pore fluid conditions (pH > 12) typical for initial cement alteration. To assess this stability, the impact of the **S**olid **Y**oung **F**luid (SYF) [1] on the clay mineralogy of the Callovo-Oxfordian argillite has been studied experimentally under oxidizing conditions which are expected to occur in the excavation disturbed zone (EDZ) during the installation of the repository shafts and galleries. Indeed, in the alteration experiments performed by [2], the clay mineralogy is little affected as compared to analogue studies with pure smectite systems [3] even though the pH is still high after long reaction times. This low reactivity of clay minerals has been attributed to the presence of organic matter in the samples [2], and an important release of organic colloids has been observed. Because the marine/terrestrial deposition of argillite and shale generally occurs in the presence of organic material [4] and because the P/T evolution during burial diagenesis/catagenesis can change drastically the organic composition in these systems [5], reliable clay stability predictions can only be drawn if the NOM-clay association is precisely characterized. As a consequence, the present study focuses on (1) the C(1s) and K($L_{2,3}$) NEXAFS (**N**ear **E**dge **X**-ray **A**bsorption **F**ine **S**tructure) spectromicroscopic characterization of the initial clay-NOM association in the Callovo-Oxfordian argillite and Opalinus shale, (2) investigation of the role of NOM on clay dissolution kinetics and (3) the critical evaluation of NOM as a potential source for humic & fulvic acid colloids in solution under oxidizing conditions.

2. EXPERIMENTAL

The clay fraction (< 2 μm) of four MHM samples (447, 490, 494, 516 m below surface - borehole EST 104) and one Opalinus shale sample (579.19-579.45m - borehole Benken) were selected as representative of the two mineralogical sequences. For details on clay fraction preparation, mineralogical characterization and batch experimental setup under alkaline conditions it is referred to [2, 6]. The TOC concentration in the Bure argillite is depth independent ~1.3 wt% and < 0.4 wt% in the Opalinus clay [2, 6]. Scanning transmission X-ray microscopy (STXM) investigations were performed at the beamline X1A (NSLS) op-

erated by the State University of New York at Stony Brook. The principle of the method and the sample preparation using a wet cell assembly is described in [7,8]. STXM images of clay suspensions were recorded at the carbon K-edge and potassium L-edge. In the NEXAFS spectra illitic clays are identified using the X-ray absorption double feature at 297.3 eV (L_3-edge) and 300 eV (L_2-edge) of interlayer potassium. STXM investigations on alkaline treated samples are limited to sample 447. For C(1s) NEXAFS spectra deconvolution ionization threshold (IP) was set to 290.5 eV and a single arctangent function was used to generate the continuum spectrum up to 295 eV. FWHM of Gaussian peaks was set to 0.4 eV and 7 Gaussian functions representing the main π^* transitions were used (Fig. 1A). Two additional σ^*-transitions were simulated by simplified Gaussian shape function with a FWHM of 0.6 eV and 0.8 eV, respectively.

3. RESULTS & DISCUSSION

3.1 Untreated clay

The simultaneous measurement of the C(1s) NEXAFS and the potassium L-edge in the same pixel area clearly indicates an association of NOM with K-rich clay phases (illite) in the Callovo-Oxfordian argillite (Fig. 1A). Furthermore no significant depth dependent C(1s) variations in the average spectra are noticeable after deconvolution of the spectra (Tab.1). The observed clay-NOM association can be interpreted as a so-called sorptive protection mechanism preventing diagenetic degradation of NOM via sorption on clays [9]. The microscopy of the clay-NOM associates (Fig. 1B) shows no homogeneous clay coverage in form of a monolayer coating as proposed by [10], but rather a blurred patchy distribution [11]. The noted association implies that NOM sequestration may be more closely related to patterns of continental weathering and clay mineralogy than to ocean water chemistry or marine productivity as already pointed out by Kennedy and co-workers [12]. Isolated organic areas with high aromatic content known as amorphous organic matter (AOM) typical for Type II kerogen [13] were also observed (Fig. 1B). This discrete AOM constitutes usually only a minor portion (<10%) of the total organic carbon [12] in which oxidized organic compounds (benzoquinone type groups) are detectable.

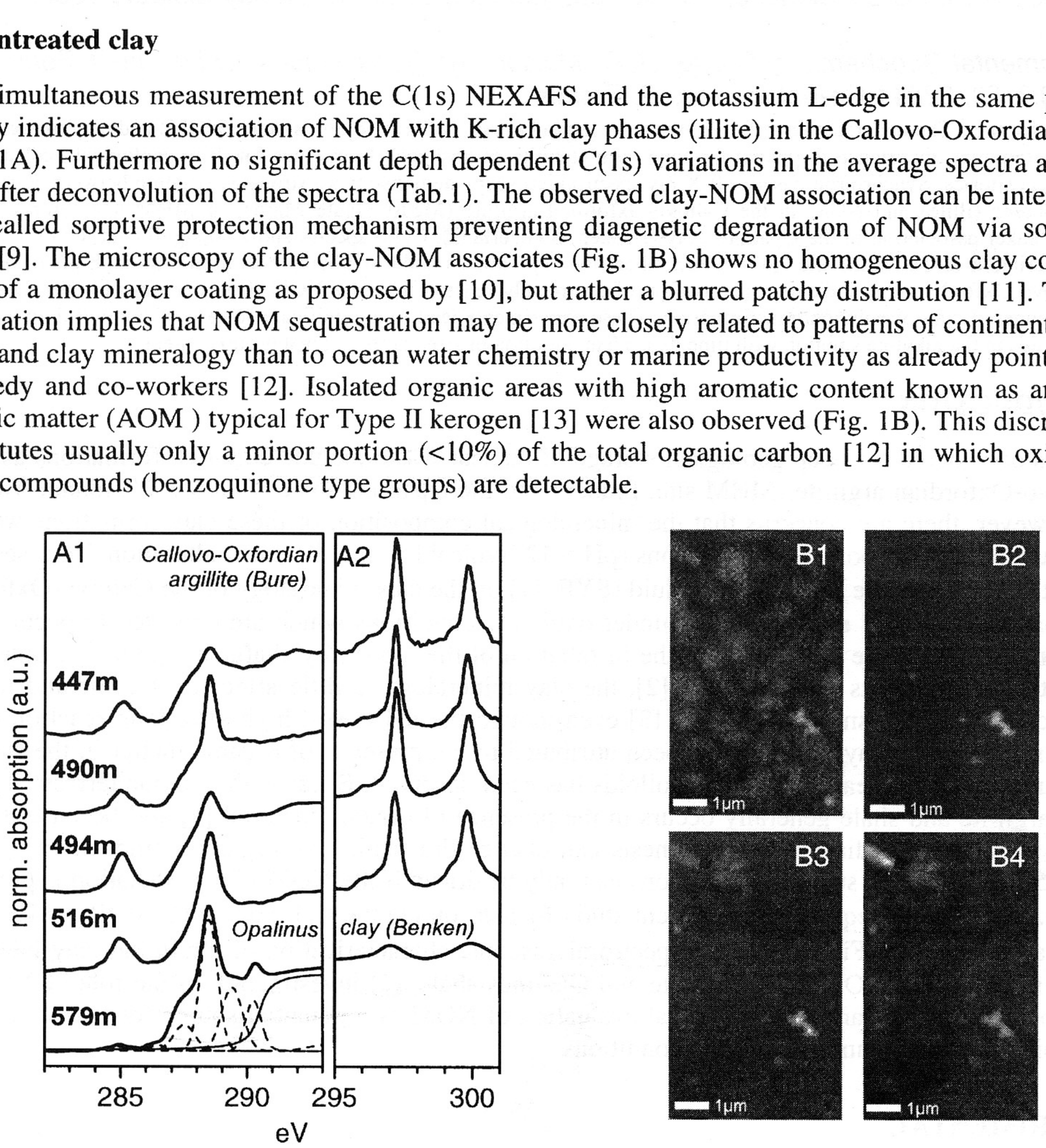

Figure 1: A1: C K-edge spectra of the Bure and Opalinus untreated clay fraction and Gaussian functions used for deconvolution. A2: Potassium $L_{2,3}$ edges of the samples. B: Ratio images (-log [I/I_0]; I_0= Σ(280-283eV)) of sample 490m. B1: Potassium distribution, I=297.2eV; B2: aromatics, I=285eV; B3: aliphatics, I=287.6eV; B4: carboxyl, I=288.4eV.

In addition, enrichment in carboxyl groups has been observed in the K-rich areas (thick illite platelets) in samples of the MHM site. In comparison, the untreated Opalinus clay (Fig. 1A) shows lower potassium L-edges absorption in the C-edge normalized spectra, therefore indicating a weaker association of NOM

with K-rich illite. This might point to a preferential association with other clay mineral phases (kaolinite, chlorite) as indicated by additional FT-IR measurements. Furthermore Opalinus clay is significantly depleted on aromatic functional groups in comparison with the samples from the MHM site. The ratio of the 1s-π^* transition at 285eV and of aromatic carbon bonded to oxygen (286.6eV; phenol type groups) in Opalinus clay is similar to values reported for hydroquinone and implies an average degree of hydroxylation close to 2OH/ring and lower than reported values for phenol indicating an average hydroxylation ~1OH/ring in the Bure argillite [14, 15]. A possible explanation for the significant lower aromatic band intensities (285 eV) in the Opalinus shale might be the polycondensation associated relative increase of carboxyl and aliphatics according to the P/T history of the sediment. In addition, oxidation of the Callovo-Oxfordian argillite increases the content of triaromatic steroids (phenanthrene) in the total aromatic fraction [16].

Table 1: Semiquantitative analysis of the average Carbon K-edge by spectra de-convolution in the energy range 280-295eV. Values given are proportion in % of the sum of the seven π^* Gaussian peaks used.

Sample	C_{arom}-C_{arom}, C_{arom}-H	phenol type	CH_2, CH_3	carboxyl	carbonyl	carbonate	$\Sigma(I_{fit}-I_{meas.})^2$
Opalinus	1.6	3.0	18.4	38.8	23.1	15.2	0.03297
Bure 447m	12.0	4.1	18.9	31.4	21.4	12.1	0.26007
Bure 490m	10.1	3.3	19.7	36.3	23.6	7.0	0.04825
Bure 494m	12.4	2.4	15.2	35.6	23.0	11.4	0.04678
Bure 516m	11.9	3.2	17.6	35.0	22.1	10.2	0.16874

3.2 High alkaline solution reaction of Callovo-Oxfordian argillite

After 2 years reaction in SYF the NOM is still partly associated with clay and covers clay particle edge Si, Al functional groups (Fig. 2C), whereas basal surfaces appear to be depleted of their initial organic coverage [2]. Spectra of the clay associated NOM after SYF reaction show features similar to that observed for the untreated clay material (Fig. 2A). After two years reaction time bonding of organic ligands to crystal edges is still effective, and the limited increase of carboxyl groups in released DOC (Fig. 2B)

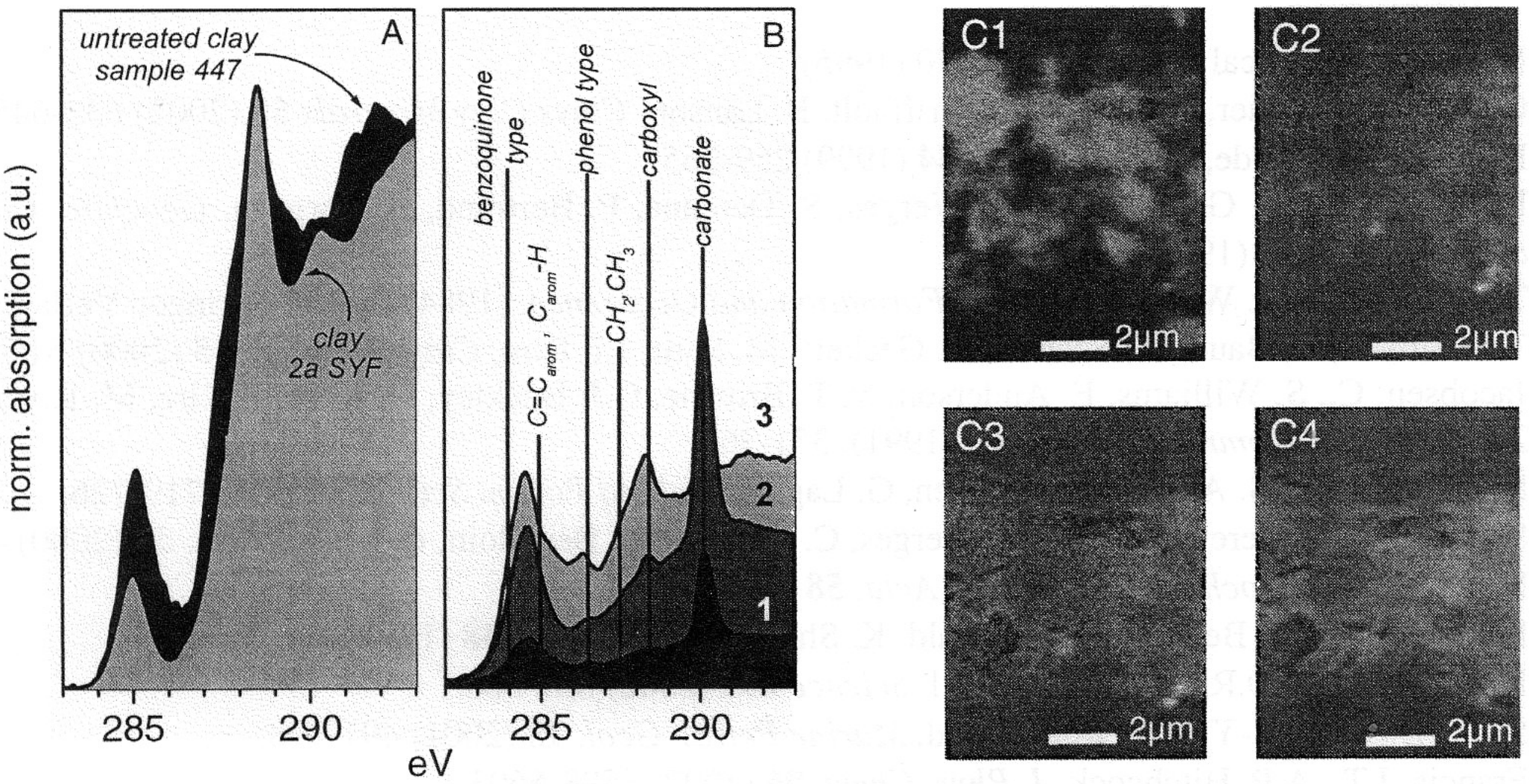

Figure 2: Clay sample 447 m (MHM site) after alkaline alteration. A: C K-edge spectra of the untreated clay fraction and after two years reaction time in SYF solution. B: Carbon functional group characterization in reaction solution (DOC), 1: 3d in SYF; 7.1% of TOC released. 2: 74d in SYF (25.8%) 3: 350d in SYF (40.9 %). All absorption spectra initially normalized to 1 at 295 eV and spectra in B are weighted on the relative amount of DOC released. C: Ratio images (-log [I/I_0]; I_0= Σ(280-283eV)) of sample 490m 2a treated in SYF. C1: Potassium distribution, I=297.2eV; C2: aromatics, I=285eV; C3: aliphatics, I=287.6eV; C4: carboxyl, I=288.4eV.

suggests a carboxyl mediated strong NOM surface complexation. The observed passivation of these reactive clay edge sites is likely responsible for the very limited mineralogical transformation in SYF as discussed by [2]. In addition, enrichment in carboxyl groups has been observed in the K-rich areas (thick illite platelets) in samples of the MHM site. The organic matter (DOC) released from clay after one year reaction in SYF represents ~40% of the total C_{org} content. Under high alkaline conditions expected in the near-field of a nuclear-waste repository with cement waste packages, such high concentrations of hydrophilic organic substances are generated by conversion of initially clay associated mainly hydrophobic natural organic matter. This DOC is quantitatively HA & FA and shows a continuous decrease in colloid size to 80% < 1kDa after one year reaction time [2]. The released HA/FA C(1s) spectra differ significantly from the clay associated NOM and shows benzoquinone type (284 eV) functional groups indicative for oxidative processes (photodegradation). Additional fluorescence spectroscopy studies reveal a significant red shift of the isolated HA to 520 nm in the emission spectra with a excitation wavelength of 260 nm [17]. This red shift can be related to a significant contribution of quinone type groups to the overall HA fluorescence as pointed out by [18]. These results together with the above mentioned observation of benzoquinone type groups on AOM support the sorptive protection mechanism of NOM via clay association proposed by [9]. Furthermore a pronounced increase of phenol type groups (286.6 eV) and, to a lesser extent, of carboxyl groups (288.6 eV) with time is observable. FT-IR investigations showed comparable spectra independent of sampling depth for the HA isolates after one year SYF reaction [17]. However, a decrease in released DOC concentration can be observed with sediment depth [2] leading to two possible explanations: (a) Diagenetic differences in the Callovo-Oxfordian formation resulting in a stronger polycondensation and insolubilization (humin) of HA/FA in the lower sediments or (b) considerable land derived organic matter in the upper part of the formation, where HA and FA can still amount from 5-70% after complete diagenetic insolubilization.

Acknowledgments

The results presented in the article were partly collected during the Ph.D. thesis of F. Claret granted by Andra (French National Agency for Nuclear Waste Disposal). Spectromicroscopic data was collected using the X1-A1 STXM developed by the group of Janos Kirz and Chris Jacobsen at SUNY Stony Brook.

References

[1] NAGRA, Technical report NTB 95-70 (1995).
[2] Claret, F., A. Bauer, T. Schäfer, L. Griffault, B. Lanson, *Clays Clay Minerals* **50** (2002) 632-645.
[3] Bauer, A., B. Velde, *Clay Minerals* **34** (1999) 259-265.
[4] Boussafir, M., F. Gelin, E. Lallier-Verges, S. Derenne, P. Bertrand, C. Largeau, *Geochim. Cosmochim. Acta* **59**/18 (1995) 3731-3747.
[5] Tissot, B.P., D.H. Welte, *Petroleum Formation and Occurence*. (1984) Berlin: Springer-Verlag.
[6] Taubald, H., A. Bauer, T. Schäfer, H. Geckeis, M. Satir, J.I. Kim, *Clay Minerals*, **35** (2000) 515-524.
[7] Jacobsen, C., S. Williams, E. Anderson, M.T. Browne, C.J. Buckley, D. Kern, J. Kirz, M. Rivers, X. Zhang, *Optics Communications*, **86** (1991). 351-364.
[8] Neuhäusler, U., S. Abend, C. Jacobsen, G. Lagaly, *Colloid Polym. Sci.*, **277** (1999) 719-726.
[9] Salmon, V., S. Derenne, E. Lallier-Verges, C. Largeau, B. Beaudoin, *Org. Geochem.* **31** (2000) 463.
[10] Mayer, L.M., *Geochim. Cosmochim. Acta*, **58** (1994) 1271-1284.
[11] Ranson, B., R.H. Bennett, R. Baerwald, K. Shea, *Marine Geol.* **138** (1997) 1-9.
[12] Kennedy, M.J., D.R. Pevear, R.J. Hill, *Science* **295** (2002) 657-660.
[13] Stow, D.A.V., A.-Y. Huc, P. Bertrand, *Marine Petrol. Geol.* **18** (2001) 491-498.
[14] Francis, J.T., A.P. Hitchcock, *J. Phys. Chem.* **96** (1992) 6598-6603.
[15] Cody, G.D., R.E. Botto, H. Ade, S. Behal, M. Disko, S. Wirick, *Energy & Fuels*, **9** (1995) 525-533.
[16] Elie, M., P. Faure, R. Michels, P. Landais, and L. Griffault, *Energy & Fuels* **14** (2000) 854-861.
[17] Claret, F., T. Schäfer, A. Bauer, G. Buckau, *Sci. Total Environ.* (submitted).
[18] Klapper, L., D.M. McKnight, J.R. Fulton, E.L. Blunt-Harris, K.P. Nevin, D.R. Lovley, P.G. Hatcher, *Environ. Sci. Technol.* **36** (2002) 3170-3175.

Generation of humic and fulvic acid from Callovo- Oxfordian clay under high alkaline conditions.

Sci. Total Environ. (2003) **317**(1-3), 189.

Claret F., Schäfer T., Bauer A., and Buckau G.

Available online at www.sciencedirect.com
SCIENCE DIRECT®
The Science of the Total Environment 317 (2003) 189–200
the Science of the Total Environment
An International Journal for Scientific Research into the Environment and its Relationship with Man
www.elsevier.com/locate/scitotenv

Generation of humic and fulvic acid from Callovo-Oxfordian clay under high alkaline conditions

Francis Claret, Thorsten Schäfer, Andreas Bauer, Gunnar Buckau*

Forschungszentrum Karlsruhe, Institut für Nukleare Entsorgungstechnik, Karlsruhe D-76021, Germany

Received 23 September 2002; received in revised form 20 March 2003; accepted 30 April 2003

Abstract

Low-carbon-containing clay from four different depths (447 to 516 m) of the Meuse Haute Marne (MHM) site is kept in contact with alkaline solution simulating conditions expected from cement dissolution in the near-field of a nuclear waste repository. Original organic material in the clay consists mainly of aliphatic hydrophobic compounds basically without oxygen-containing functional groups. After contact with 'solid young fluid' (mimicking cement dissolution, initial pH 13.22) for approximately one and a half years, high concentrations of hydrophilic organic matter are found (243–355 mg DOC/L). Characterization by solubility behavior, UV/Vis absorption, IR and fluorescence properties show that the dissolved hydrophilic organic matter has the characteristic features of humic and fulvic acids. Estimation of humic and fulvic acid content via UV/Vis spectroscopy results in 97.5 ($\pm$9.7)% of DOC being humic and fulvic acid. The results indicate that this could be an important source of complexing mobile organic matter influencing the mobility of radionuclides in a nuclear waste repository under consideration for this site. Investigations were conducted under oxic conditions representing the situation in the excavation disturbed zone (EDZ) of an underground facility. Sample amounts were very small and thus some characterization results are partly of preliminary character.

Keywords: Clay organic matter; Humic substancesl; Disposal; Radioactive waste; High pH

1. Introduction

Geologic disposal of radioactive waste is under consideration for a number of different geological settings. These include clay, salt and crystalline rock. Within these different types of basic host rocks, great individual variations are found. One site under consideration in France is at the Meuse Haute Marne (MHM) in the Eastern Paris basin, where the French nuclear agency (ANDRA) is currently setting up an underground laboratory. The sedimentary host formation is an approximately 130 m thick clay-rich Callovo-Oxfordian formation at approximately 350–550 m depth below ground surface in the selected area. The origin of the clay organic matter, identified by biomarkers, in the Oxfordian series is mainly terrestrial-derived (type III kerogen), whereas organic carbon in the Callovian series is mainly of marine origin (type

*Corresponding author. Tel.: +49-7247-824461; fax: +49-7247-82-4308.
E-mail address: buckau@ine.fzk.de (G. Buckau).

0048-9697/03/$ - see front matter © 2003 Elsevier Science B.V. All rights reserved.
doi:10.1016/S0048-9697(03)00337-1

II kerogen). These variations have been related to paleoenvironmental changes occurring during the Callovo-Oxfordian period (Landais and Elie, 1999). Various studies carried out on clay mineralogy, fluid inclusions and organic matter suggest that the maximum burial temperature recorded for the Callovo-Oxfordian formation has not exceeded 40 °C (Elie et al., 2000). Under these burial temperature conditions humic substances that represent part of the immature organic material are decreased, but not fully degraded (Tissot and Welte, 1984; Huang, 1999).

Cement may be present in a nuclear waste repository as a waste form and/or as part of engineered structures. In case of water intrusion, cement dissolution will, amongst others, lead to high pH values. Such high pH values are expected to result in clay mineral dissolution (Eberl et al., 1993; Bauer and Velde, 1999). The impact of such high pH values on the clay is studied under oxic conditions relevant for the excavation-disturbed zone (EDZ). Mobilization of dissolved organic carbon (DOC) is well known from extraction procedures to be released from soils under alkaline conditions (e.g. NaOH method (Swift, 1996)). Furthermore, humic-like substances can be generated via oxidative conversion of clay organic matter (Vilks et al., 1998). Substantial generation of hydrophilic dissolved organic carbon from hydrophobic clay organic matter has also been observed by alkaline extended treatment of clay (Claret et al., 2002).

Humic substances are operationally classified into humic acids (HA) and fulvic acid (FA), based on differences in solubility in acidic and alkaline media. Humic and fulvic acids are soluble in alkaline media, whereas humic acid flocculates under acidic conditions. Humic substances are mixtures of natural organic substances showing a distribution in mass and functional entities. Examples of different functional entities are aromatics, aliphatics, phenolics and quinones (Gaffney et al., 1996). For characterization of the humic substances and their functional entities, spectroscopic methods amongst others are applied. Frequently used spectroscopic methods are UV/Vis, Fourier-transform infrared (FTIR) and fluorescence. UV/Vis absorption shows a monotonous increase with decreasing wavelength due to aromatic and other organic chromophores (Traina et al., 1990; Chen et al., 2002). The fluorescence (excitation and emission) gives information related to the structure, functional groups, conformation and heterogeneity (Mobed et al., 1996; Chen et al., 2003). Due to significant overlapping and peak broadening linked to the multicomponent nature, straightforward identification and interpretation of fluorescence signatures is difficult. A blue shift in the emission is indicative of a higher degree of condensed and/or higher substituted aromatic character (Miano et al., 1988). A red shift in the fluorescence emission of fulvic acid is attributed to the presence of high molecular weight fractions with a high degree of conjugation and extended electron delocalization and electron-withdrawing groups on delocalized electron structures (Mobed et al., 1996). Electron-donating groups result in a corresponding blue shift (Mobed et al., 1996).

Humic substances in natural groundwater are present in the form of humic colloids, consisting of the organic entities and associated mineral structures and complexed metal ions. These humic colloids can play a major role in radionuclide migration in natural aquifer systems (Choppin, 1992). The potential impact of humic-colloid-mediated radionuclide transport depends on (i) the sources/concentrations of humic substances, (ii) their stability and mobility, and (iii) the interaction with radionuclides (McCarthy and Zachara, 1989; Buckau, 2000a). Humic substances in natural aquifer systems show no sign of retention or decomposition but migrate like ideal tracers (Buckau et al., 2000b,c). Carboxylic functional groups generally dominate the metal ion complexation behavior (Pompe et al., 2000; Sachs et al., 2003; Schmeide et al., 2003). Differences between humic and fulvic acids may lead to small differences in the metal complexation behavior. In addition, to the complexation strength, the complex kinetic behavior needs to be considered (Buckau, 2000a; Schuessler et al., 2000; King et al., 2001; Artinger et al., 2002).

The origin of humic substances is the subject of the present paper. DOC generated by alkaline treatment of clay is characterized by spectroscopic methods and it is shown that the DOC has the typical properties of humic and fulvic acids. Consequently, this is an additional potential source for

Table 1
Sampling depth of MHM site clay samples, conditions for leaching experiment, and pH, Eh, DOC and sulfate concentration of final solutions

Sample no.	Sampling depth (m)	Clay to liquid ratio	Liquid volume* (ml)	Fe chip (g)	Fe powder (g)	Contact time (days)	pH	Eh (mV)	DOC (mgC/l)	Sulfate (mmol/l)
1	447	1:20	10	3.61	–	537	12.3	13	299	2.52
2	447	1:20	10	3.59	0.20	538	12.4	12	260	2.17
3	490	1:20	10	3.58	–	537	13.2	−29	243	1.90
4	490	1:20	10	3.37	0.20	538	13.2	−29	267	2.06
5	494	1:20	10	3.60	–	537	13.3	−36	270	1.34
6	494	1:20	10	3.60	0.20	538	13.3	−28	252	1.21
7	516	1:20	10	3.60	–	537	13.2	−35	355	3.97
8	516	1:20	10	3.53	0.20	538	13.3	−28	324	3.04

* 'Solid young fluid' to mimic conditions expected for cement dissolution; NaOH: 65.2 mmol/l; KOH: 161 mmol/l; $Ca(OH)_2$: 2.24 mmol/l. Initial pH is 13.2.

humic substances that needs to be considered for the humic colloid mediated radionuclide transport.

2. Experimental

Clay samples are from four different depths of the borehole EST 104 (Claret et al., 2002). Sampling depth and experimental conditions are shown in Table 1. The total organic carbon content in the four clay samples is approximately 1.3 wt.% (Claret et al., 2002). Experimental samples were prepared in PE vials with 0.5 g of clay to 10 ml of 'solid young fluid' (see bottom of Table 1). Iron chips and powder were added to simulate real repository conditions, as steel containers are one waste package process under consideration in the multi-barrier concept. The variation between iron chips and powders was used to monitor the effect of iron-reactive surface area in contact with the clay and the solution. After 537 or 538 days pH, Eh and chemical composition were determined. Solution (4 ml) was withdrawn from each sample for characterization of the dissolved organic carbon (DOC). HCl (1 M) was added until solutions were around pH 2 (pH indicator strips). After centrifugation the supernatant (containing fulvic acid) was withdrawn and pH adjusted to pH neutral range (pH indicator strip). The brown flocculate (humic acid) was washed with 2 ml 0.01 M HCl, redissolved in 4 ml 0.01 M $HClO_4$ and brought to neutral pH (1 M NaOH, pH indicator strip). An exception was humic acid where the flocculate at low pH was dried for preparation of IR spectroscopy KBr pellets.

UV/Vis spectra were recorded from 250 to 900 nm with a Hewlett Packard HP 8451A diode array spectrometer. Due to the small amount of sample, the fulvic acid samples were not isolated and purified but were measured in a matrix of high concentrations of the various salts present. UV/Vis classification of humic and fulvic acids is frequently based on absorption ratios between two wavelengths as a descriptor for the degree of absorption increase with decreasing wavelength. In this paper the absorption ratio between 300 and 400 nm is used. Investigations of a large number ($n=49$) of humic and fulvic acids of different origin has shown that this absorption ratio (E3/E4) correlates with the specific absorption at a given wavelength (Kim et al., 1995; Artinger et al., 2000). However, this empirical relationship cannot be generalized without caution. Nevertheless, for the purpose of estimating the humic and fulvic acid content in the present samples, the specific absorptions at 300 and 400 nm of individual samples are deduced from their respective E3/E4 absorption ratios and this empirical relationship as shown in Fig. 1.

Fluorescence spectra were recorded with a FA-256 SLM AMINCO Bowman Series 2 fluorometer with a 150 W continuous Xenon lamp source. FTIR spectra were obtained using a Bruker IFS 55 in the wavenumber range of 360–4000 cm^{-1}, collecting 256 scans at a resolution of 2 cm^{-1}

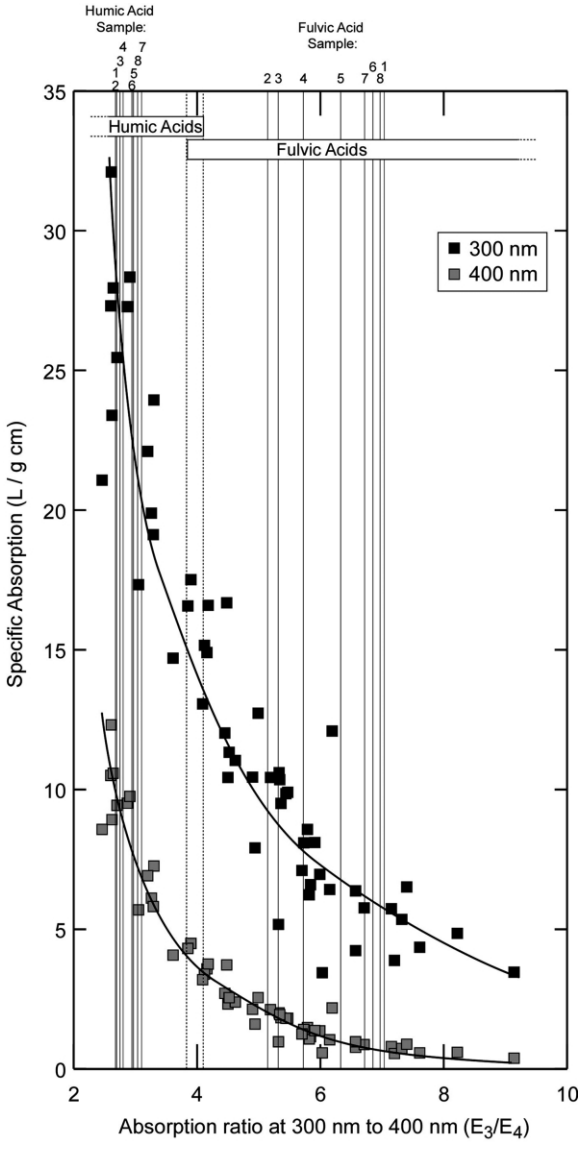

Fig. 1. Specific absorption at 300 and 400 nm versus absorption ratio at 300–400 nm (E_3/E_4) of humic and fulvic acids from different groundwaters and sediments (Kim et al., 1995). For the samples of the present investigations, vertical lines are drawn for the known E_3/E_4 absorption ratios. From these lines and the shown empirical relationship between absorption ratio and specific absorption, the specific absorptions of the respective samples are deduced.

after 20–30 min N_2 gas flow purging of the measurement chamber to avoid carbon dioxide and moisture interference. Samples were freeze-dried prior to preparation of pressed pellets containing 0.1 or 0.2 mg material (for humic and fulvic acid, respectively) in 100 mg KBr. Due to the hygroscopic nature, KBr powder of spectroscopic grade was kept in moisture free atmosphere at 50 °C.

3. Results and discussion

The pH values dropped from 13.2 to 12.4 and 12.3 in the samples from 447 m depth whereas the pH values of the other samples were scattered around the value of the initial solution (Table 1). The generation of hydrophilic organic matter becomes obvious from the high DOC concentrations in the supernatant solutions. Previous investigations (Claret et al., 2002) showed that this high-pH plume has a minor effect on clay mineralogy of the Callovo-Oxfordian formation over the experimental period of one year, but lead to a high release of dissolved organic carbon (DOC). Under alkaline conditions, the size distribution of the organic matter was shifted to smaller entities as also found in other alkaline hydrolysis investigations on natural organic matter (Kumke et al., 2001). The most likely reaction was considered to be ester and ether cleavages resulting in an increase in carboxyl and hydroxyl content (Wallis, 1971). Gas chromatography-mass spectrometry (GC-MS) on a set of samples similar to the present ones (neighbour borehole in the same area) but on a different extracted fraction (Elie et al., 2002) shows a shift in the distribution of the chromatograms towards low molecular weights for both aliphatic and aromatic compounds with increasing oxidation time of alkali extracts. These previous investigations show that the organic matter is subjected to chemical conversion under such conditions with an increase in hydrophilic nature via oxidative cleavage.

In Fig. 2, the generation of DOC from MHM clay samples under alkaline conditions is shown (data from Claret et al., 2002). The sedimentary organic carbon (SOC) content is approximately 1.3% in all samples from the four different depths. The upper sample (447 m depth) is of terrestrial

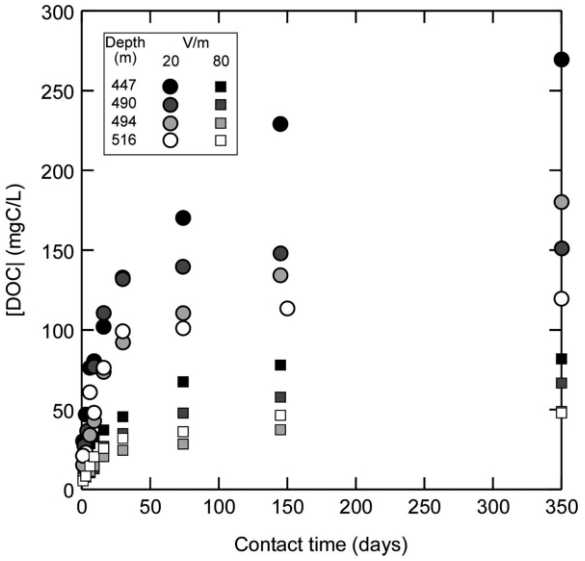

Fig. 2. Dissolved organic carbon (DOC) in alkaline 'solid young fluid', mimicking cement dissolution conditions, as a function of contact time with clay samples from different depths of the MHM site.

origin whereas the sample from 516 m depth is of marine origin (Landais and Elie, 1999). In between is a transition zone. The DOC concentrations show a steady increase over approximately one and a half years of reaction time, to a great extent following a logarithmic dependency of the contact time. In two samples (490 and 516 m depth with the lower volume to mass ratio of 20), however, the increase in the DOC concentration with time levels off after approximately 50 days instead of showing continued increase as in the other samples. This may result from progressive consumption of SOC constituents that are more easily chemically converted, saturation (low volume to mass ratio) and consumption of alkali.

The in-growth of DOC over such a long time is not likely to be a dissolution process. Back-extrapolation to zero contact time results in an 'instant release' of 0.49 ± 0.32 mg DOC per gram clay, equivalent to approximately 3.8% of SOC. In Fig. 3, the generation of DOC is plotted against the logarithm of the contact time from a few days of contact time and with the exception of some data with low volume to mass ratio that level off at long contact times (cf. Fig. 2). The generation of DOC (per gram clay) can be described by:

$$[\mathrm{DOC}] = \mathrm{A} \times \log(\text{contact time}) + \mathrm{B} \quad (1)$$

where the factor 'A', describing the release rate amounts for 2.39 ± 0.30, 2.33 ± 0.15, 1.43 ± 0.13 and 1.72 ± 0.32 for the sequence 447, 490, 494 and 516 m depth. In Fig. 3 the total fractions of DOC after 537 and 538 days, relative to the SOC, are also shown. The numbers vary from 53% in the sample of terrestrial origin (447 m depth) to 27% in the sample of marine origin at 516 m depth. To which extent these numbers represent only conversion of SOC to DOC or also mineralization of DOC to DIC cannot be determined from these numbers.

The IR spectra of humic and fulvic acids and of original clay samples, are shown in Fig. 4a,b,c. On top of the Figures regions are given with bands found in humic and fulvic acids as well as bands typical for silica clay minerals. The spectra in Fig.

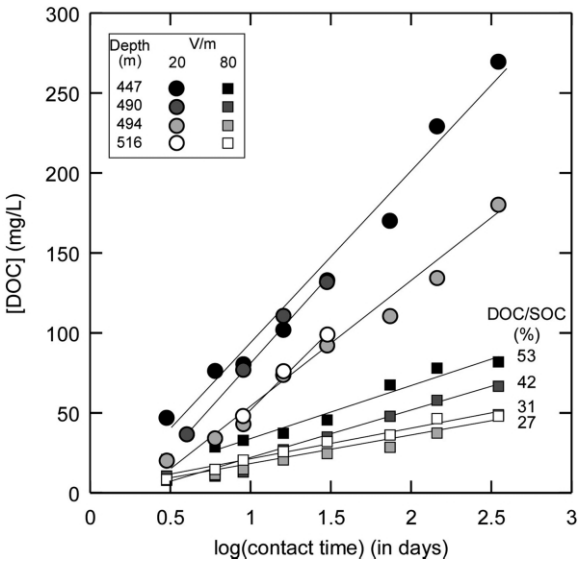

Fig. 3. Dissolved organic carbon (DOC) in alkaline 'solid young fluid', mimicking cement dissolution conditions, as a function of log(contact time) with clay samples from different depths of the MHM site (selected data from Fig. 2). Also shown is the fraction of sedimentary organic carbon (SOC) found as DOC after a contact time of 537/538 days for samples with a V/m ratio of 80.

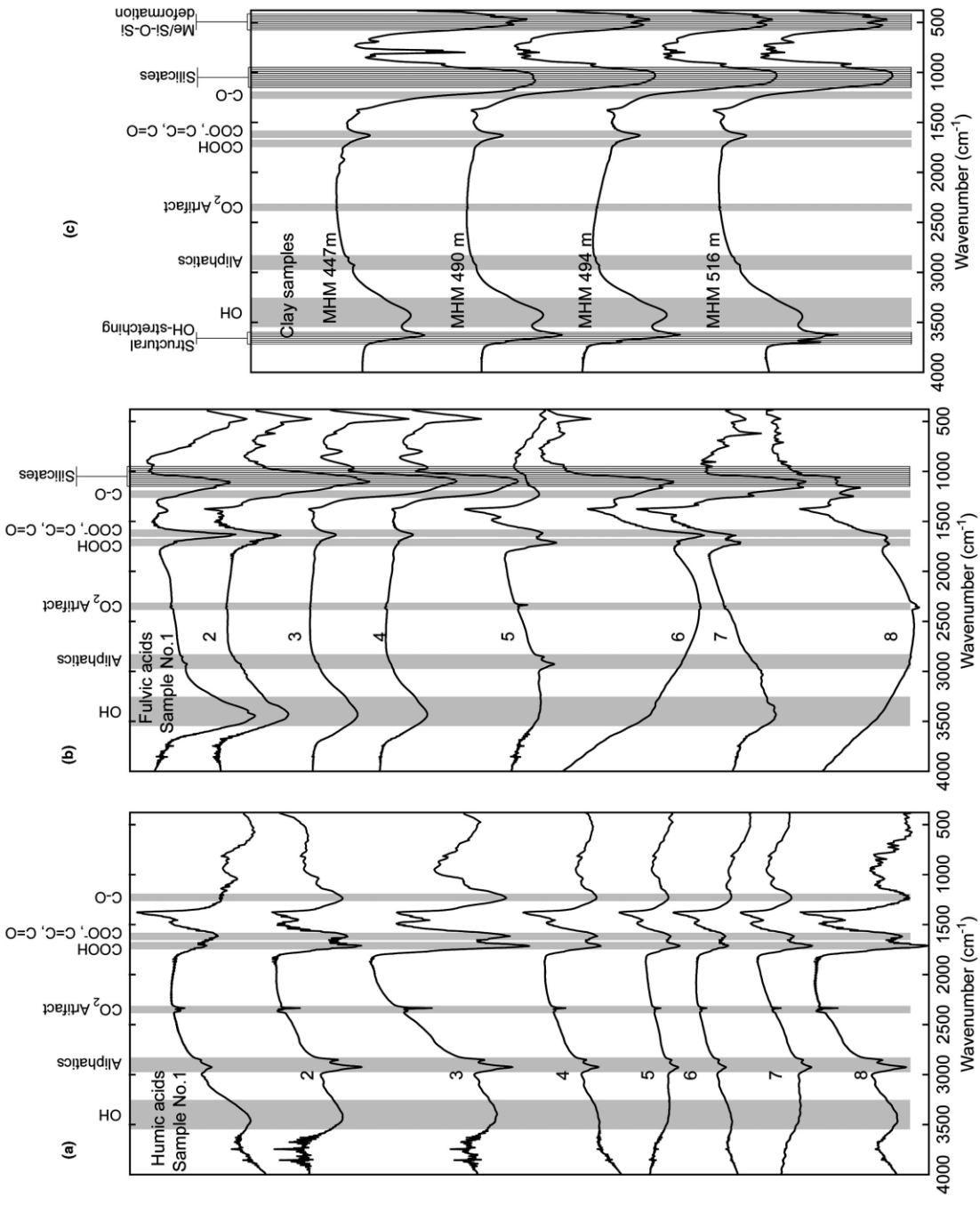

Fig. 4. (a) IR spectra of humic acids from alkaline 'solid young fluid' treatment of MHM site clay. The different numbers of spectra refer to sample numbers given in Table 2. Typical bands for humic and fulvic acids are given as gray vertical lines. (b) IR spectra of fulvic acids from alkaline 'solid young fluid' treatment of MHM site clay. The different numbers of spectra refer to sample numbers given in Table 2. Typical bands for humic and fulvic acids are given as gray vertical lines. (c) IR spectra of MHM site clay samples (cf. Table 1). Typical bands for humic and fulvic acids are given as gray vertical lines. Typical bands for clay mineral are given as striped vertical lines.

4a show the characteristic features expected for isolated protonated humic acid (Kim et al., 1990). This includes the expected band at 1720 cm^{-1} for protonated carboxylic groups. One exception is the spectrum of the humic acid No. 1, which is of very poor quality. Humic acids Nos. 2, 3 and 8 show the pronounced bands of aliphatic groups (approx. 2900 cm^{-1}). The spectra of the fulvic acids (Fig. 4b) are less clear because of the small amounts of sample and the inorganic matrix present as the small sample amounts of fulvic acids did not allow isolation from solution matrix and acids and base used for sample treatment. Consequently, bands typical for silicates also appear in the spectra. Due to the ill-defined pH conditions in preparation of fulvic acid samples, the band at 1720 cm^{-1} from protonated carboxylic groups is only pronounced in some of the samples. Within these limitations, other features of these spectra are as expected for fulvic acid (Kim et al., 1995).

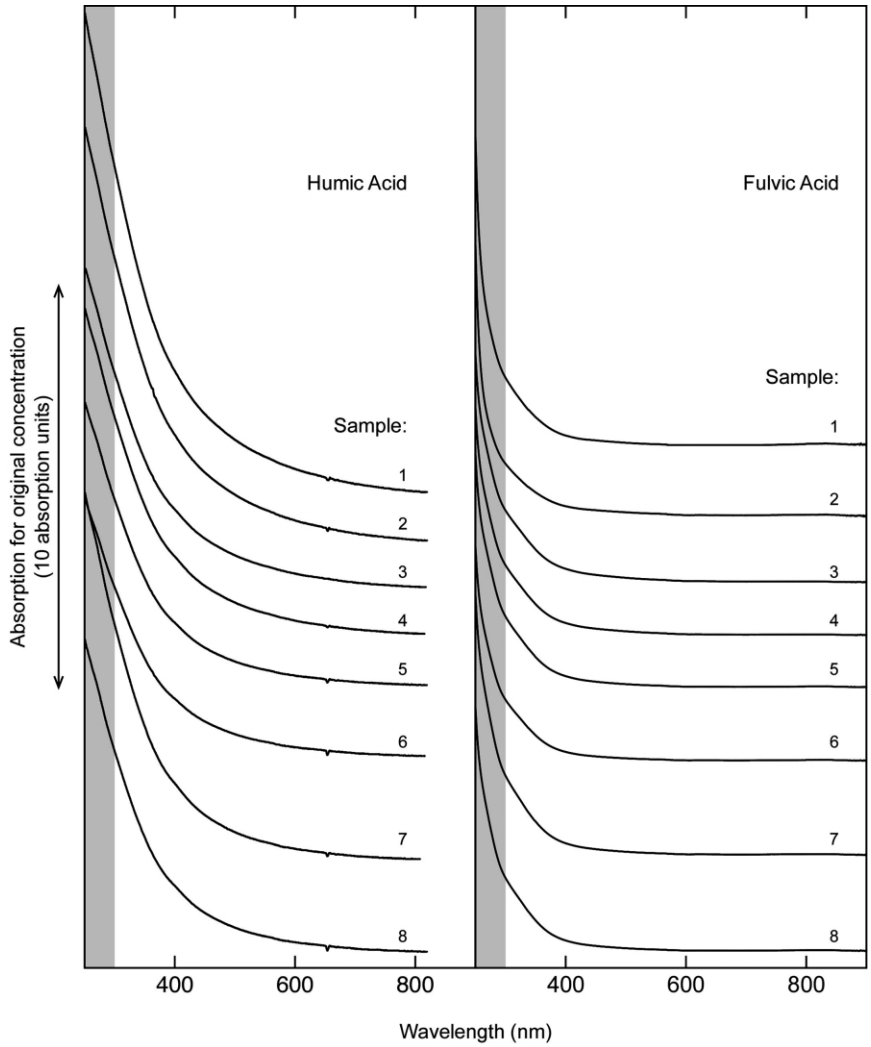

Fig. 5. UV/Vis absorption spectra of MHM site humic and fulvic acid samples from alkaline 'solid young fluid' treatment of MHM site clay (cf. Table 2).

Table 2
Calculation of humic and fulvic acid concentrations in MHM site clay alkaline extracts by UV/Vis spectroscopy

Sample	Absorption at 300 nm	Absorption at 400 nm	Abs. ratio E3/E4	Specific abs. at 300 nm (from Fig. 3) (l/g cm)	Specific abs. at 400 nm (from Fig. 3) (l/g cm)	Concentration calculated at 300 nm (g/l)	Concentration calculated at 400 nm (g/l)	Mean value from 300 and 400 nm (g/l)	Standard deviation	Standard deviation (%)
Humic Acid										
1	8.12	3.02	2.69	28.25	9.77	0.29	0.31	0.30	0.015	5.1
2	7.04	2.64	2.67	28.75	9.95	0.25	0.26	0.25	0.014	5.5
3	5.34	1.94	2.75	26.72	9.28	0.20	0.21	0.20	0.006	3.1
4	5.41	1.93	2.80	25.30	8.84	0.21	0.22	0.22	0.003	1.5
5	4.63	1.56	2.97	22.22	7.65	0.21	0.20	0.21	0.003	1.5
6	4.21	1.43	2.94	22.64	7.81	0.19	0.18	0.18	0.002	1.0
7	5.86	1.89	3.10	20.38	7.85	0.29	0.24	0.26	0.033	12.4
8	5.00	1.65	3.03	21.19	7.22	0.24	0.23	0.23	0.005	2.3
Fulvic Acid										
1	1.68	0.24	7.03	5.74	0.64	0.29	0.37	0.33	0.057	17.2
2	1.32	0.26	5.14	9.22	2.03	0.14	0.13	0.13	0.012	8.7
3	1.79	0.34	5.31	8.75	1.82	0.20	0.19	0.19	0.014	7.1
4	1.75	0.31	5.72	7.80	1.40	0.22	0.22	0.22	0.004	1.9
5	1.76	0.28	6.32	6.76	0.96	0.26	0.29	0.28	0.021	7.6
6	1.52	0.22	6.85	5.99	0.70	0.25	0.32	0.29	0.045	15.7
7	1.98	0.30	6.71	6.18	0.75	0.32	0.39	0.36	0.052	14.5
8	1.82	0.26	6.97	5.83	0.66	0.31	0.40	0.35	0.059	16.6

Table 3
DOC content from humic and fulvic acid by UV/Vis spectroscopy compared to measured DOC values (in mgC/l)

	Clay horizon									
	1	2	3	4	5	6	7	8		
Sum DOC (UV/Vis):*	349	219	222	242	266	258	342	322		
DOC (measured):	299	260	243	267	270	252	354	324		
% DOC by UV/Vis:	116.9	84.3	91.3	90.8	98.4	102.5	96.7	99.4	Mean value:	97.5 ± 9.7

* Values for carbon content used are 0.58 and 0.53% for humic and fulvic acid, respectively (Kim et al., 1995).

The original untreated organic rich MHM site clay samples (Fig. 4c) show a depth-dependent increase of OH-stretching modes of inner surface hydroxyl groups typical for kaolinite ($n_{OH}=3694$ cm^{-1}, 3653 cm^{-1}, 3620 cm^{-1}) (Madejova and Komadel, 2001). This result confirms X-ray diffraction pattern analysis showing the same relative increase of the kaolinite content (Claret et al., 2002). Strong spectral features at 778 cm^{-1} and 798 cm^{-1} in the sample from 447 m depth are due to Si–O stretching vibrations of quartz and silica (Farmer, 1968, 1974; Farmer and Palmieri, 1975). All original clay sample spectra also display characteristic bands of CH_2, CH_3 aliphatic groups (2855 cm^{-1}, 2920 cm^{-1} and 1455 cm^{-1}), a denoted wide band approximately 1710 cm^{-1} (C=O groups of ketones, acids, esters) and a band superposition approximately 1630 cm^{-1} of mostly aromatic C=C and OH deformation of water (Tissot and Welte, 1984). The results confirm the association of organic compounds with the clay fraction in the initial clay as found by X-ray spectromicroscopic investigations (Schäfer et al., in press).

UV/Vis absorption spectra of humic and fulvic acids show no specific features but a strong steady increase with decreasing wavelength, as also found for the spectra of the humic and fulvic acids from the present investigation (Fig. 5). Below 300 nm a sharp increase in absorption is seen in all fulvic acid samples. This is linked to the sample preparation (small amount and high salt matrices) Applying the empirical method based on the E3/E4 ratio described above, specific absorptions of individual samples were deduced and the humic and fulvic acid concentrations were calculated (Table 2). In this Table the mean value, with standard deviation, between estimations based on 300 and 400 nm absorption wavelengths is listed in absolute numbers as well as in percent. The agreement between determinations at the two different wavelengths is 5.5% or less for the humic acids. One exception is humic acid from sample 7 with 12.4% deviation. This higher deviation reflects the overall different shape of this absorption spectrum (Fig. 5). The reason for this deviation is not known. Because of the low concentrations and lack of purification, fulvic acid samples show an overall higher deviation between determination at 300 and 400 nm (Table 2). In Table 3, the sum of humic and fulvic acid in individual samples is compared with the measured DOC values. A mean value of $97.5 \pm 9.7\%$ of DOC is evaluated to consist of humic and fulvic acids. Despite the required caution in the approach used, this result allows the conclusion that DOC consists mainly of humic and fulvic acids generated during contact of the clay with the alkaline 'solid young fluid'.

Fluorescence spectroscopy is a useful tool for identification and characterization of humic and fulvic acids. Comparison of results from different investigations, however, must be viewed with caution because of the sensitivity to experimental setup, chemical conditions and background compensation. This is especially true for excitation spectra (Kim et al., 1995). In Fig. 6, the excitation and emission spectra of the studied humic and fulvic acids are shown. Published values for the wavelength of maximum excitation vary widely and the numbers reported reach from 315 to 480 nm for humic and fulvic acids (Hayase, 1985; Miano et al., 1988; Kim et al., 1995) The excitation spectra of the investigated humic and fulvic

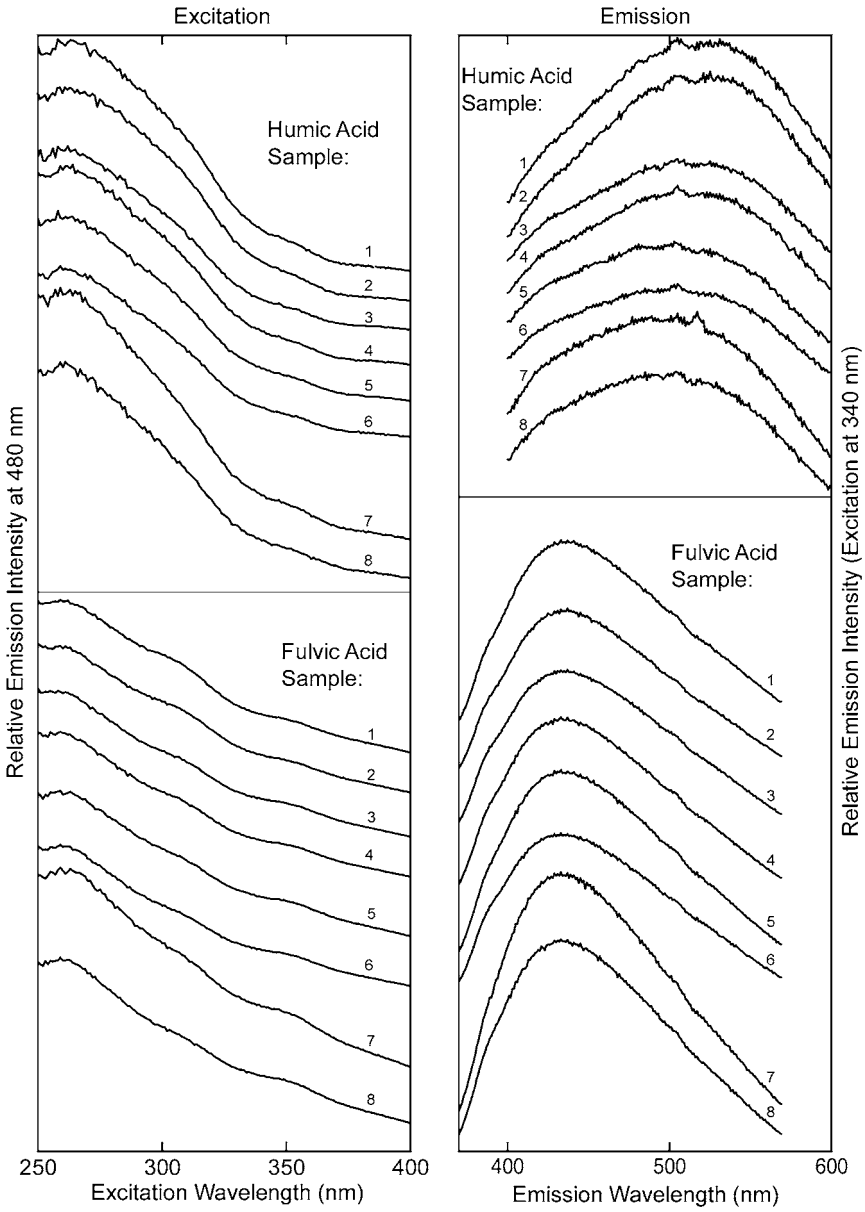

Fig. 6. Excitation and emission spectra of MHM site humic and fulvic acids (cf. Table 2).

acids show maxima approximately 260 nm. There is no significant difference between respective results from humic and fulvic acids. The very short and comparable excitation wavelengths indicate similarities in the common origin of the humic and fulvic acids present, and may reflect a distinct structural feature compared to other humic and fulvic acids (cf. below) or the high sensitivity to experimental setup and chemical conditions (cf. above).

For the purpose of recording the emission spectra, the excitation wavelength is used reflecting

the excitation maximum. In the above referenced investigation on a large number of humic and fulvic acids from different groundwaters and sediments (Kim et al., 1995; Artinger et al., 2000), emission maxima of humic acids are found approximately 440 nm and those of fulvic acids approximately 430 nm. In the present investigation the respective broad maxima are found approximately 520 and 435 nm for humic and fulvic acids, respectively. Thus, the emission spectra of the fulvic acids from the two investigations are found to be very similar, whereas there is a strong redshift in the emission spectra of the present humic acids. The latter may reflect a more extended delocalization/extension of the electronic systems in the humic acids present (Seitz, 1981; Hayase, 1985; Miano et al., 1988). The fluorescence properties of anthraquinone-2,6-disulfonate, a model compound that has been used to study electron-shuttling properties of humic and fulvic acids, are characterized by excitation and emission in the ranges of the humic and fulvic acids present (Klapper et al., 2002). Carbon edge XANES of humic and fulvic acids comparable to the ones present, show a high quinone content (Schäfer et al., in press). One may, therefore, conclude that a comparably high quinone content is the characteristic for the present humic and fulvic acids generated by conversion of the MHM site clay organic matter under high alkaline conditions.

4. Summary and conclusions

The original organic matter in the clay material is mainly hydrophobic and with a low solubility in aqueous solution. Under conditions expected in the near-field of a nuclear waste repository with cement as waste packages or part of engineered structures, high concentrations of hydrophilic organic substances are generated by conversion of the original organic matter. The dissolved organic matter is shown to be dominated by humic and fulvic acids. These humic and fulvic acids may significantly change the solubility and mobility of radionuclides. The present initial study will be followed by more detailed investigations under reducing conditions with more material and more detailed characterization.

Acknowledgments

Parts of the results presented in the present paper were collected during a Ph.D. thesis of Francis Claret with financial support from ANDRA (French National Agency for nuclear waste disposal). ANDRA is also acknowledged for making the MHM site clay samples available. The work is also supported by a Marie Curie fellowship of the European Commission programme 'Nuclear Fission' under the contract number MCFI-2001-01983.

References

Artinger R, Buckau G, Geyer S, Wolf M, Kim JI, Fritz P. Characterization of groundwater humic substances: influence of sedimentary organic carbon. Appl Geochem 2000;15/:97–116.

Artinger R, Schuessler W, Schäfer T, Kim JI. A kinetic study of Am(III)/humic colloid interactions. Environ Sci Technol 2002;36:4358–4363.

Bauer A, Velde B. Smectite transformation in high molar KOH solutions. Clay Miner 1999;34:259–273.

Buckau G. (ed) Effects of Humic Substances on the Migration of Radionuclides: Complexation and Transport of Actinides (Final Report). Report of the Europeean Commission: EUR 19610 EN, 2000a.

Buckau G, Artinger R, Fritz P, Geyer S, Kim JI, Wolf M. Origin and mobility of humic colloids in the gorleben aquifer system. Appl Geochem 2000b;15/2:171–179.

Buckau G, Artinger R, Kim JI, Geyer S, Fritz P, Wolf M, Frenzel B. Development of climatic and vegetation conditions and the geochemical and isotopic composition in the franconian albvorland aquifer system. Appl Geochem 2000c;15/8:1191–1201.

Chen J, Gu BH, LeBoeuf EJ, Pan HJ, Dai S. Spectroscopic characterization of the structural and functional properties of natural organic matter fractions. Chemosphere 2002;48:59–68.

Chen J, LeBoef EJ, Dai S, Gu BH. Fluorescence spectroscopic studies of natural organic matter fractions. Chemosphere 2003;50:639–647.

Choppin GR. The role of natural organics in radionuclide migration in natural aquifer systems. Radiochim Acta 1992;58–9:113–120.

Claret F, Bauer A, Schafer T, Griffault L, Lanson B. Experimental investigation of the interaction of clays with high-pH solutions: a case study from the Callovo-Oxfordian formation, Meuse-Haute Marne underground laboratory (France). Clay Clay Miner 2002;50:633–646.

Eberl DD, Velde B, Mc Cormick T. Synthesis of illite-smectite from smectite at Earth surface temperatures and high pH. Clay Miner 1993;28:49–60.

Differences in Properties and Cm(III) Complexation behavior of isolated humic and fulvic acid derived from Opalinus Clay and Callovo-Oxfordian argillite.

Appl. Geochem. (2005) 20, 1158.

Claret, F., Schäfer, T., Rabung, Th., Wolf, M., Bauer, A.,Buckau, G.

Available online at www.sciencedirect.com
SCIENCE DIRECT®
Applied Geochemistry 20 (2005) 1158–1168
Applied Geochemistry
www.elsevier.com/locate/apgeochem

Differences in properties and Cm(III) complexation behavior of isolated humic and fulvic acid derived from Opalinus clay and Callovo-Oxfordian argillite

Francis Claret [a,*], Thorsten Schäfer [a,*], Thomas Rabung [a], Manfred Wolf [b], Andreas Bauer [a], Gunnar Buckau [a]

[a] *Forschungszentrum Karlsruhe, Institut für Nukleare Entsorgung, P.O. Box 3640, D-76021 Karlsruhe, Germany*
[b] *GSF-National Research Center for Environment and Health, Institute of Hydrology, D-85764 Neuherberg, Germany*

Received 20 May 2004; accepted 9 January 2005
Editorial handling by J.-C. Petit
Available online 21 April 2005

Abstract

Fulvic acids from deep clay formations have been isolated by the International Humic Substances Society (IHSS) standard protocol and analyzed. Near edge X-ray absorption fine structure (NEXAFS) spectroscopy reveals, that the basic structural features relating to the origin of the clay organic matter (i.e., terrestrial or marine) are preserved even after the around 150 Ma since deposition (Jurassic sediment). Analysis by asymmetrical flow field flow fractionation (AFFFF) shows the size distribution peak found for typical fulvic acids. In addition, a second larger size peak is found for the fulvic acids influenced by marine deposition. These fulvic acids also have a considerable content of organic material which does not absorb in the visible range. The Cm(III) complexation behavior has been studied by time-resolved laser fluorescence spectroscopy (TRLFS). Despite considerable fluorescence quenching, the complexation constant is shown to be in the same range as published values found for different typical fulvic acids.

1. Introduction

The purpose of the present study is to characterize humic substances extracted from Opalinus clay and Callovo-Oxfordian argillite with respect to complexing properties. As these two geological formations are under investigation as potential host rocks for a nuclear waste repository (Thury, 2002; Lebon and Mouroux, 1999; Jorda, 2000), physico-chemical perturbations induced by the storage concept (i.e., Multi Barrier System) and potential consequences for the host rock retention capacity should be taken into account and investigated. Cement may be present in a nuclear waste repository as a waste form or as part of engineered structures. In the case of water intrusion, cement alteration will generate highly alkaline solutions (initial pH $\sim$ 13) that can influence clay reactivity via mineral dissolution and/or transformation (Chermak, 1992, 1993; Eberl et al., 1993; Bauer and Velde, 1999). Recently, Claret et al. (2002) and Schäfer et al. (2003b) showed that the clay dissolution expected under the above conditions was strongly influenced by the presence of natural organic matter present in the starting clay sediment (total organic

* Corresponding authors. Tel.: +49 7247 82 5294; fax: +49 7247 82 3927 (T. Schäfer).
E-mail addresses: francis.claret@cae.fr (F. Claret), schaefer@ine.fzk.de (T. Schäfer).

0883-2927/$ - see front matter © 2005 Elsevier Ltd. All rights reserved.
doi:10.1016/j.apgeochem.2005.01.008

carbon (TOC), 0.4–1.4 wt%). Furthermore, these studies demonstrated that a high concentration (~300 mg L^{-1}) of humic substances can be generated. The latter are widely recognized as important complexing agents towards inorganic and organic pollutants in the geosphere and therefore can play a major role in radionuclide migration in natural aquifers systems (Choppin, 1992; Moulin and Ouzounian, 1992; Vilks et al., 1998; Artinger et al., 2002; Schäfer et al., 2003a).

On a short time scale, a minor fraction (a few percent) of the clay organic matter is dissolved. With prolonged alkaline solution contact time a large portion (up to around 50% after about 1.5 a) of the hydrophobic clay associated organic matter becomes chemically converted into hydrophilic humic and fulvic acids (HAs and FAs) (Claret et al., 2003).

In the present paper, HAs and FAs extracted and isolated from Callovo-Oxfordian and Opalinus Clay using a slightly modified International Humic Substance Society (IHSS) protocol were investigated by UV/Vis spectroscopy, asymmetrical flow field-flow fractionation (AFFFF) and near edge X-ray absorption fine structure (NEXAFS) spectroscopy. The latter technique can offer practically the same level of information as nuclear magnetic resonance (NMR) (Scheinost et al., 2002; Schäfer et al., 2003c) but requires a very small amount of sample (~10^{-3} mg). The complexation behavior with trivalent actinides (Cm^{3+}) is studied by time resolved fluorescence spectroscopy (TRFLS).

2. Experimental

2.1. Sample origin and HAs and FAs extraction protocol

Callovo-Oxfordian clay samples from the Meuse Haute Marne site (MHM) and the Opalinus shale were investigated. The Opalinus clay sample is from 579.45 m depth of the investigation borehole Benken. Three samples from different depths of the MHM site were studied, representative for the full mineralogical sequence. These samples are from the borehole EST 104 at 447, 494 and 516 m depth (Claret et al., 2002, 2004). The TOC content in the MHM argillite clay fraction is depth independent at around 1.3 wt%. The TOC content in the Opalinus clay fraction is lower (around 0.4 wt%, Schäfer et al., 2003b). In the Callovo-Oxfordian sediments, biomarker analysis showed that the sedimentation environment in the upper stratigraphic layer (Oxfordian, sample 447) is mainly terrestrial (type III kerogen), whereas the lower stratigraphic layer (Callovian, sample 494 and 516) is mainly of marine influence (type II kerogen) (Landais and Elie, 1999). For the Opalinus clay the deposited sediments are of mixed terrestrial and marine origin (Mazurek et al., 2002; Nagra, 2002).

Before extracting the <2 μm size-fraction by centrifugation, carbonates were removed using the acetic acid–acetate buffer method described by Moore and Reynolds (1989). Thereafter, the humic substances were extracted using a slightly modified IHSS protocol (Swift, 1996). This extraction was done with 0.5 N NaOH under Ar and was repeated (7 times) in order to increase the extraction rate. After pH adjustment to 1 using purified 1 M HCl, the humic acid (HA) flocculate was separated by centrifugation (4300 rpm). The HA was re-dissolved in 0.1 M NaOH and NaF added. The sample was acidified again and left over night. The dissolution with NaOH was then repeated, followed by flocculation at pH 1. Finally, the flocculate was washed twice with 0.1 M HCl and freeze dried (Buckau, 1991).

After separation of the HA by flocculation from the original alkaline extract, the fulvic acid (FA) in the supernatant solution was isolated by sorption on a XAD-8 column. It was purified by two cycles of sorption on a XAD-8 column followed by alkaline elution (NaOH). Due to the small total amounts, the purified FA samples were used as the final concentrate solutions. The yield of HA from the MHM samples is between 5.2% and 7.1% TOC. The yield of FA from the MHM and Opalinus samples is between 0.5% and 1.3%. No HA was found or detectable in the Opalinus sample. The original content of TOC in the clay fraction and the yields of HAs and FAs from the different samples are given in Table 1. As the total amount of sample was in the μg range for the FAs and the HAs, NEXAFS was chosen according to its high sensitivity in this concentration range.

2.2. UV/Vis spectroscopy

UV/Vis spectroscopy was performed with a Cary 5 spectrophotometer (Cary Co., USA). UV/Vis absorption of humic substances strongly depends on the chemical conditions, namely pH, ionic strength, and the degree of complexation with metal ions (MacCarthy and Rice, 1985; Buckau, 1991). Consequently, compari-

Table 1
Total organic carbon (TOC) in the starting clay fraction samples and the fraction of TOC extracted as humic acid (HA) and fulvic acid (FA)

Sample	TOC (wt%)	HA (% of TOC)	FA (% of TOC)
447 HA/FA	1.4	5.2	1.3
494 HA/FA	1.4	5.2	1.2
516 HA/FA	1.4	7.1	0.5
OPA FA	0.4	≈0.0	1.1

*447, 494 and 516: respective depths of samples from the MHM site.
"OPA FA": fulvic acid extracted from Opalinus clay.

son of spectra from different samples requires well-defined measurement conditions. Therefore, in the present study a background electrolyte of 0.1 M $NaClO_4$ was used with solutions buffered at pH 8.5 by 10^{-3} mol/L TRIS (tris(hydroxomethyl)aminomethane). In addition, 10^{-3} M EDTA was added to avoid the possible influence of higher valent metal ions complexing with humic substances. For HA measurement, Milli-Q water was used as a blank solution. For FA, NaOH passed through the XAD-8 column prior to the FA concentration/purification was used.

2.3. NEXAFS

NEXAFS carbon K-edge spectra were measured at the scanning transmission X-ray microscopy (STXM) beamline X1A1 (NSLS), operated by the State University of New York at Stony Brook. The principle of the method is described in detail elsewhere (Jacobsen et al., 1991). The absorption by different C structures follows the Lambert–Beer Law, i.e., the absorption is directly proportional to the different mass absorption coefficients of different C functionalities as a function of the X-ray wavelength. Images are recorded between 280 and 305 eV, using the image stack option (Jacobsen et al., 2000). Image alignment of the stack sequence is used for correcting small sample stage displacement during the scan. NEXAFS spectra are then extracted from the region of interest, setting the $I_o(E)$ in a region free of sample.

STXM sample preparation was performed by drying 1 μL of HA or FA solution on a Si_3N_4 window (100 nm thick). Energy calibration of the spherical grating monochromator was achieved by using the photon energy of the CO_2 gas adsorption band at 290.74 eV (Ma et al., 1991; Hitchcock and Mancini, 1994). The X-ray absorption double feature at 297.3 eV (L_3-edge) and 300 eV (L_2-edge) of potassium (Henke et al., 1993) was used for the identification of inorganic clay constituents (e.g., illite).

For the comparison of NEXAFS spectra, a baseline correction and normalization to 1 at 295 eV prior to peak fitting was performed. The spectra were then deconvoluted following the protocol used by (Schäfer et al., 2003c):

(i) an arctangent function for the ionization potential at 290.5 eV of aromatic/aliphatic C (Hitchcock and Ishii, 1987; Hitchcock et al., 1992),
(ii) six Gaussian functions (284.4, 285.0, 286.6, 287.4, 288.6 and 289.4 with a FWHM of 0.4 eV) for the 5 π* transitions below the ionization energy. The 287.4 eV band also fitted using a gaussian function is a mixed Rydberg/valence state transition. Additionally two second, higher transition (1s–2π* for aromatic C bonded to either H or C and for aromatic C bonded to O approximately 4 eV above the energy of the 1s–π* transition with a quarter of the 1s–π* intensity were implemented. (Francis and Hitchcock, 1992),
(iii) and two additional Gaussian functions for the σ*-transitions.

2.4. AFFFF

AFFFF was carried out with a system from Wyatt Technology (USA) using a fractionation channel from ConSenxus (Germany) and regenerated cellulose membrane from Wyatt Technology (USA) with a nominal cut-off of 1 kDa (the nominal cut-off size related to the mass of 1000 Dalton of globular proteins). The asymmetrical channel has a length of 286 mm and a spacer thickness of 0.54 mm. As mobile phase, 5 mM Tris buffer (pH ~ 9.1, Thang et al., 2001) was used at a channel flow of 0.6 mL min^{-1} and a cross-flow of 3 mL min^{-1}. The absorbance of the effluent was recorded with an UV/Vis detector (K-2500, Knauer, Germany) at 210 nm. A detection wavelength of 210 nm was chosen because of the low sample concentrations and in order to monitor also constituents that, contrary to HAs and FAs do not show significant absorption in the visible range. The fractionated sample volume was 20 μL. For calibration of the AFFFF system, polyacrylic acid (PAA) standards were used from American Polymer Standards Corp. (USA) and Polymer Laboratories, Germany (Hoque et al., 2003; Wolf et al., 2005).

2.5. TRFLS

TRFLS measurements were performed using a pulsed Nd:YAG-pumped dye laser system (Continuum, Powerlite 9030, ND 6000). An optical multichannel analyzer consisting of a polychromator (Chromex 250) with a 1200 lines/nm grating was used for detection of the fluorescence emission. To fade out any light scattering and background fluorescence, the emission spectra of Cm(III) were recorded 1 ms after the exciting laser pulse (laser dye: Exalite 396.6 nm) in the wavelength range of 580–620 nm in a time window of 1 ms. For lifetime measurement, the delay time between laser pulse and camera gating was scanned with time intervals of 20 μs. Samples were prepared in a glove box under Ar atmosphere by adding 2×10^{-7} mol/L of Cm^{3+} to the 3 different HA solutions ([HA] = 10 mg DOC/L; DOC = Dissolved Organic Carbon), and 1×10^{-7} mol/L to the 4 different FA solutions ($6.6 < [FA] < 10$ mg DOC/L; see Table 3). Investigations were conducted at pH 5.7–6.0. In this range hydrolysis is negligible and only two species are formed in significant concentrations. These species are the Cm FA complex and the non-complexed Cm^{3+} ion. Thereby, spectral evaluation is straightforward.

Furthermore, the results can be readily compared with published data.

3. Results and discussion

3.1. UV/Vis spectroscopy

UV/Vis adsorption spectra of HA and FA are featureless over the whole UV/Vis wavelength range showing only a strong absorption increase with decreasing wavelength linked to aromatic and other organic chromophores (Traina et al., 1990; Chen et al., 2002). Evaluation of UV/Vis spectra is either achieved by comparing absorption measurement at a specific wavelength or absorption ratios at two different wavelengths. The UV absorptivity at 260 nm is commonly used to determine the relative abundance of aromatic C=C content (Traina et al., 1990; Chin et al., 1994). However, the sharp increase below 300 nm can be considerably biased by salt presence or limited sample amount, as in the case of this study. For characterization/classification of HAs and FAs, a frequently used absorption ratio is E_4/E_6 (absorption at 465 over 665 nm, Chen et al., 1977). This ratio can presumably be used for estimating the degree of humification. Due to the low absorption at 665 nm, however, the results become strongly influenced by the quality of the background compensation. In samples of limited concentration, reproducibility suffers under this background compensation problem. Given that the relative shape of HA and FA spectra are similar, any absorption ratios can be used for classification of HAs and FAs. A ratio that is not sensitive to background compensation and is not affected by high absorption of salt and contaminants in the UV range is E_3/E_4 (absorption at 300 nm over the absorption at 400 nm, Artinger et al., 2000).

The UV/Vis spectra of the samples are shown in Fig. 1. The absorption is normalized to the DOC content. The large differences in this "specific absorption" reflect differences in the humic substances. It also, however, reflects the presence of low-absorbing organic compounds.

The specific absorptions at 300 and 400 nm, and the absorption ratio E_3/E_4 of the samples are shown in Fig. 2. In this figure also the correlation regions are shown for a large number of HAs and FAs from 4 different aquifer systems and some HAs and FAs isolated from deep and near surface groundwater sediments (Artinger et al., 2000). The results show, that both the HAs and FAs from the present study fall in a range rather typical for HAs (high specific absorption and high absorption ratio). The specific absorption of 447 HA is somewhat high. The data for the other two HAs and the FA 447 FA fall within the typical range. The FAs 494 FA, 516 FA and OPA FA, however, show very low specific absorptions. Given that the relative absorption curve shapes are so similar for all FAs of the present study (cf. Fig. 1, lower part), the low specific absorption may indicate the presence of low UV/Vis absorbing organic constituents.

3.2. AFFFF

The size distribution of the different FAs is determined using AFFFF. The data are presented in Fig. 3.

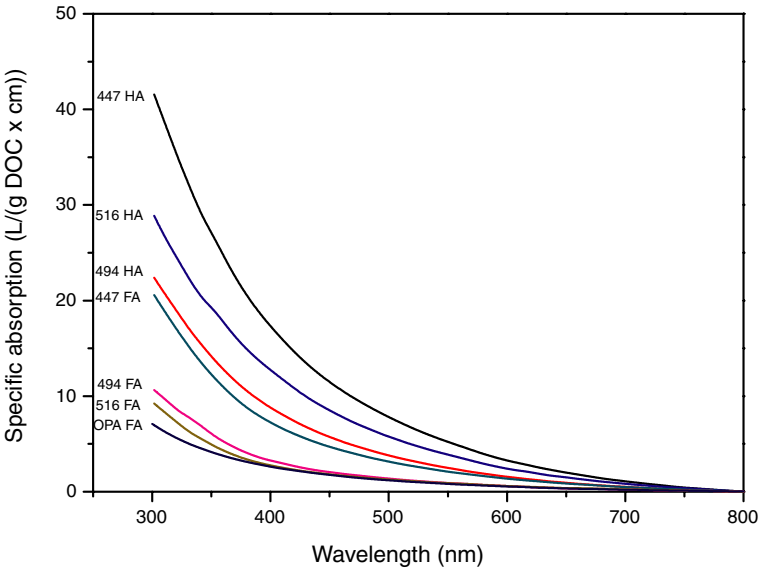

Fig. 1. UV/Vis spectra of humic and fulvic acid samples, normalized to the DOC concentration.

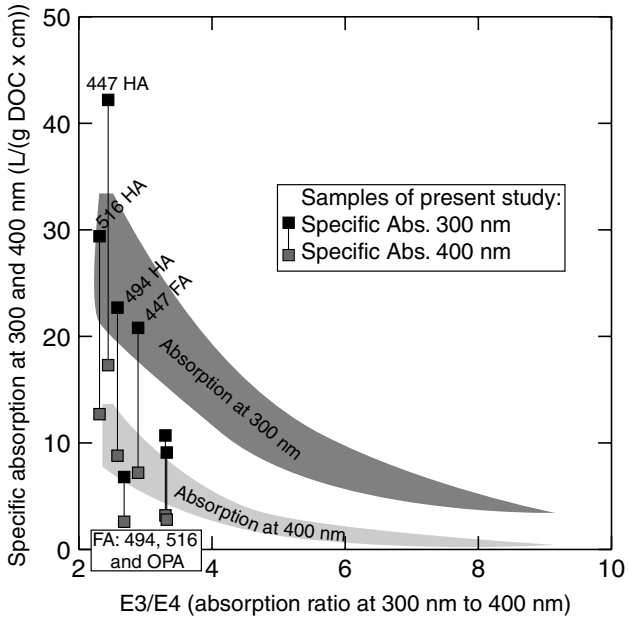

Fig. 2. UV/Vis absorption properties (specific absorption at 300 and 400 nm, as well as absorption ratio E_3/E_4) of a large number of groundwater and sediment humic and fulvic acid samples from 4 aquifer systems (shaded areas from Artinger et al., 2000) and samples from the present investigation.

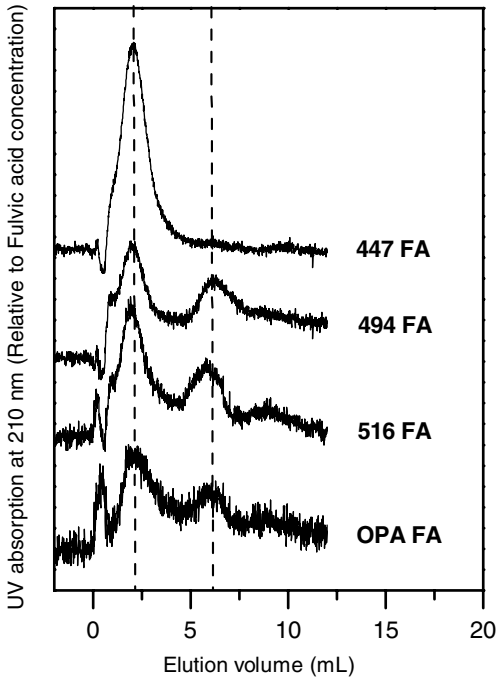

Fig. 3. AFFFF of fulvic acid samples recorded at pH 9.1 in 0.005 mol/L Tris buffer.

The size distribution of the sample 447 FA from the MHM site shows the typical size distribution of FA (Wolf et al., 2005). The other MHM FA isolates derived from sediments of marine origin, in contrast to the sample 447 FA isolated from terrestrial deposited sediments, show a bi-modal distribution. The first peak of the smaller size fraction fits well with FAs in general and also with the FA from the 447 FA (terrestrial origin). The second peak indicates a larger size fraction of atypical size for FAs. The same bi-modal size distribution is found for the isolated FA from the Opalinus clay. The results support the indications from UV/Vis spectroscopy, namely that, with exception for 447 FA, there are additional components in the FA samples. These components are obviously of organic nature (lowering the specific UV/Vis absortion), are larger in size and show some chemical similarities with FA (being sorbed on the XAD-8 column in the acidic range and elute in the alkaline range). Aiming at identifying the nature of the samples, they were also characterized by NEXAFS.

3.3. NEXAFS

The NEXAFS spectra of the samples are shown in Fig. 4. In this figure, the measured spectra are given together with the Gaussian functions used for different C functionalities and the arctangent function representing the ionization potential. The outcome of spectra deconvolution is shown exemplarily by sample 516 HA. The results for all the HAs and FAs are summarized in Table 2. As expected, the dominant oxygen containing functional group is of carboxyl type, more pronounced in FAs than in HAs.

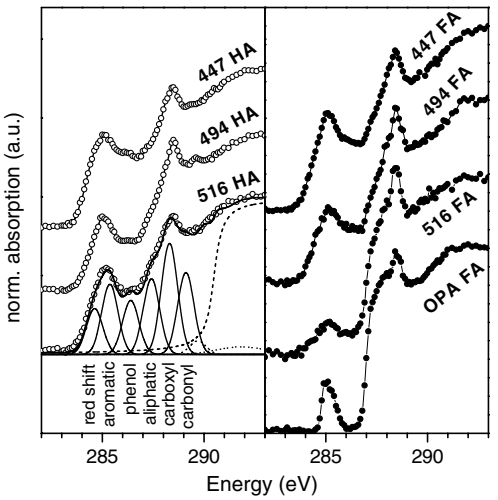

Fig. 4. NEXAFS spectra of the isolated humic and fulvic acid samples together with the peaks of individual carbon functionalities and additional transitions used for peak deconvolution on the example of 516 HA.

According to Rice and MacCarthy (1991), HAs from different sources suggest a "preferred" composition for each environment, with the aliphaticity of humic material from marine sources being higher than for those of terrestrial origin. A direct quantification of the relative composition by NEXAFS is hampered by the lower sensitivity for the mixed Valence/Rydberg state transition of methyl and methylene groups compared to intense 1s–π* transitions of aromatics or C=C, as well as phenol or carboxyl type groups. Nevertheless, the data in Table 2 can be used to draw some important conclusions, especially trends between the different substances.

A clear trend of depositional transition from a terrestrial to marine environment is not well reflected in the Callovo-Oxfordian argillite extracted HAs. In contrast to this, the aliphaticity as well as carboxyl and carbonyl type functional groups of the MHM FAs show a clear trend with an enrichment with depth. Furthermore the red-shift area, aromatic C=C and C—H and phenol-type functional groups show an apparent decrease. These observations are consistent with the higher H/C ratio in the case of type II kerogen. Marine organic detritus is predominantly of algal origin and therefore of highly aliphatic nature (Nissenbaum and Kaplan, 1972), whereas soil organic matter is more aromatic in nature due to the ubiquity of lignin in terrestrial plants (Flaig, 1972).

In the case of the Opalinus clay, the isolated FAs show an unexpected high aliphatic nature typical for marine derived organic material, whereas the whole sediment is of mixed terrestrial–marine origin (Nagra, 2002). The observed discrepancy could either by interpreted as a preferential release of marine-derived organic material or might be due to the thermal overprint with burial temperatures of ~80 °C (Nagra, 2002) in comparison to the Callovo-Oxfordian argillite (approx. 40 °C, Elie et al., 2000). These higher burial temperatures can lead to the observed elevated aliphaticity and the high degree of aromatic ring condensation indicated by a near disappearance of aromatic associated oxygen containing functional groups (red shift area and phenol) in the C(1s) NEXAFS.

In Fig. 5, the aromaticity determined by C(1s) NEXAFS is plotted against the E_3/E_4 absorption ratio for the samples analyzed in this study together with HAs and FAs of different origin in the Gorleben aquifer system (Artinger et al., 2000; Schäfer et al., 2005). In the Gorleben system the E_3/E_4 absorption ratio increases from isolated HAs via FAs derived from microbiological turnover of deep brown coal sands to the highest values found in soil-derived FAs from recharge-dominated aquifer systems. The Gorleben HAs do not show a specific trend, but for the Gorleben FAs the increase in the E_3/E_4 absorption ratio is associated with a decrease in aromaticity (Fig. 5). The absorption ratios of the isolated HAs and FAs discussed in this paper are all in the range of or slightly lower than the Gorleben HAs with a low overall E_3/E_4 variation. The C(1s) NEXAFS determined aromaticity of the FAs investigated here, however, decreases with an increasing contribution of marine origin and becomes exceptionally low for the

Table 2
Distribution of carbon among the main structural groups of FA and HA as determined from their carbon K-edge spectra deconvolution

Sample	Red shift area[a]	C=C	Phenol	Aliphatic	Carboxyl	Carbonyl
447 HA	10	19	15	16	26	14
494 HA	6	17	12	18	30	17
516 HA	7	19	14	18	27	15
447 FA	8	19	14	18	28	13
494 FA	8	15	12	18	30	17
516 FA	2	7	4	27	39	21
Opa FA	0	10	0	29	39	22

[a] Red shift due to heteroatom substitution/aromatic ring destabilization or benzoquinone type functional groups.

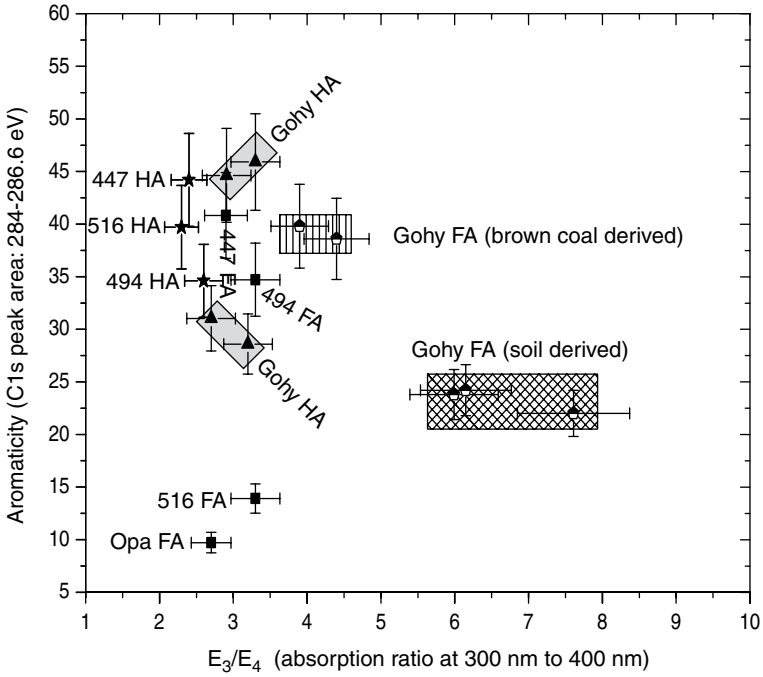

Fig. 5. Aromaticity (peak area between 284 and 286.6 eV (quinone, C=C and phenolic groups, cf. Table 2) plotted against the absorption ratio E_3/E_4 for the present samples and for comparison, samples of different origin from the Gorleben aquifer system (Artinger et al., 2000).

samples 516 FA and OPA FA. The "clustering behavior" of the sample 516 FA and OPA FA is striking. To what extent this reflects an explicit marine origin (516 FA) or a mixed effect of marine influence and higher burial temperature (OPA FA) can not be clarified at this point. Although 447 FA and 494 FA were extracted, respectively, from Oxfordian and Callovian stratigraphic layers, they also cluster together which, at first glance, does not reflect the contrasting origin of the initial organic matter input. However, Landais and Elie (1999) have shown that the transition between the two types of organic matter does not strictly coincide with the mineralogical transition (Claret et al., 2004) occurring in the Callovo-Oxfordian. The sample situated at −494 m belongs precisely to this mineralogical transition (Claret et al., 2004).

3.4. Cm(III) complexation behavior

The complexation behavior was studied using TRFLS. By this method metal ion speciation can be done with respect to excitation and emission band shapes, and fluorescence decay behavior (Kim et al., 1991a,b). In the present study, the emission spectra show the characteristic shape of humate and fulvate Cm complexes with a peak maximum around 600 nm, compared to 593.8 nm for the non-complexed Cm^{3+} ion (Fig. 6) (Buckau et al., 1992; Czerwinski et al., 1996). The Cm(III) fluorescence decay and derived lifetimes of the different FA samples show quite similar temporal behavior as found for the Cm(III)–Aldrich HA complex (Fig. 7). The small differences are caused by different amounts of free, uncomplexed Cm^{3+} in the samples. In the HA, almost all Cm(III) is complexed, whereas for FA free Cm^{3+}_{aq} ion is still present (Fig. 6).

Determination of the Cm^{3+}_{aq} and Cm fulvate concentration is done normally by peak deconvolution. Thereby, the fluorescence intensity of the complex, relative to that of the free ion, needs to be taken into account. The fluorescence intensity of the complex depends on the excitation wavelength, but is always higher than that of the free ion. The reason is that the excitation of the complexed ion takes place by a combination of direct excitation and energy transfer via the fluorescent organic ligand. The relative fluorescence intensity of the complexed Cm ion is normally expressed by this so called fluorescence intensity factor.

Curium(III) fluorescence in the present samples is strongly quenched. As a result, fluorescence intensities of Cm complexed with brown coal derived FAs is more than one order of magnitude higher than that obtained for the FAs described in this present study. The reason for the low fluorescence intensities in the present samples may be related to structural properties and to quenching. Given the high iron contents of the present samples (up to 15%, determined by ICP-MS analysis) this is expected

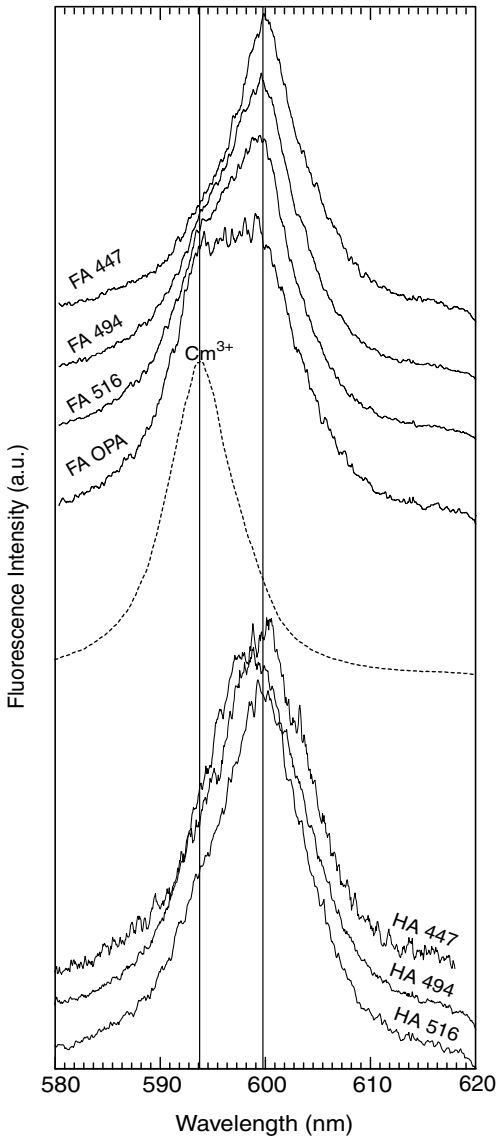

Fig. 6. Fluorescence spectra of Cm(III) with the different humic and fulvic acids. Vertical lines represent the positions of the two components humic/fulvic complex and the non-complexed Cm^{3+} ion (cf. reference spectrum).

to be the main cause. The Fe is not distributed equally over the samples, but AFFFF coupled with ICP-MS shows that it is concentrated in large particles (40–200 nm, Bouby, personal communication). It is well known that interaction with Fe oxide/hydroxide surfaces leads to the formation of non-fluorescent Cm complexes and even to the complete extinction of the fluorescence light (Stumpf, 2004). In the present case, the strong quenching is probably due to non-radiative energy transfer to the colloidal Fe(III). Quenching of Fe^{3+}-ions in fulvic acid solution is less pronounced and only relevant at very high concentrations ($>10^{-4}$ mol/L, Stumpf, 2004).

Since the free Cm^{3+}_{aq} ion is not affected by this quench process one can estimate its concentration after peak deconvolution of the mixed spectra by comparison with the intensity of a Cm(III) standard solution containing 2×10^{-7} mol/L Cm^{3+} in 0.1 M $HClO_4$ under identical experimental conditions. Small losses of laser energy due to light scattering and absorption within the FA containing cuvettes were not taking into account. The Cm(III) fulvate concentration is then calculated from the total Cm(III) concentration and subtracting the aqueous ion concentration. The results are presented in Table 3.

The complexation constants ($\log\beta = 6.05 \pm 0.42$) are calculated from the values in Table 3 by using the charge neutralization model (Kim and Czerwinski, 1996). Values used for evaluation are 5.7 meq/g for the proton exchange capacity, a C content of 45% and a loading capacity of 60% (Kim et al., 1990; Buckau et al., 1992; Czerwinski et al., 1996). These values are typical for purified natural HAs and FAs (Kim et al., 1991b; Buckau et al., 1992), and the same is true for the resulting complexation constant.

Based on the intense quenching, one may consider the possibility that Cm(III) interacts directly with Fe colloids. The study of the influence of HA on Eu(III)/Cm(IIII) sorption onto hematite and γ-Al_2O_3 colloids performed by Rabung et al. (1998) and Wang et al. (2004), indicates that the formation of ternary surface complexes where HA is strongly involved in the complexation. Reiller et al. (2002) have also shown that the sorption on Fe oxides is inhibited when HA is present where there is an excess of HA sites compared

Table 3
Cm(III) complexation results with fulvic acid samples at pH 5.7–6 in 0.2 mol/L $NaClO_4$

Sample	DOC[a]	Cm^{3+}(10^{-9} mol/L)	CmFA (10^{-8} mol/L)	Log β[b] (L/mol)
447 FA	8.7	1.17	9.88	6.59
494 FA	8.7	4.18	9.58	6.02
516 FA	10.4	9.32	9.07	5.57
OPA FA	6.6	5.70	9.43	6.01

[a] DOC: dissolved organic carbon.
[b] Calculated with a proton exchange capacity of 5.7 meq/g, a loading capacity of 60% and a carbon content of 45%.

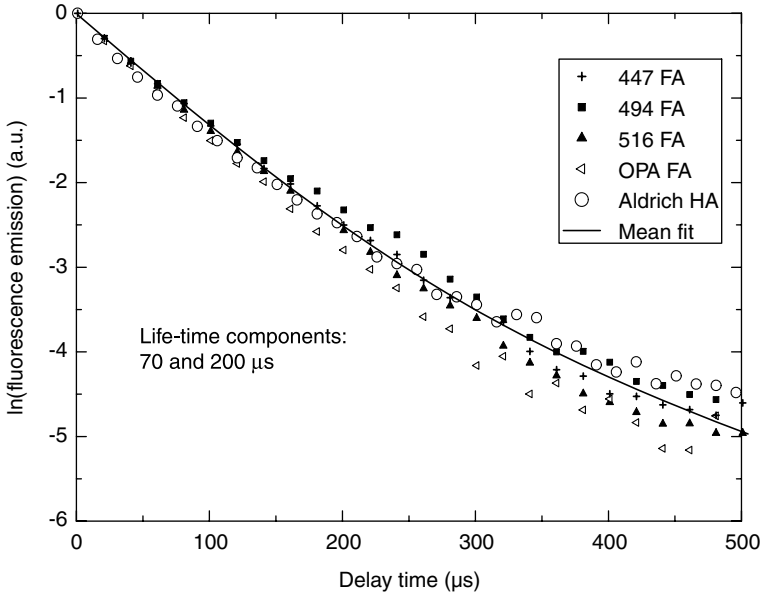

Fig. 7. Fluorescence lifetime of Cm(III) complexed with fulvic acids of the present study and for reference, Aldrich humic acid. The fluorescence decay of Cm(III) humate and fulvate complexes consists of two components with 70 and 200 μs lifetime.

to Fe oxide sites. These published observations and the agreement between the complexation constant found in the present study with that of different other humic and fulvic acids indicates the predominance of the fulvic acids in the complexation process.

4. Summary and conclusion

Up to about 8% of rapidly released clay organic matter (within about 24 h in alkaline medium) from Callovo-Oxfordian argillite or Opalinus clay is identified as hydrophilic humic and fulvic acid (standard IHSS protocol conditions). Characterization shows that especially in the Callovo-Oxfordian clay, original features of the organic matter, reflecting terrestrial and marine deposition around 150 Ma ago, are preserved in the HAs and FAs. FA influenced by marine origin shows a separate size peak, atypical for FA of terrestrial origin, and a low content of chromophoric C functionalities. Curium(III) is complexed by both the HAs and FAs. Differences in fluorescence behavior of complexed Cm(III) are most probably related to the fluorescence quenching by Fe colloids. The complexation constants $\log(\beta)$ indicate a typical complexation behavior in comparison with brown coal derived FAs. The present study is made with total FA amounts in the μg range. Further characterization and complexation studies by additional analytical methods and approaches will require larger amounts of material not presently available.

Acknowledgments

The results presented in the present paper were collected during work supported by a Marie Curie fellowship of the European Commission programme "Nuclear Fission" under the contract number FIKW-CT2002-50509. ANDRA and NAGRA are also acknowledged for making, respectively, the MHM site clay and the Opalinus Clay from Benken samples available. We are grateful for beamtime allotment by BNL/NSLS. Spectromicroscopic data were collected using the X1A1 STXM developed by the group of Janos Kirz and Chris Jacobsen at SUNY Stony Brook, with support from the Office of Biological and Environmental Research, US DoE under Contract No. DE-FG02-89ER60858, and from the NSF under Grant No. DBI-9605045. The zone plates were developed by Steve Spector and Chris Jacobsen of Stony Brook and Don Tennant of Lucent technologies Bell Labs with support from the NSF under Grant No. ECS-9510499. Dr. Muriel Bouby-Laliron is also thanked for additional AFFFF coupled ICP-MS measurements.

References

Artinger, R., Buckau, G., Geyer, S., Wolf, M., Fritz, P., Kim, J.I., 2000. Characterization of groundwater humic substances: influence of sedimentary organic carbon. Appl. Geochem. 15, 97–116.

Artinger, R., Schuessler, W., Schäfer, T., Kim, J.I., 2002. A kinetic study of Am(III)/humic colloid interactions. Environ. Sci. Technol. 36, 4358–4363.

Bauer, A., Velde, B., 1999. Smectite transformation in high molar KOH solutions. Clay Miner. 34, 259–273.

Buckau, G., 1991. Komplexierung von Americium (III) mit Huminstoffen in natürlichen Grundwässern. Ph.D. Thesis, Technical Univ., München, Germany.

Buckau, G., Kim, J.I., Klenze, R., Rhee, D.S., Wimmer, H., 1992. A comparative spectroscopy study of the fulvate complexation of trivalent transuranium ions. Radiochim. Acta 57, 105–111.

Chen, J., Gu, B.H., LeBoeuf, E.J., Pan, H.J., Dai, S., 2002. Spectroscopic characterization of the structural and functional properties of natural organic matter fractions. Chemosphere 48, 59–68.

Chen, Y., Senesi, N., Schnitzer, M., 1977. Information provided on humic substances by E_4/E_6 ratios. Soil Sci. Am. J. 41, 352–358.

Chermak, J.A., 1992. Low temperature experimental investigation of the effect of high pH NaOH solutions on the Opalinus shale, Switzerland. Clay Clay Miner. 40, 650–658.

Chermak, J.A., 1993. Low temperature experimental investigation of the effect of high pH KOH solutions on the Opalinus shale, Switzerland. Clay Clay Miner. 41, 365–372.

Chin, Y.P., Aiken, G., Oloughlin, E., 1994. Molecular-weight, polydispersity, and spectroscopic properties of aquatic humic substances. Environ. Sci. Technol. 28, 1853–1858.

Choppin, G.R., 1992. The role of natural organics in radionuclide migration in natural aquifer systems. Radiochim. Acta 58-9, 113–120.

Claret, F., Bauer, A., Schäfer, T., Griffault, L., Lanson, B., 2002. Experimental investigation of the interaction of clays with high-pH solutions: a case study from the Callovo-Oxfordian formation, Meuse-Haute Marne underground laboratory (France). Clay Clay Miner. 50, 633–646.

Claret, F., Schäfer, T., Bauer, A., Buckau, G., 2003. Generation of humic and fulvic acid from Callovo-Oxfordian clay under high alkaline conditions. Sci. Total Environ. 317, 189–200.

Claret, F., Sakharov, B.A., Drits, V.A., Velde, B., Meunier, A., Griffault, L., Lanson, B., 2004. Clay minerals in the Meuse-Haute Marne underground laboratory (France): possible influence of organic matter on clay mineral evolution. Clay Clay Miner. 52, 515–532.

Czerwinski, K.R., Kim, J.I., Rhee, D.S., Buckau, G., 1996. Complexation of trivalent actinide ions (Am^{3+}, Cm^{3+}) with humic acid: the effect of ionic strength. Radiochim. Acta 72, 179–187.

Eberl, D.D., Velde, B., Mc Cormick, T., 1993. Synthesis of illite-smectite from smectite at Earth surface temperatures and high pH. Clay Miner. 28, 49–60.

Elie, M., Faure, P., Michels, R., Landais, P., Griffault, L., 2000. Natural and laboratory oxidation of low-organic-carbon-content sediments: comparison of chemical changes in hydrocarbons. Energ. Fuel 14, 854–861.

Flaig, W., 1972. Biochemical factors in coal formation. In: Von Gaertner, H.R., Wehner, H. (Eds.), Advances in Organic Geochemistry. Pergamon Press, Oxford.

Francis, J.T., Hitchcock, A.P., 1992. Inner-shell spectroscopy of *p*-benzoquinone, hydroquinone, and phenol: distinguishing quinoid and benzenoid structures. J. Phys. Chem. 96, 6598.

Henke, B.L., Gullikson, E.M., Davis, J.C., 1993. X-Ray interactions: photoabsorption, scattering, transmission, and reflection at $E = 50$–$30{,}000$ eV, $Z = 1$–92. Atom. Data Nucl. Data Tables 54, 181–342.

Hitchcock, A.P., Ishii, I., 1987. Carbon K-shell excitation spectra of linear and branched alkanes. J. Electron. Spectrosc. 42, 11–26.

Hitchcock, A.P., Mancini, D.C., 1994. Bibliography of atomic and molecular inner-shell excitation studies. J. Electron. Spectrosc. 67, 1–132.

Hitchcock, A.P., Urquart, S.G., Rightor, E.G., 1992. Inner shell spectroscopy of benzaldehyde, terephthalaldehyde, ethyl benzoate, terephthaloyl chloride, and phosgene: models for core excitation of poly(ethylene terephathalate). J. Phys. Chem. 96, 8736–8750.

Hoque, E., Wolf, M., Teichmann, G., Peller, E., Schimmack, W., Buckau, G., 2003. Influence of ionic strengh and organic modifier concentration on characterization of aquatic fulvic and humic acids by high-performance size-exclusion chromatography. J. Chromatogr. A 1017, 97–105.

Jacobsen, C., Williams, S., Anderson, E., Browne, M.T., Buckley, C.J., Kern, D., Kirz, J., Rivers, M., Zhang, X., 1991. Diffraction-limited imaging in a scanning transmission X-ray microscope. Opt. Commun. 86, 351–364.

Jacobsen, C.J., Zimba, C., Flynn, G., Wirick, S., 2000. Soft X-ray microscopy from sub-100 nm regions. J. Microsc. 197, 173–184.

Jorda, M., 2000. Geologic storage of high-level longlived radioactive waste – the situation of France. Atw-Int. Z. Kernenerg. 45, 29.

Kim, J.I., Czerwinski, K.R., 1996. Complexation of metal ions with humic acid: metal ion charge neutralization model. Radiochim. Acta 73, 5–10.

Kim, J.I., Buckau, G., Li, G.H., Duschner, H., Psarros, N., 1990. Characterization of humic and fulvic acids from Gorleben groundwater. Fresen. J. Anal. Chem. 338, 245–252.

Kim, J.I., Klenze, R., Wimmer, H., 1991a. Fluorescence spectroscopy of curium(III) and application. Eur. J. Sol. State Inorg. 28, 347–356.

Kim, J.I., Wimmer, H., Klenze, R., 1991b. A study of curium(III) humate complexation by time resolved laser fluorescence spectroscopy (TRLFS). Radiochim. Acta 54, 35–41.

Landais, P., Elie, M., 1999. Utilisation de la géochimie organique pour la détermination du paléoenvironnement et de la paléothermicité dans le Callovo-Oxfordien du site de l'Est de la france. Etude de l'Est du bassin de Paris. Edition EDP Sciences.

Lebon, P., Mouroux, B., 1999. Knowledge of the three French underground laboratory sites. Eng. Geol. 52, 251–256.

Ma, Y., Chen, C.T., Meigs, G., Randall, K., Sette, F., 1991. High-resolution-shell photoabsorption measurements of simple molecules. Phys. Rev. A 44, 1848–1858.

MacCarthy, P., Rice, J.A., 1985. Spectroscopic methods (other than NMR) for determining functionality in humic substances. In: Aiken, G.R., MacCarthy, P., McKnight, D.S., Wershaw, R.L. (Eds.), Humic Substances in Soil, Sediment

and Water: Geochemistry, Isolation and Charaterization. Wiley-Interscience, New York, pp. 457–476.

Mazurek, M., Elie, M., Hurford, A., Leu, W., Gautschi, A., 2002. Burial history of Opanilus clay. In: Proc. Int. Conf., Clays in Natural and Engineered Barriers for Radioactive Waste Confinement, Reims, pp. 101–102.

Moore, D.M., Reynolds Jr., R.C., 1989. X-Ray Diffraction and the Identification and Analysis of Clay Minerals. Oxford University Press, Oxford and New York.

Moulin, V., Ouzounian, G., 1992. Role of colloids and humic substances in the transport of radio-elements through the geosphere. Appl. Geochem. Suppl. 1, 179–186.

Nagra, 2002. Technical Report NTB 0205.

Nissenbaum, A., Kaplan, I.R., 1972. Chemical and isotopic evidence for the in situ origin of marine humic substances. Limnol. Oceanog. 17, 570–582.

Rabung, T., Geckeis, H., Kim, J.I., Beck, H.P., 1998. The influence of anionic ligands on the sorption behaviour of Eu(III) on natural hematite. Radiochim. Acta 82, 243–248.

Reiller, P., Moulin, V., Casanova, F., Dautel, C., 2002. Retention behaviour of humic substances onto mineral surfaces and consequences upon thorium (IV) mobility: case of iron oxides. Appl. Geochem. 17, 1551–1562.

Rice, J.A., MacCarthy, P., 1991. Statistical evaluation of the elemental composition of humic substances. Org. Geochem. 17, 635–648.

Schäfer, T., Artinger, R., Dardenne, K., Bauer, A., Schuessler, W., Kim, J.I., 2003a. Colloid-borne americium migration in Gorleben groundwater: significance of iron secondary phase transformation. Environ. Sci. Technol. 37, 1528–1534.

Schäfer, T., Claret, F., Bauer, A., Griffault, L., Ferrage, E., Lanson, B., 2003b. Natural organic matter (NOM)–clay association and impact on Callovo-Oxfordian clay stability in high alkaline solution: spectromicroscopic evidence. J. Phys. IV 104, 413–416.

Schäfer, T., Hertkorn, N., Artinger, R., Claret, F., Bauer, A., 2003c. Functional group analysis of natural organic colloids and clay association kinetics using C(1s) spectromicroscopy. J. Phys. IV 104, 409–412.

Schäfer, T., Buckau, G., Artinger, R., Kim, J.I., Geyer, S., Bleam, W.F., Wirick, S., Jacobsen, C., 2005. Origin an mobility of fulvic acids in the Gorleben Aquifer system: implications from isotopic data and carbon/sulfur XANES. Org. Geochem. 36, 567–582.

Scheinost, A.C., Kretzschmar, R., Christl, I., Jacobsen, C., 2002. Carbon group chemistry of humic and fulvic acid: a comparison of C-1s NEXAFS and 13C-NMR spectroscopies. Spec. Pub. Roy. Soc. Chem., 273.

Stumpf, S., 2004. Spektroskopische Untersuchungen zu Sorptionmechanismen von dreiwertigen Actiniden an Feldspäten, Quartz und Ferrihydrit (Investigation of mechanisms of trivalent actinide sorption onto feldspars, quartz and ferrihydrite). Ph.D. Thesis, Univ. Heidelberg, Germany.

Swift, R.S., 1996. Organic matter characterization. In: Sparks, D.L. (Ed.), Methods of Soil Analysis. Part 3 – Chemical Methods, vol. 5. Soil Science Society of America, Madison, WI, USA, pp. 1011–1069.

Thang, N.M., Geckeis, H., Kim, J.I., Beck, H.P., 2001. Application of the flow field flow fractionation (FFFF) to the characterization of aquatic humic colloids: evaluation and optimization of the method. Coll. Surf. A 181, 289–301.

Thury, M., 2002. The characteristics of the Opalinus Clay investigated in the Mont Terri underground rock laboratory in Switzerland. C. R. Phys. 3, 923–933.

Traina, S.J., Novak, J., Smeck, N.E., 1990. An ultraviolet absorbance method of estimating the percent aromatic carbon content of humic acids. J. Environ. Qual. 19, 151–153.

Vilks, P., Stroes-Gascoyne, S., Goulard, M., Haveman, S.A., Bachinski, D.B., 1998. The release of organic material from clay based buffer materials and its potential implications for radionuclide transport. Radiochim. Acta 82, 385–391.

Wang, X., Rabung, T., Panak, P., Geckeis, H., Klenze, R., Fanghänel, T., 2004. Effect of humic acid on the sorption of Cm(III) onto γ-Al2O3 studied by the time-resolved laser fluorescence spectroscopy. Radiochim. Acta 92, 691–695.

Wolf, M., Buckau, G., Chanel, V., 2005. Asymmetrical flow field-flow fractionation of humic substances: comparison of polyacrylic acids and polystyrene sulfonates as molecular mass standards. In: Ghabbour, E.A., Davies, J. (Eds.), Humic Sustances: Molecular Details and Aplications in Land and Water Conservation. Taylor & Francis, New York (in press).

Source identification and characterization of humic and fulvic acids from Oxfordian argillite and Opalinus Clay

In: E.A. Ghabbour and J. Davies (eds.): Humic Substances: Molecular Details & Applications in Land and Water Conservation (2005) Chapter 4, Taylor & Francis, New York (USA).

Schäfer T., Claret F., Lerotic M., Buckau G., Rabung T., Bauer A., and Jacobsen C.

Chapter 4

SOURCE IDENTIFICATION AND CHARACTERIZATION OF HUMIC AND FULVIC ACIDS ISOLATED FROM OXFORDIAN ARGILLITE AND OPALINUS CLAY

Thorsten Schäfer,[1] Francis Claret,[1] Mirna Lerotic,[2] Gunnar Buckau,[1] Thomas Rabung,[1] Andreas Bauer[1] and Chris Jacobsen[2]

[1] Institute für Nukleare Entsorgung (INE), Forschungszentrum Karlsruhe, 76021 Karlsruhe, Germany
[2] Department of Physics & Astronomy, State University of New York, Stony Brook, New York 11794, USA

4.1. INTRODUCTION

Clay-organic matter studies focus predominantly on the process of biogeochemical carbon cycling and the understanding of carbon degradation/preservation pathways in aquatic systems. About 90 % of the preserved organic material (OM) in the global carbon cycle resides in amorphous, kerogen-type macromolecules disseminated in shale or other sedimentary rocks [1]. Over ninety percent of this total sedimentary organic matter cannot be physically separated from its mineral matrix. The observed mineral surface area loading for continental shelf sediments characteristically approaches a mono-layer mineral surface coverage [2]. Mechanisms governing sedimentary organic matter preservation in marine environments (< 0.5 % efficiency [3,4]) have remained unclear. Several theories have been proposed.

Besides the classical degradation-recondensation [5], selective preservation [6] and the natural sulphurization [7] pathways, a new mechanism recently has been proposed [8]. The preservation theory via an sorptive protection pathway [8] is based on the partition coefficient (K_D), which has to be in the order of 10^2-10^4 mL/g or higher to prevent OM degradation. Clay mineral natural biopolymer K_D values (illite 10^2 mL/g; montmorillonite 10^4mL/g) can explain protein preservation via this model [9]. Model refinement includes the combination of the mineral sorption and aggregate formation process to describe the OM preservation mechanism [10,11]. In this case, the OM distribution should be patchy, rather than a monolayer mineral surface coverage. OM distribution in Cenomanian black shale showing an alteration

of organic and clay layers of approx. 100 nm thickness rather than molecular monolayers is in accordance with this theory [12]. Pyrolysis-GC/MS analysis of clay-organic associates in recent soils have demonstrated an enrichment of polysaccharides in kaolinite-dominated soils, whereas smectite-dominated soils contained larger amounts of aromatic compounds [13]. However, in ref 13 the total amount of organic carbon in the clay fraction was independent of the clay mineralogy. Combined transmission electron microscopy (TEM) and electron energy-loss spectroscopy (EELS) studies showed a preferential association of organic matter with Ca-containing smectite single platelets rather than with kaolinite and illite [14].

Residual organic matter in diagenetic overprinted shales or argillites of marine or terrestrial origin still show some extractable humic and/or fulvic acid [15-18]. Clay-rich low organic carbon sediments are considered as possible host rock formations for deep geological disposal of nuclear waste. This poses the question, if mineral preserved mostly insoluble organic matter (kerogen) can generate soluble compounds (humic and fulvic acids) having complexation properties with respect to radionuclides, then that might change the radionuclide transport mechanism (for example, colloidal transport) [19-22]. Another aspect (not discussed in detail in this paper) that has to be considered with respect to the long-term evolution of different barriers in the multi-barrier concept of a repository is the change in chemical stability of backfill clay and/or host rock clay due to clay-organic association [17,23,24].

The application of carbon x-ray absorption near edge structure (XANES) in environmental studies includes work on coal, aquatic humic and fulvic acids [23,25-27] and the reactivity of natural organic matter (NOM) inorganic mineral associates [23,24]. The objective of our investigation is to compare XANES spectra measured at the carbon K-edge, potassium L-edge, calcium L-edge, oxygen K-edge and iron L-edge with synchrotron based mid-infrared microspectroscopy and time-resolved laser fluorescence spectroscopy (TRLFS) measurements in order to determine

(a) the nanoscale spatial distribution and functional group composition of organic matter in two different clay-rich, low-carbon sedimentary rocks, namely the Callovo-Oxfordian argillite and the Opalinus shale considered as possible host rock formations for storage of high level nuclear waste (HLW),
(b) to localize possible sources for humic and/or fulvic acid release in these undisturbed sediments, and
(c) to investigate spectroscopically the trivalent actinide complexation behavior of these terrestrial sediment derived HA/FA like materials.

The analytical approach used in this study to localize and characterize HA/FA and NOM is to find natural groupings of spectromicroscopic data without prior knowledge of the spectra of all components [28,29]. This was performed with principal component analysis (PCA) [30] to orthogonalize spectromicroscopic data and to eliminate analytical noise. Subsequently, cluster analysis [31] was used to classify pixels according to their spectral similarity, and then recover gradations of thickness of representative materials using the observable spectra. Furthermore, the same set of principal components in combination with carbon K-edge target spectra of isolated humic and fulvic acids were used to define possible source regions of released humic and fulvic acids in these whole rock samples.

4.2. MATERIALS AND METHODS

4.2.1. Sample Origins

Callovo-Oxfordian sedimentary rock samples representative of the future French underground laboratory located in Bure (eastern Paris Basin, departments Meuse and Haute-Marne) were taken from four burial depths (447m, 490m, 494m, 516m) of the exploration borehole EST 104 [23,24]. The formation can be classified as argillite containing 40-45% clay minerals and ~50% calcite and quartz. Detailed mineralogical studies on the composition of the clay fraction < 2μm revealed in the upper part (447 to 490m) higher amounts of 2:1 layer silicates (13-20% smectite), whereas the lower rock formations have a decreased smectite content (~2%) and show considerable amounts of kaolinite (4-9%) and chlorite (1-2%) [24,32]. In this study we present data on the smectite-containing terrestrial sedimentation environment influenced sample of the argillite (sample 447m) [33]. For comparison, one Opalinus shale sample (579.19-579.45m) of the borehole Benken provided by the Swiss National Cooperative for the Disposal of Radioactive Waste (NAGRA) was selected [34]. The total organic carbon (TOC) concentration in the clay fraction is depth independent: ~1.3 wt% in the Bure argillite and < 0.4 wt% in the Opalinus clay. The maximum burial temperature of the Bure probably never exceeded 40°C, as indicated by organic matter characterization and fluid inclusions [35,36], whereas the Opalinus shale has seen a higher maximal burial temperature of 59°C to 78°C [37]. Additionally the < 2μm size-fraction of these rock samples, separated by centrifugation and pre-treated according to ref. 38, was investigated for comparison.

4.2.2. Sample Preparation

To prevent cross-contamination with organic embedding materials (e.g., epoxy-resin) the untreated rock samples and clay fractions were embedded in sulfur and ultra-microtomed (MVA, Inc., Norcross, GA) to a thickness of 100 nm and transferred to low carbon Formvar® grids for spectroscopic investigations. Aliquots of the clay fractions used for ultra-microtoming were repeatedly humic and fulvic acid extracted using the modified [18] isolation procedure [39] of the standard method developed by the International Humic Substance Society (IHSS) [40]. 5.2 % HA and 1.3 % FA of total clay fraction associated carbon were isolated from the argillite sample 447, whereas only 1.1 % FA could be extracted from the Opalinus clay. HA/FA sample preparation for scanning transmission x-ray microscope (STXM) analysis was performed by drying a 0.5 to 1 μL droplet of the suspension on a 100 nm thick Si_3N_4 window.

4.2.3. X-Ray Absorption Near Edge Structure (XANES) Spectromicroscopy

Measurements were performed at the Scanning Transition X-Ray Microscope (STXM) of the National Synchrotron Light Source (NSLS) at Brookhaven National Laboratory (BNL) in Upton, New York: undulator beamlines X1A1 (elements C, K and Ca) and X1A2 (elements O and Fe), operated by the State University of New York at Stony Brook [41]. The principle of this method is described in detail elsewhere [41,42]. Carbon K-edge, potassium L-edge and oxygen K-edge spectra

were recorded using an undulator gap of 36.8 mm, whereas for iron L-edge and calcium L-edge measurements an undulator gap of 41.7 mm was used. The Fresnel zone plate utilized for C-, K- and Ca-edge measurements had a diameter (a) of 160 μm and an outermost zone width (δ) of 45 nm, whereas for O- and Fe-edge measurements a zone plate with a = 80 μm and δ = 30 nm was used. The larger 180 μm diameter zone plate needed for wet cell measurements [43] on X1A1 gives a theoretical spatial resolution (Rayleigh criterion) of 55 nm at a focal length of 1.7 mm [44]. Energy calibration of the spherical grating monochromators was performed with the photon energy of the CO_2 gas adsorption band at 290.74 eV (X1A1) and the O_2 gas adsorption band at 532.82 eV (X1A2), respectively [45,46]. The X1A1 STXM exit and entrance slit set-up was chosen to obtain an energy resolution ΔeV of 0.1 eV at the C K-edge [47]. XANES spectra were recorded using the image stack option [48]. Only spectra with at least 1% x-ray transmittance of the incoming flux were used to avoid spectral distortion.

STXM measurements give information on the product of sample thickness d and the mass absorption coefficient μ(E), which is related to the quotient of the incident flux on the sample $I_0(E)$ and the flux detected behind the sample I(E) by $\mu(E)*d = \ln[I_0(E)/I(E)]$. Image stacks are measured as a function of photon energy and the XANES spectra were extracted after stack alignment. Image regions free of particles or separately measured XANES spectra without samples gave the $I_0(E)$ information. All carbon XANES spectra were treated according to the deconvolution procedure described in ref. 48 for semi-quantitative analysis of functional group content. In order to compare isolated HA/FA spectra with cluster regions of the whole rock microtomes in both deconvolution procedures, a Gaussian peak at 290.2 eV for carbonate was implemented as shown in Table 4.1.

4.2.4. Synchrotron FT-IR Microspectroscopy

Infrared measurements were performed at the U10B beamline (National Synchrotron Light Source) using a Spectra-Tech Continuum IR microscope coupled to a Nicolet Magna 860 FTIR. The microscope utilizes a dual remote masking aperture and matching 32x Schwartzchild objectives [50]. Area mapping was performed using the dual remote masking aperture to define the sample area and spectra were collected with 10 μm x 10 μm aperture by averaging 1024 scans in the wavenumber range 650 – 4000 cm^{-1} per point in transmission mode at 4 cm^{-1} resolution using Atlμs software (Thermo Nicolet Instruments). Background information is collected through the blank Si_3N_4 window and the final data format is absorbance.

4.2.5. Time Resolved Fluorescence Laser Spectroscopy (TRFLS)

TRFLS measurements were performed with a pulsed Nd:YAG pumped dye laser system (Continuum, Powerlite 9030, ND 6000). An optical multichannel analyser consisting of a polychromator (Chromex 250) with a 1200 lines/nm grating is used for detection of the fluorescence emission. To fade out any light scattering and background fluorescence, the emission spectra of curium(III) were recorded 1 μs after the exciting laser pulse (laser dye: Exalite 398, excitation wavelength 396.6 nm) in the wavelength range 580-620 nm in a time window of 1 ms. For lifetime

Table 4.1 Semiquantitative analysis of the average carbon K-edge by spectral deconvolution in the energy range 280 – 295 eV. Values given are in proportion (%) of the area sum of the seven π* and the C_{aliph} mixed valence state/Rydberg transition simulated by Gaussian peaks

Sample	benzoquinone-type	$C_{arom.}$	phenol-type	$C_{aliph.}$	carboxyl-type	O-alkyl-type	carbonate	$\sum(I_{fit}-I_{meas})^2$
447 HA isolate	9	17	14	12	22	8	14	0.033840
447 FA isolate	6	17	12	16	26	12	11	0.037275
OPA FA isolate	0	8	0	24	30	17	21	0.079951
Microtome 447								
smectite region	9	17	16	16	16	12	14	0.038092
illite/MLM region	0	8	3	23	15	25	26	0.060050
carbonate region	8	15	14	16	16	13	18	0.044007
Microtome Opalinus								
illite/MLM region (cluster B)	1	12	0	25	20	16	26	0.116719
illite/MLM region (cluster C)	3	13	2	24	13	19	26	0.071879
AOM[a]-type region	0	7	4	32	26	8	23	0.104606

[a] AOM: amorphous organic matter without identification of inorganic mineral association.

measurements, the delay time between laser pulse and camera gating was scanned with time intervals of 20 µs. Samples were prepared by adding 2 x 10^{-7} mol L^{-1} Cm^{3+} to the humic acid (447 HA: 10 mg L^{-1} DOC) solution, and 1 x 10^{-7} mol L^{-1} to the two different fulvic acids (447 FA: 8.7 mg L^{-1} DOC, OPA FA: 6.6 mg L^{-1} DOC) solutions in a glove box under an argon atmosphere. Investigations were conducted at pH 5.7-6. In this range Cm^{3+} hydrolysis is negligible and only two species are formed in significant concentrations. These species are the Cm fulvic acid complex and the non-complexed Cm^{3+} ion. Therefore, spectral deconvolution is straightforward.

4.3. RESULTS AND DISCUSSION

4.3.1. X-Ray Absorption Near Edge Structure (XANES) Spectromicroscopy

Combination of the carbon, calcium, potassium, oxygen and iron edge spectra in this study gives the possibility to differentiate nanoscopically between organic association to carbonate minerals (strong Ca K-edge and carbon K-edge π^* resonance at 290.2 eV), illitic clays (potassium $L_{2,3}$-edge), smectitic clays (Ca-edge and carbon K-edge absorption without the 290.2 eV carbonate peak) and pyrite/iron oxide (Fe $L_{2,3}$-edge absorption) in the heterogeneous mineral assemblage of the whole rock microtome.

Oxfordian Argillite (447 m Depth). STXM analysis of the Oxfordian argillite microtome sample (447 m burial depth) shows a strong increase of organic content in the smectite microtome region as indicated by the optical density (OD) shown in Figure 4.1.

This smectite rich region was identified in the upper microtome sector (Figure 4.2B) because of the absence of absorption bands 1) in the energy region of the potassium L2,3-edge, and 2) at the energy of 290.2eV (π^*-transitions for carbonate); and 3) a detectable absorption at the calcium K-edge representing the exchangeable interlayer cations (Figure 4.2E). In the lower part of the microtome section, two regions of generally lower overall organic carbon content can be differentiated. One region (Figure 4.2C) shows a significant absorption at the potassium L2,3-edge, a considerable calcium K-edge absorption and some iron L2,3-edge absorption (Figure 4.2E), indicative of illitic clays or smectite/illite mixed layer minerals (MLM). This region shows significantly different carbon edge spectra, with lower absorption in the aromatic carbon region and higher aliphaticity (Table 4.1). The second region (Figure 4.2D) that could be identified in the lower part of the microtome section displays very strong calcium K-edge absorption, the highest iron L_3-edge absorption and a strong absorption band at 290.2 eV in the carbon K-edge spectra indicative of carbonate. From the spectroscopic results we can deduce that this organic matter is associated with carbonate phases, most probably a mixed (Fe,Ca)-carbonate or nano-crystalline intergrowth of pure siderite and calcite end members, not resolved by the resolution of STXM (<50 nm). The carbon edge of the smectite rich regions (Figure 4.2B) and the carbonate rich region (Figure 4.2D) are surprisingly very similar in the overall features, with the sole difference of increased absorption at the C(1s) π^*-transition at 290.2 eV for carbonate and the

generally lower organic association with carbonate, as indicated by the optical density (Figure 4.1).

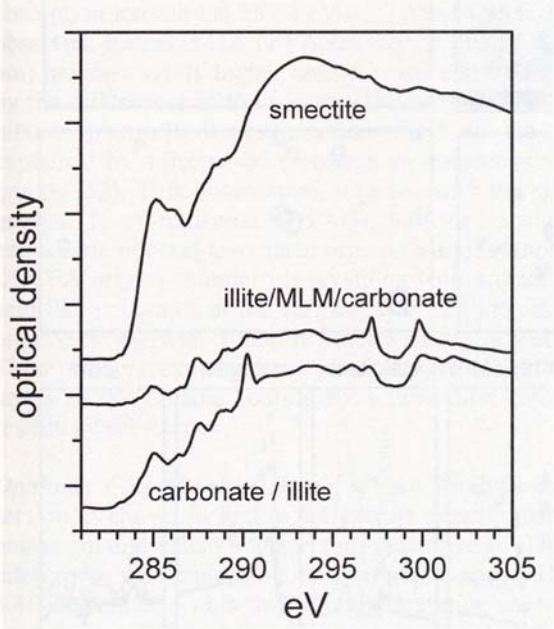

Figure 4.1 Optical density of different principal components identified in microtome section 447 of the Oxfordian argillite

Overall, these data clearly demonstrate a higher natural organic matter concentration with smectite type clay minerals. ^{14}C activity measurements in a recent Savanna system have demonstrated that clay mineralogy has a strong influence on organic matter preservation, with smectite having significantly lower organic matter turnover and higher mean residence time [51]. Therefore, the mineralogically-dependent organic carbon concentration differences observed in both the ancient Callovo-Oxfordian sediments (sample 447 m) and recent soils leads to the preliminary conclusion that only a minor organic matter overprint by diagenesis has occurred in the Bure sample. In this case, the functional group composition should change significantly with the clay mineralogy. The deconvolution of the average spectra (Table 4.1) extracted from the smectite rich region revealed a significantly higher proportion of aromatic carbon (42%) and a lower aliphatic carbon content (16%) compared to the illite/mixed layer mineral (MLM) region with 11% aromatic carbon and 23% aliphatic carbon, respectively. No particulate or amorphous organic matter (AOM) without mineral association could be observed in sample 447 under the given resolution of the STXM.

To estimate the source of soluble organic matter (that is, isolated humic and fulvic acid) in the whole rock samples, the FA/HA spectra shown in Figure 4.3C are used as target spectra to fit the first four principal components from the PCA [29]. As expected, deconvolution of the isolated HA (Table 4.1) generally showed a higher humic acid aromaticity ($\sum$(hydroquinone, C_{arom}, phenol-type) ~ 40%) compared to 35 % for the isolated FA and a lower aliphaticity of approximately 12% to 16% in FA, respectively.

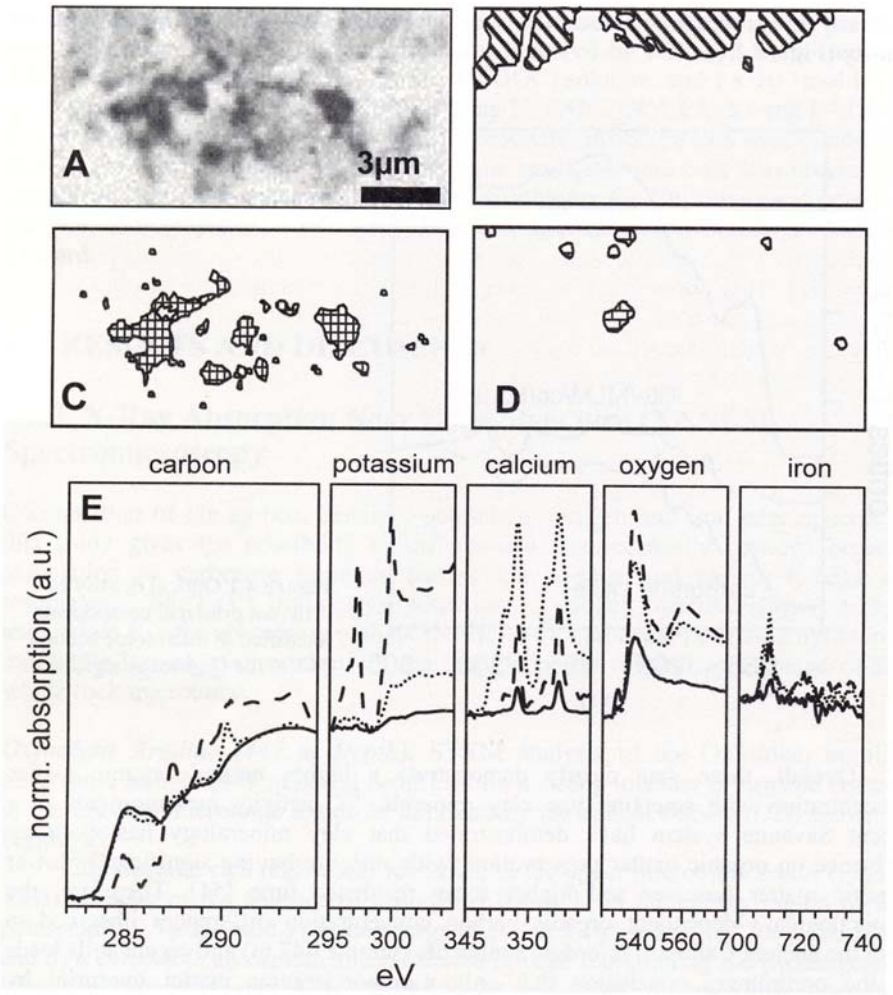

Figure 4.2 STXM analysis of whole rock microtome sample 447. In the upper part of the figure, the absorption image at 280 eV below the carbon K-edge (A) and three clusters identified using the first eight significant principle components from the PCA analysis are shown (B, C, D). Cluster analysis was performed over the energy range 280 to 740 eV with the following set-up: 4 clusters seeking procedure, eigenimage scaling factor: 0.2, first principal component removed, Euclidean distance measurement (for details see ref. 29). E: Carbon, potassium, calcium, oxygen and iron absorption spectra of the clusters found (cluster B solid line, cluster C dashed line, cluster D dotted line)

The maps of the raw target spectra (isolated FA, HA; not shown separately) and the fitted target spectra show a good correlation with light gray regions indicating high concentrations of spectral constituents and dark areas being a sign of depleted regions of target spectra. From the fitted target spectra maps (Figures 4.3A and 4.3B) and the results of the cluster analysis (Figure 4.2), the smectite rich region can be identified as a source of isolated HA in sample 447, whereas the isolated FA shows more similarities to the illite/MLM region of the microtome. However, detailed comparison of HA and FA target spectra with the fitting results

shows systematic variations as well as good conformity (σ = 0.0206-0.0248). Both the isolated FA and HA have a significantly higher amount of carboxylic groups (288.6 eV) as well as C_{arom} = C_{arom} or C_{arom}-H (285.2 eV), whereas a lower absorption intensity at 287.4 eV (C_{aliph}) and 286.6 eV (phenol type), respectively, is observed. Released HA or FA are most probably coming from surface layers (~ 10 nm) having slightly higher aromatic and carboxylic acid-like structure as indicated by the differences in the spectra. The decreased 287.4 eV intensity assigned to the mixed valence/Rydberg transition C-H* in the HA/FA target spectra can be explained by a decreased carbon atom number (chain length) in the alkyl pendant groups [52]. This observation, together with the significantly lower carboxyl type groups (1s-π* transition of C=O), indicates a higher polymerization of the non extractable mineral-associated organic matter compared to the organic surface layer (HA/FA origin). Similar observations with aromatic, carbohydrate and carboxylic acid-like structures in the surface layer and increased aliphatic content in the bulk organic matter were found in studies of recent wetland soil in Saskatchewan [53]. These authors explained the observations of labile aliphatic structures in deeper layers of the organic coating by a protection mechanism involving surface layer refractory substances.

Opalinus Clay (Benken Depth 579m). Analysis of the Opalinus Clay microtome section as shown in Figure 4.4 reveals organic matter in regions where significant potassium and calcium absorption indicative of illite/mixed layer minerals (MLM) intergrown with nanocrystalline carbonate appear. Both clusters (Figures 4.4A and 4.4B) separated within this microtome region are very similar and show in the de-convolution (Table 4.1) a low aromaticity ($\sum$ (benzoquinone-type, C_{arom} = C_{arom}, phenol-type = 13-18%) with a low amount of C_{arom} associated oxygen containing functional groups (phenol-type 0-2%) and a high aliphaticity (24-25%). These values are in good agreement with the results found for illite/MLM region in the Oxfordian argillite 447 (see Table 4.1) and show that the illite/MLM associated organic matter of both host rock types is comparable with respect to organic functionality.

This observation raises the question of whether the illite/MLM region serves as a source of fulvic acid-like organics in the Opalinus shale. Therefore, the spectra of the isolated Opalinus FA (OPA FA, see Figure 4.5B1) were used as target spectra to fit the first four principal components of PCA [29]. From the fitted target spectral map and the results of the cluster analysis, the illite/MLM region (Figure 4.5B1) can be identified with a high certainty (σ= 0.0365) as a source of the isolated FA. Differences between the combination of the first four principal components and the target spectra (isolated FA) are a lower absorption in the phenol-type group region and a higher absorption in the C_{aliph} region of the isolated OPA FA. Additional analysis on various other regions of the microtome section (not shown in detail) revealed that besides the illite/MLM association, particulate organics or amorphous organic carbon (AOM) without significant absorption on the potassium, calcium and iron-edge also could be the source of extractable FA (Figure 4.5B2). Besides the good correlation (σ = 0.0195), significantly higher amounts of C_{aliph} and lower carboxyl and O-alkyl type groups (47% in OPA FA versus 34% in AOM) are found in the AOM, indicating a higher hydrophobicity of this material and therefore a less probable FA source.

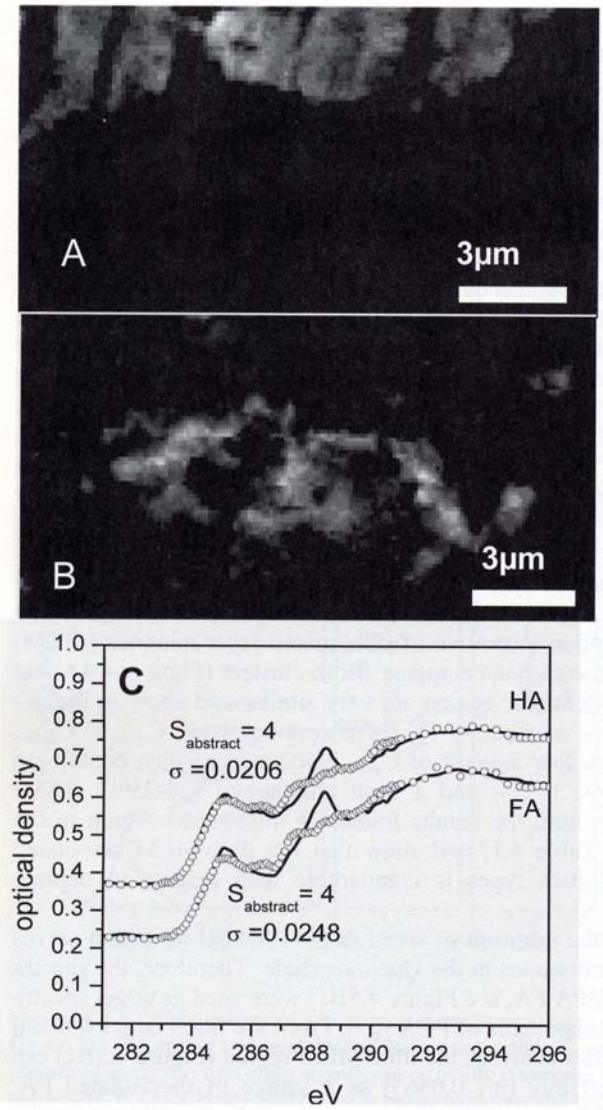

Figure 4.3 Target spectral analysis of the STXM data. In the upper part the generated maps from target spectra fits (A, B) are shown. C: shows the fit of isolated HA and FA target spectra using the first four significant principle components $S_{abstract}$ from the PCA (open circles) and the original isolated HA and FA target spectra (solid lines)

4.3.2. Synchrotron Based FT-IR Microspectroscopy

Oxfordian Argillite (Depth 447 m). The infrared spectra of the microtome section 447 is shown in Figure 4.6. A differentiation of the clay mineral assemblage as performed by X-Ray diffraction could not be accomplished from the spectra of the separated clay fraction and the rock microtome shown in Figure 4.6 [18,32]. In the region of Al-OH stretching vibrations of the aluminosilicate layers, a broad absorption at 3625 cm^{-1} and two additional significant humps at 3666 cm^{-1} and 3694 cm^{-1} could be identified. This broad hydroxyl absorption is typical of random substitution present in dioctahedral micas and smectites, where the MgAlOH absorption at 3687 cm^{-1} could not be resolved from the Al_2OH absorption at 3620-

3630 cm^{-1} [54]. The additional hump at 3666 cm^{-1} can be assigned to a weak OH-stretching feature of trioctrahedral chlorites. Kaolinite group minerals typically show three sharp high frequency features at 3697, 3669 and 3652 cm^{-1}, and the 3620 cm^{-1} inner hydroxyl group band could not be differentiated, as expected [54]. The band at 1161 cm^{-1} can be assigned to the C-C bond in aliphatics and polymeric substances or to a Si-O-C bond, which might indicate a linkage of some organic macromolecules to the clay Si-O groups [55]. The absorption bands around 1076, 1039 and 916 cm^{-1}, and the doublet around 800 cm^{-1} can be identified as Si-O or Al-OH vibrations in quartz and/or aluminosilicates, whereas the absorption band near 1415 cm^{-1} can be assigned to the asymmetrical stretch of CO_3^{-2} in carbonates [54].

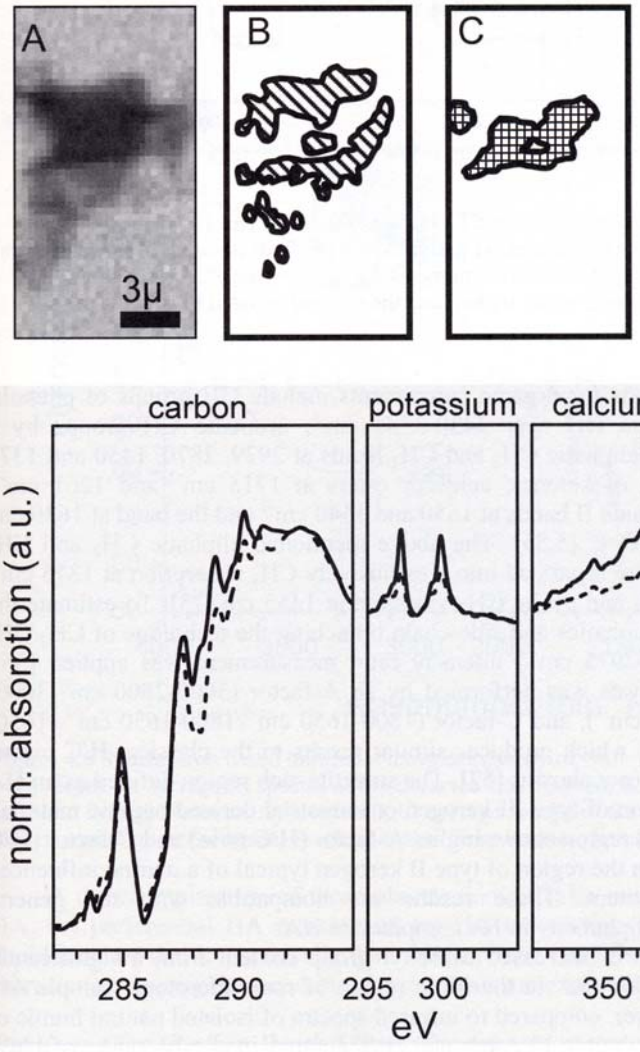

Figure 4.4 STXM analysis of whole rock microtome sample Opalinus. Upper part: the absorption image at 280 eV below the carbon K-edge (A) and two clusters identified using the first seven significant principle components from the PCA (B, C). Cluster analysis was performed over the energy range 280 to 360 eV with the following set-up: 4 clusters-seeking procedure, eigenimage scaling factor 0.2, first principal component removed, Euclidean distance measurement (for details see ref. 29). Lower part: Carbon, potassium and calcium absorption spectra of the clusters found (cluster B solid line, cluster C dashed line. No iron $L_{2,3}$- edge absorption could be detected)

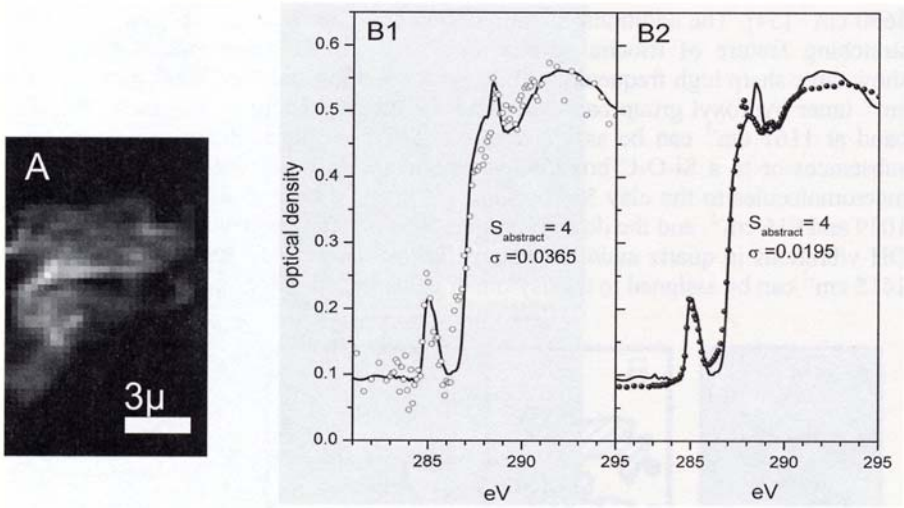

Figure 4.5 Target spectral analysis of the STXM data. The upper part (A) is the generated map from the target spectral fit. Figures B1 and B2 show the fit of isolated FA target spectra using the first four significant principal components $S_{abstract}$ from the PCA (B1: illite/MLM region; B2: amorphous organic matter region) and the original isolated FA target spectra (solid lines)

Characteristic bands for organic components include OH groups of phenols, alcohols and carboxylic OH near 3430-3383 cm^{-1}, aromatic CH groups by a shoulder at 3073 cm^{-1}, aliphatic CH_2 and CH_3 bands at 2929, 2870, 1450 and 1375 cm^{-1}, a carbonyl band of ketones, acids or esters at 1715 cm^{-1} and 1261 cm^{-1}, peptidic amide I and amide II bands at 1650 and 1540 cm^{-1} and the band at 1630 cm^{-1} for mostly aromatic C=C [5,55]. The above mentioned aliphatic CH_2 and CH_3 bands can be furthermore separated into a exclusively CH_3 absorption at 1375 cm^{-1} and a mixed linear CH_3 and cyclic CH_2 vibration at 1455 cm^{-1} [5]. To estimate the length, the degree of aliphatics and side-chain branching the technique of CH_2/CH_3 (2915-2940 cm^{-1}/2950-2975 cm^{-1}) intensity ratio measurement was applied [56]. Furthermore, data analysis was performed by an A-factor (3000-2800 cm^{-1}/3000-2800 cm^{-1}+1650-1520 cm^{-1}), and C-factor (1800-1650 cm^{-1}/1800-1650 cm^{-1}+1650-1520 cm^{-1}) calculation, which produces similar results to the classical H/C versus O/C van Krevelen plot (not shown) [57]. The smectite-rich region defined as an HA source plots in the region of type III kerogen or terrestrial derived organic material, whereas the illite/MLM region shows higher A-factor (H/C ratio) and C-factor (O/C ratio) values and falls in the region of type II kerogen typical of a marine influenced sedimentation environment. These results are compatible with the general observation of higher aliphaticity in FA compared to HA.

A clear indication of increased carboxyl group content from a significantly higher absorption at 1709 cm^{-1} in the illitic region of rock microtome sample 447 can be detected. However, compared to infrared spectra of isolated natural humic or fulvic acids [55,58] or humic-like substances generated in the presence of clays [59], this C=O band intensity of all clay associated organics is significantly reduced, indicating a loss of oxygen-containing functional groups as already shown by

XANES analysis. A second difference between regions B and C (Figure 4.6) is the band at 1161 cm^{-1}, which can be identified in the illite rich region C, but cannot be resolved in the smectite rich region B. Taking into account the C(1s) XANES target spectra analysis derived information of smectite as the potential HA source and the higher HA extraction yield compared to FA [18] of these sediments, a possible explanation of the higher HA mobilisation can be the missing Si-O-C linkage of humic macromolecules.

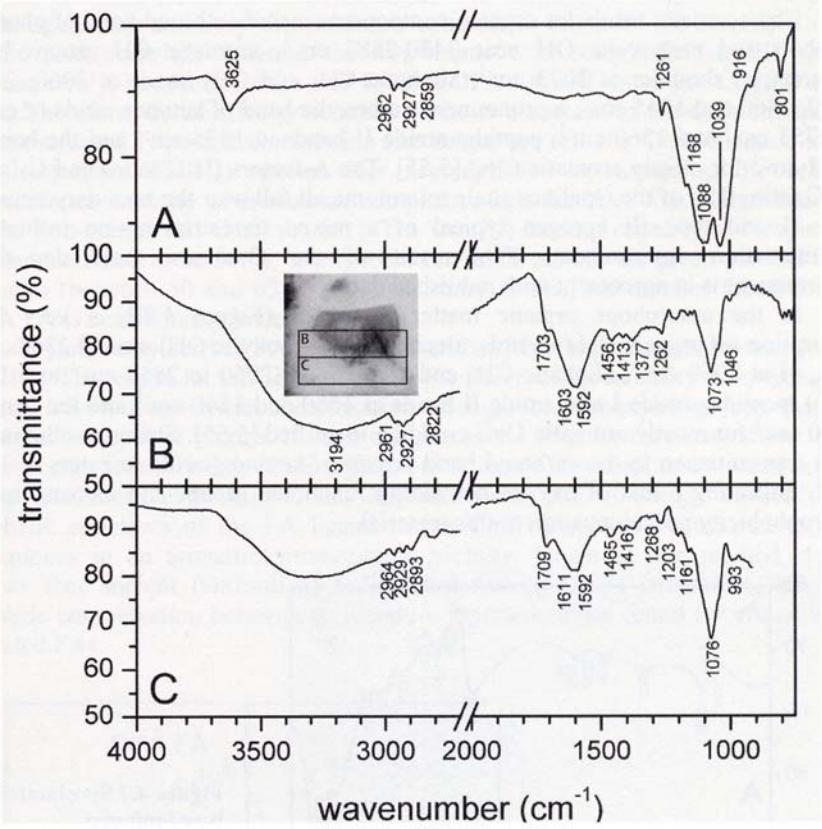

Figure 4.6 Synchrotron based infrared microspectroscopy of Oxfordian argillite sample 447m depth. A: average IR spectra of the extracted clay fraction, B: average spectra extracted from the smectite rich region B, C: average spectra of the illite/MLM region C. Size of square gives the spatial resolution used for spectra acquisition (10µm)

A direct implication of these observations is (a) a missing Si-O-C linkage of HA, (b) preferential HA release and (c) HA association with smectitic minerals could indicate that in chemically disturbed environments (high pH plume of cement corrosion) primarily the smectitic clay minerals are expected to react.

Opalinus Clay (Benken Depth 579m). The infrared spectrum of the Opalinus shale microtome section is shown in Figure 4.7. In the upper spectra (Figure 4.7), extracted from the clay-rich region A kaolinite group mineral, specific sharp high frequency features at 3696, 3669 and 3651 cm^{-1} besides the 3619 cm^{-1} inner

hydroxyl group band could by identified [54]. The additional hump at 3666 cm^{-1} can be interpreted as a weak OH-stretching feature of trioctrahedral chlorites. The band observed at 1163 cm^{-1} can be assigned again to the C-C bond in aliphatics and polymeric substances or to a Si-O-C bond, which might indicate a linkage of some organic macromolecules to the clay Si-O groups [55]. The absorption bands around 1076 cm^{-1} and 1039 cm^{-1}can be identified as Si-O or Al-OH vibrations in quartz and/or aluminosilicates, whereas the absorption band near 1426 cm^{-1} can be assigned to the asymmetrical stretch of CO_3^{-2} in carbonates [54].

Characteristic bands for organic components include a broad band of phenols, alcohols and carboxylic OH near 3430-3383 cm^{-1}, aromatic CH groups by a pronounced shoulder at 3073 cm^{-1}, aliphatic CH_2 and CH_3 bands at 2960, 2922, 2857, 1460 and 1345 cm^{-1}, a pronounced carboxylic band of ketones, acids or esters at 1753 cm^{-1} and 1260 cm^{-1}, peptidic amide II bands at 1575 cm^{-1} and the band at 1631 cm^{-1} for mostly aromatic C=C [5,55]. The A-factors (H/C ratio) and C-factor (O/C ratio) data of the Opalinus shale microtome all fall near the boundary between type II and type III kerogen typical of a mixed terrestrial/marine influenced sedimentation environment. This result of the Opalinus shale deposition environment is in agreement with published data [37].

In the amorphous organic matter region B (Figure 4.7B) a very high absorption for organic OH (phenols, alcohols and carboxylic OH) around 3300 cm^{-1}, C_{arom}-H at 3069 cm^{-1}, aliphatic CH_2 and CH_3 bands (2960 to 2850 cm^{-1} and 1453 cm^{-1}), peptidic amide I and amide II bands at 1650 and 1540 cm^{-1} and the band at 1630 cm^{-1} for mostly aromatic C=C could be identified [5,55]. Striking is the rather high transmittance in the carbonyl band region of ketones, acids or esters at 1753 cm^{-1}, indicating a loss of oxygen containing functional groups and increase in the hydrophobicity/polymerization of this material.

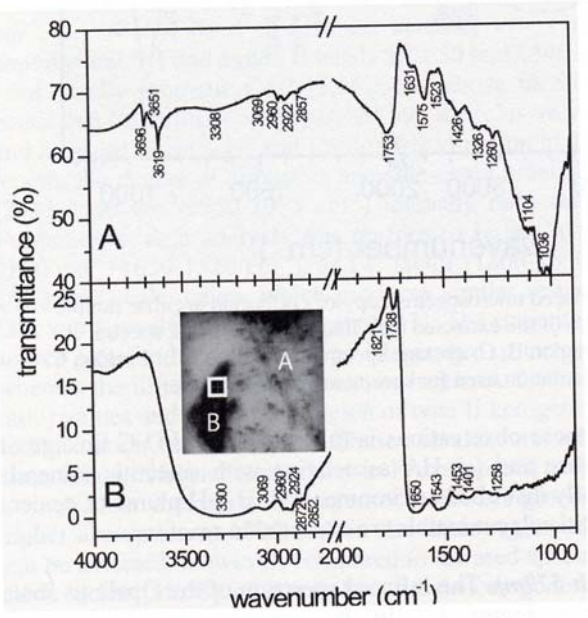

Figure 4.7 Synchrotron based infrared microspectroscopy of Opalinus clay microtome. A: average IR spectra of the clay rich region A, B: average spectra extracted from the amorphous organic matter(AOM) type material. Size of square gives the spatial resolution used for spectra acquisition (10µm)

4.3.3. Curium(III) Complexation Behavior

The trivalent actinide complexation behavior of isolated HA/FA was studied using time resolved fluorescence spectroscopy (TRFLS) on Cm(III) [60]. The emission spectra show the characteristic shape of humate and fulvate curium complexes with a peak maximum around600 nm, compared to 593.8 nm for the non-complexed Cm^{3+} aqua-ion as shown in Figure 4.8 [61]. The curium(III) fluorescence decay and derived lifetimes of the investigated humic and fulvic acid samples are basically indistinguishable and show the same time behavior as found for the Cm(III)-Aldrich humic acid complex. Whereas the 447 humic acid complexes Cm(III) almost quantitatively, both fulvic acids 447 FA and OPA FA still show free Cm(III) aqua-ions. Therefore, the relative peak areas of the two species in the different spectra were evaluated by peak deconvolution (for details see ref. 18). Quantification of the two respective Cm(III) species was accomplished by assuming the relative fluorescence intensity of the fulvate complex to be a factor of four higher than that of the non-complexed Cm^{3+} ion [61]. The Cm(III) loading capacity of sample 447 FA is calculated to be 58 %, as expected for fulvic acid at the given pH and ionic strength (between 50 and 63 % [62]). Contrary to this, the number found for the OPA FA is considerably lower (7.9 %).

The Opalinus clay derived FA shows a lower Cm(III) complex intensity than for the 447 FA. The reason for this lower Cm(III) FA fluorescence intensity is not yet clear. It may result from lower complexation strength of carboxylic groups that are adjacent to aliphatic groups. If such complexes are formed, they may show lower fluorescence intensity than those adjacent to aromatic/chromophoric structures. The lower fluorescence intensity could originate from lack of energy transfer from aliphatic structures of the FA ligand to the Cm(III) complex compared to such complexes in an aromatic/chromophoric vicinity. However, the method clearly shows that ancient (Oxfordian) sediment derived FA has comparable trivalent actinide complexation behavior to literature reported values found for groundwater isolated FAs.

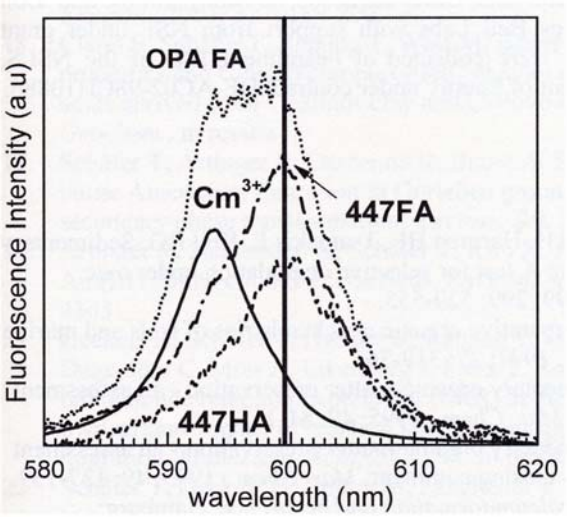

Figure 4.8 Cm(III) fluorescence spectra of isolated FA (447 FA, OPA FA) and HA (447 HA) investigated in this study. The vertical line gives the position of the humic/fulvic acid complex

4.5. CONCLUSIONS

The combination of carbon, potassium, calcium, oxygen and iron XANES spectra using PCA and cluster as well as target spectra analysis revealed a mineral dependent organic matter functionality in Jurassic low-carbon sedimentary formations, namely Oxfordian argillite and Opalinus shale. Furthermore, this method is capable of identifying the sources of isolated humic and fulvic acids in an undisturbed rock sample with nanoscopic spatial resolution. By employing synchrotron based FT-IR microspectroscopy with its high sensitivity to aliphatic carbon, it was also possible to retrieve additional information on the deposition environment. These results demonstrate that even in approximately 160 Ma old geological formations, part of the organic inventory keeps the structure/functionality of HA/FA. Investigations with time-resolved laser fluorescence spectroscopy (TRLFS) clearly showed that Oxfordian sediment derived FA-like material has not only kept its structure/functionality, but also shows comparable trivalent actinide complexation behavior, as expected for FA from literature data.

ACKNOWLEDGEMENTS

The results presented in this paper were partly collected during research supported by a Marie Curie fellowship of the European Commission programme "Nuclear Fission" under contract number FIKW-CT2002-50509. The authors are indebted to L. Griffault (ANDRA, France) and A. Gautschi (NAGRA, Switzerland) for providing core samples of the Callovo-Oxfordian argillite and Opalinus shale (Benken), respectively. We are grateful for beamtime allotment by BNL/NSLS. Spectromicroscopic data were collected using the X1A STXM developed by the group of Janos Kirz and Chris Jacobsen at SUNY Stony Brook, with support from the Office of Biological and Environmental Research, U.S. DOE under contract DE-FG02-89ER60858, and from the NSF under grant DBI-9605045. The zone plates were developed by Steve Spector and Chris Jacobsen of Stony Brook and Don Tennant of Lucent Technologies Bell Labs with support from NSF under grant ECS-9510499. The FTIR data were collected at beamline U10B of the NSLS, supported by the U.S. Department of Energy under contract DE-AC02-98CH10886.

REFERENCES

1. Hedges JI, Hu FS, Devol AH, Hartnett HE, Tsamakis E, Keil RG. Sedimentary organic matter preservation: A test for selective degradation under oxic conditions. *Am. J. Sci.*, 1999; 299: 529-555.
2. Hedges JI, Oades JM. Comparative organic geochemistries of soils and marine sediments. *Org. Geochem.*, 1997; 27: 319-361.
3. Hedges JI, Keil RG. Sedimentary organic-matter preservation - an assessment and speculative synthesis. *Mar. Chem.*, 1995; 49: 81-115.
4. Hedges JI, Keil RG. Sedimentary organic-matter preservation - an assessment and speculative synthesis - closing comment. *Mar. Chem.*, 1995; 49: 137-139.
5. Tissot BP, Welte DH, *Petroleum formation and occurence*. Hamburg: Springer, 1984.

6. Tegelaar EW, Deleeuw JW, Derenne S, Largeau, C. A Reappraisal of kerogen formation. *Geochim. Cosmochim. Acta*, 1989; 53: 3103-3106.
7. Sinninghe Damst'e JS, Rijpstra WIC, Kock-van Dalen AC, De Leeuw JW, Schenck PA. Quenching of labile functionalised lipids by inorganic sulphur species: Evidence for the formation of sedimentary organic sulphur compounds at the early stages of diagenesis. *Geochim. Cosmochim. Acta*, 1989; 53: 1343-1355.
8. Henrichs SM. Sedimentary organic-matter preservation - an assessment and speculative synthesis - a comment. *Mar. Chem.*, 1995; 49: 127-136.
9. Ding XL, Henrichs SM. Adsorption and desorption of proteins and polyamino acids by clay minerals and marine sediments. *Mar. Chem.*, 2002; 77: 225-237.
10. Bock MJ, Mayer LM. Mesodensity organo-clay associations in a near-shore sediment. *Marine Geol.*, 2000; 163: 65-75.
11. Ransom B, Bennett RH, Baerwald R, Shea K. TEM study of in situ organic matter on continental margins: Occurrence and the "monolayer" hypothesis. *Marine Geol.*, 1997; 138: 1-9.
12. Salmon V, Derenne S, Lallier-Verges E, Largeau C, Beaudoin B. Protection of organic matter by mineral matrix in a Cenomanian black shale. *Org. Geochem.*, 2000; 31: 463-474.
13. Wattel-Koekkoek EJW, van Genuchten PPL, Buurman P, van Lagen B. Amount and composition of clay-associated soil organic matter in a range of kaolinitic and smectitic soils. *Geoderma*, 2001; 99: 27-49.
14. Furukawa Y. Energy-filtering transmission electron microscopy (EFTEM) and electron energy-loss spectroscopy (EELS) investigation of clay-organic matter aggregates in aquatic sediments. *Org. Geochem.*, 2000; 31: 735-744.
15. Khalili F. Isolation and characterization of humic-acid from Jordanian oil shale. *Fuel*, 1990; 69: 151-156.
16. Krumholz LR, Harris SH, Suflita JM. Anaerobic microbial growth from components of cretaceous shales. *Geomicrobiol. J.*, 2002; 19: 593-602.
17. Claret F, Schäfer T, Bauer A, Fanghänel T. Generation of humic and fulvic acid from Callovo-Oxfordian clay under high alkaline conditions. *Sci. Tot. Environ.*, 2003; 317: 189-200.
18. Claret F, Schäfer T, Rabung T, Wolf M, Bauer A, Buckau G. Differences in properties and Cm(III) complexation behavior of isolated humic and fulvic acids derived from Opalinus clay and Callovo-Oxfordian argillite. *Appl. Geochem.*, in review.
19. Schäfer T, Artinger R, Dardenne K, Bauer A, Schuessler W, Kim JI. Colloid-borne Americium migration in Gorleben groundwater: Significance of iron secondary phase transformation. *Environ. Sci. Technol.*, 2003; 37: 1528-1534.
20. Artinger R, Schuessler W, Schäfer T, Kim JI. A kinetic study of Am(III)/humic colloid interactions. *Environ. Sci. Technol.*, 2002; 36: 4358-4363.
21. Geckeis H, Schäfer T, Hauser W, Rabung T, Geyer FW, Götz R, Missana T, Degueldre C, Möri A, Eikenberg J, Fierz T. Results of the colloid and radionuclide retention experiment (CRR) at the Grimsel test site (GTS), Switzerland-Impact of reaction kinetics and speciation on radionuclide migration. *Radiochim. Acta*, 2004; 92: in press.
22. Schäfer T, Geckeis H, Bouby M, Fanghänel T. U, Th, Eu and colloid mobility in a granite fracture under near-natural flow conditions. *Radiochim. Acta*, 2004; 92: in press.

23. Schäfer T, Claret F, Bauer A, Griffault L, Ferrage E, Lanson B. Natural organic matter (NOM)-clay association and impact on Callovo-Oxfordian clay stability in high alkaline solution: Spectromicroscopic evidence. *J. Phys. IV*, 2003; 104: 413-416.
24. Claret F, Bauer A, Schäfer T, Griffault L, Lanson B. Experimental investigation of the interaction of clays with high-pH solutions: A case study from the Callovo-Oxfordian formation, Meuse-Haute Marne underground laboratory (France). *Clay Clay Min.*, 2002; 50: 633-646.
25. Cody GD, Botto RE, Ade H, Behal S, Disko M, Wirick S. Inner-shell spectroscopy and imaging of a sub-bituminous coal: *In-situ* analysis of organic and inorganic microstructure using C(1s)-, Ca(2p)-, and Cl(2s)-NEXAFS. *Energy Fuels*, 1995; 9: 525-533.
26. Plaschke M, Rothe J, Schäfer T, Denecke MA, Dardenne K, Pompe S, Heise KH. Combined AFM and STXM in situ study of the influence of Eu(III) on the agglomeration of humic acid. *Colloids Surf. A*, 2002; 197: 245-256.
27. Schäfer T, Buckau G, Artinger R, Geyer S, Bleam WF, Wirick S, Jacobsen C. Origin and mobility of fulvic acids in the Gorleben aquifer system: Implications from isotopic data and carbon/sulfur XANES. *Org. Geochem.*, in review.
28. Jacobsen C, Feser M, Lerotic M, Vogt S, Maser J, Schäfer T. Cluster analysis of soft X-ray spectromicroscopy data. *J. Phys. IV*, 2003; 104: 623-626.
29. Lerotic M, Jacobsen C, Schäfer T, Vogt S. Cluster analysis of soft x-ray spectro-microscopic data. *Ultramicroscopy*, 2004, in press.
30. Malinowski E. *Factor analysis in chemistry*. New York: Wiley, 1991.
31. Everett B, Landau S, Leese M. *Cluster analysis.* London: Arnold Publishers, 2001.
32. Claret F. Caractérisation structurale des transitions minéralogiques dans les formations argileuses: Contrôles et implications géochimiques des processus d'illitisation. Cas particulier d'une perturbation alcaline dans le Callovo-Oxfordien Laboratoire souterrain Meuse-Haute-Marne. PhD Thesis, Université Joseph Fourrier, Grenoble, France, 2001:174 pp.
33. Landais P, Elie M. Utilisation de la géochimie organique pour la détermination du paléoenvironnement et de la paléothermicité dans le Callovo-Oxfordien du site de l´Est de la france. Etude de l´Est du bassin de Paris, Edition EDP Sciences, 1999: pp. 35-61.
34. The Swiss National Cooperative for the Disposal of Radioactive Waste (NAGRA). Project Opalinus clay - safety report - demonstration of disposal feasibility for spent fuel, vitrified high-level waste and long-lived intermediate level waste (Entsorgungsnachweis). NTB 02-05, Nagra, Wettingen (Switzerland), 2003.
35. Pellenard P, Deconinck JF, Marchand D, Thierry J, Fortwengler D, Vigneron G. Controle geodynamique de la sedimentation argileuse du Callovien-Oxfordien moyen dans l'Est du bassin de Paris: influence eustatique et volcanique. *C.R. Acad. Sci. Paris, Sciences de la terre et des planetes*, 1999; 328: 807-813.
36. Elie M, Faure P, Michels R, Landais P, Griffault L. Natural and laboratory oxidation of low-organic-carbon-content sediments: Comparison of chemical changes in hydrocarbons. *Energy Fuels*, 2000; 14: 854-861.
37. The Swiss National Cooperative for the Disposal of Radioactive Waste (NAGRA). Projekt Opalinuston -Synthese der geowissenschaftlichen

Untersuchungsergebnisse: Entsorgungsnachweis für abgebrannte Brennelemente, verglaste hochaktive sowie langlebige mittelaktive Abfälle-. NTB 02-03, NAGRA, Wettingen (Switzerland), 2003.
38. Moore DM, Reynolds RC. *X-ray diffraction and the identification and analysis of clay minerals.* New York: Oxford University Press, 1989.
39. Buckau, G. Komplexierung von Americium (III) mit Huminstoffen in natürlichen Grundwässern. PhD Thesis, Free University of Berlin, Berlin, 1991.
40. Swift RS. Organic matter characterization. In: Bartels JM ed. *Methods of soil analysis. Part 3: Chemical methods*. Madison, WI: Soil Science Society of America Book Series, 1996: pp. 1390.
41. Jacobsen C, Williams S, Anderson E, Browne MT, Buckley CJ, Kern D, Kirz J, Rivers M, Zhang X. Diffraction-limited imaging in a scanning transmission x-ray microscope. *Optics Commun.*, 1991; 86: 351-364.
42. Zhang X, Ade H, Jacobsen C, Kirz J, Lindaas S, Williams S, Wirick S. Micro-XANES: chemical contrast in the scanning transmission x-ray microscope. *Nucl. Instrum. Methods Phys. Res. A*, 1994; 347: 431-435.
43. Neuhäusler U, Abend S, Jacobsen C, Lagaly G. Soft X-Ray spectromicroscopy on solid-stabilized emulsions. *Colloid Polym. Sci.*, 1999; 277: 719-726.
44. Spector S, Jacobsen C, Tennant D. Process optimization for production of sub-20 nm soft x-ray zone plates. *J. Vacuum Sci. Technol. B*, 1997; 15: 2872-2876.
45. Hitchcock AP, Mancini DC. Bibliography of atomic and molecular inner-shell excitation studies. *J. Electron Spectrosc.*, 1994; 67: 1-132.
46. Ma Y, Chen CT, Meigs G, Randall K, Sette F. High-resolution-shell photoabsorption measurements of simple molecules. *Phys. Rev. A*, 1991; 44: 1848-1858.
47. Winn B, Ade H, Buckley C, Howells M, Hulbert S, Jacobsen C, Kirz J, McNulty I, Miao J, Oversluizen T, Pogorelsky I, Wirick S. X1A: Second generation undulator beamlines serving soft x-ray spectromicroscopy experiments at the NSLS. *Rev. Sci. Instrum.*, 1996; 67: 1-4.
48. Jacobsen CJ, Zimba C, Flynn G, Wirick S. Soft x-ray microscopy from sub-100nm regions. *J. Microsc.*, 2000; 197: 173-184.
49. Schäfer T, Hertkorn N, Artinger R, Claret F, Bauer A. Functional group analysis of natural organic colloids and clay association kinetics using C(1s) spectromicroscopy. *J. Phys. IV*, 2003; 104: 409-412.
50. Dumas P, Miller L. The use of synchrotron infrared microspectroscopy in biological and biomedical investigations. *Vibrational Spectrosc.*, 2003; 32: 3-21.
51. Wattel-Koekkoek EJW, Buurman P, van der Plicht J, Wattel E, van Breemen N. Mean residence time of soil organic matter associated with kaolinite and smectite. *Europ. J. Soil Sci.*, 2003; 54: 269-278.
52. Kikuma J, Tonner BP. Photon energy dependence of valence band photoemission and resonant photoemission of polystyrene. *J. Electron Spectrosc. Relat. Phenom.*, 1996; 82: 41-52.
53. Jokic A, Cutler JN, Ponomarenko E, van der Kamp G, Anderson DW. Organic carbon and sulphur compounds in wetland soils: Insights on structure and transformation processes using K-edge XANES and NMR spectroscopy. *Geochim. Cosmochim. Acta*, 2003; 67: 2585-2597.
54. Farmer VC ed. *The infrared spectra of minerals.* Mineralogical Society Monograph 4. London: Mineralogical Society, 1974: 539 pp.

55. Naidja A, Huang PM, Anderson DW, van Kessel C. Fourier transform infrared, UV-visible, and X-ray diffraction analyses of organic matter in humin, humic acid, and fulvic acid fractions in soil exposed to elevated CO_2 and N fertilization. *Appl. Spectrosc.*, 2002; 56: 318-324.
56. Painter PC, Starsinic M, Coleman MM. Determination of functional groups in coal by fourier transform interferometry. In: Ferraro JR, Basile LJ eds. *Fourier transform infrared spectroscopy*. New York: Academic Press, 1985: 169-240.
57. Ganz, Kalkreuth. *Fuel*, 1987; 66: 708.
58. Schmeide K, Sachs S, Bubner M, Reich T, Heise KH, Bernhard G. Interaction of uranium(VI) with various modified and unmodified natural and synthetic humic substances studied by EXAFS and FTIR spectroscopy. *Inorg. Chim. Acta*, 2003; 351: 133-140.
59. Bosetto M, Arfaioli P, Pantani OL. Study of Maillard reaction products formed by glycine and D-glucose on different mineral substrates. *Clay Min.*, 2002; 37: 195-204.
60. Kim JI, Wimmer H, Klenze R. A study of curium(III) humate complexation by time resolved laser fluorescence spectroscopy (TRLFS). *Radiochim. Acta*, 1991; 54: 35-41.
61. Buckau G, Kim JI, Klenze R, Rhee DS, Wimmer H. A comparative spectroscopy study of the fulvate complexation of trivalent transuranium ions. *Radiochim. Acta*, 1992; 57: 105-111.
62. Kim JI, Czerwinski KR. Complexation of metal ions with humic acid: Metal ion charge neutralization model. *Radiochim. Acta*, 1996; 73: 5-10.

Functional group analysis of natural organic colloids and clay association kinetics using C(1s) spectromicroscopy.

J. Phys. IV (2003) **104**, 409.

Schäfer T., Hertkorn N., Artinger R., Claret F., and Bauer A.

J. Phys. IV France **104** (2003)

DOI: 10.1051/jp4:20030110

Functional group analysis of natural organic colloids and clay association kinetics using C(1s) spectromicroscopy

T. Schäfer, N. Hertkorn[1], R. Artinger, F. Claret and A. Bauer

Forschungszentrum Karlsruhe, Institut für Nukleare Entsorgung, INE, P.O. Box 3640, 76021 Karlsruhe, Germany

[1] *GSF-Forschungszentrum für Umwelt und Gesundheit, Institut für Ökologische Chemie, P.O. Box 1129, 85758 Neuherberg, Germany*

Abstract. The quantification of natural humic colloid functional group content and chemical association of humic substances with clay minerals exerts a crucial role in the colloid-borne mobility of actinides due to the functional group dependent strong interaction with multivalent metal ions. Functional group quantification in isolated fulvic acids of the Gorleben groundwater (Lower Saxony, NW Germany) by comparison of high resolution C(1s) NEXAFS spectra deconvolution with ^{13}C-NMR measurements showed good correlation ($r^2 > 0.9$) and gives a potential quantification tool in complex natural groundwater systems. Time resolved soft X-ray spectromicroscopy on dissolved organic carbon stabilized SWy-2 smectite colloids revealed an enrichment of carboxyl groups on broken edges (silanol/aluminol groups) at short contact times (1h). With longer contact times (7d, 6 months) the clay associated organic carbon increases and significantly higher aromatic content associated with basal surfaces were detected. The enhanced sorption of aromatic compounds can be related to an increase in mineral surface hydrophobicity and/or preferential sorption on charged siloxane surfaces.

1. INTRODUCTION

In natural aquifers, organic and inorganic colloids are ubiquitous and take part in geochemical solid-water-interface reactions. Due to their strong interaction with multivalent metal ions humic colloids exert a crucial influence on the mobility of actinides in natural [1] and anthropogenic influenced aquifer systems [2]. The importance of colloid enhanced contaminant transport depends preliminary on the colloid chemistry, their stability in the geochemical environment and the reversibility of metal/colloid association. Numerous electro kinetic experiments have been performed to elucidate the effect of humic (HA) and fulvic (FA) acids sorption onto inorganic colloid (clay, iron oxide) surface charge and coagulation kinetics. The natural groundwater and the isolated HA/FA used in this study origin from the Gorleben aquifer (Lower Saxony, Germany) representing the far-field of a potential deep geological final storage site for heat-generating high level radioactive waste in Germany. The sediments covering the Permian salt dome host rock formation consist of a complex system of confined and unconfined groundwater horizons [3] with various geochemical zones influenced by (i) recharge, (ii) transition, (iii) enhanced DOC and (iv) brines. Due to local Miocene brown coal and Pleistocene peat deposits, dissolved organic carbon increases locally (enhanced DOC groundwater) up to 200 mgC/L [4].

The aim of this study is to demonstrate (1) the possibility of functional group quantification in complex natural organic matter by comparison of high resolution C(1s) NEXAFS spectra deconvolution with ^{13}C-NMR measurements and (2) to elucidate the FA/HA stabilization/association of inorganic colloids and the time dependent C(1s) functional group changes.

2. EXPERIMENTAL

Scanning transmission X-ray microscopy (STXM) investigations were performed at the beam line X1A (NSLS) operated by the State University of New York at Stony Brook. The principle of the method is described in [5]. Details on isolation and characterization of the isolated HA/FA from the Gorleben groundwater DOC can be found in [6,7]. Na-montmorillonite (SWy-2) was obtained from the Source Clay repository of the Clay Minerals Society. The Clay fraction < 2 μm was separated by centrifugation. Suspensions of 10 g/L montmorillonite in natural groundwater (GoHy-2227) were prepared for kinetic sorption experiments. For detailed description of the groundwater composition and the Gorleben site it is

referred to the studies of [6,7]. Samples were taken after 1h, 7d and 6 months Swy-2/DOC reaction time, centrifuged and the supernatant discarded. The centrifugate was resuspended with MilliQ water and 1μL was taken immediately and squeezed between two SiN_3 windows of the wet cell assembly designed by [8] for spectromicroscopic analysis. To compare directly the different spectra the linear pre-edge background was set to zero. Additionally to the untreated original groundwater and the SWy-2/DOC associates isolated freeze dried HA and FA were characterized by X-Ray spectromicroscopy. Two ionization thresholds (IP) were set for C(1s) NEXAFS spectra deconvolution (arctangent function at 290.4eV for aromatic/aliphatic carbon and at 292eV for hydroxylated aromatic carbon) with FWHM of 0.5 eV to generate the continuum spectrum up to 295 eV. Their magnitude was assessed by the atomic ratio of carbon to oxygen tabulated in [7]. FWHM of Gaussian peaks was set to 0.4 eV and 6 Gaussian functions representing the main 1s-π^* transitions (284.0, 285.0, 286.6, 287.6, 288.6 and 289.4eV) were used (Fig. 1A). The aromatic carbon in Fig. 1 is the sum of the 284 eV (benzoquinone) and 285 eV (C_{arom}-C_{arom}, C_{arom}-H) Gaussian peaks, respectively. Additionally two second, higher transitions (1s-2π^*) for aromatic carbon bonded to either hydrogen or carbon and for aromatic carbon bonded to oxygen approximately 4 eV above the energy of the 1s-π^* transition with nearly one-quarter of the intensity were implemented. σ^*-transitions (~293eV, ~294eV) were simulated by simplified Gaussian shape function with a FWHM of 1 eV and 2 eV. For quantitative analysis ^{13}C NMR spectra were acquired with a Bruker DMX 500 NMR spectrometer. For details on the principle and the analytical setup it is referred to [9,10]. The spectra deconvolution procedure described here is comparable to the approach used by [11] on subbituminous coal and by [12] on different size fractions of HA.

3. RESULTS & DISCUSSION

3.1 Fulvic acid functional group quantification

The isolated Gorleben groundwater fulvic acids, namely GoHy-421, -711, -182 and –2221, show in the C(1s) spectrum deconvolution a significant variation of phenol, aromatic carbon and aliphatic content (Tab. 1). Furthermore a slight variation in carbonyl groups and almost no variation in the carboxyl group content could be observed. Isolated FA of the groundwater recharge dominated areas show thereby the highest aliphatic content with the lowest aromatic and phenol content, whereas FA of the enhanced DOC groundwater have the highest aromatic and phenol group content. C(1s) NEXAFS of huminitic macerals in Wyodak subbituminous coal measured by [11] reveal comparable high aromatic spectral features, therefore indicating that indeed the mobilization of Miocene brown coal and Pleistocene peat deposits is the process of DOC enhancement. To evaluate if the deconvolution procedure used in this study is capable to give at least semi-quantitative information in complex natural organics the results were compared with quantitative ^{13}C-NMR measurements. A good linear correlation ($r^2 > 0.9$) of aromatic C=C and C-H, phenol, aliphatic and carbonyl groups between the ^{13}C-NMR and C(1s) NEXAFS (Fig. 1B, Tab. 1) were found. Due to the low variation in the carboxyl group content of the samples no linear correlation coefficient could be determined for this functional group.

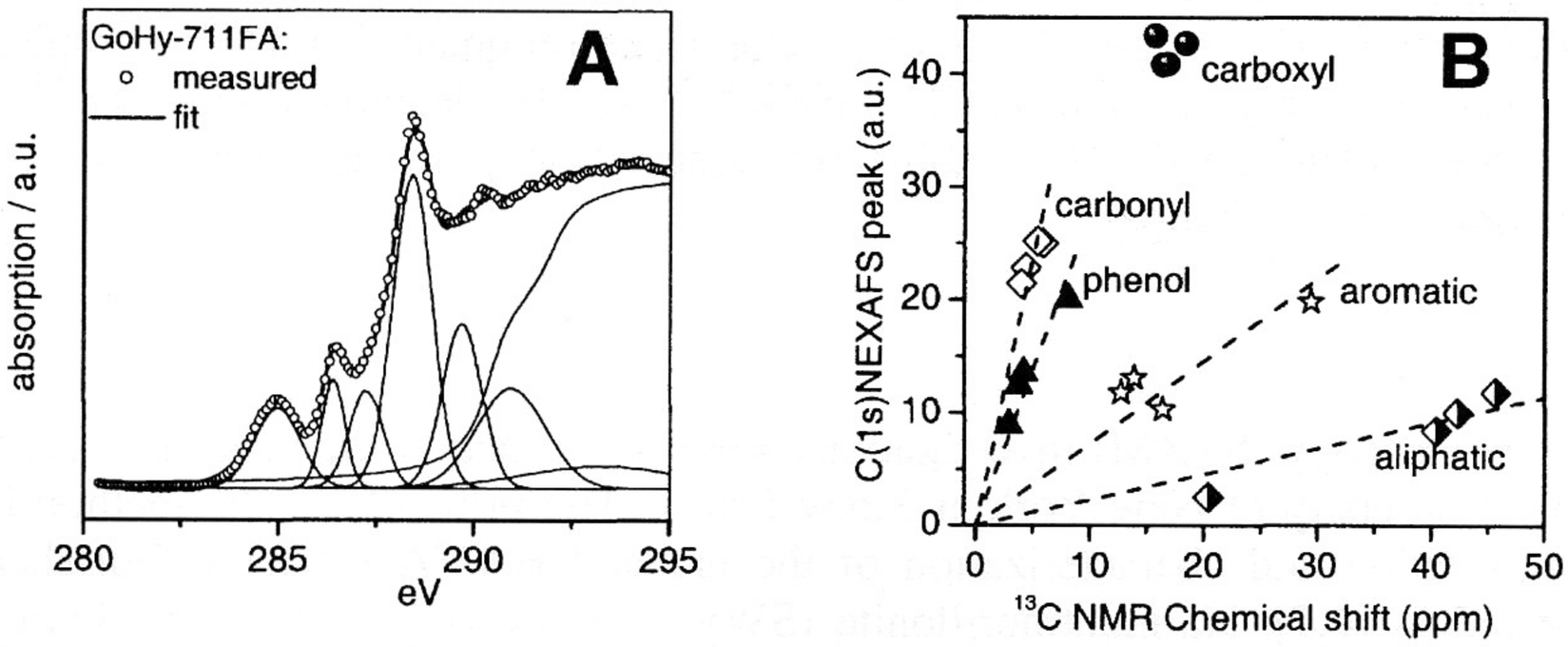

Figure 1: A: C(1s) spectra deconvolution of sample GoHy-711 isolated fulvic acid showing the main □*-transitions, the two □* transitions and the arctangent step function. 1s-2□* transitions are not shown. **B**: Correlation of C(1s) NEXAFS peak areas and ^{13}C-NMR chemical shifts.

However, the promising small scattering in the carboxyl data points of Fig. 1B gives strong hints that the deconvolution procedure is as well applicable in the carboxyl group region. Overall the results presented clearly demonstrate that C(1s) NEXAFS deconvolution can be used in the Gorleben system to quantify functional group content of highly complex isolated natural fulvic acids. The transferability of this procedure to other natural systems has to be proved and is under investigation.

Table 1. Linear correlation of ^{13}C-NMR measurements (chemical shifts in ppm) and C(1s)-NEXAFS peak de-convolution (peak position in eV) of isolated Gorleben groundwater fulvic acids of different origin and calculated correlation coefficient

	Recharge		*Transition*	*Enhanced DOC*	
Functional group	421 FA	711FA	182FA	2211FA	r^2
C_{arom}-H, C_{arom}=C_{arom} (285 eV)	11.8	13.1	10.3	19.8	0.90537
arom. carbon (105-145 ppm)	12.8	13.9	16.4	29.4	
Phenol type (286.6 eV)	12.4	8.9	13.5	20	0.98017
Phenol type (145-165 ppm)	3.8	2.9	4.2	8.1	
aliphatic (287.6eV)	10	11.8	8.4	2.5	0.98692
aliphatic (0-50ppm)	42.3	45.7	40.4	20.4	
carboxyl (288.6 eV)	40.8	43.4	42.7	40.9	-*
carboxyl (165-185 ppm)	16.4	15.7	18.4	16.8	
carbonyl (289.4 eV)	25	22.8	25.2	21.4	0.95344
carbonyl (185-220 ppm)	5.9	4.4	5.4	4	

* Data point cluster, no linear fit possible

3.2 Clay-Organic association kinetic

Spectra de-convolution of isolated fulvic acid (FA) from Gorleben groundwater (GoHy-2227) shows twice as much carboxyl groups and lower amounts of aromatics, phenol type groups and aliphatics compared to the humic acid (HA) isolate (Tab. 2). The deconvolution results demonstrate clearly a higher density of functional groups (69.9% of total area) in FA relative to HA (54.1% of total area) as already pointed out by [13]. The original GoHy-2227 groundwater DOC (mixture of HA, FA and hydrophilic compounds) however has lower aromatic and phenol type groups than the measured HA/FA isolates, but even slightly higher carboxyl groups than the FA isolate. Kinetic investigations on the GoHy-2227 DOC uptake of smectite particles display at short contact times a carboxyl functional group dominated C (1s) spectrum (Tab. 2). Microscopic investigations showed that the organic carbon is preliminary concentrated at the particle broken edges silanol/aluminol groups (Fig. 2, B3). Minor proportions of aromatic compounds are furthermore localized at these edge sites and at the basal surfaces (Fig. 2, B2). A possible explanation for the observed high carboxyl group content associated with clay edges after short reaction times might be a multiple adsorption bond (surface complexation) via carboxyl groups at Al sites as proposed by [13]. Furthermore a diffusion related higher attachment probability of small FA molecules compared to larger HA molecules can effect the sorption results at short contact times. With increasing reaction time (7d, 6months) the clay associated organic carbon increases as documented by the optical density increase (Fig. 2A). Carbon functional groups on edge sites still remains, but significantly higher aromatic content associated with basal surfaces and also broken edge sites can be observed (Fig.2, B2). The enhanced sorption of aromatic compounds with increasing reaction time can be related to an increase in mineral surface hydrophobicity of broken edge and isomorphous substitution sites by low polar organic acids. Investigations by Angove and co-workers [14] demonstrated e.g. an anthracene adsorption enhancement in the presence of low polar benzene carboxylates on clay.

Table 2. C(1s)-NEXAFS peak de-convolution area (peak position in eV) of isolated Gorleben groundwater fulvic acid, humic acid, groundwater DOC and Swy-2 smectite particle associated DOC after different contact times.

Functional group		285 eV	286.6 eV	287.6 eV	288.6 eV	289.4 eV
GoHy-2227 fulvic acid		20.9	17.2	9.2	40.0	12.7
GoHy-2227 humic acid		29.2	21.4	16.7	20.6	12.1
GoHy-2227 groundwater DOC		13.3	14.0	5.3	42.2	25.1
Swy-2/GoHy-2227	*1h*	6	2.6	19.5	47.7	24.2
Swy-2/GoHy-2227	*7d*	13.3	11.4	22.6	34.5	16.6
Swy-2/GoHy-2227	*6m*	37.5	17.8	18.6	16.6	9.4

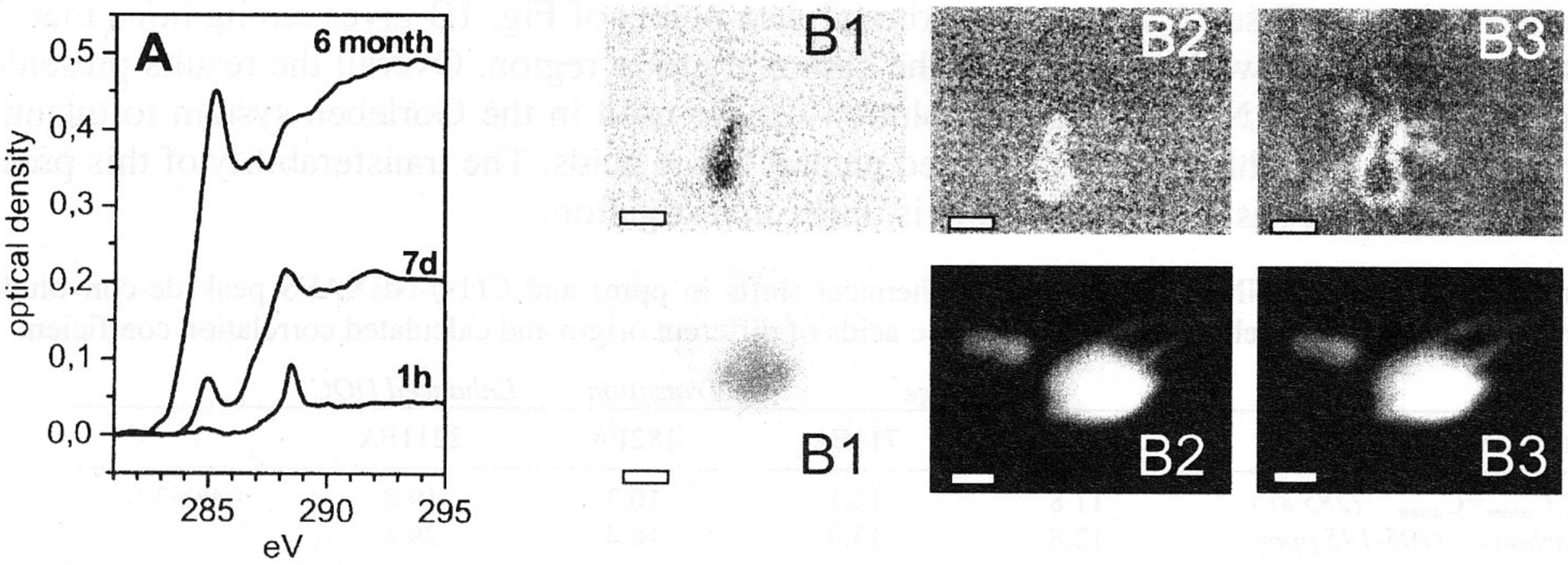

Figure 2: A: Optical density and functional group changes with increasing SWy-2 smectite/organic contact time. Spectra pre-edge optical density set to zero. Right: B1 pre-edge images taken at 280 eV. Ratio images (-log [I/I_0]; I_0= Σ(280-283eV)) of sample 1h contact time (upper row) and 6 months contact time (lower row); B2: aromatics, I=285eV; B3 carboxyl, I=288.4eV. (scale bar is equivalent to 1µm).

Charged siloxane surfaces can act as soft Lewis base (delocalised octahedral substitution) or hard Lewis base (localized tetrahedral substitution), which has an important impact e.g. on organic acid sorption. It could be shown e.g. that quinoline adsorption [15] and sorption of aromatic compounds [16] is strongly enhanced by charged siloxane sites of montmorillonite as also demonstrated in this study. The observed slow functional group change on inorganic colloid associated organics can have a significant influence on colloid stability predictions and might also serve as an explanation for the often observed changes of metal/colloid association reversibility.

Acknowledgments

We are grateful for beam time allotment by BNL/NSLS. Spectromicroscopic data were collected using the X1-A1 STXM developed by the group of Janos Kirz and Chris Jacobsen at SUNY Stony Brook [5], with support from the Office of Biological and Environmental Research, U.S. DoE under contract DE-FG02-89ER60858, and from the NSF under grant DBI-9605045. The zone plates were developed by Steve Spector and Chris Jacobsen of Stony Brook and Don Tennant of Lucent technologies Bell Labs with support from the NSF under grant ECS-9510499.

References

[1] Kim, J.I., G. Buckau, H. Rommel, B. Sohnius, *Mat. Res. Soc. Symp. Proc.* **127** (1989) 849-854.
[2] Vilks, P., H.G. Miller, D.C. Doern, *Appl. Geochem.*, **6** (1991) 565-574.
[3] BGR, *Übertägige geowissenschaftliche Erkundung des Standortes Gorleben*. (1991), Bundesanstalt für Geowissenschaften und Rohstoffe: Hannover.
[4] Buckau, G., *Komplexierung von Americium (III) mit Huminstoffen in natürlichen Grundwässern*. (1991), Ph.D. Thesis, Freie Universität Berlin: Berlin.
[5] Jacobsen, C., S. Williams, E. Anderson, M.T. Browne, C.J. Buckley, D. Kern, J. Kirz, M. Rivers, X. Zhang, *Optics Communications*, **86** (1991) 351-364.
[6] Buckau, G., R. Artinger, P. Fritz, S. Geyer, J.I. Kim, M. Wolf, *Appl. Geochem.*, **15** (2000) 171-179.
[7] Artinger, R., G. Buckau, S. Geyer, P. Fritz, M. Wolf, J.I. Kim, *Appl. Geochem.*, **15** (2000) 97-116.
[8] Neuhäusler, U., S. Abend, C. Jacobsen, G. Lagaly, *Colloid Polym. Sci.*, **277** (1999) 719-726.
[9] Hertkorn, N., A. Permin, I. Perminova, M. Yudov, A. Kettrup, *J. Environ. Qual.* **31** (2002) 375-387.
[10] Hertkorn, N., T. Schäfer, R. Artinger, and P. Schmitt-Kopplin, *Org. Geochem.* (in prep.)
[11] Cody, G.D., R.E. Botto, H. Ade, S. Behal, M. Disko, S. Wirick, Energy & Fuels **9** (1995) 525-533.
[12] Scheinost, A., R. Kretzschmar, I. Christl, C. Jacobsen, *Spec. Pub. Roy. Soc. Chem.* **273** (2002) 39-47.
[13] Schulthess, C.P. C.P. Huang, *Soil Sci. Soc. Am. J.* **55** (1991) 34-42.
[14] Angove, M.J., M.B. Fernandes, J. Ikhsan, *J. Coll. Interface Sci.* **247/2** (2002) 282-289.
[15] Burgos, W.D., N. Pisutpaisal, M.C. Mazzarese, J. Chorover, *Environ. Eng. Sci.* **19/2** (2002) 59-68.
[16] Wattel-Koekkoek, E., P. van Genuchten, P. Buurman, B. van Lagen, *Geoderma* **99** (2001) 27-49.

Combined AFM and STXM in situ study of the influence of Eu(III) on the agglomeration of humic acid.

Colloids Surf. A (2002) **197**(1-3), 245.

Plaschke M., Rothe J., Schäfer T., Denecke M. A., Dardenne K., Pompe S., and Heise K. H.

ELSEVIER

Colloids and Surfaces
A: Physicochemical and Engineering Aspects 197 (2002) 245–256

COLLOIDS AND SURFACES A

www.elsevier.com/locate/colsurfa

Combined AFM and STXM in situ study of the influence of Eu(III) on the agglomeration of humic acid

Markus Plaschke [a,*], Jörg Rothe [a,*], Thorsten Schäfer [a], Melissa A. Denecke [a], Kathy Dardenne [a], Susanne Pompe [b], Karl-Heinz Heise [b]

[a] *Institut für Nukleare Entsorgung, Forschungszentrum Karlsruhe GmbH, Postfach 3640, D-76021 Karlsruhe, Germany*
[b] *Forschungszentrum Rossendorf, Institut für Radiochemie, Postfach 510119, D-01314 Dresden, Germany*

Received 19 March 2001; accepted 8 August 2001

Abstract

Humic acid (HA) agglomerates formed in aqueous solutions in the presence of trivalent Eu cations were investigated in situ with a combination of atomic force microscopy (AFM) and scanning transmission X-ray microscopy (STXM). The micromorphologies of both natural HA and a melanoidine based synthetic HA observed by AFM in electrolyte solution are in fair agreement with previous AFM studies on humic substances. STXM micrographs of Eu(III) induced HA agglomeration reveal zones of high and low optical density with markedly distinct *C* K-NEXAFS, indicative of different humic functionalities. Particulate agglomerates observed by AFM can be correlated to the dense zones, whereas fibrous structures in AFM images can be associated with the low density areas. The Eu cation distribution within the agglomerates cannot be unambiguously deduced from their *C* K-NEXAFS spectra. The near edge X-ray absorption fine structure spectra can be correlated to a segregation of different HA fractions, possibly due to the presence of humic species with different affinities for metal cation complexation. STXM micrographs of purified Aldrich HA exhibit the presence of other yet unidentified, carbon-rich particles, independent of the addition of Eu(III). Both AFM and STXM results for the synthetic melanoidine based HA demonstrate a homogeneous morphology and chemical structure.

Keywords: Humic acid; Synthetic humic acid; Atomic force microscopy; Scanning transmission X-ray microscopy; *C* K-NEXAFS

1. Introduction

Long term isolation and immobilization of long-lived radionuclides, especially actinide elements, is the major goal of nuclear waste repositories in geological formations. To ensure this goal, the impact of colloid-borne actinide transport in the geosphere must be understood. Actinide ions can form either 'eigen-colloids', or adsorb onto aquatic colloids formed by organic materials such as humic substances (HS) or inorganic materials such as hydrous ferric oxides (HFO) or clays. These colloids can be mobile in groundwater aquifers and thus enhance radionuclide migration [1].

* Corresponding author. Tel.: +49-7247-82-4747; fax: +49-7247-82-3927.
E-mail addresses: plaschke@ine.fzk.de (M. Plaschke), rothe@ine.fzk.de (J. Rothe).

0927-7757/02/$ - see front matter
PII: S0927-7757(01)00901-3

Aquatic HS are natural organic colloids with a high affinity for complexing metal cations. Although HS have been studied extensively for their environmental and biochemical importance, their high structural diversity has been a limiting factor in the search of their basic building blocks as well as in the understanding of their secondary structure [2]. Investigations of actinide binding properties of humic acids (HA) implicate carboxylate groups as the primary functional groups complexing metal ions [3,4]. However, variations in morphologies of the colloid sorbents are thought to be correlated to variations in their metal affinities. For example, the sorption properties of HS-inorganic mineral mixtures is often different than that observed for the separate pure phases [5,6]. This is attributed to a mineral surface coating by HS [7,8]. As the underlying processes are not understood in detail, the necessity for combining morphological studies with chemical, functional group information and their correlation to actinide sorption properties is obvious.

Atomic force microscopy (AFM) or scanning force microscopy is a scanning probe technique, which has already been employed to study the morphologies of humic and fulvic acids [9–15]. Compared to electron microscopy, AFM offers more flexibility in sample preparation, three-dimensional imaging and, in many cases, better image resolution. The advantage of scanning probe techniques is the ability to image microstructures not only on dried samples, but also in aqueous solutions, with a spatial resolution in the nanometer range. Thus, AFM is a valuable tool allowing to visualize small colloids, as well as colloid agglomeration, adsorption onto surfaces, or morphological changes affected by interaction with ions.

Non-contact mode AFM (or tapping-mode AFM) is a technique, which uses an oscillating cantilever to maintain a constant distance between the AFM tip and the sample surface [16]. This is preferable for investigations of soft materials (i.e., organic or biological), because lateral frictional forces between tip and sample are reduced in this mode. For this reason, the AFM results presented here were obtained using non-contact mode in aqueous electrolyte solution.

Recent publications of AFM studies on HS differ from one another in the humic material used and in sample preparation techniques. Soil and stream fulvic acids deposited on muscovite followed by air-drying were studied by Namjesnik-Dejanovic and Maurice [12,13]. Sponge-like structures, small spheres (10–50 nm in diameter, 2–10 nm in height), agglomerates of spheres, chain-like assemblies and perforated sheets were found. In situ investigations of purified commercial HA were performed in electrolyte solutions, showing humic particles (diameters 8–13 nm, heights 1–3 nm) to agglomerate in dependence of pH [9] and in the presence of polyvalent cations (e.g., Eu(III)) [10]. Similar observations were made by Balnois et al. investigating effects of pH and ionic strength on two different HA in air-dried samples [11]. Wilkinson et al. observed various structures of natural organic matter (NOM) and reference compounds. Particulate structures of HS (particle heights ~ 1 nm) and agglomerates, as well as fibrous structures originating from decomposition of natural polysaccharides were detected [14].

For the highly heterogeneous natural colloidal systems, morphological characterization is not sufficient to distinguish between different colloid species. Therefore, in this study, AFM investigations were combined with a complementary scanning technique, scanning transmission X-ray microscopy (STXM). Employing diffractive Fresnel zone plate lenses as focussing optics, STXM is an ideal tool for obtaining both morphological and chemical state information in situ on aqueous colloid species within the 'water window' (i.e., between the *C* K and *O* K absorption edges at 284 and 537 eV, respectively). The spatial resolution of STXM allows imaging of structures with dimensions ranging from sub-micron to several microns.

By varying the energy of the incident radiation, the absorption contrast can be tuned to reveal the spatial distribution of a selected element, as well as its chemical state [17]. As shown in a previous study, differentiation of inorganic from organic components and visualization of their interaction is possible through comparison of micrograph images recorded at photon energies above and

below the *C* K absorption edge [18]. Simultaneously, the high energy resolution of near edge X-ray absorption fine structure (NEXAFS) in the soft X-ray regime provides a tool for direct speciation of carbon containing macromolecules from characteristic spectral transition resonances. Following changes in *C* K-NEXAFS associated with actinide complexation onto HS will aid in identifying HS functional groups involved in cation binding.

Despite these advantages, only a few reports of X-ray microscopy on NOM have been published [18–20]. For example, in an earlier investigation it was observed that HA agglomerates formed at pH 4.4 appear in STXM micrographs as both globular and filament-type particles, with only very diffuse contours and dimensions in the μm range [18]. The *C* K-NEXAFS of these agglomerates revealed electronic transitions, which were identified as fingerprints of carbon containing functional groups and structural elements (phenyl groups, C = O). The assignment of the individual carbon peaks to functional groups was based on comparison to spectra of known organic compounds reported in the literature [21,22]: phenyl group; π_1^* (aromatic carbon)—284.8 eV, carboxyl group; π^* (C = O)—288.4 eV, phenyl group; σ_1^* (aromatic carbon)—293.0 eV. In mixed suspensions containing both HA and montmorillonite clay colloids, HA was always associated with the mineral component, i.e., no separate clustering of HA was found [18]. STXM images of HA + clay at near-neutral pH conditions showed HA to coat the clay surface, leading to a fractal-like manner of agglomeration. These agglomerates appear no longer as diffuse structures, but exhibit remarkably sharp contours.

This paper presents results obtained from combining two scanning imaging techniques, STXM and AFM, in investigations of the chemical species and micromorphologies of HA complexed with Eu(III) (as a homologue for trivalent actinide cations). Both purified Aldrich HA and a melanoidine based synthetic HA, designated as 'M42' [23], were used. M42 is made from xylose, a reducing sugar, and glutamic acid, a monoamino dicarboxylic acid. In many respects, M42 is known to behave chemically similar to natural HA, e.g., its proton exchange capacity was determined to 3.9 ± 0.18 meq g^{-1}, which is comparable to natural HA [23].

The objective of these AFM and STXM investigations was to identify HA functional groups involved in actinide cation binding and to associate morphological structures with cation complexation. The AFM studies compared the micromorphology of HA agglomerates formed following addition of Eu(III) and sorbed onto natural muscovite to those formed using M42. Parallel STXM investigations were performed and extended to include recording *C* K-NEXAFS for both the HA/Eu(III) and the M42/Eu(III) samples. In addition, comparative STXM studies of mixed colloidal suspensions of HA and HFO were carried out.

2. Experimental section

2.1. Sample preparation

The compositions of the experimental systems under investigation in this study are summarized in Table 1. All chemicals used in this study were analytical grade, unless mentioned otherwise. Commercial HA (Aldrich, Steinheim, Germany) was purified according to a procedure described by Kim and Buckau [24]. The HA proton exchange capacity, determined by potentiometric pH titration, is 5.43 ± 0.16 meq g^{-1} [24]. A stock solution of 200 mg l^{-1} HA, with an electrolyte content of 0.1 mol l^{-1} NaCl (Merck suprapur, Darmstadt, Germany), was prepared, adjusted to pH 6.0 and stored at 5 °C. Sample solutions for AFM were prepared by diluting the stock solution to a HA content of 100 mg l^{-1}, adding the desired amount of a Eu(III) solution and adjusting to the required pH. All measurements were performed in an electrolyte solution with an ionic strength of 0.1 mol l^{-1} NaCl, at a pH between 5.3 and 6.

The amount of Eu(III) (ICP-AES standard, Johnson Matthey GmbH, Karlsruhe, Germany, diluted to 6.3×10^{-3} mol l^{-1}, pH adjusted to 4.2) added to aliquots of the HA stock solutions for STXM samples was calculated to saturate the

total loading capacity of Aldrich HA [25]. After addition of Eu(III), rapid flocculation and sedimentation of the colloidal suspensions was observed. Mounting large flocs from the HA/Eu(III) solutions into STXM sample cells was avoided by pipetting 1 μl aliquots of the suspension located above the settled agglomerates.

The preparation of 6-line HFO is reported elsewhere [26].

2.2. Soft X-ray spectromicroscopy

Soft X-ray spectromicroscopy investigations of HA were performed at the STXM endstation (X1A Outboard-STXM) at the National Synchrotron Light Source, Brookhaven, NY [27]. All samples were investigated as a thin film of colloid suspension in a fully hydrated state using silicon nitride wet cells. The sample preparation technique for STXM measurements has been described elsewhere [28].

STXM images of HA agglomerates formed following addition of Eu(III) and of agglomerates found in mixed suspensions of HA/HFO were recorded. Changes in the *C* K-NEXAFS upon Eu(III) cation complexation by HA and M42 at a pH value of 5.5 were recorded and compared to *C* K-NEXAFS of both HA agglomerates at low pH and HA/HFO agglomerates. The STXM images of the pure solution of Aldrich HA at pH 5.5 already showed some very dense particles. In order to generate HA agglomerates for STXM investigations, either addition of HFO or Eu(III) solution was necessary at the concentrations and ionic strength given in these sample systems.

Colloid suspensions containing HA were adjusted to near-neutral pH (5.3–5.5) in order to minimize effects on the *C* K-NEXAFS possibly exerted by conformational changes and/or variations in the overall molecular charge, due to protonation/deprotonation of HA functional groups. This was to separate spectral variations caused by complexation of Eu(III) from those associated with protonation/deprotonation of HA carboxyl groups.

At the X1A Outboard-STXM, a Fresnel zone plate was used to focus the undulator beam into a spot of soft X-rays. The zone plate had a diameter of 160 μm and a width of 45 nm of the outer most ring segment, giving a resolution (Rayleigh criterion) of 55 nm [29]. The STXM endstation provides a flux of about 10^7 photons s^{-1}, with an energy bandwidth of about 0.1 eV at the *C* K-edge [30]. The spherical grating monochromator was calibrated against the *C* K absorption threshold resonance of carbon dioxide at 292.76 eV [31].

Stacks of images from selected sample regions were recorded as a function of incident photon energy *E*. *C* K-NEXAFS spectra were extracted through the analysis of the absorption variation, $\mu(E) \times d = \ln(I_0(E)/I(E))$, of vertical projections onto aligned image stacks. Image regions free of particles supply information on the I_0-signal. The transmitted intensity (I) is derived from image regions containing particles of interest. For a review of the procedure for image stack data analysis, see [32]. All *C* K-NEXAFS spectra were obtained from stacks of 210 images, recorded at *E*

Table 1
Colloid suspension content, concentrations and pH values for STXM and AEM sample systems

Sample	Method	Concentration	pH, I = 0.1 mol l^{-1} NaCl
HA	STXM	200 mg l^{-1}	5.3
	AFM	l00 mg l^{-1}	6.0
M42	AFM	200 mg l^{-1}	5.5
HA/HFO	STXM	80 mg l^{-1} (HA), 770 mg l^{-1} (HFO)	5.5
M42/HFO	STXM	80 mg l^{-1} (M42), 770 mg l^{-1} (HFO)	5.5
HA/Eu(III)	STXM	190 mg l^{-1} (HA), 3.2×10^{-4} mol l^{-1} (Eu(III))	5.5
	AFM	100 mg l^{-1} (HA), 1×10^{-5} mol l^{-1} (Eu(III))	6.0
M42/Eu(III)	STXM	190 mg l^{-1} (M42), 3.2×10^{-4} mol l^{-1} (Eu(III))	5.5
	AFM	200 mg l^{-1} (M42), $1 \times l0^{-5}$ mol l^{-1} (Eu(III))	5.5

ranging between 275 and 310 eV. E was varied for recording images in 1 eV steps in the range 275–282 eV, in 0.1 eV steps for 282–300 eV, and in 0.5 eV steps at energies 300–309 eV. A linear pre-edge background (275–280 eV) was subtracted from the extracted spectra, followed by normalization ($\mu \times d = 1$) at 305 eV.

2.3. Atomic force microscopy

Pieces of natural muscovite (Piano, Wetzlar, Germany) with dimensions of $\sim 1 \times 2$ cm^2 were freshly cleaved and placed in polypropylene sample beakers containing the sample suspensions. The mica sheets were positioned vertically in order to avoid deposition of agglomerates by sedimentation. Colloids were allowed to adsorb from the solution onto the mica surface for a period of 24 h ($T = 22$ °C). The mica was then withdrawn from the solution and rinsed with de-ionized water in order to remove any non-sorbed HA. AFM measurements were performed in 0.1 mol l^{-1} NaCl solution containing the same Eu(III) concentration used for the sorption experiment. This solution was free of HA colloids, because high colloid concentrations in solution would disturb the imaging process.

Non-contact mode AFM imaging was performed in electrolyte solution using a Topometrix TMX 2000 Explorer, which was equipped with cantilever oscillating hardware. Triangular probes with silicon nitride tips (radius < 50 nm; nominal resonance frequency 17 kHz, cantilever spring constant about 0.06 N m^{-1}) were mounted on a liquid scanner with a maximum range of 2.3 μm in the x–y-direction and 900 nm in the z-direction.

3. Results

3.1. Soft X-ray spectromicroscopy

Agglomerates in the HA/HFO suspension appear very dark and dense above the *C* K edge (Fig. 1) with less distinct contours than those previously observed for HA + clay agglomerates [18]. These dark agglomerates are not observed in images of HFO alone (not shown). The *C* K-NEXAFS of the HA/HFO agglomerates is depicted in Fig. 2(a). The absorption spectrum is invariant to the position on particles in the image stack, from which it was extracted. The HA/HFO *C* K-NEXAFS is nearly indistinguishable from that of a pure HA agglomerate reported in [18].

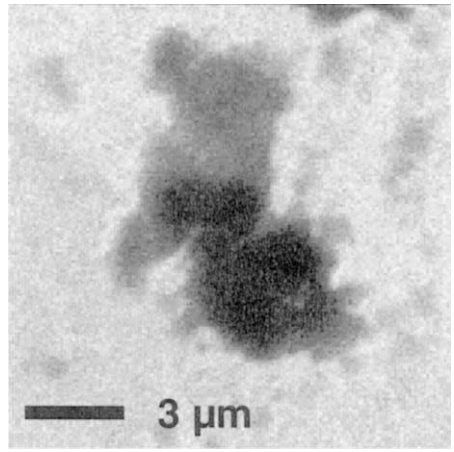

Fig. 1. STXM image of Aldrich HA/HFO agglomerate recorded at 288.7 eV.

If metal cation complexation is selectively mediated by specific HA functional groups such as carboxylate groups, changes in the corresponding HA *C* K-NEXAFS 1s → π* transition peak might be expected upon complexation. However, instead of mere intensity and/or energy changes in the 288.4 eV NEXAFS feature assigned to carboxylate functions, the micrographs indicate segregation of different HA species upon Eu cation-mediated HA agglomeration. A STXM micrograph (150×150 pixel, 200 nm x/y step width) of one of these agglomerates, with typical diameters of several μm, is depicted in Fig. 3. The image shows darker, dense patches of organic material dispersed in lighter, less dense regions with nearly one third of the absorption. Pixel for pixel extraction of NEXAFS spectra from the aligned image stacks reveals that these dark and light regions have differing *C* K-NEXAFS. The dark patches exhibit a NEXAFS spectrum (Fig. 2(b)) similar to both that recorded for the HA/HFO suspension (Fig. 2(a)) and the HA alone. Two additional absorption peaks, not observed in the other HA spectra, appear at 282.4 and 286.5 eV in the

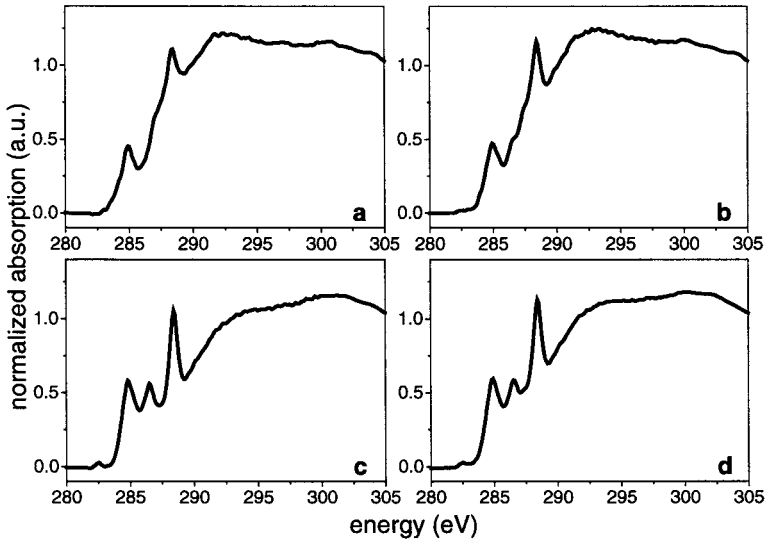

Fig. 2. *C* K-NEXAFS of (a) Aldrich HA/HFO agglomerates (agglomerates in Fig. 1), (b) Aldrich HA agglomerates formed following Eu(III) complexation (dark regions in Fig. 3), (c) Aldrich HA agglomerates formed following Eu(III) complexation (light regions in Fig. 3), (d) spatially averaged spectrum extracted from the entire agglomerate in Fig. 3.

NEXAFS (Fig. 2(c)) extracted from the lighter regions of the image in Fig. 3. Moreover, the intensity of the carboxylate peak at 288.4 eV remains almost unaffected by the Eu complexation, within the error introduced by spectrum normalization. This peak appears more exposed in Fig. 2(c) due to intensity loss in the broad 'shape' resonance above 290 eV. For comparison, an average spectrum, as it would have been recorded with spatial resolution less than 200 nm, is shown in Fig. 2(d). Had the NEXAFS been extracted from a large agglomerate at a lower resolution, then only a change in the spectra following Eu(III) complexation would have been observed; the similarity of the NEXAFS of the dark regions to HA alone would have remained undetected.

In contrast to the natural HA, homogeneous agglomerates of M42 are observed in STXM micrographs following addition of Eu(III); there is no separation into dense and less dense areas. This likely reflects the greater homogeneity of M42 compared to natural HA [33]. The *C* K-NEXAFS for M42 shown in Fig. 5(a) differs from that obtained for natural HA. The lower amplitude of resonances at 284.8 and 293 eV in the spectrum reflects the low amount of phenyl groups in the melanoidine based compound. This is due to the low aromatic content in the precursors used in the M42 synthesis. However, there is a similarity of the spectral trends observed upon addition of Eu(III) to both the Aldrich HA and to M42, the 286.5 eV peak intensity increases. Simi-lar to the observation for the Aldrich HA, the carboxylate peak near 288 eV is nearly unaffected by the interaction with Eu cations (Fig. 5(b)).

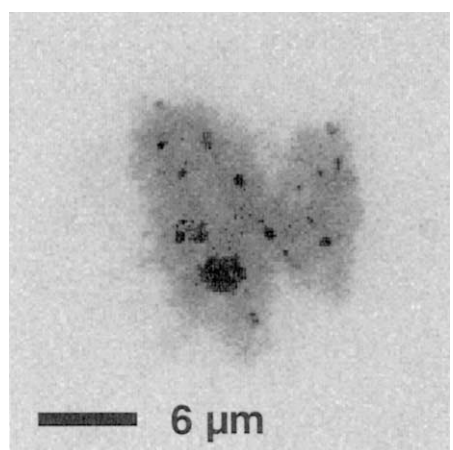

Fig. 3. STXM image of Aldrich HA agglomerate formed after addition of Eu(III), recorded at 288.7 eV.

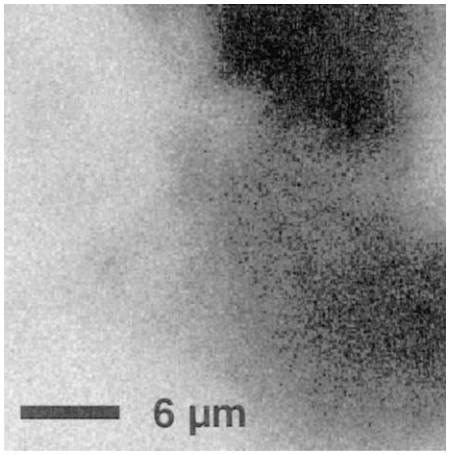

Fig. 4. STXM image of M42 agglomerate formed after addition of Eu(III), recorded at 288.7 eV.

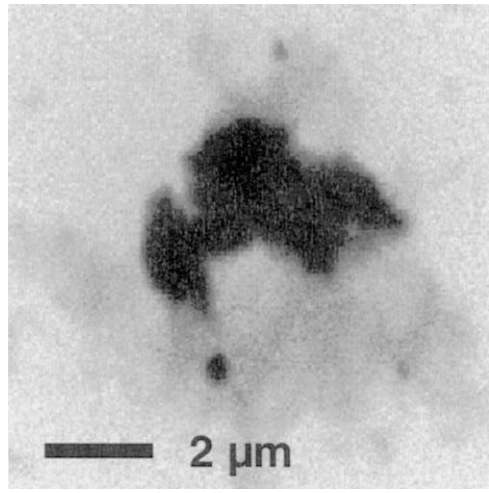

Fig. 6. STXM image (288.7 eV) showing persistent dense, carbon-rich particles in a mixture of Aldrich HA/HFO.

The observation of an additional type of particles—already present in solutions of Aldrich HA before Eu(III) complexation or addition of HFO—was mentioned above. An example for the morphology of these dense, strongly absorbing carbon-rich particles is shown in Fig. 6. In this example, the particles appear as dense structures, surrounded by HFO particles (note that these carbon-rich particles are observed prior to HFO addition). The HFO appears as diffuse, light structures, due to their higher transparency at 288.7 eV. These dense particles exhibit only saturated NEXAFS spectra with markedly dampened features, thus they cannot be unambiguously identified as HS.

3.2. Atomic force microscopy

The agglomeration of purified Aldrich HA induced by Eu(III) cations was subject of a previous study [10]. Typical HA morphologies in the presence of Eu(III), at a concentration of 10^{-5} mol l^{-1}, are shown in Fig. 7. Large agglomerates are observed, which partially combine with one another. The agglomerates show lateral dimensions up to 300 nm and maximum heights in the range from 4 to 20 nm. These are distinctly higher than particles observed in the absence of Eu(III) [10]. In Fig. 7, the well-resolved morphology of Eu(III)-complexed HA agglomerates is an apparent arrangement of smaller particles, indicating agglomeration of HA particles as subunits. In-

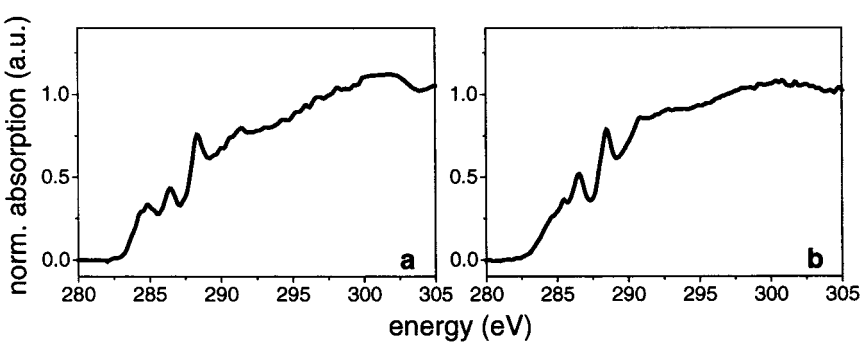

Fig. 5. *C* K-NEXAFS of (a) M42/HFO agglomerates, (b) M42 agglomerates after Eu(III) complexation.

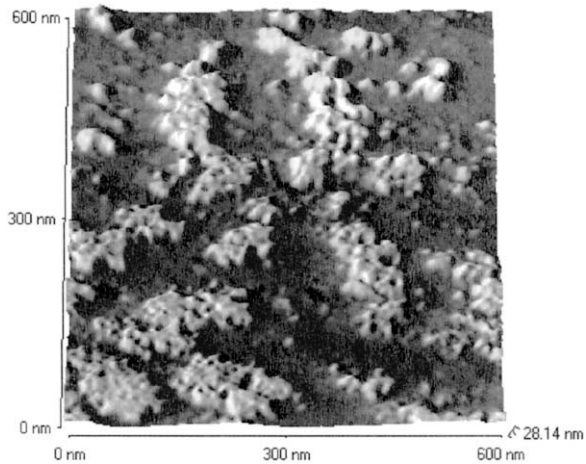

Fig. 7. AFM image of Aldrich HA sorbed onto mica in the presence of 10^{-5} mol l^{-1} Eu(III): agglomerated particles [11] (height scale 0–28 nm).

creased agglomeration and sorption of HA onto mineral surfaces induced by Eu(III) cations is supported by surface force measurements [10].

The surface structures in the same sample were found to be heterogeneous: separated from the particulate agglomerates additional fibrous structures were observed. These fibrous structures appear in the AFM image, depicted in Fig. 8, arranged nearly parallel without crossing each other. These kind of structures can be easily removed by the AFM tip, as shown in Fig. 9 for a

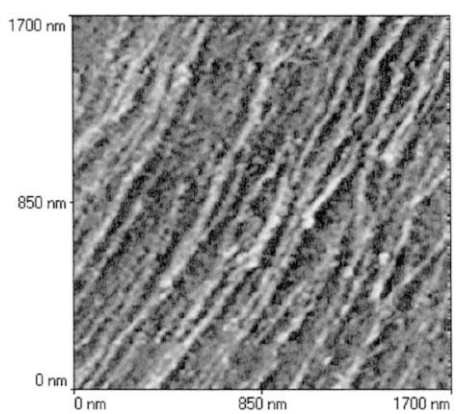

Fig. 8. AFM image of Aldrich HA sorbed onto mica in the presence of 10^{-5} mol l^{-1} Eu(III): fibrous structures (height scale 0–3.4 nm).

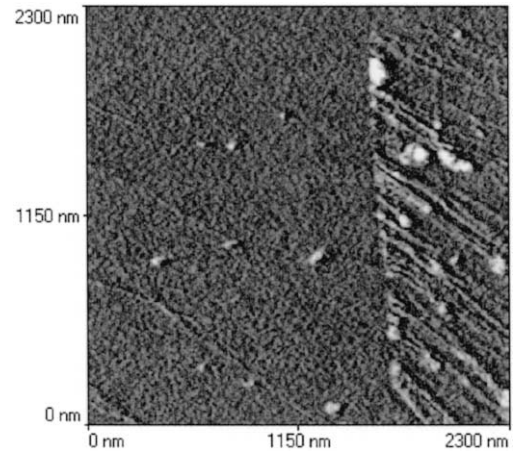

Fig. 9. AFM image of a natural HA sorbed onto mica in the presence of 10^{-5} mol l^{-1} Eu(III): fibrous structures are shown to be removed by the cantilever tip at left part of the image (height scale 0–17 nm).

similar sample. The left part of the image in Fig. 9 had been previously scanned at a higher loading force. It is evident that many fibrous structures were completely removed, whereas some larger particles remained on the surface. Therefore, weakly bound, fibrous structures actually present on the surface may be inadvertently removed and remain unobserved in the AFM images; they are not AFM image artifacts.

The synthetic model HA M 42 was investigated under the same experimental condition as the Aldrich HA. An in situ AFM image of this material sorbed onto mica can be seen in Fig. 10. Both particles with apparent diameters of 20–40 nm and heights of 2–5 nm and fibrous-like structures with lengths in the 150 nm range and diameters in the 10 nm range are visible. In the presence of 10^{-5} mol l^{-1} Eu(III) cations, the material forms widely branched, sponge-like structures covering the mica surface. This is depicted in Fig. 11. The pores of these structures have diameters in the range of 20–50 nm and the height of the HA microstructure is in the range of 1–2.5 nm. Particles and fibers are indistinguishable from one another in the sponge-like structure. This diffuse network of M42 dominates the micromorphology of the synthetic HA under the conditions applied in our investigation. Only a few agglomerated

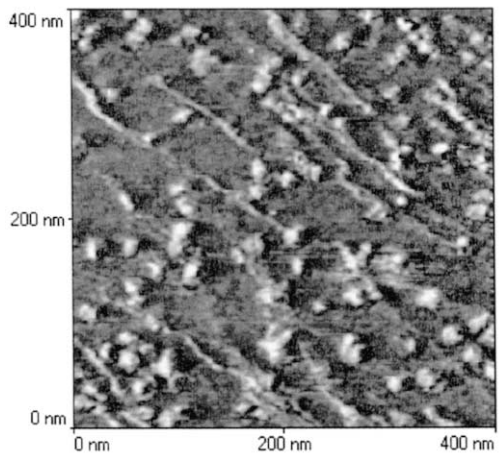

Fig. 10. AFM image of the M42 sorbed onto mica: particulate and fibrous structures (height scale 0–12 nm).

large particles were observed (diameter ~80 nm, height ~8 nm, Fig. 11(a)).

4. Discussion

Variable micromorphologies, both particulate and fibrous structures, of hydrated HA complexed with Eu(III) are observed by AFM. This is in agreement with previous studies reporting on various HA micro-structures, such as small spheres, agglomerates of spheres, sponge-like structures, chain-like assemblies or 'perforated sheets' [13,14]. The well-resolved morphology of HA/Eu(III) agglomerates sorbed onto mica reveals that they are partly composed of smaller particles. Humic particles appear to agglomerate, resulting in more dense species (Fig. 7). In contrast, the fibrous structures observed to form are flat, showing a nearly parallel organization with very little branching (Fig. 8). The parallel organization of the fibers may possibly be due to repulsive interactions between them. The lack of branching may indicate that there is a lack of binding sites for fiber-attachment, which would allow more branched structures to form. The fibrous structures are presumably less dense than the agglomerated particles.

The synthetic M42 exhibits a micromorphology somewhat different than that observed for the natural HA; in addition to small particles, short fibers are observed in their AFM micrographs (Fig. 10). In contrast to that, in the presence of Eu(III) highly branched structures form, resulting in a network covering the mineral surface (Fig. 11). This HA network exhibits a uniform, sponge-like morphology, enclosing only a few larger particles (Fig. 11(a)). This behavior may be due to the more homogeneous chemical nature of the synthetic M42, compared to that of natural HA.

It is a key question of our study, whether these morphological differences indicate a difference in

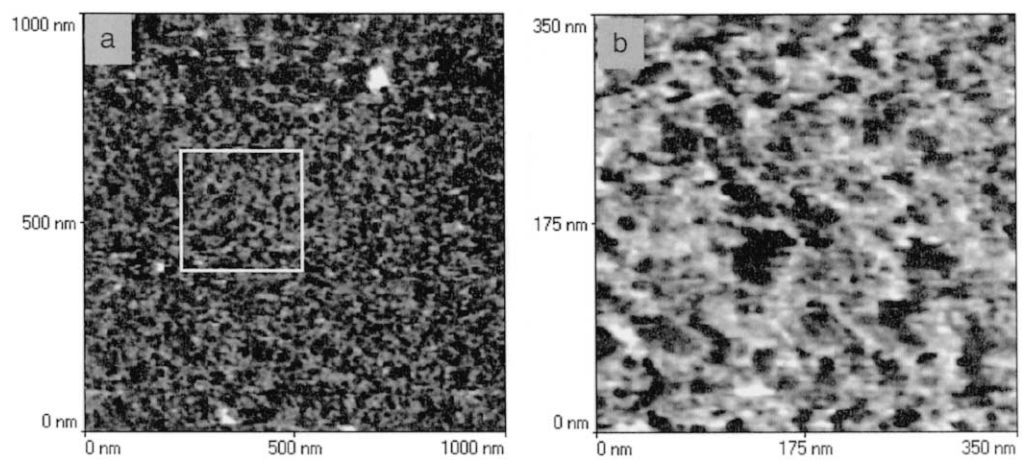

Fig. 11. AFM image of M42 sorbed onto mica in the presence of 10^{-5} mol l^{-1} Eu(III): sponge-like structures are covering the surface; different magnifications in images (a) and (b) (height scale (a) 0–15 nm, (b) 0–6 nm).

the chemical functionalities of the species. This may effect the physiochemical behavior of humic colloids, e.g., binding forces to the mineral surfaces, complexation of metal ions, or agglomeration behavior. Two regions in HA/Eu(III) agglomerates with different spectral features can be derived from the STXM micrographs and the NEXAFS measurements. The *C* K-NEXAFS spectrum of the light, less-dense regions of agglomerates (Fig. 2(c)) resembles that reported by Schmidt et al. for aqueous colloids of a natural soil HA [34]. Comparison to spectra of known organic compounds reported in the literature allows tentative assignment of the absorption peak at 286.5 eV to aliphatic $-CH_3$ and $-CH_2-$ groups [21]. However, these functional groups are not expected to be involved in metal cation complexation. The observed decrease of the broad resonance between 290 and 295 eV following complexation in the agglomerate light regions might reflect a decrease in the amount of aromatic groups present in these regions. The separation of HA into light and dark regions with varying amounts of aliphatic and aromatic carbon groups probably induced by Eu(III) may be equivalent to segregation of structurally dissimilar HA.

Previous gel permeation chromatography (GPC) investigations by Kim et al. disclosed the presence of different size fractions in purified Aldrich HA and in HA obtained from groundwater ('Gohy-573', Gorleben, Germany) [24]. IR-spectra of the different fractions indicate that the minor fraction of larger molecular size contains a relatively low amount of carboxyl groups compared to the smaller molecular size fraction. The major fraction of smaller molecular size presumably contains a number of different species. The observed segregation of HA species in the STXM may reflect a separation within this HA fraction, whereas the minor, high molecular weight fraction detected by GPC might be correlated to the persistent dense particles in Fig. 6.

At neutral pH conditions, loading HA with multivalent metal cations is expected to compensate for the HA molecule overall negative charge. The changes in molecular charge reduces the inter-particular repulsion forces affecting their agglomeration. In addition, it may stimulate intra-particular rearrangement, such as folding and coiling of HA to more dense agglomerates. Hence one would expect the dark regions in Fig. 3 to be enriched in HA species with a high affinity for Eu(III), whereas those with a lower affinity remain less densely agglomerated and uncoiled to form the surrounding lighter, less dense matrix. However, the *C* K-NEXAFS of the dark regions does not directly reflect Eu(III) complexation. Likewise, no distinct spectral changes are observed for HA–HFO interaction, compared to the HA alone. The differences in the NEXAFS of the dark and light regions in the Eu(III)–HA agglomerates reflects rather a species separation.

The STXM micrograph of M42 agglomerates formed after addition of Eu(III) shows formation of homogeneous agglomerates (Fig. 4) without separation into dense and less dense areas. This corroborates the interpretation of the AFM results that the model compound morphology reflects its being chemically more homogeneous compared to natural HA.

5. Summary and conclusions

This investigation into the micromorphology and the chemical functionality of HA complexed with Eu(III) benefits from two state of the art microscopy techniques. Combining the high spatial resolution of AFM with the chemical sensitivity of STXM provides complementary information. Both methods together disclose regions in samples containing HA–Eu(III) complexes, which markedly differ in their micomorphology and chemical functionality. The dark regions in STXM micrographs may be equivalent to the dense agglomerates found by AFM, whereas the light regions observed by STXM may be correlated to the less dense, fibrous regions observed in AFM images. The different morphologies observed likely result from HA species with different cation affinities. That no separation into dark and light regions in STXM images occurs for the homogeneous M42 supports this hypothesis. The morphology observed by AFM for M42 following complexation with Eu(III) is a uniform, sponge-like network,

reflecting the homogeneous chemical composition of this model compound. One important area for future study is to provide experimental evidence for the hypothesis that the dense regions observed in the HA/Eu(III) agglomerates are regions of high metal cation affinity. Any detection of the enrichment of Eu in the dense regions of the agglomerate would support this hypothesis.

Natural HA is a heterogeneous material with a distribution of chemical functional groups. Combination of AFM and STXM results show that this heterogeneity leads to at least two particle micromorphologies or HA fractions upon complexation with Eu(III) cations. Both large particle agglomerates and fibrous structures are formed. Although the formation of the different HA agglomerates is induced by the addition of the trivalent cations, no unambiguous conclusions as to if, or how, Eu(III) is distributed among the two HA fractions can be made. Additionally, STXM micrographs of natural Aldrich HA exhibit the presence of other yet unidentified, carbon-rich particles, independent of the addition of Eu(III) or HFO.

As shown in our previous study and in X-ray microscopy work published by Thieme et al. [20] and Myneni et al. [19], the interaction of HA and mineral colloids such as HFO induces drastic changes in colloid morphology of the binary systems. From comparison of the *C* K-NEXAFS of the HA/HFO agglomerates to HA alone, we conclude that this interaction does not measurably effect the HA macromolecule functionality. Although introduction of HFO colloids to HA leads to their agglomeration, whereby the HA appears dense in STXM images and in intimate contact with the inorganic colloids, the HA *C* K-NEXAFS does not undergo any distinct changes. The question arises, to what extent sorption of metal cations onto such systems are influenced by the morphology of the sorbent substrates.

Further investigation should be helpful in understanding the reversibility of the HA cation complexation after prolonged contact times [35]. Investigations to follow the time-dependent behavior of the morphology and *C* K-NEXAFS of the Eu(III)–HA agglomerates, as well as the changes induced by a systematic variation of the solution parameters pH, ionic strength, and metal cation concentration, are planned. Because the origin of the spectral changes between the different HA regions observed in this study is yet unclear, the analysis of well-characterized model compounds will aid continued understanding of HA metal complexation reactions. For example, interpretation of the NEXAFS carboxyl peak intensity through comparison of spectra from known mono- and bidentate organic-metal complexes will be possible.

Acknowledgements

We are grateful for beam-time allotment by BNL/NSLS and assistance from SUNY-Stony Brook X-ray Microscopy Group. Special thanks to S. Wirick and C. Jacobsen. G. Buckau is acknowledged for helpful discussion. The Aldrich HA was purified and kindly provided by T. Rabung.

References

[1] J.I. Kim, MRS Bulletin 19 (12) (1994) 47.
[2] L.T. Sein Jr., J.M. Varnum, S.A. Jansen, Environ. Sci. Technol. 33 (1999) 546.
[3] M.A. Denecke, D. Bublitz, J.I. Kim, H. Moll, I. Farkes, J. Synchrotron Rad. 6 (1999) 394.
[4] M.A. Denecke, T. Reich, S. Pompe, M. Bubner, K.-H. Heise, H. Nitsche, P.G. Allen, J.J. Bucher, N.M. Edelstein, D.K. Shuh, K.R. Czerwinski, Radiochim. Acta 82 (1998) 103.
[5] T. Zuyi, C. Taiwei, D. Jinzhou, D. Xiong Xin, G. Yingjie, Appl. Geochem. 15 (2000) 133.
[6] Th. Rabung, Einfluss von Huminstoffen auf die Europium(III)-Sorption an Hämatit, PhD Thesis, Universität Saarbrücken, Germany, 1998.
[7] G. Sposito, The Surface Chemistry of Soils, Oxford University Press, New York, 1984 Chapter 4.
[8] R. Kretzmar, D. Hesterberg, H. Sticher, Soil Sci. Soc. Am. 61 (1997) 101.
[9] M. Plaschke, J. Römer, R. Klenze, J.I. Kim, Colloids Surf. A 160 (1999) 269.
[10] M. Plaschke, J. Römer, R. Klenze, J.I. Kim, Surf. Interface Sci. 30 (2000) 293.
[11] E. Balnois, K.J. Wilkinson, J.R. Lead, J. Buffle, Environ. Sci. Technol. 33 (1999) 3911.
[12] P.A. Maurice, Colloids Surf. A 107 (1996) 57.
[13] K. Namjesnik-Dejanovic, P.A. Maurice, Colloids Surf. A 120 (1997) 77.
[14] K.J. Wilkinson, E. Balnois, G.C. Leppard, J. Buffle, Colloids Surf. A 155 (1999) 287.

[15] M. Mertig, D. Klemm, W. Pompe, H. Zänker, M. Böttger, Surf. Interface Anal. 27 (1999) 426.
[16] P.K. Hansma, J.P. Cleveland, M. Radmacher, D.A. Walters, P.E. Hillner, M. Bezanilla, M. Fritz, D. Vie, H.G. Hansma, C.B. Prater, J. Massie, L. Fukunaga, J. Gurley, V. Elings, Appl. Phys. Lett. 64 (13) (1994) 1738.
[17] J. Rothe, F.M. Kneedler, K. Pecher, B.P. Tonner, K.H. Nealson, T. Grundl, W. Meyer-Ilise, T. Warwick, J. Synchrotron Rad. 6 (1999) 359.
[18] J. Rothe, M.A. Denecke, K. Dardenne, J. Colloid Interface Sci. 231 (2000) 91.
[19] S.C.B. Myneni, J.T. Brown, G.A. Martinez, W. Meyer-Ilse, Science 286 (1999) 1335.
[20] J. Thieme, J. Niemeyer, Progr. Colloid Polym. Sci. 111 (1998) 193.
[21] I. Ishii, A.P. Hitchcock, J. Electron Spectroscopy Relat. Phenomena 46 (1988) 55.
[22] H. Ade, D.A. Winesett, A.P. Smith, S. Qu, S. Ge, J. Sokolov, M. Rafailovich, Europhys. Lett. 45 (4) (1999) 526.
[23] S. Pompe, A. Brachmann, M. Bubner, G. Geipel, K.-H. Heise, G. Bernhard, H. Nitsche, Radiochim. Acta 82 (1998) 89.
[24] J.I. Kim, G. Buckau, G.H. Li, H. Duschner, N. Psarros, J. Fresenius, Anal. Chem. 338 (1990) 245.
[25] J.I. Kim, D.-S. Rhee, G. Buckau, Radiochim. Acta 53 (1991) 49.
[26] U. Schwertmann, R.M. Cornell, Iron Oxides in the Laboratory, VCH, Weinheim, 1991 Chapter 8.
[27] C. Jacobsen, S. Williams, E. Anderson, M.T. Browne, C.J. Buckley, D. Kern, J. Kirz, M. Rivers, X. Zhang, Opt. Commun. 86 (1991) 351.
[28] U. Neuhäusler, S. Abend, C. Jacobsen, G. Lagaly, Colloid Polym. Sci. 277 (1999) 719.
[29] S. Spector, C. Jacobsen, D. Tennant, in: J. Thieme, G. Schmahl, E. Umbach, D. Rudolph (Eds.), X-ray microscopy and spectromicroscopy, Springer, Heidelberg, 1998.
[30] B. Winn, H. Ade, C. Buckley, M. Howells, S. Hulbert, C. Jacobsen, J. Kirz, I. McNulty, J. Miao, T. Oversluizen, I. Pogorelsky, S. Wirick, Rev. Sci. Instrum. 67 (1996) 1.
[31] A.P. Hitchcock, D.C. Mancini, J. Electron Spectroscopy 67 (1994) 1.
[32] Stack software manual in http://xrayl physics.sunysb.edu/~jacobsen/stack/stack.html.
[33] S. Pompe, M. Bubner, M.A. Denecke, T. Reich, A. Brachmann, G. Geipel, R. Nicolai, K.H. Heise, H. Nitsche, Radiochim. Acta 74 (1996) 135.
[34] C. Schmidt, J. Thieme, U. Neuhäusler, U. Schulte-Ebbert, G. Abbt-Braun, C. Specht, C. Jacobsen. In: W. Meyer-Ilse, T. Warwick, D. Attwood (Eds.), Proceedings 6 Intl. Conf. X-Ray Microscopy, Berkeley, California, August 1999, American Institute of Physics, 2000.
[35] G. Buckau (Ed.), Effects of Humic Substances on the Migration of Radionuclides: Complexation and Transport of Actinides (Final Report), Report EUR 19610 EN, 2000.

5.0 Conclusions

In order to understand and especially predict over historical or even geological timescales the migration behaviour of hazardous metals (i.e. radionuclides) in the geosphere the fundamental processes of metal mobilization/retention have to be clarified. For example, the comparison between calculated Am(III) column distributions deviate by almost a factor of 10 in peak arrival from the experimental data (Artinger et al., 2002b) although the principle trend and the shape of the breakthrough curves is reproduced by the model (Figure 8). The deviation is probably due to an oversimplified treatment of the Am(III) sand surface interaction, which leads to an underestimation of the Am(III) mobility.

This example shows clearly, that the metal mineral-water interface processes as shown schematically in Figure 9 and the kinetics involved have to be understood on a molecular level in order to reliable predict the retention behaviour in the near and far-field of a nuclear waste repository over historical and even geological timescales.

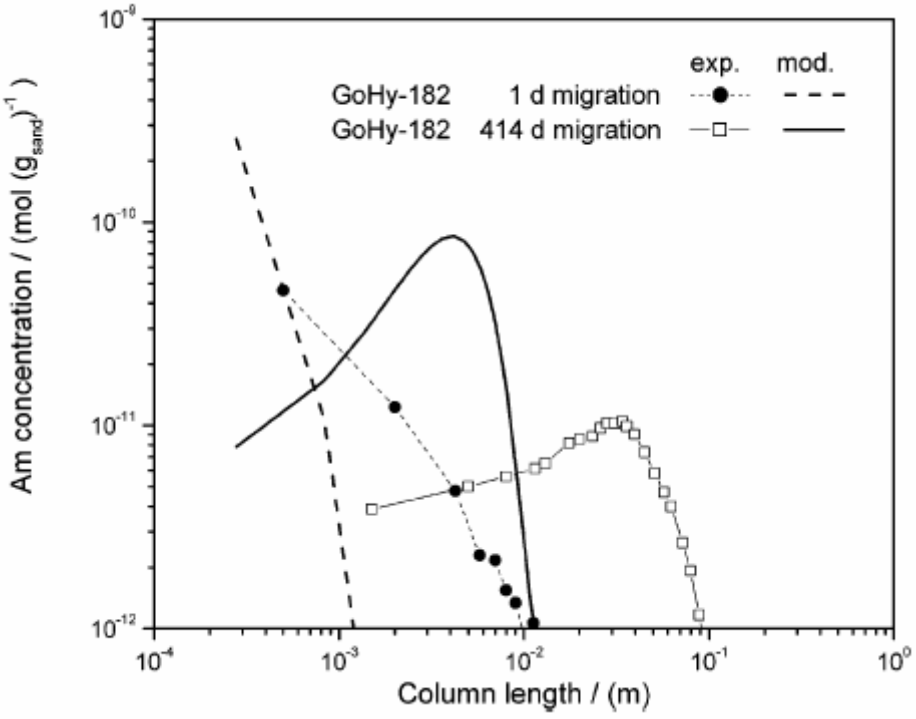

Figure 8: *Comparison of experimental data obtained and values calculated using the K1D code (Schuessler et al., 2001) and KICAM for the Am distribution in the sand columns (Artinger et al., 2002b).*

The manuscript pinpoints approaches by applying various synchrotron- or laser- based spectroscopic and microscopic techniques to elucidate underlying fundamental interaction mechanisms. For example, solely based on surface complexation modelling of isotherm data no mechanistic conclusions on trivalent lanthanide/actinide ferrihydrite surface complexes could

be drawn. In combination with molecular level X-ray absorption spectroscopy data it was possible to identify the surface complex and implement the gained knowledge in the advanced modelling exercise (Dardenne et al., 2001). Another example are the observed actinide-smectite desorption kinetics in the migration studies of the CRR experiment. The tailing of the migration experiment breakthrough curves indicated a reversibility of sorption and additional time resolved laser fluorescence spectroscopy measurements could indeed show a slow reversible inner sphere complexation of trivalent actinides (Cm^{3+}). Furthermore, the spectroscopic studies showed no evidence for actinide smectite incorporation (irreversible association), which is a very important information for the long-term actinide mobility estimations.

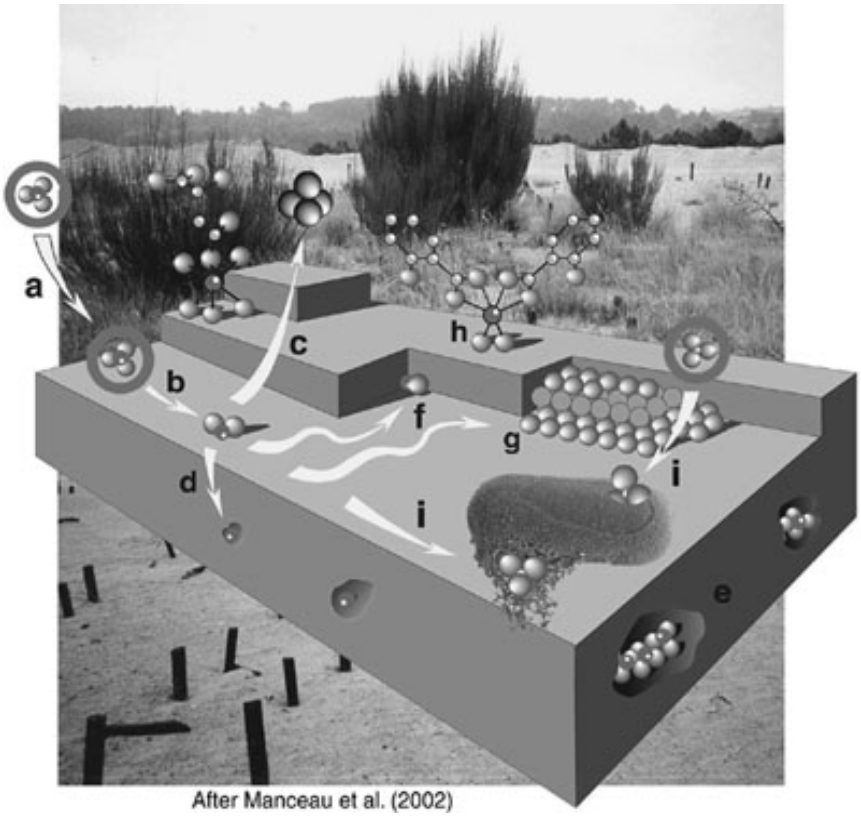

Figure 9: *Schematic overview of mineral-metal interaction processes: a) physisorption; b) chemisorption; c) detachment; d) absorption or inclusion (impurity ion that has a size and charge similar to those of one of the ions in the crystal); e) occlusion (pockets of impurity that are literally trapped inside the growing crystal); f) attachment; g) hetero-nucleation (epitaxial growth); h) organo-mineral complexation; i) complexation to bacterial exopolymer (Manceau et al., 2002).*

However, there are still quite a lot of open questions that are the focus of ongoing research. For example, the Grimsel groundwater system is considered to be a worst case scenario for colloidal transport based on electrostatic considerations, as the hydrochemistry is favouring colloid stability (low ionic strength, high pH value). However, laboratory experiments clearly show a flow velocity dependent recovery of colloids (Schäfer et al., 2004). If this colloid sur-

face attachment is due to fracture surface roughness or surface charge heterogeneity or another process is still unanswered.

Overall, taking into account the rapid development of computational methods and new analytical techniques, including synchrotron-based spectroscopy and microscopy, there will be exciting new opportunities for addressing these issues.

6.0 References

Adhiya, J. and Chisholm, S.W., 2001. Is ocean fertilization a good carbon sequestration option? 02-001, Massachusetts Institute of Technology, Laboratory for Energy and the Environment, Cambridge, MA.

Ahn, J., Kawasaki, D. and Chambre, P.L., 2002. Relationship among performance mid disposal of geologic repositories, canister-array configuration, and radionuclide mass in waste. Nuclear Technology, 140(1): 94-112.

Andra, 2001. Dossier 2001 Argile sur l'avancement des études et recherches relatives à la faisabilité d'un stockage de déchets à haute activité et à vie longue en formation géologique profonde: Rapport de synthèse, Agence nationale pour la gestion des déchets radioactifs (Andra), Châtenay-Malabry, France.

Andra, 2005. Dossier 2005 Synthèse Évaluation de la faisabilité du stockage géologique en formation argileuse., Agence nationale pour la gestion des déchets radioactifs (Andra), Châtenay-Malabry, France.

Archer, D.E. and Johnson, K., 2000. A Model of the iron cycle in the ocean. Global Biochemical Cycles, 14(1): 269-279.

Arcos, D., Bruno, J. and Karnland, O., 2003. Geochemical model of the granite-bentonite-groundwater interaction at Aspo HRL (LOT experiment). Applied Clay Science, 23(1-4): 219-228.

Artinger, R. et al., 2000. Characterization of groundwater humic substances: influence of sedimentary organic carbon. Applied Geochemistry, 15(1): 97-116.

Artinger, R. et al., 2003. Humic colloid mediated transport of tetravalent actinides and technetium. Radiochimica Acta, 91(12): 743-750.

Artinger, R., Schuessler, W., Schäfer, T. and Kim, J.I., 2002a. A kinetic study of Am(III)/humic colloid interactions. Environmental Science & Technology, 36(20): 4358-4363.

Artinger, R., Schuessler, W., Scherbaum, F., Schild, D. and Kim, J.I., 2002b. Am-241 migration in a sandy aquifer studied by long-term column experiments. Environmental Science & Technology, 36(22): 4818-4823.

Atkinson, A., 1985. The time dependence of pH within a repository for radioactive waste disposal. AERE Harwell Report No. DOE/RW/85.062.

Banfield, J.F. and Navrotsky, A. (Editors), 2001. Nanoparticles and the Environment. Rev. Mineral. Geochem., 44. Mineral. Soc. Am., Washington, D.C., 349 pp.

Bauer, A. and Berger, G., 1998. Kaolinite and smectite dissolution rate in high molar KOH solutions at 35 degrees and 80 degrees C. Applied Geochemistry, 13(7): 905-916.

Berner, U., 2003. Project Opalinus Clay: Radionuclide Concentration Limits in the Cementious Near-Field of an ILW Repository. NTB 02-22, Paul Scherrer Institut, Villigen PS, Wettingen (Switzerland).

BfS, 2002. Auswertung von Langzeitsicherheitsanalysen hinsichtlich Kriterien für die Auswahl von Endlagerstandorten. Schlussbericht NPB 01-31, Bundesamt für Strahlenschutz (BfS).

Biber, M.V., Afonso, M.D. and Stumm, W., 1994. The Coordination Chemistry of Weathering .4. Inhibition of the Dissolution of Oxide Minerals. Geochimica Et Cosmochimica Acta, 58(9): 1999-2010.

Blowes, D.W. et al., 2000. Treatment of inorganic contaminants using permeable reactive barriers. Journal of Contaminant Hydrology, 45: 123-137.

Bond, A.E. et al., 1997. Assessment of a spent fuel disposal canister, assessments studies for a copper canister with cast steel inner component. SKB technical report TR 97-19, Swedish Nuclear Fuel and Waste Management Company (SKB).

Bouby, M. et al., 2004. Laser-Induced Breakdown Detection (LIBD) Combined with Flow Field-Flow Fractionation: Application to the Characterization of Polystyrene and Iron Oxi/hydroxide Colloids. Journal of Chromatography A, 1040: 97-104.

Bouby, M., Manh, T.N., Geckeis, H., Scherbaum, F. and Kim, J.I., 2002. Characterization of aquatic colloids by a combination of LIBD and ICP-MS following the size fractionation. Radiochimica Acta, 90(9-11): 727-732.
Bowyer, W.H., 1999. A study of defects which might arise in the copper steel canister. SKI Report 00:19, Swedish Nuclear Power Inspectorate (SKI).
Bradbury, M.H. and Baeyens, B., 2005. Modelling the sorption of Mn(II), Co(II), Ni(II), Zn(II), Cd(II), Eu(III), Am(III), Sn(IV), Th(IV), Np(V) and U(VI) on montmorillonite: Linear free energy relationships and estimates of surface binding constants for some selected heavy metals and actinides. Geochimica Et Cosmochimica Acta, 69: 875-892.
Bradbury, M.H., Baeyens, B., Geckeis, H. and Rabung, T., 2005. Sorption of Eu(III)/Cm(III) on Ca-montmorillonite and Na-illite. Part 2: Surface complexation modelling. Geochimica Et Cosmochimica Acta, 69(23): 5403-5412.
Bruno, J., de Pablo, J., Duro, L. and Figuerola, E., 1995. Experimental study and modeling of the U(VI)-Fe$(OH)_3$ surface precipitation/coprecipitation equilibria. Geochimica & Cosmochimica Acta, 59(20): 4113-4123.
Buckau, G. et al., 2000a. Origin and mobility of humic colloids in the Gorleben aquifer system. Applied Geochemistry, 15(2): 171-179.
Buckau, G. et al., 2000b. 14C dating of Gorleben groundwater. Appl. Geochem., 15: 583-597.
Buckau, G. et al., 2000c. Groundwater in-situ generation of aquatic humic and fulvic acids and the mineralization of sedimentary organic carbon. Applied Geochemistry, 15(6): 819-832.
Buesseler, K.O., Andrews, J.E., Pike, S.M. and Charette, M.A., 2004. The effects of iron fertilization on carbon sequestration in the Southern Ocean. Science, 304(5669): 414-417.
Buesseler, K.O. and Boyd, P.W., 2003. Will ocean fertilization work? Science, 300: 67-68.
Buffle, J. and van Leeuwen, H.P. (Editors), 1993. Environmental Particles. Environmental analytical and physical chemistry series, 2. Lewis Publisher, Boca Raton, 426 pp.
Bundschuh, T., Knopp, R. and Kim, J.I., 2001. Laser-induced Breakdown Detection (LIBD) of Aquatic Colloids with Different Laser Systems. Colloids and Surfaces A, 177: 47-55.
Cantrell, K.J. and Kaplan, D.I., 1997a. Injection of Colloidal Fe0 Paricles inSand Columns with Shearthining Fluids. J. Environ. Eng., 123: 786-791.
Cantrell, K.J. and Kaplan, D.I., 1997b. Zero-valent iron colloid emplacement in sand columns. J. Environ. Eng., 123: 499-505.
Cantrell, K.J., Kaplan, D.I. and Wietsma, T.W., 1995. Zero-valent iron for in-situ remediation of selected metals in groundwater. Journal of Hazardous Materials, 42(2): 201-212.
Carlson, L. and Schwertmann, U., 1987. Iron and manganese oxides in Finnish ground water treatment plants. Water Research, 21(2): 165-170.
Catalano, J.G. and Brown, G.E., 2005. Uranyl adsorption onto montmorillonite: Evaluation of binding sites and carbonate complexation. Geochimica Et Cosmochimica Acta, 69(12): 2995-3005.
Catalano, J.G., Heald, S.M., Zachara, J.M. and Brown, G.E., 2004. Spectroscopic and diffraction study of uranium speciation in contaminated vadose zone sediments from the Hanford site, Washington state. Environmental Science & Technology, 38(10): 2822-2828.
Charlet, L. and Manceau, A.A., 1992. X-ray absorption spectroscopic study of the sorption of Cr(III) at the oxide/water interface. II. Adsorption, coprecipitation, and surface precipitation on hydrous ferric oxide. J. Colloid Interface Sci., 148: 443-458.
Chen, G. and Flury, M., 2005. Retention of mineral colloids in unsaturated porous media as related to their surface properties. Colloids and Surfaces a-Physicochemical and Engineering Aspects, 256(2-3): 207-216.
Chen, G., Flury, M., Harsh, J.B. and Lichtner, P.C., 2005. Colloid-facilitated transport of cesium in variably saturated Hanford sediments. Environmental Science & Technology, 39(10): 3435-3442.
Claret, F., 2001. Caractérisation structurale des transitions minéralogiques dans les formations argileuses : Contrôles et implications géochimiques des processus d'illitisation.

Cas particulier d'une perturbation alcaline dans le Callovo-Oxfordien Laboratoire souterrain Meuse-Haute-Marne. Ph.D. thesis Thesis, Université Joseph Fourrier, Grenoble, France, 174 pp.
Claret, F., Bauer, A., Schäfer, T., Griffault, L. and Lanson, B., 2002. Experimental investigation of the interaction of clays with high-pH solutions: A case study from the Callovo-Oxfordian formation, Meuse-Haute Marne underground laboratory (France). Clays and Clay Minerals, 50(5): 633-646.
Claret, F., Schäfer, T., Bauer, A. and Buckau, G., 2003. Generation of humic and fulvic acid from Callovo- Oxfordian clay under high alkaline conditions. Science of the Total Environment, 317(1-3): 189-200.
Claret, F. et al., 2005. Differences in properties and Cm(III) complexation behavior of isolated humic and fulvic acid derived from Opalinus clay and Callovo-Oxfordian argillite. Applied Geochemistry, 20: 1158-1168.
Coale, K.H. et al., 2004. Southern ocean iron enrichment experiment: Carbon cycling in high- and low-Si waters. Science, 304(5669): 408-414.
Cornell, R.M. and Schwertmann, U., 1996. The Iron Oxides -structure, properties, reactions, occurrence and uses-. VCH-Verlag, Weinheim, 573 pp.
Dardenne, K., Schäfer, T., Denecke, M.A., Rothe, J. and Kim, J.I., 2001. Identification and characterization of sorbed lutetium species on 2-line ferrihydrite by sorption data modeling, TRLFS and EXAFS. Radiochimica Acta, 89(7): 469-479.
Dardenne, K. et al., 2002. Low temperature XAFS investigation on the lutetium binding changes during the 2-line ferrihydrite alteration process. Environmental Science & Technology, 36(23): 5092-5099.
Degueldre, C., Pfeiffer, H.-R., Alexander, W., Wernli, B. and Bruetsch, R., 1996. Colloid properties in granitic groundwater systems. I: Sampling and characterisation. Appl. Geochem., 11: 677-695.
DeNovio, N.M., Saiers, J.E. and Ryan, J.N., 2004. Colloid movement in unsaturated porous media: recent advances and future directions. Vadose Zone Journal, 3: 338-351.
Drever, J.I., 1994. The Effect of Land Plants on Weathering Rates of Silicate Minerals. Geochimica Et Cosmochimica Acta, 58(10): 2325-2332.
Drever, J.I. and Stillings, L.L., 1997. The role of organic acids in mineral weathering. Colloids and Surfaces a-Physicochemical and Engineering Aspects, 120(1-3): 167-181.
Drits, V.A., Sakharov, B.A., Salyn, A.L. and Manceau, A., 1993. Structural model for ferrihydrite. Clay Minerals, 28: 185-207.
Duckworth, O.W. and Martin, S.T., 2001. Surface complexation and dissolution of hematite by C-1-C-6 dicarboxylic acids at pH=5.0. Geochimica Et Cosmochimica Acta, 65(23): 4289-4301.
Duckworth, O.W. and Martin, S.T., 2003. Connections between surface complexation and geometric models of mineral dissolution investigated for rhodochrosite. Geochimica Et Cosmochimica Acta, 67(10): 1787-1801.
Duker, A. and Ledin, A., 1998. Properties of the particulate phase in deep saline groundwater in Laxemar, Sweden. Water Research, 32(1): 186-192.
Dzombak, D.A. and Morel, F.M.M., 1990. Surface complexation modeling- hydrous ferric oxide. Wiley & Sons, New York, 393 pp.
EC, 2005. Treatment of radionuclide transport in geosphere within safety assessments (RETROCK): Final report. report EUR 21230 EN, European Commission; European Atomic Energy Community (Euratom), Brussels (Belgium).
EPA, 1998. Permeable Reactive Barrier Technologies for Contaminant Remediation. EPA report no. EPA /600/R-98/125, United States Environmetal Protection Agency (US EPA), Washington DC.
Fanghanel, T. and Neck, V., 2002. Aquatic chemistry and solubility phenomena of actinide oxides/hydroxides. Pure and Applied Chemistry, 74(10): 1895-1907.
Fein, J.B., Boily, J.F., Guclu, K. and Kaulbach, E., 1999. Experimental study of humic acid adsorption onto bacteria and Al-oxide mineral surfaces. Chemical Geology, 162(1): 33-45.

Feng, X. et al., 1994. Characteristics of Colloids Generated During the Corrosion of Nuclear Waste Glasses in Groundwater. Radiochimica Acta, 66-7: 197-205.
Filella, M., Zhang, J.W., Newman, M.E. and Buffle, J., 1997. Analytical applications of photon correlation spectroscopy for size distribution measurements of natural colloidal suspensions: Capabilities and limitations. Colloids and Surfaces a-Physicochemical and Engineering Aspects, 120(1-3): 27-46.
Filius, J.D., Meeussen, J.C.L., Lumsdon, D.G., Hiemstra, T. and Van Riemsdijk, W.H., 2003. Modeling the binding of fulvic acid by goethite: The speciation of adsorbed FA molecules. Geochimica Et Cosmochimica Acta, 67(8): 1463-1474.
Fujita, T., Sugiyama, D., Swanton, S.W. and Myatt, B.J., 2003. Observation and characterization of colloids derived from leached cement hydrates. Journal of Contaminant Hydrology, 61(1-4): 3-16.
Furrer, G. and Stumm, W., 1986. The Coordination Chemistry of Weathering .1. Dissolution Kinetics of Delta-Al2o3 and Beo. Geochimica Et Cosmochimica Acta, 50(9): 1847-1860.
Gamerdinger, A.P. and Kaplan, D.I., 2001a. Colloid transport and deposition in water-saturated yucca mountain tuff as determined by ionic strength. Environmental Science & Technology, 35(16): 3326-3331.
Gamerdinger, A.P. and Kaplan, D.I., 2001b. Physical and chemical determinants of colloid transport and deposition in water-unsaturated sand and Yucca Mountain tuff material. Environmental Science & Technology, 35(12): 2497-2504.
Geckeis, H. et al., 1998. Formation and stability of colloids under simulated near field conditions. Radiochimica Acta, 82: 123-128.
Geckeis, H., Manh, T.N., Bouby, M. and Kim, J.I., 2003. Aquatic colloids relevant to radionuclide migration: characterization by size fractionation and ICP-mass spectrometric detection. Colloids and Surfaces a-Physicochemical and Engineering Aspects, 217(1-3): 101-108.
Geckeis, H. et al., 2004. Results of the Colloid and Radionuclide Retention experiment (CRR) at the Grimsel Test Site (GTS), Switzerland -Impact of reaction kinetics and speciation on radionuclide migration-. Radiochimica Acta, 92(9-11): 765-774.
Geist, A., Gompper, K., Weigl, M. and Fanghänel, T., 2004. Reduzierung der Radiotoxizität abgebrannter Kernbrennstoffe durch Abtrennung und Tranmutation von Actiniden: Partitioning. Nachrichten, 36(2): 97-102.
Geist, A., Weigl, M. and Gompper, K., 2002. Minor actinide partitioning by liquid-liquid extraction: Using a synergistic mixture of bis(chlorophenyl)dithiophosphinic acid and TOPO in a hollow fiber module for americium(II)-lanthanides(III) separation. Separation Science and Technology, 37(15): 3369-3390.
Grolimund, D. et al., 1998. Transport of in situ mobilized colloidal particles in packed soil columns. Environ. Sci. Technol., 32: 3562-3569.
Haese, R. et al., 1997. Iron species determination to investigate early diagenetic reactivity in marine sediments. Geochimica Cosmochimica Acta, 61(1): 63-72.
Hauser, W., Geckeis, H., Kim, J.I. and Fierz, T., 2002. A mobile laser-induced breakdown detection system and its application for the in situ-monitoring of colloid migration. Colloids and Surfaces a-Physicochemical and Engineering Aspects, 203(1-3): 37-45.
Heron, G., Crouzet, C., Bourg, A.C.M. and Christensen, T.H., 1994. Speciation of Fe(II) and Fe(III) in contaminated aquifer sediments using chemical extraction techniques. Environ. Sci. Technol., 28: 1698-1705.
Higgo, J.J.W. et al., 1993. Colloid Transport in a Glacial Sand Aquifer - Laboratory and Field Studies. Colloids and Surfaces a-Physicochemical and Engineering Aspects, 73: 179-200.
Hochella, M.F., 2002a. Nanoscience and technology the next revolution in the Earth sciences. Earth and Planetary Science Letters, 203(2): 593-605.
Hochella, M.F., 2002b. There's plenty of room at the bottom: Nanoscience in geochemistry. Geochimica Et Cosmochimica Acta, 66(5): 735-743.
Hochella, M.F., 2003. Nanoscience and technology: the next revolution in the Earth sciences (vol 203, pg 593, 2002). Earth and Planetary Science Letters, 207(1-4): 183-185.

Houben, G.J., 2004. Modeling the buildup of iron oxide encrustations in wells. Ground Water, 42(1): 78-82.
Howe, J.A., Loeppert, R.H., Derose, V.J., Hunter, D.B. and Bertsch, P.M., 2003. Localization and speciation of chromium in subterranean clover using XRF, XANES, and EPR spectroscopy. Environmental Science & Technology, 37(18): 4091-4097.
ISRN, 2006. Avis de l'Institut de radioprotection et de sûreté nucléaire sur le Dossier 2005 Argile. Report DSU No. 106, ISRN Institut de Radioprotection et de sûreté Nucléaire.
ITRC, 2005. Permeable Reactive Barriers: Lessons Learned/New Directions. Interstate Technology & Regulatory Council report PRB-4, Washington, DC.
Jambor, J.L. and Dutrizac, J.E., 1998. Occurrence and constitution of natural and synthetic ferrihydrite, a widespread iron oxyhydroxide. Chem. Rev., 98: 2549-2585.
Johnson, L.H. and Smith, P.A., 2000. The interaction of radiolysis products and canister corrosion products and the implications for radionuclide transport in the near field of a repository for spent fuel. Nagra Technical Report NTB 00-04, Nagra, Wettingen, Switzerland.
Johnson, S.B., Yoon, T.H. and Brown, G.E., 2005. Adsorption of organic matter at mineral/water interfaces: 5. Effects of adsorbed natural organic matter analogues on mineral dissolution. Langmuir, 21(7): 2811-2821.
Johnson, S.B., Yoon, T.H., Kocar, B.D. and Brown, G.E., 2004. Adsorption of organic matter at mineral/water interfaces. 2. Outer-sphere adsorption of maleate and implications for dissolution processes. Langmuir, 20(12): 4996-5006.
Kamat, P.V. and Meisel, D., 2003. Nanoscience opportunities in environmental remediation. Comptes Rendus Chimie, 6: 999-1007.
Kaplan, D.I., Cantrell, K.J., Wietsma, T.W. and Potter, M.A., 1996. Formation of a chemical barrier with zero-valent iron colloids for groundwater remediation. J. Environ. Qual., 25: 1086-1094.
Karlsruhe, F., 2001. Radioaktivität und Kernenergie. Stabsabteilung Öffentlichkeitsarbeit, Karlsruhe, Germany, pp. 203.
Kennedy, M.J., Pevear, D.R. and Hill, R.J., 2002. Mineral surface control of organic carbon in black shale. Science, 295(5555): 657-660.
Kersting, A.B. et al., 1999. Migration of plutonium in ground water at the Nevada Test Site. Nature, 397: 56-59.
Kim, J.I., 1994. Actinide colloids in natural aquifer systems. Mat. Res. Soc. Bull., 19(12): 47-53.
Kim, J.I., Buckau, G., Baumgärtner, F., Moon, H. and Lux, D., 1984. Colloid generation and the actinide migration in Gorleben groundwaters. Mater. Res. Soc. Symp. Proc., 26: 31-40.
Kim, J.I. and Grambow, B., 1999. Geochemical assessement of actinide isolation in a German salt repository environment. Engineering Geology, 52: 221-230.
Kim, J.I., Zeh, P. and Delakowitz, B., 1992. Chemical Interaction of Actinide Ions with Groundwater Colloids in Gorleben Aquifer Systems. Radiochim. Acta, 57/58: 147.
King, F., Quinn, M.J. and Miller, N.H., 1999. The effect of hydrogen and gamma radiation on the oxidation of UO_2 in 0.1 mol dm^{-3} NaCl solution. SKB Technical Report TR-99-27, Swedish Nuclear Fuel and Waste Management Co., Stockholm, Sweden.
Kretzschmar, R., Borkovec, M., Grolimund, D. and Elimelech, M., 1999. Mobile subsurface colloids and their role in contaminant transport. Advances in Agronomy, 66: 122.
Kretzschmar, R. and Schäfer, T., 2005. Metal retention and transport on colloidal particles in the environment. Elements, 1(4): 205-210.
Kretzschmar, R. and Sticher, H., 1997. Transport of humic-coated iron oxide colloids in a sandy soil: influence of Ca2+ and trace metals. Environ. Sci. Technol., 31: 3497-3504.
Ledin, A., Karlsson, S., Duker, A. and Allard, B., 1993. Applicability of Photon-Correlation Spectroscopy for Measurement of Concentration and Size Distribution of Colloids in Natural-Waters. Analytica Chimica Acta, 281(2): 421-428.

Ledin, A., Karlsson, S., Duker, A. and Allard, B., 1994. Measurements in-Situ of Concentration and Size Distribution of Colloidal Matter in Deep Groundwaters by Photon-Correlation Spectroscopy. Water Research, 28(7): 1539-1545.
Lerotic, M., Jacobsen, C., Schäfer, T. and Vogt, S., 2004. Cluster analysis of soft x-ray spectromicroscopic data. Ultramicroscopy, 100(1-2): 35-57.
Liang, L.Y., Moline, G.R., Kamolpornwijit, W. and West, O.R., 2005. Influence of hydrogeochemical processes on zero-valent iron reactive barrier performance: A field investigation. Journal of Contaminant Hydrology, 80(1-2): 71-91.
Lichtner, P.C. and Waber, N., 1992. Redox front geochemistry and weathering: theory with applications to the Osamu Utsumi uranium mine, Pocos de Caldas, Brazil. J. Geochem. Expl., 45: 521-564.
Liger, E., Charlet, L. and Van, C.P., 1999. Surface catalysis of uranium(VI) reduction by iron(II). Geochim. Cosmochim. Acta, 63: 2939.
Liu, J. and Neretnieks, I., 1996. A model for radiation energy deposition in natural uranium-bearing systems and its consequences to water radiolysis. Journal of Nuclear Materials, 231: 103.
Liu, L., 2001. Oxidative Dissolution of Spent Fuel and Release of Nuclides from a Copper/Iron Canister: Model Developments and Applications. Ph.D. thesis Thesis, Royal Institute of Technology (KTH), Stockholm, Sweden, 68 pp.
Ludwig, C., Casey, W.H. and Rock, P.A., 1995. Prediction of Ligand-Promoted Dissolution Rates from the Reactivities of Aqueous Complexes. Nature, 375(6526): 44-47.
Magill, J. et al., 2003. Impact limits of partitioning and transmutation scenarios on the radiotoxicity of actinides in radioactive waste. Nuclear Energy-Journal of the British Nuclear Energy Society, 42(5): 263-277.
Manceau, A. and Drits, V.A., 1993. Local structure of ferrihydrite and feroxyhite by EXAFS spectroscopy. Clay Minerals, 28: 165-184.
Manceau, A. and Gates, W.P., 1997. Surface structural model for ferrihydrite. Clays and Clay Minerals, 45(3): 448-460.
Manceau, A., Marcus, M.A. and Tamura, N., 2002. Quantitative speciation of heavy metals in soils and sediments by synchrotron X-ray techniques. In Applications of Synchrotron Radiation in Low-Temperature Geochemistry and Environmental Science. In: M.R. P. Fenter, N.C. Sturchio, S. Sutton (Editor), Reviews in Mineralogy and Geochemistry. Mineralogical Society of America, Washington, DC, pp. 341-428.
Manceau, A. et al., 2005. Natural speciation of Mn, Ni, and Zn at the micrometer scale in a clayey paddy soil using X-ray fluorescence, absorption, and diffraction. Geochimica Et Cosmochimica Acta, 69(16): 4007-4034.
McCarthy, J.F. and McKay, L.D., 2004. Colloid transport in the subsurface: past, present, and future challenges. Vadose Zone Journal, 3: 326-337.
McCarthy, J.F. and Shevenell, L., 1998. Processes controlling colloid composition in a fractured and karstic aquifer in eastern Tennessee, USA. Journal of Hydrology, 206(3-4): 191-218.
McCarthy, J.F. and Zachara, J.M., 1989. Subsurface transport of contaminants: Mobile colloids in the subsurface environment may alter the transport of contaminants. Environ. Sci. Technol., 23(5): 497-502.
McHale, J.M., Auroux, A., Perrotta, A.J. and Navrotsky, A., 1997. Surface energies and thermodynamic phase stability in nanocrystalline aluminas. Science, 277(5327): 788-791.
Missana, T., Alonso, T. and Turrero, M.J.S., 2003. Generation and stability of bentonite colloids at the bentonite/granite interface of a deep geological radioactive waste repository. Journal of Contaminant Hydrology, 61(1-4): 17-31.
Möri, A. et al., 2003. The colloid and radionuclide retardation experiment at the Grimsel Test Site: influence of bentonite colloids on radionuclide migration in a fractured rock. Colloids and Surfaces a-Physicochemical and Engineering Aspects, 217(1-3): 33-47.
Moridis, G.J., Hu, Q., Wu, Y.S. and Bodvarsson, G.S., 2003. Preliminary 3-D site-scale studies of radioactive colloid transport in the unsaturated zone at Yucca Mountain, Nevada. Journal of Contaminant Hydrology, 60(3-4): 251-286.

Morris, D.E. et al., 1996. Speciation of uranium in Fernald soils by molecular spectroscopic methods: Characterization of untreated soils. Environmental Science & Technology, 30(7): 2322-2331.
Morrison, S.J., Metzler, D.R. and Carpenter, C.E., 2001. Uranium precipitation in a permeable reactive barrier by progressive irreversible dissolution of zero-valent iron. Environmental Science & Technology, 35: 385-390.
Naftz, D.L., Morrison, S.J., Fuller, C.C. and Davis, J.A. (Editors), 2002. Handbook of Groundwater Remediation Using Permeable Reactive Barriers, Applications to Radionuclides, Trace Metals, and Nutrients. Academic Press, Amsterdam (Netherland).
Nagano, T., Mitamura, H., Nakayama, S. and Nakashima, S., 1999. Formation of goethite and hematite from Neodymium-containing ferrihydrite suspensions. Clays Clay Minerals, 47(6): 748-754.
Nagra, 1994a. Kristallin-I - Conclusions from the regional investigation programme for siting a HLW respository in the crystalline basement of Northern Switzerland. NTB 93-09E, Nagra, Wettingen (Switzerland).
Nagra, 1994b. Kristallin I -Safety assessment report-. NTB 93-22E, Nagra, Wettingen (Switzerland).
Nagra, 2002a. Project Opalinus Clay: FEP Management for Safety Assessment - Demonstration of disposal feasibility for spent fuel, vitrified high-level waste and long-lived intermediate-level waste- (Entsorgungsnachweis). NTB 02-23, Nagra, Wettingen (Switzerland).
Nagra, 2002b. Projekt Opalinuston -Konzept für die Anlage und den Betrieb eines geologischen Tiefenlagers- Entsorgungsnachweis für abgebrannte Brennelemente, verglaste hochaktive sowie langlebige mittelaktive Abfälle. NTB 02-02, Nagra, Wettingen (Switzerland).
Nagra, 2003a. Project Opalinus Clay - Safety Report - Demonstration of disposal feasibility for spent fuel, vitrified high-level waste and long-lived intermediate level waste (Entsorgungsnachweis). NTB 02-05, Nagra, Wettingen (Switzerland).
Nagra, 2003b. Projekt Opalinuston -Synthese der geowissenschaftlichen Untersuchungsergebnisse: Entsorgungsnachweis für abgebrannte Brennelemente, verglaste hochaktive sowie langlebige mittelaktive Abfälle-. NTB 02-03, Nagra, Wettingen (Switzerland).
Nagra, 2005. Geologische Tiefenlagerung der abgebrannten Brennelemente, der hochaktiven and langlebigen mittelaktiven Abfälle. Darstellung und Beurteilung der aus sicherheitstechnisch-geologischer Sicht möglichen Wirtsgesteine und Gebiete. NTB 05-02, Nagra, Wettingen (Switzerland).
Navrotsky, A., 2004. Energetic clues to pathways to biomineralization: Precursors, clusters, and nanoparticles. Proceedings of the National Academy of Sciences of the United States of America, 101(33): 12096-12101.
NEA, 2004. Safety of Disposal of Spent Fuel, HLW and Long-lived ILW in Switzerland. An international peer review of the post-closure radiological safety assessment for disposal in the Opalinus Clay of the Zürcher Weinland. NEA No. 5568, OECD/NEA, Paris, France.
NEA, O.N.E.A., 1999. Actinide and fission product partitioning and transmutation -status and assessment report-, Paris (France).
NEA, O.N.E.A., 2003a. Engineered barrier systems and the safety of deep geological repositories -State of the art report-. 19964 EN, Paris (France).
NEA, O.N.E.A., 2003b. The French R&D Programme on Deep Geological Disposal of Radioactive Waste - An International Peer Review of the "Dossier 2001 Argile"-, Paris (France).
NEA, O.N.E.A., 2003c. SAFIR 2: Belgian R&D programme on the deep disposal of high-level and long-lived radioactive waste - An International Peer Review-, Paris (France).
Neall, F.B. et al., 1994. Kristallin-I -Results in perspective-. NTB 93-23, Nagra, Wettingen (Switzerland).
Neck, V. et al., 2003. Solubility of crystalline thorium dioxide. Radiochimica Acta, 91(5): 253-262.

Neck, V. et al., 2002. Solubility of amorphous Th(IV) hydroxide - application of LIBD to determine the solubility product and EXAFS for aqueous speciation. Radiochimica Acta, 90(9-11): 485-494.
O'Hannesin, S.F. and Gillham, R.W., 1998. Long-term performance of an in situ "iron wall" for remediation of VOCs. Ground Water, 36: 164-170.
Payne, T.E., Davis, J.A. and Waite, T.D., 1996. Uranium adsorption on ferrihydrite- effects of phosphate and humic acid. Radiochimica Acta, 74: 239-243.
Pedersen, K., 2002. Microbial processes in the disposal of high level radioactive waste 500 m underground in Fennoscandian Shield rocks. Interactions of Microorganisms with Radionuclides. In: M.J. Keith-Roach and F.R. Livens (Editors). Elsevier, Oxford, UK, pp. 279-312.
Persson, P. et al., 1998. Comparison of the adsorption of o-phthalate on boehmite (gamma-AlOOH), aged gamma-Al2O3, and goethite (alpha-FeOOH). Journal of Colloid and Interface Science, 206(1): 252-266.
Pirlet, V., 2001. Overview of actinides (Np, Pu, Am) and Tc release from waste glasses: influence of solution composition. Journal of Nuclear Materials, 298(1-2): 47-54.
Pittman, E.D. and King, G.E., 1986. Petrology and formation damage control, Upper Cretaceous sandstone, offshore Gabon. Clay Minerals, 21(4): 781-790.
Plaschke, M. et al., 2002. Combined AFM and STXM in situ study of the influence of Eu(III) on the agglomeration of humic acid. Colloids and Surfaces a-Physicochemical and Engineering Aspects, 197(1-3): 245-256.
Plaschke, M. et al., 2001. Size characterization of bentonite colloids by different methods. Analytical Chemistry, 73(17): 4338-4347.
Potter, J.M. and Dibble Jr., W.E., 1985. Chemical aspects of Iron Colloid Plugging in Quartz sands and Implications for Formation Damage. Soc. of Petrol. Eng. J., SPE 11801: 1682-1687.
Powell, R.M. and Puls, R.W., 1997. Proton generation by dissolution of intrinsic or augmented aluminosilicate minerals for in situ contaminant remediation by zero-valence-state iron. Environ. Sci. Technol., 31(8): 2244-2251.
Pratt, A.R., Blowes, D.W. and Ptacek, C.J., 1997. Products of chromate reduction on proposed remediation material. Environ. Sci. Technol., 31: 2492-2498.
Puls, R.W., Blowes, D.W. and Gillham, R.W., 1999. Long-term performance monitoring for a permeable reactive barrier at the U.S. Coast Guard Support Center, Elizabeth City, NC. Journal of Hazardous Materials, 68: 109-124.
Rabung, T. et al., 2005. Sorption of Eu(III)/Cm(III) on Ca-montmorillonite and Na-illite. Part 1: Batch sorption and time-resolved laser fluorescence spectroscopy experiments. Geochimica Et Cosmochimica Acta, 69(23): 5393-5402.
Ranade, M.R. et al., 2002. Energetics of nanocrystalline TiO2. Proceedings of the National Academy of Sciences of the United States of America, 99: 6476-6481.
Robinson, B.A., Li, C.H. and Ho, C.K., 2003. Performance assessment model development and analysis of radionuclide transport in the unsaturated zone, Yucca Mountain, Nevada. Journal of Contaminant Hydrology, 62-3: 249-268.
Ryan, J.N. and Gschwend, P.M., 1990. Colloid Mobilization in Two Atlantic Coastal Plain Aquifers: Field Studies. Water Resour. Res., 26(2): 307-322.
Ryan, J.N. and Gschwend, P.M., 1994. Effect of solution chemistry on clay colloid release from an iron oxide-coated aquifer sand. Environmental Science & Technology, 28(9): 1717-1726.
Sakamoto, Y., Ohnuki, T. and Senoo, M., 1994. Redistribution of Neptunium(V) during the alteration of ferrihydrite. Radiochim. Acta, 66/67: 285-289.
Schäfer, T. et al., 2003a. Colloid-borne Americium migration in Gorleben groundwater: Significance of iron secondary phase transformation. Environmental Science & Technology, 37(8): 1528-1534.
Schäfer, T. et al., 2005a. Origin and mobility of fulvic acids in the Gorleben aquifer system: implications from isotopic data and carbon/sulfur XANES. Organic Geochemistry, 36(4): 567-582.

Schäfer, T. et al., 2003b. Natural organic matter (NOM)-clay association and impact on Callovo-Oxfordian clay stability in high alkaline Solution: Spectromicroscopic evidence. Journal de Physique IV, 104: 413-416.
Schäfer, T. et al., 2005b. Source identification and characterization of humic and fulvic acids from Oxfordian argillite and Opalinus Clay. In: E.A. Ghabbour and J. Davies (Editors), Humic Sustances: Molecular Details and Applications in Land and Water Conservation. Taylor & Francis, New York, pp. 268.
Schäfer, T., Geckeis, H., Bouby, M. and Fanghänel, T., 2004. U, Th, Eu and colloid mobility in a granite fracture under near-natural flow conditions. Radiochimica Acta, 92: 731-737.
Schäfer, T., Hertkorn, N., Artinger, R., Claret, F. and Bauer, A., 2003c. Functional group analysis of natural organic colloids and clay association kinetics using C(1s) spectromicroscopy. Journal de Physique IV, 104: 409-412.
Scheckel, K.G. and Ryan, J.A., 2004. Spectroscopic speciation and quantification of lead in phosphate-amended soils. Journal of Environmental Quality, 33(4): 1288-1295.
Scherbaum, F.J., Knopp, R. and Kim, J.I., 1996. Counting of particles in aqueous sulutions by laser-induced photoacoustic breakdown detection. Applied Physics B, 63: 299-306.
Schuessler, W., Artinger, R., Kienzler, B. and Kim, J.I., 2000. Conceptual modeling of the humic colloid-borne Americium(III) migration by a kinetic approach. Environ. Sci. Technol., 34: 2608-2611.
Schuessler, W., Artinger, R., Kim, J.I., Bryan, N.D. and Griffin, D., 2001. Numerical modeling of humic colloid borne Americium(III) migration in column experiments using the transport/speciation code K1D and the KICAM model. Journal of Contaminant Hydrology, 47(2-4): 311-322.
Schulten, H.R. and Leinweber, P., 2000. New insights into organic-mineral particles: composition, properties and models of molecular structure. Biol. Fertil. Soils, 30: 399-432.
Seaman, J.C., Bertsch, P.M. and Miller, W.P., 1995. Chemical controls on colloid generation and transport in a sandy aquifer. Environmental Science & Technology, 29(July '95): 1808-1815.
SKB, 1996. SKB Annual Report 1995 - Including Summaries of Technical Reports Issued during 1995-. 95-37.
SKB, 2005. RETROCK Project (Treatment of geophere retention phenomena in safety assessment models), SKB report R-04-48, Sweden.
SLAC, 2004. Molecular Environmental Science: An Assessment of research accomplishments, available synchrotron radiation facilities, and needs. SLAC-Report-704, National Technical Information Service, U.S. Department of Commerce, Springfield, VA, United States.
Smith, P.A. et al., 2001. Development and testing of radionuclide transport models for fractured rock: examples from the Nagra/JNC Radionuclide Migration Programme in the Grimsel Test Site, Switzerland. Journal of Contaminant Hydrology, 47(2-4): 335-348.
Smith, P.A. and Curti, E., 1995. Some variations of the Kristallin-I near-field model. NTB 95-09, Nagra, Wettingen (Switzerland).
Spahiu, K., Werme, L. and Eklund, U.-B., 2000. The influence of near field hydrogen on actinide solubilities and spent fuel leaching. Radiochim. Acta, 88/9-11: 507-511.
Stevenson, F.J., 1982. Humus chemistry, genesis, composition, reactions. Wiley, New York.
Stöber, W. and Arnold, M., 1961. Anomalien bei der Ablösung von Kieselsäure von der Oberläche feinkörniger Siliziumdioxidpulver. Kolloid Z., 174: 20-27.
Stumm, W., 1993. From surface acidity to surface reactivity; inhibition of oxide dissolution. Aquatic Sciences, 55(4): 273-280.
Stumm, W. and Morgan, J.J., 1996. Aquatic Chemistry. John Wiley & Sons, New York, 1022 pp.
Stumpf, T., Bauer, A., Coppin, F., Fanghanel, T. and Kim, J.I., 2002. Inner-sphere, outer-sphere and ternary surface complexes: a TRLFS study of the sorption process of Eu(III) onto smectite and kaolinite. Radiochimica Acta, 90(6): 345-349.

Stumpf, T., Bauer, A., Coppin, F. and Il Kim, J., 2001. Time-resolved laser fluorescence spectroscopy study of the sorption of Cm(III) onto smectite and kaolinite. Environmental Science & Technology, 35(18): 3691-3694.
Stumpf, T. and Fanghanel, T., 2002. A time-resolved laser fluorescence spectroscopy (TRLFS) study of the interaction of trivalent actinides (Cm(III)) with calcite. Journal of Colloid and Interface Science, 249(1): 119-122.
Sun, T., Paige, C.R. and Snodgrass, W.J., 1996. The effect of cadmium on the transformation of ferrihydrite into crystalline products at pH 8. Water,Air, and Soil Pollution, 91: 307-325.
Sunder, S. and Shoesmith, D.W., 1991. Chemistry of UO_2 fuel dissolution in relation to the disposal of used nuclear fuel. AECL-10395, Atomic Energy of Canada Limited.
Swartz, C.H. and Gschwend, P.M., 1998. Mechanisms controlling release of colloids to groundwater in a southeastern coastal plain aquifersand. Environ. Sci. Technol., 32: 1779-1785.
Tamura, H., Goto, K. and Nagayama, M., 1976. The effect of ferrous hydroxide on the oxygenation of ferrous ions in neutral solutions. Corros. Sci., 16: 197.
Taubald, H. et al., 2000. Experimental investigation of the effect of high-pH solutions on the Opalinus Shale and the Hammerschmiede Smectite. Clay Minerals, 35(3): 515-524.
Ternes, T.A. et al., 2002. Removal of pharmaceuticals during drinking water treatment. Environmental Science & Technology, 36(17): 3855-3863.
Tessier, A., Campbell, P.G.C. and Bisson, M., 1979. Sequentiel extraction procedure for the speciation of particulate trace metals. Anal. Chem, 51: 844-851.
Thury, M. and Bossart, P., 1999. The Mont Terri rock laboratory, a new international research project in a Mesozoic shale formation, in Switzerland. Engineering Geology, 52(3-4): 347-359.
Toulhoat, P., 2002. Confinement and migration of radionuclides in a nuclear waste deep repository. C.R. Physique 3: 975-986.
Trolard, F., Bourrie, G., Jeanroy, E., Herbillon, A.J. and Martin, H., 1995. Trace metals in natural iron oxides from laterites: A study using selective kinetic extraction. Geochim. Cosmochim. Acta, 59(7): 1285-1297.
Vieno, T. and Nordman, H., 1999. Safety assessment of spent fuel disposal in Hästholmen, Kivetty, Olkiluoto and Romuvaara, TILA-99. Report POSIVA 99-07, Posiva Oy.
Vilks, P. and Bachinski, D.B., 1996. Colloid and suspended particle migration experiments in a granite fracture. Journal of Contaminant Hydrology, 21(1-4): 269-279.
Vilks, P., Caron, F. and Haas, M.K., 1998. Potential for the formation and migration of colloidal material from a near-surface waste disposal site. Applied Geochemistry, 13(1): 31-42.
Vilks, P., Frost, L.H. and Bachinski, D.B., 1997. Field-Scale colloid migration experiments in a granite fracture. Journal of Contaminant Hydrology, 26(1-4): 203-214.
Walther, C., 2003. Comparison of colloid investigations by single particle analytical techniques - a case study on thorium-oxyhydroxides. Colloids and Surfaces a-Physicochemical and Engineering Aspects, 217(1-3): 81-92.
Wan, J. and Tokunaga, T.K., 1997. Film straining of colloids in unsaturated porous media: conceptual model and experimental testing. Environmental Science & Technology, 31: 2413-2420.
Wan, J. and Wilson, J.L., 1994. Visualization of the role of the gas-water interface on the fate and transport of colloids in porous media. Water Resources Research, 30(1): 11-23.
Wang, X.X., Li, Q.M., Hu, H.F., Zhang, T.L. and Zhou, Y.Y., 2005. Dissolution of kaolinite induced by citric, oxalic, and malic acids. Journal of Colloid and Interface Science, 290(2): 481-488.
Weigl, M. et al., 2003. Alkyl-substituted 2,6-dioxadiazolylpyridines as selective extractants for trivalent actinides. Journal of Radioanalytical and Nuclear Chemistry, 256(3): 403-412.
Werme, L., Sellin, P. and Forsyth, R., 1990. Radiolytically induced oxidative dissolution of spent nuclear fuel. SKB technical report TR 90-08, Swedish Nuclear Fuel and Waste Management Company (SKB).

Wickham, S.M., Bennett, D.G. and Higgo, J.J.W., 2000. Evaluation of Colloid Transport Issues and Recommendations for SKI Performance Assessments, SKI (The Swedish Nuclear Power Inspectorate), Stockholm, Sweden.
Wieland, E., Tits, J. and Bradbury, M.H., 2004. The potential effect of cementitious colloids on radionuclide mobilisation in a repository for radioactive waste. Applied Geochemistry, 19(1): 119-135.
Wu, J., Boyle, E., Sunda, W. and Wen, L.-S., 2001. Soluble and colloidal iron in the oligotrophic North Atlantic and North Pacific. Science, 293: 847-849.
Yoon, T.H., Johnson, S.B. and Brown, G.E., 2004. Adsorption of Suwannee River fulvic acid on aluminum oxyhydroxide surfaces: An in situ ATR-FTIR study. Langmuir, 20(14): 5655-5658.
Zänker, H. et al., 2002. The colloid chemistry of acid rock drainage solution from an abandoned Zn-Pb-Ag mine. Applied Geochemistry, 17(5): 633-648.
Zänker, H., Richter, W. and Hüttig, G., 2003. Scavenging and immobilization of trace contaminants by colloids in the waters of abandoned ore mines. Colloids and Surfaces a-Physicochemical and Engineering Aspects, 217(1-3): 21-31.
Zinder, B., Furrer, G. and Stumm, W., 1986. The Coordination Chemistry of Weathering .2. Dissolution of Fe(Iii) Oxides. Geochimica Et Cosmochimica Acta, 50(9): 1861-1869.